

# Evaluation of the Hydrocarbon Exploration Potential in the Tail End Graben

Finn Christian Jakobsen, Karen Dybkjær, Mette Olivarius, Niels Hemmingsen Schovsbo,  
Rikke Weibel, Morten Bjerager, Finn Mørk, Sofie Lindström, Anders Mathiesen,  
Margrethe Thorup Nielsen, Jørgen Bojesen-Koefoed, Paul Knutz,  
Christian Knudsen, Michael B.W. Fyhn, Claus Andersen,  
Lars Kristensen, Peter Johannessen &  
Bodil Wesenberg Lauridsen

CONFIDENTIAL  
FORTROLIG

# Evaluation of the Hydrocarbon Exploration Potential in the Tail End Graben

Finn Christian Jakobsen, Karen Dybkjær, Mette Olivarius, Niels Hemmingsen Schovsbo,  
Rikke Weibel, Morten Bjerager, Finn Mørk, Sofie Lindström, Anders Mathiesen,  
Margrethe Thorup Nielsen, Jørgen Bojesen-Koefoed, Paul Knutz,  
Christian Knudsen, Michael B.W. Fyhn, Claus Andersen,  
Lars Kristensen, Peter Johannessen &  
Bodil Wesenberg Lauridsen

Confidential report

Copy No.

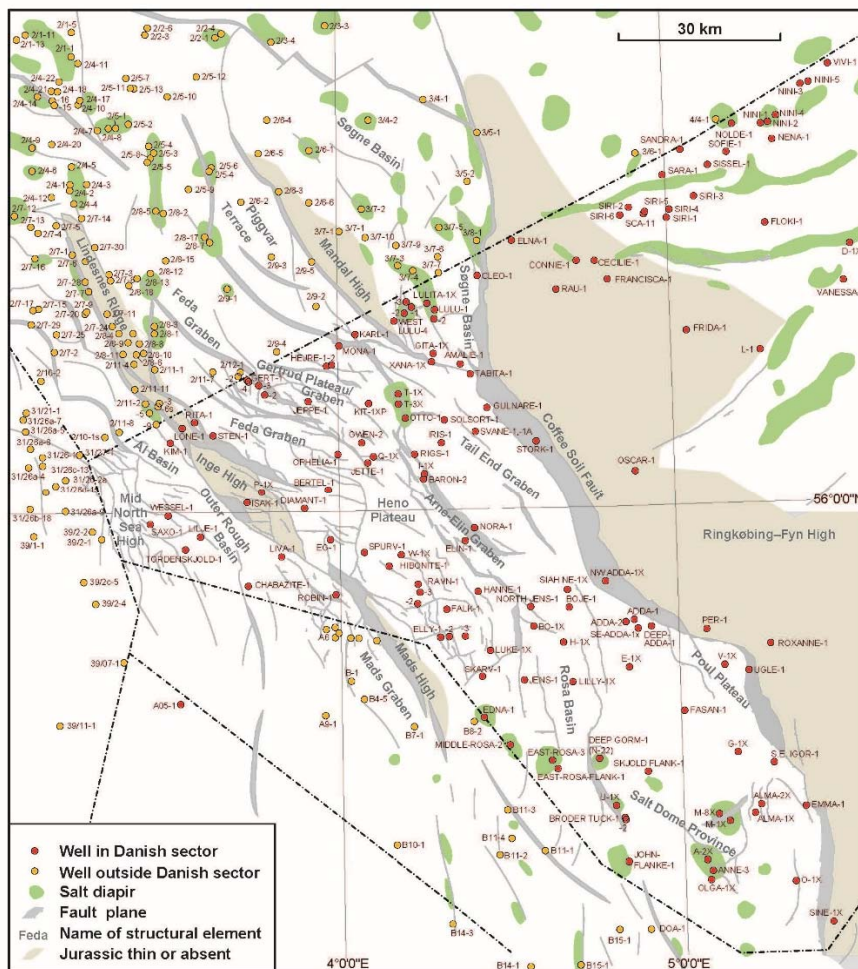
To be released 01.07.2021

# Executive summary

## Prospectivity of the Tail End Graben

A new study was initiated to re-evaluate the remaining hydrocarbon potential in the Tail End Graben, primarily based on the results from the recent Gita-1, Xana-1 and Svane-1/1A wells.

Shows of hydrocarbons have been found in Upper Jurassic sandstones in a number of wells in the Tail End Graben area but only considered as discoveries in the Xana-1 and Svane-1/1A wells. The Xana and Svane discoveries represent two different, separate structures. The Xana structure is located to the north across the Amalie Cross Fault (the boundary between the Søgne Basin and the Tail End Graben). The Svane structure is located in the basin center of the Tail End Graben. Both the Xana-1 and Svane-1/1A wells have been abandoned due to poor reservoir quality and limited volumens of hydrocarbons. Furthermore, the HPHT conditions in the Svane-1/1A well resulted in severe technical challenges. However, data from the two discoveries provide important information which can be used to evaluate the prospectivity in the Tail End Graben. The two discoveries represent different structural and depositional settings and show different reservoir properties.



## Reservoir properties in the Xana and Svane discoveries

The Xana structure is located along the Amalie Cross Fault and comprises a number of Upper Kimmeridgian sandstone intervals. These sandstones have been drilled by the Xana-1 well located south of the Cross Fault, and by the Gita-1 well located in the northern part of the structure, north of the Amalie Cross Fault. The top of the structure is located at approximately 4350 m's depth in Gita-1 and at 4625 m's depth in Xana-1.

The Upper Kimmeridgian gravity flow sandstones in the Gita-1 and Xana-1 wells have been interpreted to be part of the same submarine fan system and show comparable sand-thicknesses. However, the reservoir properties indicate a division of the structure into a northern and southern part separated by the Amalie Cross Fault. Data from the present study indicate that the porosities in the oil-bearing sandstones in the Xana-1 well generally are low, with average porosity up to 10 %. The Gita-1 well shows better reservoir properties (higher net sand percentage and an average porosity up to 15 %), but this well was dry.

The Svane structure is located on an inversion ridge in the basin center of the Tail End Graben and comprises thin-bedded, Upper Kimmeridgian gravity flow deposits. The top of the Svane structure is located at approximately 5400 m. The porosity in the sandstone is generally low (average porosities below 10%).

A comparison of the Xana and Svane discoveries reveal some differences in the reservoir properties. The slight difference in porosity may reflect different depths of burial, where the deep seated Svane-1/1A well exhibits the lowest porosities. The depth of burial influences the diagenesis in several ways, e.g. by the complex interaction of increased dissolution of feldspar with increased temperature on one hand and on the other hand increased precipitation of albite. Such diagenetic changes makes it difficult to predict the porosities in the reservoirs.

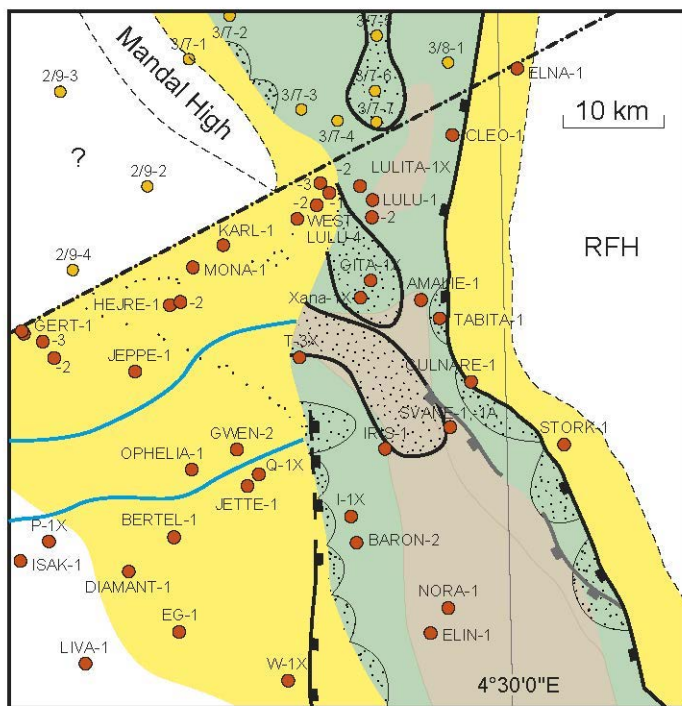
In addition to the differences in burial depth, the differences in depositional facies may be responsible for variations in reservoir parameters. The Upper Kimmeridgian sands in the Gita-1, Xana-1 and Svane-1/1A wells correlate stratigraphically and have previously been interpreted to be part of the same prograding fan system. In this model, the Xana/Gita wells were interpreted to be associated with the proximal part of the fan system whereas the Svane well was associated with the distal part of the fan system.

## New results and interpretations

The overall conclusion of the new study indicates that the Tail End Graben during the Upper Jurassic formed part of a rift system dominated by open marine claystones and siltstones interbedded with sandstones related to gravity flows. The rift system was surrounded by plateaus and highs which acted as potential source-areas for the reservoir sandstones. Upper Kimmeridgian back barrier and shallow marine sandstones are found on the Heno Plateau, and floodplain deposits (found as transgressive lag clasts) have been found as far east as in the Gwen-2 well, indicating that land-areas existed close to the Tail End Graben at this time. Deep marine gravity flow sandstones have been found in the Tail End Graben (Amalie-1 and Svane-1/1A) and on the Gita Plateau (Gita-1 and Xana-1), where they seem to occur in separate lobal systems. Additional deep marine gravity flow sandstones may be present in other parts of the Søgne Basin and Tail End Graben.

New geochemical data indicate that the Lower Kimmeridgian gravity flow deposits in the Amalie-1 well was sourced from the Ringkøbing-Fyn High. The data further demonstrate clear differences in the geochemical composition of the Upper Kimmeridgian reservoir sand in the Xana- and Svane areas, respectively, which

not only relate to depositional facies variations (proximal contra distal parts of a fan system) but indicate two different source areas for the sands. Based on this information, combined with the basin history, it is suggested that the sand in the Xana Field were sourced from the Mandal High to the north, while the sand in Svane-1/1A were sourced from the Heno Plateau area, see figure below. This suggests the presence of at least two different Upper Kimmeridgian fan-systems with different sediment sources.



**Kimm-3a LST-TST**

The presence of several fan systems is in accordance with the interpretation of the basin development. It is however difficult to map out the fan systems because these often are associated with the basin margins located in complex fault zones.

The distribution of Upper Jurassic sand in the Tail End Graben area is not very well understood. Very few wells penetrate the Upper Jurassic succession and a detailed seismic mapping is hindered by complex fault zones. The indications of more than one depositional fan system opens up for the possibility of the presence of new prospects. The palaeogeographical interpretations suggest the possibility for the presence of further sandstone deposits, e.g. deltas to shallow marine environments, incised valleys, slope aprons and submarine fans, in the transition zone between the Heno Plateau area and the deep Tail End Graben. Equal depositional sand systems may occur along the complex Coffee Soil Fault.

The known sandstone reservoirs, drilled in the Amalie-1, Gita-1, Xana-1 and Svane-1 wells show variable net sand values and -ratios up through the Kimmeridgian succession. The variations in net sand values in the Gita/Xana wells on one hand and the Svane-1 well on the other hand does not correlate. The highest net sand values in the Gita/Xana wells are found in the Upper Kimmeridgian only. In the Svane-1 well high net sand values occur from the Lower Kimmeridgian up to the lower part of the Upper Kimmeridgian.

## Source rock

Mature source rocks are present in all of the Tail End Graben area. The Middle Jurassic Bryne, Lulu and Middle Graben formations and the whole Farsund Formation are good to very good source rocks throughout the Tail End Graben with a mixed oil-gas generative potential. The Bo Member in the uppermost Farsund Formation comprises an exceptionally TOC- and oil-rich source interval. However, because the Upper Volgian - Ryazanian Bo Member seldom are in juxtaposition with the Kimmeridgian sandstones, we do not consider it likely that the Bo Member source has contributed to the filling of these sandstone reservoirs. Instead, the Middle Jurassic and the lower Farsund formations are considered as source rocks for the hydrocarbons encountered in the Xana-1 and Svane-1/1A wells.

## Conclusion

In spite of the rather poor reservoir properties in the two discoveries, Xana and Svane in Upper Kimmeridgian gravity flow sandstones, we consider the Tail End Graben to be an interesting basin for future hydrocarbon exploration. Mature source rock is present in all of the graben area. The new study reveals that several fan systems comprising gravity flow sandstones are present, at different stratigraphic levels and with different sand source areas. These fan systems are not well understood and explored. In addition to more fan systems, also incised valleys and shallow marine reservoir sandstone deposits may be present along the basin margins.

# Deposition and diagenesis of Upper Kimmeridgian (Upper Jurassic) reservoir sandstones in the Søgne Basin and Tail End Graben, the Danish Central Graben

Finn Jakobsen, Morten Bjerager, Karen Dybkjær, Finn Mørk, Rikke Weibel, Mette Olivarius, Niels H. Schovsbo, Paul Knutz, Michael Bryld Wessel Fyhn, Margrethe T. Nielsen, Sofie Lindström, Claus Andersen, Lars Kristensen, Hans Peter Nytoft, Jørgen Bojesen-Koefoed, Peter Johannessen

## Contents

0. Abstract .....	5
1. Introduction.....	6
2. Geological setting .....	7
2.1 Basin development of the Danish Central Graben .....	7
2.2 Potential sand-source areas .....	8
3. Data base .....	10
4. Stratigraphy .....	11
4.1 Bio- and chronostratigraphy.....	11
4.2 Lithostratigraphy .....	11
4.3 Sequence stratigraphy.....	12
4.4 Chemostratigraphy and mineralogy.....	16
5. Seismic interpretation and mapping .....	20
5.1 Interpretation .....	20
5.2 Regional structural setting .....	21
5.3 Upper Jurassic basin development in the Gita-Xana-Svane area.....	22
5.4 Mapping of the sand.....	23
5.5 Detailed depositional geometries and potential source areas .....	23
5.6 Summary.....	26
6. Petrophysical evaluation .....	27
7. Reservoir characteristics.....	29
7.1 Reservoir petrography.....	29
7.2 Reservoir properties .....	31
7.3 Discussion .....	32
8. Provenance .....	33
8.1 Methods .....	33
8.2 Results .....	33
8.3 Discussion .....	34
8.4 Conclusion .....	35
9. Source rock .....	36
10. Basin development of the Tail End Graben .....	38
10.1 Depositional environments and palaeogeography .....	38
11. Discussion .....	42

11.1 Prospectivity of the Tail End Graben .....	42
12. Conclusion .....	45
References .....	46
Figures .....	50
Tables.....	55
Appendix 1.....	56
Amalie Member .....	56
Svane Member .....	56
Gita Member .....	57



## 0. Abstract

The aim of this study was to re-evaluate the remaining hydrocarbon potential in the Tail End Graben, primarily based on the results from the recent Gita-1, Xana-1 and Svane-1/1A wells.

Shows of hydrocarbons have been found in Upper Jurassic sandstones in a number of wells in the Tail End Graben area but only considered as discoveries in the Xana-1 and Svane-1/1A wells. The discoveries were made in Upper Kimmeridgian gravity flow sandstones, previously interpreted to be part of the same submarine fan system. However, both wells have been abandoned due to poor reservoir quality and limited volumes of hydrocarbons. Furthermore, the HPHT conditions in the Svane-1/1A well resulted in severe technical challenges.

Our study demonstrates differences in the geochemical composition of the reservoir sand in the Xana- and Svane areas, respectively. These differences not only relate to depositional facies variations (proximal contra distal parts of a fan system) but indicate two different source areas for the sands. We suggest that the sand in the Xana Field are associated with a source area from the Mandal High to the north, while the geochemical composition of the Svane sand are comparable with the sand deposited on the Heno Plateau. This suggests the presence of at least two different Upper Kimmeridgian fan-systems with different sediment sources. The presence of several fan systems is in accordance with our interpretation of the basin development. It is however difficult to map out the fan systems because these often are associated with the basin margins located in complex fault zones.

The indications of more than one depositional fan system opens up for the possibility of the presence of new prospects. The palaeogeographical interpretations based on the present study suggest the possibility for presence of further sandstone deposits, e.g. incised valleys, deltas, shallow marine deposits and shallow and deep shelfal lobes in the transitional zone between the Heno Plateau area and the deep Tail End Graben. Equal depositional sand systems may occur along the complex Coffee Soil Fault.

Three new lithostratigraphic members are defined herein; 1) The Svane Member comprising the Upper Kimmeridgian gravity-flow sandstone interval in the Svane-1/1A well located in the Tail End Graben. 2) The Gita Member comprising the Upper Kimmeridgian gravity-flow sandstone intervals in the Gita-1 and Xana-1 wells, located in the transitional area between the Søgne Basin and the Tail End Graben. The Gita-1 well is located in the northern part of the Xana structure, north of the Amalie Cross Fault while the Xana-1 well is located south of the Amalie Cross Fault. 3) The Amalie Member comprising the Lower Kimmeridgian sandstone interval in the Amalie-1 well located in the Danish part of the Søgne Basin.

## 1. Introduction

Due to the extremely thick Upper Jurassic succession in the Tail End Graben, hydrocarbon exploration in this area has focused on shallower stratigraphic levels such as the Upper Cretaceous Chalk and the Jurassic sands on highs and along basin margins.

In 2002 a gas discovery was made in Upper Jurassic gravity flow sandstones in the Svane-1/1A well located in the northern part of the Tail End Graben and recently an oil discovery was made in the Xana-1 well, located at the transition between the Tail End Graben and the Søgne Basin (SB) (Fig. 1.1). Time-equivalent gravity flow sandstones in the Gita-1 well, located 3 km north of the Xana-1 well in the southernmost part of the Søgne Basin, did not encounter any hydrocarbons.

The Svane discovery in sandstones buried more than 6000 m below the seafloor, was considered to be a giant gas field but was relinquished in 2013 due to a poor quality reservoir combined with technical challenges associated with HPHT conditions.

The Xana discovery, located somewhat shallower, at approximately 4500 m below the seafloor, was evaluated to be un-economical due to the low oil saturation/incomplete filling of the gravity flow deposits.

The hydrocarbon discoveries in both Svane-1/1A and Xana-1 sandstones have increased the interest for Upper Jurassic gravity flow deposits as reservoirs in the Tail End Graben. However, the dry well Gita-1 well indicates the need for further studies on these reservoir sandstones.

Neither the provenance nor the distribution of these sandstones are well known. Very few wells penetrate the Upper Kimmeridgian succession in the Tail End Graben and the wells are typically located on structural highs. The deep burial depths and the lack of cores have resulted in poor biostratigraphic data. Also the quality of the existing seismic data is poor. Likewise, the large variations in reservoir quality of these deeply buried HTHP sandstone deposits are not well understood. These variations may be related to depositional environments, provenance, burial history and/or diagenesis, all of which are poorly evaluated in the area.

This study aims to describe the present distribution and reservoir quality of these sandstones, located in the southern part of the Søgne Basin and in the Tail End Graben, and their relationship to the aforementioned factors.

A very comprehensive study on the Jurassic succession in the Danish Central Graben (PETSYS) was performed from 2011- 2014 and a detailed stratigraphic framework was established based on more than 80 Danish wells. This framework forms the basis for the present study. Data from the Gita-1 and Xana-1 wells was not included in the PETSYS study.

The present study includes re-interpretation of a new seismic dataset, implementation of data from Gita-1 and Xana-1 and a re-evaluation of Svane-1/1A and other older selected wells. New broadband seismic data have been acquired in the Tail End Graben and improved the resolution in the deeper part of the Central Graben. New results from geochemical/diagenesis and provenance studies are included in this study.

## 2. Geological setting

### 2.1 Basin development of the Danish Central Graben

The depositional pattern of clastic sediments in an extensional rift basin is primarily controlled by fault activity, forming accommodation space and sediment source areas (Ravnås & Steel 1998; Gawthorpe & Leeder, 2000). This was also the case for the Upper Jurassic deposits within the Danish Central Graben (Fig. 1.1). The structural development of the Central Graben has been described in a series of papers, e.g. Andersen et al. (1982), Gowers & Sæbøe (1985), Møller (1986), Michelsen et al. (1987), Cartwright (1987), Korstgård et al. (1993), Møller & Rasmussen (2003), Japsen (2003), Andsbjerg & Dybkjær (2003), Bruhn & Vagle (2005) and Verreussel et al (2018), and is briefly summarized below.

The Danish Central Graben forms the southern arm of the Middle Jurassic – Early Cretaceous North Sea rift complex, comprising the Viking Graben, the Outer Moray Firth and the Central Graben (Roberts et al. 1990; Ziegler 1990). It is bounded by the Ringkøbing-Fyn High to the east and by the Mid North Sea High to the west and consists of a series of minor NW-SE trending half-grabens mainly dipping eastwards (Andersen et al. 1982; Gowers & Sæbøe 1985; Møller 1986; Cartwright 1987; Korstgård et al. 1993; Møller & Rasmussen 2003; Japsen 2003). The Middle to Late Jurassic rifting resulted in the stepwise formation of this series of half-grabens, the largest and deepest of which is the Tail End Graben. The Tail End Graben is located in the easternmost part of the Danish Central Graben, bounded by the Coffee Soil Fault towards the Ringkøbing-Fyn High to the east, and the Heno- and Gertrud Plateau areas to the west. Northwards the Tail End Graben is bounded by the Piggvar Terrace and the Mandal High and towards the south the Tail End Graben gradually transposes into the Salt Dome Province (Fig. 1.1).

During the Early Jurassic all of the Danish area was probably covered by the sea and a relatively uniform succession of marine shales is believed to have been deposited over most of the Danish North Sea region (Michelsen 1978; Koch et al. 1982; Michelsen et al. 2003; Andsbjerg & Dybkjær 2003). Doming of parts of the Central Graben area during the Toarcian and Aalenian resulted in the transition from marine to terrestrial conditions in large areas. Associated with this uplift, erosion removed most of the Lower Jurassic succession in these areas (Hallam & Sellwood 1976; Ziegler 1990; Underhill & Partington 1993; Andsbjerg et al. 2001).

In the Danish Central Graben rifting began during the Late Aalenian along the Coffee Soil Fault zone and culminated during the Oxfordian to Early Kimmeridgian (Jensen et al. 1986; Rasmussen 1995; Andsbjerg et al. 2001; Andsbjerg & Dybkjær 2003; Bruhn & Vagle 2005). The major faults probably re-activated older faults systems (Gowers & Sæbøe 1985; Møller & Rasmussen 2003). The orientation of these faults was mainly N-S.

Rifting started in the north (Norwegian sector) and propagated southwards during the initial rift phase. The oldest sediments in the rift system are Bathonian–Middle Callovian in age (paralic and lagoonal) and are found in the Danish and Norwegian Søgne Basin and in the Tail End Graben. In the latest Callovian, marine conditions prevailed in the rift basin.

During the succeeding Kimmeridgian rift phase the platform areas adjacent to the graben were affected. Subsidence in the graben axis continued, but the change in tectonic regime led to activation of NW–SE-striking normal faults affecting the Heno/Gertrud Plateau. The Heno and Gertrud Plateaus together formed

a flat-lying, slowly subsiding platform until the Late Jurassic (Söderström et al. 1991, Rasmussen 1995, Johannessen et al 1996). Initial subsidence of the Gertrud Graben took place along the active Mona fault.

After a period of relative tectonic quiescence, rifting resumed in the Late Kimmeridgian and new NNW-SSE trending faults formed (Gowers & Sæbøe 1985; Møller & Rasmussen 2003). This rift phase demonstrated divergent basin development in the Danish sector.

The rifting gradually ceased during the late Middle Volgian – Ryazanian and during the latest Early Cretaceous the Central Graben entered a post-rift phase with thermal cooling, resulting in regional subsidence, punctured by episodes of significant inversion in the Early and Late Cretaceous (Vejbæk & Andersen 1987).

In the deepest parts of the Tail End Graben a greater than 3600 m thick succession of Upper Jurassic clastic deposits are present. Most of this succession consists of deep marine shales and siltstones referred to the Lola and Farsund Formations, while gravity flow sandstones occur locally at several stratigraphic levels (Fig. 2.1). Shallow marine sands and siltstones appear along the rim of the basin.

During the Early Volgian, the depositional area reached its maximum extent (when the Inge and Mads highs and Outer Rough Basin became active). At the same time, basin development became increasingly complex due to salt movement along the Central Graben axis (Lulu area) and differential subsidence. Uplift and erosion is observed at the graben axis (in the southern part of the Norwegian Søgne Basin).

## 2.2 Potential sand-source areas

During the Late Kimmeridgian the rift system was surrounded by plateaus and highs which acted as potential sand-source areas or by-pass areas for coarse grained sediments and gravity flow sandstones. Some of the plateau areas were gradually submerged during the latest Kimmeridgian – Early Volgian, and downgrading the potential sand-source areas for the deeper marine parts of the basin.

### *The Mandal High*

To the north, the Tail End Graben is bounded by the Mandal High. The Mandal High was a high-lying area during the Upper Jurassic and is considered as a source area for the reservoir sands in the rift system. Sand intervals in the Kimmeridgian succession in the Søgne Basin may originate from the Mandal High.

### *Heno- and Gertrud Plateaus*

To the west of the Tail End Graben the Heno- and Gertrud Plateaus existed. These plateaus formed a continuous flat-lying, slowly subsiding platform bounded by the Mandal High/Piggvar Terrace to the north and the Mid North Sea High to the west. The plateau area was subaerially exposed during the Middle Jurassic but was covered by a relatively shallow sea during the Kimmeridgian which received a lot of clastic input from the surrounding land-areas. This resulted in the formation of back-barrier and shoreface deposits referred to as the Heno Formation.

The Heno Plateau may have acted as a source area or a by-pass area for the sand deposits in the Tail End Graben during the Kimmeridgian. The transitional area between the Heno Plateau areas and the deep Tail

End Graben is not well understood and is seismically obscured by the Arne Elin Graben. Therefore the identification of shelf edge deltas, feeder channels and fan deposits in the Tail End Graben related to the Heno Plateau have not been properly studied.

### *The Ringkøbing-Fyn High*

The Tail End Graben rift system is bounded by the Coffee Soil Fault to the east, separating the graben from the Ringkøbing-Fyn High. The Ringkøbing-Fyn High is a basement high displaying a major stratigraphic hiatus from the Rotliegendes to the Upper Cretaceous. The deep erosion on the Ringkøbing-Fyn High is clear evidence for the presence of a major sediment source area where sediments were shed into the rift graben across the Coffee Soil Fault. Thin sand intervals of Kimmeridgian, Volgian, Ryazanian and Valanginian age are penetrated in the wells located in the Coffee Soil Fault zone. These sands are interpreted to represent deep marine fan deposits to marginal shallow marine deposits. The Coffee Soil Fault may have acted as the shelf edge during the Upper Jurassic but due to poor seismic resolution in the chaotic and heavily faulted fault zone, it has not been possible to identify coastlines, slopes etc. for paleogeographical purposes.

### 3. Data base

The aim of the present study is to re-examine the hydrocarbon potential in the Tail End Graben by implementation of new data from among others the recent wells Gita-1 and Xana-1 into the comprehensive work on the Jurassic succession carried out in the PETSYS project. Here we present a detailed study on the stratigraphy, depositional environments, petrography, diagenesis, provenance and source rock potential in and around the Tail End Graben. The study also includes interpretation of new broadband seismic data (PGS15).

The study area and the location of the wells included in the study are shown in Fig. 1.1. The methodology and results of the various disciplines are described below.

## 4. Stratigraphy

### 4.1 Bio- and chronostratigraphy

The chronostratigraphic frame for the present study are based on dinoflagellate cyst (dinocyst) stratigraphy (Fig. 4.1). The first and last occurrences of stratigraphically important dinocyst taxa in the wells included in the study have been extracted from reports and publications. Most of this evaluation and interpretation work was done as part of the PETSYS project. In addition, data from new palynological analysis of samples from the Gita-1, Xana-1, Svane-1/1A, and Stork-1 wells have been included.

Based on the extensive literature on the correlation of dinocyst bioevents with the boreal ammonite zonation (e.g. Davey 1982; Heilmann-Clausen 1987; Costa & Davey 1992; Riding & Thomas 1992; Poulsen 1996; Poulsen & Riding 2003) the Upper Jurassic succession has been subdivided in the wells included in the study (Fig. 4.1).

The results are outlined in a series of stratigraphic summary charts, which also includes the sequence stratigraphic subdivision and the stratigraphic position of the seismic markers defined in the present study (Figs. 4.2-4.13; Table 4.1).

An update of the stratigraphy in the Amalie-1 well based on existing palynological data is presented (Fig. 4.2). Furthermore, a revision of the lower part of the succession in Stork-1 is included here (Fig. 4.11).

### 4.2 Lithostratigraphy

The lithostratigraphic subdivision of the Upper Jurassic succession in the Danish Central Graben is illustrated schematically in Fig. 2.1. The Upper Jurassic succession in the Danish Central Graben rests on the Callovian-Oxfordian paralic and mudstone-dominated Middle Graben Formation in the south and the shallow marine and paralic sandstone-dominated Lulu Formation in the north (Fig. 2.1). The overlying Oxfordian-Volgian marine shale- and siltstone intervals are referred to the Lola- and Farsund Formations, respectively. The back-barrier to shoreface sandstones deposited on the Heno- and Gertrud Plateau areas in the Late Kimmeridgian are referred to the Heno Formation and subdivided into the Gert- and Ravn Members, respectively (Jensen et al. 1986; Michelsen et al. 2003).

The Kimmeridgian sandstones in the Tail End Graben (Svane-1/1A well) and in the Danish part of the Søgne Basin (Amalie-1, Gita-1 and Xana-1 wells) have not previously been defined as separate lithostratigraphic units and interpretations of the age and the depositional environments of the sandstones in the Gita-1 and Xana-1 wells have not been published previously. Based on comparison of log-signatures from the cored gravity-flow sandstones in the Norwegian 3/7-6 well located in the Søgne Basin, the sandstones in the Svane-1/1A well was also suggested to represent gravity-flow deposits intercalated the shale- and siltstone succession of the Farsund Formation. The Svane-1/1A sandstones were referred to the Upper Kimmeridgian – Lower Volgian, although the quality of the datings are very poor due to the deep burial (Johannessen et al. 2010). Based on new stratigraphic and seismic data the interval with gravity flow sandstones in the lower part of Amalie-1 is now referred to the Amalie Member in the Lola Formation. The interval with gravity sandstones in Svane-1/1A well area are referred to the Svane Member of Farsund Formation. In the Gita-1 and Xana-1 wells area the interval with gravity flow sandstones are referred to the Gita Member also of the Farsund Formation (Fig. 2.1, Appendix 1).

The marine shales of the Farsund Formation extends into the Ryazanian and include locally the Volgian shallow marine and informal “Outer Rough Sand” in the west, the Volgian – Ryazanian coarse-grained slope apron of the Poul Member in the east, and centrally the Volgian- Ryazanian organic rich shales of the Bo Member (Fig. 2.1, Michelsen et al. 2003). The Farsund Formation is erosionally overlain by Lower Cretaceous sediments of the Cromer Knoll Group in the study area.

### 4.3 Sequence stratigraphy

The sequence stratigraphic framework of the log correlation panels (Figs 4.14-4.16) follows essentially the concepts of the Exxon Group as also presented in the PETSYS project. Recorded sequence stratigraphic units include Kimm-1 – Kimm-4, Volg-1 – Volg-4 and Ryaz-1. The sequence stratigraphic framework is considered within a mainly mud-dominated basinal to lower slope setting in the studied area of the Tail End Graben. Identified systems tracts comprise mainly TST (Transgressive Systems Tracts) and HST (Highstand Systems Tracts), and occasionally LST (Lowstand Systems Tracts). Sequence boundaries (SB) are placed at the base of TST or LST and maximum flooding surfaces (mfs) are placed at the base of HST.

The sequence stratigraphic framework presented here is modified from Andsbjerg & Dybkjær (2003) and the PETSYS project. The subdivision into sequences and the correlations between wells are based on integration of biostratigraphic data, petrophysical log interpretation, seismic data, cuttings descriptions and sedimentology of conventional cores and sidewall cores. The biostratigraphic datings of the sequences are based on palynology (mainly dinocyst stratigraphy) as outlined in Andsbjerg & Dybkjær (2003) and Johannesen et al. (2010). New data from selected intervals in the Gita-1, Xana-1, Svane-1/1A and Stork-1 wells are included in the present study.

The Upper Jurassic depositional sequences are subdivided into one Oxfordian sequence, Ox-1, four Kimmeridgian sequences, Kimm-1 to Kimm-4, four Volgian sequences, Volg-1 to Volg-4, and one Ryazanian sequence, Ryaz-1, as revised from Andsbjerg & Dybkjær (2003) and the PETSYS project in the Amalie-1, Gwen-2, Jeppe-1, Karl-1 and Nora-1 wells. In addition, the Kimm-1 to Kimm-3 sequences are further subdivided into A and B for detailed correlation and they are regarded as subordinate sequences. The Kimmeridgian sequences correlates to some extent with the Sequences 0–2 from the Heno – Gertrud Plateau area in Johannesen (2003) as represented in e.g. the Gwen-2, Jeppe-1 and Q-1 wells.

Three log correlation panels of wells are presented to illustrate the recorded depositional sequences in the study area (Figs. 4.14-4.16). The panels include the following wells: Amalie-1, Gita-1, Gwen-2, Hejre-2, Jeppe-1, Karl-1, Lulu-2, Nora-1, Q-1X, Stork-1, Svane-1/1A, Gita-1 and two Norwegian wells, 3/7-6 and 3/7-7 (Marsvin). For location of the wells, see Fig. 1.1. The correlated surfaces comprise sequence boundaries and maximum flooding surfaces, linked to seismic markers. Interpreted systems tracts are likewise inserted.

#### *Ox-1*

This sequence is recorded in the Tail End Graben and Søgne Basin and the southern part of the Heno Plateau and correlate mainly/only to the Ox-1 sequence in e.g. Elly-2 by Andsbjerg & Dybkjær (2003). It is revised up to about 100 m thick in Nora-1 based on the new high resolution 3D seismic data. The Oxfordian is 70 m thick in Gita-1 and 50 m in Amalie-1 and comprises up to three transgressive-regressive units in the GR log. In the southern part of the Heno Plateau area as represented by e.g. Ravn-1, -2, Elly-2, the sequence is interpreted to comprise shoreface sandstone in the lower part overlain by offshore mudstones.

In more basinal settings, in the Tail End Graben, the sequence is mainly composed of offshore mudstones and thin < 5 m sandstone units of probable gravity flow origin. Proximal to the Coffee Soil Fault, in the easternmost part of the Tail End Graben, e.g. in Amalie-1, the lower part comprise possible shoreface sandstones succeeded by offshore mudstones. The sequence is not present in the northern part of the Heno- Gertrud Plateau area.

#### *Kimm-1a*

The age of this sequence is tentatively assigned to the Early Kimmeridgian Baylei–Cymodoce Zones and corresponds e.g. to the lowermost part of the Ox-1 in Nora-1 of Andsbjerg & Dybkjær (2003). The sequence is recorded in the Søgne Basin and Tail End Graben, where it is at least up to 150 m thick (Gita-1) and on the Heno Plateau it is 30–45 m thick (Gwen-2, Q-1). It is absent in the northern part of the Heno – Gertrud Plateau on the Gertrud Plateau (Hejre-2, Jeppe-1).

The base is located at a GR low in Nora-1 and Gita-1, and the lower part comprises here a TST represented by an increasing GR interval in marine mudstones, culminating with a mfs at the GR peak and succeeded by a decreasing GR trend. Prominent intercalated “blocky” low GR units up to 7 m thick of coarse-grained probably gravity flow sandstones occur in the middle and upper part of the sequence in Amalie-1.

#### *Kimm-1b*

This sequence is tentatively assigned to the Early Kimmeridgian Baylei–Cymodoce Zones and corresponds e.g. to the upper part of Kimm-2 in Amalie-1 as defined by Andsbjerg & Dybkjær (2003). The sequence is recorded in the Søgne Basin and Tail End Graben where it is 50–280 m thick (e.g. Gita-1, Nora-1) and 70 – 85 m thick on the Heno- Gertrud Plateau (e.g. Gwen-2, Q-1).

At the Heno Plateau the base is located at a GR low followed by a GR increase in a shallow marine, mainly sandstone dominated, succession. In the Søgne Basin (Gita-1 and Amalie-1) it comprises mainly offshore mudstones characterised by two couplets of subtle increase and decrease GR readings.

In the Tail End Graben a similar trend is recorded in the Nora-1 well. In contrast, Svane-1/1AA records a 120 m interval of mudstones with intercalated low GR gravity flow sandstones, 1-10 m thick.

The Kimm-1b sequence is interpreted as mainly drowning of the Heno Plateau from the south with predominantly deposition of offshore mudstones and similarly offshore mudstone deposition in the Tail End Graben that also shows a deepening towards the south. The interpreted gravity flow sandstones recorded in the Svane-1/1ASvane-1/1A/1A probably represents distal turbidite fan deposits.

#### *Kimm-2a*

This sequence is assigned to the Late Kimmeridgian Mutabilis Zone e.g. corresponding to the lower part of Kimm-2 in Jeppe-1 of Andsbjerg & Dybkjær (2003). It is recorded in the Søgne Basin and Tail End Graben, where it is up to 190 m thick or more (e.g. Svane-1/1ASvane-1/1A/1AA). It is generally condensed/thin on the Heno – Gertrud Plateau, 0-25 m thick, and in the northern part it forms the basal part of the Jurassic succession erosionally overlying Permian deposits (e.g. wells Jeppe-1, Hejre-2 and Karl-1).

Cores from the Heno-Gertrud Plateau record mainly shallow marine deposits represented by a transgressive unit of upper shoreface sandstones with an upwards transition into lower shoreface sandstone and mudstone, and a highstand unit of upper shoreface sandstones (e.g. Hejre-2). Locally on the Gertrud Plateau back-barrier sediments precedes the shoreface sediments (e.g. Gert-1, -2, -4) (Johannessen 2003).

In contrast, the Søgne Basin and Tail End Graben represent deeper water facies of basinal and slope mudstones and intercalated of gravity flow sandstones units up to 10 m thick. The lower boundary is a subtle GR low in mudstone representing the sequence boundary in a basinal setting with a succeeding GR increase culminating in a GR high and maximum flooding level (e.g. Gita-1, Amalie-1, Svane-1/1ASvane-1/1A/1A). The overlying succession comprise intercalated mudstone and gravity flow sandstones with characteristic blocky GR recordings.

#### *Kimm-2b*

This sequence is also assigned to the Late Kimmeridgian Mutabilis Zone, e.g. corresponding upper part of Kimm-2 in Jeppe-1 of Andsbjerg & Dybkjær (2003). The unit is about 100 m thick in the Søgne Basin and Tail End Graben (e.g. Gita-1 and Nora-1). On the Heno Plateau the unit is <10 m (e.g. Gwen-2, Q-1), and on the Gertrud Plateau and Piggvar Terrace it is 25-70 m thick (e.g. Jeppe-1, Hejre-2, Karl-1).

The base of the sequence is a marked erosional boundary on the Gertrud Plateau with a prominent conglomeratic and pebbly unit a few metre thick of mainly upper shoreface deposits (e.g. Hejre-2 core), succeeded by a transgressive interval grading upwards into lower shoreface mudstones. The interpreted HST represents an upwards shallowing into upper shoreface sandstones. The thin or missing succession representing this sequence at the Heno Plateau is interpreted as mainly sand- dominated shallow marine deposits (e.g. Gwen-2, Q-1). In the Søgne Basin and Tail End Graben a lowstand systems tract, 3–15 m thick, of probable gravity flow sandstones is interpreted at the base of the sequence and is succeeded by a thick mudstone succession of transgressive and highstand systems tracts (e.g. Gita-1, Amalie-1).

#### *Kimm-3a*

This sequence is assigned to the latest Kimmeridgian Eudoxus – Autissiodorensis Zones and corresponds to the lower part of Kimm-3 in e.g. Jeppe-1 of Andsbjerg & Dybkjær (2003). The sequence is 5-30 m thick on the Gertrud Plateau and Piggvar Terrace (e.g. Jeppe-1, Hejre-2, Karl-1) and 10–15 m thick on the Heno Plateau (e.g. Gwen-2). The thickness increases to 70-150 m in the Søgne Basin (e.g. Amalie-1, Gita-1, Xana-1) and to 200 m in the Tail End Graben (e.g. Svane-1/1ASvane-1/1A/1A).

The base comprises prominent pebbly sandstone units on the Gertrud Plateau (e.g. Jeppe-1 core) and on the Heno Plateau (e.g. corresponding to SB2 in Gwen-2 core of Johannessen 2003) interpreted as representing marked erosion. The correlative interval in the Søgne Basin and Tail End Graben comprises thick gravity flow sandstone and intercalated mudstones representing a lowstand systems tract. Thick blocky sandstone units (based on the GR-log) are recorded in Gita-1 and correlated to thinner sandstones units and intercalated thicker mudstones in Gita-1 and Svane-1/1ASvane-1/1A/1A, respectively. These sandstone units are interpreted to represent a proximal to distal turbidite fan system. Accordingly, the sandstones units thins markedly towards the Coffee Soil Fault (e.g. in the Amalie- 1 well) and in the Arne Elin Graben (e.g. Nora-1) in this interval.

The upper part of the sequence comprises offshore mudstones on the Gertrud Plateau with an upwards decreasing GR trend (e.g. Jeppe-1, Hejre-2) representing initial phase of increased drowning/subsidence from the Feda Graben in the north. Similar trends are recorded in the Søgne Basin and Tail End Graben areas.

#### *Kimm-3b*

This sequence is assigned to the latest Kimmeridgian Eudoxus – Autissiodorensis Zones and corresponds to the upper part of Kimm-3 in e.g. Jeppe-1 of Andsbjerg & Dybkjær (2003). The sequence is 10 -15 m thick on the Heno Plateau (e.g. Gwen-2) and up to 20 m thick on the Gertrud Plateau (e.g. Hejre-2), whereas it is probably absent on the Piggvar Terrace (Karl-1). The thickness increases to 150 m in the Søgne Basin (e.g. Gita-1) and to 200 m in the Tail End Graben (e.g. Svane-1/1ASvane-1/1A/1A).

The sequence comprises offshore mudstones on the Gertrud Plateau e.g. Jeppe-1 and Hejre-2 representing a continued drowning in this area from the Feda Graben in the north (Sequence 2 in Johannessen 2003). In contrast, the Piggvar Terrace (e.g. Karl-1) received no sediment or was eroded. Parts of the Heno Plateau area continued with deposition of shallow marine sandstones (e.g. Gwen-2, Q-1). In the Søgne Basin Kimm-3b is represented by a basal lowstand systems tract, 10-15 m thick of probable gravity flow sandstone in the Gita-1 and Gita-1 wells, that wedges out towards the Svane 1 and Amalie-1 wells. It is succeeded by a transgressive unit of offshore mudstones that thins towards the north in the Søgne Basin. Two prominent gravity flow sandstone units are intercalated in the mudstone successions in the upper part of the sequence in the Gita-1 and Gita-1 wells. They correlate to similar units in the 3/7-6 and 3/7-7 wells located in the Norwegian part of the Søgne Basin. The correlative succession in the Tail End Graben comprises mudstones.

#### *Kimm-4*

This sequence is assigned to the latest Kimmeridgian Autissiodorensis Zone and corresponds partly to the Kimm-4 in e.g. Nora-1 of Andsbjerg & Dybkjær (2003). Newer data, including palynological data generated in connection with the present study, support these datings. The unit is rather condensed up to 50 m thick on the Heno Plateau (Gwen-2, Q-1), it is 60-170 m thick on the Gertrud Plateau/Graben (Jeppe-1, Hejre-2, Karl-1), 20-170 m thick in the Søgne Basin (e.g. Gita-1, Xana-1) and 250 m or more in the Tail End Graben (e.g. Svane-1/1A, Stork-1).

The base of the sequence marks a major flooding zone and offshore – basinal mudstones prevail on the Gertrud and Heno Plateaus as well as in the Søgne Basin and Tail End Graben.

#### *Volg 1–4*

Sequences Volg 1-4 were dated as Early to Late Volgian by Andsbjerg & Dybkjær (2003). Newer data, including palynological data generated in connection with the present study, support these datings. The succession shows variable thicknesses in the study area due to major rift-/fault-associated subsidence in the Gertrud Plateau/Graben area and in the Tail End Graben where the sequences show a combined thickness of up to 800 m. A rather condensed succession, 50 – 70 thick, is present on the Heno Plateau and in the Søgne Basin they only comprise a 0–200 m thick succession.

The Volgian is dominated by offshore – basinal mudstones throughout the area. Intercalating gravity flow sandstones are present at several stratigraphic levels in the Søgne Basin and Tail End Graben.

Possibly shallow marine Upper Kimmeridgian - Lower Volgian sandstones are present in a detached fault block along the Coffee Soil Fault in the Stork-1 well.

#### *Ryaz-1*

This sequence spans the uppermost Volgian – Ryazanian and represent the upper part of the Farsund Formation including the organic rich Bo Member (Andsbjerg & Dybkjær, 2003). The sequence consists of turbidite sandstones and marine mudstones and has depocentres in the Gertrud Graben and Arne–Elin Graben, with thicknesses of 45 m (Jeppe-1) and > 200 m (Elin-1) respectively (Ineson et al. 2003).

### 4.4 Chemostratigraphy and mineralogy

#### *4.4.1 Methods and samples*

Mineral quantification by the Mineralscan method is performed on carbon coated polished thin sections analysed by a scanning electron microscope (SEM) coupled with 2 energy dispersive X-ray spectrometers (EDS) to image and chemically/mineralogically map samples. Mineralscan uses the level of backscatter electron brightness to distinguish the sample from the impregnated epoxy, i.e. ‘background’, in the sample thin section. Therefore, at each stepping interval, a backscatter electron (BSE) brightness reading is taken and, if above a ‘background’ threshold, an X-ray spectrum is acquired. Each analysis point (each pixel in the mineralogical image) is made with a distance of 10 µm. Based on the X-ray spectra the wt% of each element identified in each spectrum is quantified. The classification of minerals is based on quantitative chemical composition as compared to known compositions in Deer et al. (1966) and the online databases [www.webminerals.com](http://www.webminerals.com) and [www.mineralienatlas.com](http://www.mineralienatlas.com). If an unclassified mineral phase is encountered during analysis, it is marked as ‘unclassified’. The Mineralscan method cannot distinguish between authigenic and detrital phases. Rock fragments are not identified by the Mineralscan method, but split into separate minerals. Some minerals are grouped due to similar chemical composition. The group illite-mix was for instance created to cover mud composed of a mixture of Illite and small particles of carbonate and pyrite, but may also comprise e.g. glauconitic and smectitic compositions as these mineral groups have similar chemical compositions.

Geochemical analyses were performed on crushed samples, which were manually pulverized by mortar and pestle. Major oxides several minor elements were measured by ICP-OES (inductively coupled plasma optical emission spectrometry) after lithium borate fusion. Trace elements were measured by ICP-MS (inductively coupled plasma-mass spectrometry) after lithium borate fusion. For oxides measured by ICP-OES, the detection limit of 0.04% for Fe<sub>2</sub>O<sub>3</sub>, 0.002% for Cr<sub>2</sub>O<sub>3</sub> and 0.01 % for the rest of the oxides. For minor elements measured by ICP-OES, the detection limit is for Ba (5 ppm), Nb (5 ppm), Ni (20 ppm), Sc (1 ppm), Sr (2 ppm), Y (3 ppm), Zr (5 ppm). For trace elements measured by ICP-MS the detection limits are 1 or less than 1 ppm. Total S and C were analysed by LECO with detection limits of 0.02%. Loss on ignition (LOI) was given as weight difference after ignition at 1000°C with a detection limit of 0.1%.

#### 4.4.2 Results

In the following the results of the geochemical analysis are presented for the sandstone intervals and the mudstone intervals, respectively. The subdivision into seismic sequences, referred to here, are presented in Chapter 5.

##### 4.4.2.1 Sandstones

The multivariate analyses show that the geochemical signal from the sand fraction is mainly from  $\text{SiO}_2$ ,  $\text{Na}_2\text{O}$ , Zr and Hf in both the Xana-1 and Gita-1 wells and partly in the Svane-1 well (Fig. 4.17). This is supported from the mineralogical study showing abundant quartz, common albite and the presence of zircon grains in the sandstone intervals.

##### Seismic sequence TEG 15-TEG 20

The lowermost Gita Member has a relatively high dolomite content and hence a high Mg/Ca ratio (Fig. 4.18). Though, the Na/Zr, Na/Si, Na/Al, Na/Ti and Ce/Na ratios in the Xana-1, Gita-1 and Svane-1 well are similar, the resemblance is mainly due to the common albite content. Other sand-prone element ratios like Zr/Si and Zr/ $\text{Na}_2\text{O}$  are different for the Svane Member in the Svane-1 well (Fig. 4.20). It is uncertain whether the intense milling of the cuttings samples from the Svane-1 well could have affected the minerals differently, hence zircon being a mechanical very stable mineral may be concentrated relatively to other minerals. However, when zircon is abundant in the Svane-1 well it occurs in sandstone fragments together with quartz, albite and calcite. In addition, the Svane Member differs geochemically from the Gita Member by having generally higher Zr/Ti, P/Ti, Nb/Zr and lower K/Al ratios (Fig. 4.20).

##### Seismic sequence TEG20-TEG25

The intermediate Gita Member in the Xana-1 and Gita-1 wells have low Cr/Ti, Th/Ti P/Ti and P/Zr ratios. Most of these elements are associated with stable heavy minerals, though Ti is commonly also incorporated in clay minerals. When comparing the sand-prone elements (Si, Na, Zr) in the lower Gita Member with the intermediate Gita Member in the Xana-1 well they show equally low Na/Si and Na/Al ratios. This probably reflects similar abundances of sand, which are related to the position in the basin.

The highest K/Al ratios are found in the intermediate Gita Member, in both the sandstones and mudstones in the Xana-1 and Gita-1 wells (Fig. 4.18).

##### Seismic sequence TEG25-TEG30

The upper Gita Member sandstone in the Xana-1 well show high Ce/Na ratios and low Na/Ti, Na/Al, Na/K and Mg/Ca ratios. This probably reflects upward increasing calcite content followed by decreasing albite content (Fig. 4.19). However, when comparing elements associated with heavy minerals (Cr/Ti, Zr/Ti), rather than the sand-prone elements, the upper Gita Member sandstones resembles the lower Gita Member sandstone in the Xana-1 well and the intermediate Gita Member sandstones in the Gita-1 well.

#### 4.4.2.2 Mudstones

Although the focus is on the sandstone intervals, information of the geochemical composition and trends of the surrounding and interbedded mudstone intervals may be applied for correlation of the sandstones or in a specific framework. If the sandstone intervals are influenced by local sediment sources, they may show some geochemical differences. The mudstones from all wells tend to plot together in several of the binary diagrams, simply because mudstones have some general geochemical differences to sandstones. Overall, there is a larger geochemical affinity between the mudstones from the Xana-1 and Gita-1 wells than with those from the Svane-1/1A and Amalie-1 wells.

#### Seismic sequence TEG10-TEG15

The dataset for the mudstones below the Gita Member, does not indicate any clear geochemically based correlation between the Gita-1, Xana-1 and Svane-1/1A wells (Fig. 4.18).

#### Seismic sequence TEG15-TEG25

The mudstones interbedded with gravity flow sandstones in the Xana-1 well, resembles geochemically the interbedded mudstones in the Gita-1 well. These mudstones have similar K/Ti, Na/Ti, K/Al, P/Al, Nb/Zr, Ce/Na, U/V, Y/P and partly Na/Zr ratios (some of which are illustrated in Fig. 4.18). Despite several exceptions, the mudstones in this interval in the Xana-1 and Gita-1 wells generally resembles each other more than they resemble any of the other mudstones.

#### Seismic sequence TEG30-TEG50

The uppermost mudstones of Kimm-4 and Volg-1 in the Xana-1 and Gita-1 wells have similar Zr/Ti, K/Ti, Na/Ti, K/Al, Na/K, Nb/Zr, Na/Zr, Na/Si, Ce/Na, U/V and Y/P ratios (some of which are illustrated in Fig. 4.18). Despite several exceptions, the mudstones in this interval in the Xana-1 and Gita-1 wells resemble each other geochemically and probably can be correlated.

#### 4.4.3 Discussion of sediment composition / provenance

Rounded dolomite clasts with rhombohedral ankerite clasts occur in the Gita Member sandstones in the Søgne Basin and in the Tail End Graben. These carbonate clasts are in particular common in the Heno Formation from the western part of the Danish Central Graben (Weibel et al. in prep.). The geographically restricted distribution strongly suggest that the dolomite clasts originate from the Mid North Sea High or the Mandal High. At the time of deposition (of the Heno and Farsund formations), Zechstein deposits were exposed on the Mid North Sea High and Mandal High (Weibel et al. 2010). The dolomite clasts may thus have been sourced from the Zechstein deposits exposed on intrabasinal highs.

The differences in K-feldspar abundances between the gravity flow sandstones in the Søgne Basin and the Tail End Graben, respectively, could be due to 1) different sediment sources or 2) preferential dissolution of K-feldspar in the Xana-1, Gita-1 and Svane-1/1A wells. Feldspar dissolution is identified in all investigated wells. K-feldspar (in particular overgrowths) and albite grains are partly dissolved in the 3/7-6 and 3/7-7

wells, contrary to the authigenic albite forming in secondary porosity after dissolved feldspar grains in the Xana-1 wells. These dissolved feldspar grains might have been K-feldspar, though this is difficult to confirm. Increased influx of sediments from the Søgne Basin to the Tail End Graben during deposition of the middle part of the Gita Member may have delivered the K-feldspar to the sandstones in this interval in contrast to the under- and overlying successions characterized by absence of K-feldspar.

## 5. Seismic interpretation and mapping

The seismic interpretation in this study has been carried out on new high quality broad band seismic data (PGS15015 PH1 and PH2) and supplemented by seismic interpretation from previous studies in the area (e.g. PETSYS) where the seismic interpretation was carried out on older data (NACS, PAM-99South). Only the final stack version of the seismic data has been used. Seismic inversion and AVO studies are not applied in this study.

The seismic interpretation was carried out in order to evaluate the basin development during deposition of the Upper Jurassic sandstones identified in the Gita-1 and Xana-1 wells. Therefore the emphasis for the seismic interpretation has been on the northern part of the Tail End Graben comprising the Svane-1/1A, Xana-1 Gita-1 and Amalie-1 wells.

The distribution of reservoir sand in the Upper Jurassic in the Tail End Graben is closely related to the basin development and from the seismic data and maps it has been possible to establish a relatively detailed description of the basin development in the Tail End Graben.

### 5.1 Interpretation

In total 8 horizons of structural and stratigraphic relevance were selected for mapping. The marker horizons have been annotated with pre-fix TEG (for Tail End Graben) and with increasing number from below (Fig. 5.1). Four horizons (TEG10, TEG15, TEG20 and TEG30) are closely related to the sand units in the Gita-1 and Xana-1 wells.

The seismic line in Fig. 5.1 shows the composite nature of the seismic sequences. Each sequence comprises a varying number of individual lobe features with varying sand thickness in response to basin-tectonic developments and activation of source areas. The change in reflectivity towards the deep-lying basin is interpreted as a result of decreasing sand content, but dimming due to loss of energy with burial depth may also be a factor.

It is not possible to interpret the individual sands in the conventional seismic. The seismic markers are instead used for delineation of sandy intervals (Fig. 5.2). The seismic sequences have been evaluated individually and coordinated with the sequence stratigraphic approach being aware of the composite nature of the package.

A brief characterization in stratigraphic order of the interpreted horizons (from oldest to youngest) is given below:

**Base Upper Jurassic (TEG\_BUJ):** The reflector is picked on top of a generally high amplitude reflector zone and marks the Near Top Middle Jurassic level. In the Gita-1 and Amalie-1 wells the reflector corresponds with the top of a coal bearing interval.

**TEG10** is picked in a distinct amplitude trough below a thin sand stringer within a shale dominated interval in Gita-1. In the Norwegian wells 3/7-6 and 3/7-7 the marker is picked at the base of a distinct sandy unit. The reflector is interpreted to represent the sequence boundary SBKimm-1b.

**TEG15** follows a strong amplitude trough picked at the base of the sand-rich interval in the Gita-1 and Xana-1 wells. In the western part of the Danish Central Graben the TEG15 marks the lithological boundary at the base of the Ravn Mb of the Heno Formation.

**TEG20** is a high amplitude peak defined internally in the Gita Member interval in the Gita-1 well. The marker correlates with the sequence boundary SBKimm-3.

**TEG25** is a high amplitude peak in the upper part of the Gita member in the Gita-1 and Xana-1 wells. The marker is linked to the sequence boundary SBKimm-3b

**TEG30** is associated with the top of the Gita Member in the Gita-1 and Xana-1 wells. Here the reflector appears as a bright trough. In the deeper part of the Tail End Graben the marker weakens, probably due to a lateral change towards more shaly deposits. In the Søgne Basin the TEG30 marker ties to the top of turbiditic sands drilled in N3/7-5 and N3/7-6. To the west- and northwest of the Tail End Graben the seismic marker interferes with the distinct erosional surface at the top of the Heno Formation. The TEG30 marker is associated with the sequence boundary SBKimm-4

**TEG40** is picked in the lower reflector of a characteristic double marker (peaks/troughs?), which can be traced with high confidence in the Tail End Graben. TEG40 is an intra-Farsund Formation horizon that is stratigraphically close to the Volgian-Kimmeridgian boundary and is associated with the sequence boundary SBVolg-1.

The **TEG50** reflector is a distinct marker corresponding to a marked downward increase in acoustic impedance in the Farsund Formation close to the Lower-Middle Volgian boundary. In the north and northwest, e.g. the Søgne Basin, it represents a structural unconformity truncating underlying strata.

**BCU** (Base Cretaceous Unconformity) is a distinct regional marker representing the transition from the Jurassic to the Cretaceous. It is an easily recognized seismic event (strong peak) marking the top of the low impedance Farsund Formation.

## 5.2 Regional structural setting

The Søgne Basin and Tail End Graben forms part of the Upper Jurassic rift system and the basin development is closely related to the tectonic activity associated with the rifting. The basins are bounded by the Ringkøbing Fyn High (Coffee Soil Fault) to the east, the Mandal High to the north and to the west by the Heno Plateau and Gertrud Plateau/Graben (Fig. 5.3).

The rifting initiated at the end of the Middle Jurassic and created an elongated basin with a basin axis parallel to the Coffee Soil Fault. During the succeeding Kimmeridgian rift phase, the platform areas adjacent to the graben were affected. Subsidence in the graben axis continued, but the change in tectonic regime led to activation of NW–SE-striking normal faults. In the basin, the Amalie Cross Fault and the Lulu Fault (Fig. 5.3) became active. Initial subsidence of the Gertrud Plateau took place along the Mona fault.

In the Late Kimmeridgian, rifting resumed and new NNW-SSE trending faults formed. This rift phase demonstrates a divergent basin development in the area.

A W-E trending structural profile from the Heno Plateau to the southern part of the Tail End Graben is shown in Fig. 5.4. The section ties to the Jette-1, Gwen-2, Q-1, Iris-1 and Svane-1/1A wells. The profile shows the existence of the Heno Platform to the west being active during the Late Jurassic. The Heno

platform is separated from the Tail End Graben by the Arne-Elin Graben, which is a complex fault zone active during the Cretaceous dominated by wrenching and inversion influenced by salt tectonics. The basin development of the Tail End Graben shows evidence of a rapid subsidence throughout the Late Jurassic but also evidence of wrenching and inversion, notably the Svane Ridge.

A W-E trending structural profile from the Gertrud Graben through the southern part of the Mandal High to the Gita Plateau is shown in Fig. 5.5. The section ties to the Jeppe-1, Hejre-1 and -2, Gita-1, Amalie-1, Gulnare-1 and Tabita-1 wells. The profile highlights the marked difference in basin development between the Gertrud Graben and the Gita Plateau. The Gertrud Graben is dominated by thick Volgian deposits revealing a basin development initiated in the Kimmerigian. On the Gita Plateau the thick lower units show evidence of basin subsidence during the earlier part of the Late Jurassic. In the Gertrud Graben subsidence took place during the latest Jurassic (Volgian) when evidence of uplift is observed for the Gita Plateau. The uppermost Jurassic deposits in the Gita area are considered to be a condensed section associated with hiatus developments.

Fig. 5.6 displays a N-S trending profile from the Søgne Basin in the north to the Tail End Graben in the south. The section ties to the 3/7-5, 3/7-6, 3/7-7, Lulu-1 and-2, Gita-1, Xana-1 and Svane-1/1A wells. The profile shows the differences in basin development between the Søgne Basin, Gita Plateau and Tail End Graben. The beginning of the Late Jurassic is characterized by a relatively uniform basin development (similar thickness of lowermost units throughout the area). Conversely, during the late Late Jurassic, the Lulu area in the southern part of the Søgne Basin was affected by uplift and associated truncation. The Gita Plateau is likewise influenced by uplift but is less affected by truncation. The uppermost Jurassic deposits are interpreted to be condensed sections associated with hiatus. The basin development of the Tail End Graben shows evidence of a constant and rapid subsidence throughout the Late Jurassic.

A 3D visualization of the basin development during Upper Jurassic is summarized in Fig. 5.7. Isochore maps of the seismic sequences indicate a slight change in depocentres during the Upper Jurassic. Two overall phases of basin development and subsidence can be recognized in the Tail End Graben: (1) a Kimmeridgian phase of subsidence and (2) a Volgian phase following a period of uplift and erosion (Fig. 5.8). The initial subsidence of the Gertrud Graben began during Kimmeridgian times. This phase also marks a slight change in the location of the depocentres toward west. Inversion along the Svane Ridge began in Late Kimmeridgian and introduced a separate depocenter east of the Svane Ridge adjacent to the Coffee Soil Fault (Fig. 5.7).

### 5.3 Upper Jurassic basin development in the Gita-Xana-Svane area

The basin development is primarily evaluated based on isochore maps of the seismic sequences.

A structure map of the top of the Gita Member (TEG30) outlines the main structural elements in the study area e.g. the Gita Plateau to the north and the Tail End Graben to the south separated by the Amalie Cross Fault (Fig. 5.9). The Svane Ridge in the Tail End Graben is flanked by deeper basins on both sides.

The seismic data show significant variation in the thickness of the various seismic sequences in the study area. The variation is closely related to the structural setting. A series of seismic cross sections illustrate the thickness variation and the structural style in the study area (Figs. 5.10 - 5.13).

Fig. 5.10 is a N-S trending line that extends from the Gita Plateau in the north to the Tail End Graben crossing the Amalie Cross Fault. The profile shows a general thickening of the seismic units toward the south. A local thickness maximum of the TEG25-TEG30 interval is seen north of the Amalie Cross Fault.

Fig. 5.11 is a SW-NE line (inline 15440) through the Amalie-1 well crossing the Amalie Cross Fault. In the Tail End Graben the sequences are thinning towards the Svend Salt structure to the west.

Fig. 5.12 is a W-E cross section through the Gita-1 and Amalie -1 wells. The profile shows a thickness maximum of the TEG15-TEG20 between the wells. The interval is characterized by low amplitudes. A hummocky reflection pattern is seen in the TEG25-TEG30 interval. The interval is getting truncated by TEG40.

Fig. 5.13 is a cross section (inline 14440) through the complex faulted Svane Ridge. The profile show evidence of onlap toward the west.

For illustration of the basin development during the Upper Jurassic isochore maps of all the seismic sequences have been generated (Fig. 5.14). The isochore maps exhibit an overall comparable basin subsidence throughout the Kimmeridgian. The isochore maps show detailed variations in thickness distribution that indicate a general westward shift of the depocenter locations. The Svane Ridge became active during Late Kimmeridgian separating an eastern basin along the Coffee Soil Fault from the main depocenter to the west (TEG15-TEG20, Fig. 5.14).

#### 5.4 Mapping of the sand

To identify and outline areas with sandy intervals an attribute analysis have been carried out for the 6 seismic sequences. The sandy interval in the Gita-1 and Xana-1 wells is associated with high amplitude reflectivity whereas the reflectivity decreases basinwards corresponding to a change toward more shaly deposits (Fig. 5.15). The close relationship between high reflectivity and sandy intervals are used to outline and map out the presence of sandy deposits (evt REF). The result of the attribute analysis in the seismic sequences varies and a clear outline of sandy unit is only possible in some of the sequences. In the BUJ-TEG10 interval a high amplitude anomalies are identified along the Coffee Soil Fault (Fig. 5.16). In the TEG15-TEG20 and TEG20-TEG30 intervals anomalies are concentrated to the western part of the Gita Plateau. In the TEG20-TEG30 interval the anomalies extent into the Tail End Graben south of the Amalie Cross Fault.

#### 5.5 Detailed depositional geometries and potential source areas

An analysis of seismic geometries in combination with isochore maps (Fig. 5.14) was carried out with the aim of understanding the sedimentary response to subsidence and uplift in different compartments of the Tail End Graben rift basin. Moreover, the seismic facies within the mapped seismic units potentially contain information on depositional environment and sediment transport direction (Mitchum et al., 1977). The seismic geometries mapped within the Middle-Late Jurassic interval are illustrated by six seismic sections (Figs. 5.17-5.22). As a tool for interpretation horizon flattening is applied to enhance depositional geometries and reduce the post-depositional structural overprint.

### 5.5.1 Tail End Graben

The seismic data south of Svane-1/1A well is influenced by noise and low reflectivity, which impedes the quality of the interpretation. The main horizons and units can be identified but the interpretation of internal horizons TEG15 and TEG25 is uncertain (therefore not shown on Fig. 5.17).

In the southern part of Tail End Graben, the interval TEG10 to TEG20 (Kimm-1 – Kimm-2) is marked by low amplitudes and vaguely defined continuous reflections (Figs. 5.17 and 5.18). These reflections represent strata infill of an elongate depocentre that is primarily developed over and west of the Svane Ridge. The low-amplitude to nearly transparent character makes it difficult to interpret internal geometries but it appears that the reflections onlap the base horizon TEG10 and the bounding faults on the eastern flank of the basin (against Ringkøbing Fyn High) – this is highlighted by the flattened sections in Figs. 5.17 and 5.18. The elongate distribution of the TEG15-TEG20 interval below the western basin margin (Fig. 5.14C) and the apparent continuation of strata toward west (Fig. 5.18) may imply that the sediment source mainly lay to the west, e.g. Heno Plateau.

The interval TEG20-TEG30 (Kimm-3 - lowermost Kimm-4) is marked by medium to high-amplitude, semi-continuous reflections that generally diverge in an east-west direction. The general thinning of this interval from east to west across the Svane Ridge and the mounded anomalies below the eastern basin flank, corresponding to local depocentres (Figs. 5.14D-E), suggests that the Ringkøbing Fyn High was a likely sediment source for the Upper Kimmeridgian deposits in the Tail End Graben. In N-S profiles, the eastern depocentre is seen as a lenticular wedge expressed by the TEG20-TEG25 (Kimm-3a) interval (Fig. 5.20). This gently mounded sediment geometry occurring below the footwall of a rifted margin is typically associated with sand-rich submarine fans (Mattern, 2005).

Both packages – TEG10-TEG20 and TEG20-TEG30 – show a northward thinning with reflector terminations, e.g. apparent onlap, observed both in the basin and against the Gita Plateau. These strata configurations in combination with the thickness distribution, indicating extremely elongated depocentres, may suggest a sediment transport direction along the basin axis. This pattern is particularly prominent for the interval TEG15-TEG20 where apparent low-angle clinoform features are observed both in the basin and on the Gita Plateau. Possibly, sediments were carried northward away from the proximal input sources, i.e. the aforementioned submarine fans, along the basin flanks. Possible mechanisms include dilute suspension currents directed northward by the Coriolis effect (if source was located on the eastern basin margin) (Normark, 1970; Normark et al., 1980) or oceanographic contour currents (Stow et al., 1998; Stow and Piper, 1984). If the elongate depocentre geometry developed as a consequence of along-slope transport it would require that an open connection to adjoining oceanic regions had developed by middle Jurassic. However, present paleogeographic reconstructions suggests that the Jurassic rift basin was closed toward south (Verreussel et al. 2018).

### 5.5.2 Gita Plateau

The internal seismic stratigraphy and the isochore distribution of the interval TEG10-TEG20 (Kimm-1 – Kimm-2) suggests that the depositional system, involving the subsidiary sedimentary packages TEG10-TEG15 (Kimm-1) and TEG15-TEG20 (Kimm-2), extends across the Gita Plateau. The thickest of these intervals, TEG15-TEG20, display onlap onto the Gita Plateau in a northerly direction (Figs. 5.19; 5.20). In E-W profiles across the Gita Plateau the interval TEG15-TEG20 displays reflection terminations that are generally dipping toward west (Fig. 5.21) and south-west (Fig. 5.22). A depositional reconstruction of the

TEG15-TEG20 interval may be attempted by flattening of TEG15 suspected to be a marine flooding surface (Fig. 5.22B). The geometries after flattening resemble a series of depocentres that were likely syn-depositional with the formation of small half-grabens along the main faults. The eastward depocentre is interpreted as a slope apron generated by sediments coming from the Ringkøbing-Fyn High. This sedimentary system may have been a key source for sediments transported westward over what is presently the Gita Plateau. In addition, sediments for the interval TEG15-TEG20 may have come from the south, carried by distal suspension-driven turbidites or alternatively some form of contour current. We cannot rule out any local input sources for this interval but as far as the sedimentary geometries are concerned, areas to the north and immediately west of the Gita Plateau were unlikely major source areas for sand below TEG20 in the Gita-1 well.

For the package TEG20-TEG25 (Kimm-3a), an along-strike onlap configuration toward the Gita Plateau is noted, similar to the package below the TEG20 horizon (Fig. 5.19; 5.20). However, for TEG20-TEG25 we do not observe a connection in the depositional system between Tail End Graben and Gita Plateau as suggested for the strata geometries in the underlying section. This is illustrated by the dissociation between the depocentres in the Tail End Graben and the basins toward NE (Fig. 5.15D). In sections transverse to the basin orientation, the interval TEG20-TEG25 is relatively thin and of equivalent thicknesses across the Gita Plateau. The local depocentres north-east of the plateau may relate to eastern sources (Ringkøbing-Fyn High) but there are no particular indications from the depositional geometries that TEG20-TEG25 sediments on the Gita Plateau, e.g. at the position of Gita-1, are derived from the east.

The development into more confined depocentres that began with TEG20-TEG25 is seen to continue for the TEG25-TEG30 (Kimm-3b – lowermost Kimm-4) interval. Presumably, this ensuing separation between the more widespread depositional systems of the Tail End Graben and the more local depocentres on the Gita Plateau and farther toward NE marks the progressive tectonic phase resulting in uplift of the Gita Plateau.

The sand-rich package TEG25-TEG30 (Kimm-3b – lowermost Kimm-4) at the crest of the Gita Plateau displays a series of slightly elongate convex features, marked by very strong reflectivity and apparent erosion along flanks (Figs. 5.19; 5.21; 5.22). Internal reflections vary from semi-continuous to discontinuous with parallel to mounded geometries. Consistent directional indices, e.g. in the form of clinoform dips, are not observed. N-S oriented sections show that the package covers the flanks of the Mandal High with vague indications of basal onlap (Fig. 5.19). The above characteristics suggests that unlike the similarities in seismic facies observed for the older sand-rich interval TEG15-TEG20, the uppermost sand package at the position of the Gita-1 well bears little or no resemblance with the time-equivalent package of the Tail End Graben.

The multi-panel cross-section in Fig. 5.22 shows a thickening of the TEG25-TEG30 interval in what appears to be a synclinal basin below the Ringkøbing Fyn High. Clinoform features are observed but with strong lateral variations in geometries that complicates interpretation. In the example shown in Fig. 5.22 eastward dipping clinoforms are observed that would suggest a transport direction from the Gita Plateau and toward the Ringkøbing Fyn High. This depositional system, however, is separated from the section of the TEG25-TEG30 interval that was drilled by the Gita-1 on the western part of the plateau. Although, no firm conclusions can be made based on the seismic data alone, the separation of the sand-rich TEG25-TEG30 interval over the western Gita Plateau from time-equivalent systems to the south and the east may point to a sediment source originating from the north, i.e. Mandal High.

## 5.6 Summary

The seismic basin analyses indicate distinct changes in basin evolution between the early rift phase (Early Kimmeridgian), and the later tectonic phases (Late Kimmeridgian to Volgian). During the early phase, TEG10-TEG20, sedimentation is influenced by a N-S elongate depocentre probably reflecting multiple input sources active along both basin margins (e.g. Heno Plateau, Gertrud High, Ringkøbing-Fyn High) and a general northward movement of fine-grained sediments along the basin axis. During the late rift phase (TEG20-TEG40) sedimentation becomes progressively influenced by uplift of the Gita Plateau and the major NW-SE trending faults, e.g. Amalie Cross Fault. Inversion of the Svane Ridge starts to compartmentalize the Tail End Graben from TEG25. The late rift phase also marks the build out of more distinct fan lobes, notably in the Tail End Graben along the Ringkøbing-Fyn High. The seismic analyses (geometries and attributes) and well information indicate that these fan systems are potentially sand-prone in vicinity of the input source. The sand-rich TEG25-TEG30 package on the Gita Structure is likely a result of the change in the tectonic re-orientation of the basin and the activation of the nearby sources areas, e.g. the Mandal High.

## 6. Petrophysical evaluation

The petrophysical evaluation is based on wireline log data and supplemented in places with cores, side-wall cores and cutting analysis. The principal logs for this study was the gamma ray (GR), the sonic (DT), resistivity logs, density (RHOB) and neutron density (NPHI) where available. The volume of shale (VSH) was calculated both as a function of the GR, as well as NPHI-RHOB log data. In most cases these methods result in similar VSH. Hence, in order to have similar approaches to all wells in the study area the GR-derived VSH has been used. The effective porosity (PHIE) was calculated using the NPHI-RHOB plots with the formation temperature and the resistivity as supplementary information and a grain density of the sand being 2.65 g/cm<sup>3</sup>.

The stratigraphic tops are based on an integrated approach applying seismic stratigraphy, log stratigraphy, sequence stratigraphy, geochemistry and biostratigraphy.

Figs. 6.1 – 6.11 illustrate the CPI's for 11 selected wells in the study area in alphabetic order. The CPI's show the measured depth (M), the seismically intervals, the gamma ray, sonic, resistivity, density, neutron porosity, effective porosity and the lithological interpretation.

Based on the CPIs table 6.1 lists the thicknesses of the TEG units along with the net-to-gross ratio and the average effective porosity of the sand units within the Upper Jurassic in 17 wells within the study area.

The seismic interval between BUJ and TEG10 is not represented in many of the wells. It is most thick in the Gita-1 well where the thickness is 246 m, of which 37 m are sand units. However, the seismic marker TEG BUJ marks the top of the coal layers, as described in Chapter 5. In the Gita-1 well there are two thin coal layers above the seismic marker, which therefore could indicate that the lowermost section of this interval should be included in the Middle Jurassic succession. All of the sand units in this interval are below the uppermost coal layer. In the Gwen-2 well a fluctuating high frequency but low GR succession is observed in this interval consisting of shale with a relatively high content of terrestrial input. Three sandy units of combined 18 m are encountered in the Amalie-1 well. The seismic data (e.g. Fig. 5.11) demonstrate that this sand was sourced from the Ringkøbing-Fyn High, which is also supported by the geochemical provenance data.

The TEG10 – TEG15 interval ranges from 10s of metres on the Heno Plateau to nearly 200 m in the Svane-1/1A well. On the Heno Plateau this interval consists of high portions of sand, while the net-to-sand ratio in the basin is lower. In the Svane-1/1A well this interval comprises 44 m of hydrocarbon bearing sand units. Most of these sand units are clustered in the middle of this seismic interval and are thin, i.e. > 2 m, but some are as thick as 7 m. Both the geochemical data and the seismic data (e.g. Fig. 5.13) indicate that the sand in the Svane-1/1A well in this interval are transported down-slope from the Heno Plateau.

During the interval TEG15 – TEG20 the net-to-gross ratio in the wells located on the Heno Plateau continues to be high, while sand units are evident in the Xana-1 and Gita-1 wells in the Kimm-2a sequence (Fig. 4.15). The sand units are thicker and more porous in the Gita-1 well compared to the corresponding sand units in the Xana-1 well. The geochemical data indicate that this sand was sourced from the northwest, i.e. from the Mandal High.

A high net-to-gross ratio is still dominating in the wells on the Heno Plateau during the seismic interval TEG20 - TEG30, although within the Hejre-1 and -2 wells the lithology is fine grained. In the Svane-1/1A well this seismic interval is 205 m thick, of which 30 m is sand. Most of these sand units thin, < 2 m, and

probably represent the distal portion of a submarine fan system. In the Gita-1 and Xana-1 wells the net-to-gross ratio is approximately 50%. The log shape in these wells indicates that the sand units represent the proximal part of a submarine fan system. The seismic attributes mapped for this interval are illustrated in Fig. 5.16 and show a coherent high amplitude area from the Mandal High into the deep basin. Other areas of similar high amplitude observed on this map are features that could be submarine fans feed from the Ringkøbing-Fyn High, as well as sand rich units along the slope of the Heno Plateau facing the Tail end Graben. Faults seem to control the depositional environment, timing and the distribution of the sand during this seismic interval.

For the seismic interval TEG30 – BCU mainly fine grained material was deposited throughout the study area, including on the Heno Plateau. In the Svane-1/1A well stringers of sand are present. An Upper Kimmeridgian - Lower Volgian 30 m thick sand unit has been drilled in the Stork-1 well at the base of this seismic interval. This sand unit is located within a structure interpreted to represent a detached fault block, from the Ringkøbing-Fyn High. The sandy interval is interpreted as being shallow marine.

Comparing the porosity in the Xana-1 and Gita-1 wells indicates that the highest porosities are associated with thick sand units. The sandstone might be prone to calcilte-cementation in proximity to the mudstone, hence thin units are often cemented as well as the edges of the thicker sand units.

## 7. Reservoir characteristics

### 7.1 Reservoir petrography

#### 7.1.1 *Methods and samples*

The gravity flow sandstones are represented by cuttings samples in the Xana-1, Gita-1 and Svane-1/1A wells, supplemented by 11 side wall cores from the Xana-1 well. Additionally, 10 core samples from the 3/7-6 and 3/7-7 wells from the Norwegian sector have assisted in the understanding of the mineralogical and diagenetic variations. Ditch cuttings samples were cleaned by dichloromethane in soxhlet for up to 10 days washed, dried and sieved in order to obtain the 0.5-4 mm fraction. Core plugs for porosity and permeability measurements were cleaned in methanol using soxhlet. Core samples for thin section preparation and geochemical analysis were not cleaned.

Polished thin sections were prepared from core and cuttings samples using blue dyed epoxy to improve pore space visibility. The different lithologies present in each sample were documented by transmitted and reflected optical microscopy. The mean grain diameter in the thin sections was obtained by long-axis measurement of about 60 grains intersecting a number of arbitrary straight lines in polarization microscope. All sand grains, either present in sandstone fragments, embedded in drilling mud or occurring as loose grains are regarded part of the gravity flow sandstones and included in the grain size average. Many grains have been crushed during drilling, thus deviations from formational grain-size means must be expected. The grain size nomenclature is applied according to the Wentworth Class (Wentworth, 1922). Calculation of the degree of sorting is according to Folk (1966). The mineralogical and petrographical relationships were supplemented by investigations of carbon coated thin sections by scanning electron microscopy (SEM) using a back-scatter electron (BSE) detector. The SEM applied for this study was a Zeiss Sigma 300 VP operating at 10–15 kV. The chemistry of the mineral phases was documented using energy dispersive X-ray spectroscopy (EDS).

Porosity was measured on several core pieces, whereas only one plug was available for permeability measurement. Porosity and permeability were measured according to the API RP-40 standard (API 1998). Steady state gas permeability was measured at a confining pressure of ~ 2.8 MPa (400 psi), and at a mean N<sub>2</sub> gas pressure of ~ 1.5 bar (bar absolute) = 0.15 MPa. He-porosity was measured at room conditions. The density was measured using the Archimedes method by submerging the plugs into mercury at room conditions.

#### 7.1.2 *Results: Mineralogy and petrography*

The cuttings samples comprise a variety of different components. The brown and black mudrocks, probably of the clayey part of the Farsund Formation, and light brown mudrocks rich in barite, which are considered drilled mud clusters, are omitted from the description of the sandstones. Sandstones intervals are represented by carbonate- and quartz cemented sandstones, sandstones with clayey matrix and loose quartz grains. Only the quartz-cemented sandstone cuttings fragments contains porosity and hence show that cuttings samples may underestimate the porosity of the reservoir, when compared with the side wall cores in the Xana-1 well.

### *Tail End Graben*

The average grain sizes in sandstone fragments and single grains are 150  $\mu\text{m}$  in the Xana-1 well, 140  $\mu\text{m}$  in the Gita-1 well and 120  $\mu\text{m}$  in the Svane-1/1A well. The Gita-1 well is characterized by moderately well – moderately sorted sand. The Xana-1 well has moderately – poorly sorted sand and the Svane-1/1A well vary from poorly to moderately well sorted (Fig. 7.1).

Quartz is the dominant detrital grain in all sandstone cuttings fragments and common as loose grains. Albite is the most common feldspar type in both the Xana-1, Gita-1 and Svane-1/1A wells (Fig. 4.3). K-feldspar is generally rare in the Svane-1/1A well, and in the uppermost and lowermost sandstone intervals of the Xana-1 and Gita-1 wells, though with a slightly higher abundance in the middle sandstone intervals. K-feldspar remnants enclosed in calcite cement is common. Secondary porosity after feldspar grains outlined by clay rims is common. Muscovite and biotite are rare. Glauconite is rare in the Gita-1 and Xana-1 wells. Chert is rare in the Xana-1 and the Svane-1/1A wells. Metamorphic rock fragments are present as rare components only in the Xana-1 well. Quartz grains occasionally have rounded 2<sup>nd</sup> cycle overgrowths. Volcanic rock fragments are rare in the Xana-1 well. Rounded dolomite clasts are common in both the Xana-1 and Gita-1 wells, whereas micritic calcite clasts are typical in the Svane-1/1A and Xana-1 wells (dolomite is in particular abundant in the lowermost sandstone intervals in the Xana-1 and Gita-1 wells). Rare heavy minerals comprise rutile, zircon and Fe-Ti oxides and apatite in the Svane-1/1A well, though mainly rutile and apatite in the Xana-1 and Gita-1 wells. Detrital clays occurs as grain coatings on detrital grains and as clusters in the Gita-1, Xana-1 and Svane-1/1A wells. The detrital clay abundance seems to be highest in the Xana-1 well.

Micro- and occasionally cryptocrystalline quartz coatings are one of the earliest forming authigenic phases in the gravity flow sandstones (Fig. 7.2B). Microquartz additionally occurs as dispersed crystals between pore-filling clays in the Gita-1 and Svane-1/1A well. Microquartz coatings occurs in all investigated sandstones from the Gita-1 well, whereas only in few samples from the Xana-1 and Svane-1/1A wells. Pyrite and anatase are common but volumetrically unimportant early diagenetic phases. Illitic clays coatings are in particular common in the Xana-1, where it typically rims secondary porosity after dissolved feldspar grains (Fig. 7.2A). This fragile appearance has little survival potential in cuttings samples and hence may be much more common in the Gita-1 and Svane-1/1A wells than estimated. Illitic clays have additionally formed by illitization of mica (kaolinised mica?), illitization of detrital mud and in secondary porosity after dissolved feldspar grains. Kaolinite has in rare cases observed between the cleavage planes in mica, possibly formed prior to deposition. Authigenic chlorite is rare and typically occurring in secondary porosity after grain dissolution. Early siderite rhombs occur locally, possibly initiating between cleavage planes in mica. Ankerite forms rhombohedral overgrowths on rounded dolomite clasts in the Gita-1 and Xana-1 wells (Fig. 7.2E, F). Ankerite may continue outwards into the adjacent pore space. Calcite cement encloses quartz overgrowths and hence formed much later than ankerite cement. Quartz overgrowths enclose brownish dust rim and are commonly interlocked and only occasionally forming prismatic terminations in the Xana-1 well (Fig. 7.2C, D). Quartz overgrowths are locally hindered by illitic or microquartz coatings or reduced to outgrowths in the Svane-1/1A and Gita-1 wells (Fig. 7.2B, D). Albite overgrowths occasionally occur on detrital albite in the Svane-1/1A well. Authigenic albite is common in secondary porosity after dissolved feldspar grains in the Xana-1 side wall cores (Fig. 7.2A).

## Søgne Basin

Monocrystalline quartz is the dominant mineral. Few quartz grains from the 3/7-6 core have rounded 2<sup>nd</sup> cycle overgrowths. K-feldspar and albite are common (Fig. 4.3). Detrital carbonate comprise rounded dolomite and micritic calcite clasts, besides bioclasts (shells and foraminifera). Mica is mainly muscovite and minor amounts of biotite. Green chlorite is rare. Metamorphic rock fragments are rare. Volcanic rock fragments have been identified in one sample only in 3/7-7 well. Chalcedony clasts are rare. Glauconite grains are rare. Heavy minerals such as apatite, leucoxene-altered ilmenite, tourmaline, rutile and zircon are rare.

The first phase to precipitate after deposition of the sandstone were pyrite and crypto- and microcrystalline quartz (Fig. 7.3C, F). Microquartz coatings are locally more common in the 3/7-6 core than in the 3/7-7 core. Kaolinite occurs as common pore-filling clays and as crystals forming between the cleavage-planes in mica (Fig. 7.3A). Illitic clays are volumetrically less abundant than kaolinite. Illitic grain coatings are common, especially around secondary porosity after partly dissolved K-feldspar (Fig. 7.3B). K-feldspar overgrowths on detrital K-feldspar are common (Fig. 7.3C). Most K-feldspar overgrowths show dissolution features except when enclosed in calcite cement. Albite overgrowths may enclose kaolinite. Quartz overgrowths are common on detrital quartz without grain coatings. Quartz overgrowths are hindered when microquartz or illite coatings cover the detrital quartz grains, and authigenic quartz may locally form outgrowths (Fig. 7.3A, D, F). Hence, quartz overgrowths are more abundant in the 3/7-7 well than the 3/7-6 well. Quartz overgrowths encloses kaolinite. Ankerite forms rhombohedral overgrowths on detrital rounded dolomite clasts (Fig. 7.3E). Poikilotopic calcite cement occurs as pore-filling or patchy cement. Calcite cement encloses K-feldspar and quartz overgrowths besides ankerite overgrowths. Occasionally, late anatase crystals and barite cement has been observed in the 3/7-7 well.

## 7.2 Reservoir properties

Petrophysical log evaluation shows a slightly higher net sand percentage in the Gita-1 well compared with the Xana-1 well, e.g. for the seismic interval TEG25-TEG30, the Gita-1 and Xana-1 wells have 50% and 40% net sand, respectively (Table 6.1). In addition, the porosity of the sand intervals are generally higher for the Gita-1 well than the Xana-1 well, e.g. for the seismic interval TEG25-TEG30, the sandstone intervals have porosities of 13 % and 6% in the Gita-1 and Xana-1 wells, respectively (Table 6.1). Porosities of up to 21 % and permeabilities of maximum 2 mD have been measured on the side wall cores from the Xana-1 well (Fig. 7.4). The log-panel shows the porosities measured in the side wall cores plotted along the log derived porosities. It is demonstrated that the porosities derived from the logs correspond well with the measured porosities. In the track showing the clay and sand content the sand is shaded with a range of yellow to orange scale according to the density of the intervals. Dense sandy intervals are interpreted to represent carbonate-cemented sandstone with probably low primary porosity and permeability, while the lighter intervals comprise pure (sometimes unconsolidated) sands with correspondingly high porosity and permeability. Thus, the lighter intervals (shaded yellow) have the best reservoir properties. Carbonate-cemented sandstone intervals are common in the upper part of most sandstone intervals in the Xana-1 well (Fig. 6.11). Comparing the permeability from the side wall cores to the log derived permeabilities illustrate a poor relation (Fig. 7.5). However, there the trends of high and low permeable intervals are represented in the log derived permeabilities.

The wells from the Søgne Basin have equally net sand percentages to those from the Tail End Graben, e.g. for the seismic interval TEG20-TEG25, the 3/7-6 and 3/7-7 wells have 47% and 63% net sand. The porosities

of 19% for both wells are higher in the Søgne Basin than in the Tail End Graben. The average sandstone porosity of 19% is supported by conventional core analysis showing porosities 15–27% with the exception of likely carbonate-cemented sandstones having low porosities (3–6%) and permeabilities. Porosities up to 25 % and a permeability of minimum 81 mD have been documented for the 3/7-7 core (Fig. 7.4). This value lies on the porosity–permeability trend of the best reservoir sandstones in the Heno Formation from Diamant-1 and Gert-1 cores and hence seems to be slightly higher than the trend for the 3/7-6 core.

### 7.3 Discussion

The highest porosities and permeabilities occur in the Tail End Graben in the Gita-1 well, not the Xana-1 well, and in the Søgne Basin in the 3/7-7 well rather than the 3/7-6 well. Microquartz coatings occur on many detrital grains in the sandstones from the Gita-1, 3/7-6 and 3/7-7 wells and have preserved much of the primary porosity by inhibiting the precipitation of larger quartz overgrowths. One successful permeability measurement was achieved from the 3/7-7 core support a relatively high permeability and porosity, which seems to have a higher permeability than the 3/7-6 core at similar porosity (Fig. 7.4). This variation may be due to a slightly larger grain size in the 3/7-7 compared with the 3/7-6 core (Fig. 7.1). The porosity and permeability is similar to those of the Heno Formation in the Diamant-1 well, which is likewise characterised by abundant microquartz coatings (Fig. 7.4; Weibel et al. in prep.). Reservoir sandstones with exceptionally high porosity and permeability have previously been associated with early microquartz coatings which inhibited the otherwise succeeding macroquartz precipitation (e.g. Vagle et al. 1994; Aase et al. 1996; Jahren and Ramm 2000; Maast et al. 2011). Siliceous sponge spicules has been suggested as an important silica source, as the biogenic opal-A becomes unstable during burial and results in oversaturation with respect to opal-CT or quartz (e.g. Hendry and Trewin 1996; Nielsen et al. 2019). Siliceous sponge spicules are common in the Farsund Formation gravity flow sandstones encountered along the Ringkøbing–Fyn High, e.g. in the Tabita-1, NW Adda-1 and Deep Adda-1 wells (Nielsen et al. 2015).

In the sandstones from the Xana-1 well, the porosity is mainly secondary after feldspar grain or carbonate clast dissolution. This mouldic porosity after feldspar grains is surrounded by illitic clay coatings (Fig. 7.2A, C) and hence the permeability is relatively low due to poor connection between the large pores. The secondary porosity seems to have formed after dissolution of K-feldspar, whereas albite remains little altered or is healed due to later albite precipitation. The stability of albite during late diagenesis is evident from albite crystals commonly forming on small remnants of intensively dissolved feldspar grains (Fig. 7.2A).

Interlocking quartz overgrowths are more common in the Xana-1 well than the Gita-1 well. Crypto- and microcrystalline quartz coatings cover many detrital quartz in both wells, but have not entirely inhibited macroquartz. Quartz outgrowths occurs in the Gita-1 well where holes in the crypto- or microquartz coatings allow direct contact to the detrital quartz grains. These quartz outgrowths may have expanded into interlocking overgrowths with clearly visible dust rims. The quartz diagenesis may have proceeded longer in the Xana-1 well due approximately 200 m deeper burial compared with the Gita-1 well. The more abundant presence of calcite-cement in the Xana-1 well compared with the Gita-1 well is an additional porosity- and permeability-reducing factor.

Calcite-cemented intervals have by log interpretation in particular been referred to thin sandstone intervals or those adjacent to mudstones. Other calcite-cemented sandstones are associated with abundant calcite clasts and fossil fragments – locally even ooids or oncoids.

## 8. Provenance

### 8.1 Methods

Radiometric U-Pb age dating of detrital zircon and rutile grains were performed by LA-ICPMS (laser ablation inductively coupled plasma mass spectrometry) by the procedure described in Olivarius et al. (this volume). Zircon ages were obtained from 14 samples from Upper Jurassic sediments in the Xana-1, Gita-1, Svane-1/1A, Amalie-1, Stork-1, Gwen-2 and 3/7-7 wells, and 3 of these samples contained rutile grains such that rutile ages could also be obtained from Gwen-2 and 3/7-7. Only the concordant ages are shown in the probability density distributions (Thomsen et al., 2016).  $^{207}\text{Pb}/^{206}\text{Pb}$  ages are used for zircon grains older than 700 million years (Ma), whereas  $^{206}\text{Pb}/^{238}\text{U}$  ages are used for younger zircons, and  $^{206}\text{Pb}/^{238}\text{U}$  ages are used for all rutile grains.

Pb-Pb isotopic analyses of detrital K-feldspar grains were carried out by HR MC-ICPMS (high-resolution multicollector inductively coupled plasma mass spectrometry) by the procedure explained in Olivarius et al. (this volume). Upper Jurassic sandstones were analyzed in 8 samples from the Hejre-2, Jeppe-1, Ophelia-1 and 3/7-7 wells. Only data with one standard error of  $< 0.25$  are plotted.

### 8.2 Results

The age distributions of the rutile versus zircon grains from the Upper Jurassic sediments in the greater Tail End Graben area are significantly different (Fig. 8.1). The zircon age distributions of all the individual samples are so similar that they have been plotted together to show the merged provenance signal that characterizes these sediments, and the same is the case for the rutile age distributions. The merged zircon age distribution comprises a large amount of age data whereas the rutile age distribution includes much fewer ages, but still it is evident that some of the age populations seen in the zircon age distribution are absent in the rutile age distribution. These comprise the Archean, Baltica/Laurentia (formation age), Cadomian and Variscan age populations. Caledonian ages dominate the rutile age distribution, whereas Grenvillian/Sveconorwegian and Paleoproterozoic ages constitute small populations. It is noteworthy that these three age populations have older rutile peak ages than the corresponding zircon peak ages. The primary formation age of the rutile grains is calculated to be 496-486 Ma (Olivarius et al., this volume).

The stratigraphic correlation between the Xana-1 and Gita-1 wells in the Tail End Graben divides the Upper Jurassic sandstones into a number of gravity-flow units that can be distinguished in both wells (Fig. 8.2). The gravity-flow sandstones are all included in the Gita Member, which is divided into lower, middle and upper sections. Each of these sections were sampled for zircon geochronology in both the Xana-1 and Gita-1 wells, where cuttings were sampled over a depth interval to obtain sufficient material (Fig. 8.2). Some differences in the zircon age distributions occur between the lower, middle and upper sections of the Gita Member, and most of these variations are identified both in the Xana-1 and Gita-1 wells such that certain features in the zircon age distributions characterize each of the lower, middle and upper sections. These characteristics may help correlate the lower, middle and upper sections of the Gita Member in other wells; however, the variations in the zircon age distributions are not large.

The lower Gita Member samples from Xana-1 and Gita-1 have larger contents of Archean zircons than the rest and also the Cadomian, Caledonian and Variscan ages are pronounced compared to the other samples. Furthermore, the dominant age peaks correspond to each other. The middle Gita Member samples from

Xana-1 and Gita-1 have more restricted age distributions with strong dominance of Proterozoic age populations and a comparable distribution of peak ages. The upper Gita Member samples from Xana-1 and Gita-1 resemble the lower Gita Member samples more than the middle Gita Member samples, but with fewer Archean ages and a younger distribution of Baltica/Laurentia formation ages and Grenvillian/Sveconorwegian ages.

The Pb isotopic signatures of the K-feldspar grains in the Upper Jurassic sandstones show that they originate from several source areas (Fig. 8.3). An Archean source is found for some of the K-feldspars from the 3/7-7 and Hejre-2 wells and also for a few grains from Jeppe-1, whereas slightly more grains from 3/7-7 and Hejre-2 have a Proterozoic II age and many grains from Jeppe-1 fall in this category. A few grains from 3/7-7 fall evidently in the Proterozoic I category, whereas the few grains with ages that overlap with the Avalonian source may rather belong to another category. Few grains from 3/7-7, Hejre-2 and Jeppe-1 are of Variscan affinity. The few analyzed K-feldspar grains from Ophelia-1 fall both within the Proterozoic I and II categories. However, the high frequency of data points all across the Proterozoic II domain makes it most likely that the overlapping grains belong to this category. Some of the grains from especially Jeppe-1 fall outside the basement domains defined by Tyrrell et al. (2007).

### 8.3 Discussion

The Variscan and Cadomian zircon age populations (Fig. 8.1) show that some of the sediment is derived from the Variscan Orogen in central Europe. This sediment was probably transported northwards by aeolian and fluvial processes during the Triassic continental setting (McKie and Williams, 2009), which evidently happened in the eastern part of the basin (Olivarius et al., 2017). Thus, reworking of Triassic sediment has contributed to the deposition of the studied Upper Jurassic sediments, and Triassic sediments were exposed on the Mid North Sea High, the Heno Plateau, the Mandal High and the Ringkøbing-Fyn High at the time so one or several of these areas could have sourced the sediment.

The dominance of the two zircon age populations in the 1.7-0.9 Ga interval (Fig. 8.1) show that most of the zircons are derived either from Baltica to the northeast or from Laurentia to the northwest since the formation ages and Sveconorwegian/Grenvillian metamorphic overprint ages are similar. However, the presence of Archean zircons and the pronounced Caledonian age peak reveal that a large part of the zircons must originate from the northwest so only a smaller part can potentially stem from Baltica. The zircons may have been transported from Laurentia to the North Sea during the Devonian or Carboniferous and reworked into Permian and Triassic sediments. Thus, the zircon ages cannot be used to show which sediments in the Tail End Graben are derived from east versus west of the basin, although the 1.5 Ga zircon age peak found in the Stork-1 sandstone may point to a sediment supply from exposed basement at the western end of the Ringkøbing-Fyn High (Olivarius et al., this volume). However, a northern source of the sediment via fan deposition in the Tail End Graben can be rejected since the Fennoscandian Shield was not a major sediment source of these sediments.

The stratigraphic trends observed in the distribution of zircon ages show that although much of the sediment has been reworked one or several times and is derived from multiple source areas, still the individual pulses of gravity-flow sand into the Tail End Graben were of slightly different composition. These differences are recognized both in the Xana-1 and Gita-1 wells such that each of the lower, middle and upper sections of the Gita Member correlate between the wells (Fig. 8.2). This explains why chemostratigraphic correlation between the wells is possible and it shows that the supplied sediment has not been completely homogenized prior to its Late Jurassic deposition or that the pulses of sediment supplying each of the gravity-flow units

were sourced from different parts of the Mandal High or Heno Plateau. The absence of Variscan zircons in the middle samples indicates perhaps that reworking of Triassic sediment was not happening during Kimm-3a and lower part of Kimm-3b.

The results of the K-feldspar Pb isotopic signatures are of great importance since they reveal that some of the grains have been sourced by distant Archean and Variscan basement (Fig. 8.3), which implies that the K-feldspar grains can survive long-distance transport without complete breakdown. Furthermore, this shows that zircon age dating is a valuable tool for provenance studies in the North Sea since the provenance interpretation made on this basis does not only apply to the very stable zircon grains but presumably also to the bulk part of the sediment. The relative proportion between Archean and Proterozoic grains is different for zircon and K-feldspar, which shows that the relationship is complex and it depends on a number of factors such as mineral fertility in the source rocks and hydraulic sorting during transport (Melusà et al., 2016).

#### 8.4 Conclusion

The provenance interpretation reveals that the Upper Jurassic sediments in the greater Tail End Graben area are derived from reworking of older sediments besides a possible small input from local basement. Triassic sandstones have supplied some of the sediment and contributions from Permian sandstones and volcanics and Carboniferous sandstones are also plausible. Local erosion of such lithologies on intra-basinal highs has sourced the sediment, which has slightly different provenance signal in the different gravity-flow pulses and this can be used as a stratigraphic indicator.

## 9. Source rock

A review is made of the source rock quality and maturity, based on an integrated sequence stratigraphic-geochemical investigation to identify and better understand the effective source rocks in the DCG (Schovsbo et al., this volume). The review is based on 5556 Rock Eval pyrolysis data and total organic carbon measurements from 78 wells, and 1175 vitrinite reflectance measurement from 55 wells representing the most data extensive study to date. The thermal maturity is evaluated through 1D- basin modelling and the key driving factors on the position of the top of the oil window such as temperature and pressure are presented.

Statistical parameters (average, median, low (P90) and high (P10)) describing the distribution of TOC, HI and  $T_{max}$  are presented for the Lower Jurassic marine Fjerritslev Formation, the Middle Jurassic Bryne, Lulu, and Middle Graben terrestrial-paralic formations and the Upper Jurassic-lowermost Cretaceous marine Lola and Farsund formations in six areas in the DCG (Table 9.1). A further stratigraphic breakdown of the source rock richness in the Farsund Formation is made for selected Volgian sequences and for the lowermost Cretaceous Ryazanian sequence (Fig. 9.1).

In the DCG, additional contribution are from Middle Jurassic coaly units of the Bryne and Lulu formations, whereas unknown contribution may come from other source rocks including the Upper Jurassic Lola Formation, the Lower Jurassic Fjerritslev Formation, Permian shales and Carboniferous coals (Damtoft et al., 1987; 1992; Petersen & Nytoft, 2007; Petersen et al., 2016).

The study document that the Middle Jurassic Bryne, Lulu and Middle Graben formations and the whole Farsund Formation throughout the DCG are good to very good source rocks with a mixed oil-gas generative potential. The Bo Member located in the uppermost Farsund Formation (Volg-4 and Ryaz-1 sequences) comprises exceptionally TOC- and oil-rich source intervals. These very rich units are characterized by being both laterally and stratigraphically quite variable reflecting the depositional depth and degree of condensation (Fig. 9.1).

Two main oil types occur in the DCG. A fully marine type sourced by the Farsund Formation (type 1) and a terrestrial influenced oil type (Type 2 and 3) sourced by the fluvatile-paralic source rocks of the Middle Jurassic. In the Tail End Graben the marine oil type 1 from Chalk and Paleogene reservoirs bear geochemical similarities to a contribution from the topmost Farsund Formation, the Bo Member, that is particularly rich and mature here (Fig 9.2). Additional oil contribution from the Middle Jurassic is also documented and thus also Mid Jurassic sourced oils are present here as well as it is common in the Søgne Basin (Fig. 9.2). These terrestrial influenced oil types are also characterised by being much more mature than the marine Jurassic oils. This again suggests contributions from both shallow and deep Jurassic sources in the Tail End Graben

Oil in the Salt Dome Province is of a subtype characterised by being very immature and lack the geochemical signature from the Bo Member. This oil type mostly originated from deeper levels in the Farsund Formation.

Two maturity maps of the upper and middle part of the Farsund Formation, respectively, and one representing the Lower to Middle Jurassic formations show that the uppermost Farsund Formation are immature in the southern part of the Salt Dome Province and in the late mature in and near the Tail End Graben and the Søgne Basin (Fig. 9.3). The middle part of the Farsund Formation are immature in local areas, but are post mature in the Tail End Graben and in the Rosa Basin within the Salt Dome Province. The Lower Jurassic and the Middle Jurassic Bryne, Lulu and Middle Graben formations are gas prone in most of the DCG.

1-D petroleum modelling shows that the uppermost source rock interval (Ryaz-1) in deep wells representing the Gertrud, Søgne and Tail End grabens entered the oil window in the late Paleogene reaching the main oil within the last c. 5–10 Ma (Fig. 9.4).

## 10. Basin development of the Tail End Graben

A number of sandy reservoir intervals are found in the Upper Jurassic in the Tail End Graben. Different models for the deposition and origin of the sandy intervals have been proposed, e.g. submarine fan deposits with prograding lobes from the north (Søgne Basin) to the south and turbidite and mass flow deposits shed into the basin from the nearby highs (Heno Plateau and Ringkøbing-Fyn High).

Our study involves bio-, litho- and chemostratigraphic aspects, seismic interpretation, petrophysics and mineralogy in order to verify the origin of the sand and identify good reservoirs.

In the following the basin development and the distribution and origin of the sand are discussed by implementing the results from the seismic interpretation, sequence and biostratigraphy, petrophysical logs and mineralogy/chemostratigraphy.

### 10.1 Depositional environments and palaeogeography

Late Jurassic depositional environments in the studied northern part of the Danish Central Graben ranged from shallow marine shelf, slope, and deeper basinal settings (Fig. 10.1). Accumulation space is often restricted on the shelf resulting in relatively thin, but massive, sand units. Beyond the shelf edge, i.e. on the slope, sand may be found in submarine channels. At the base of the slope, basinal fans may occur at the end of submarine channels. Sand may also be transported further into the basin by turbidity currents. In general, for the basinal setting, sand is more voluminous distributed close to the channels and more sparse distally.

The Upper Jurassic geological setting of the study area comprises a shallow marine area to the west, the Heno- and Gertrud plateau area, and land areas (Mid North Sea High) farther to the west and southwest (Fig. 1.1). Very little data and knowledge exist on the relief of the Ringkøbing-Fyn High in the eastern part of the study area, but it is likely that this area was elevated during the Late Jurassic with regional drainage towards the east (Andsbjerg et al. 2001, Weibel et al. 2010) and local clastic supply towards the west along the complex fault configuration of the Coffe Soil Fault (Bruhn and Vagle 2005). Between the Ringkøbing-Fyn High and the Heno Plateau a deep basin developed – the Tail End Graben - that continues northwards via the Gita Plateau into the Søgne Basin (Fig. 5.3).

The presented high resolution sequence stratigraphic framework in chapter 4.3 form the basis for the series of paleogeographic maps (Figs. 10.2), where two maps illustrate the depositional environments for each identified sequence, as the first map represents the time near the sequence boundary, the lowstand systems tract and transgressive systems tract, while the second map represents the time of maximum flooding and the highstand system tract.

#### *Ox-1*

The Ox-1 sequence is only penetrated in a few of the wells in the study area and is mainly distributed in the Tail End Graben and Søgne Basin (Fig 10.2A, B). It represents the lower part of the BUJ–TEG 10 seismic interval. The Heno Plateau is generally devoid of Oxfordian sediments except in the southeastern part, where deposition occurred in a shallow marine shelf environment (e.g. Elly-2, Ravn-2). In the Gita-1 and

Amalie-1 wells (i.e. on Gita Plateau) thin coal stringers are present in the lower parts of the sequence and the depositional environment is interpreted as a prograding shelf. The upper part of the Ox-1 sequence is characterized by a more deep marine setting with deposition of thick clay units in the Amalie-1, 3/7-7, Nora-1, Lulu-2 (e.g. Figs 4.15–16). The base of the slope is identified based on these wells and on the isopack map showing the thickness of the succession between the base of the Upper Jurassic (BUJ) and the TEG10 seismic horizons (Fig. 5.14A). The deep marine environment is present in a sub-triangular outline in the southern part of the Tail End Graben, extending from south of the Elin-1 well to the area west of the Tabita-1 well. A marine environment is recorded in the Norwegian part of the Søgne Basin (Mellere et al. 2016).

#### *Kimm-1a, b*

The sequences represent the upper part of the BUJ–TEG10 and the TEG10–15 seismic intervals. Deposition is dominated by marine mudstone in a connected/coherent deep marine basin extending throughout the Tail End Graben and Søgne Basin (Figs. 10.2C–F). Prominent gravity flow sandstone units of the Amalie Member (see definition in Appendix 1) were deposited in the eastern part of the Gita Plateau (Amalie-1) and possibly along the eastern part of the Tail End Graben. The sand was probably derived locally from the Ringkøbing-Fyn High. The three marked sand units in the Amalie-1 well has a total thickness of 20 m and represent submarine channels on the slope/submarine fans (Figs. 4.2, 10.2C). The sand units in the Svane-1 well (lower part of the Svane Member, Appendix 1) probably represent the distal parts of a submarine fan system derived from the Heno Plateau as indicated by seismic attributes (Fig. 5.14A,B) and geochemical data (Fig. 4.20). The deposition of the sand may be linked with base level falls, progradation of sandy shelf and/or fault-induced sandy shelf collapse, in a complex intermix of eustatic sea level change and tectonic activity.

The eastern part of the Heno Plateau (Gwen-2 area) gets transgressed and represents a shallow shelf with predominantly sandy deposition (Figs 4.2, 10.2C–F). The western part of the Heno Plateau was probably still an emerged area.

#### *Kimm-2a, b*

The sequences represent the TEG15–20 seismic interval. The Heno Plateau gets fully transgressed in this interval, and a sandy back barrier depositional environment was established in the Gert-1 area in the northwestern part of the study area, forming the southernmost part of the Feda Graben (Johannesen et al. 2010) (Fig. 10.2H).

During the Kimm-2a HST, gravity flow sand deposition began in the Xana-1 and Gita-1 wells. Based on the paleogeography as well as seismic attributes analysis it is likely that the sediments are transported from the Mandal High area to the Gita Plateau (Fig. (Figs. 5.14C; 10.2H). Also in the Svane-1 well gravity flow sand is present, probably sourced from the Heno Plateau (Fig. 10.2H).

Prominent erosion/by-pass occurred during base level falls with formation of pebbly sand and conglomerates (e.g. Gwen-2, Hejre-2) and with associated deposition of thin lowstand fan systems in the Svane area in the central part of the Tail End Graben and on the Gita Plateau, respectively (Figs 10.2I). The seismic data show the formation of small half grabens creating a series of depocentres parallel to the Coffee Soil Fault (Fig 5.22), which controlled the distribution of sand deposition. Potential lowstand

submarine fans/slope aprons were sourced from the Ringkøbing Fyn-High, confirming the interpretation of Bruhn and Vagle (2005). The area represented by the Amalie-1 well received only small amounts of sand in this interval (Fig 4.15). In the Svane-1 well the sand units seem more stacked, as the GR pattern fluctuates (Fig 4.14). The sand units here are approximately 8 m thick and are also interpreted to represent a distal part of a submarine fan system (Figs 10.2I).

The map representing the Kimm-2b HST illustrates the onset of subsidence of the area between the Mandal High and the Heno Plateau, indicated by fine-grained sediments in e.g. the Hejre-2 well (initial formation of the hereafter termed Gertrud Graben, Fig. 10.2J). On the Heno Plateau the log shape of the Jeppe-1, Q-1 and Gwen-2 wells indicate a prograding coastal region, as these sediments are becoming increasingly more coarse grained (Figs. 4.14; 4.15).

### *Kimm-3a, b*

The sequences correspond to the seismic interval TEG20–30. During deposition of the LST and the TST of the Kimm-3a sequence, a sandy, shallow shelf environment prevailed on the Heno Plateau, and associated prominent sandy lowstand fans were deposited in the western part of the Gita Plateau area (Gita-1, Xana-1 wells) and also in the Svane area in the central part of the Tail End Graben (Fig 10.2K). Potential sand units could further be present as slope aprons along the Ringkøbing-Fyn High within this sequence (e.g. Fig 5.15, 10.2K). Thick sand units are found in the Xana-1 and Gita-1 wells within the Kimm-3a LST. These are interpreted to have been sourced from the Mandal High area. Comparing the log shapes of the Xana-1 and Gita-1 wells show that the sand units in Gita-1 are thicker and more homogenous, as the GR fluctuated much more in the Xana-1. In addition, the net-to-gross for this interval is 51% for Gita-1 and 46% in Xana-1 (Table 6.1), which indicates that the Gita-1 well probably is located more centrally in the submarine fan system compared to Xana-1, as also illustrated on the paleogeographic map for Kimm-3A LST-TST (Fig. 10.2K). The submarine fan system in the Svane area is interpreted to have been sourced from the Heno Plateau based on the geochemical data and the seismic attribute map (Figs. 4.20; 5.14D; 5.16; 5.17).

Thick sand units have also been found in the 3/7-6 and 3/7-7 wells located in the Søgne Basin, northeast of the Mandal High, having similar log shapes as observed in Gita-1 (Fig. 4.16). These units have also been interpreted as representing submarine fans, deposited near the base of the slope. As the net-to-gross ratio is higher in the 3/7-6 well compared to the 3/7-7 well, it could indicate that the latter is located on the fringe of the fan, while the former is located more centrally. Due to the fact, that 3/7-6 is located further away from the Mandal High area and further to the north, it is likely that the sediments were transported from the north, as indicated by the outline of the fan on the paleogeographic map (Fig. 10.2K).

During deposition of the Kimm-3a TST and HST, fine-grained sediments were deposited in the Hejre-1 and -2 wells, indicating that the Gertrud Graben has developed into a deep marine depositional basin (Figs 4.15, 10.2L). On the Heno Plateau, the log shapes indicate proximity to the coast, as the sediments contain clean sand.

Deposition of submarine fans occurred in the Kimm-3b sequence on the Gita Plateau and in the Søgne Basin (Figs 4.16, 10.2M, N), although, during this time interval, it seems that the central part of the Gita Plateau fan is represented by the Xana-1 well, while the Gita-1 well represents the fringe of the fan.

#### *Kimm-4 – Ryaz-1*

These sequences correspond to the seismic interval TEG 30–BCU. As the study area gets flooded at the end of Kimm-4, the depositional environment becomes deep marine, with clays being deposited (Fig. 10.20). Only along the Ringkøbing–Fyn High there seem to be high-energy deposition, where shallow marine sand are recorded in the Volg-1 sequence in the Stork-1 well (Fig 4.14). The well is located in a detached block related to a back-stepping in the Coffee Soil Fault that bounds the Tail End Graben towards east. The Volgian intensification of tectonic activity in this region is associated with deep subsidence of the Gertrud and Tail End Grabens.

## 11. Discussion

### 11.1 Prospectivity of the Tail End Graben

The aim of this study was to re-evaluate the remaining hydrocarbon potential in the Tail End Graben, primarily based on the results from the recent Gita-1, Xana-1 and Svane-1/1A wells.

Shows of hydrocarbons have been found in Upper Jurassic sandstones in a number of wells in the Tail End Graben area but only considered as discoveries in the Xana-1 and Svane-1/1A wells. The Xana and Svane discoveries represent two different, separate structures. The Xana structure is located to the north across the Amalie Cross Fault (the boundary between the Søgne Basin and the Tail End Graben). The Svane structure is located in the basin center of the Tail End Graben. Both the Xana-1 and Svane-1/1A wells have been abandoned due to poor reservoir quality and limited volumens of hydrocarbons. Furthermore, the HPHT conditions in the Svane-1/1A well resulted in severe technical challenges. However, data from the two discoveries provide important information which can be used to evaluate the prospectivity in the Tail End Graben. The two discoveries represent different structural and depositional settings and show different reservoir properties.

#### *11.1.1 Reservoir properties in the Xana and Svane discoveries*

The Xana structure is located along the Amalie Cross Fault and comprises a number of Upper Kimmeridgian sandstone intervals. These sandstones have been drilled by the Xana-1 well located south of the Cross Fault, and by the Gita-1 well located in the northern part of the structure, north of the Amalie Cross Fault. The top of the structure is located at approximately 4350 m's depth in Gita-1 and at 4625 m's depth in Xana-1.

The Upper Kimmeridgian gravity flow sandstones in the Gita-1 and Xana-1 wells have been interpreted to be part of the same submarine fan system and show comparable sand-thicknesses. However, the reservoir properties indicate a division of the structure into a northern and southern part separated by the Amalie Cross Fault. Data from the present study indicates that the porosities in the oil-bearing sandstones in the Xana-1 well generally are low, with average porosity up to 10 %. The Gita-1 well shows better reservoir properties (higher net sand percentage and an average porosity up to 15 %), but this well was dry.

The Svane structure is located on an inversion ridge in the basin center of the Tail End Graben and comprises thin-bedded Upper Kimmeridgian gravity flow deposits. The top of the Svane structure is located at approximately 5400 m. The porosity in the sandstone is generally low (average porosities below 10%).

A comparison of the Xana and Svane discoveries reveal some differences in the reservoir properties. The slight difference in porosity may reflect different depths of burial, where the deep seated Svane-1/1A well exhibits the lowest porosities. The depth of burial influences the diagenesis in several ways, e.g. by the complex interaction of increased dissolution of feldspar with increased temperature on one hand and on the other hand increased precipitation of albite. Such diagenetic changes makes it difficult to predict the porosities in the reservoirs.

The Upper Kimmeridgian sands in the Gita-1, Xana-1 and Svane-1/1A wells correlate stratigraphically and have previously been interpreted to be part of the same prograding fan system. In this model, the Xana/Gita wells were interpreted to be associated with the proximal part of the fan system whereas the

Svane well was associated with the distal part of the fan system. In addition to the differences in burial depth, these differences in depositional facies may be responsible for the differences in reservoir parameters.

### *11.1.2 New results and interpretations*

The overall conclusion of the present study indicates that the Tail End Graben during the Upper Jurassic formed part of a rift system dominated by open marine claystones and siltstones interbedded with sandstones related to gravity flows. The rift system was surrounded by plateaus and highs which acted as potential source-areas for the reservoir sandstones. Upper Kimmeridgian back barrier and shallow marine sandstones are found on the Heno Plateau, and floodplain deposits (found as transgressive lag clasts) have been found as far east as in the Gwen-2 well, indicating that land-areas existed close to the Tail End Graben at this time. Deep marine gravity flow sandstones have been found in the Tail End Graben (Amalie-1 and Svane-1/1A) and on the Gita Plateau (Gita-1 and Xana-1), where they seem to occur in separate lobal systems.

Three new lithostratigraphic units are defined herein; 1) The Svane Member comprising the Upper Kimmeridgian gravity-flow sandstone interval in the Svane-1/1A well located in the Tail End Graben. 2) The Gita Member comprising the Upper Kimmeridgian gravity-flow sandstone intervals in the Gita-1 and Xana-1 wells, located in the transitional area between the Søgne Basin and the Tail End Graben. The Gita-1 well is located in the northern part of the Xana structure, north of the Amalie Cross Fault while the Xana-1 well is located south of the Amalie Cross Fault. 3) The Amalie Member comprising the Lower Kimmeridgian sandstone interval in the Amalie-1 well located in the Danish part of the Søgne Basin.

Additional deep marine gravity flow sandstones may be present in other parts of the Søgne Basin and Tail End Graben.

The new geochemical data indicate that the Lower Kimmeridgian gravity flow deposits in the Amalie-1 well was sourced from the Ringkøbing-Fyn High. Our study further demonstrates clear differences in the geochemical composition of the Upper Kimmeridgian reservoir sand in the Xana- and Svane areas, respectively, which not only relates to depositional facies variations (proximal contra distal parts of a fan system) but indicate two different source areas for the sands. Based on this information combined with the basin history as outlined above, we suggest that the sand in the Xana Field, the Gita Member, are associated with a source area from the Mandal High to the north, while the geochemical composition of the sand in Svane-1/1A, the Svane Member, are comparable with the sand deposited on the Heno Plateau. This suggests the presence of at least two different Upper Kimmeridgian fan-systems with different sediment sources.

The presence of several fan systems is in accordance with our interpretation of the basin development. It is however difficult to map out the fan systems because these often are associated with the basin margins located in complex fault zones.

The indications of more than one depositional fan system opens up for the possibility of the presence of new prospects. The palaeogeographical interpretations based on the present study suggest the possibility for the presence of further sandstone deposits, e.g. deltas to shallow marine environments, incised valleys, slope aprons and submarine fans, in the transition zone between the Heno Plateau area and the deep Tail End Graben. Equal depositional sand systems may occur along the complex Coffee Soil Fault.

The known sandstone reservoirs, drilled in the Amalie-1, Gita-1, Xana-1 and Svane-1 wells show variable net sand values and -ratios up through the Kimmeridgian succession;

- In the interval from BUJ-TEG10 (Ox-1 – lower Kimm-1), the net sand value is close to 20 m in the Amalie-1 well, and 37 m in Gita-1. The Svane-1/1A and Xana-1 wells did not reach this interval.
- In the interval TEG10-TEG15 (Kimm-1) the net sand value in Svane-1 is close to 44 m.
- In the interval TEG15-TEG20 (Kimm-2a,b), the net sand is between 30-44 m in the Gita-1, Xana-1 and Svane-1 wells.
- In the interval TEG20-TEG25 (Kimm-3a), the net sand increases to 50-68 m in the Gita-1 and Xana-1 wells, whereas the net sand in Svane-1 decreases to 30 m. In Amalie-1 the net sand is 10 m.
- In the interval TEG25-TEG30 ( Kimm-3b – lowermost Kimm-4), the net sand value is approximately 60 m in both Gita-1 and Xana-1.

The net sand values in Gita-1 and Xana-1 are very similar, whereas the net sand in Amalie-1 is distinctly lower for each of the intervals. The net sand values in Amalie-1 generally does not exceed 19 m in the studied succession. The variations in net sand values in the Gita/Xana wells on one hand and the Svane-1 well on the other hand does not correlate. The highest net sand values in the Gita/Xana wells are found in the intervals TEG15-TEG20, TEG20-TEG25 and TEG25-TEG30, while in Svane-1 the highest values are found in the intervals TEG10-TEG15, TEG15-TEG20 and TEG20-TEG 25. Relatively high net sand values (of approximately 50-60 m) and ratios close to 50% are found in the Gita-1 and Xana-1 wells, in the interval from TEG20-TEG30 (Kimm-3a-Kimm-3b).

The best sandstone reservoirs within the gravity flow fan systems should be found in the proximal parts of the fans, where the thickest sand-layers, the largest grainsizes and the shallowest burial depths are found. Furthermore, the sediment source area is important, e.g. mature sediments with low feldspar content are generally preferable. In the deeper parts of the basin, the diagenetic alterations generally result in decreased porosities and thus in poorer reservoir properties.

The distribution of Upper Jurassic sand in the Tail End Graben area is not very well understood. Very few wells penetrate the Upper Jurassic succession and detailed seismic mapping is hindered by complex fault zones. Our study further indicates that the previous models for deposition of gravity flow fan systems may need revision, as the new data suggest the presence of several fan systems with different source areas (Fig. 11.1).

### *11.1.3. Source rock*

Mature source rocks are present in all of the Tail End Graben area. The Middle Jurassic Bryne, Lulu and Middle Graben formations, and the whole Farsund Formation are good to very good source rocks throughout the Tail End Graben with a mixed oil-gas generative potential. The Bo Member in the uppermost Farsund Formation comprises an exceptionally TOC- and oil-rich source interval. However, because the Upper Volgian - Ryazanian Bo Member source rock seldom are in juxtaposition with the Kimmeridgian sandstones, we do not consider it likely that the Bo Member source has contributed to the filling of these sandstone reservoirs. Instead, the Middle Jurassic and the lower Farsund formations are considered as source rocks for the hydrocarbons encountered in the Xana-1 and Svane-1/1A wells.

## 12. Conclusion

In spite of the rather poor reservoir properties in the two discoveries, Xana and Svane, in Upper Kimmeridgian gravity flow sandstones, we consider the Tail End Graben to be an interesting basin for future hydrocarbon exploration. Mature source rock is present in all of the graben area. The present study reveals that several fan systems comprising gravity flow sandstones are present, at different stratigraphic levels and with different sand source areas. These fan systems are not well understood and explored. In addition to more fan systems, also incised valleys, shallow marine and shelf apron reservoir sandstone deposits may be present along the basin margins.

## References

- Aase, N. E., Bjørkum, P. A., Nadeau, P. H., 1996. The effect of grain-coating microquartz on preservation of reservoir porosity. *AAPG bulletin* **80**, 1654–1673.
- Andersen, C., Olsen, J.C., Michelsen, O., Nygaard, E., 1982. Structural outline and development. In: Michelsen, O. (ed.): *Geology of the Danish Central Graben. Danmarks Geologiske Undersøgelse, Serie B*, **8**, 9–26.
- Andsbjerg, J. & Dybkjær, K., 2003. Sequence stratigraphy of the Jurassic of the Danish Central Graben. In: Ineson, J.R. & Surlyk, F. (eds): *The Jurassic of Denmark and Greenland. Geological Survey of Denmark and Greenland Bulletin*, **1**, 301–348.
- Andsbjerg, J., Nielsen, L.H., Johannessen, P.N., Dybkjær, K., 2001. Divergent development of two neighbouring basins following the Jurassic North Sea doming event: the Danish Central Graben and the Norwegian-Danish Basin. In: Martinsen, O.J. & Dreyer, T. (eds): *Sedimentary environments offshore Norway – Palaeozoic to Recent. NPF Special Publication*, **10**, 175–197.
- Bjørlykke, K., Jahren, J., 2015. Sandstone and sandstone reservoirs. In: Bjørlykke, K. (Ed.) *Petroleum geoscience: From sedimentary environments to rock physics*. Springer, 119–150.
- Bruhn, R., Vagle, K., 2005. Relay ramp evolution and mass flow deposition (Upper Kimmeridgian – Lower Volgian) in the Tail End Graben, Danish North Sea. *Basin Research*, **17**, 551–567.
- Cartwright, J., 1987. Transverse structural zones in continental rifts – an example from the Danish sector of the North Sea. In Brooks, J. & Glennie, K.W. (eds.), *Petroleum Geology of North West Europe*. Graham & Trotman, 441–453.
- Damtoft, K., Nielsen, L.H., Johannessen, P.N., Thomsen, E., Andersen, P.R., 1992. Hydrocarbon plays of the Danish Central Trough. In: Spencer, A.M. (ed.), *Generation, accumulation and production of Europe's hydrocarbons II. Special Publications of the European Association of Petroleum Geoscientists*, **2**, Springer, Berlin, 35–58.
- Gawthorpe, R.L., Leeder, M.R., 2000. Tectono-sedimentary evolution of active extensional basins. *Basin Research* **12**, 195–218.
- Gowers, M.B., Sæbøe, A., 1985. On the structural evolution of the Central Trough in the Norwegian and Danish sectors of the North Sea. *Marine and Petroleum Geology*, **2**, 298–318.
- Hallam, A., Sellwood, B.W., 1976. Middle Mesozoic sedimentation in relation to tectonics in the British area. *Journal of Geology*, **84**, 301–321.
- Ineson, J.R., Bojesen-Koefoed, J.A., Dybkjær, K., Nielsen, L.H. 2003. Volgian–Ryazanian ‘hot shales’ of the Bo Member (Farsund Formation) in the Danish Central Graben, North Sea: stratigraphy, facies and geochemistry. In: Ineson, J.R. & Surlyk, F. (eds): *The Jurassic of Denmark and Greenland. Geological Survey of Denmark and Greenland Bulletin*, **1**, 403–436.
- Japsen, P., Britze, P., Andersen, C., 2003. Upper Jurassic – Lower Cretaceous of the Danish Central Graben: structural framework and nomenclature. In: Ineson, J.R. & Surlyk, F. (eds): *The Jurassic of Denmark and Greenland. Geological Survey of Denmark and Greenland Bulletin*, **1**, 233–246.

- Jensen, T.F., Holm, L., Frandsen, N., Michelsen, O., 1986. Jurassic – lower Cretaceous lithostratigraphic nomenclature for the Danish Central Trough. *Danmarks Geologiske Undersøgelse, Serie A*, **12**, 65pp.
- Johannessen, P.N., Dybkjær, K., Andersen, C., Kristensen, L., Hovikoski, J., Vosgerau, H., 2010. Upper Jurassic reservoir sandstones in the Danish Central Graben: new insights on distribution and depositional environments. In: Vining, B.A. & Pickering, S.C. (eds): *Petroleum Geology: From mature basins to new frontiers*. Proceedings of the 7<sup>th</sup> Petroleum Geology Conference. Geological Society London, 127–143. doi: 10.1144/0070127.
- Koch, J.-O., Holm, L., Michelsen, O., 1982. Jurassic. In Michelsen, O. (ed.), *Geology of the Danish Central Graben*. *Danmarks Geologiske Undersøgelse, Serie B*, **8**, 37–454.
- Korstgård, J.A., Lerche, I., Mogensen, T.E., Thomsen, R.O., 1993. Salt and fault interactions in the northeastern Danish Central Graben: observations and inferences. *Bulletin of the Geological Society of Denmark*, **40**, 197–255.
- Maast, T. E., Jahren, J., Bjørlykke, K. 2011. Diagenetic controls on reservoir quality in middle to upper Jurassic sandstones in the South Viking Graben, North Sea. *AAPG Bulletin* **95**, 1937–1958.
- Malusà, M.G., Resentini, A., Garzanti, E., 2016. Hydraulic sorting and mineral fertility bias in detrital geochronology. *Gondwana Research* **31**, 1–19.
- Mattern, F., 2005. Ancient sand-rich submarine fans: depositional systems, models, identification, and analyses. *Earth Science Reviews*, **70**, 167–202.
- McKie, T., Williams, B., 2009. Triassic palaeogeography and fluvial dispersal across the northwest European Basins. *Geol. J.* **44**, 711–741.
- Michelsen, O., Frandsen, N., Holm, L., Jensen, T.F., Møller J.J., Vejrbæk, O.V. (1987). Jurassic-Lower Cretaceous of the Central Trough; depositional environments, tectonism and reservoirs. *Danmarks Geologiske Undersøgelse, Serie A*, **16**, 45pp.
- Michelsen, O., Nielsen, L.H., Johannessen, P.N., Andsbjerg, J., Surlyk, F., 2003. Jurassic lithostratigraphy and stratigraphic development onshore and offshore Denmark. In: Ineson, J.R. & Surlyk, F. (eds): *The Jurassic of Denmark and Greenland*. Geological Survey of Denmark and Greenland Bulletin, **1**, 147–216.
- Mitchum, R.M., Vail, P.R., Sangree, J.B., 1977. Seismic stratigraphy and global changes of sealevel, Part 6: Stratigraphic interpretation of seismic reflection in depositional sequences Application of Seismic Reflection Configuration to Stratigraphic Interpretation Memoir, **26**, 117–133.
- Møller, J.J., 1986. Seismic structural mapping of the Middle and Upper Jurassic in the Danish Central Trough. *Danmarks Geologiske Undersøgelse, Serie A*, **13**, 40pp.
- Møller, J.J. & Rasmussen, E.S., 2003. Middle Jurassic – Early Cretaceous rifting of the Danish Central Graben. In: Ineson, J.R. & Surlyk, F. (eds): *The Jurassic of Denmark and Greenland*. Geological Survey of Denmark and Greenland Bulletin, **1**, 247–264.
- Nielsen, M.T., Weibel, R., Friis, H., 2015. Provenance of gravity flow sandstones from the Upper Jurassic-Lower Cretaceous Farsund Formation, Danish Central Graben, North Sea. *Marine and Petroleum Geology*, **59**, 371–389.

Nielsen, M.T., Weibel, R., Therkelsen, J., Friis, H., submitted. Distribution of porosity-preserving microquartz coatings in sandstones, Upper Jurassic Danish Central Graben. Review of Survey Activities 2018.

Normark, W.R., 1970. Growth patterns of deep-sea fans. American Association of Petroleum Geologists Bulletin, **54**, 2170–2195.

Normark, W.R., Hess, G.R., Stow, D.A.V., Bowen, A.J., 1980. Sediment waves on the Monterey Fan levee: a preliminary physical interpretation. Marine Geology, **37**, 1–18.

Norske shell A/S. 1997. Final well report. Well 3/7-6. PL 147. NESP 97-02, 32p.

Olivarius, M., Friis, H., Kokfelt, T.F., Wilson, R. 2015. Proterozoic basement and Palaeozoic sediments in the Ringkøbing–Fyn High characterized by zircon U-Pb ages and heavy minerals from Danish onshore wells. Bulletin of the Geological Society of Denmark, **63**, 29–44.

Olivarius, M., Weibel, R., Friis, H., Boldreel, L.O., Keulen, N., Thomsen, T.B., 2017. Provenance of the Lower Triassic Bunter Sandstone Formation: implications for distribution and architecture of aeolian vs. fluvial reservoirs in the North German Basin. Basin Research **29** (Suppl. 1), 113–130.

Olivarius, M., Knudsen, C., Weibel, R., Lahaye, Y., Thomsen, T.B., Serre, S.H., Jakobsen, F.C., Bjerager, M., Mørk, F., Dybkjær, K., this volume. Combined K-feldspar, zircon, rutile and apatite provenance interpretation, Upper Jurassic sandstones, Danish North Sea.

Petersen, H.I., Nytoft, H.P. Vosgerau, H., Andersen, C., Bojesen-Koefoed, J.A., Mathiesen, A., 2010. Source rock quality and maturity and oil types in the NW Danish Central Graben: implications for petroleum prospectivity evaluation in an Upper Jurassic sandstone play area. In: Vining, B.A. & Pickering, S.C. (eds): Petroleum Geology: From mature basins to new frontiers. Proceedings of the 7<sup>th</sup> Petroleum Geology Conference. Geological Society London, 95–111. doi: 10.1144/0070095.

Rasmussen, E.S., 1995. Structural evolution of the Gert-Mjølner area. Marine and Petroleum Geology, **12**, 377–383.

Ravnås, R. & Steel, R., 1998. Architecture of marine rift-basin successions. American Association of Petroleum Geologists Bulletin, **82**, 110–146.

Rider, M. 1986. The geological interpretation of well logs. Blackie, Halsted Press, New York, 175 pp.

Schovsbo, N., Ponsaing, L., Mathiesen, A., Bojesen-Koefoed, J.A., Kristensen, L., Dybkjær, K., Johannessen, P.N., Jakobsen, F., this volume. Review of quality and maturity of Lower Jurassic to lowermost Cretaceous petroleum source rocks in the Danish Central Graben.

Spathopoulos, F., Doubleday, P.A., Hallsworth, C.R., 2000. Structural and depositional controls on the distribution of the Upper Jurassic shallow marine sandstones in the Fife and Angus fields area. Quadrants 31 and 39, UK Central North Sea. Marine and Petroleum Geology, **17**, 1053–1082.

Stow, D.A.V., Faugeres, J.C., Viana, A., Gonthier, E., 1998. Fossil contourites: a critical review. Sedimentary Geology, **115**, 3–31.

Stow, D.A.V., Piper, D.J.W., 1984. Deep-water fine-grained sediments: facies models. In: Stow, D.A.V., Piper, D.J.W. (Eds.), Fine-Grained Sediments: Deep-Water Processes and Facies. Geol. Soc. London Spec. Publ., 611–646.

Thomsen, T.B., Heijboer, T., Guarnieri, P., 2016. jAgeDisplay: software for evaluation of data distributions in U-Th-Pb geochronology. *Geological Survey of Denmark and Greenland Bulletin* **35**, 103–106.

Tyrrell, S., Haughton, P.D.W., Daly, J.S., 2007. Drainage reorganization during breakup of Pangea revealed by in-situ Pb isotopic analysis of detrital K-feldspar. *Geology* **35**, 971–974.

Underhill, J.R., Partington, M.A., 1993. Jurassic thermal doming and deflation in the North Sea: implications of the sequence stratigraphic evidence. In: Parker, J.R. (Ed.): *Petroleum Geology of the Northwest Europe: Proceedings of the 4<sup>th</sup> Conference*. The Geological Society of London, 337–345.

Vejbæk, O., 1997. Dybe strukturer i danske sedimentære bassiner. *Geologisk Tidsskrift*, **4**, 40pp.

Verreussel, R.M.C.H., Bouroullec, R., Munsterman, D.K., Dybkjær, K. Geel, C.R., Houben, A.J.P. Johannessen, P.N., Kerstholt-Boegehold, S.J., 2018. Stepwise basin evolution of the Middle Jurassic–Early Cretaceous riftphase in the Central Graben area of Denmark, Germany and The Netherlands. *Geological Society, London, Special Publications* **469**, 305–340.

Weibel, R., Keulen, N., 2008. Diagenesis influencing the porosity of Upper Jurassic reservoir sandstones, Danish North Sea. *Geological Survey of Denmark and Greenland Bulletin*, **15**, 9–12.

Weibel, R., Friis, H., Kazerouni, A. M., Svendsen, J. B., Stokkendahl, J. & Poulsen, M. L. 2010. Development of early diagenetic silica and quartz morphologies – Examples from the Siri Canyon, Danish North Sea. *Sedimentary Geology* **228**, 151–170.

Weibel, R., Johannessen, P.N., Dybkjær, K., Rosenberg, P., Knudsen, C., 2010. Chemostratigraphy of upper Jurassic reservoir sandstones, Danish Central Graben, North Sea. *Marine and Petroleum Geology*, **27**, 1572–1594.

Weibel, R., Johannessen, P.N., Dybkjær, K., Rosenberg, P. & Knudsen, C., 2010. Chemostratigraphy of Upper Jurassic reservoir sandstones, Danish Central Graben, North Sea. *Marine and Petroleum Geology* **27**, 1572–1594.

Weibel, R., Nielsen, M.T., Therkelsen, J., Jakobsen, F.C., Bjerager, M., Mørk, F., Mathiesen, A., Johannessen, P.N., Dybkjær, K., this volume. Illite distribution and morphology explaining basinal variations in reservoir properties of Upper Jurassic sandstones, Danish North Sea.

Ziegler, P.A., 1990. *Geological atlas of western and central Europe*. 2<sup>nd</sup> edition, 239pp. Amsterdam: Elsevier for Shell Internationale Petroleum Maatschappij.

## Figures

The figure- and table numbers refer to the number of the chapter in which reference to the figure/table is mentioned for the first time.

*Figure 1.1: Main structural elements of the Tail End Graben area and the location of wells.*

*Figure 2.1: Lithostratigraphy*

*Figure 4.1: Chronostratigraphic chart showing the chronostratigraphic subdivision of the Upper Jurassic and part of the Lower Cretaceous, the boreal ammonite zonation, first- and last occurrences of stratigraphically important dinocyst taxa, the sequence stratigraphic subdivision and the seismic markers defined in the present study.*

*Figure 4.2: Stratigraphic summary chart for Amalie-1.*

*Figure 4.3: Stratigraphic summary chart for Gita-1.*

*Figure 4.4: Stratigraphic summary chart for Gwen-2.*

*Figure 4.5: Stratigraphic summary chart for Hejre-2.*

*Figure 4.6: Stratigraphic summary chart for Jeppe-1.*

*Figure 4.7: Stratigraphic summary chart for Karl-1.*

*Figure 4.8: Stratigraphic summary chart for Lulu-2.*

*Figure 4.9: Stratigraphic summary chart for Nora-1.*

*Figure 4.10: Stratigraphic summary chart for Q-1.*

*Figure 4.11: Stratigraphic summary chart for Stork-1.*

*Figure 4.12: Stratigraphic summary chart for Svane-1/1A/1A.*

*Figure 4.13: Stratigraphic summary chart for Xana-1.*

*Figure 4.14: Log correlation panel of the Upper Jurassic succession trending W-E in the central part of the Danish Central Graben with main lithologies based on Gamma Ray and Density logs, interpreted main sedimentary environments, sequences and systems tracts for the Kimmeridgian interval, and linked with mapped seismic horizons (BUJ, TEG10 –TEG50, BCU). SB Sequence boundary, LST lowstand systems tract, TST Transgressive systems tract, HST high stand systems tract, K Kimmeridgian, Ox Oxfordian, R Ryazanian, V Volgian.*

*Figure 4.15: Log correlation panel of the Upper Jurassic succession trending W-E in the northern part of the Danish Central Graben with main lithologies based on Gamma Ray and Density logs, interpreted main sedimentary environments, sequences and systems tracts for the Kimmeridgian interval, and linked with mapped seismic horizons (BUJ, TEG10 –TEG50, BCU). SB Sequence boundary, LST lowstand systems tract, TST Transgressive systems tract, HST high stand systems tract, K Kimmeridgian, Ox Oxfordian, R Ryazanian, V Volgian.*

Figure 4.16: Log correlation panel of the Upper Jurassic succession trending N–S from Søgne Basin and into the Tail End Graben with main lithologies based on Gamma Ray and Density logs, interpreted main sedimentary environments, sequences and systems tracts for the Kimmeridgian interval, and linked with mapped seismic horizons (BUJ, TEG10 –TEG50, BCU). SB Sequence boundary, LST lowstand systems tract, TST Transgressive systems tract, HST high stand systems tract, K Kimmeridgian, Ox Oxfordian, R Ryazanian, V Volgian.

Figure 4.17: Principal component analysis of geochemical data from the Xana-1 well. **A.** The sand fraction in Xana-1 is positively correlated with quartz ( $\text{SiO}_2$ ), albite ( $\text{Na}_2\text{O}$ ) and zircon (Zr, Hf) and depth, and negatively correlated with clay minerals as observed from the principal component 1 (PC1). The sand fraction is negatively correlated with carbonate abundance (CaO, TOTAL C, volatiles) as given by principal component 2 (PC2). **B.** Sulphides, base metals and MnO and MgO are negatively correlated with clay minerals and sand composition as shown by the third principal component (PC3).

Figure 4.18: Chemical correlation of the wells Xana-1, Gita-1, Svane-1/1A and Nora-1 exemplified by Si/Al, K/Al, Ti/Zr and Ce/Na ratios.

Figure 4.19: Mineralscan show that albite, with minor amounts of K-feldspar in the intermediate sandstones, is the dominant feldspar in the Tail End Gaben, whereas K-feldspar and albite are equally common in the Søgne Basin. Dolomite is most abundant in the lowermost part of the Xana-1 well. Repeated samples show the variation for cuttings samples.

Figure 4.20: Geochemical cross plots of sand- and mudstones from the Gita-1, Xana-1, Svane-1 and Amalie-1 wells showing differences between the Gita-, Svane- and Amalie members;

- A. Zr (corresponding to zircon grains) versus  $\text{Na}_2\text{O}$  (roughly corresponding to albite).
- B. U versus V, both elements affected by redox conditions.
- C. Zr versus  $\text{TiO}_2$  (corresponding to heavy minerals, like Fe-Ti oxides, and clay minerals).
- D. Nb versus Zr, both elements corresponding to heavy minerals.
- E.  $\text{P}_2\text{O}_5$  (corresponding to apatite and other phosphoreous heavy minerals) versus  $\text{TiO}_2$ .
- F.  $\text{K}_2\text{O}$  versus  $\text{Al}_2\text{O}_3$  indicating the relative K-feldspar and illite+muscovite content.

Figure 5.1: Cross section showing the correlation of the sandy intervals from Gita-1 to Svane-1/1A. The seismic line shows the composite nature of the seismic sequences. Each sequence comprises a varying number of individual lobe features with varying sand thickness. The change in reflectivity towards the basin is interpreted as a result of decreasing sand content.

Figure 5.2: W-E trending seismic section tying to the Gita-1 well demonstrating the lithological complexity and reflectivity in the various seismic sequences.

Figure 5.3: Location map of the Søgne Basin and Tail End Graben.

Figure 5.4: W-E trending structural profile with tie to the Jette-1, Q-1 and Svane-1/1A wells.

Figure 5.5: W-E trending structural profile with tie to the Jeppe-1, Hejre-2 and Gita-1 wells.

Figure 5.6: N-S trending structural profile along the basin axis of the Søgne Basin and Tail End Graben ties to the 3/7-5, 3/7-6, 3/7-7, Lulu-1 and-2, Gita-1, Xana-1, Svane-1/1A, Nora-1 and Elin-1 wells.

Figure 5.7: 3D visualization of the Upper Jurassic Basin (Base map: Upper Jurassic time isochore).

Figure 5.8: A) Time isochore map of the BUJ-TEG40 (Kimmeridgian) succession. B) Time isochore map of the TEG40-BCU (Volgian) succession.

Figure 5.9: Time structure map of the top Gita Sand (TEG30).

Figure 5.10: N-S trending seismic profile going from the Gita Plateau in the north to the Tail End Graben to the south crossing the Amalie Cross Fault. The profile shows a general thickening toward the south. A local thickness maximum of the TEG25-TEG30 interval is seen north of the Amalie Cross Fault.

Figure 5.11: SW-NE trending seismic profile (inline 15440) through the Amalie-1 well crossing the Amalie Cross Fault. In the Tail End Graben the sequences is thinning towards the Svend Salt structure to the west.

Figure 5.12: W-E cross section through the Gita-1 and Amalie -1 wells. The profile shows a thickness maximum of the TEG15-TEG20 between the wells. The interval is characterized by low amplitudes. A hummocky reflection pattern is seen in the TEG25-TEG30 interval. The interval is getting truncated by TEG40.

Figure 5.13: W-E cross section (inline 14440) through the complex faulted Svane Ridge. The profile show evidences of onlap toward the west.

Figure 5.14: Time isochore maps of the seismic sequences.

Figure 5.15: W-E trending seismic section tying to the Gita-1 well demonstrating the lithological complexity and high amplitude reflectivity in the various seismic sequences.

Figure 5.16: RMS amplitude maps for the BUJ-TEG10, TEG15-TEG20 and TEG20-TEG30 intervals

Figure 5.17: **A.** East-west profile (IL14440) running perpendicular to the basin (dip-section to Ringkøbing-Fyn High) and intersecting Svane-1/1A well. RFH = Ringkøbing-Fyn High. **B.** Similar profile flattened on TEG20. Inset map shows the seismic line positions with TEG20 structure map as background.

Figure 5.18: **A.** East-west profile (IL14680) running perpendicular to the basin (dip-section to Ringkøbing-Fyn High) and intersecting the Svane-1 well. RFH = Ringkøbing-Fyn High, HP = Heno Plateau. **B.** Similar profile flattened on TEG20. Inset map shows the seismic line positions with TEG20 structure map as background.

Figure 5.19: **A.** North-south profile (XL14540) orientated along the basin axis and intersecting the Svane-1/1A well via IL14440 (Fig. 3.4.2). MH = Mandal High. **B.** Similar profile flattened on TEG20. Inset map shows the seismic line positions with TEG20 structure map as background.

Figure 5.20: **A.** North-south profile (XL14340) orientated along the basin axis. MH = Mandal High. **B.** Similar profile flattened on TEG20. Inset map shows the seismic line positions with TEG20 structure map as background.

Figure 5.21: **A.** East-West profile (IL ) across the Gita Plateau across the flank of Ringkøbing-Fyn High (RFH) **B.** Similar profile flattened on TEG20. Inset map shows the seismic line positions with TEG20 structure map as background.

Figure 5.22: **A.** Multipanel (SW-NE/E-W) profile across the Gita Plateau toward the Ringkøbing-Fyn High (RFH) **B.** Similar profile flattened on TEG15. Inset map shows the seismic line positions with TEG20 structure map as background.

Figure 6.1: CPI of the 3/7-7 well illustrating the stratigraphy, lithology, the associated wire line logs, and the log derived porosity (PHIE) and standard Archie calculation of the saturation (SW\_AR).

Figure 6.2: CPI of the Amalie-1 well illustrating the stratigraphy, lithology, the associated wire line logs, and the log derived porosity (PHIE) and standard Archie calculation of the saturation (SW\_AR).

Figure 6.3: CPI of the Gita-1/Gita-1 well illustrating the stratigraphy, lithology, the associated wire line logs, and the log derived porosity (PHIE) and standard Archie calculation of the saturation (SW\_AR).

Figure 6.4: CPI of the Gwen-2 well illustrating the stratigraphy, lithology, the associated wire line logs, and the log derived porosity (PHIE) and standard Archie calculation of the saturation (SW\_AR). Please note that the apparent high saturation near the top is due to bad data.

Figure 6.5: CPI of the Hejre-1 well illustrating the stratigraphy, lithology, the associated wire line logs, and the log derived porosity (PHIE) and standard Archie calculation of the saturation (SW\_AR).

Figure 6.6: CPI of the Hejre-2 well illustrating the stratigraphy, lithology, the associated wire line logs, and the log derived porosity (PHIE) and standard Archie calculation of the saturation (SW\_AR).

Figure 6.7: CPI of the Jeppe-1 well illustrating the stratigraphy, lithology, the associated wire line logs, and the log derived porosity (PHIE) and standard Archie calculation of the saturation (SW\_AR).

Figure 6.8: CPI of the Jette-1 well illustrating the stratigraphy, lithology, the associated wire line logs, and the log derived porosity (PHIE) and standard Archie calculation of the saturation (SW\_AR).

Figure 6.9: CPI of the Lulu-2 well illustrating the stratigraphy, lithology, the associated wire line logs, and the log derived porosity (PHIE) and standard Archie calculation of the saturation (SW\_AR).

Figure 6.10: CPI of the Svane-1/1A/1A well illustrating the stratigraphy, lithology, the associated wire line logs, and the log derived porosity (PHIE) and standard Archie calculation of the saturation (SW\_AR). Due to the availability of data the PHIE is calculated based on the density in this particular well.

Figure 6.11: CPI of the Gita-1 well illustrating the stratigraphy, lithology, the associated wire line logs, and the log derived porosity (PHIE) and standard Archie calculation of the saturation (SW\_AR).

Figure 7.1: Lithology of the gravity flow sandstones from the Søgne Basin and northern Tail End Graben. **A.** Mean grain size. **B.** Degree of sorting as a geometrically mean (according to Folk 1966).

Figure 7.2: RW3: Petrography of the Xana-1 and Gita-1 wells from the Tail End Graben. **A.** Authigenic albite crystals (Ab) forming in secondary pores (Sp) after feldspar dissolution, which are rimmed by clay coatings (arrow). Xana-1 SWC, 4692.48 m. **B.** Crypto- and microcrystalline quartz coating on detrital quartz grains. Backscatter electron micrograph. Gita-1 well cuttings sample, 4440 m. **C.** Interlocking quartz overgrowths (arrows) next to various carbonate clasts (Cc) and secondary pores surrounded by clay coatings. Crossed nicols. Xana-1 SWC, 4692.48 m. **D.** Quartz overgrowths (Qo) and locally quartz outgrowths (arrow) probably due to local crypto- or microcrystalline quartz coatings. Gita-1 well cuttings sample, 4440 m. **E.** Dolomite (Do) clasts? enclosed in ankerite (An) cement. Backscatter electron micrograph. Xana-1 cuttings sample, 5071 m. **F.** Dolomite (Do) clast enclosed in rhombohedral ankerite (An) cement. Backscatter electron micrograph. Gita-1 well cuttings sample, 4459 m.

Figure 7.3: RW4: Petrography of the 3/7-6 and 3/7-7 cores from the Søgne Basin. **A.** Pore-filling kaolinite (Ka) partly enclosed in quartz overgrowth (Qo), backscatter electron micrograph. 3/7-6 3641.36 m. **B.** Partly dissolved albite grain (Ab) surrounded by a clay rim (arrows), which outline the original size of the grain,

backscatter electron micrograph. 3/7-7 3786.23 m. **C.** Partly dissolved/altered K-feldspar overgrowth on detrital K-feldspar with albite exsolution lamellae next to quartz grains with quartz overgrowth (Qo) or cryptocrystalline quartz coating (arrow), backscatter electron micrograph. 3/7-6 3648.08 m. **D.** Quartz overgrowths (Qo) are locally limited due to clay coatings, backscatter electron micrograph. 3/7-7 3786.23 m. **E.** Rounded dolomite clasts (Do) overgrown by rhombohedral ankerite (An) and enclosed in calcite cement (Ca), backscatter electron micrograph. 3/7-6 3646.63 m. **F.** Clay coatings has locally inhibited quartz overgrowths resulting in microquartz and small quartz overgrowths, backscatter electron micrograph. 3/7-7 3786.23 m.

Figure 7.4: Permeability versus porosity for sandstones in the Mandal Formation in the Søgne Basin, Farsund Formation in the Tail End Graben compared with the Heno Formation from the Danish Central Graben. Data for the Xana-1 side wall cores and the 3/7-6 cores are from previous studies (data from Final well reports, e.g. Norske Shell 1997).

Figure 7.5: Log panel from the Xana-1 well, showing the lithology, porosity, and permeability. Red dots represents side wall core measurements for the porosity and permeability, respectively.

Figure 8.1: Compilation of all rutile (A) and zircon (B) U-Pb age data from the Upper Jurassic sediments from Olivarius et al. (this volume) plotted as probability density distributions. The provenance areas of the age populations constitute in some cases several possibilities and resulting transport directions. The age of a grain corresponds to its ultimate basement source and the grains have most likely been recycled at least once. The basement age of the Ringkøbing-Fyn High (RFH) is here assumed representative of the intra-basinal basement highs in the central North Sea.

Figure 8.2: Well-log profile of the correlation of the gravity-flow sandstones in the Xana-1 and Gita-1 wells. The sequence stratigraphic surfaces and seismic marker surfaces are shown. The depth intervals of the cuttings samples used for zircon U-Pb analysis are shown alongside the resulting zircon age distributions. The grain no. is the number of employed concordant ages out of the total number of measured ages.

Figure 8.3: Pb isotopic composition of individual K-feldspar grains from Upper Jurassic sandstones in the greater Tail End Graben area. The basement domains are based on Tyrrell et al. (2007).

Figure 9.1: Box plot (mean, P95, P75, P50, P25 and P05) for the TOC,  $T_{max}$  and HI populations within the Farsund Formation and selected sequences.

Figure 9.2: A) Oil types and B) relative oil maturity as depicted by modelled source rock depth. Shallow depths in B indicate less mature oils. From Schovsbo et al. (2018).

Figure 9.3: 1-D modelled maturity based on 46 wells and using Easy%Ro to interpolate the maturity covering A) the Volg-2 to Ryaz-1 sequences (from near the base middle to the top of the Farsund Formation), B) the Kimm-3 to Volg-3 sequences (i.e. from near the base to the middle part of the Farsund Formation) and (C) the Lower and Middle Jurassic (i.e. from Lower Jurassic to near the top Bryne/Lulu/Middle Graben formations).

Figure 10.1: Model for marine depositional setting across the shelf, slope and basin. Sans units can develop in all these settings.

Figure 10.2 A-O: Paleogeographic maps of the sequences spanning from Oxfordian throughout Kimmeridgian and Volgian.

*Figure 11.1: Paleogeographic map of the lowstand and transgressive systems tracts of Kimm-3a, showing the presence of several prograding fan systems.*

## Tables

*Table 4.1: Well picks. The table presents the depths (in m or feet) to all stratigraphic surfaces (seismic markers, sequence stratigraphic surfaces (sequence boundaries, SB; maximum flooding surfaces, MFS; maximum regressive surface, MRS), lithostratigraphic boundaries, chronostratigraphic boundaries) from the present project.*

*Table 6.1: Spreadsheet showing the total thicknesses of the TEG-units, along with the net-to-gross ratios and the average effective porosity in the sand units.*

*Table 9.1.: Source rock characteristics of Jurassic – lowermost Cretaceous formations and selected sequences in the Danish Central Graben.*

## Appendix 1

### Amalie Member

New member in the Lola Formation.

**Name.** The member is named after the Amalie-1 well situated in the southern part of the Søgne Basin in a transitional location to the Tail End Graben and in close proximity to the Coffee Soil Fault and Ringkøbing-Fyn High (Fig. 1.1).

**Type section.** The Amalie-1 well, c. 4975-4875 m b. KB, is selected as the type section (Fig. 4.2).

**Lithology and environment.** The member comprises a heterogeneous succession of mainly fine-grained sandstones interbedded with mudstones based on cuttings and petrophysical log characteristics. Deposition took place in an offshore marine environment with periodically sandy gravity flow deposition (Johannessen et al 2010).

**Log characteristics.** The member includes blocky, low gamma-ray sandstones, the sandstone units are 3–7 m thick, alternating with high GR claystone units in the lower part, and with medium GR claystones/siltstones intercalated with 1- 10 m thick low GR sandstone units in the upper part, reflecting the heterogeneous composition of the member.

**Lower boundary.** The lower boundary is selected at the lowest of the blocky, low GR units that succeed a high GR claystone interval with an upward decreasing GR trend of the Lola Formation in the Amalie-1 well.

**Upper boundary.** The top of the member is situated at the top of the low GR sandstones units overlain by medium GR claystones/siltstones of the Farsund Formation in the Amalie-1 well.

**Distribution and thickness.** The member forms the lower part of the Lola Formation in the Amalie-1 well area. The distribution is probably linked to a submarine fan with sediment supplied from the Ringkøbing-Fyn High in the east, or alternatively along the basin axis from the Søgne Basin in the north (Johannessen et al. 2010). The thickness of the combined intercalated claystone and sandstones is 100 m in the Amalie-1 well.

**Age.** The member is of Early Kimmeridgian age in the Amalie-1 well (Johannessen et al. 2010).

### Svane Member

New member in the Lola Formation – lower Farsund Formation.

**Name.** The member is named after the Svane-1/1A well situated in the northeastern part of the Tail End Graben (Fig. 1.1).

**Type section.** The Svane-1/1A well, c. 5905-5310 m b. KB is selected as the type section (Fig. 4.12). The upper part is partly time equivalent to sandy units of the Gita Member in the Gita-1 and Xana-1 wells (for definition of the Gita Member see below).

**Lithology and environment.** The member comprises a heterogeneous succession of mainly fine-grained sandstones interbedded with mudstones based on cuttings and petrophysical log characteristics. Deposition took place in an offshore marine environment with periodically sandy gravity flow deposition (Johannessen et al. 2010).

Log characteristics. The member includes claystones with high gamma-ray and low sonic readings and intercalated sandstones commonly with a blocky low gamma-ray readings, as well as units with highly fluctuating high and low gamma-ray readings with both upwards increasing and decreasing gamma ray trends, reflecting the heterogeneous composition of the member.

Lower boundary. The lower boundary is selected at the TD in Svane-1A in the type section and is therefore poorly constrained overlying offshore mudstones/claystones of the Lola Formation.

Upper boundary. The top of the member corresponds to the uppermost level with blocky low gamma readings overlain by high gamma mudstones of the Farsund Formation.

Distribution and thickness. The member forms the lower part of the Farsund Formation in the Svane-1/1A well area in the Tail End Graben. Previously the origin of these sandstones have been suggested to be sourced from either the Søgne Basin, from the north, or from the Ringkøbing-Fyn High (Johannessen et al. 2010). However, geochemical data from the present study indicate that the sandy sediments were supplied from the Heno Plateau area. The thickness of the combined intercalated claystone and sandstones is 595 m in the Svane-1/1A well.

Age. The member is of Early to Late Kimmeridgian age in the Svane-1A well (Johannessen et al. 2010).

#### Gita Member

New member in the Farsund Formation.

Name. The member is named after the Gita-1 well situated in the southern part of the Søgne Basin in a transitional location to the Tail End Graben (Fig. 1.1).

Type section. The Gita-1 well, 4728–4344 m b. KB, 4680–4295 m b. MSL, is selected as the type section (Fig 4.3).

Reference section. The Xana-1 well, 5087–4624 m b. KB, 5033–4570 m b. MSL, situated 3 km SSE of Gita-1, is selected as the reference section (Figs. 1.1; 4.13).

Lithology and environment. The member comprises a heterogeneous succession of mainly fine-grained sandstones interbedded with mudstones. Sidewall cores from the member in the Xana-1 well record a variety of sedimentary facies comprising laminated mudstone/claystone intercalated with homogeneous light grey, fine-grained sandstones, homogenous sandstone with dispersed large mudstone intraclasts, heterolithic laminated sandstones and claystone with occasional deformed and disrupted bedding structures as well as coarse-grained sandstone with fine pebbles and large claystone clasts. Deposition took place in an offshore marine environment with periods of sandy gravity flow deposition in a submarine base of slope fan system. The member have partly experienced post-depositional deformation and injection.

Log characteristics. In the Gita-1 and Xana-1 wells the member includes claystones with high gamma-ray and low sonic readings and intercalated sandstones commonly with a blocky low gamma-ray readings, as well as units with highly fluctuating high and low gamma-ray readings with both upwards increasing and decreasing gamma ray trends, reflecting the heterogeneous composition of the member.

Lower boundary. The member sharply overlies offshore claystones of the Lola Formation in the Gita-1 well type section. The base of the member is defined by a shift to blocky lower gamma-ray and higher sonic readings.

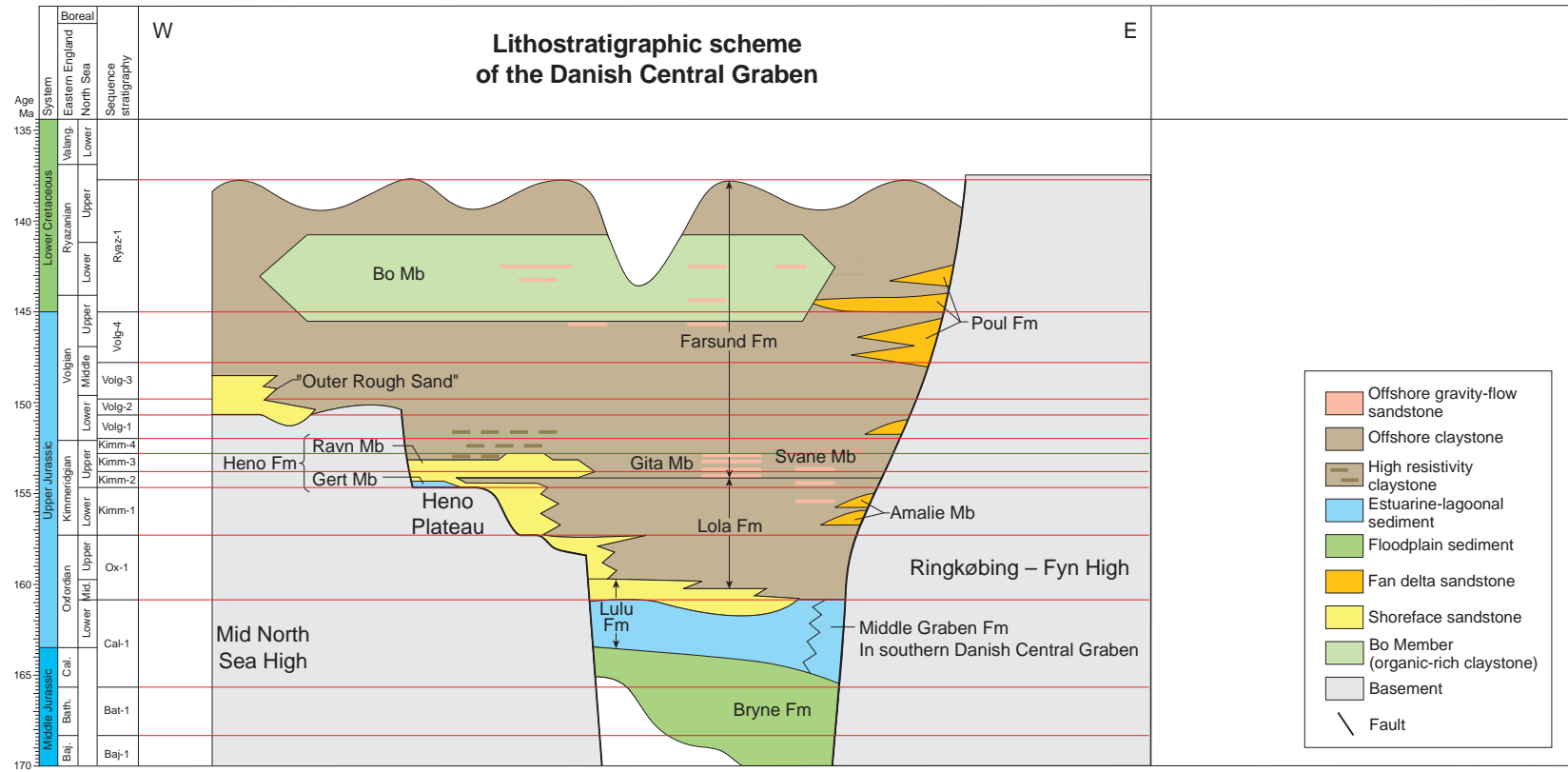
Upper boundary. The top of the member corresponds to the uppermost level with blocky low gamma readings overlain by high gamma mudstones of the Farsund Formation. The upper boundary is considered diachronous - younging towards the north.

Distribution and thickness. The member forms the base of the Farsund Formation in the Søgne Basin and with transition to the central parts of the Tail End Graben. The sandy parts of the member is associated with gravity flow type deposits in channel, fan and lobe geometries. Results from the present study indicate that the sand originated from the Mandal High - Piggvar Terrace areas or along the basin axis of the Søgne Basin from farther north. Thin sandstone units in the Amaile-1A well may represent featheredge of the sandy gravity flow units. A maximum thickness of 463 m is found in the Xana-1 well.

Age. The member is mainly of Late Kimmeridgian age and may extend into the Lower Volgian in the Norwegian part of the Søgne Basin, e.g. in the 3/7-6 well.



Fig. 2.1



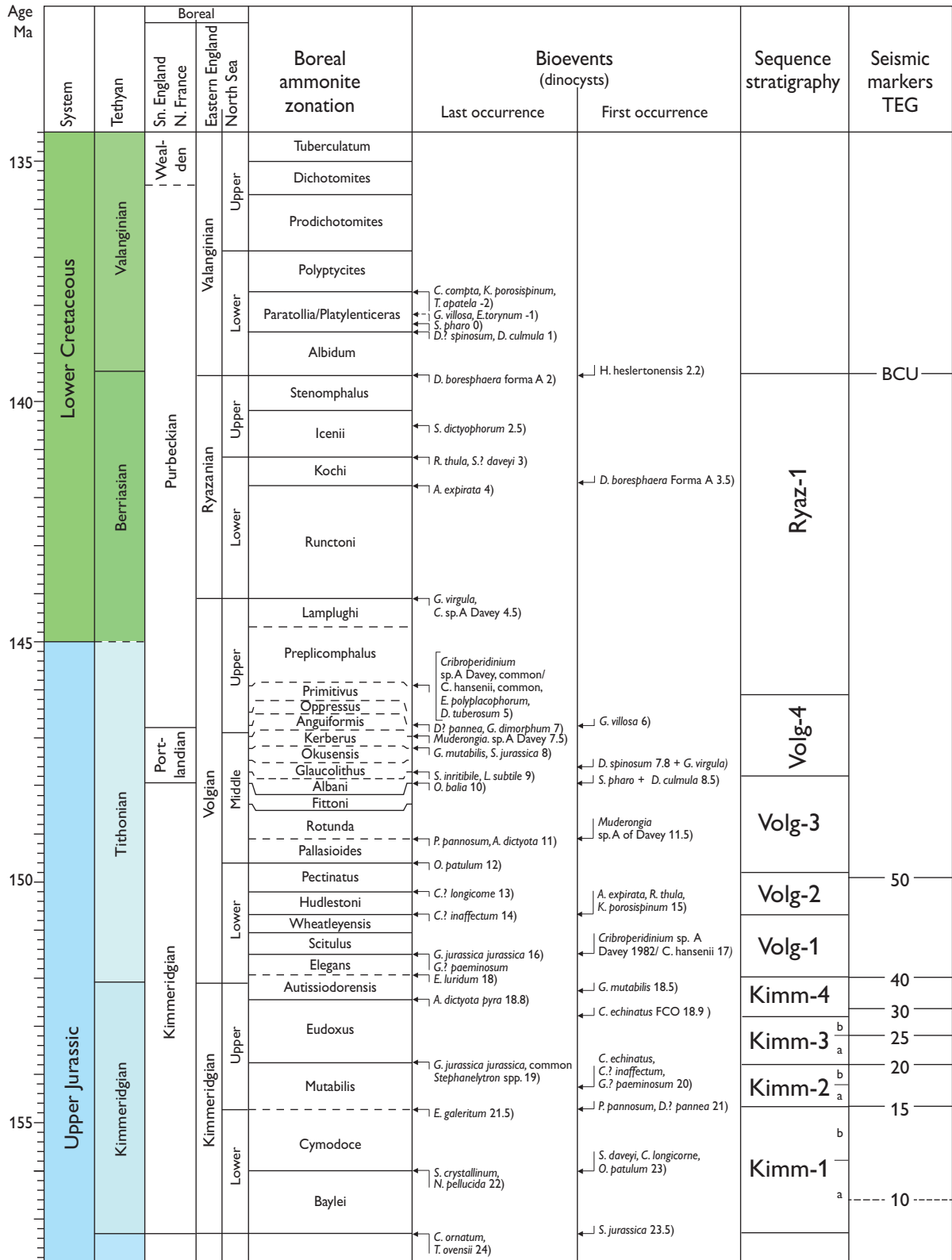


Fig. 4.1

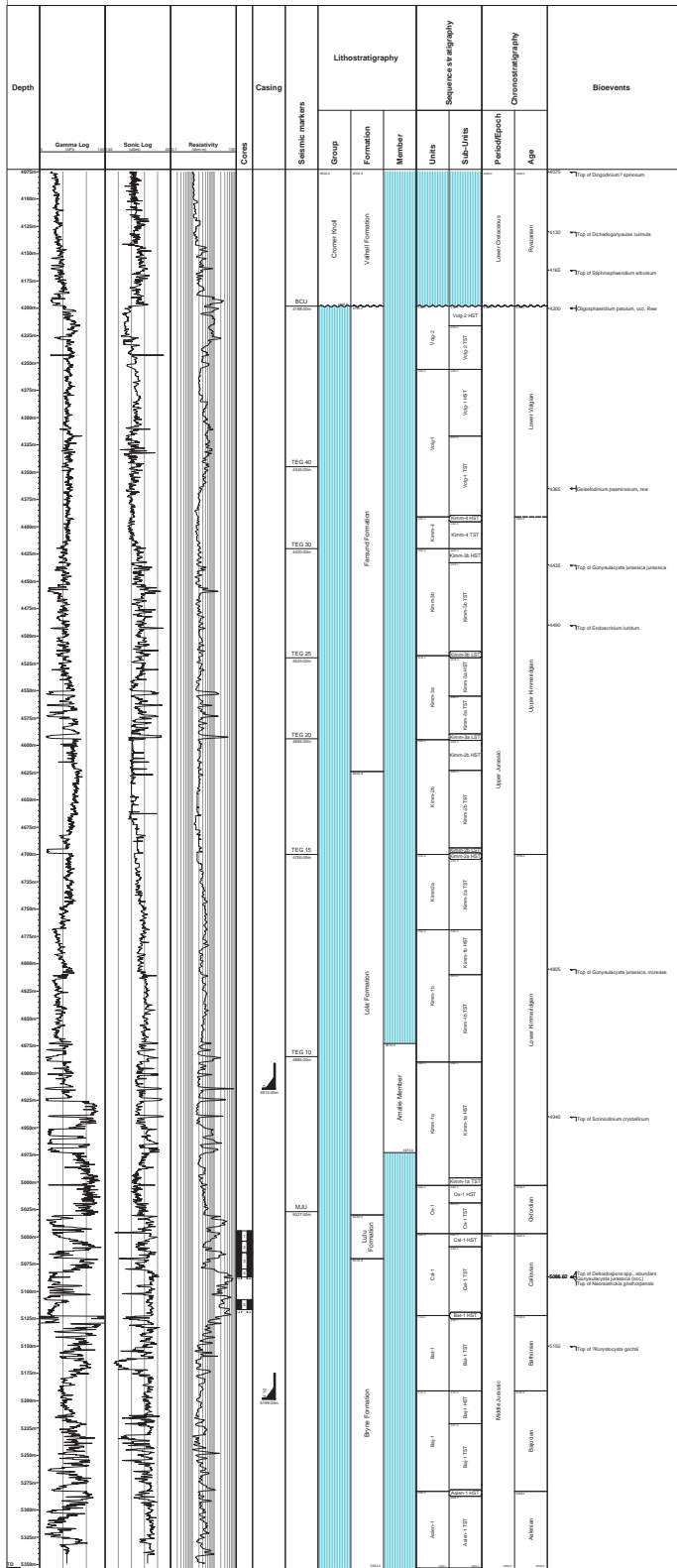


Fig. 4.2

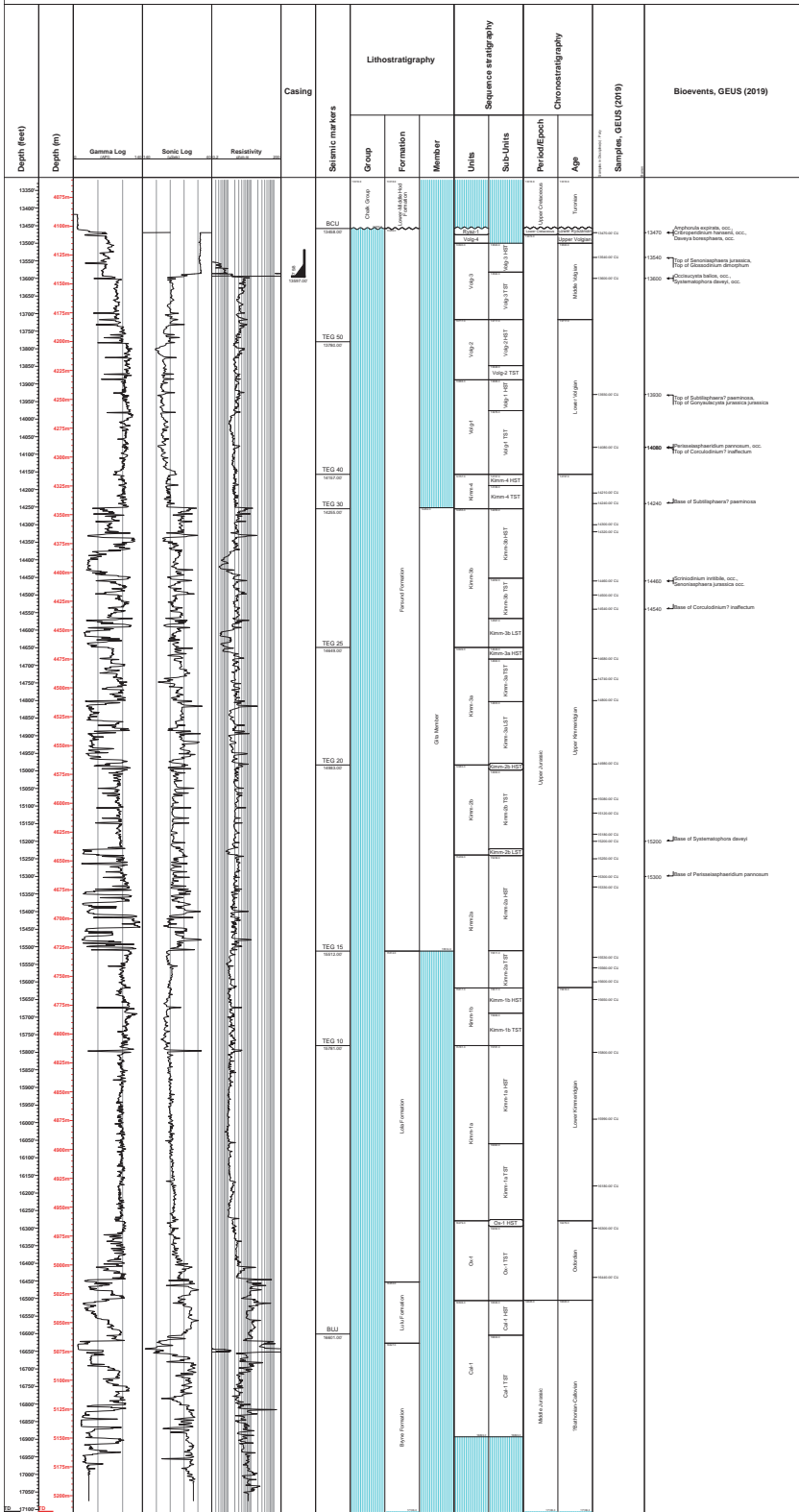


Fig. 4.3

Well Name : Gwen-2

Interval Various TEG 2019  
 Scale : 1:1000  
 Chart date: 28 May 2019

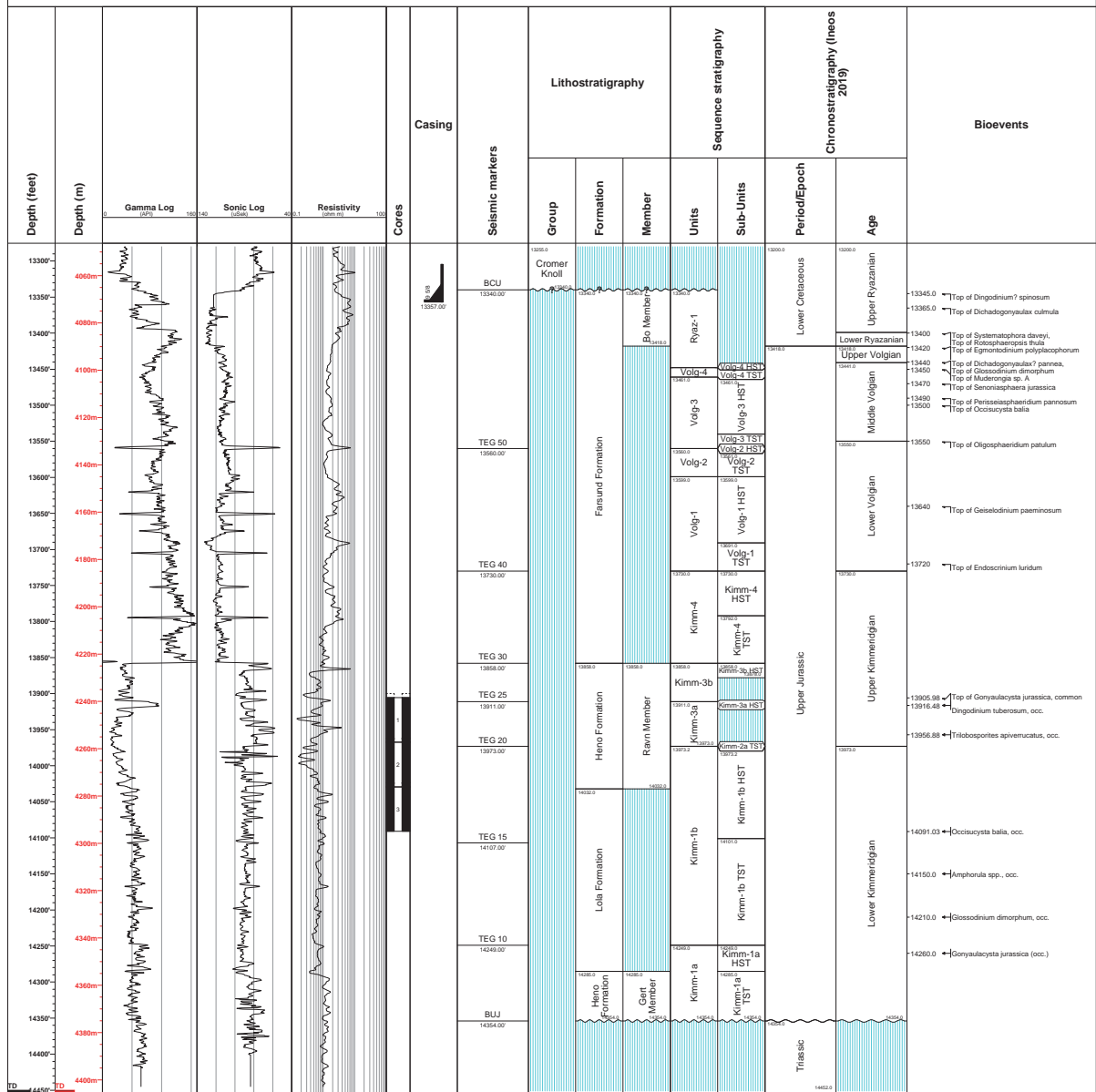


Fig. 4.4

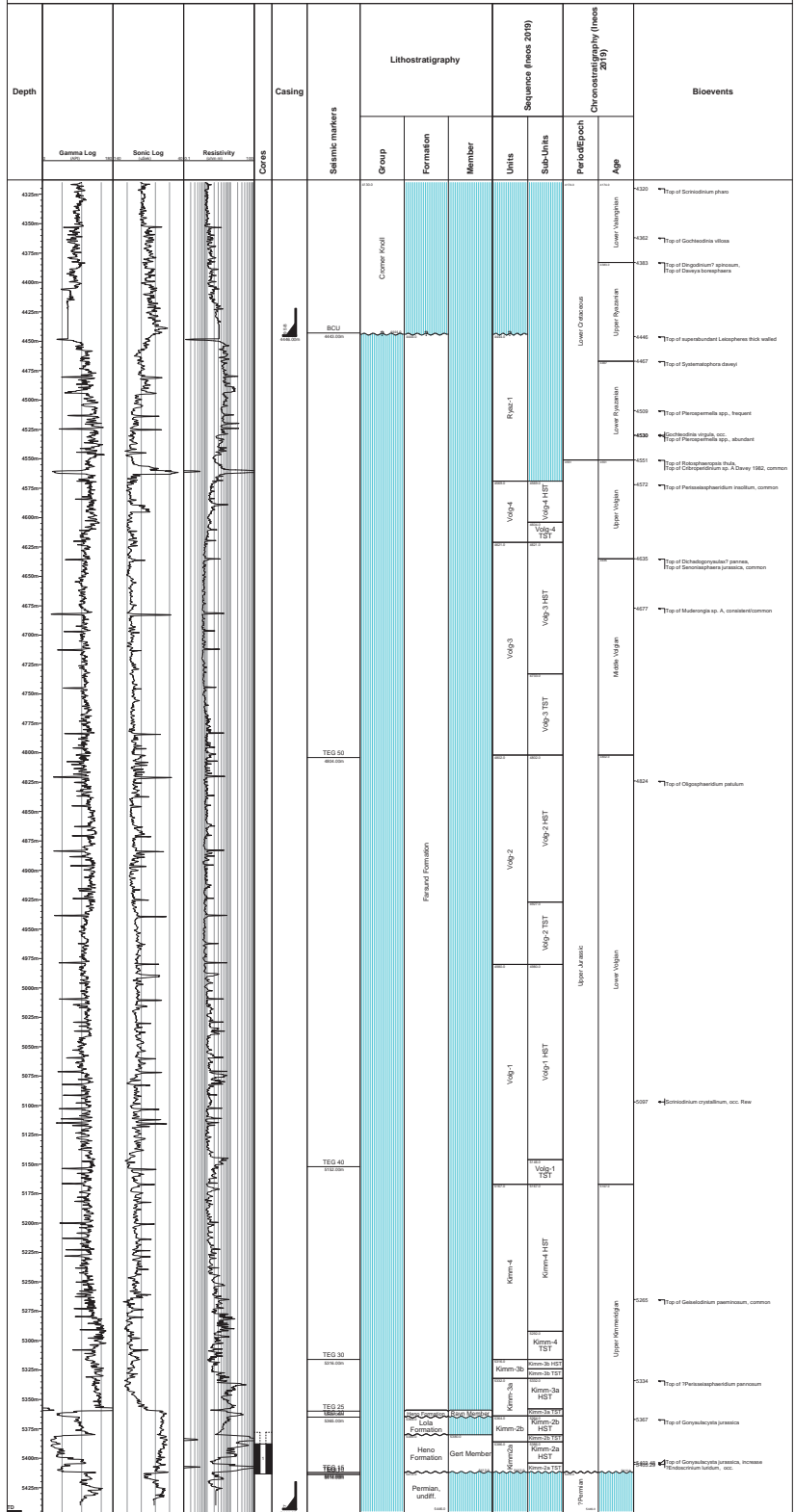


Fig. 4.5

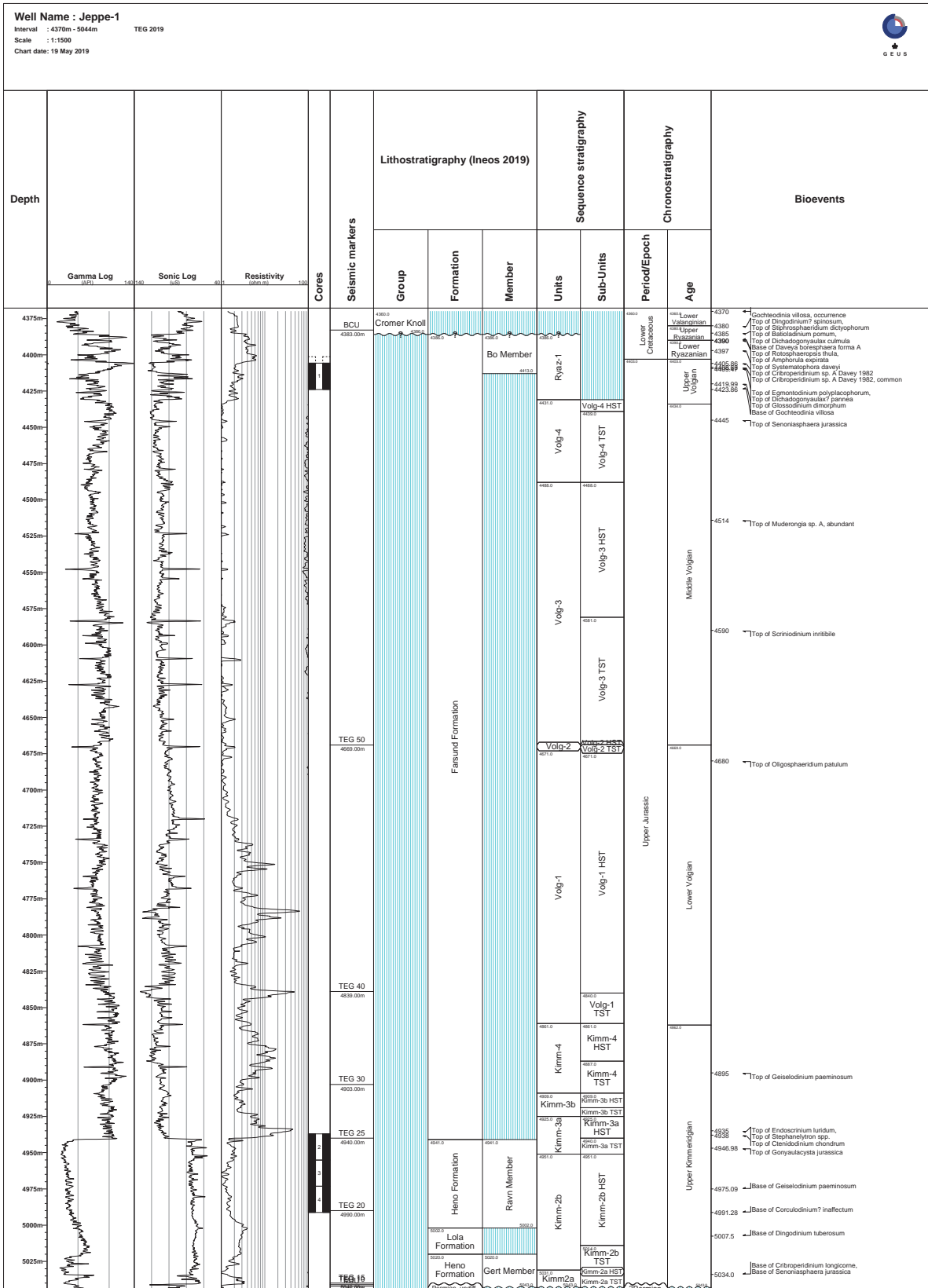


Fig. 4.6

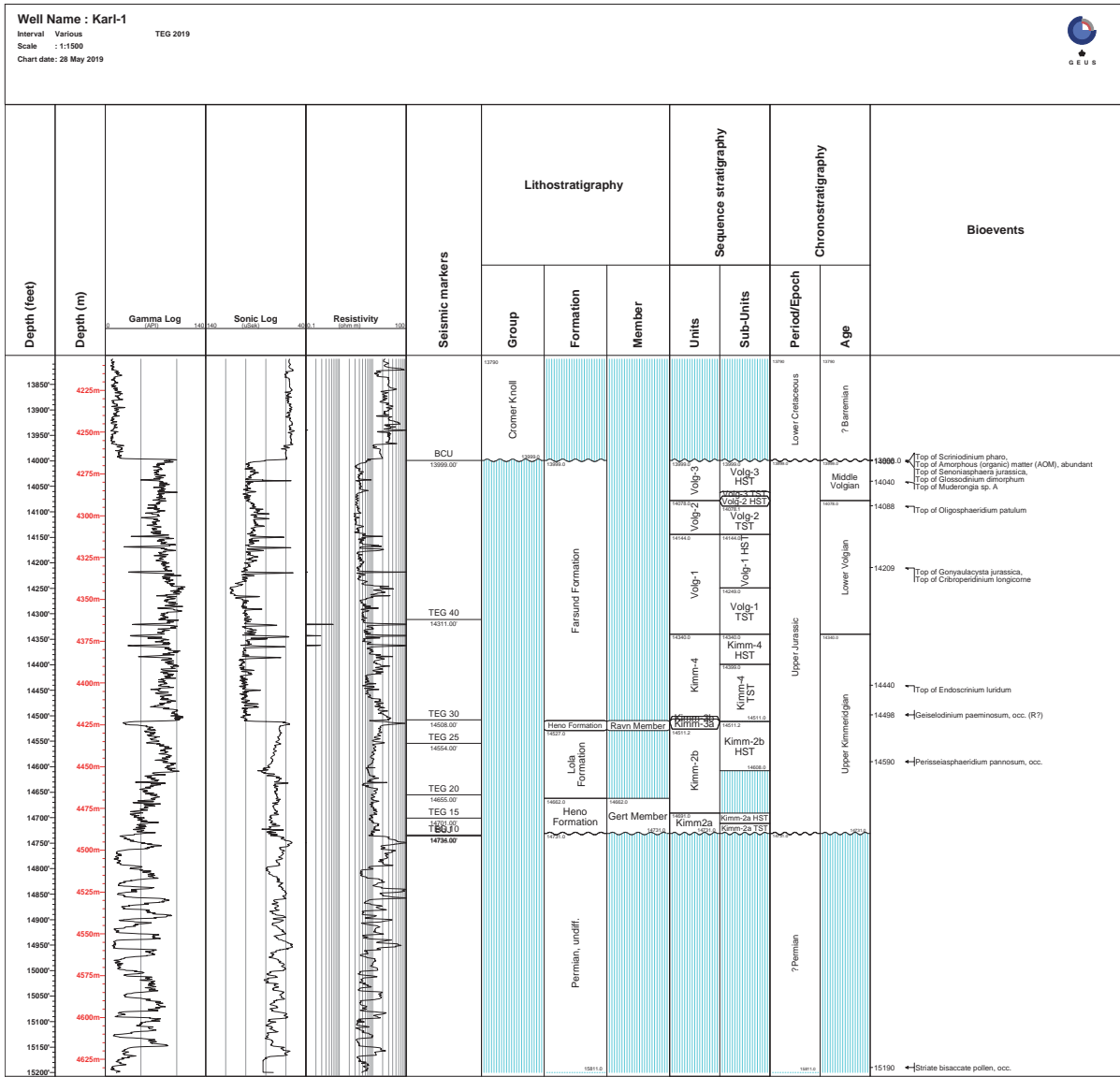


Fig. 4.7

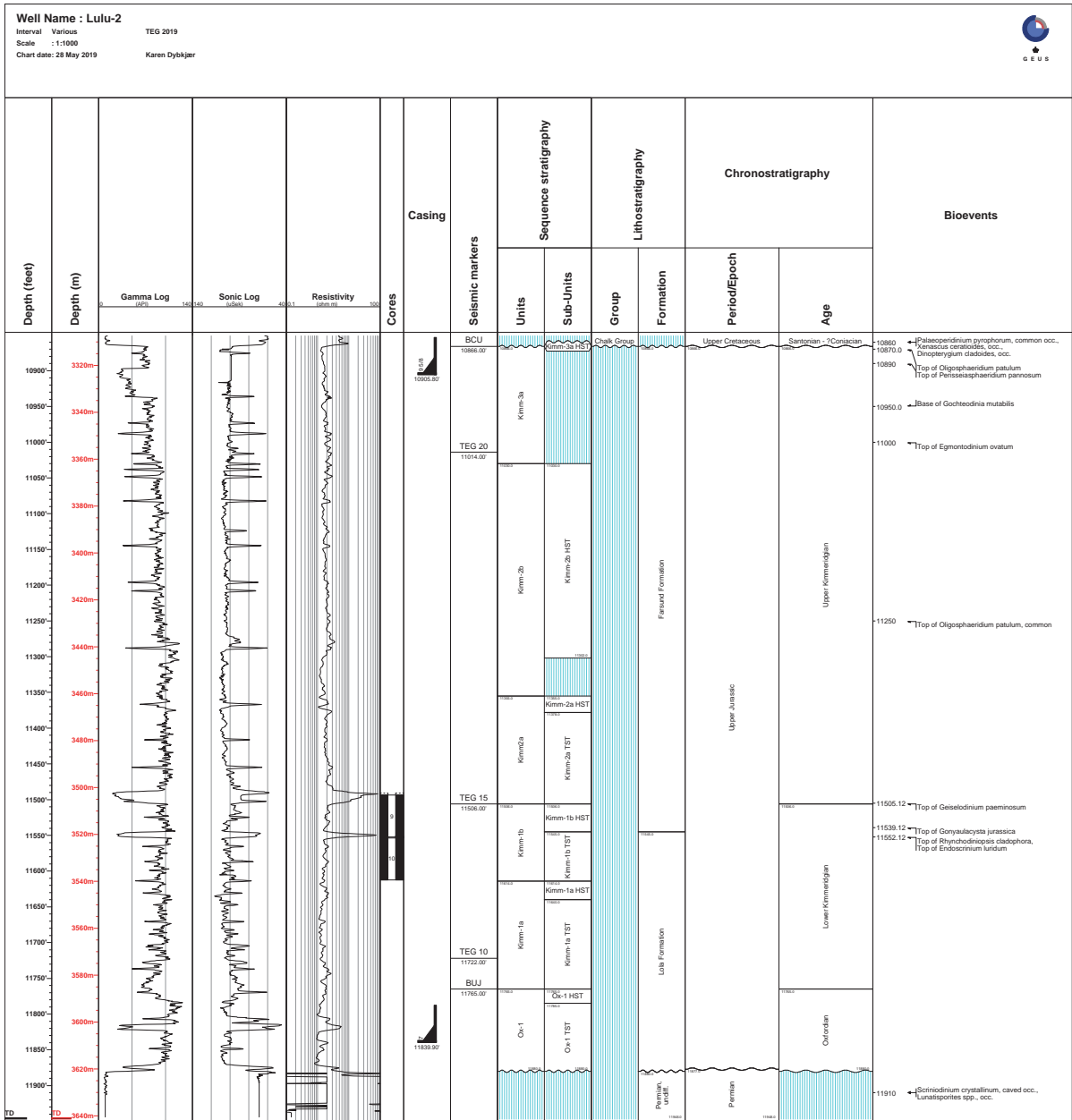


Fig. 4.8

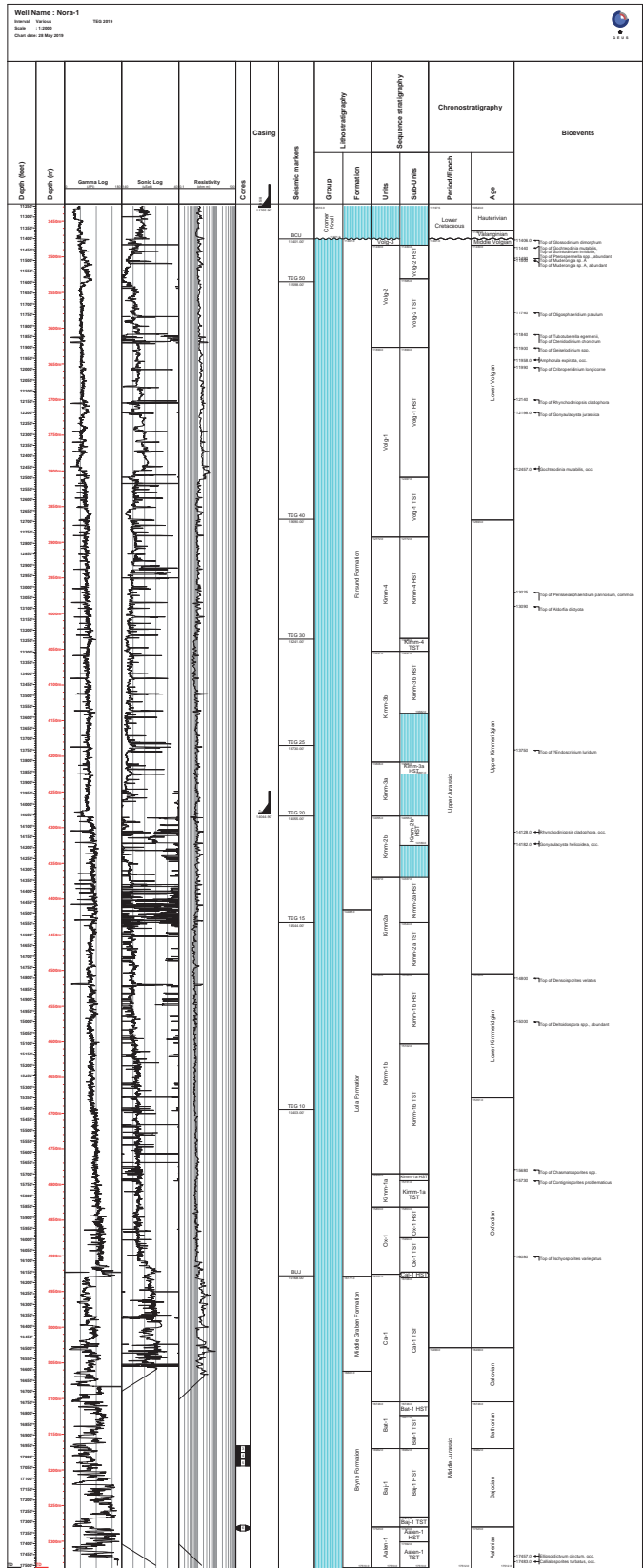


Fig. 4.9

Well Name : Q-1X  
 Interval Various  
 Scale : 1:1000  
 Chart date: 28 May 2019

TEG 2019

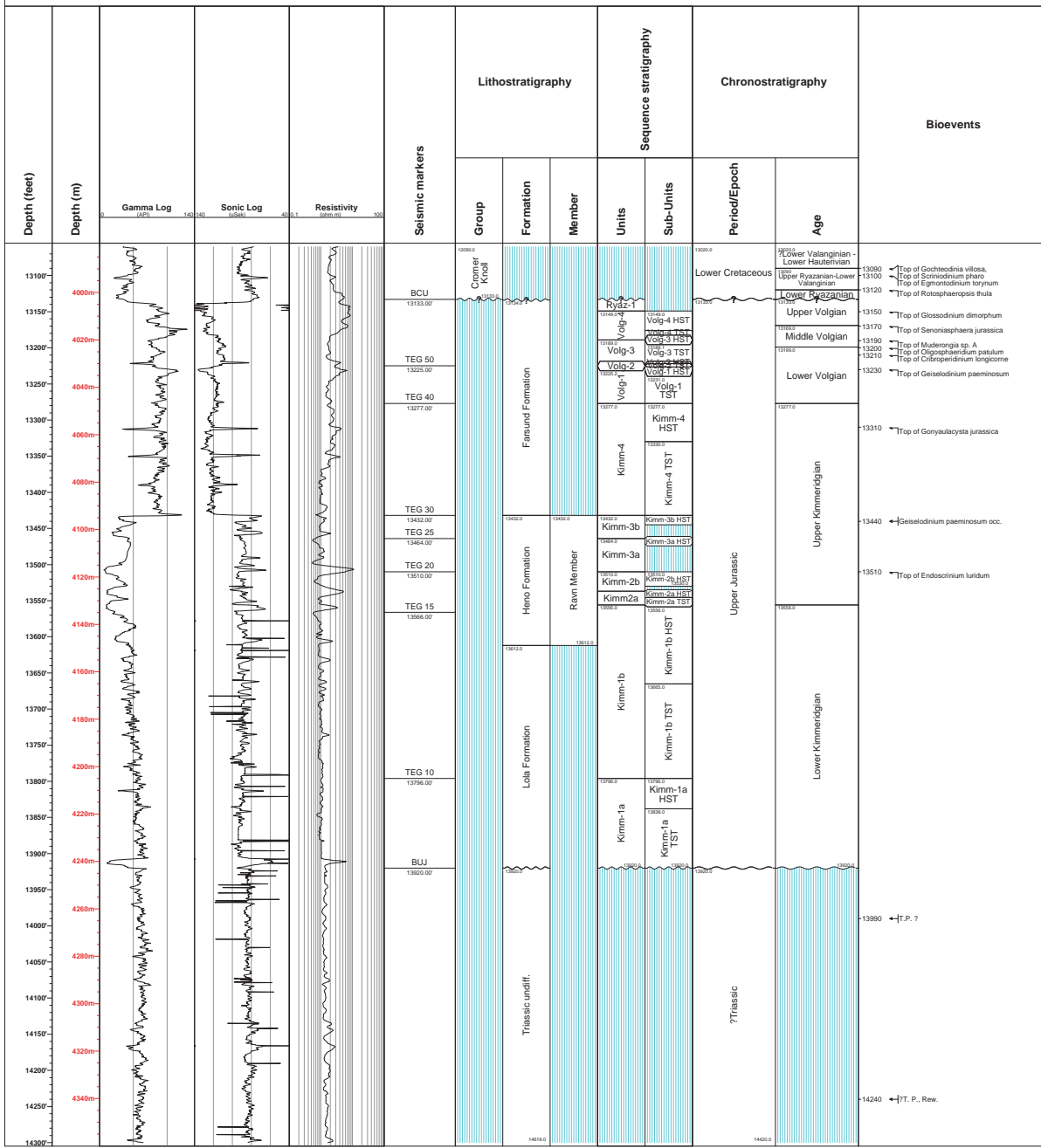


Fig. 4.10

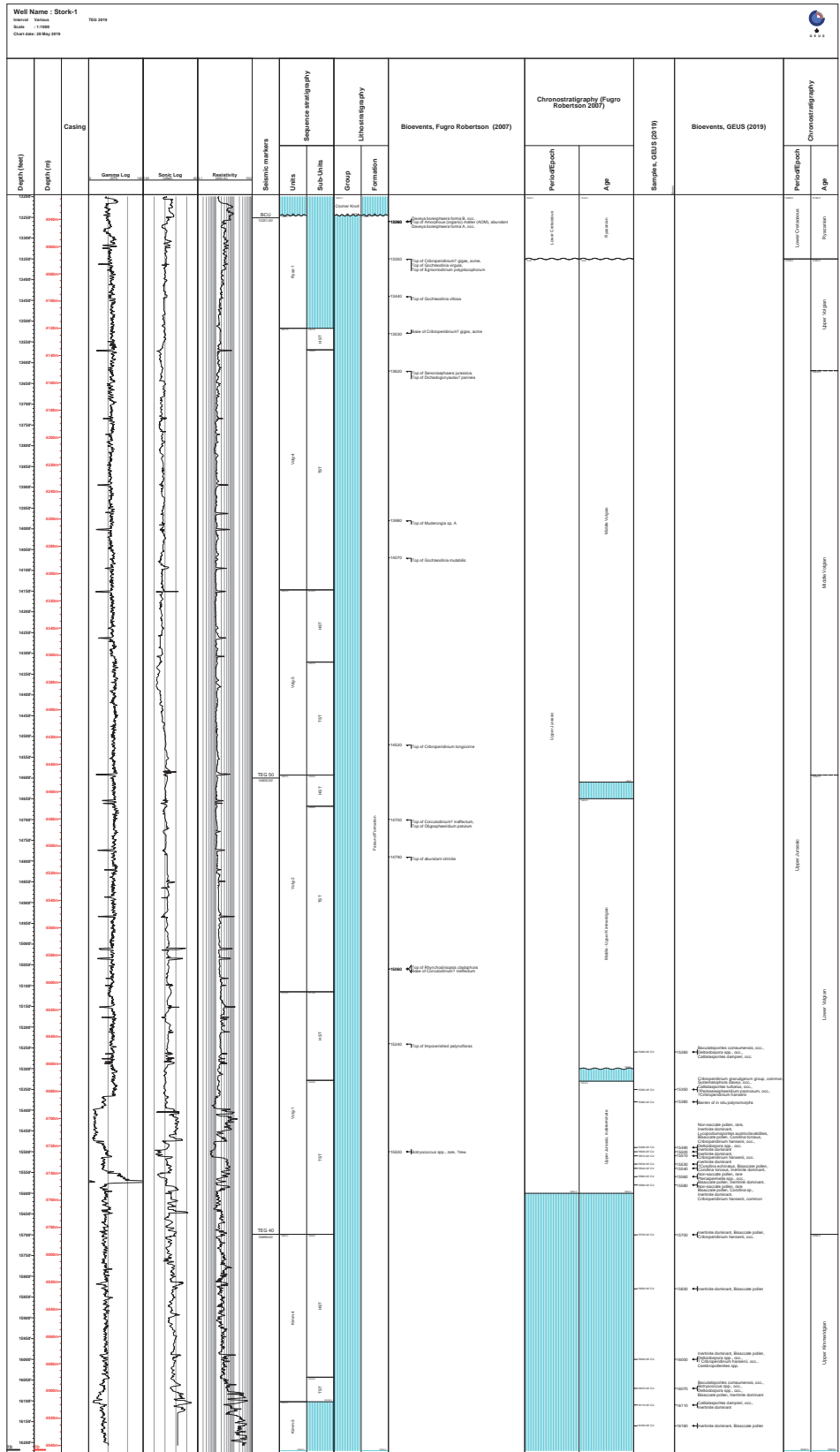


Fig. 4.11

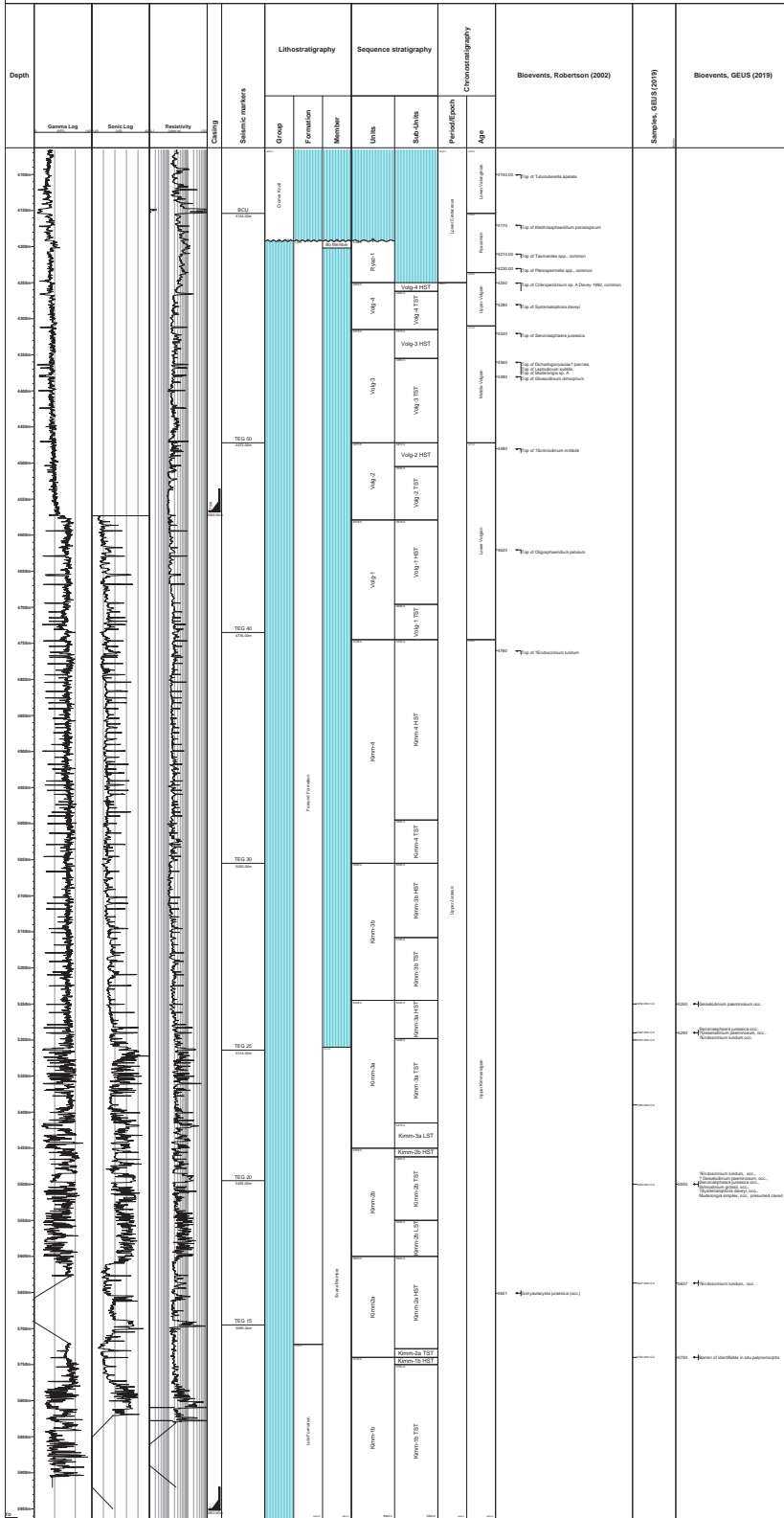


Fig. 4.12

Well Name : Xana-1  
 Interval Various  
 Scale : 1:11500  
 Chart date: 31 May 2019

TEG 2019

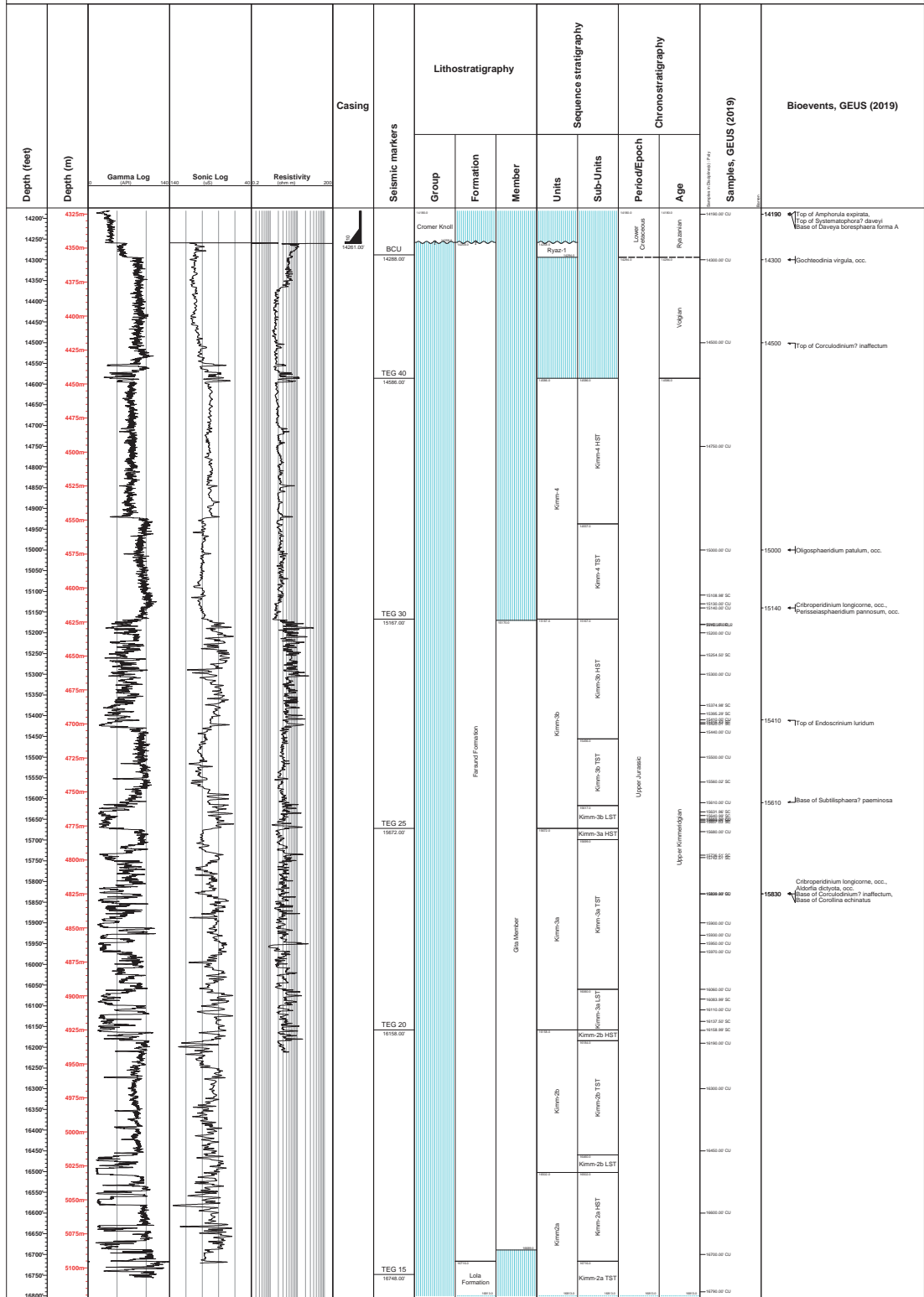


Fig. 4.13



W

E

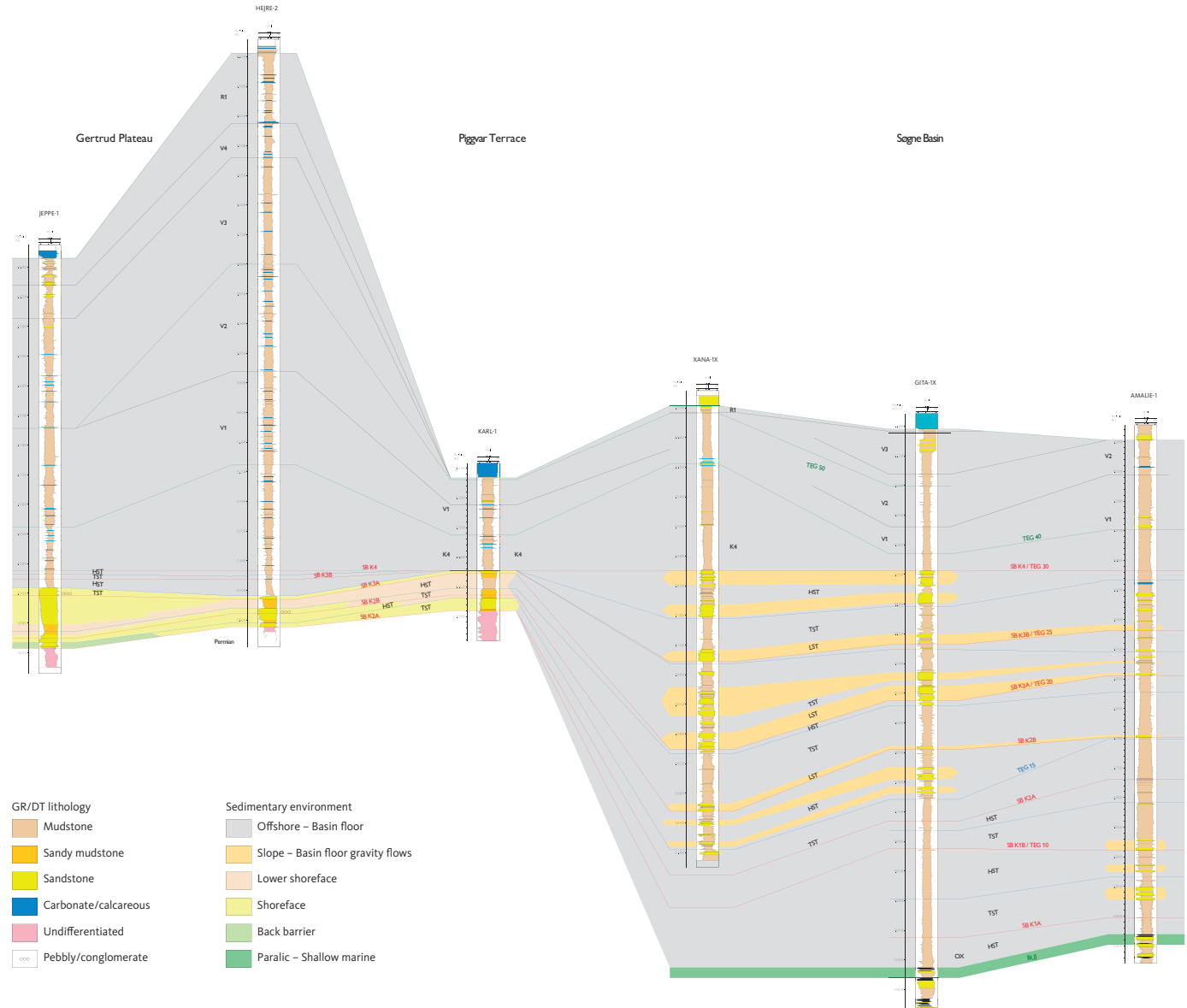


Fig. 4.15

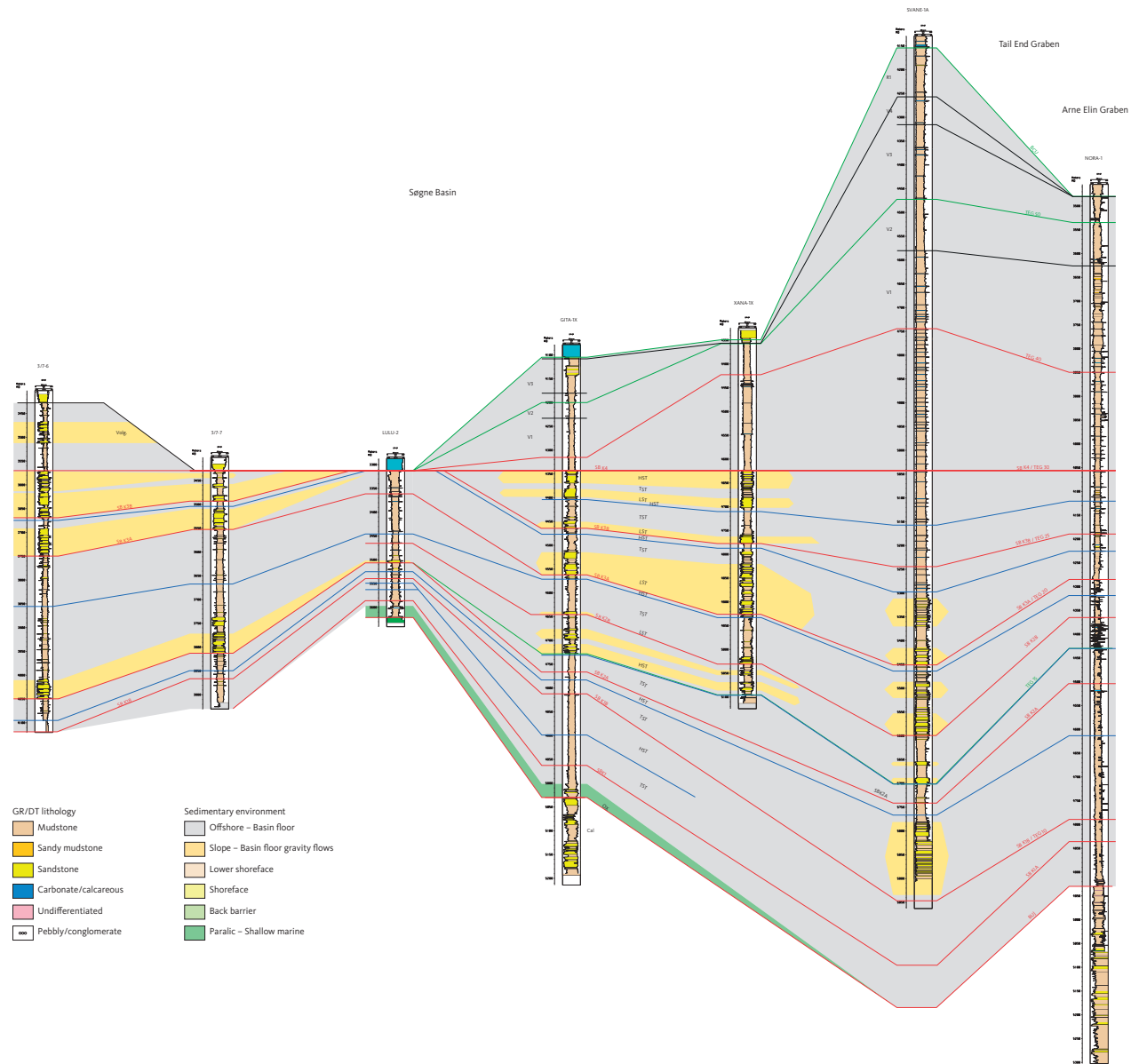


Fig. 4.16

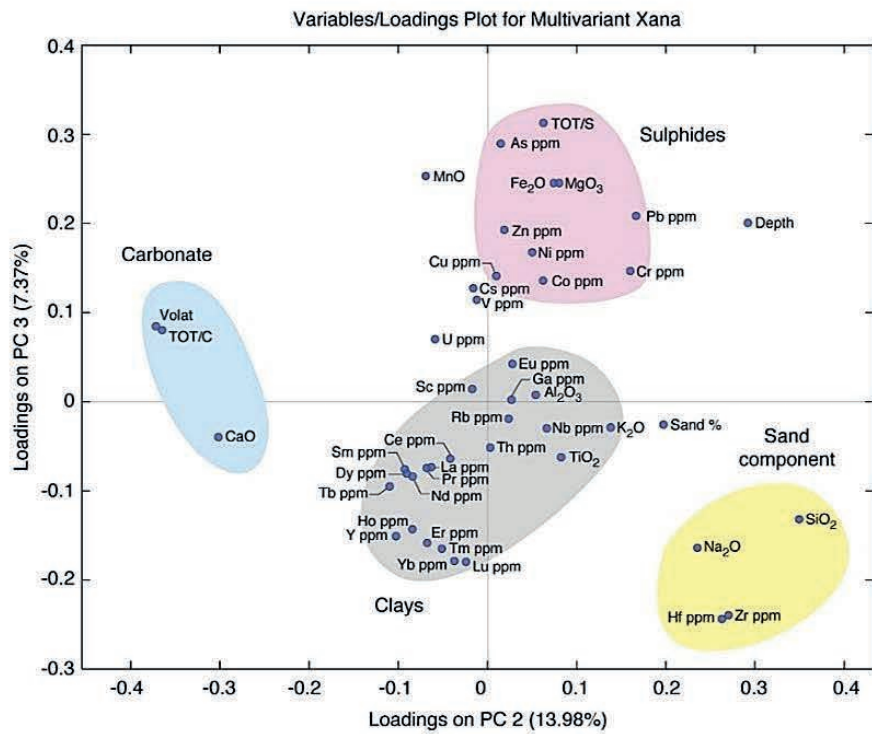
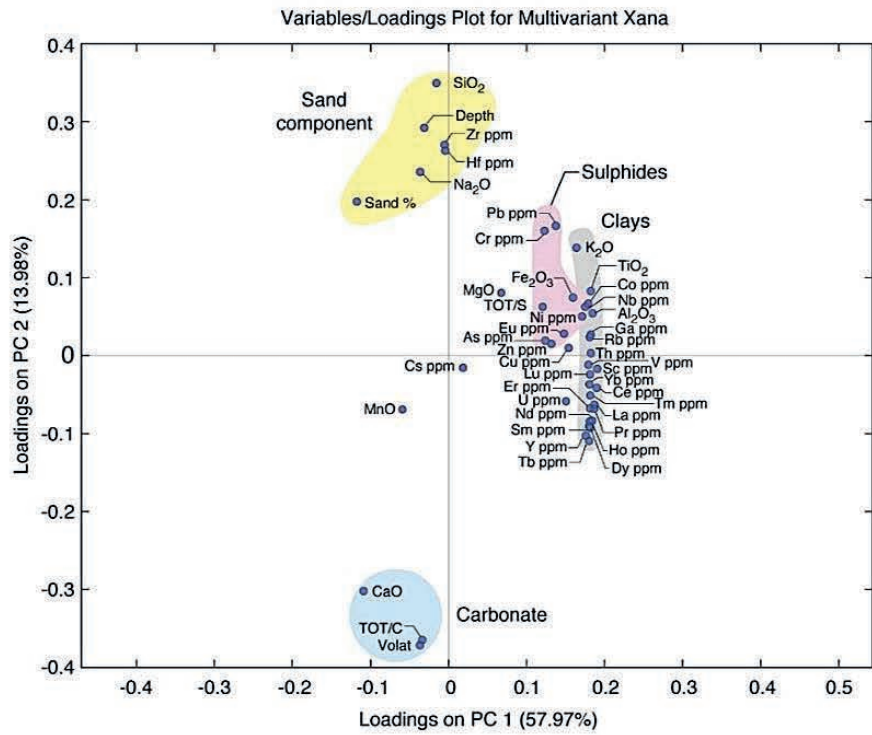


Fig. 4.17

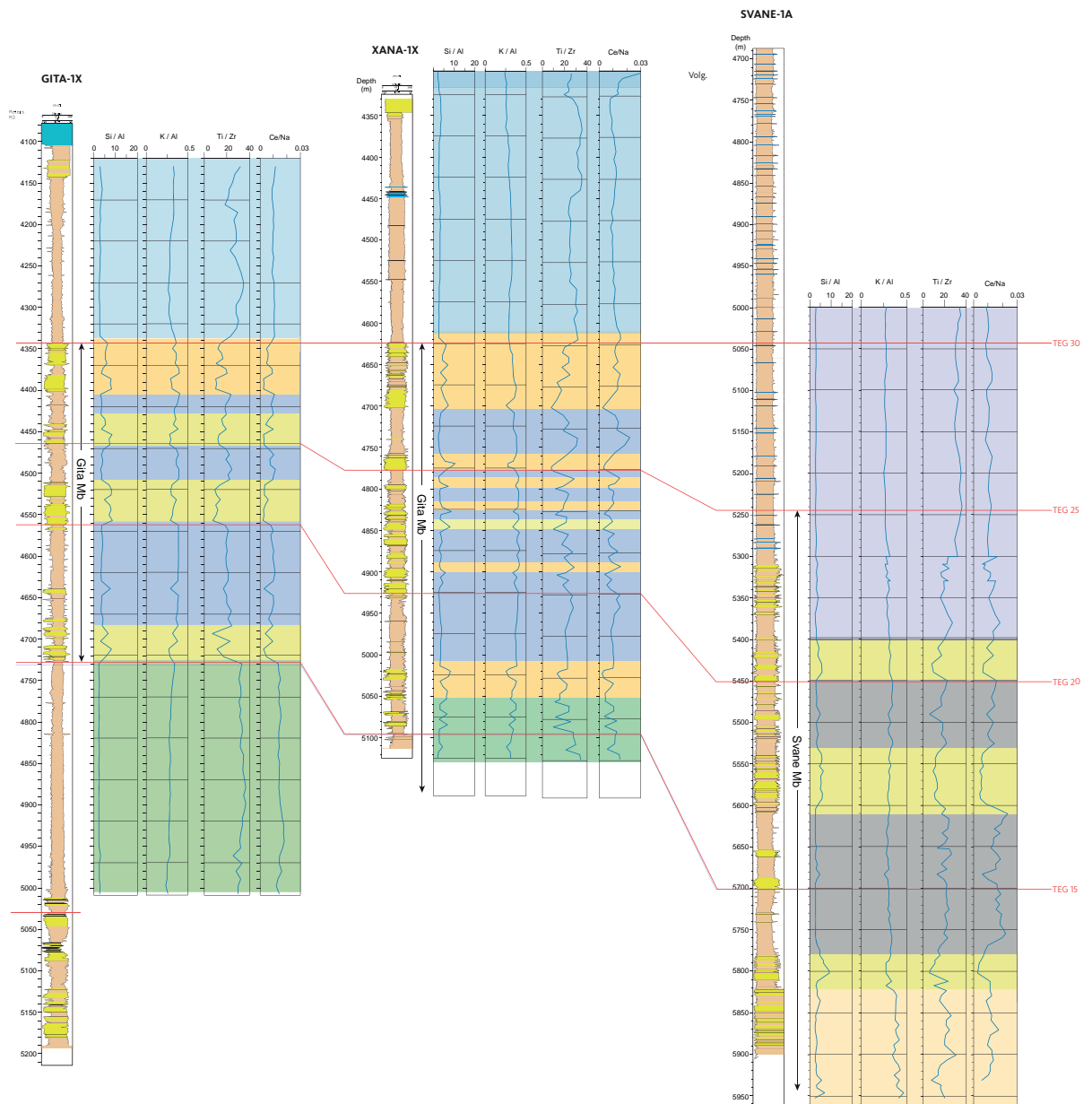


Fig. 4.18

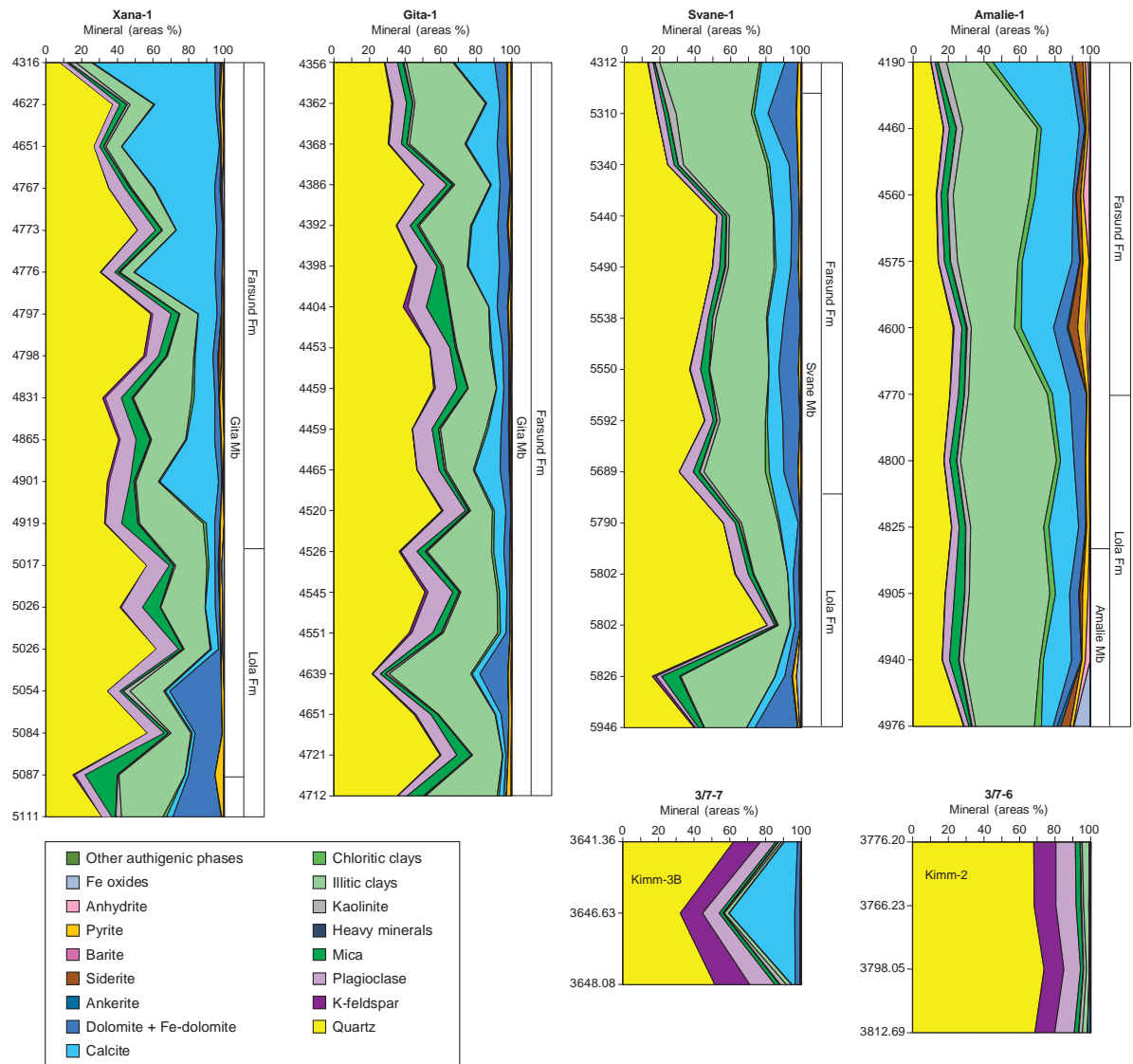
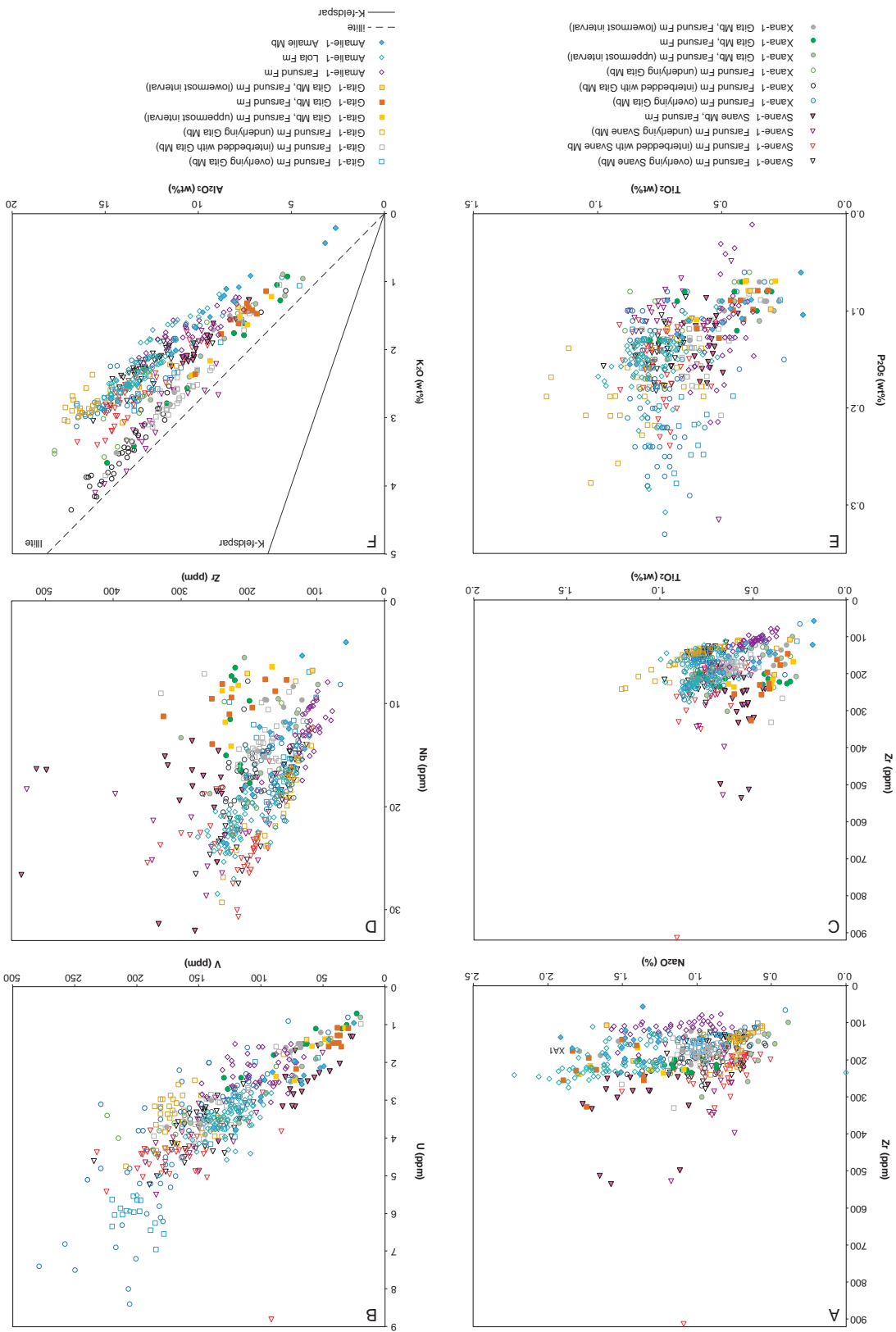


Fig. 4.19

Fig. 4.20



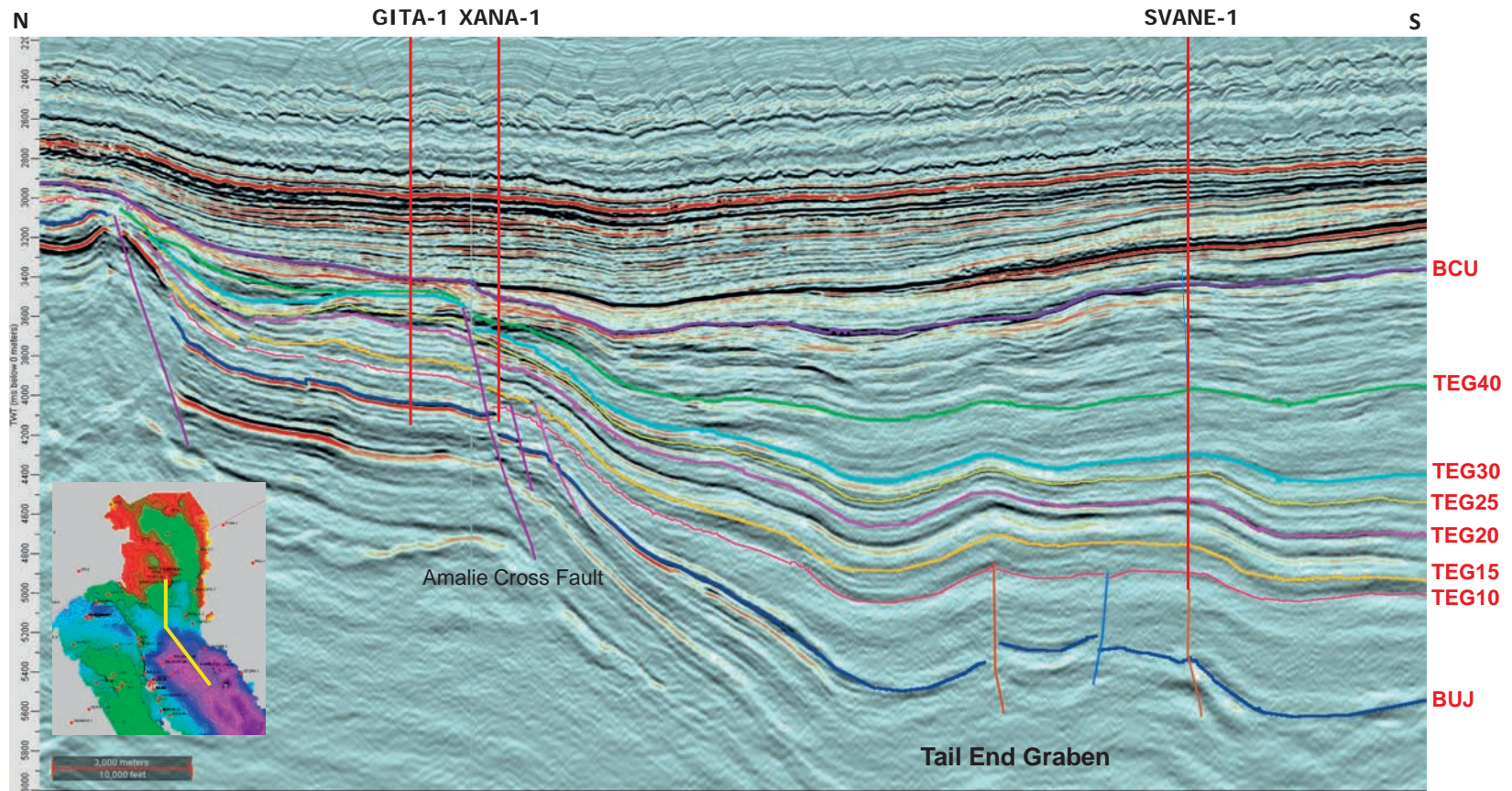


Fig. 5.1

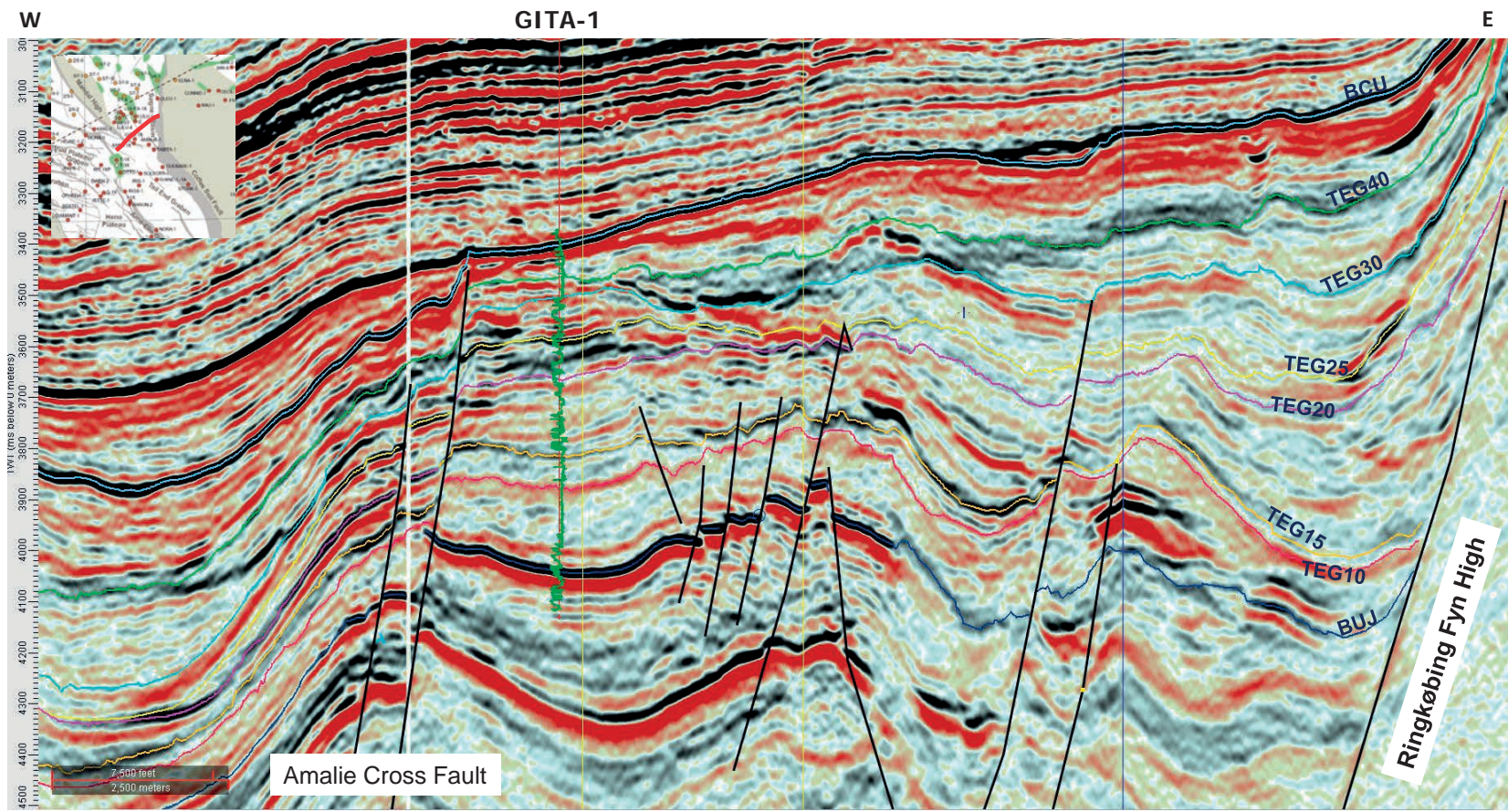


Fig. 5.2

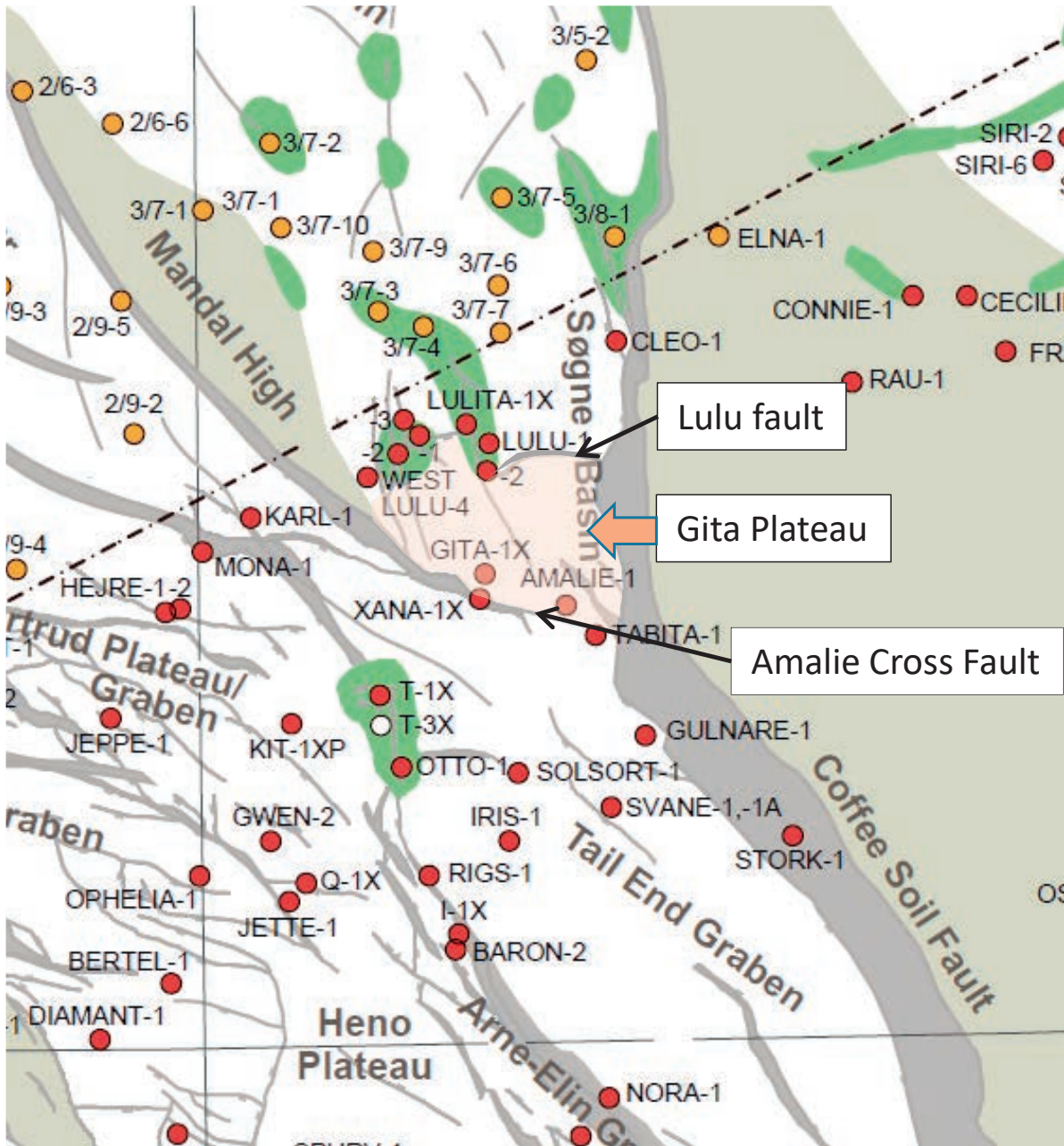


Fig. 5.3

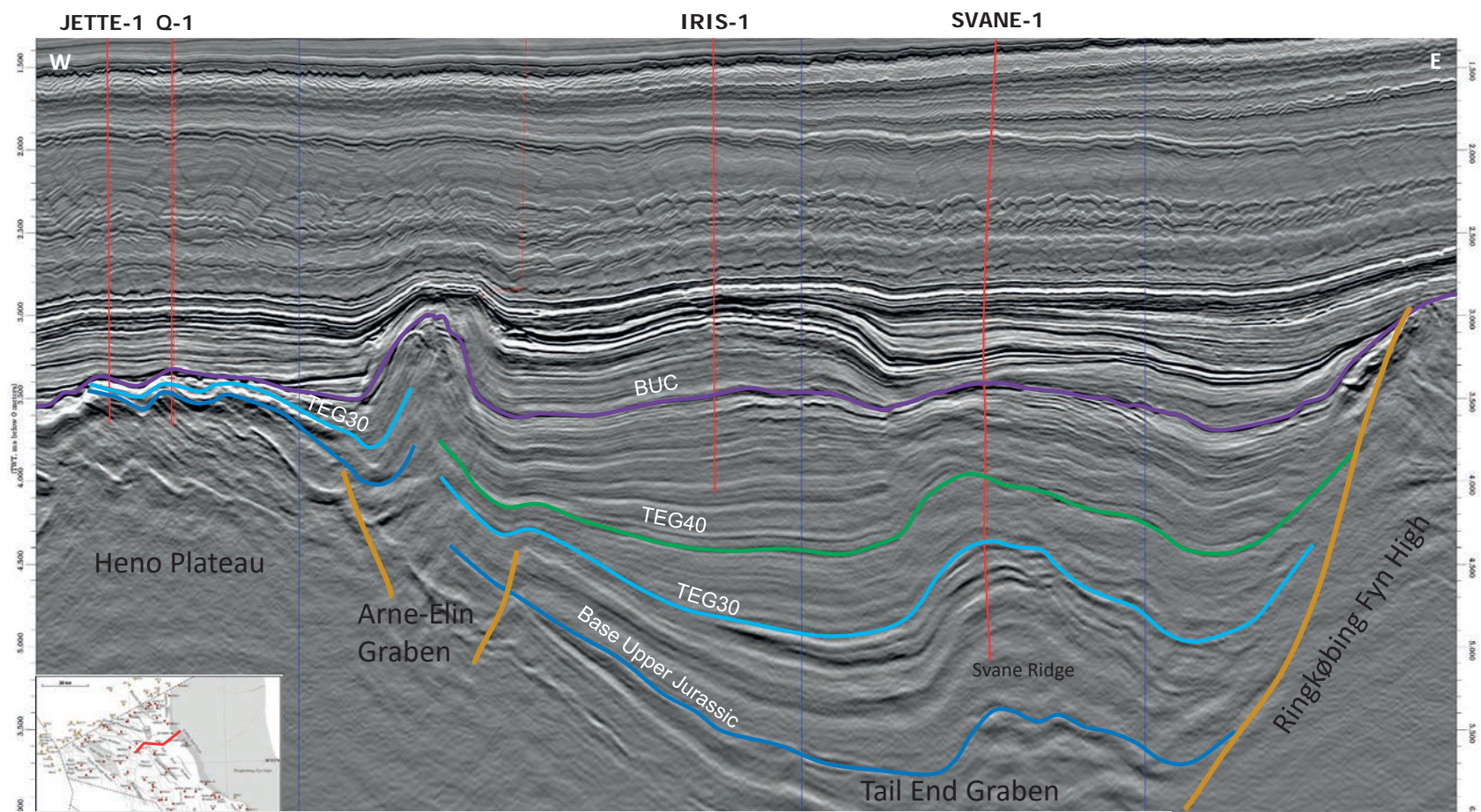
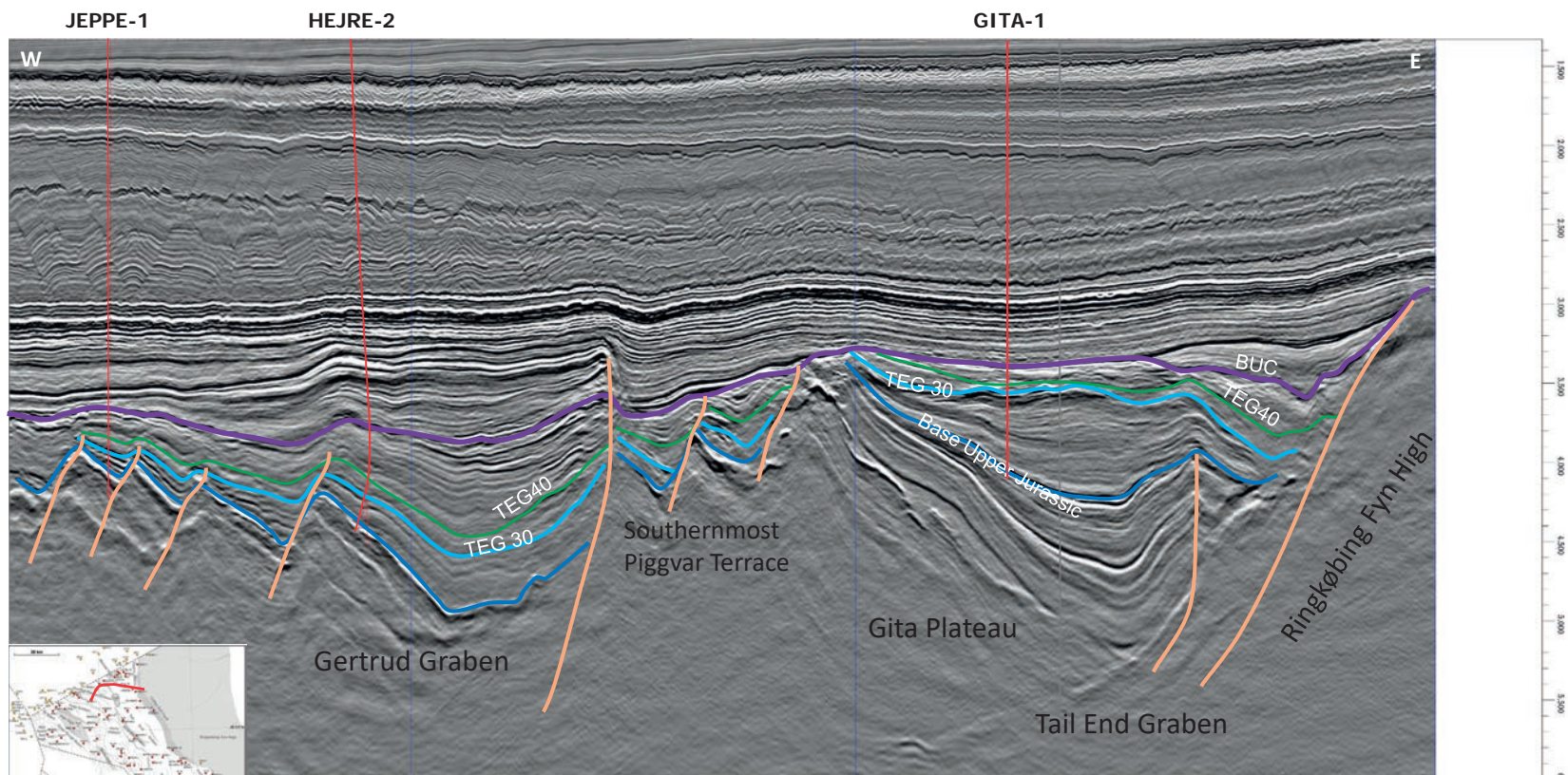


Fig. 5.4



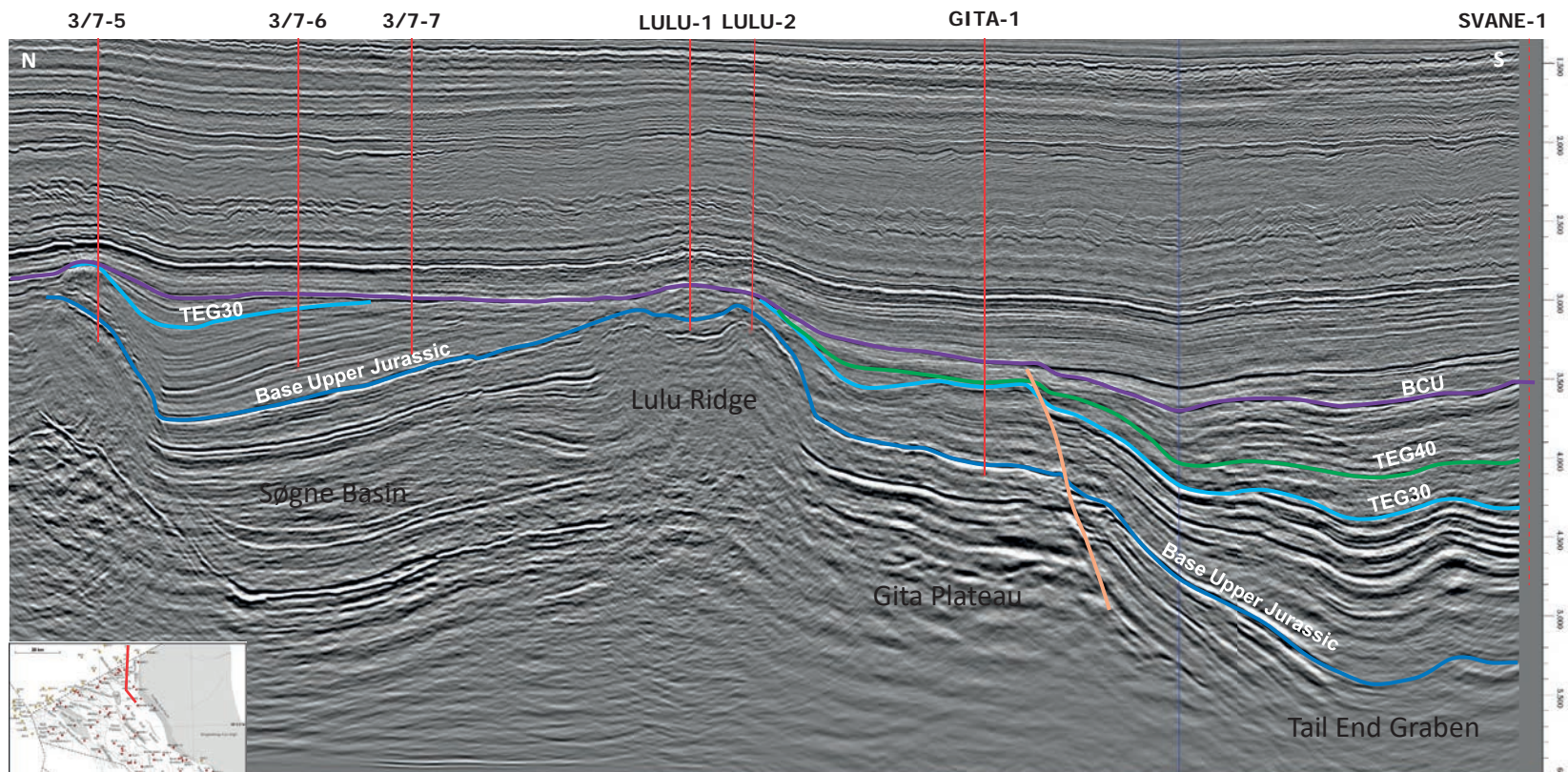


Fig. 5.6

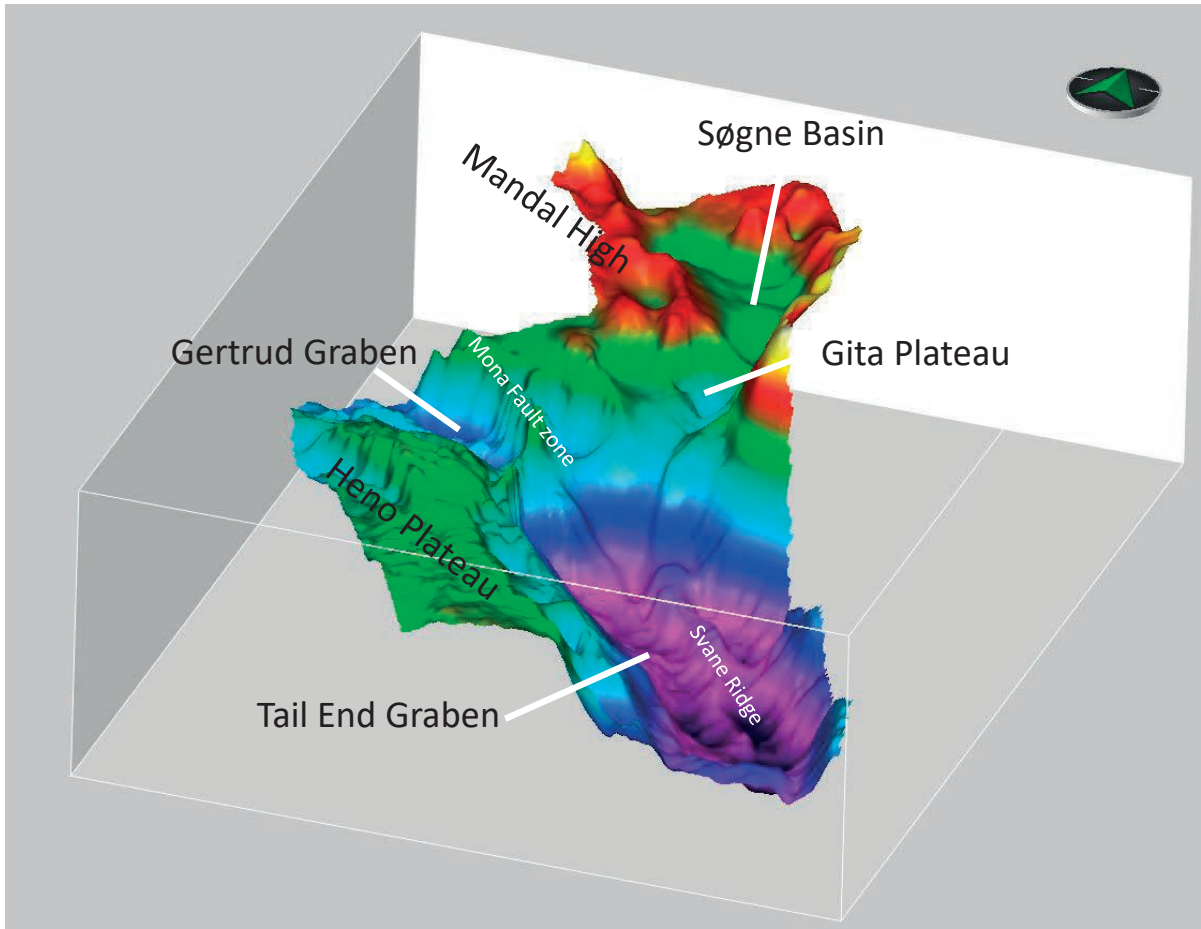


Fig. 5.7

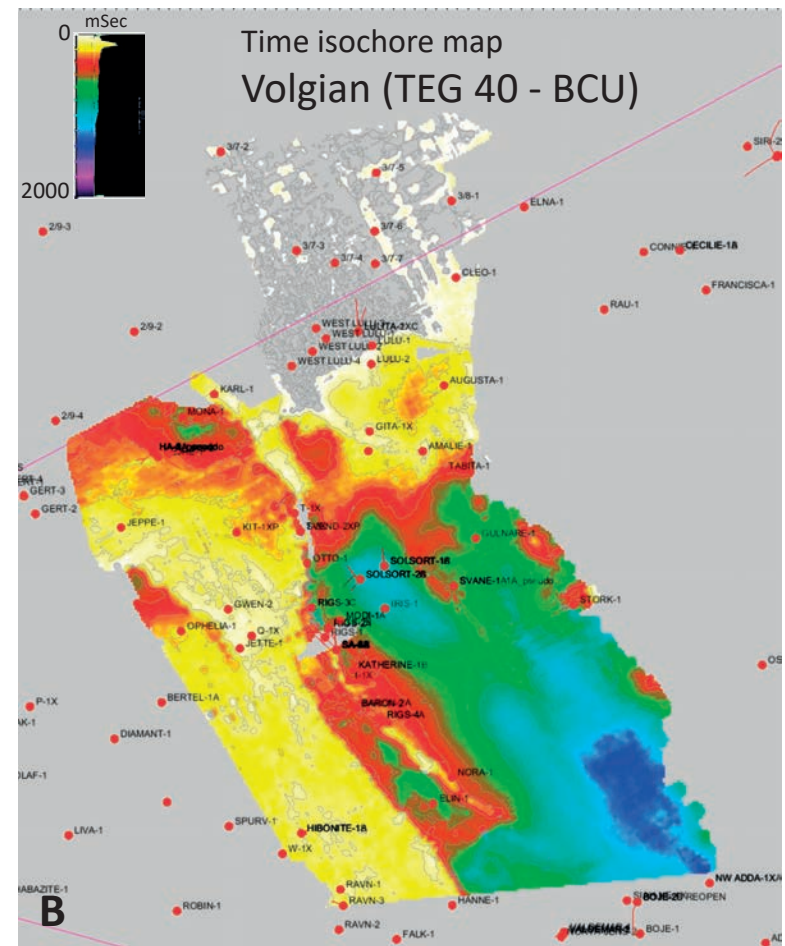
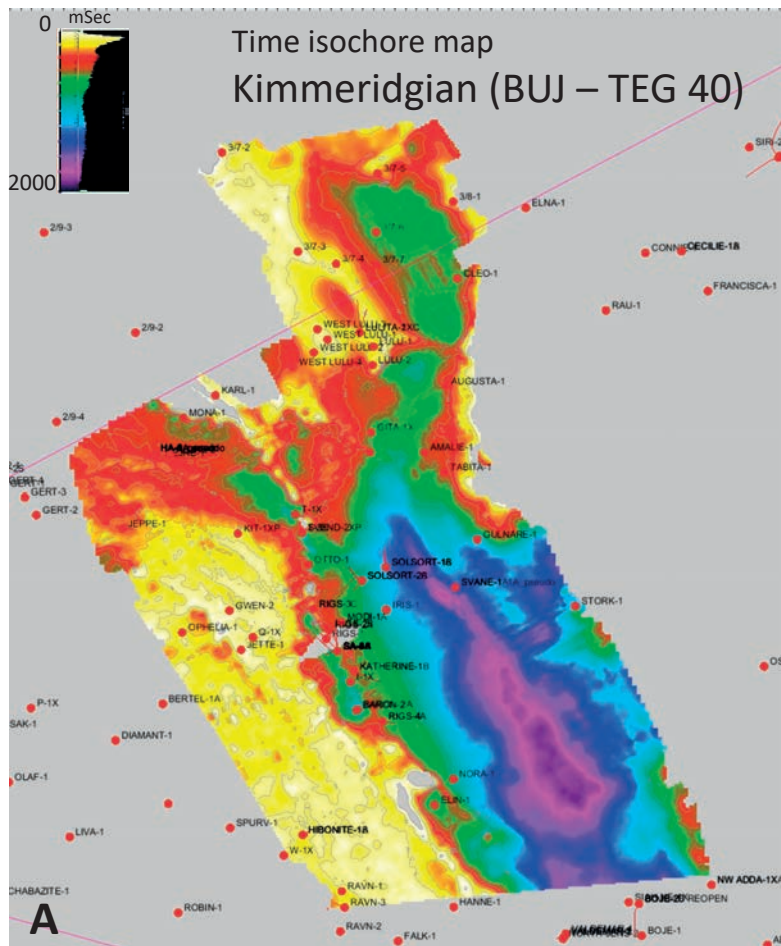


Fig. 5.8

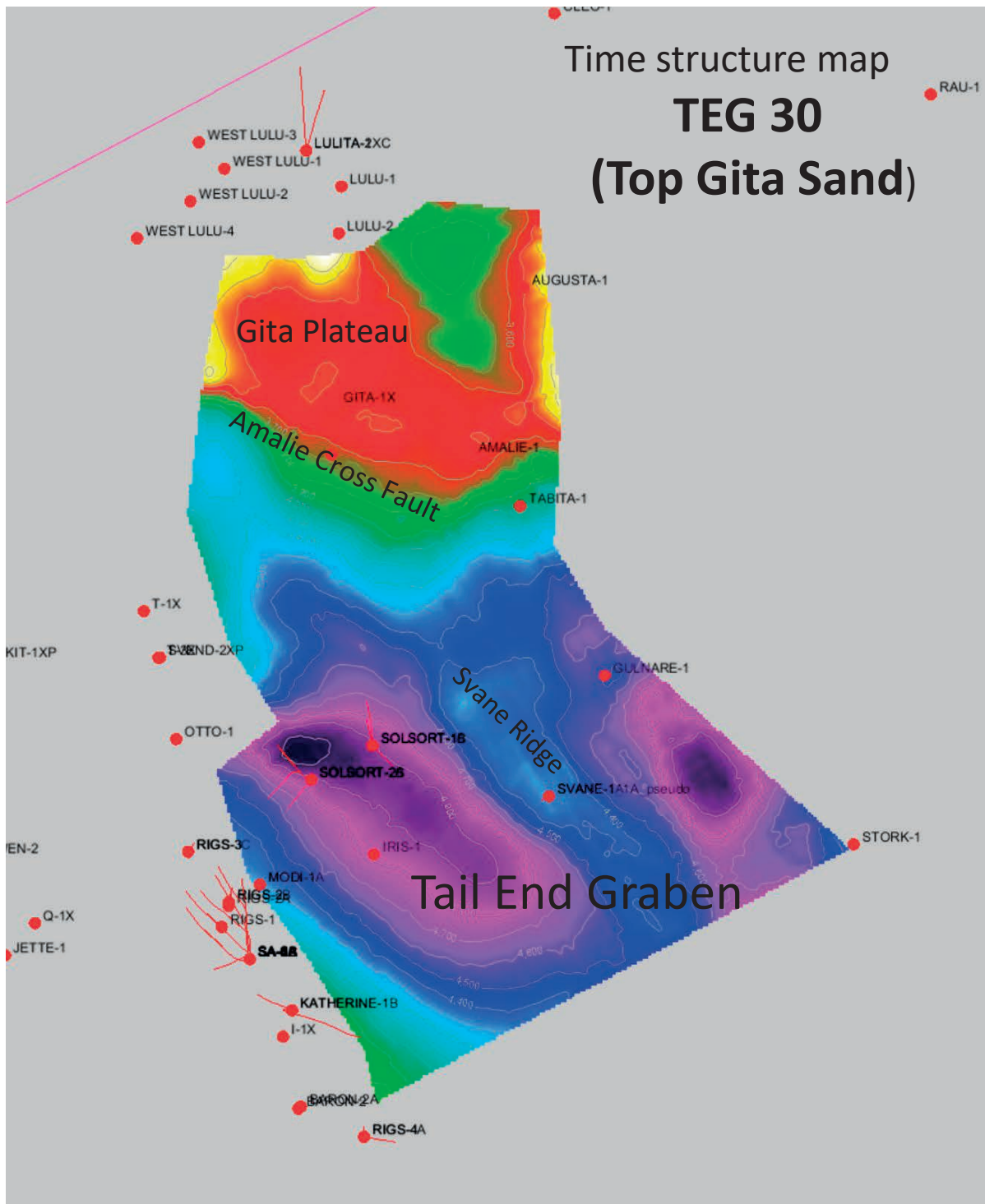


Fig. 5.9

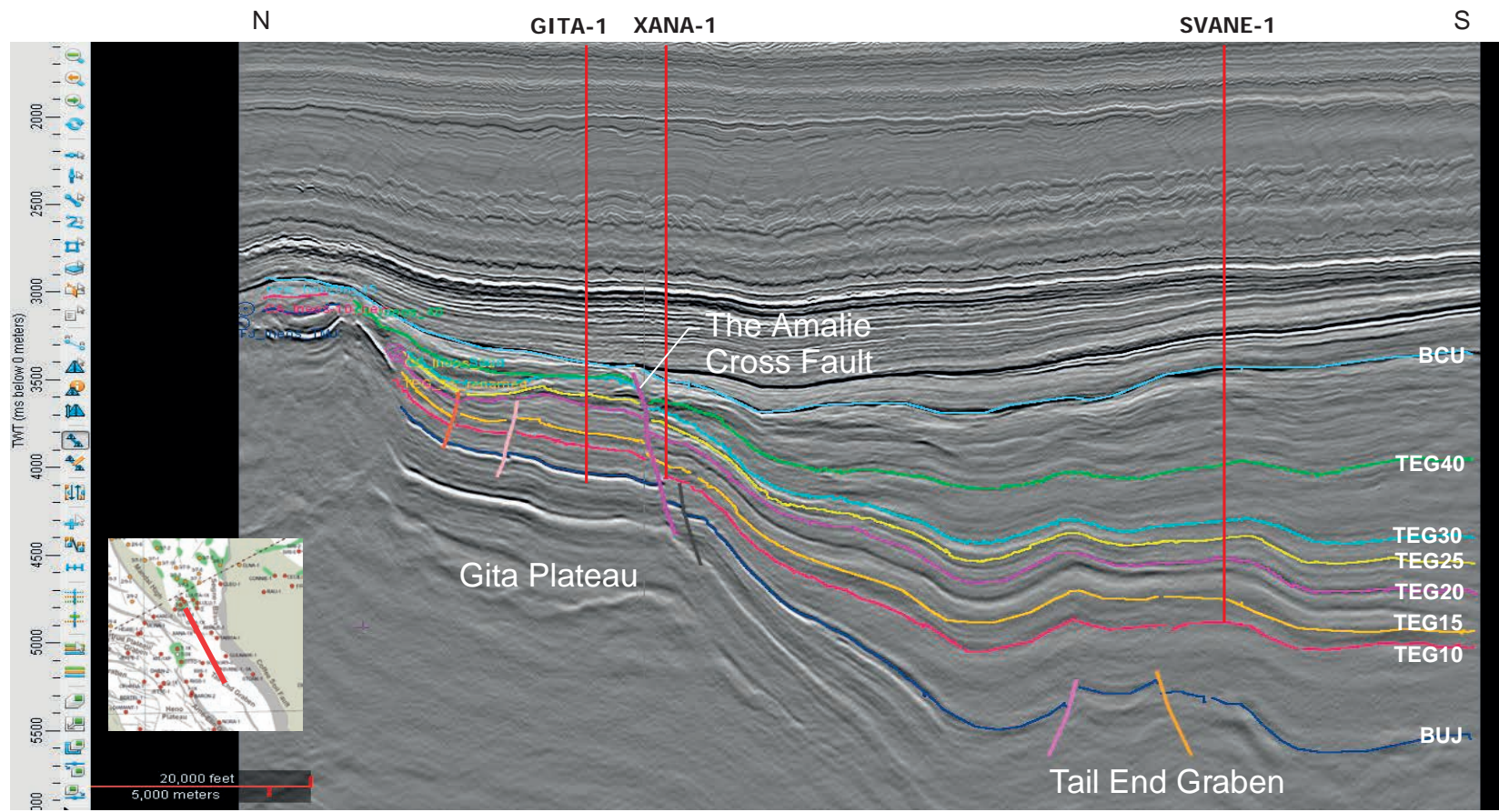


Fig. 5.10

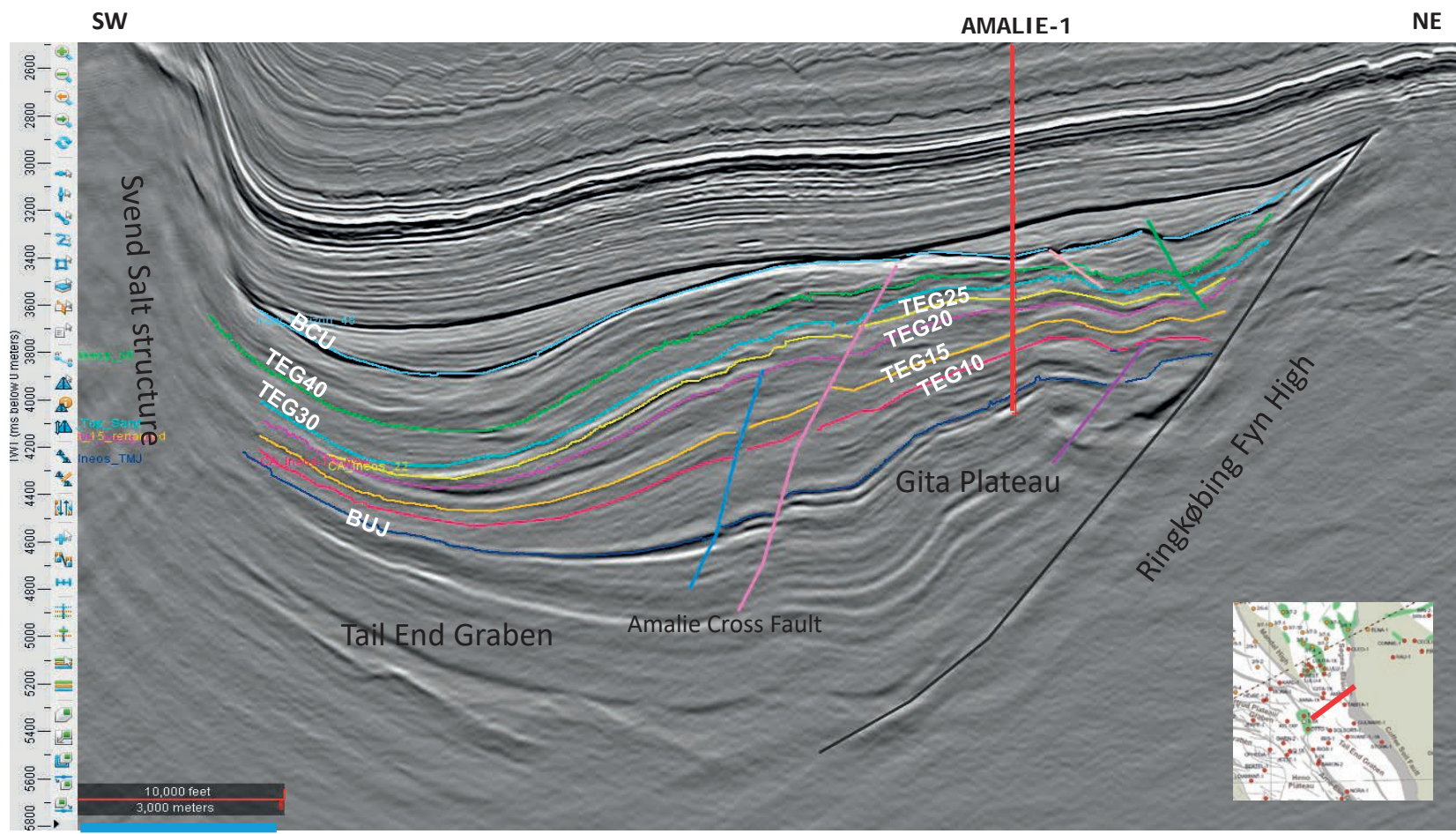


Fig. 5.11

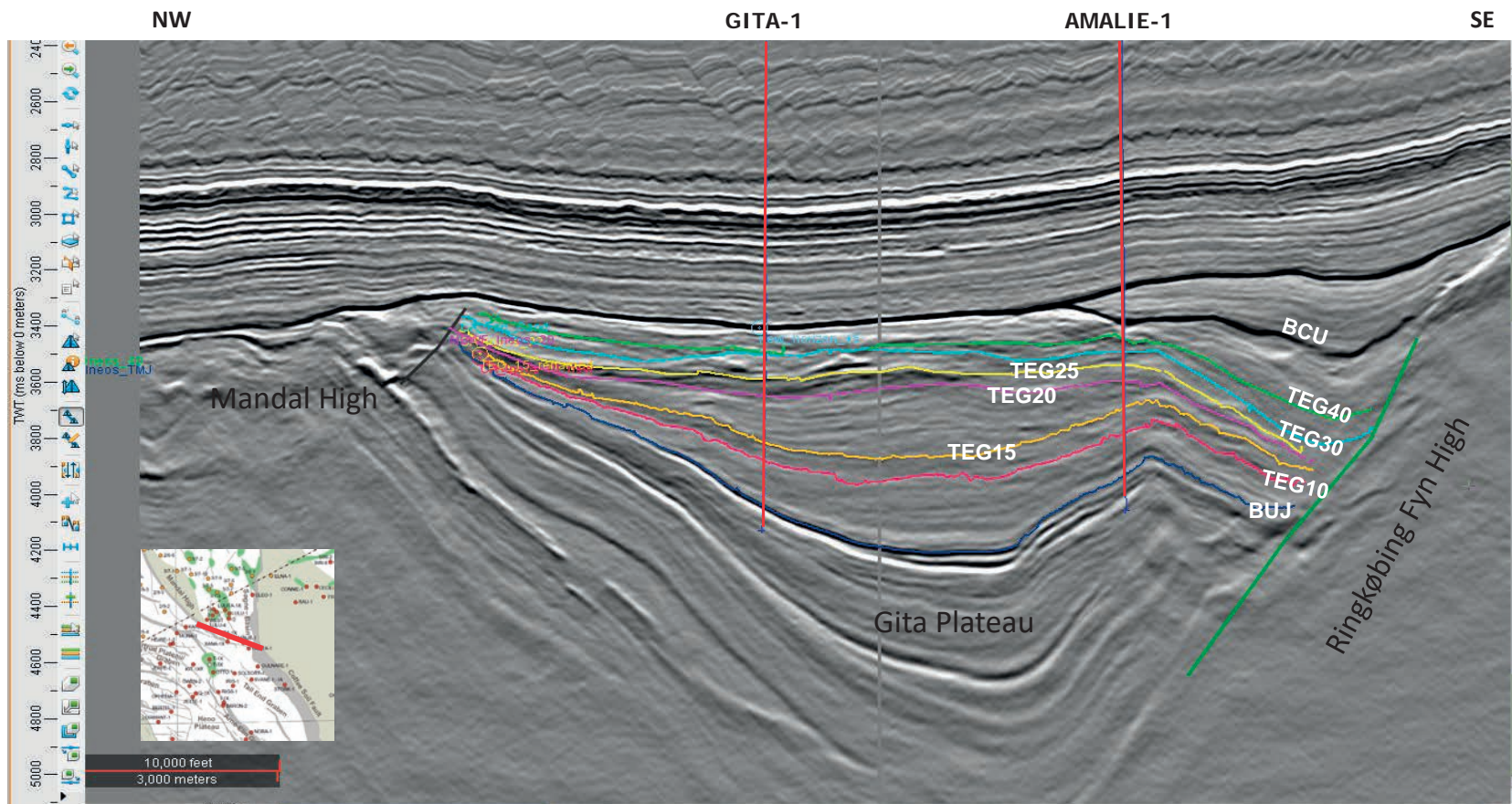


Fig. 5.12

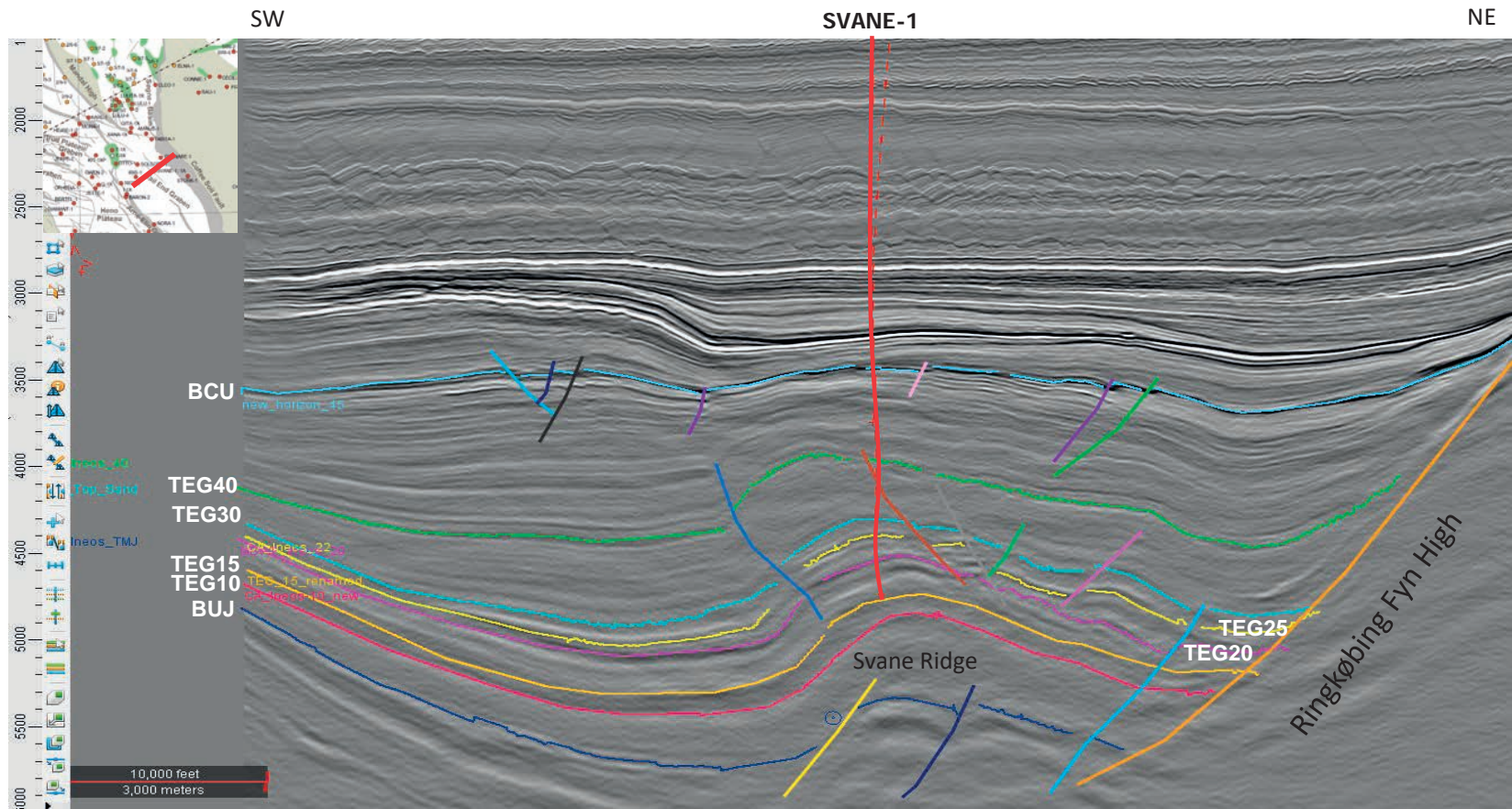
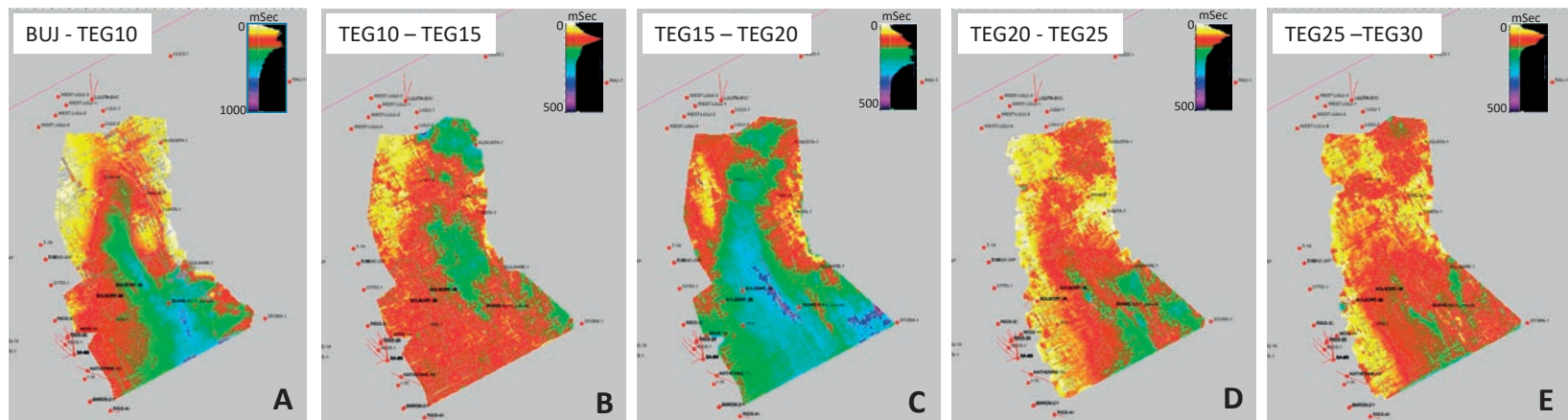
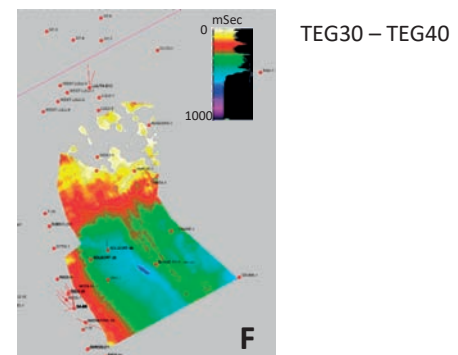


Fig. 5.13



Time isochore maps for the seismic sequences



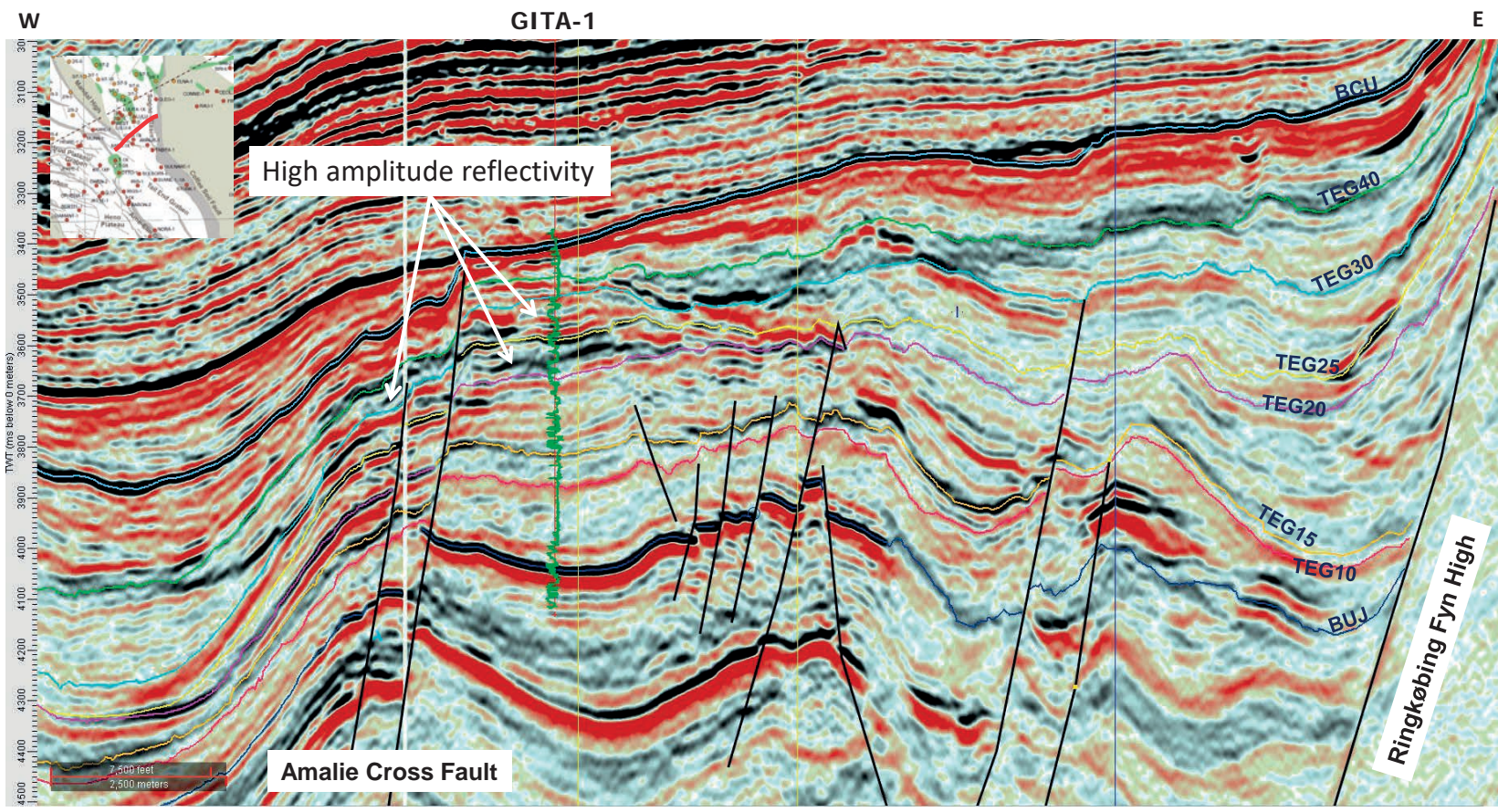
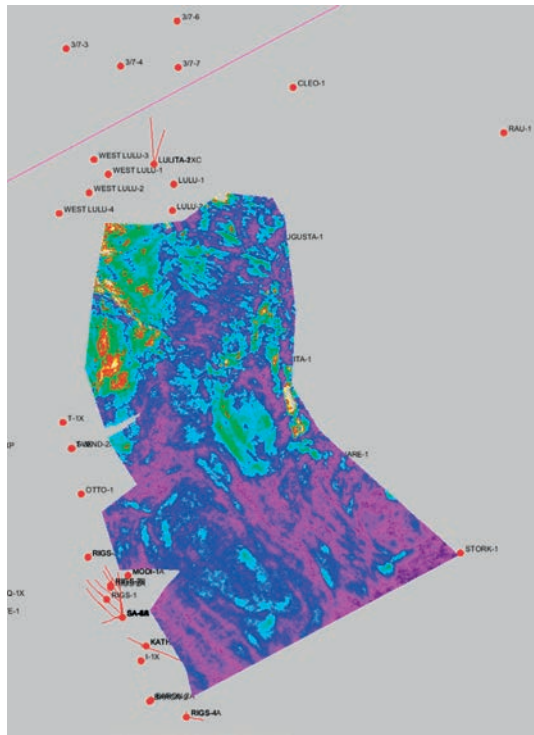
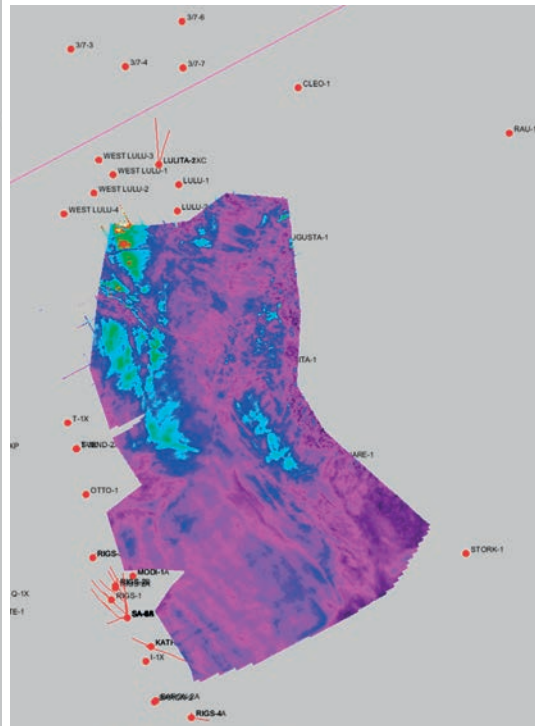


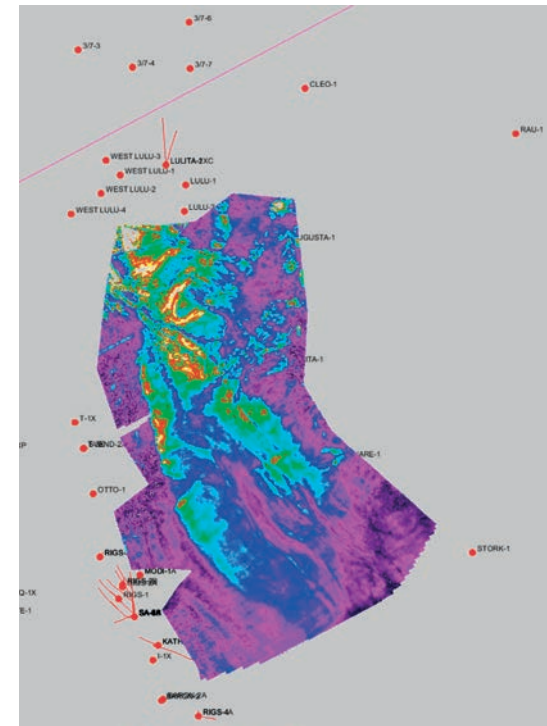
Fig. 5.15



RMS-amplitude map BUJ-TEG 10



RMS-amplitude map TEG15 – TEG20



RMS-amplitude map TEG20 – TEG30

Fig. 5.16

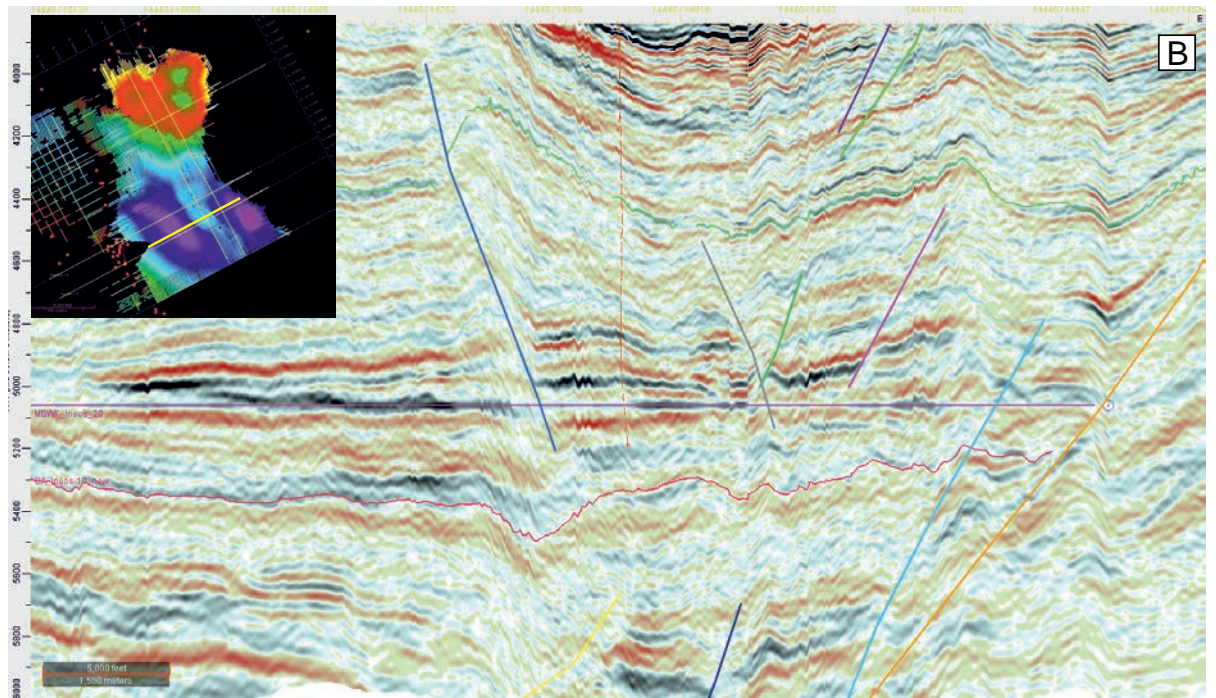
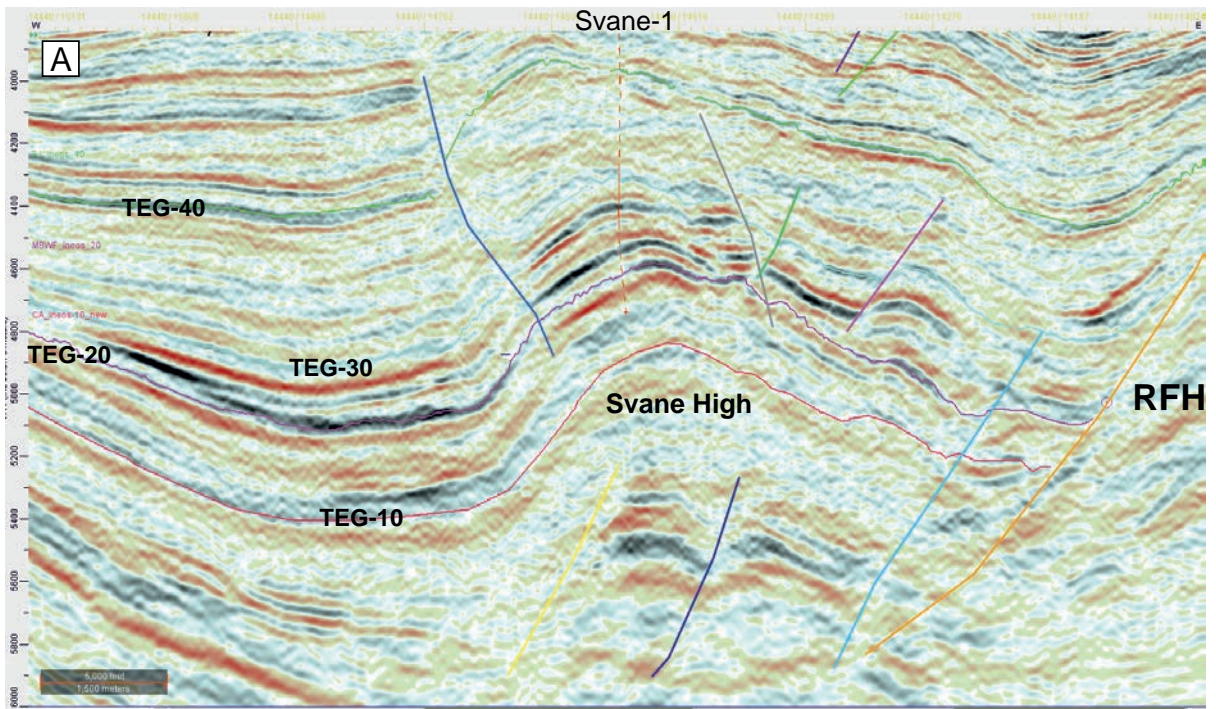


Fig. 5.17

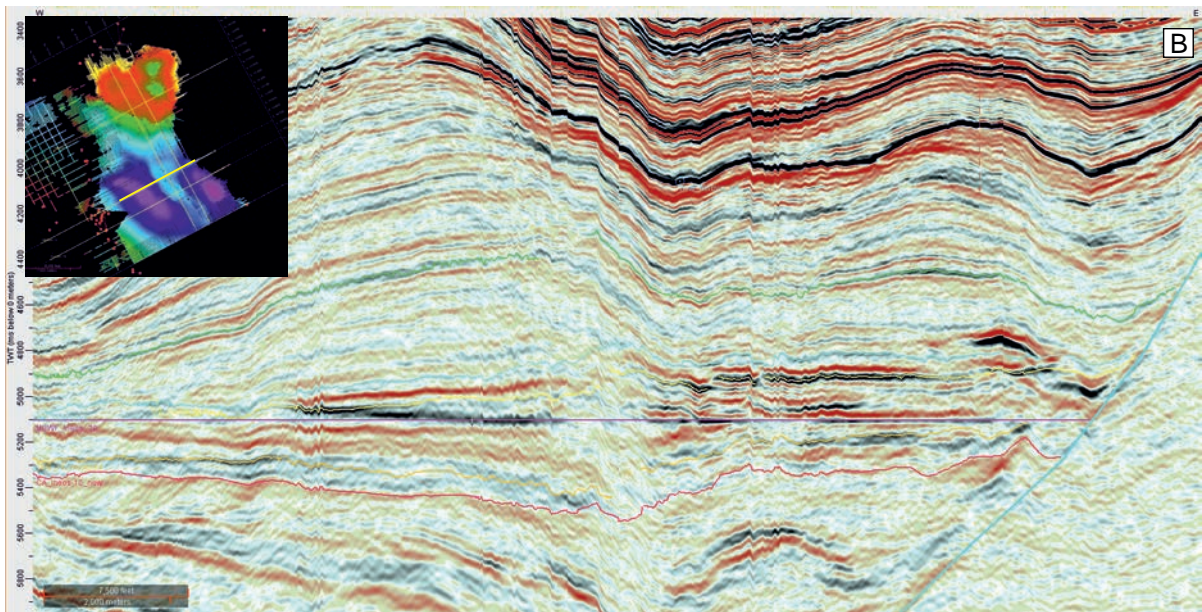
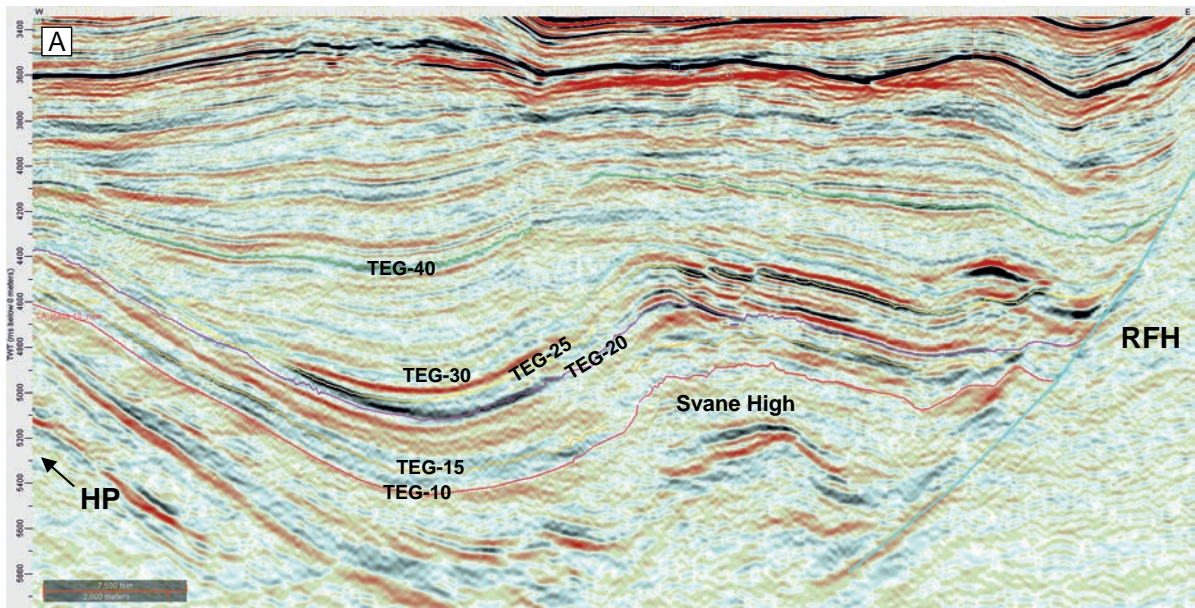


Fig. 5.18

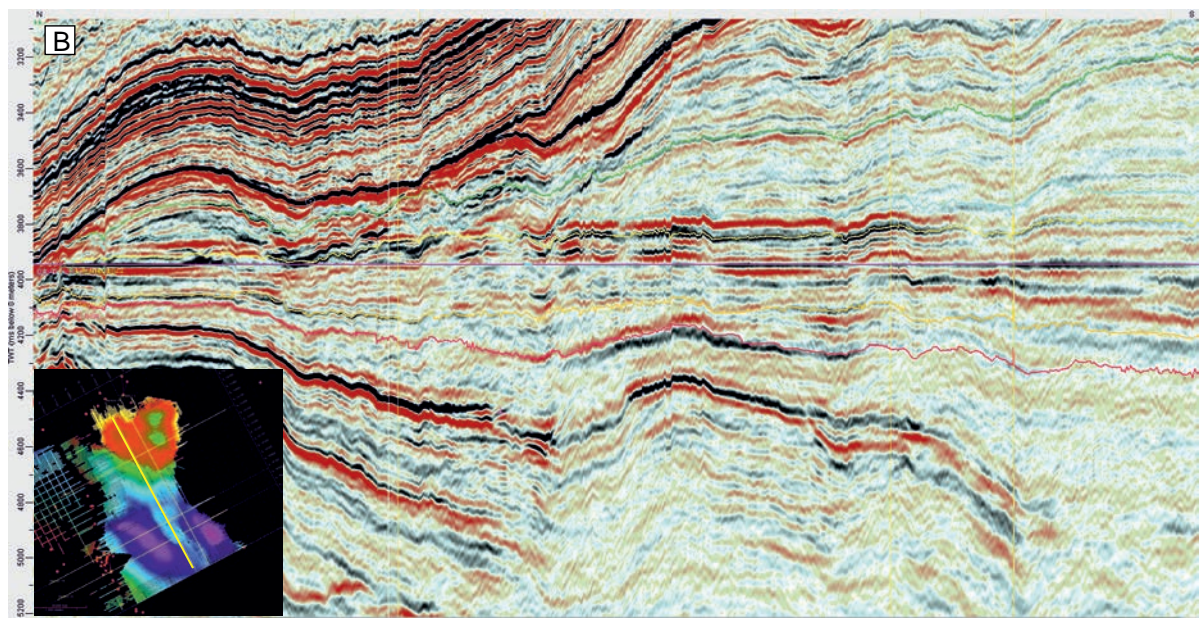
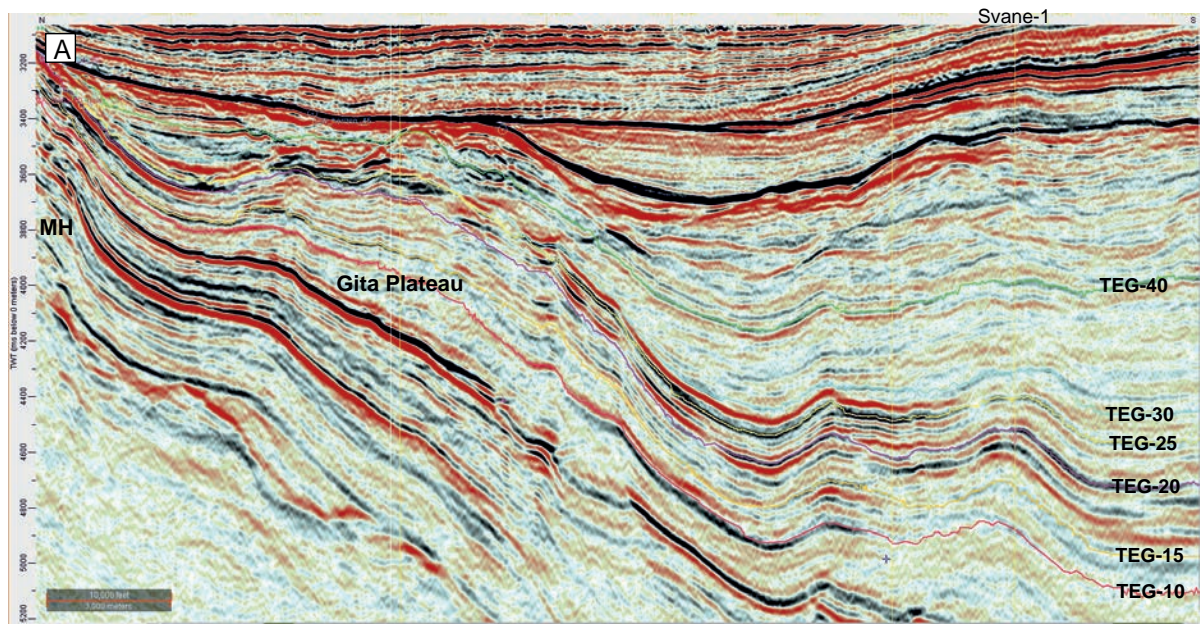


Fig. 5.19

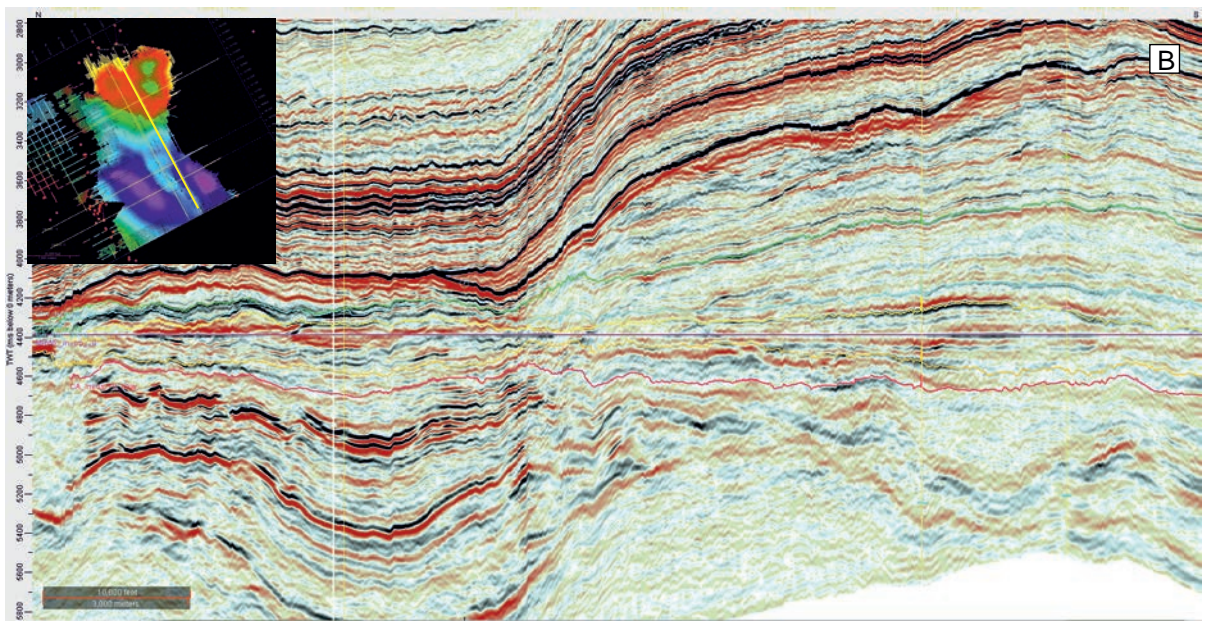
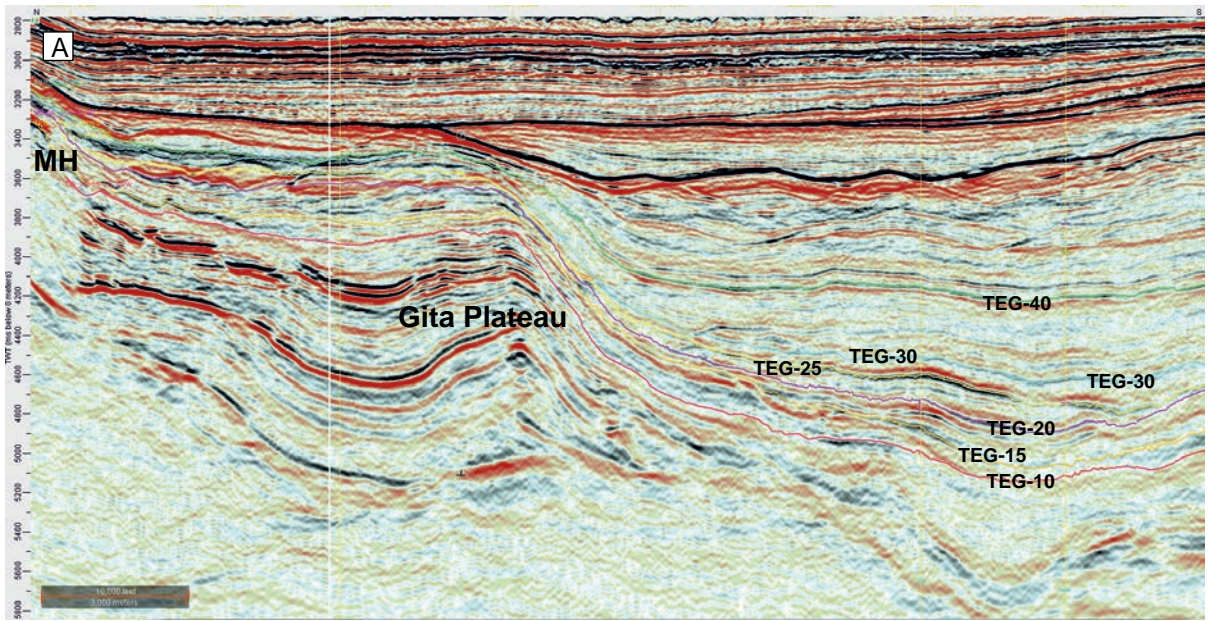


Fig. 5.20

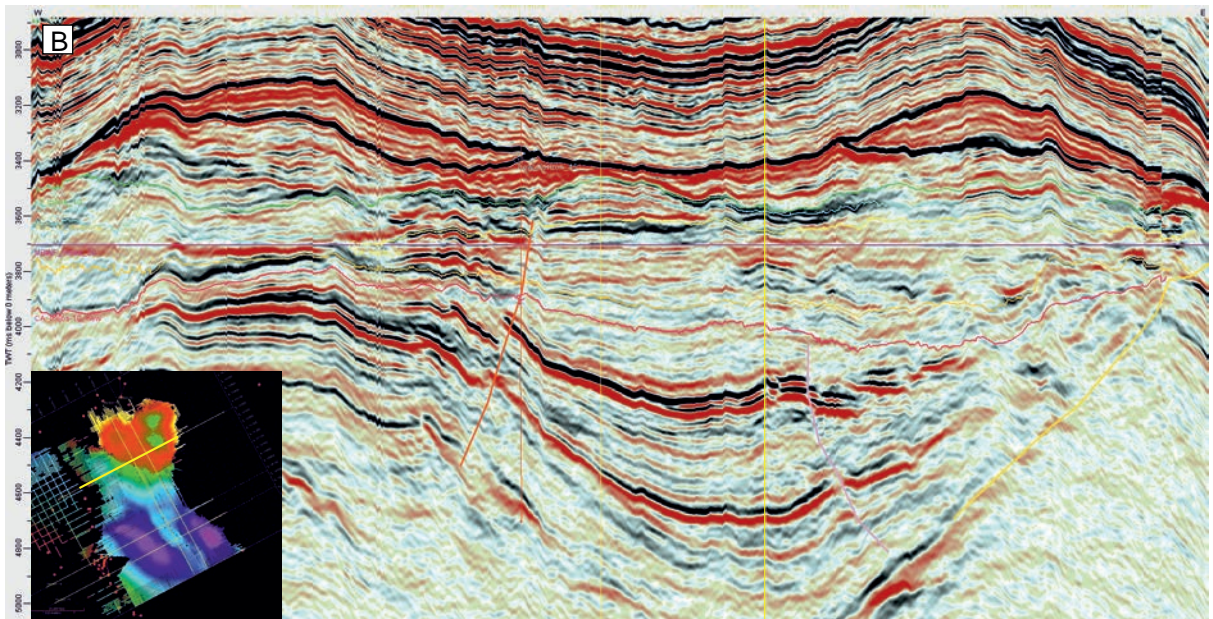
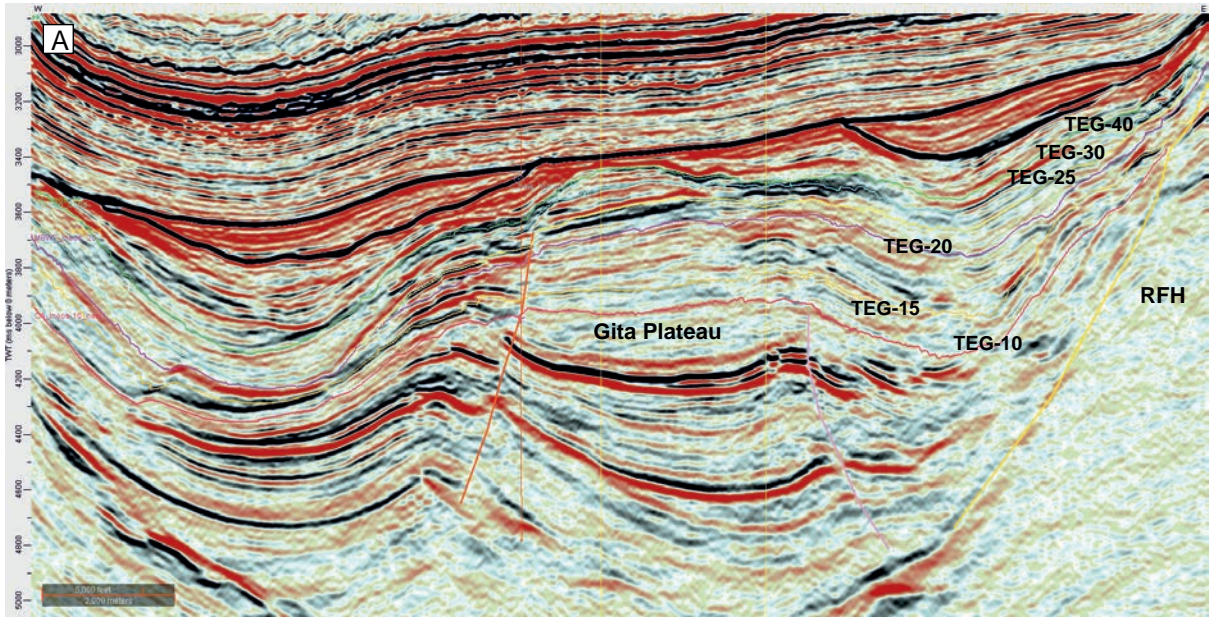


Fig. 5.21

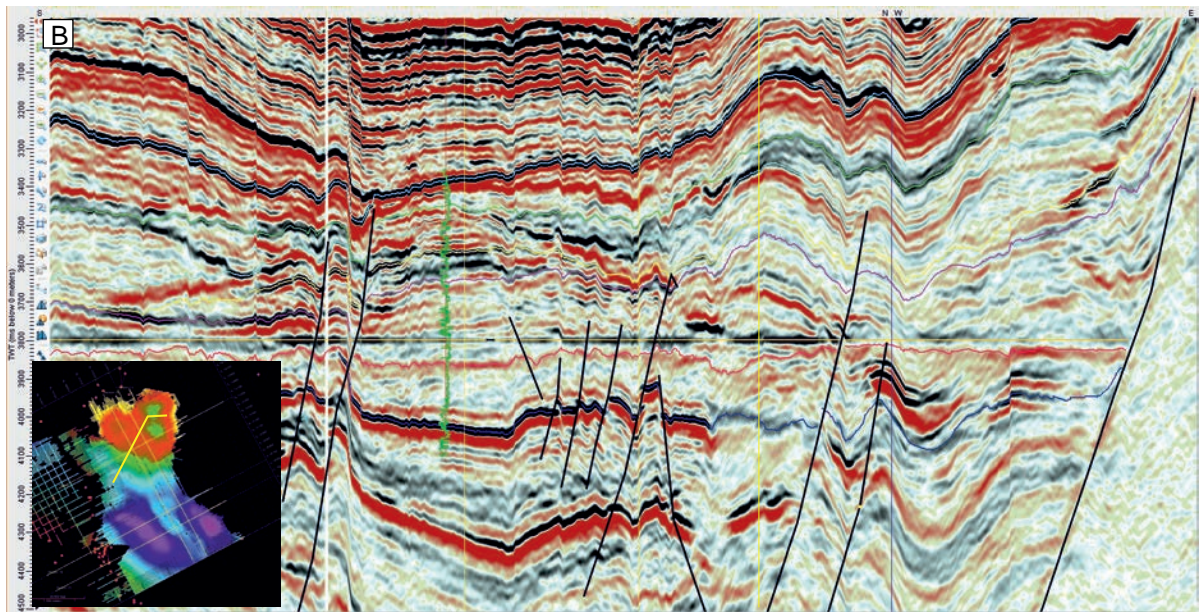
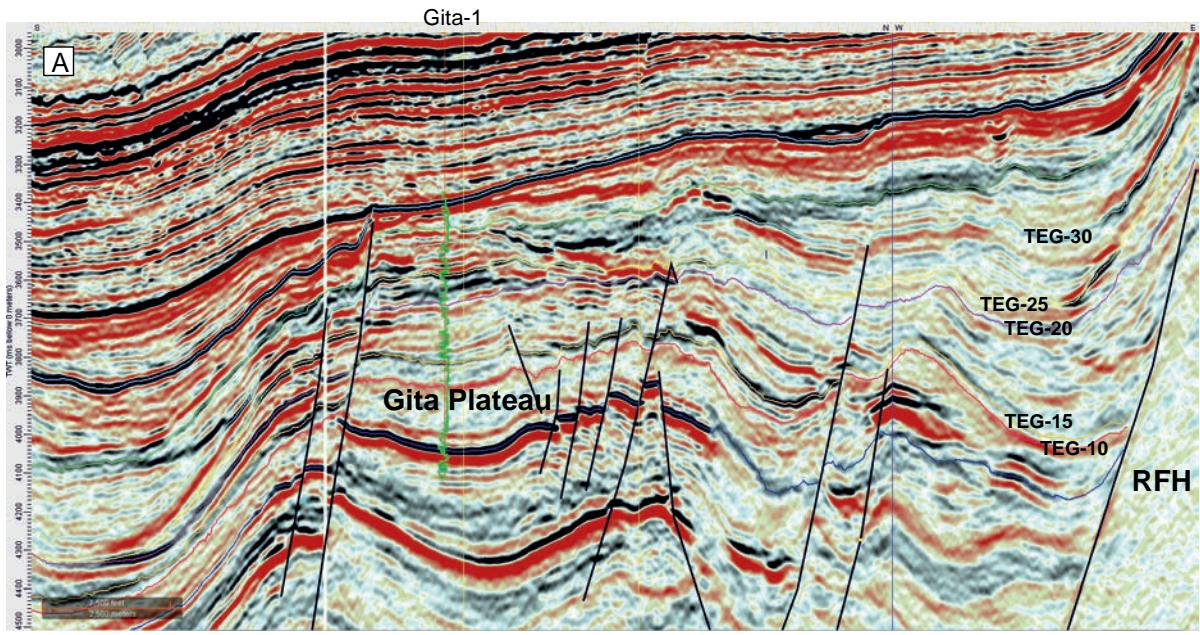


Fig. 5.22

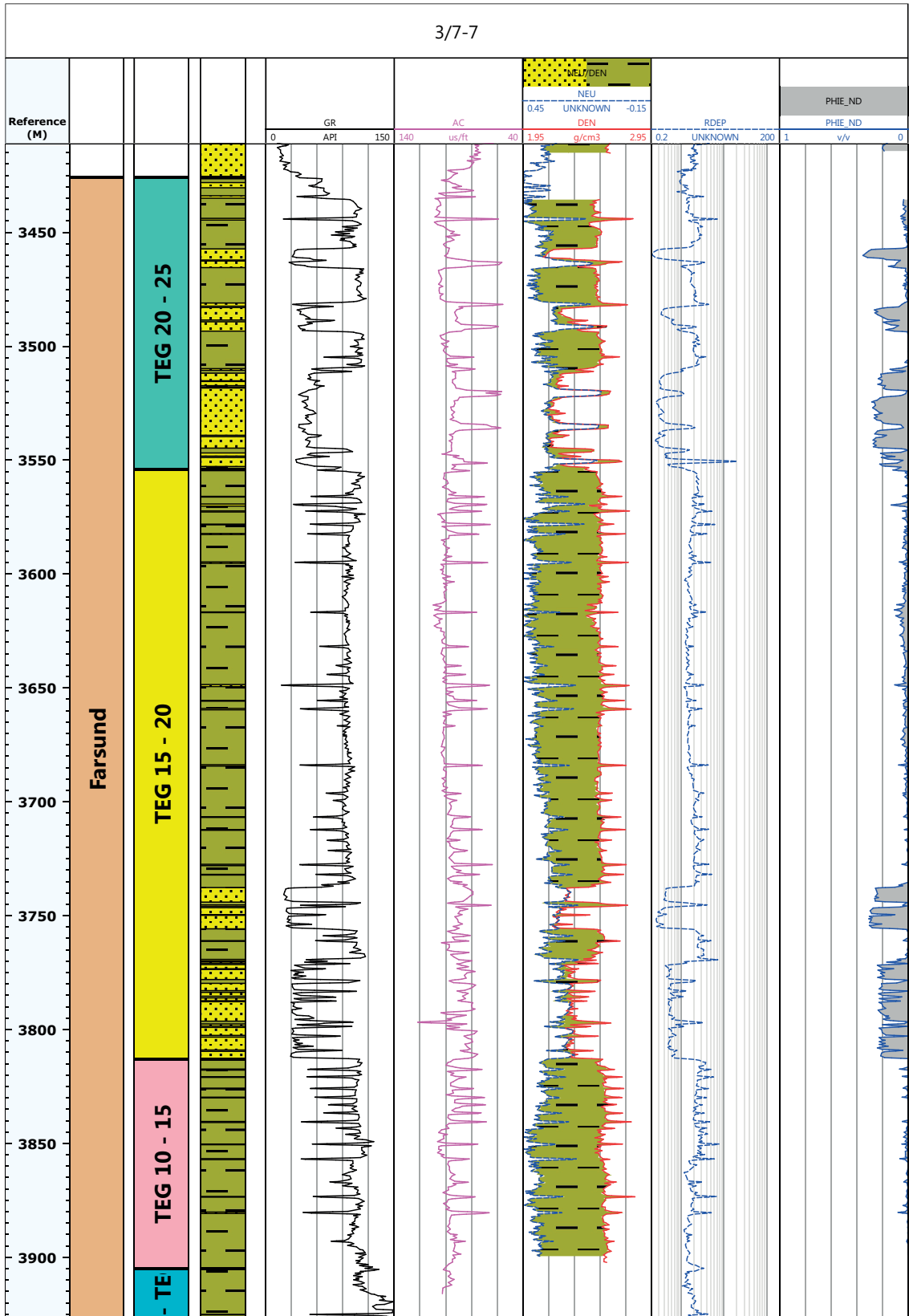


Fig. 6.1

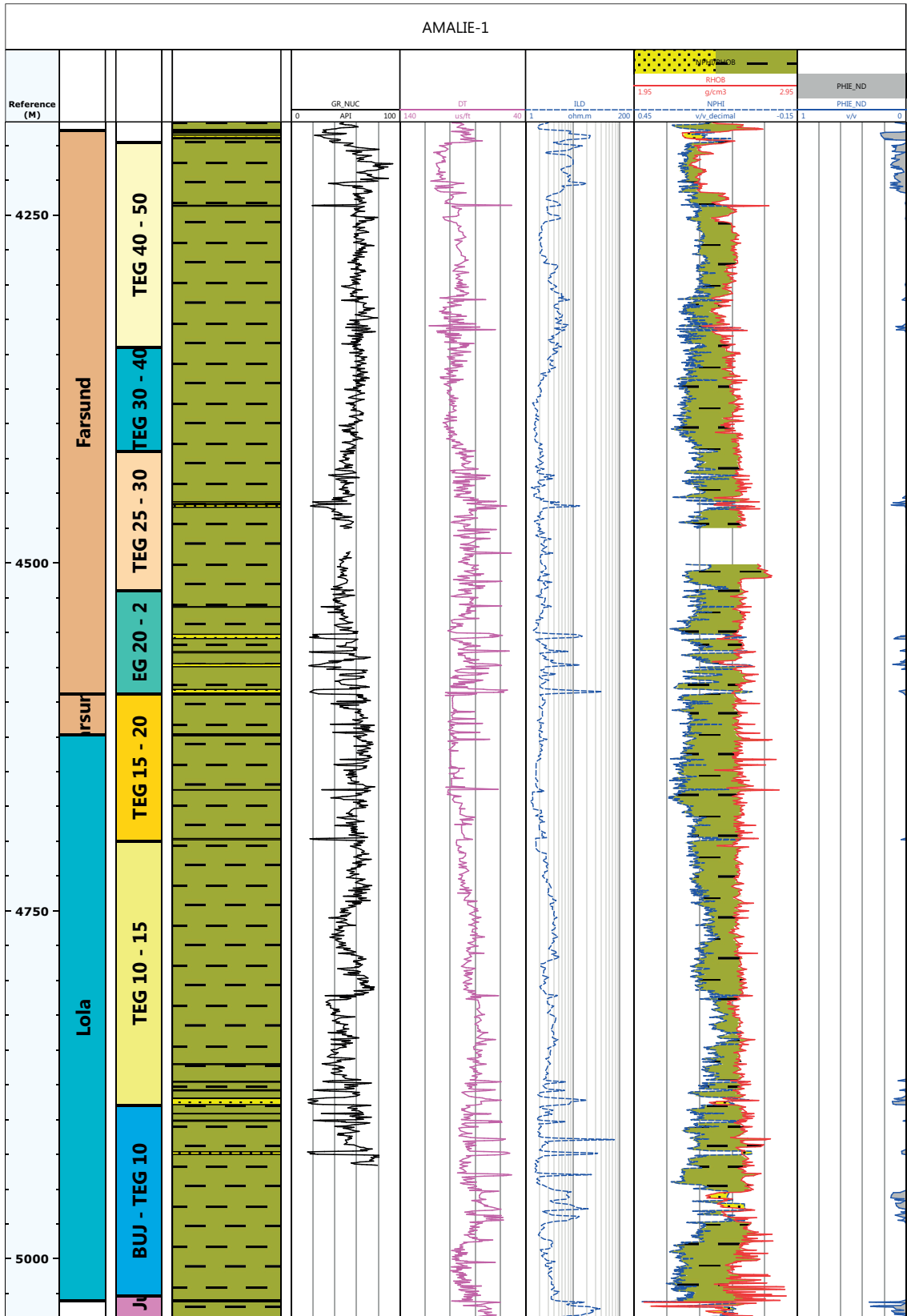


Fig. 6.2

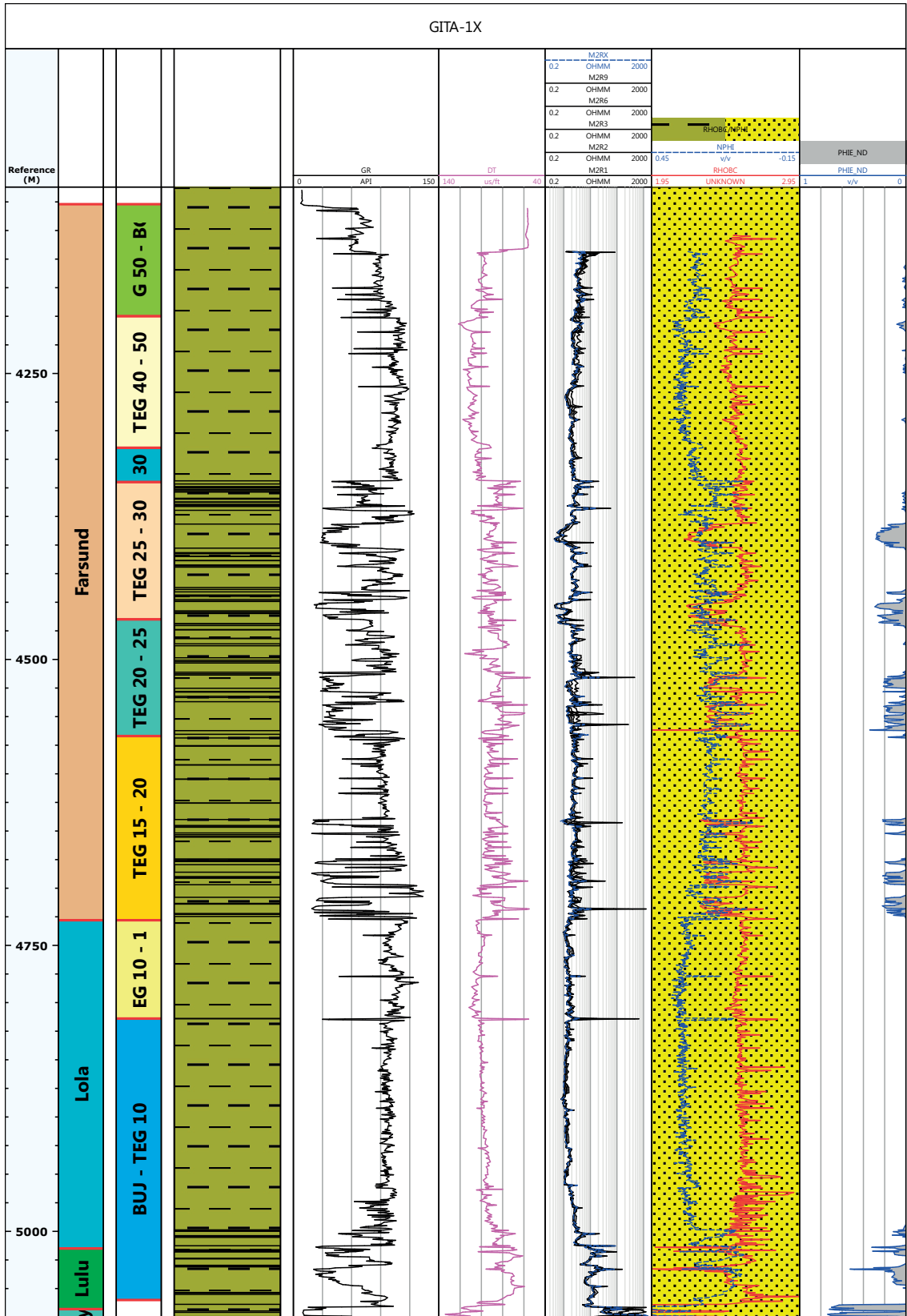


Fig. 6.3



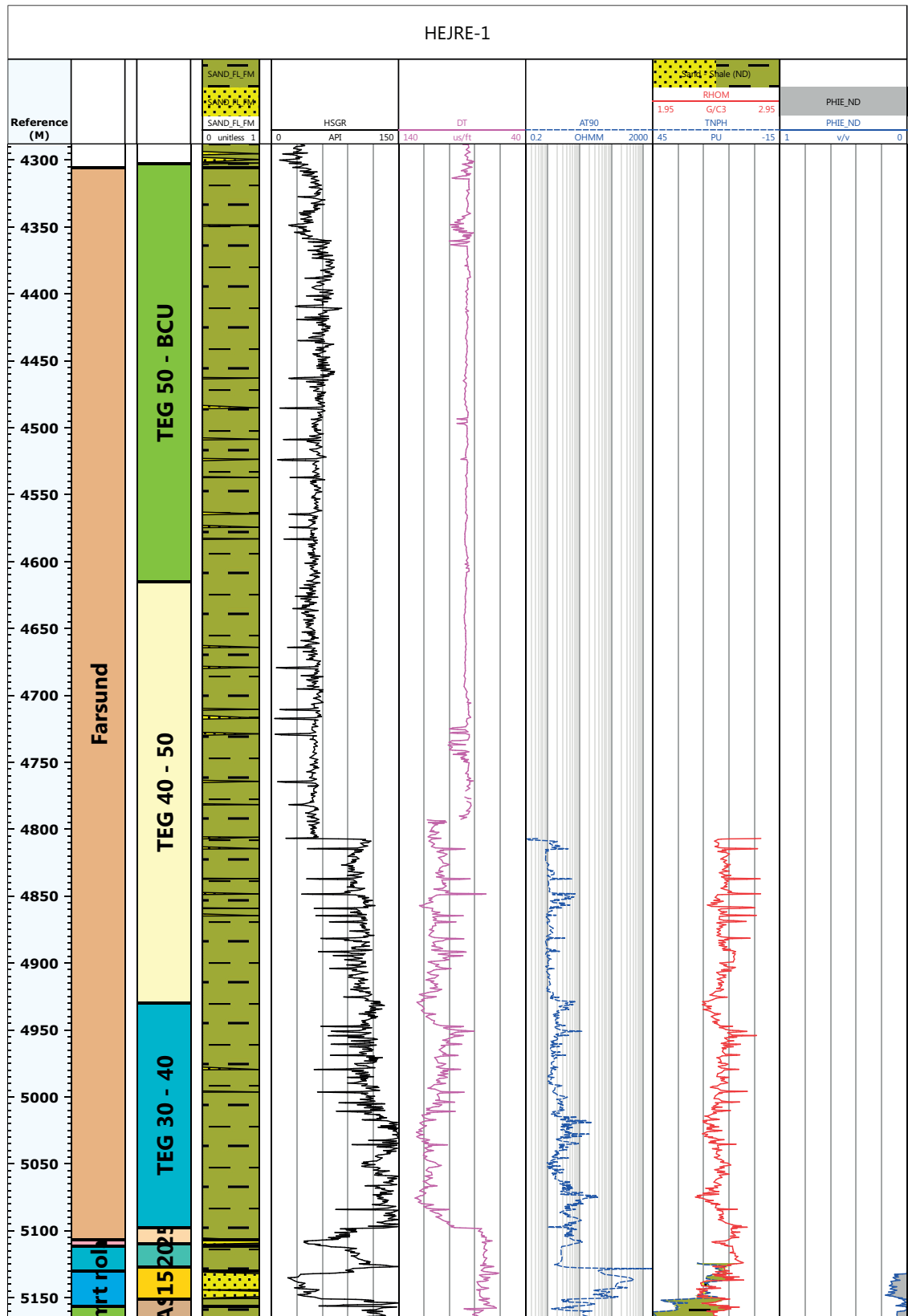


Fig. 6.5

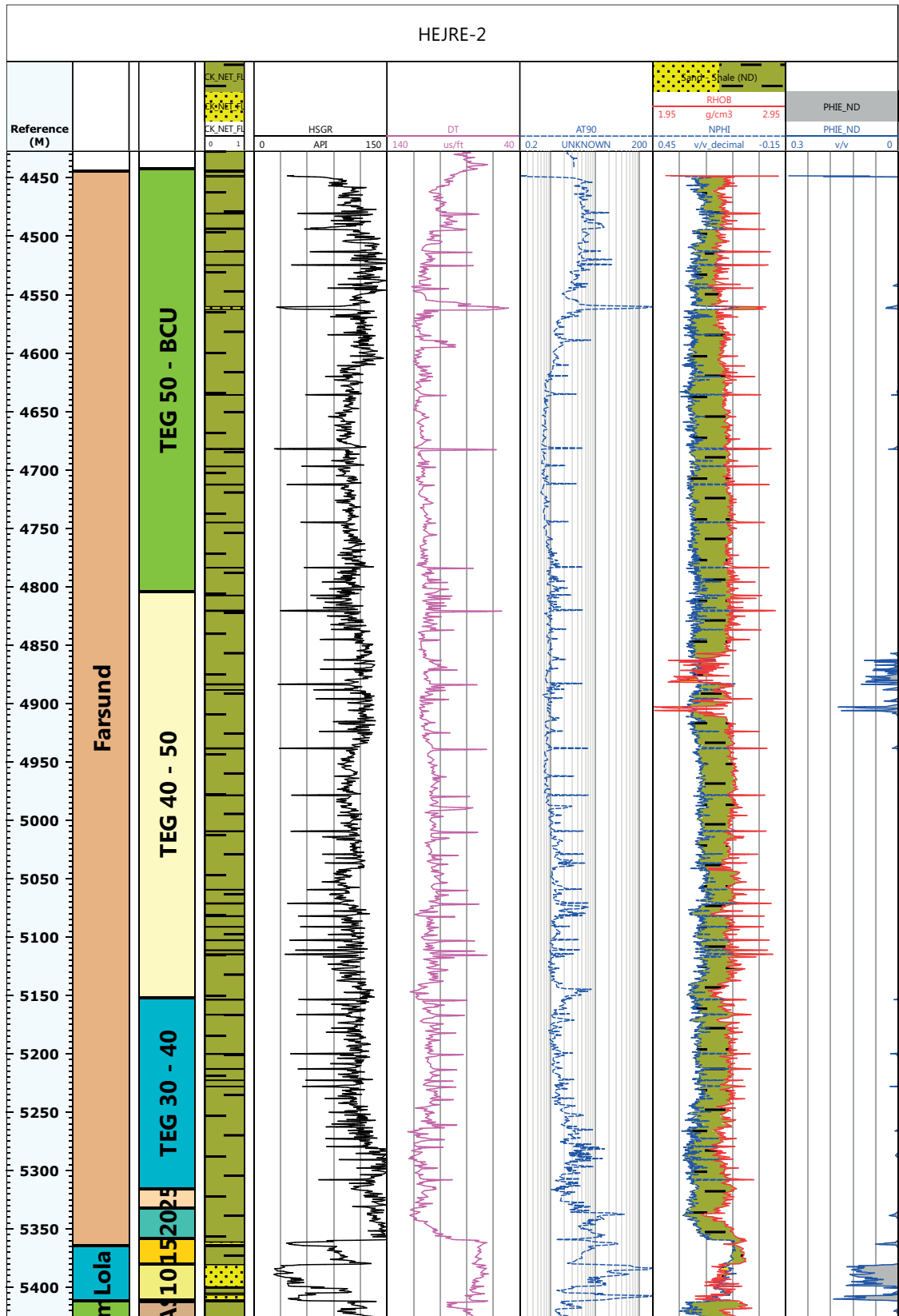


Fig. 6.6

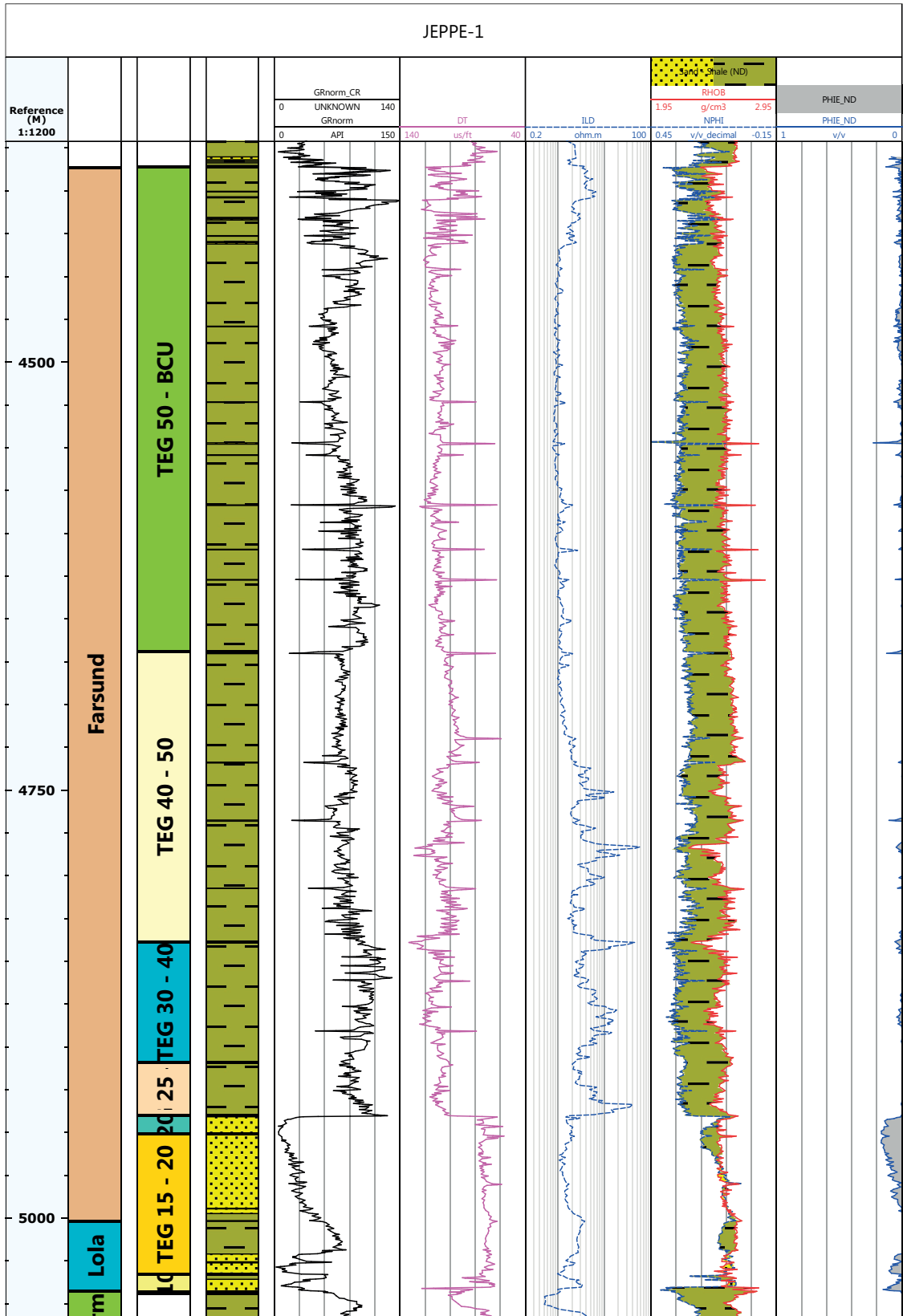


Fig. 6.7

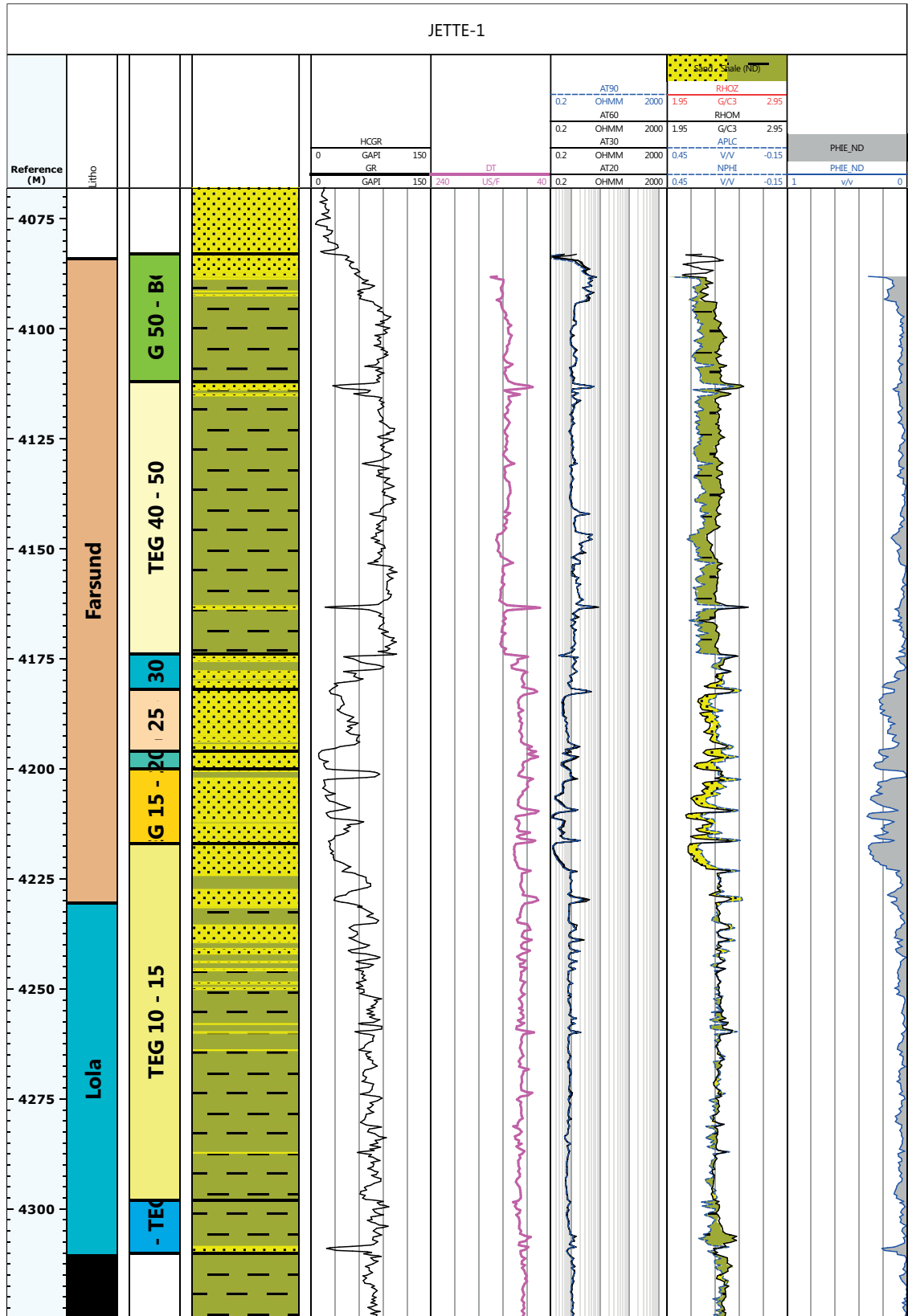


Fig. 6.8



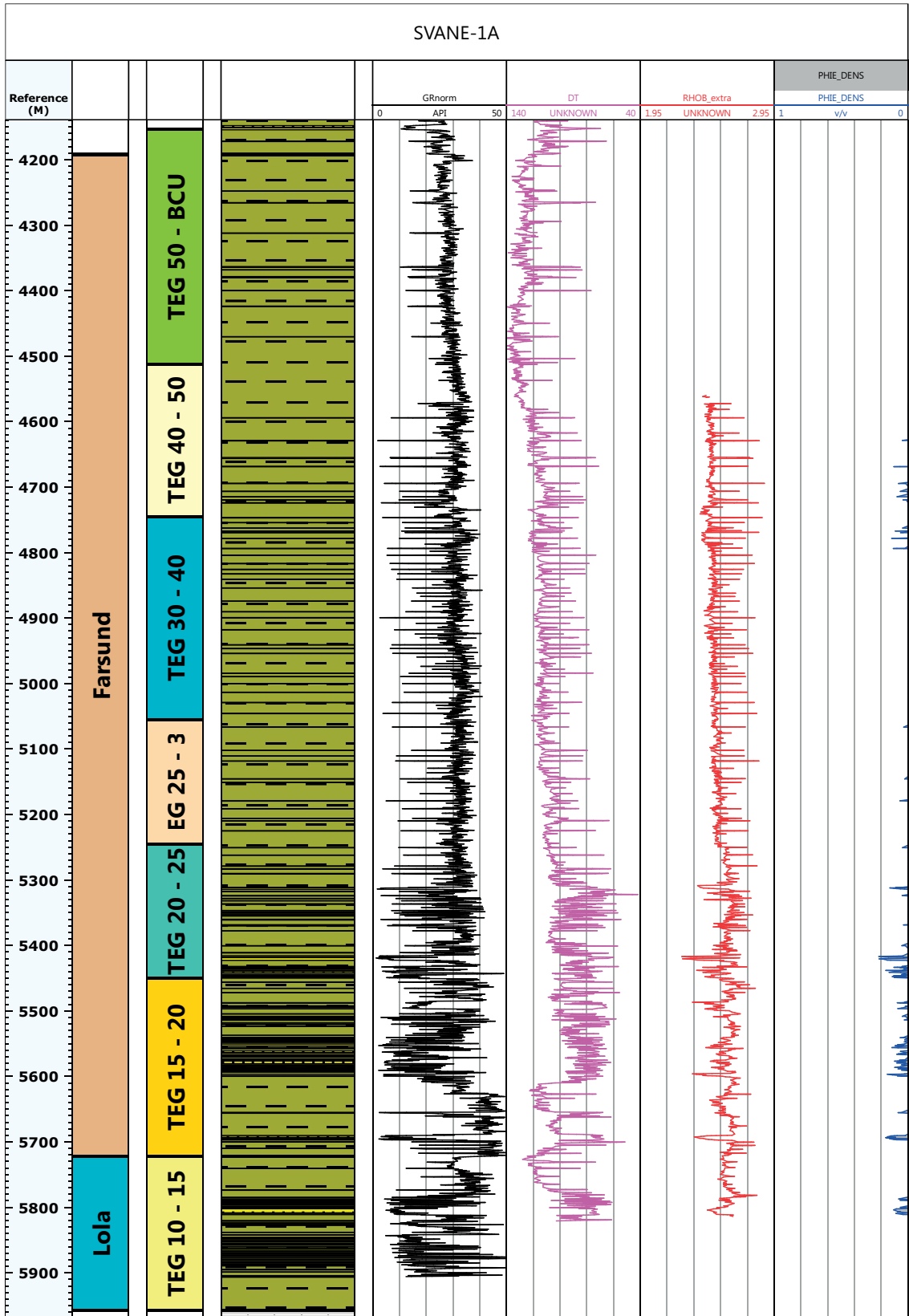


Fig. 6.10

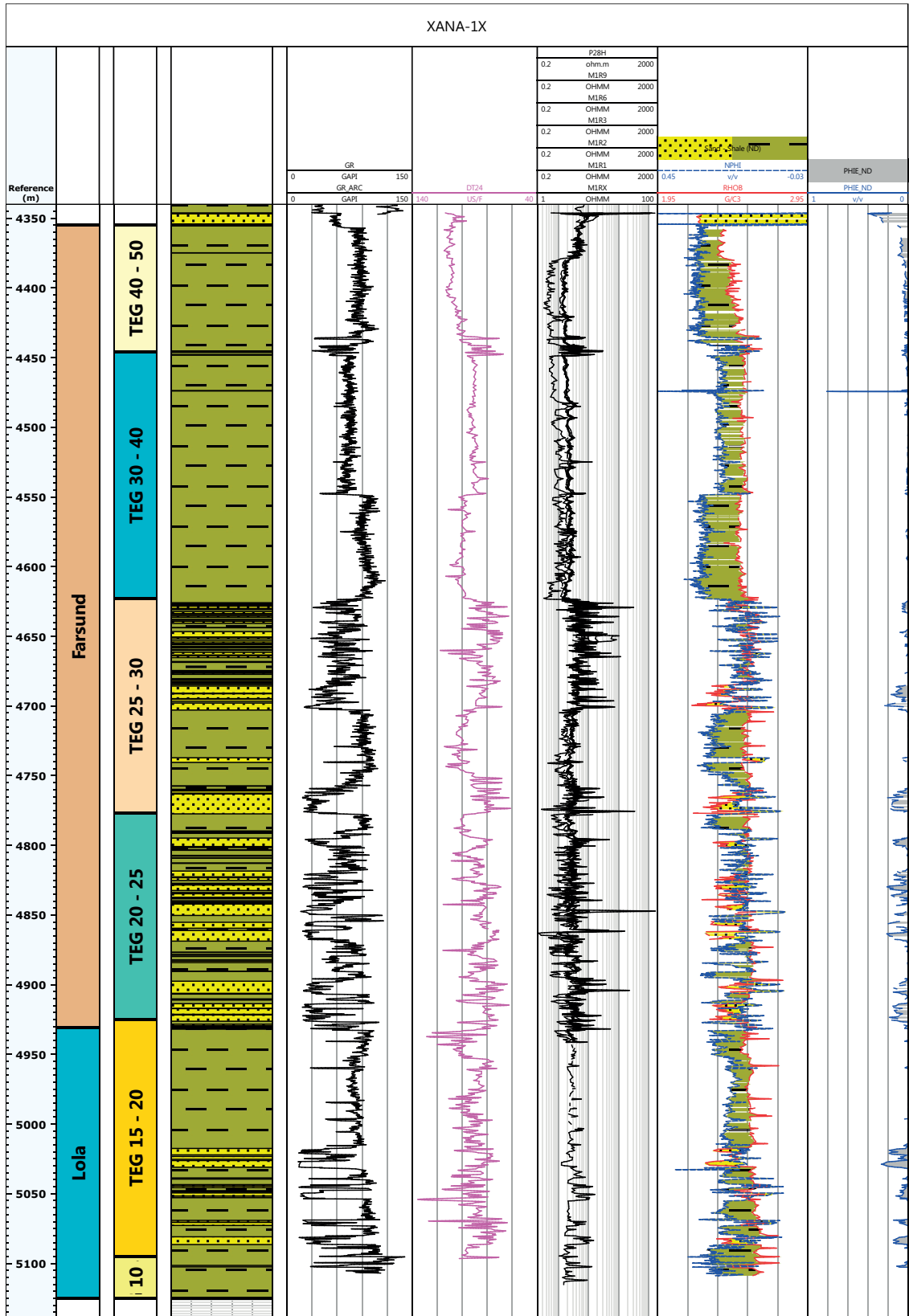
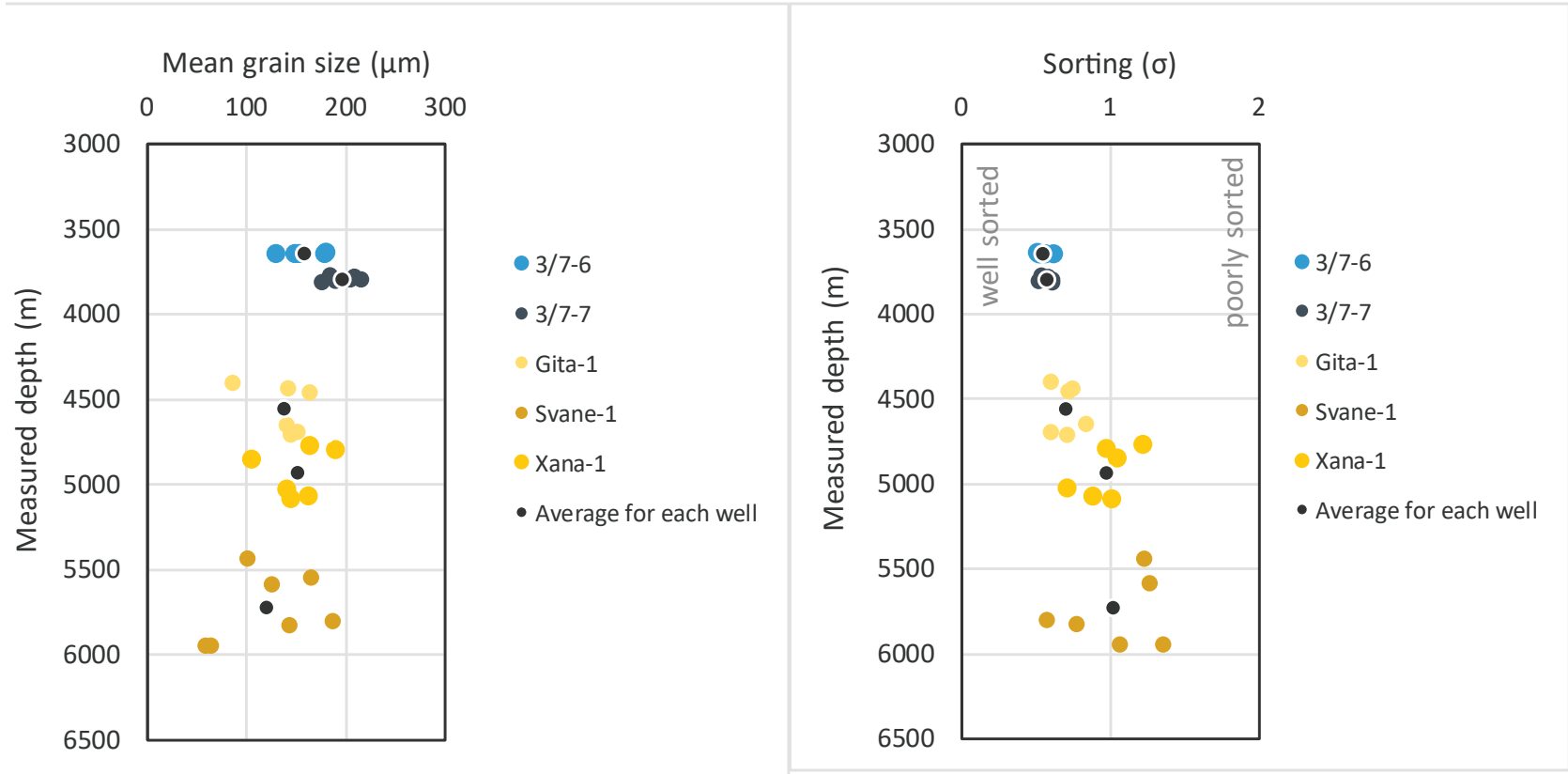


Fig. 6.11

Fig. 7.1



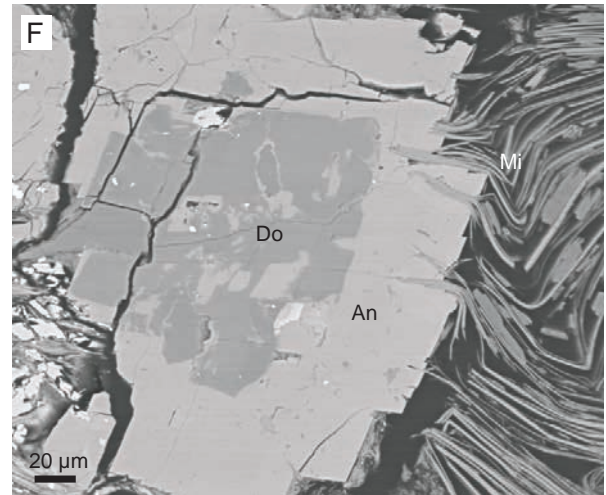
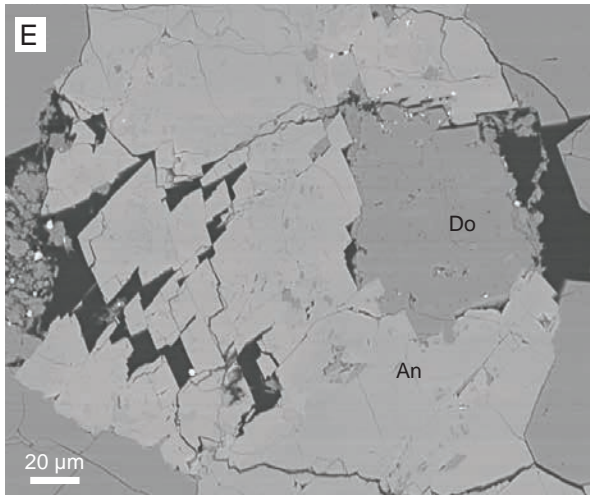
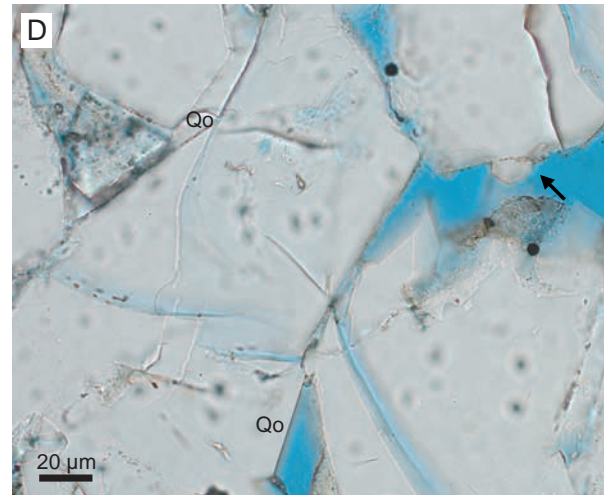
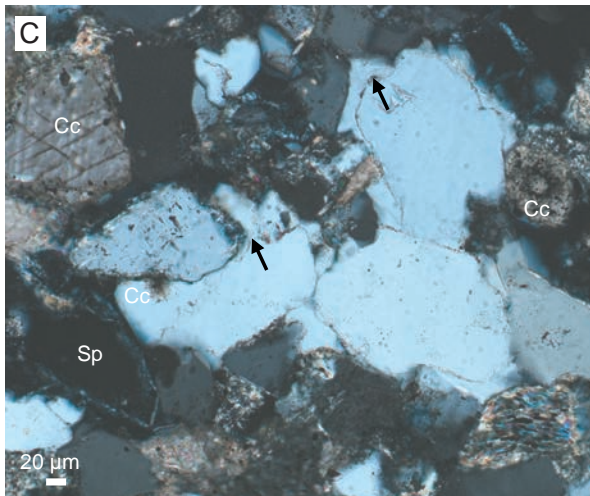
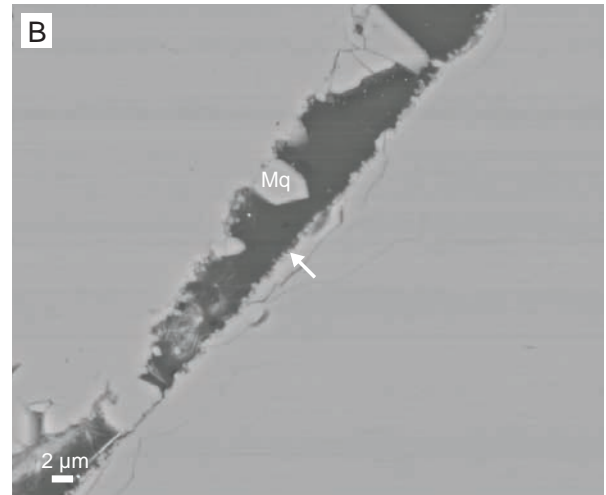
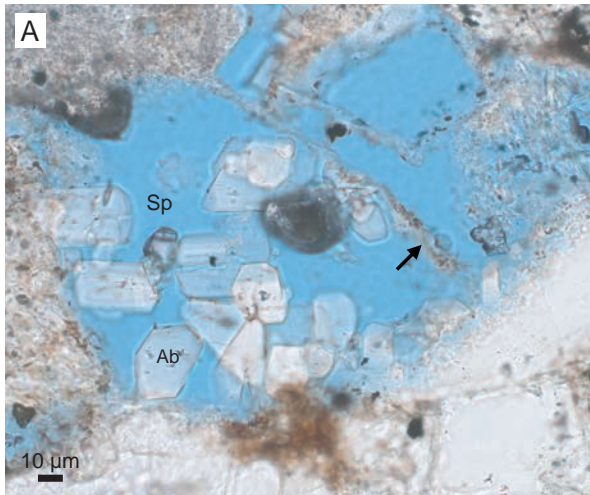


Fig. 7.2

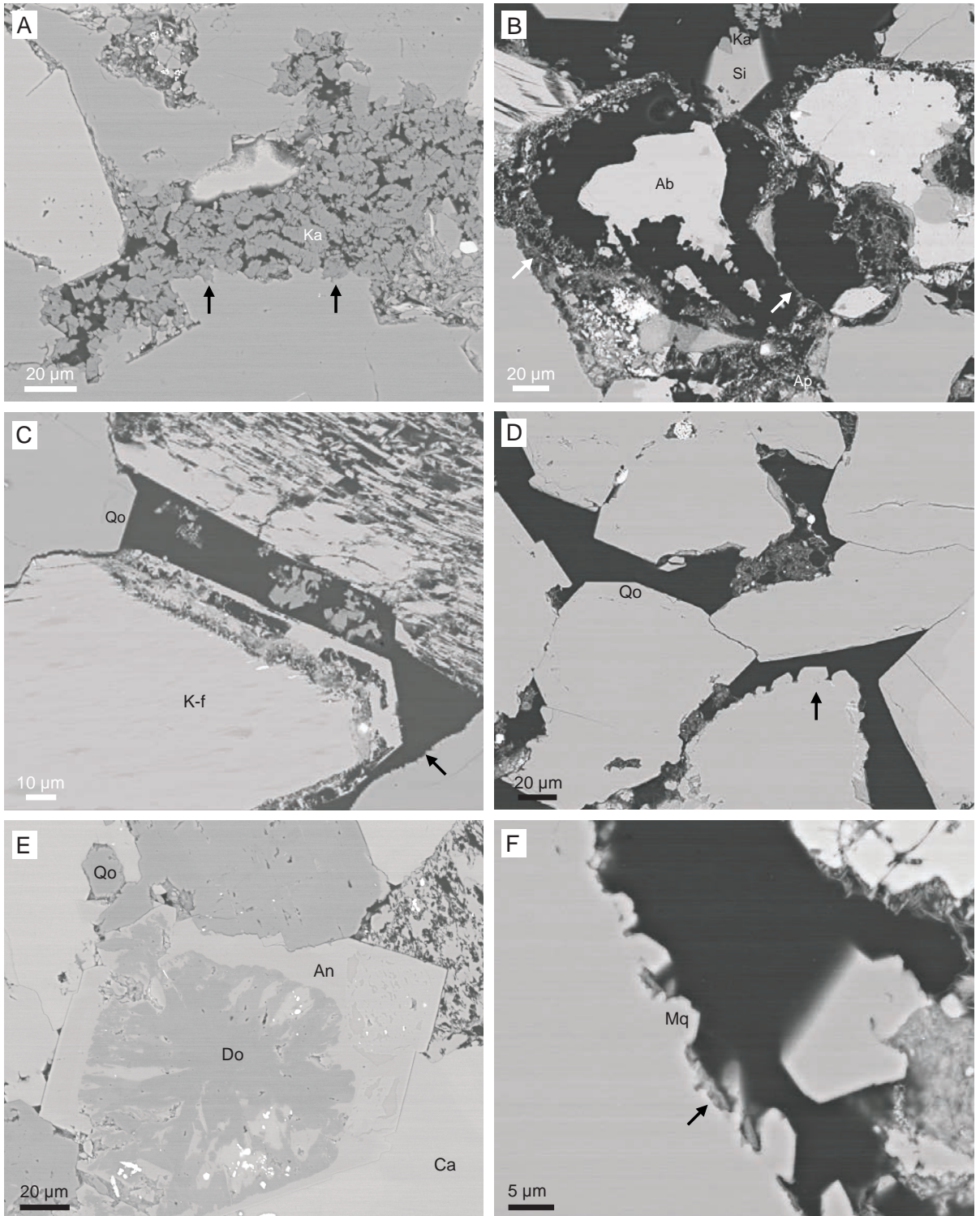


Fig. 7.3

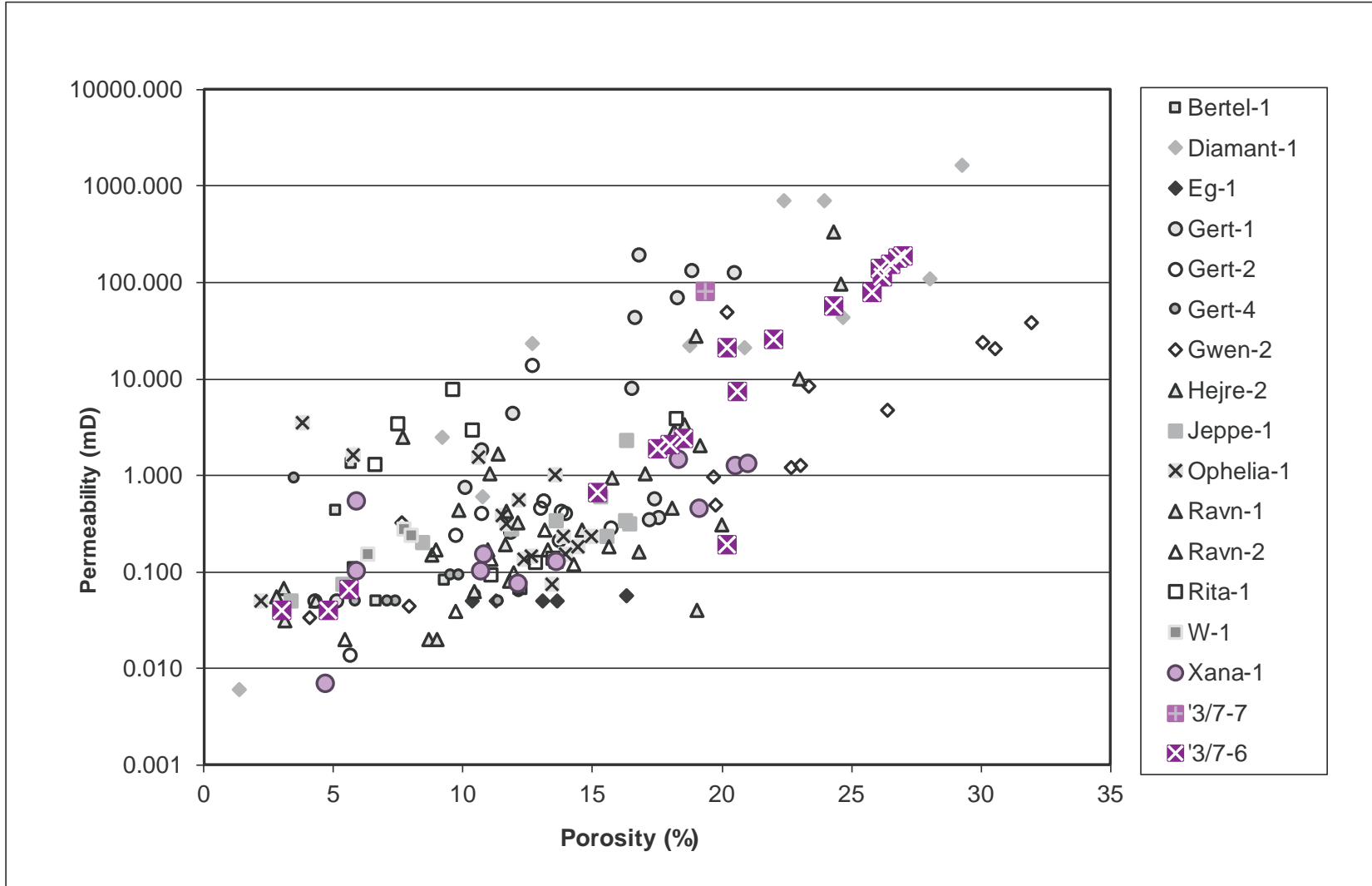


Fig. 7.4

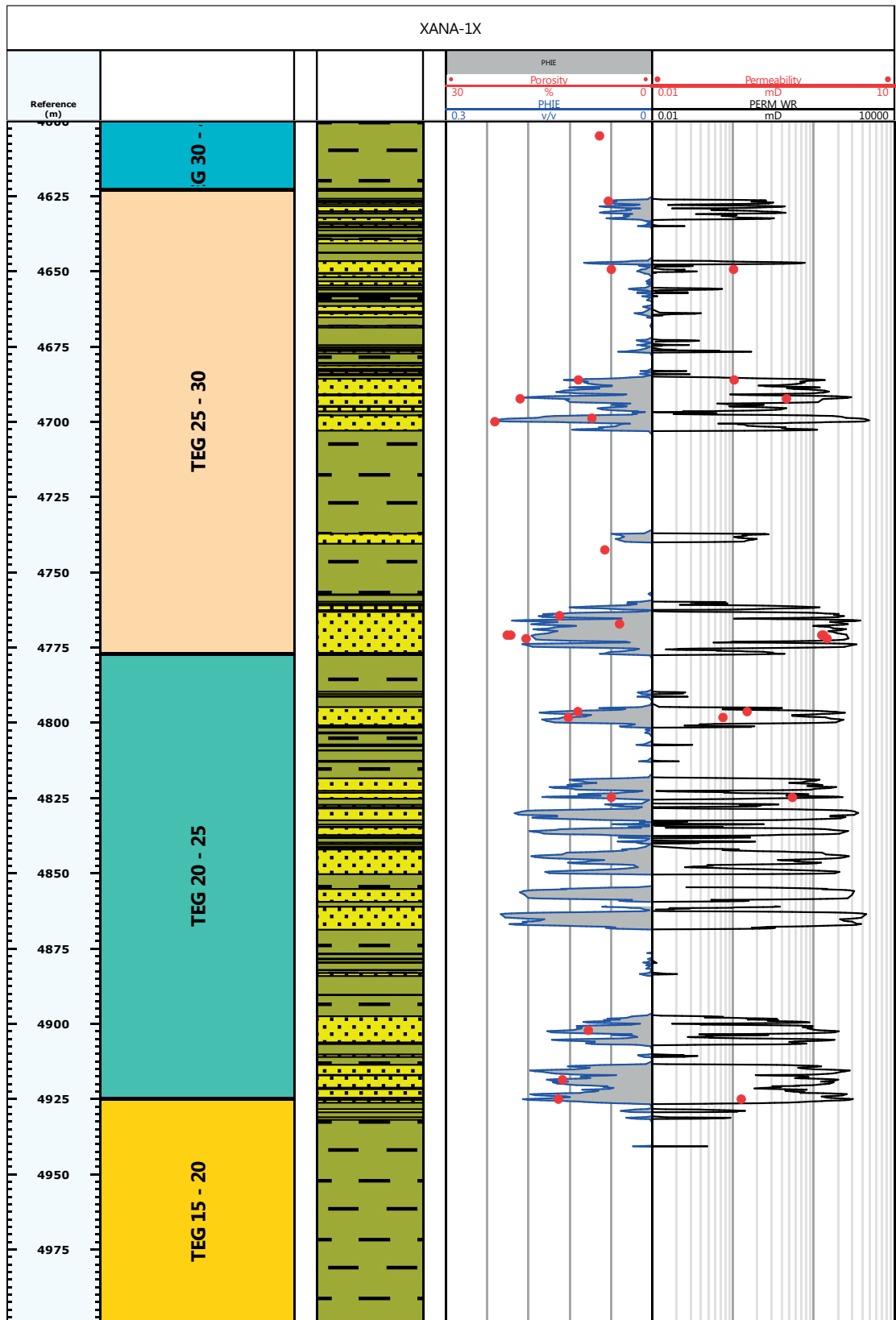


Fig. 7.5

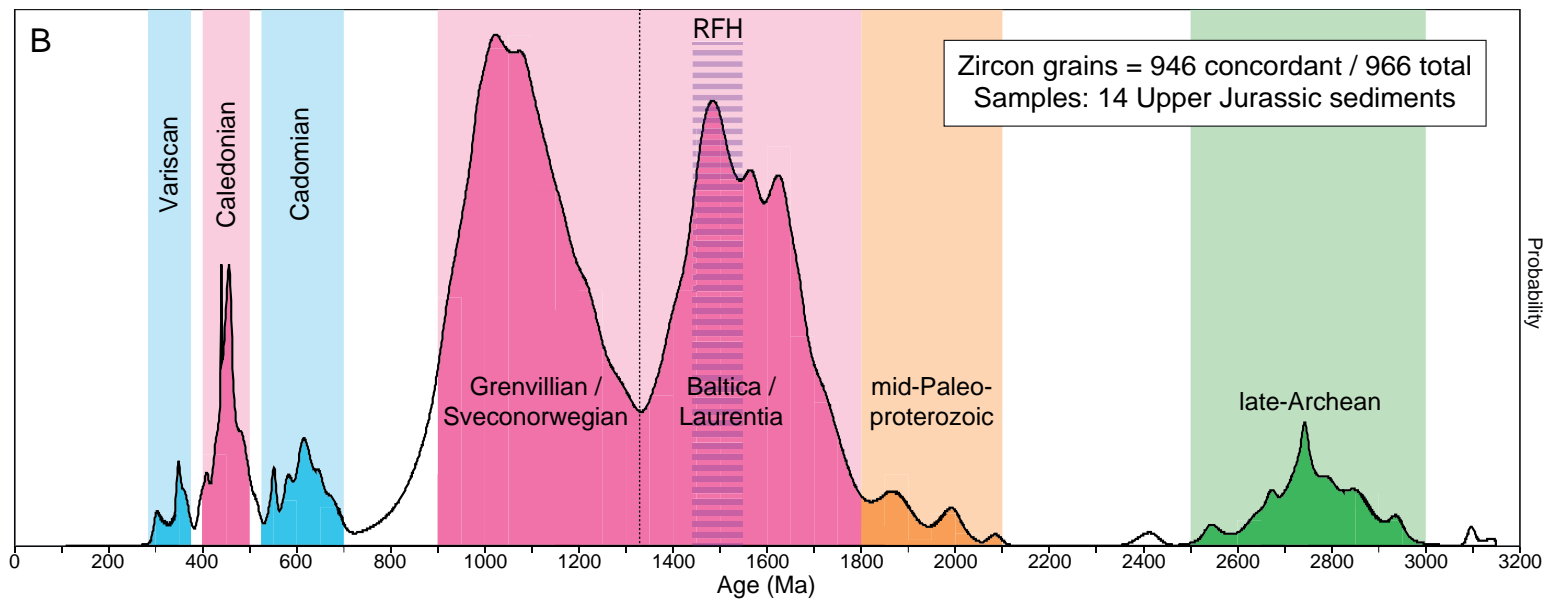
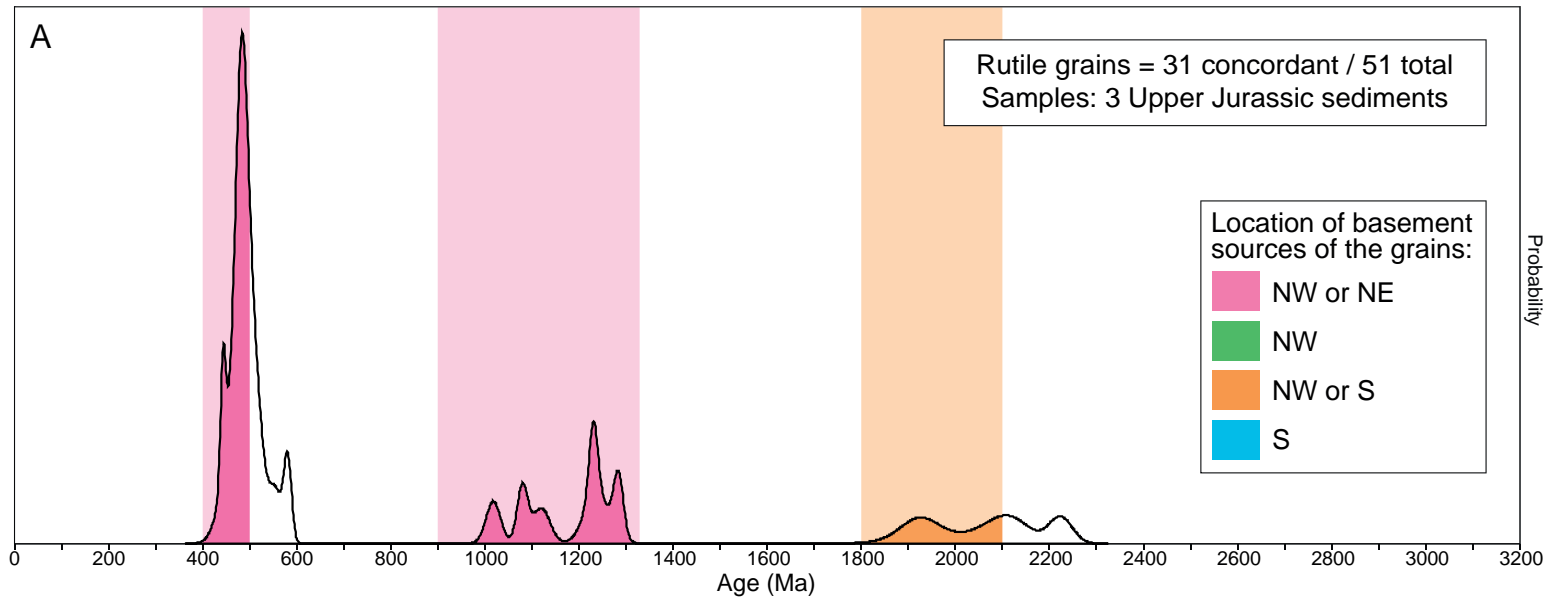


Fig. 8.1

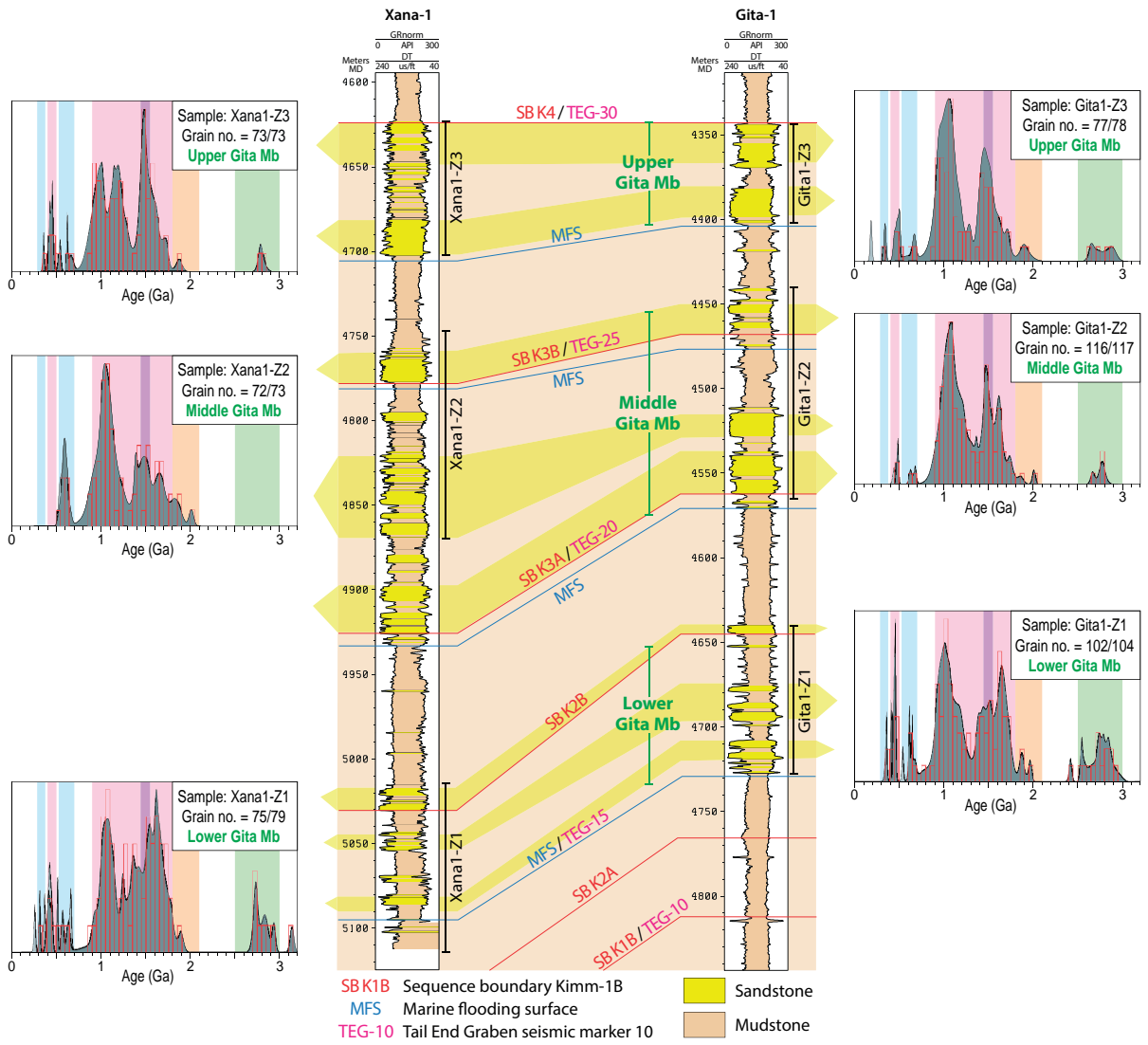


Fig. 8.2

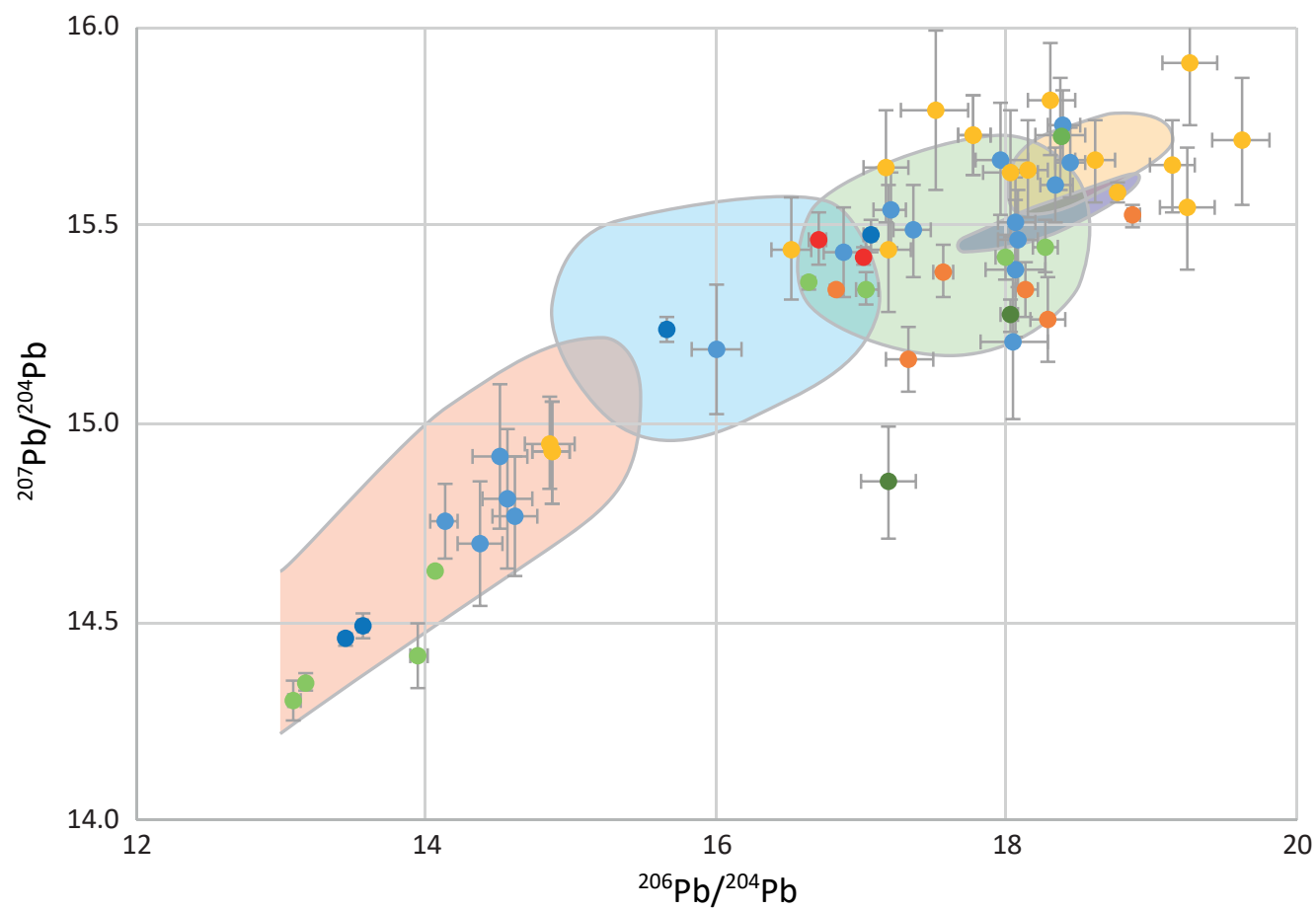


Fig. 8.3

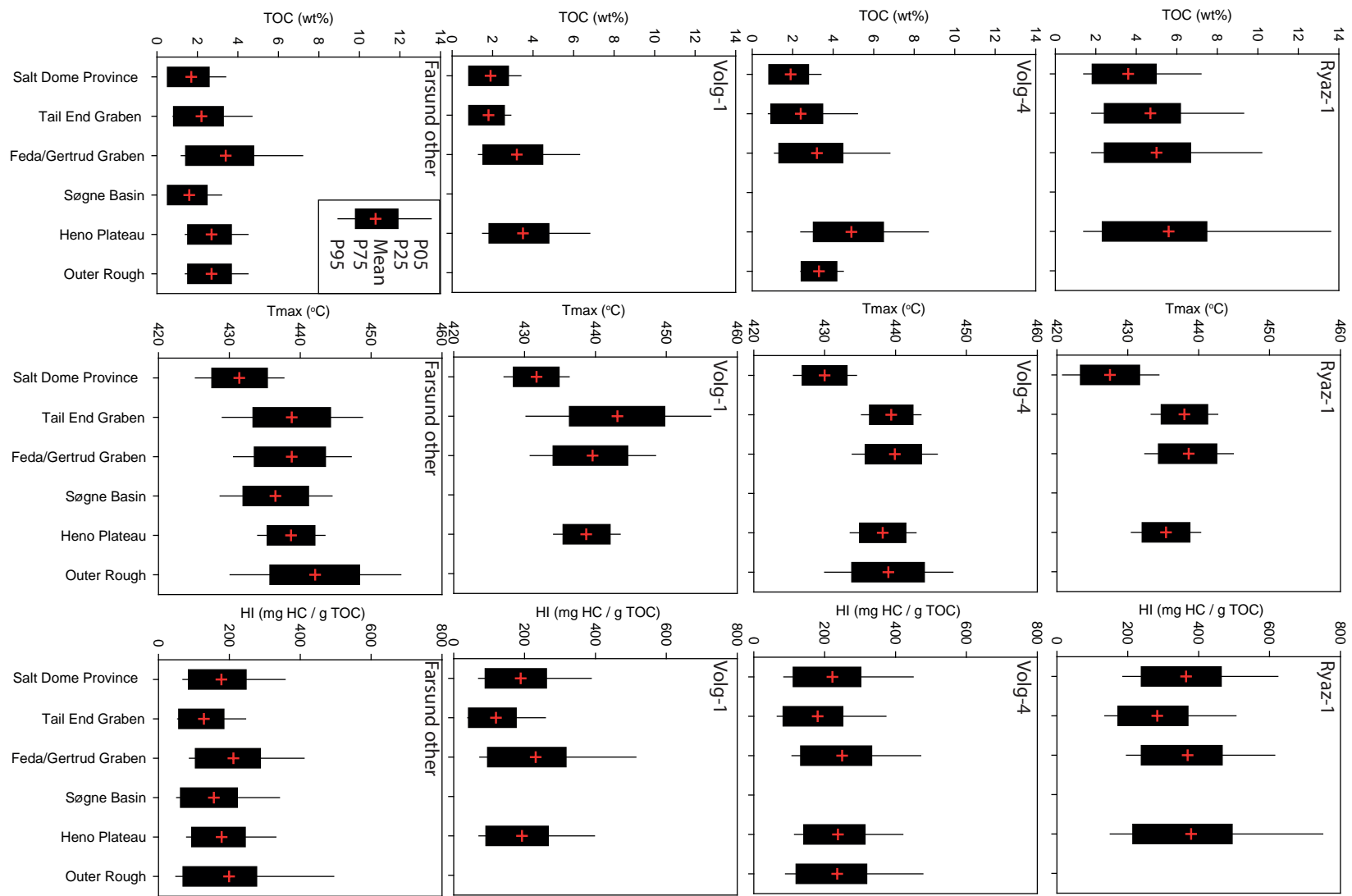


Fig. 9.1

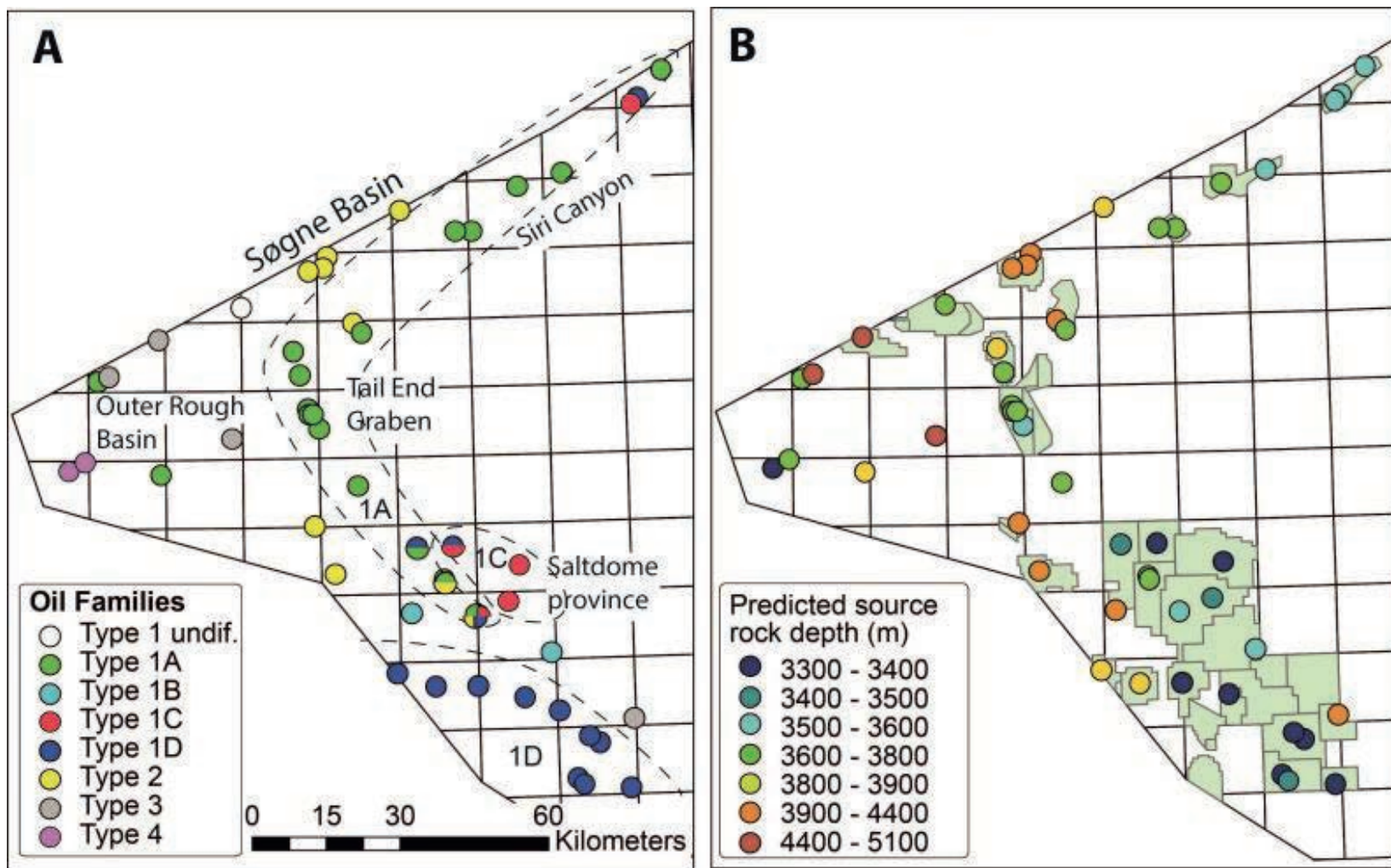


Fig. 9.2

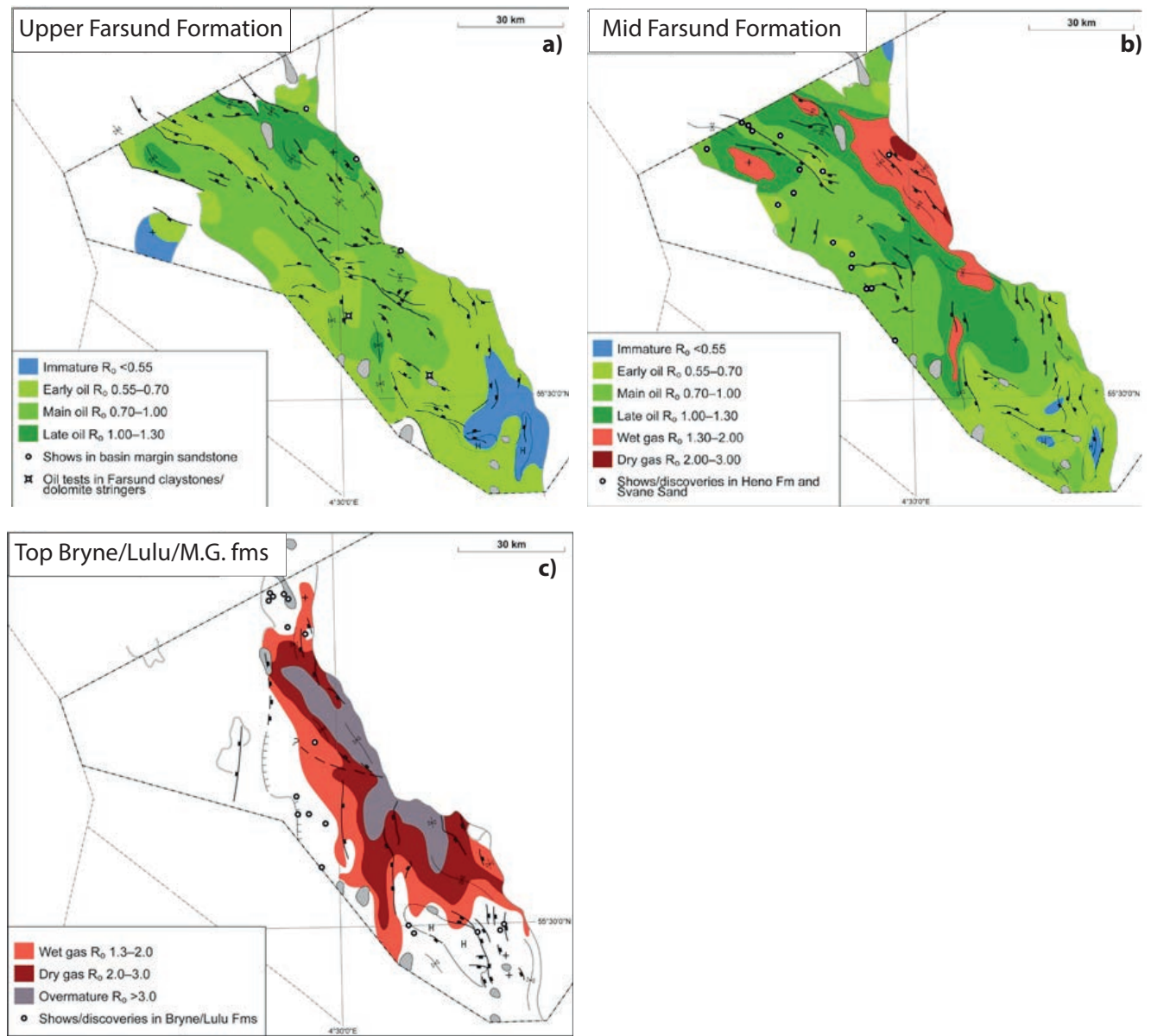


Fig. 9.3

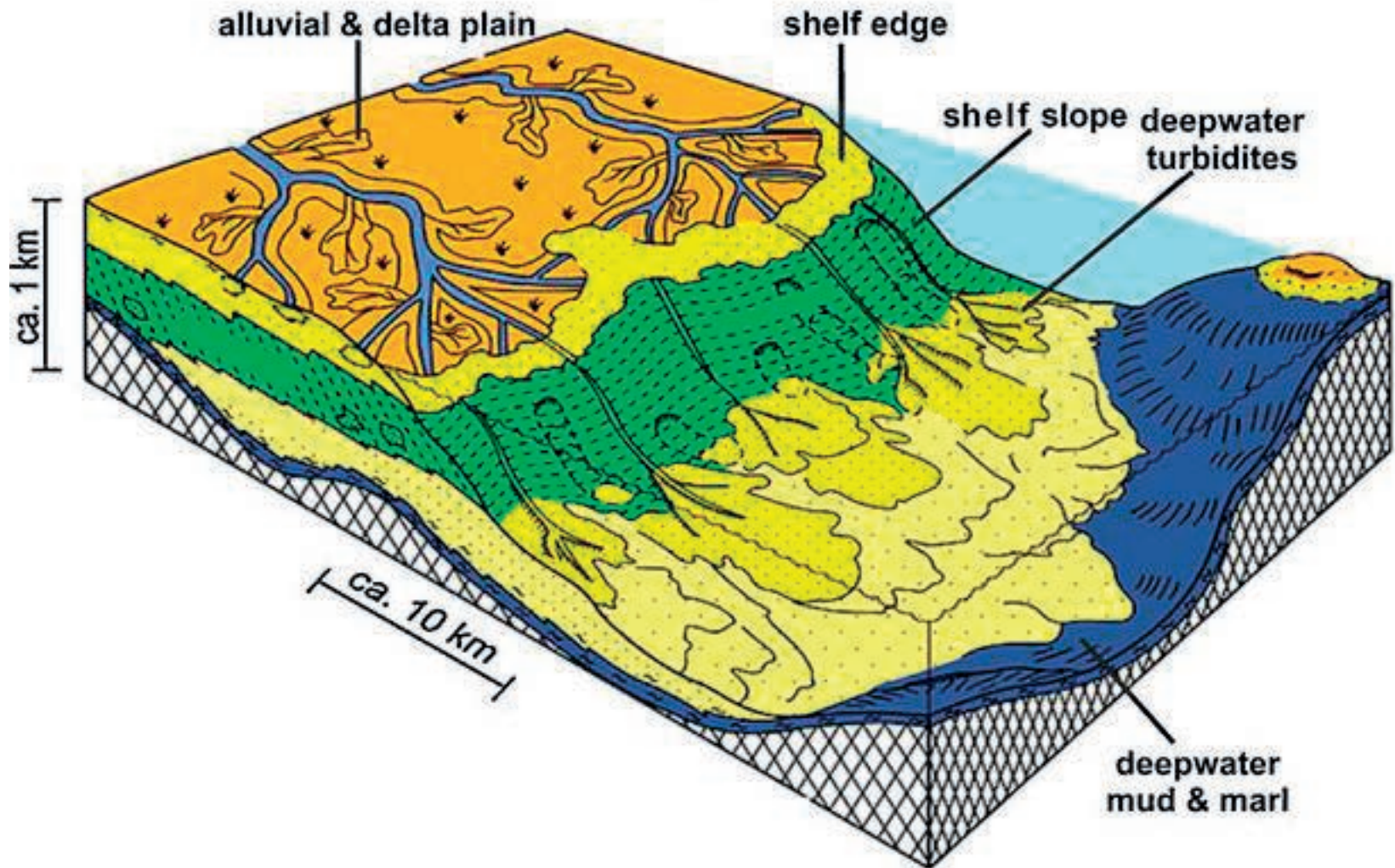
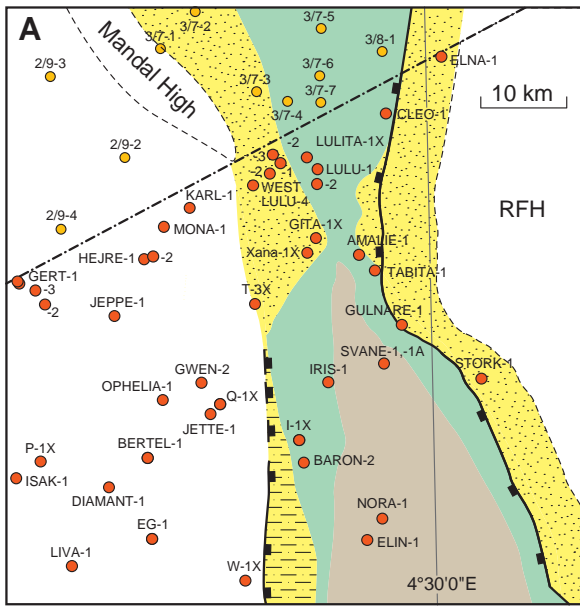
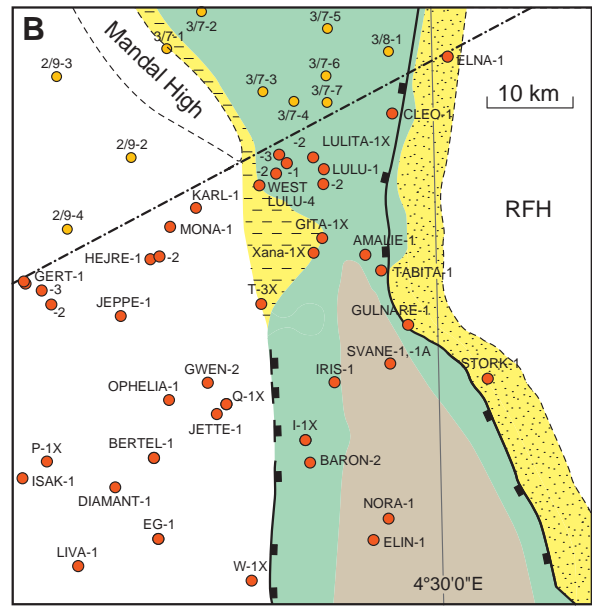


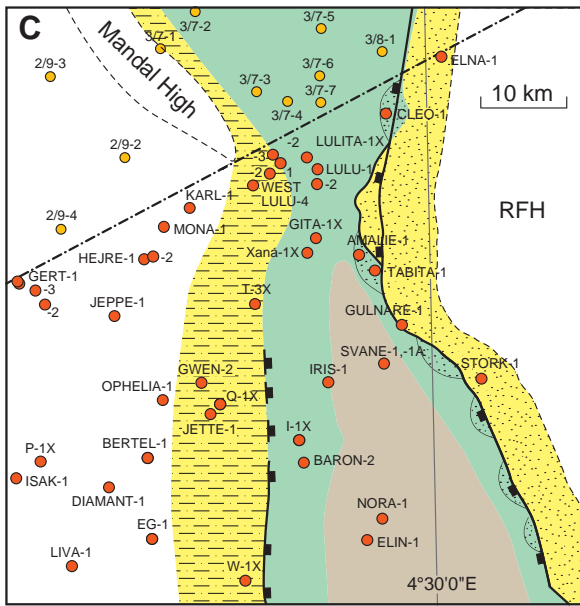
Fig. 10.1



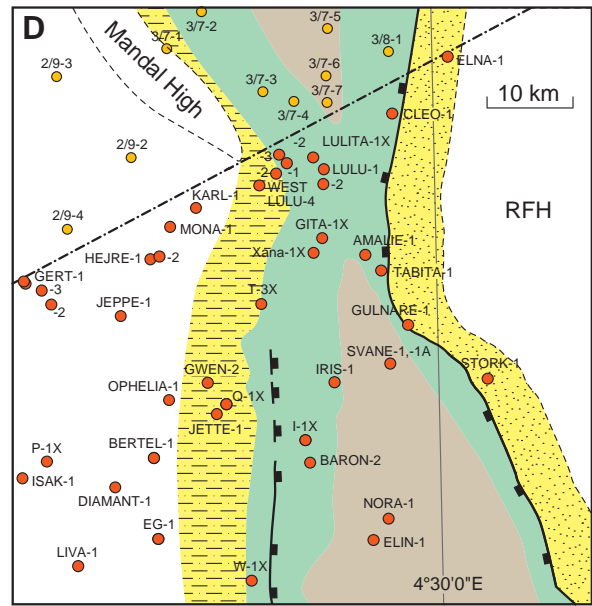
**OX-1 LST-TST**



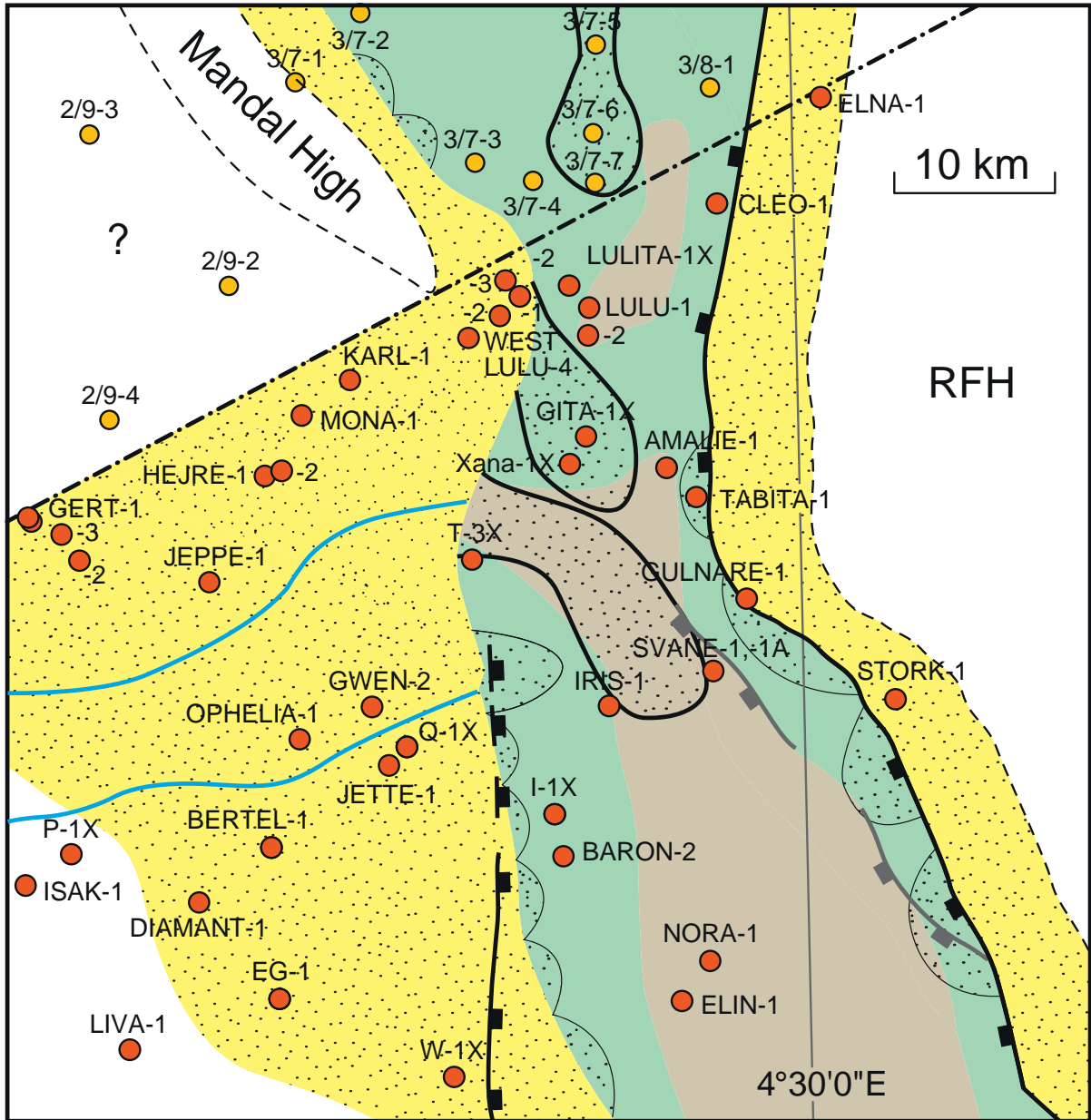
**Ox-1 HST**



**Kimm-1a LST-TST**



**Kimm-1a HST**



**Kimm-3a LST-TST**

TABLE 4.1. Well picks

ND: not defined

**AMALIE-1/1A**

**Seismic markers**

Segment name	Surface	Md (m)	TWT (mS)
Amalie-1	BCU	4198	3401
Amalie-1	TEG 40	4345	3467
Amalie-1	TEG 30	4420	3516
Amalie-1	TEG 25	4520	3562
Amalie-1	TEG 20	4594	3620
Amalie-1	TEG 15	4700	3701
Amalie-1/1A	TEG 10	4885	3790
Amalie-1A	BUJ	5027	3910

**Sequence stratigraphy**

Segment name	Unit	Surface type	Md (m)
Amalie-1	Volg-3	SB	4198
Amalie-1	Volg-2	mfs	4216
Amalie-1	Volg-2	SB	4256
Amalie-1	Volg-1	mfs	4317
Amalie-1	Volg-1	SB	4391
Amalie-1	Kimm-4	mfs	4394
Amalie-1	Kimm-4	SB	4420
Amalie-1	Kimm-3b	mfs	4433
Amalie-1	Kimm-3b	mrs	4516
Amalie-1	Kimm-3b	SB	4518
Amalie-1	Kimm-3a	mfs	4555
Amalie-1	Kimm-3a	mrs	4590
Amalie-1	Kimm-3a	SB	4595
Amalie-1	Kimm-2b	mfs	4623
Amalie-1	Kimm-2b	mrs	4694
Amalie-1	Kimm-2b	SB	4700
Amalie-1	Kimm-2a	mfs	4703
Amalie-1A	Kimm-2a	SB	4769
Amalie-1A	Kimm-1b	mfs	4810
Amalie-1A	Kimm-1b	SB	4890
Amalie-1A	Kimm-1a	mfs	4996
Amalie-1A	Kimm-1a	SB	5003
Amalie-1A	Ox-1	mfs	5019
Amalie-1A	Ox-1	SB	5048
Amalie-1A	Cal-1	mfs	5059
Amalie-1A	Cal-1	SB	5122
Amalie-1A	Bat-1	mfs	5122
Amalie-1A	Bat-1	SB	5191
Amalie-1A	Baj-1	mfs	5221
Amalie-1A	Baj-1	SB	5283
Amalie-1A	Aalen-1	mfs	5286
Amalie-1A	Aalen-1	SB	5353

**Lithostratigraphy**

Segment name	Unit	Surface type	Md (m)
Amalie-1	Cromer Knoll Group	base	4198
Amalie-1	Farsund Formation	top	4198
Amalie-1	Farsund Formation	base	4624
Amalie-1	Lola Formation	top	4624
Amalie-1	Amalie Member	top	4873

Amalie-1	Amalie Member	base	4973
Amalie-1A	Lola Formation	base	5030
Amalie-1A	Lulu Formation	top	5030
Amalie-1A	Lulu Formation	base	5070
Amalie-1A	Bryne Formation	top	5070

### Chronostratigraphy

Segment name	Unit	Surface type	Md (m)
Amalie-1	Lower Cretaceous	base	4198
Amalie-1	Ryazanian	base	4198
Amalie-1	Upper Jurassic	top	4198
Amalie-1	Lower Volgian	top	4198
Amalie-1	Lower Volgian	base	4391
Amalie-1	Upper Kimmeridgian	top	4198
Amalie-1A	Upper Kimmeridgian	base	4700
Amalie-1A	Lower Kimmeridgian	top	4700
Amalie-1A	Lower Kimmeridgian	base	5003
Amalie-1A	Oxfordian	top	5003
Amalie-1A	Oxfordian	base	5047
Amalie-1A	Upper Jurassic	base	5047
Amalie-1A	Callovian	top	5047
Amalie-1A	Middle Jurassic	top	5047
Amalie-1A	Callovian	base	5122
Amalie-1A	Bathonian	top	5122
Amalie-1A	Bathonian	base	5191
Amalie-1A	Bajocian	top	5191
Amalie-1A	Bajocian	base	5283
Amalie-1A	Aalenian	top	5283

### GITA-1

#### Seismic markers

Segment name	Surface	Md (m)	Md (ft)	TWT (mS)
Gita-1	BCU	4102	13457,84	3406
Gita-1	TEG 50	4200	13779,36	3462
Gita-1	TEG 40	4315	14156,65	3499
Gita-1	TEG 30	4345	14255,08	3509
Gita-1	TEG 25	4465	14648,77	3596
Gita-1	TEG 20	4567	14983,41	3663
Gita-1	TEG 15	4728	15511,62	3801
Gita-1	TEG 10	4810	15780,65	3888
Gita-1	BUJ	5060	16600,85	4057

#### Sequence stratigraphy

Segment name	Unit	Surface type	Md (m)	Md (ft)
Gita-1	Ryaz-2	SB	4102	13457,84
Gita-1	Ryaz-1	SB	4107	13474,25
Gita-1	Volg-4	SB	4115	13500,49
Gita-1	Volg-3	mfs	4140	13582,51
Gita-1	Volg-3	SB	4181	13717,02
Gita-1	Volg-2	mfs	4221	13848,26
Gita-1	Volg-2	SB	4233	13887,63
Gita-1	Volg-1	mfs	4260	13976,21
Gita-1	Volg-1	SB	4315	14156,65
Gita-1	Kimm-4	mfs	4325	14189,46
Gita-1	Kimm-4	SB	4345	14255,08
Gita-1	Kimm-3b	mfs	4405	14451,92
Gita-1	Kimm-3b	mrs	4440	14566,75
Gita-1	Kimm-3b	SB	4465	14648,77
Gita-1	Kimm-3a	mfs	4475	14681,58
Gita-1	Kimm-3a	mrs	4512	14802,97
Gita-1	Kimm-3a	SB	4567	14983,41
Gita-1	Kimm-2b	mfs	4570	14993,26

Gita-1	Kimm-2b	mrs	4640	15222,91
Gita-1	Kimm-2b	SB	4645	15239,32
Gita-1	Kimm-2a	mfs	4728	15511,62
Gita-1	Kimm-2a	SB	4760	15616,61
Gita-1	Kimm-1b	mfs	4782	15688,79
Gita-1	Kimm-1b	SB	4810	15780,65
Gita-1	Kimm-1a	mfs	4895	16059,52
Gita-1	Kimm-1a	SB	4962	16279,33
Gita-1	Ox-1	mfs	4966	16292,45
Gita-1	Ox-1	SB	5031	16505,7
Gita-1	Cal-1	mfs	5061	16604,13
Gita-1	Cal-1	SB	5149	16892,84

### Lithostratigraphy

Segment name	Unit	Surface type	Md (m)	Md (ft)
Gita-1	Chalk Group	base	4102	13457,84
Gita-1	Farsund Formation	top	4102	13457,84
Gita-1	Gita Member	top	4344	14251,8
Gita-1	Gita Member	base	4728	15511,62
Gita-1	Farsund Formation	base	4728	15511,62
Gita-1	Lola Formation	top	4728	15511,62
Gita-1	Lola Formation	base	5015	16453,21
Gita-1	Lulu Formation	top	5015	16453,21
Gita-1	Lulu Formation	base	5068	16627,09
Gita-1	Bryne Formation	top	5068	16627,09

### Chronostratigraphy

Segment name	Unit	Surface type	Md (m)	Md (ft)
Gita-1	Upper Cretaceous	base	4102	13457,84
Gita-1	Ryazanian	top	4102	13457,84
Gita-1	Ryazanian	base	4107	13474,25
Gita-1	Upper Volgian	top	4107	13474,25
Gita-1	Lower Cretaceous	base	4107	13474,25
Gita-1	Upper Jurassic	top	4107	13474,25
Gita-1	Upper Volgian	base	4115	13500,49
Gita-1	Middle Volgian	top	4115	13500,49
Gita-1	Middle Volgian	base	4181	13717,02
Gita-1	Lower Volgian	top	4181	13717,02
Gita-1	Lower Volgian	base	4315	14156,65
Gita-1	Upper Kimmeridgian	top	4315	14156,65
Gita-1	Upper Kimmeridgian	base	4760	15616,61
Gita-1	Lower Kimmeridgian	top	4760	15616,61
Gita-1	Lower Kimmeridgian	base	4962	16279,33
Gita-1	Oxfordian	top	4962	16279,33
Gita-1	Oxfordian	base	5031	16505,7
Gita-1	Upper Jurassic	base	5031	16505,7
Gita-1	Middle Jurassic	top	5031	16505,7
Gita-1	?Bathonian-Callovian	top	5031	16505,7

### GWEN-2

#### Seismic markers

Segment name	Surface	Md (m)	Md (ft)	TWT (mS)
Gwen-2	BCU	4066	13339,73	3405
Gwen-2	TEG 50	4133	13559,55	3439
Gwen-2	TEG 40	4185	13730,15	3484
Gwen-2	TEG 30	4224	13858,1	3534
Gwen-2	TEG 25	4240	13910,59	ND
Gwen-2	TEG 20	4259	13972,93	3592
Gwen-2	TEG 15	4300	14107,44	ND
Gwen-2	TEG 10	4343	14248,51	ND
Gwen-2	BUJ	4375	14353,5	3623

### Sequence stratigraphy

Segment name	Unit	Surface type	Md (m)	
Gwen-2	Ryaz-2	SB	4066	13339,73
Gwen-2	Ryaz-1	SB	4099	13448
Gwen-2	Volg-4	mfs	4099	13448
Gwen-2	Volg-4	SB	4103	13461,12
Gwen-2	Volg-3	mfs	4127	13539,86
Gwen-2	Volg-3	SB	4133	13559,55
Gwen-2	Volg-2	mfs	4133	13559,55
Gwen-2	Volg-2	SB	4145	13598,92
Gwen-2	Volg-1	mfs	4173	13690,78
Gwen-2	Volg-1	SB	4185	13730,15
Gwen-2	Kimm-4	mfs	4204	13792,48
Gwen-2	Kimm-4	SB	4224	13858,1
Gwen-2	Kimm-3b	mfs	4230	13877,78
Gwen-2	Kimm-3b	SB	4240	13910,59
Gwen-2	Kimm-3a	mfs	4243	13920,43
Gwen-2	Kimm-3a	SB	4259	13972,93
Gwen-2	Kimm-2	SB	4259	13972,93
Gwen-2	Kimm-1b	mfs	4298	14100,88
Gwen-2	Kimm-1b	SB	4343	14248,51
Gwen-2	Kimm-1a	mfs	4354	14284,6
Gwen-2	Kimm-1a	SB	4375	14353,5

### Lithostratigraphy

Segment name	Unit	Surface type	Md (m)	
Gwen-2	Cromer Knoll Group	base	4066	13339,73
Gwen-2	Bo Member	top	4066	13339,73
Gwen-2	Farsund Formation	top	4066	13339,73
Gwen-2	Bo Member	base	4090	13418,47
Gwen-2	Farsund Formation	base	4224	13858,1
Gwen-2	Ravn Member (Heno Fm)	top	4224	13858,1
Gwen-2	Ravn Member (Heno Fm)	base	4277	14031,98
Gwen-2	Lola Formation	top	4277	14031,98
Gwen-2	Lola Formation	base	4354	14284,6
Gwen-2	Gert Member (Heno Fm)	top	4354	14284,6
Gwen-2	Gert Member (Heno Fm)	base	4375	14353,5
Gwen-2	Triassic undiff	top	4375	14353,5

### Chronostratigraphy

Segment name	Unit	Surface type	Md (m)	
Gwen-2	Upper Ryazanian	base	4084	13398,79
Gwen-2	Lower Ryazanian	top	4084	13398,79
Gwen-2	Lower Cretaceous	base	4090	13418,47
Gwen-2	Lower Ryazanian	base	4090	13418,47
Gwen-2	Upper Jurassic	top	4090	13418,47
Gwen-2	Upper Volgian	top	4090	13418,47
Gwen-2	Upper Volgian	base	4097	13441,44
Gwen-2	Middle Volgian	top	4097	13441,44
Gwen-2	Middle Volgian	base	4130	13549,7
Gwen-2	Lower Volgian	top	4130	13549,7
Gwen-2	Lower Volgian	base	4185	13730,15
Gwen-2	Upper Kimmeridgian	top	4185	13730,15
Gwen-2	Upper Jurassic	base	4375	14353,5
Gwen-2	Upper Kimmeridgian	base	4375	14353,5
Gwen-2	Triassic	top	4375	14353,5

### HEJRE-2

#### Seismic markers

Segment name	Surface	Md (m)	TWT (mS)
Hejre-2	BCU	4443	3789

Hejre-2	TEG 50	4804	4019
Hejre-2	TEG 40	5152	4266
Hejre-2	TEG 30	5316	4345
Hejre-2	TEG 25	5360	4407
Hejre-2	TEG 20	5365	4410
Hejre-2	TEG 15	5412	4464
Hejre-2	TEG 10	5412	4464
Hejre-2	BUJ	5412	4464

### Sequence stratigraphy

Segment name	Unit	Surface type	Md (m)
Hejre-2	Ryaz-2	SB	4444
Hejre-2	Ryaz-1	SB	4569
Hejre-2	Volg-4	mfs	4604
Hejre-2	Volg-4	SB	4621
Hejre-2	Volg-3	mfs	4733
Hejre-2	Volg-3	SB	4802
Hejre-2	Volg-2	mfs	4927
Hejre-2	Volg-2	SB	4980
Hejre-2	Volg-1	mfs	5146
Hejre-2	Volg-1	SB	5167
Hejre-2	Kimm-4	mfs	5292
Hejre-2	Kimm-4	SB	5316
Hejre-2	Kimm-3b	mfs	5324
Hejre-2	Kimm-3b	SB	5332
Hejre-2	Kimm-3a	mfs	5358
Hejre-2	Kimm-3a	SB	5364
Hejre-2	Kimm-2b	mfs	5380
Hejre-2	Kimm-2b	SB	5386
Hejre-2	Kimm-2a	mfs	5404
Hejre-2	Kimm-2a	SB	5412

### Lithostratigraphy

Segment name	Unit	Surface type	Md (m)
Hejre-2	Cromer Knoll Group	base	4444
Hejre-2	Farsund Formation	top	4444
Hejre-2	Farsund Formation	base	5360
Hejre-2	Ravn Member (Heno Fm)	top	5360
Hejre-2	Ravn Member (Heno Fm)	base	5364
Hejre-2	Lola Formation	top	5364
Hejre-2	Lola Formation	base	5380
Hejre-2	Gert Member (Heno Fm)	top	5380
Hejre-2	Gert Member (Heno Fm)	base	5412
Hejre-2	Permian undiff	top	5412

### Chronostratigraphy

Segment name	Unit	Surface type	Md (m)
Hejre-2	Lower Valanginian	base	4383
Hejre-2	Upper Ryazanian	top	4383
Hejre-2	Upper Ryazanian	base	4467
Hejre-2	Lower Ryazanian	top	4467
Hejre-2	Lower Cretaceous	base	4551
Hejre-2	Lower Ryazanian	base	4551
Hejre-2	Upper Jurassic	top	4551
Hejre-2	Upper Volgian	top	4551
Hejre-2	Upper Volgian	base	4635
Hejre-2	Middle Volgian	top	4635
Hejre-2	Middle Volgian	base	4802
Hejre-2	Lower Volgian	top	4802
Hejre-2	Lower Volgian	base	5167
Hejre-2	Upper Kimmeridgian	top	5167
Hejre-2	Upper Jurassic	base	5412
Hejre-2	Upper Kimmeridgian	base	5412

Hejre-2	?Permian	top	5412
---------	----------	-----	------

## JEPPE-1

### Seismic markers

Segment name	Surface	Md (m)	TWT (mS)
Jeppe-1	BCU	4383	3659
Jeppe-1	TEG 50	4669	3842
Jeppe-1	TEG 40	4839	3971
Jeppe-1	TEG 30	4903	4036
Jeppe-1	TEG 25	4940	4081
Jeppe-1	TEG 20	4990	4116
Jeppe-1	TEG 15	5040	4147
Jeppe-1	TEG 10	5040	4147
Jeppe-1	BUJ	5040	4147

### Sequence stratigraphy

Segment name	Unit	Surface type	Md (m)
Jeppe-1	Ryaz-2	SB	4386
Jeppe-1	Ryaz-1	SB	4431
Jeppe-1	Volg-4	mfs	4439
Jeppe-1	Volg-4	SB	4488
Jeppe-1	Volg-3	mfs	4581
Jeppe-1	Volg-3	SB	4669
Jeppe-1	Volg-2	mfs	4670
Jeppe-1	Volg-2	SB	4671
Jeppe-1	Volg-1	mfs	4840
Jeppe-1	Volg-1	SB	4862
Jeppe-1	Kimm-4	mfs	4887
Jeppe-1	Kimm-4	SB	4909
Jeppe-1	Kimm-3B	mfs	4919
Jeppe-1	Kimm-3B	SB	4925
Jeppe-1	Kimm-3A	mfs	4940
Jeppe-1	Kimm-3A	SB	4951
Jeppe-1	Kimm-2B	mfs	5014
Jeppe-1	Kimm-2B	SB	5031
Jeppe-1	Kimm-2A	mfs	5033
Jeppe-1	Kimm-2A	SB	5043

### Lithostratigraphy

Segment name	Unit	Surface type	Md (m)
Jeppe-1	Cromer Knoll Group	base	4386
Jeppe-1	Bo Member	top	4386
Jeppe-1	Farsund Formation	top	4386
Jeppe-1	Bo Member	base	4413
Jeppe-1	Farsund Formation	base	4941
Jeppe-1	Ravn Member (Heno Fm)	top	4941
Jeppe-1	Ravn Member (Heno Fm)	base	5002
Jeppe-1	Lola Formation	top	5002
Jeppe-1	Lola Formation	base	5020
Jeppe-1	Gert Member (Heno Fm)	top	5020
Jeppe-1	Gert Member (Heno Fm)	base	5043
Jeppe-1	Permian undiff	top	5043

### Chronostratigraphy

Segment name	Unit	Surface type	Md (m)
Jeppe-1	Lower Valanginian	base	4380
Jeppe-1	Upper Ryazanian	top	4380
Jeppe-1	Upper Ryazanian	base	4390
Jeppe-1	Lower Ryazanian	top	4390
Jeppe-1	Lower Cretaceous	base	4403
Jeppe-1	Lower Ryazanian	base	4403

Jepe-1	Upper Jurassic	top	4403
Jepe-1	Upper Volgian	top	4403
Jepe-1	Upper Volgian	base	4434
Jepe-1	Middle Volgian	top	4434
Jepe-1	Middle Volgian	base	4669
Jepe-1	Lower Volgian	top	4669
Jepe-1	Lower Volgian	base	4862
Jepe-1	Upper Kimmeridgian	top	4862
Jepe-1	Upper Jurassic	base	5043
Jepe-1	Upper Kimmeridgian	base	5043
Jepe-1	?Permian	top	5043

## KARL-1

### Seismic markers

Segment name	Surface	Md (m)	Md (ft)	TWT (mS)
Karl-1	BCU	4267	13999,17	3491
Karl-1	TEG 50	ND	ND	ND
Karl-1	TEG 40	4362	14310,85	3532
Karl-1	TEG 30	4422	14507,7	3587
Karl-1	TEG 25	4436	14553,63	3595
Karl-1	TEG 20	4467	14655,33	3605
Karl-1	TEG 15	4481	14701,26	3615
Karl-1	TEG 10	4491	14734,07	3631
Karl-1	BUJ	4491	14734,07	3631

### Sequence stratigraphy

Segment name	Unit	Surface type	Md (m)	Md (ft)
Karl-1	Volg-4	SB	4267	13999,17
Karl-1	Volg-3	mfs	4286	14061,51
Karl-1	Volg-3	SB	4291	14077,91
Karl-1	Volg-2	mfs	4291	14077,91
Karl-1	Volg-2	SB	4311	14143,53
Karl-1	Volg-1	mfs	4343	14248,51
Karl-1	Volg-1	SB	4371	14340,38
Karl-1	Kimm-4	mfs	4389	14399,43
Karl-1	Kimm-4	SB	4423	14510,98
Karl-1	Kimm-3	SB	4423	14510,98
Karl-1	Kimm-2b	mfs	4453	14609,4
Karl-1	Kimm-2b	SB	4478	14691,42
Karl-1	Kimm-2a	mfs	4484	14711,11
Karl-1	Kimm-2a	SB	4490	14730,79

### Lithostratigraphy

Segment name	Unit	Surface type	Md (m)	Md (ft)
Karl-1	Cromer Knoll Group	base	4267	13999,17
Karl-1	Farsund Formation	top	4267	13999,17
Karl-1	Farsund Formation	base	4423	14510,98
Karl-1	Ravn Member (Heno Fm)	top	4423	14510,98
Karl-1	Ravn Member (Heno Fm)	base	4428	14527,38
Karl-1	Lola Formation	top	4428	14527,38
Karl-1	Lola Formation	base	4469	14661,9
Karl-1	Gert Member (Heno Fm)	top	4469	14661,9
Karl-1	Gert Member (Heno Fm)	base	4490	14730,79
Karl-1	Permian undiff	top	4490	14730,79

### Chronostratigraphy

Segment name	Unit	Surface type	Md (m)	Md (ft)
Karl-1	?Barremian	base	4267	13999,17
Karl-1	Lower Cretaceous	base	4267	13999,17
Karl-1	Middle Volgian	top	4267	13999,17
Karl-1	Upper Jurassic	top	4267	13999,17

Karl-1	Middle Volgian	base	4291	14077,91
Karl-1	Lower Volgian	top	4291	14077,91
Karl-1	Lower Volgian	base	4371	14340,38
Karl-1	Upper Kimmeridgian	top	4371	14340,38
Karl-1	Upper Jurassic	base	4490	14730,79
Karl-1	Upper Kimmeridgian	base	4490	14730,79
Karl-1	?Permian	top	4490	14730,79

## LULU-2

### Seismic markers

Segment name	Surface	Md (m)	Md (ft)	TWT (mS)
Lulu-2	BCU	3312	10866,01	2974
Lulu-2	TEG 20	3357	11013,65	3016
Lulu-2	TEG 15	3507	11505,77	ND
Lulu-2	TEG 10	3573	11722,3	ND
Lulu-2	BUJ	3586	11764,95	3100?

### Sequence stratigraphy

Segment name	Unit	Surface type	Md (m)	
Lulu-2	Kimm-3b	SB	3312	10866,01
Lulu-2	Kimm-3a	mfs	3312	10866,01
Lulu-2	Kimm-3a	SB	3362	11030,05
Lulu-2	Kimm-2b	mfs	3445	11302,36
Lulu-2	Kimm-2b	SB	3461	11354,85
Lulu-2	Kimm-2a	mfs	3468	11377,81
Lulu-2	Kimm-2a	SB	3507	11505,77
Lulu-2	Kimm-1b	mfs	3519	11545,14
Lulu-2	Kimm-1b	SB	3540	11614,03
Lulu-2	Kimm-1a	mfs	3548	11640,28
Lulu-2	Kimm-1a	SB	3586	11764,95
Lulu-2	Ox-1	mfs	3592	11784,63
Lulu-2	Ox-1	SB	3621	11879,78

### Lithostratigraphy

Segment name	Unit	Surface type	Md (m)	
Lulu-2	Chalk Group	base	3312	10866,01
Lulu-2	Farsund Formation	top	3312	10866,01
Lulu-2	Farsund Formation	base	3519	11545,14
Lulu-2	Lola Formation	top	3519	11545,14
Lulu-2	Lola Formation	base	3621	11879,78
Lulu-2	Permian, undiff.	top	3621	11879,78

### Chronostratigraphy

Segment name	Unit	Surface type	Md (m)	
Lulu-2	Santonian	base	3312	10866,01
Lulu-2	Upper Cretaceous	base	3312	10866,01
Lulu-2	Upper Jurassic	top	3312	10866,01
Lulu-2	Upper Kimmeridgian	top	3312	10866,01
Lulu-2	Upper Kimmeridgian	base	3586	11764,95
Lulu-2	Oxfordian	top	3586	11764,95
Lulu-2	Oxfordian	base	3621	11879,78
Lulu-2	Permian	top	3621	11879,78

## NORA-1

### Seismic markers

Segment name	Surface	Md (m)	Md (ft)	TWT (mS)
Nora-1	BCU	3475	11400,78	3141
Nora-1	TEG 50	3535	11597,63	3182

Nora-1	TEG 40	3868	12690,13	3466
Nora-1	TEG 30	4036	13241,31	3558
Nora-1	TEG 25	4185	13730,15	3659
Nora-1	TEG 20	4284	14054,95	3753
Nora-1	TEG 15	4433	14543,79	3963
Nora-1	TEG 10	4695	15403,36	4128
Nora-1	BUJ	4928	16167,78	4225

### Sequence stratigraphy

Segment name	Unit	Surface type	Md (m)	Md (ft)
Nora-1	Volg-4	SB	3475	11400,78
Nora-1	Volg-3	SB	3484	11430,31
Nora-1	Volg-2	mfs	3531	11584,5
Nora-1	Volg-2	SB	3627	11899,46
Nora-1	Volg-1	mfs	3809	12496,57
Nora-1	Volg-1	SB	3893	12772,15
Nora-1	Kimm-4	mfs	4035	13238,03
Nora-1	Kimm-4	SB	4053	13297,08
Nora-1	Kimm-3b	mfs	4140	13582,51
Nora-1	Kimm-3b	SB	4208	13805,61
Nora-1	Kimm-3a	mfs	4225	13861,38
Nora-1	Kimm-3a	SB	4284	14054,95
Nora-1	Kimm-2b	mfs	4325	14189,46
Nora-1	Kimm-2b	SB	4370	14337,1
Nora-1	Kimm-2a	mfs	4433	14543,79
Nora-1	Kimm-2a	SB	4505	14780
Nora-1	Kimm-1b	mfs	4603	15101,52
Nora-1	Kimm-1b	SB	4785	15698,63
Nora-1	Kimm-1a	mfs	4795	15731,44
Nora-1	Kimm-1a	SB	4832	15852,83
Nora-1	Ox-1	mfs	4875	15993,9
Nora-1	Ox-1	SB	4926	16161,22
Nora-1	Cal-1	mfs	4928	16167,78
Nora-1	Cal-1	SB	5105	16748,48
Nora-1	Bat-1	mfs	5124	16810,82
Nora-1	Bat-1	SB	5170	16961,74
Nora-1	Baj-1	mfs	5266	17276,69
Nora-1	Baj-1	SB	5280	17322,62
Nora-1	Aalen-1	mfs	5301	17391,52
Nora-1	Aalen-1	SB	5337	17509,63

### Lithostratigraphy

Segment name	Unit	Surface type	Md (m)	Md (ft)
Nora-1	Cromer Knoll Group	base	3475	11400,78
Nora-1	Farsund Formation	top	3475	11400,78
Nora-1	Farsund Formation	base	4415	14484,73
Nora-1	Lola Formation	top	4415	14484,73
Nora-1	Lola Formation	base	4929	16171,06
Nora-1	Middle Graben Formation	top	4929	16171,06
Nora-1	Middle Graben Formation	base	5062	16607,41
Nora-1	Bryne Formation	top	5062	16607,41
Nora-1	Bryne Formation	base	5337	17509,63

### Chronostratigraphy

Segment name	Unit	Surface type	Md (m)	Md (ft)
Nora-1	Hauterivian	base	3463	11361,41
Nora-1	Valanginian	top	3463	11361,41
Nora-1	Lower Cretaceous	base	3475	11400,78
Nora-1	Valanginian	base	3475	11400,78
Nora-1	Middle Volgian	top	3475	11400,78
Nora-1	Upper Jurassic	top	3475	11400,78
Nora-1	Middle Volgian	base	3484	11430,31
Nora-1	Lower Volgian	top	3484	11430,31

Nora-1	Lower Volgian	base	3869	12693,42
Nora-1	Upper Kimmeridgian	top	3869	12693,42
Nora-1	Upper Kimmeridgian	base	4505	14780
Nora-1	Lower Kimmeridgian	top	4505	14780
Nora-1	Lower Kimmeridgian	base	4679	15350,86
Nora-1	Oxfordian	top	4679	15350,86
Nora-1	Oxfordian	base	5029	16499,14
Nora-1	Upper Jurassic	base	5029	16499,14
Nora-1	Callovian	top	5029	16499,14
Nora-1	Middle Jurassic	top	5029	16499,14
Nora-1	Callovian	base	5105	16748,48
Nora-1	Bathonian	top	5105	16748,48
Nora-1	Bathonian	base	5170	16961,74
Nora-1	Bajocian	top	5170	16961,74
Nora-1	Bajocian	base	5280	17322,62
Nora-1	Aalenian	top	5280	17322,62

## Q-1X

### Seismic markers

Segment name	Surface	Md (m)	Md (ft)	TWT (mS)
Q-1X	BCU	4003	13133,04	3351
Q-1X	TEG 50	4031	13224,9	ND
Q-1X	TEG 40	4047	13277,4	3373
Q-1X	TEG 30	4094	13431,6	3411
Q-1X	TEG 25	4104	13464,4	3434
Q-1X	TEG 20	4118	13510,33	3450
Q-1X	TEG 15	4135	13566,11	3462
Q-1X	TEG 10	4205	13795,76	3488
Q-1X	BUJ	4243	13920,43	3509

### Sequence stratigraphy

Segment name	Unit	Surface type	Md (m)	Md (ft)
Q-1X	Ryaz-2	SB	4003	13133,04
Q-1X	Ryaz-1	SB	4008	13149,45
Q-1X	Volg-4	mfs	4016	13175,69
Q-1X	Volg-4	SB	4020	13188,82
Q-1X	Volg-3	mfs	4020	13188,82
Q-1X	Volg-2	SB	4031	13224,9
Q-1X	Volg-3	SB	4031	13224,9
Q-1X	Volg-2	mfs	4031	13224,9
Q-1X	Volg-1	mfs	4033	13231,47
Q-1X	Volg-1	SB	4047	13277,4
Q-1X	Kimm-4	mfs	4063	13329,89
Q-1X	Kimm-4	SB	4094	13431,6
Q-1X	Kimm-3b	mfs	4098	13444,72
Q-1X	Kimm-3b	SB	4104	13464,4
Q-1X	Kimm-3a	mfs	4106	13470,96
Q-1X	Kimm-3a	SB	4118	13510,33
Q-1X	Kimm-2b	mfs	4124	13530,02
Q-1X	Kimm-2b	SB	4126	13536,58
Q-1X	Kimm-2a	mfs	4129	13546,42
Q-1X	Kimm-2a	SB	4132	13556,27
Q-1X	Kimm-1b	mfs	4165	13664,53
Q-1X	Kimm-1b	SB	4205	13795,76
Q-1X	Kimm-1a	mfs	4218	13838,41
Q-1X	Kimm-1a	SB	4243	13920,43

### Lithostratigraphy

Segment name	Unit	Surface type	Md (m)	Md (ft)
Q-1X	Cromer Knoll Group	base	4003	13133,04
Q-1X	Farsund Formation	top	4003	13133,04

Q-1X	Farsund Formation	base	4094	13431,6
Q-1X	Ravn Member (Heno Fm)	top	4094	13431,6
Q-1X	Ravn Member (Heno Fm)	base	4149	13612,04
Q-1X	Lola Formation	top	4149	13612,04
Q-1X	Lola Formation	base	4243	13920,43
Q-1X	Triassic undiff	top	4243	13920,43
Q-1X	Permian undiff	top	4456	14619,24

### Chronostratigraphy

Segment name	Unit	Surface type	Md (m)	Md (ft)
Q-1X	?Lower Valanginian-Lower Hauterivian	base	3990	13090,39
Q-1X	Upper Ryazanian-Lower Valanginian	top	3990	13090,39
Q-1X	Upper Ryazanian-Lower Valanginian	base	3999	13119,92
Q-1X	Lower Ryazanian	top	3999	13119,92
Q-1X	Lower Ryazanian	base	4003	13133,04
Q-1X	Lower Cretaceous	base	4003	13133,04
Q-1X	Upper Jurassic	top	4003	13133,04
Q-1X	Upper Volgian	top	4003	13133,04
Q-1X	Upper Volgian	base	4014	13169,13
Q-1X	Middle Volgian	top	4014	13169,13
Q-1X	Middle Volgian	base	4023	13198,66
Q-1X	Lower Volgian	top	4023	13198,66
Q-1X	Lower Volgian	base	4047	13277,4
Q-1X	Upper Kimmeridgian	top	4047	13277,4
Q-1X	Upper Kimmeridgian	base	4132	13556,27
Q-1X	Lower Kimmeridgian	top	4132	13556,27
Q-1X	Lower Kimmeridgian	base	4243	13920,43
Q-1X	Upper Jurassic	base	4243	13920,43
Q-1X	?Triassic	top	4243	13920,43

### STORK-1

#### Seismic markers

Segment name	Surface	Md (m)	Md (ft)	TWT (mS)
Stork-1	BCU	4039	13251,15	3288
Stork-1	TEG 50	4450	14599,56	3536
Stork-1	TEG 40	4785	15698,63	3759
Stork-1	TEG 30	ND	ND	ND

#### Sequence stratigraphy

Segment name	Unit	Surface type	Md (m)	Md (ft)
Stork-1	Ryaz-2	SB	4037	13244,59
Stork-1	Ryaz-1	SB	4120	13516,9
Stork-1	Volg-4	mfs	4136	13569,39
Stork-1	Volg-4	SB	4312	14146,81
Stork-1	Volg-3	mfs	4365	14320,69
Stork-1	Volg-3	SB	4448	14593
Stork-1	Volg-2	mfs	4471	14668,46
Stork-1	Volg-2	SB	4607	15114,65
Stork-1	Volg-1	mfs	4672	15327,9
Stork-1	Volg-1	SB	4785	15698,63
Stork-1	Kimm-4	mfs	4890	16043,11
Stork-1	Kimm-4	SB	4908	16102,17

#### Lithostratigraphy

Segment name	Unit	Surface type	Md (m)
Stork-1	Cromer Knoll Group	base	4037
Stork-1	Farsund Formation	top	4037

#### Chronostratigraphy

Segment name	Unit	Surface type	Md (m)
Stork-1	Ryazanian	base	4069

Stork-1	Upper Volgian	top	4069	13349,58
Stork-1	Lower Cretaceous	base	4069	13349,58
Stork-1	Upper Jurassic	top	4069	13349,58
Stork-1	Upper Volgian	base	4151	13618,6
Stork-1	Middle Volgian	top	4151	13618,6
Stork-1	Middle Volgian	base	4448	14593
Stork-1	Lower Volgian	top	4448	14593
Stork-1	Lower Volgian	base	4785	15698,63
Stork-1	Upper Kimmeridgian	top	4785	15698,63

## SVANE-1

### Seismic markers

Segment name	Surface	Md (m)	TWT (mS)
Svane-1A	BCU	4154	3435
Svane-1A	TEG 50	4472	3798
Svane-1A	TEG 40	4735	3975
Svane-1A	TEG 30	5055	4290
Svane-1A	TEG 25	5314	4426
Svane-1A	TEG 20	5495	4559
Svane-1A	TEG 15	5695	4796

### Sequence stratigraphy

Segment name	Unit	Surface type	Md (m)
Svane-1A	Ryaz-2	SB	4192
Svane-1A	Ryaz-1	SB	4250
Svane-1A	Volg-4	mfs	4262
Svane-1A	Volg-4	SB	4315
Svane-1A	Volg-3	mfs	4355
Svane-1A	Volg-3	SB	4472
Svane-1A	Volg-2	mfs	4505
Svane-1A	Volg-2	SB	4579
Svane-1A	Volg-1	mfs	4696
Svane-1A	Volg-1	SB	4745
Svane-1A	Kimm-4	mfs	4995
Svane-1A	Kimm-4	SB	5055
Svane-1A	Kimm-3b	mfs	5158
Svane-1A	Kimm-3b	SB	5245
Svane-1A	Kimm-3a	mfs	5298
Svane-1A	Kimm-3a	mrs	5415
Svane-1A	Kimm-3a	SB	5450
Svane-1A	Kimm-2b	mfs	5462
Svane-1A	Kimm-2b	SB	5600
Svane-1A	Kimm-2a	mfs	5728
Svane-1A	Kimm-2a	SB	5740
Svane-1A	Kimm-1b	mfs	5750

### Lithostratigraphy

Segment name	Unit	Surface type	Md
Svane-1A	Cromer Knoll Group	base	4192
Svane-1A	Bo Member	top	4192
Svane-1A	Farsund Formation	top	4192
Svane-1A	Bo Member	base	4202
Svane-1A	Svane Member	top	5310
Svane-1A	Farsund Formation	base	5722
Svane-1A	Lola Formation	top	5722

### Chronostratigraphy

Segment name	Unit	Surface type	Md
Svane-1A	Lower Cretaceous	base	4250
Svane-1A	Lower Valanginian	base	4154

Svane-1A	Ryazanian	top	4154
Svane-1A	Ryazanian	base	4236
Svane-1A	Upper Jurassic	top	4250
Svane-1A	Upper Volgian	top	4236
Svane-1A	Upper Volgian	base	4310
Svane-1A	Middle Volgian	top	4310
Svane-1A	Middle Volgian	base	4472
Svane-1A	Lower Volgian	top	4472
Svane-1A	Lower Volgian	base	4745
Svane-1A	Upper Kimmeridgian	top	4745

## XANA-1

### Seismic markers

Segment name	Surface	Md (m)	Md (ft)	TWT (mS)
Xana-1	BCU	4355	14287,88	3478
Xana-1	TEG 40	4446	14586,44	3615
Xana-1	TEG 30	4623	15167,14	3675
Xana-1	TEG 25	4777	15672,38	3730
Xana-1	TEG 20	4925	16157,94	3803
Xana-1	TEG 15	5105	16748,48	3970

### Sequence stratigraphy

Segment name	Unit	Surface type	Md (m)	Md (ft)
Xana-1	Ryaz-2	SB	4346	14258,36
Xana-1	Ryaz-1	SB	4357	14294,45
Xana-1	Volgian undiff., top	SB	4357	14294,45
Xana-1	Volgian undiff., base	SB	4446	14586,44
Xana-1	Kimm-4	mfs	4553	14937,48
Xana-1	Kimm-4	SB	4623	15167,14
Xana-1	Kimm-3b	mfs	4711	15455,85
Xana-1	Kimm-3b	mrs	4760	15616,61
Xana-1	Kimm-3b	SB	4777	15672,38
Xana-1	Kimm-3a	mfs	4785	15698,63
Xana-1	Kimm-3a	mrs	4895	16059,52
Xana-1	Kimm-3a	SB	4925	16157,94
Xana-1	Kimm-2b	mfs	4933	16184,19
Xana-1	Kimm-2b	mrs	5017	16459,77
Xana-1	Kimm-2b	SB	5030	16502,42
Xana-1	Kimm-2a	mfs	5095	16715,68

### Lithostratigraphy

Segment name	Unit	Surface type	Md (m)	MD (ft)
Xana-1	Cromer Knoll Group	base	4346	14258,36
Xana-1	Farsund Formation	top	4346	14258,36
Xana-1	Gita Member	top	4624	15170,42
Xana-1	Gita Member	base	5087	16689,43
Xana-1	Farsund Formation	base	5095	16715,68
Xana-1	Lola Formation	top	5095	16715,68

### Chronostratigraphy

Segment name	Unit	Surface type	Md (m)	Md (ft)
Xana-1	Lower Cretaceous	base	4357	14294,45
Xana-1	Ryazanian	base	4357	14294,45
Xana-1	Upper Jurassic	top	4357	14294,45
Xana-1	Volgian	top	4357	14294,45
Xana-1	Volgian	base	4446	14586,44
Xana-1	Upper Kimmeridgian	top	4446	14586,44

Sequence stratigraphy	Seismic Interval		Gita-1X	Xana-1X	Svane-1	Amalie-1	Lulu-2	Lulu-1	3/7-7	3 7-6	Jette-1
Uppermost Volg-2 – Ryaz-1	TEG 50 - BCU	Total Thickness (m)	98		358		N/A	N/A	N/A	N/A	29
		Net Sand (m)	0		6,705						6,52
		Net Sand (%)	0		1,9						22,48
		Average Porosity %	0								15,9
Volg-1 – Volg-2	TEG 40 - 50	Total Thickness (m)	115	91	233	147	N/A	N/A	N/A	N/A	62
		Net Sand (m)	0	3,39	5,943	0,609					2,44
		Net Sand (%)	0	3,73	2,6	0,4					3,94
		Average Porosity %	0	2,6	1,4	1,4					7,59
Kimm-4	TEG 30 - 40	Total Thickness (m)	30	177	310	75	N/A	N/A	N/A	N/A	8
		Net Sand (m)	1,16	2,51	11,0	0					5,64
		Net Sand (%)	3,86	1,42	3,54	0,00					70,5
		Average Porosity %	0,1	3,4	11	0					11,16
Kimm-3b – lowermost Kimm-4	TEG 25 - 30	Total Thickness (m)	120	154,0	190	100,0	N/A	N/A	N/A	144	14
		Net Sand (m)	60,3	61,57	3,7	3,05				25,15	12,37
		Net Sand (%)	50,22	39,98	1,92	3,05				17,46	88,36
		Average Porosity %	12,7	5,5	10	3,00				21,88	16,3
Kimm-3a	TEG 20 - 25	Total Thickness (m)	102,0	148,0	205	74	45,0	55	128	202	4
		Net Sand (m)	52,3	67,4	30,0	9,504	6,2	0,91	60,05	126,49	4
		Net Sand (%)	51,29	45,5	14,64	12,8	13,88	1,66	46,91	62,62	100
		Average Porosity %	11,2	8,1	6,2	2,1	12,1	2,42	19,07	18,63	22,8
Kimm-2a,b	TEG 15 - 20	Total Thickness (m)	161	170	272	106	150	166	259	277	17
		Net Sand (m)	40,5	31,70	44,04	4,32	4,72	2,59	58,22	44,96	15,019
		Net Sand (%)	25,15	18,65	16,19	1,20	3,15	1,56	22,48	16,23	88,35
		Average Porosity %	13,1	7,2	5,8	2,50	7,9	1,42	19,38	26,21	21,6
Kimm-1	TEG 10 - 15	Total Thickness (m)	86	N/A	184	190	66	59	92	75	81
		Net Sand (m)	0,157		43,68	6,553	1,829	0	3,5	1,07	19,28
		Net Sand (%)	0,2		23,74	3,4	2,8	0	3,80	1,422	23,80
		Average Porosity %	0,1		5,3	4,3	6,4	0	4,7	15,35	14,42
Ox-1 – Lower Kimm-1	BUJ - TEG10	Total Thickness (m)	246	N/A	N/A	137	13	33	0	N/A	12
		Net Sand (m)	36,876			18,745	0,00	0	0		1,22
		Net Sand (%)	15			13,68	0,00	0	0		10,17
		Average Porosity %	7			4,4	0	0	0		16,31

Tabel. 6.1

Area	Formation / sequence	TOC (wt.%)				HI (mg HC/g TOC)				T <sub>max</sub> (°C)			
		Mean	P90	P50	P10	Mean	P90	P50	P10	Mean	P90	P50	P10
<b>Salt Dome Province</b>													
	Farsund Formation	1.8	0.8	1.6	3.2	231	186	228	280	431	426	431	436
	Ryaz-1	3.6	1.7	3.2	6.0	364	213	341	546	428	422	428	433
	Volg-4	1.9	1.0	1.7	2.9	222	102	195	374	430	427	430	433
	Volg-1	1.9	1.0	1.7	2.9	189	85	165	322	432	428	432	435
	Farsund other*	1.7	0.8	1.5	2.8	178	83	157	298	431	427	431	436
	Lola Formation	1.5	0.9	1.4	2.1	138	82	130	205	434	427	434	441
	Bryne/Lulu/M.G. fms	3.3	1.1	2.6	6.2	94	54	88	142	439	428	439	450
	Fjerritslev Formation	2.1	1.2	2.0	3.2	Bimodal distribution				436	428	436	444
<b>Tail End Graben</b>													
	Farsund Formation	2.8	0.9	2.2	5.2	171	63	141	313	439	433	439	445
	Ryaz-1	4.7	2.2	4.1	7.8	283	156	261	437	438	434	438	442
	Volg-4	2.4	1.0	2.0	4.2	180	80	157	308	439	436	439	443
	Volg-1	1.8	1.1	1.7	2.6	119	49	102	211	443	433	443	453
	Farsund other*	2.2	1.0	1.9	3.8	128	64	115	208	439	431	439	447
	Lola Formation	1.2	0.2	0.7	2.7	104	48	92	175	434	424	434	445
	Bryne/Lulu/M.G. fms	1.4	0.5	1.2	2.7	55	22	47	98	not defined			
<b>Feda and Gertrud Grabens</b>													
	Farsund Formation	3.5	1.5	3.0	6.1	238	106	207	405	439	433	439	445
	Ryaz-1	5.0	2.2	4.3	8.5	369	223	347	542	439	434	439	444
	Volg-4	3.2	1.4	2.8	5.6	249	127	226	401	440	435	440	445
	Volg-1	3.2	1.5	2.9	5.3	232	91	194	415	440	433	440	446
	Farsund other*	3.4	1.5	3.0	5.9	212	104	189	346	439	432	439	445
	Lola Formation	2.0	0.6	1.5	3.8	168	85	152	270	440	430	440	450
<b>Søgne Basin</b>													
	Farsund Fm	1.6	0.8	1.4	2.7	161	63	135	290	437	430	437	443
	Farsund other*	1.6	0.8	1.4	2.7	156	63	132	277	437	430	437	443
	Lola Fm	1.8	1.0	1.7	2.9	144	78	133	225	438	431	438	444
	Bryne/Lulu/M.G. fms (TOC< 20%)	3.5	0.7	2.2	7.6	171	99	160	256	444	436	444	452
	Bryne/Lulu/M.G. fms (TOC> 20%)	69.6	51.7	69.6	87.4								
<b>Heno Plateau</b>													
	Farsund Formation	3.2	1.5	2.8	5.2	207	94	181	351	438	434	438	442
	Ryaz-1	5.6	1.8	4.4	10.6	379	180	336	628	435	432	435	439
	Volg-4	4.9	2.8	4.6	7.6	238	133	220	364	438	435	438	442
	Volg-1	3.5	1.8	3.2	5.8	193	86	168	329	439	435	439	442
	Farsund other*	2.7	1.6	2.5	3.9	178	93	162	283	439	435	439	442
	Lola Formation	2.1	0.8	1.7	3.8	161	84	146	256	439	431	439	447
	Fjerritslev Formation	1.3	1.0	1.3	1.7	64	35	59	98	447	435	447	459
<b>Outer Rough</b>													
	Farsund Formation	2.9	1.9	2.8	4.2	213	77	174	393	441	432	441	450
	Volg-4	3.3	2.6	3.3	4.2	235	108	207	397	439	432	439	446
	Farsund other*	2.7	1.6	2.5	3.9	199	63	155	383	442	433	442	451

\*Excluding Volg-1; -4; Ryaz-1. M.G.: Middle Graben Formation. P10 indicate the value that 10% of the population will exceed; P50 indicate the median of the population; P90 indicate the value that 90% of the population will exceed.

Tabel. 9.1

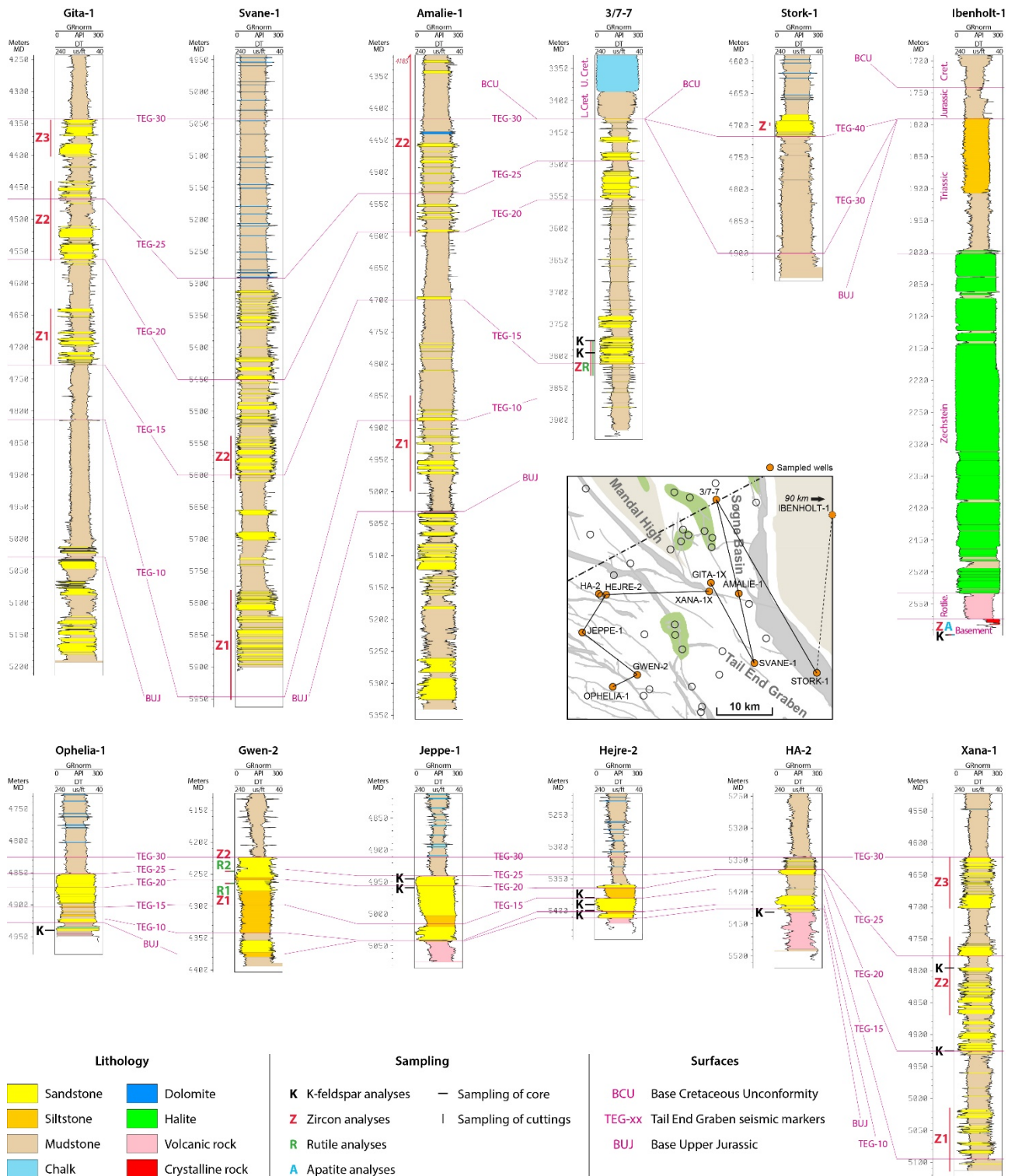


Figure 3. Well-log profile of the wells chosen for provenance analysis. The sample depths are shown for the different isotope analyses.

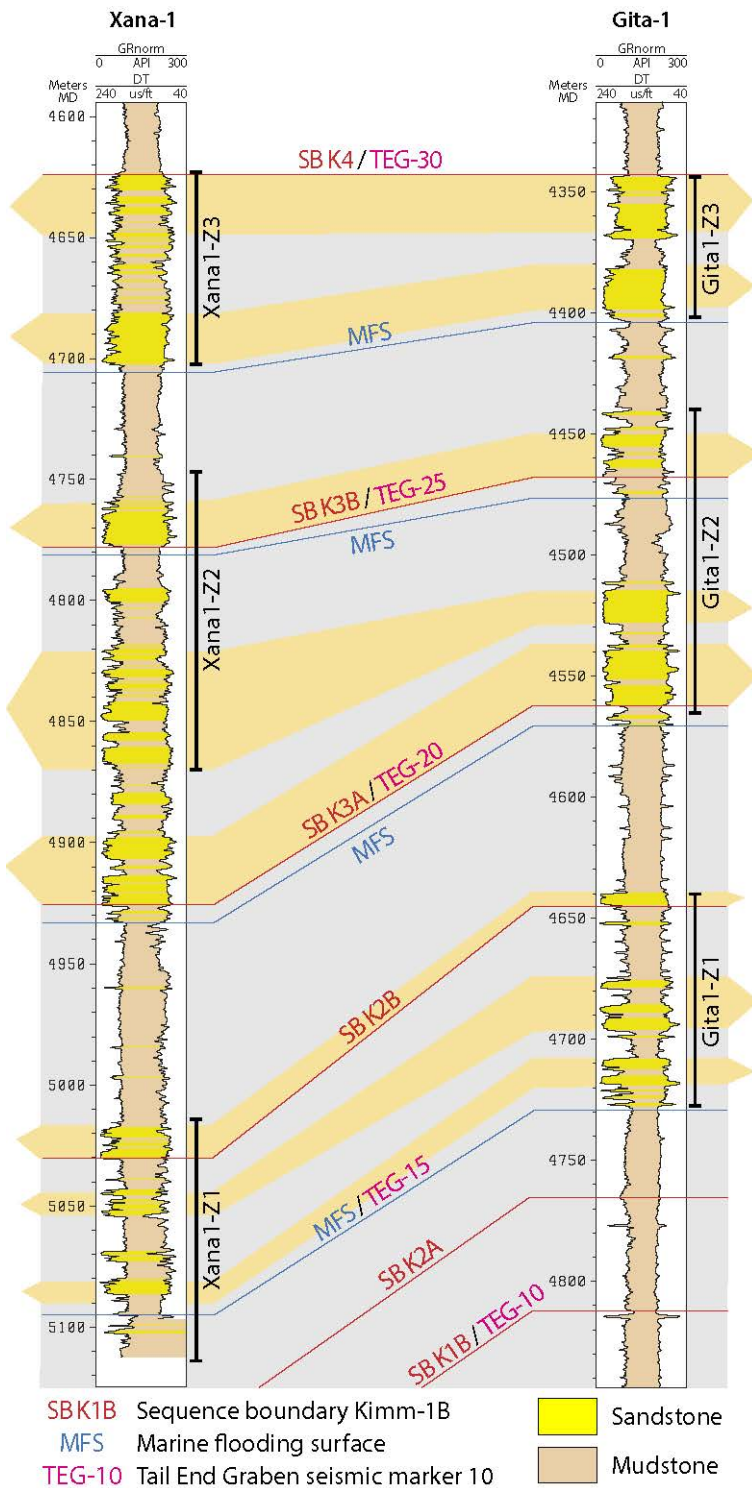


Figure 4. Well-log profile of the stratigraphic correlation of the gravity-flow sandstones in the Xana-1 and Gita-1 wells with indication of sequence stratigraphic surfaces and seismic marker surfaces (see depositional ages in Fig. 2). The depths of cuttings samples used for zircon age analysis are shown.

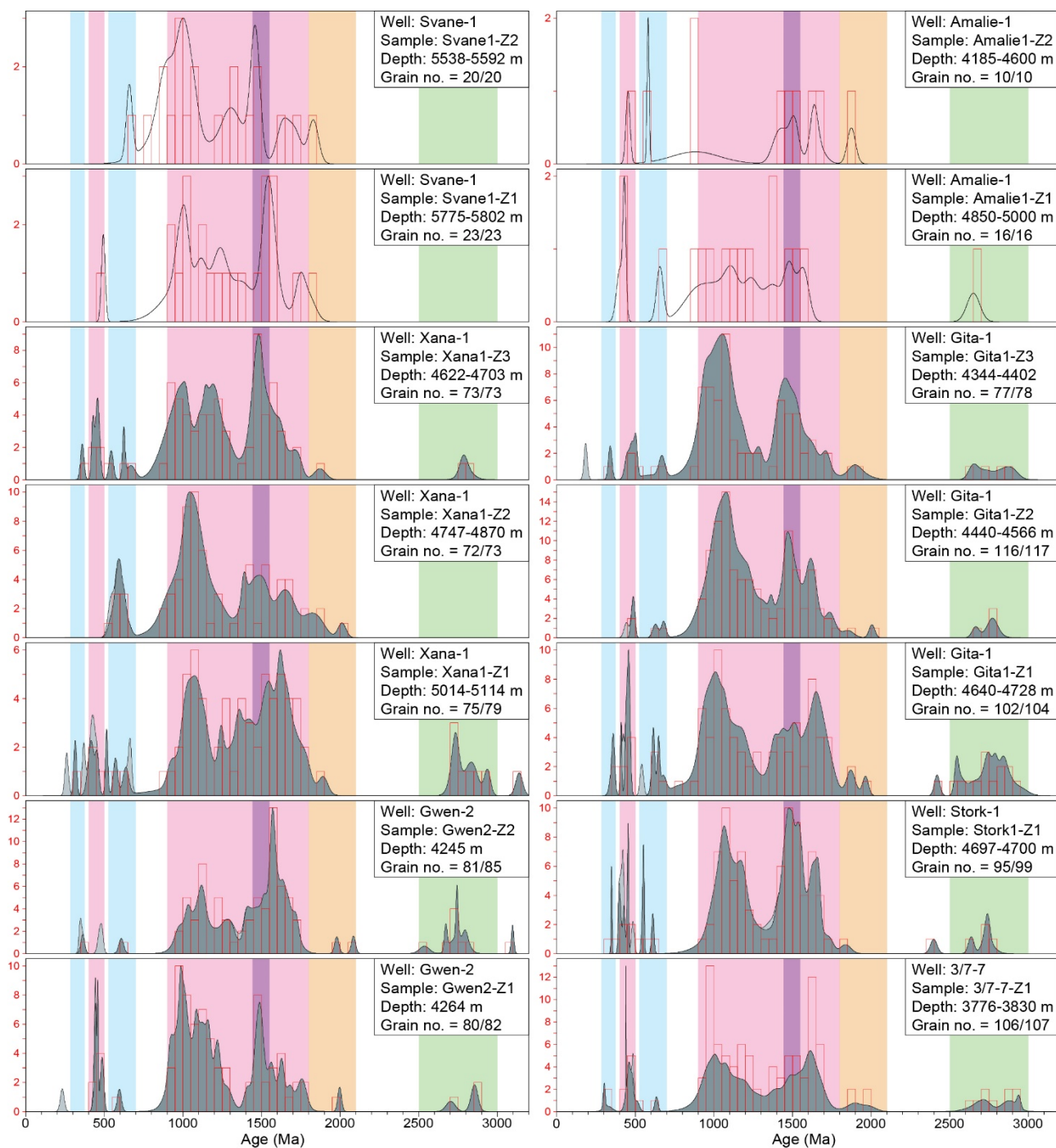


Figure 5. Zircon U-Pb ages from Upper Jurassic sediments in the greater Tail End Graben area. The results are plotted as combined histograms showing the number of concordant grains in red and as probability density distributions where the concordant ages are shown in dark grey and those with discordance >10% in light grey. The age distributions from the Svane-1 and Amalie-1 wells are not grey to signify that the number of analyzed grains is too low to be representative for the entire age spectrum in the sediments. The grain no. displays the number of employed concordant ages out of the total number of measured ages. See Fig. 6 for explanation of the colored age intervals.

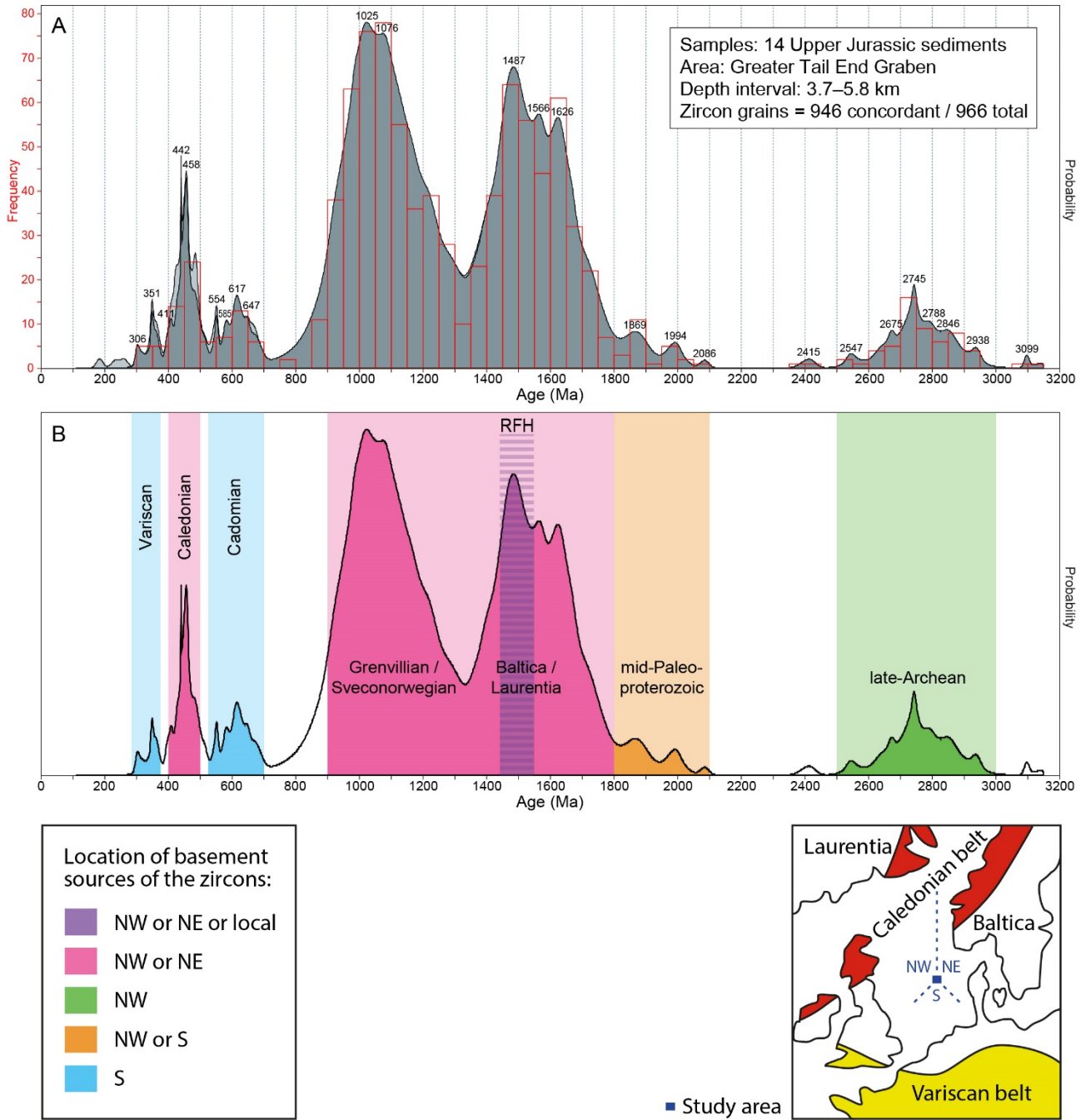


Figure 6. Compilation of all zircon U-Pb age data from Upper Jurassic sediments from this study. A: Peak ages are given in million years (Ma). B: Identification of the possible provenance areas of the age populations. The age of each zircon grain reveals its ultimate basement source, and the grains have most likely been recycled one or several times before their Late Jurassic deposition. The percentages show how large a proportion of the zircon grains have ages within each category. The basement age of the Ringkøbing-Fyn High (RFH) is here presumed to be representative of the intra-basinal basement highs.

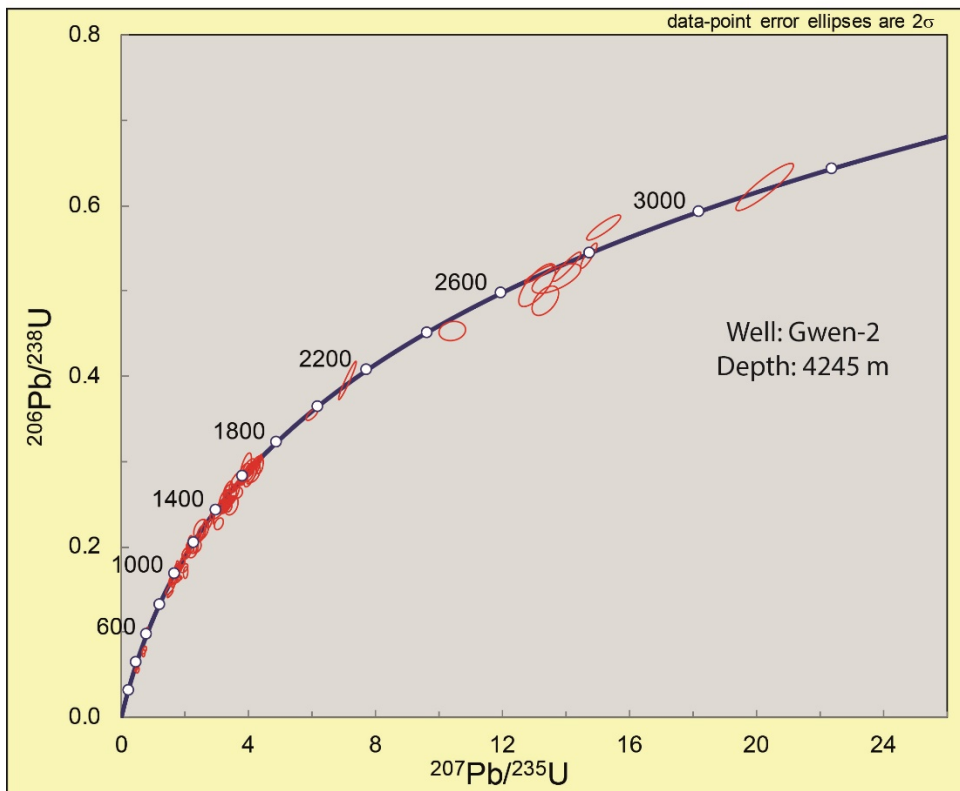
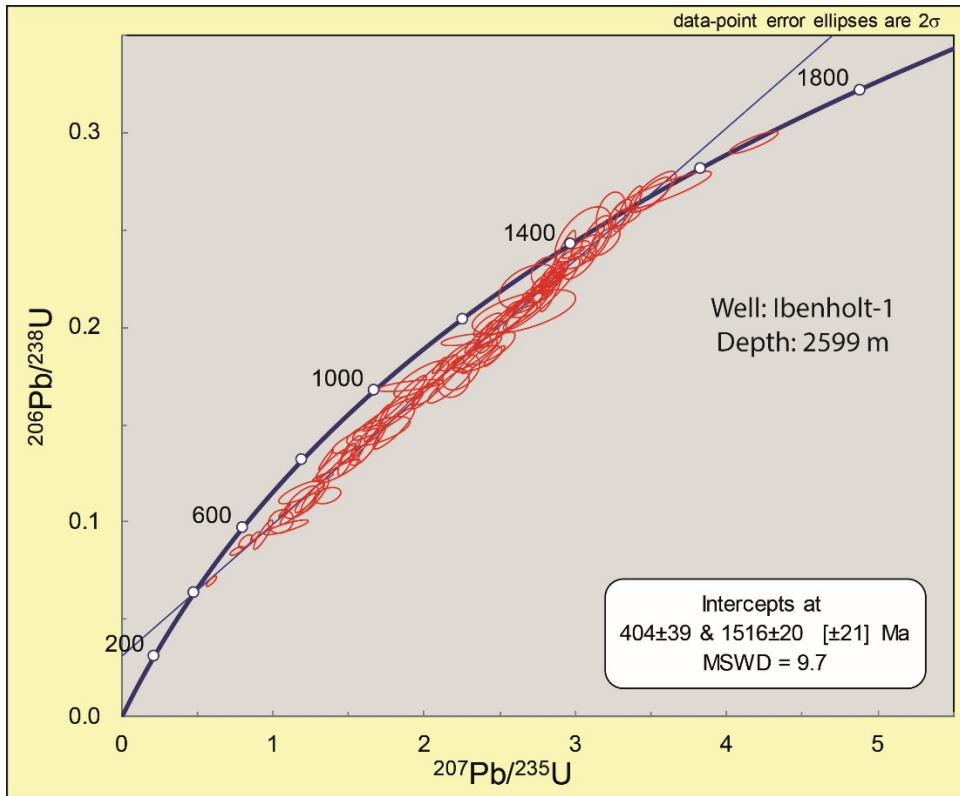


Figure 7. Concordia diagrams of zircon U-Pb data from basement in Ibenholt-1 and sandstone in Gwen-2. The concordia-intercept ages are calculated for the discordant basement ages in Ibenholt-1, whereas the detrital zircons in Gwen-2 are mostly concordant similarly to the rest of the analyzed sediments.

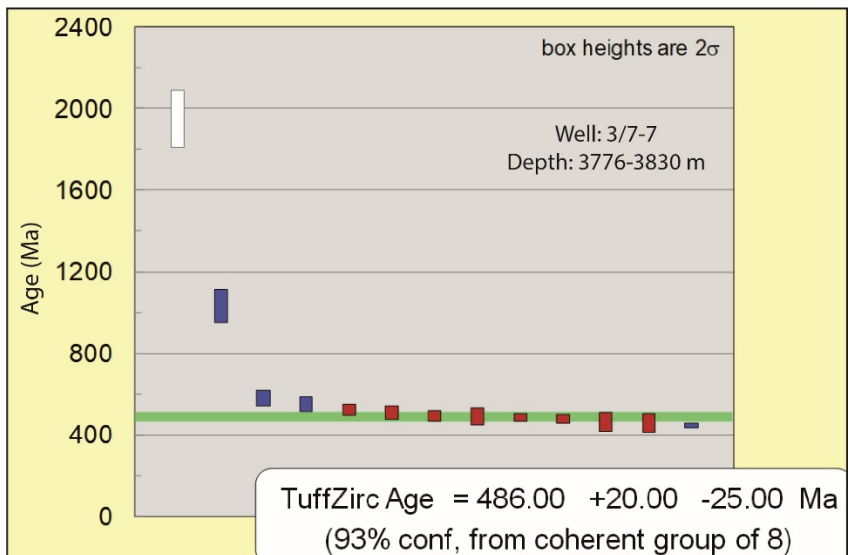
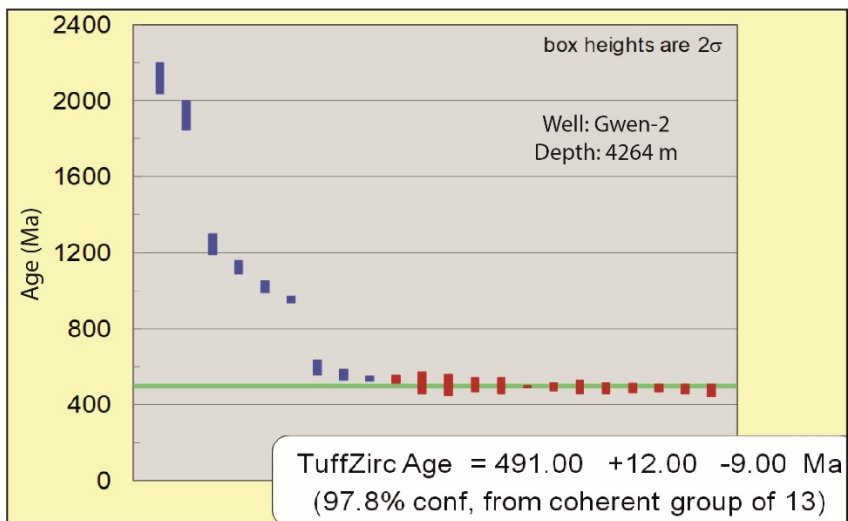
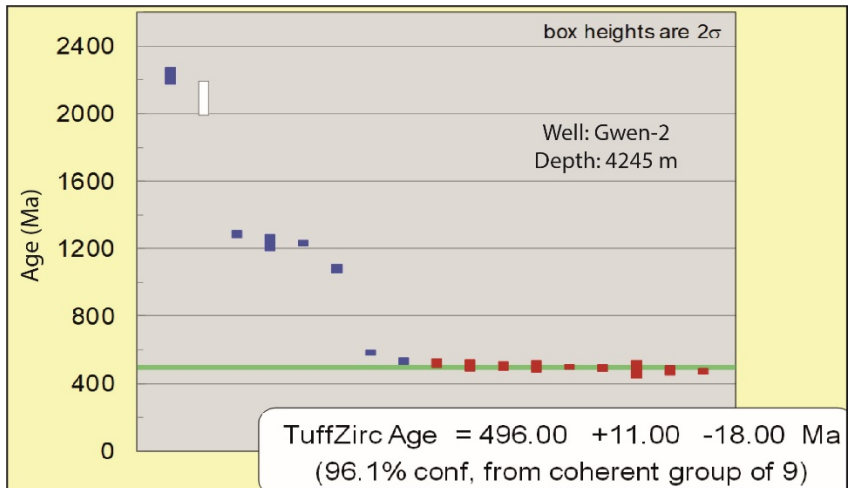


Figure 8. Rutile U-Pb ages from Upper Jurassic sediments in the greater Tail End Graben area. The internally-concordant youngest  $^{206}\text{Pb}/^{238}\text{U}$  ages (in red) are used to calculate an age (in green) of these grains. Some ages were not used in the calculation (in blue) including a few grains with anomalously high errors (in white).

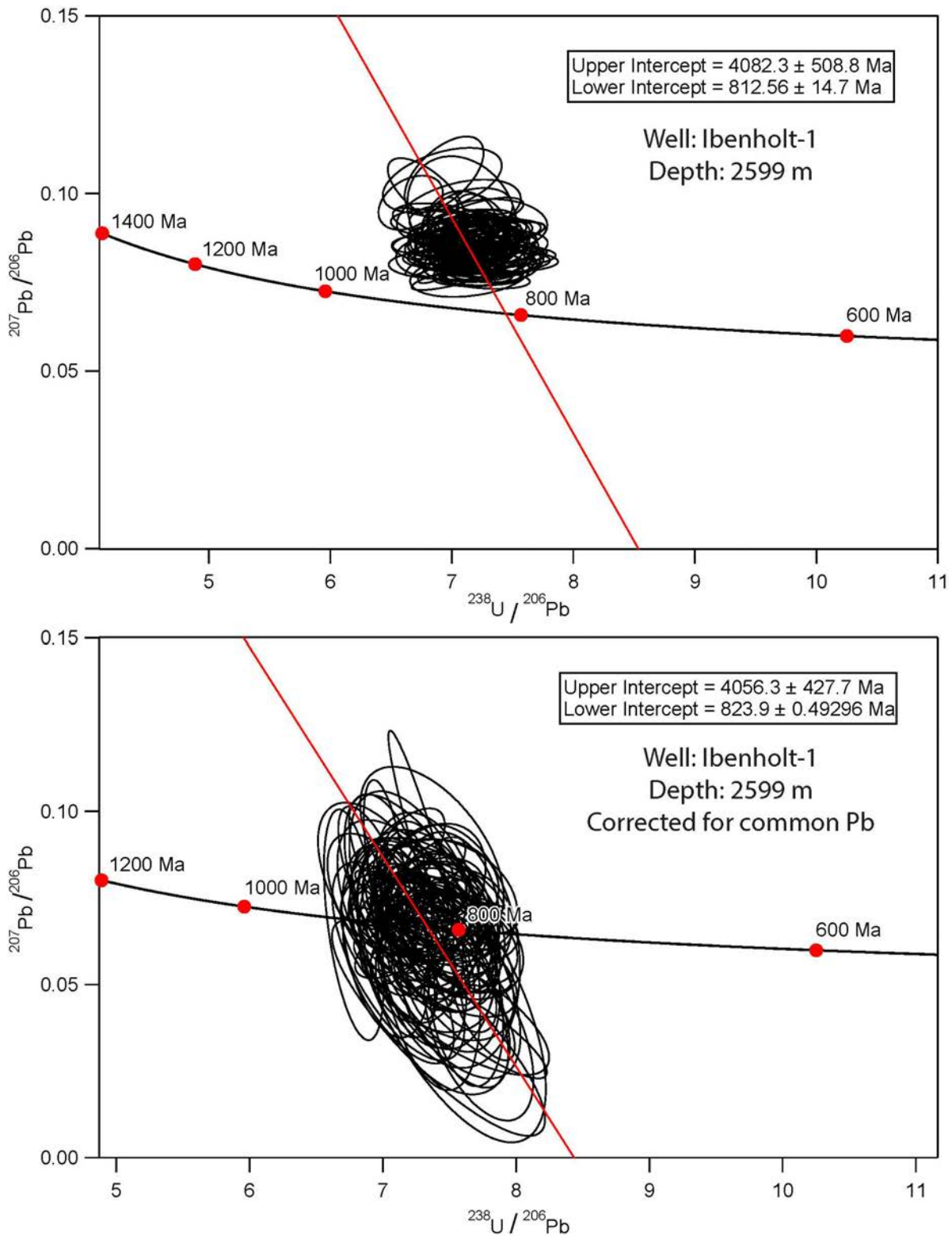


Figure 9. Concordia diagrams of apatite U-Pb data from basement in Ibenholt-1 on the Ringkøbing-Fyn High. The ages are not corrected for common Pb in the upper diagram and they are corrected in the lower diagram whereby a better estimate of the lower concordia-intercept age is made.

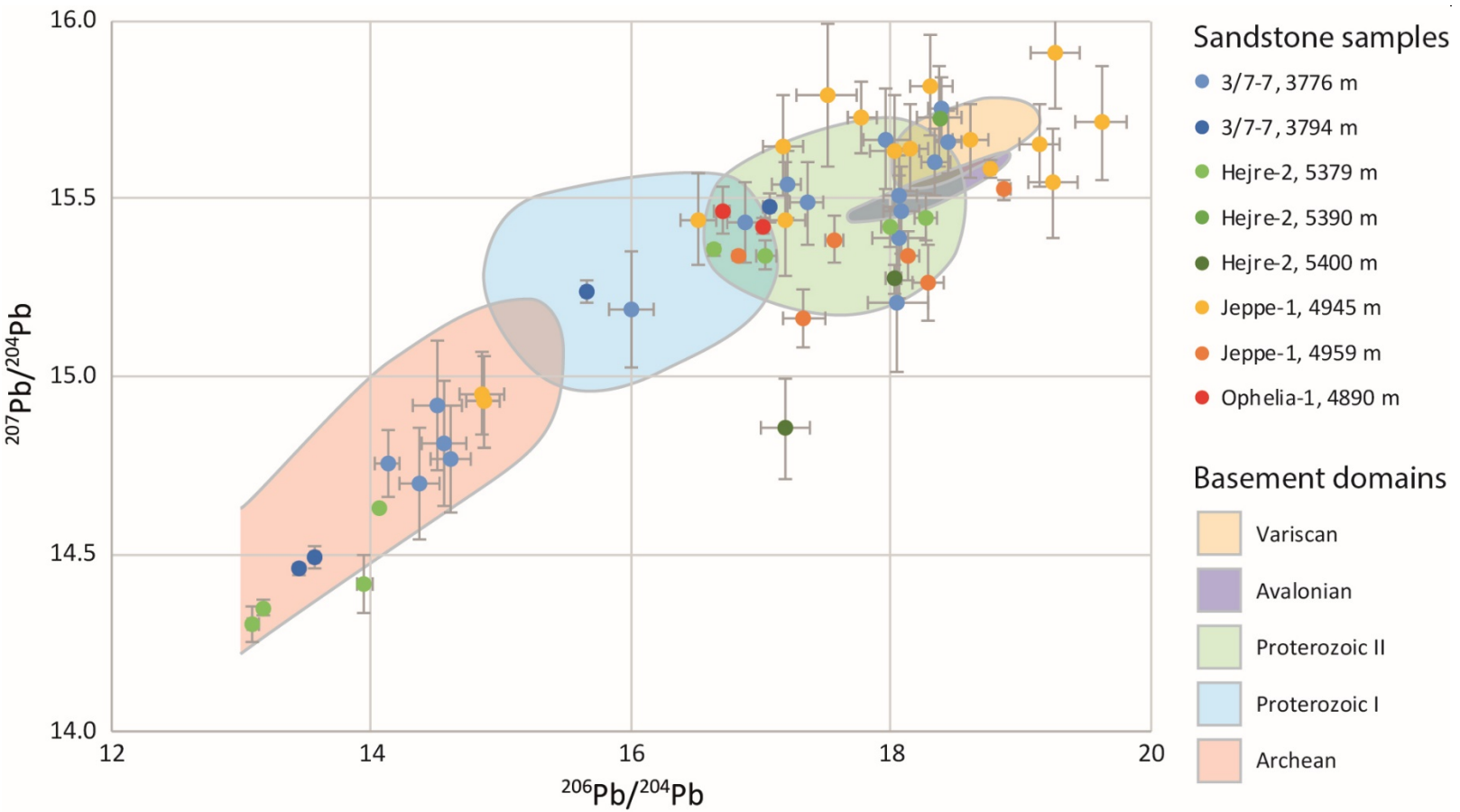


Figure 10. K-feldspar Pb-Pb isotopic signatures from Upper Jurassic sandstones in the greater Tail End Graben area, besides a basement sample from Ibenholt-1 on the Ringkøbing-Fyn High. The basement domains are from Tyrrell et al. (2007).

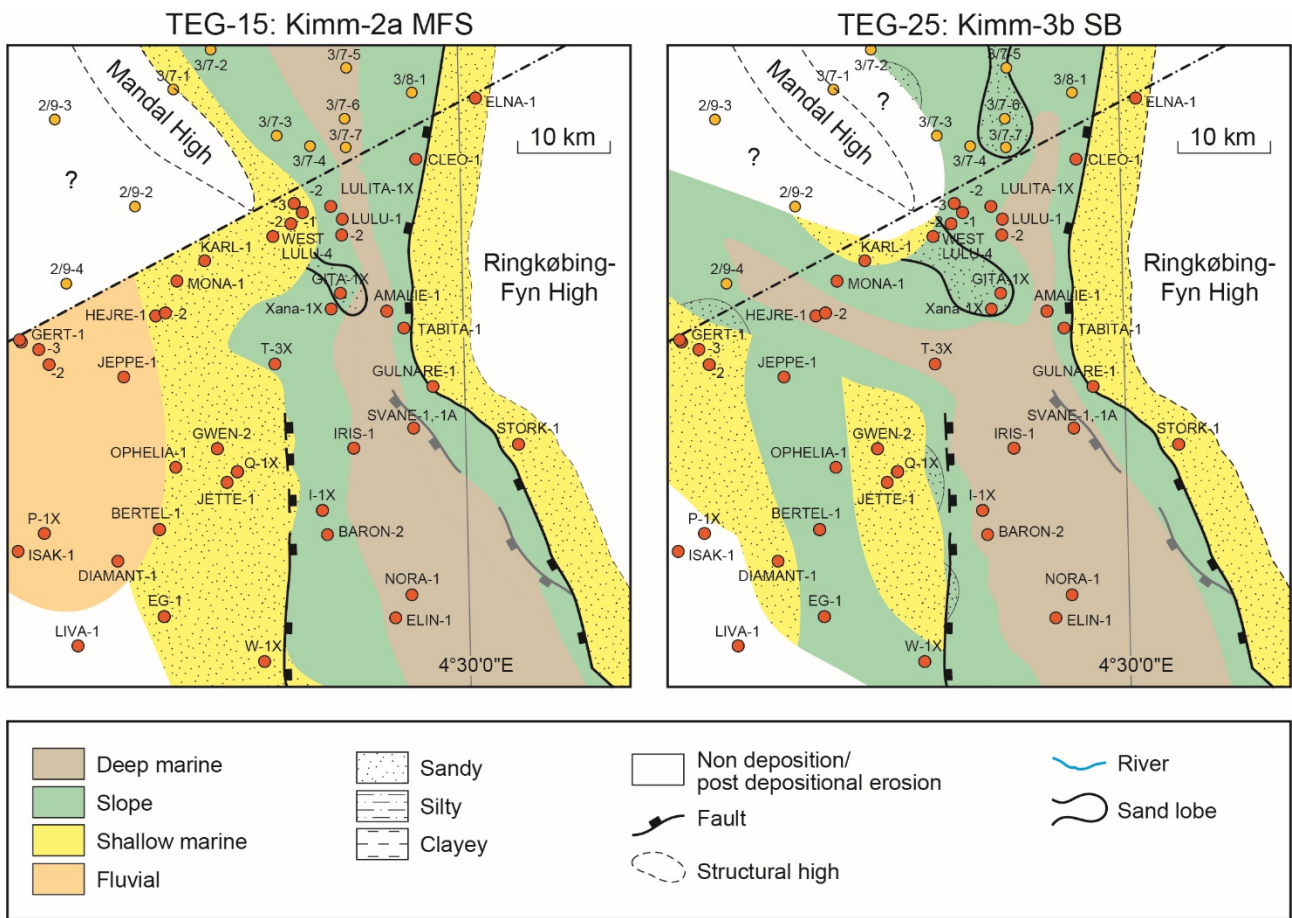


Figure 11. Paleogeographical maps showing the interpreted distribution of depositional environments for two scenarios. MFS: Marine flooding surface. SB: Sequence boundary. From Jakobsen et al. (this volume).

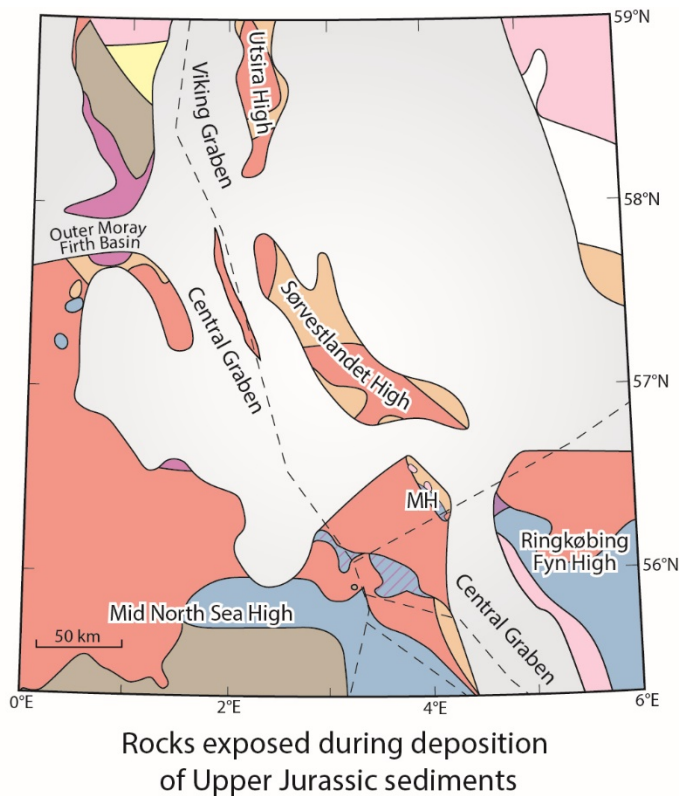
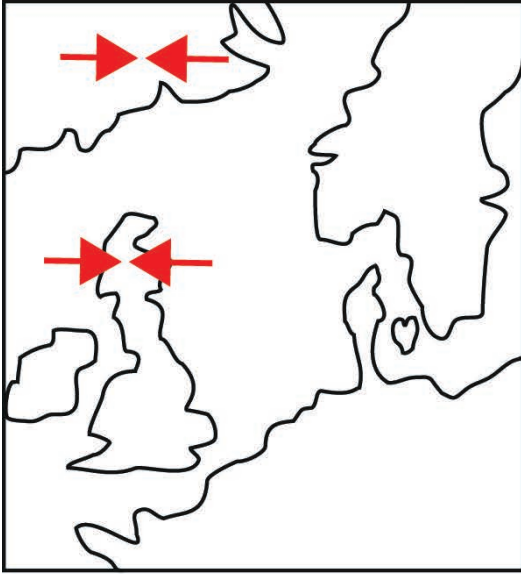
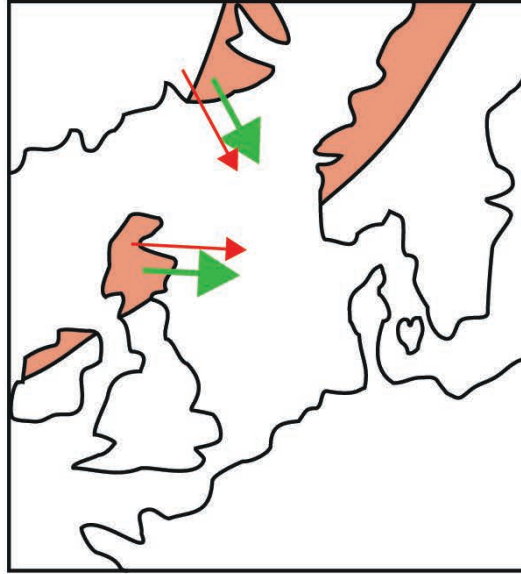


Figure 12. Map of the areas exposed for erosion in the central North Sea during the Late Jurassic. Some areas were gradually overlapped such as the Triassic sediments south of the Mandal High (MH). Modified from Weibel et al. (2010).

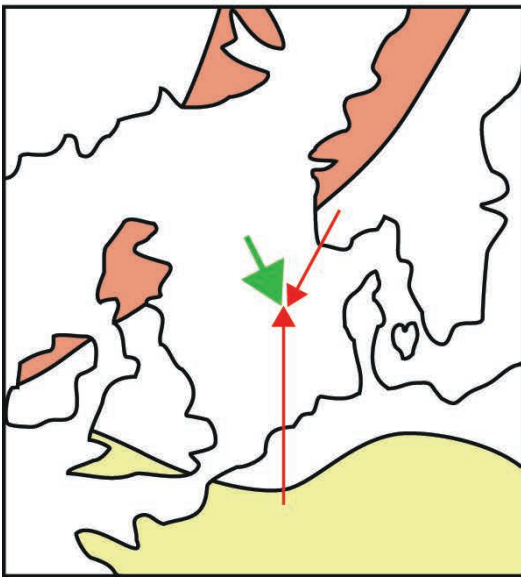
Neoproterozoic



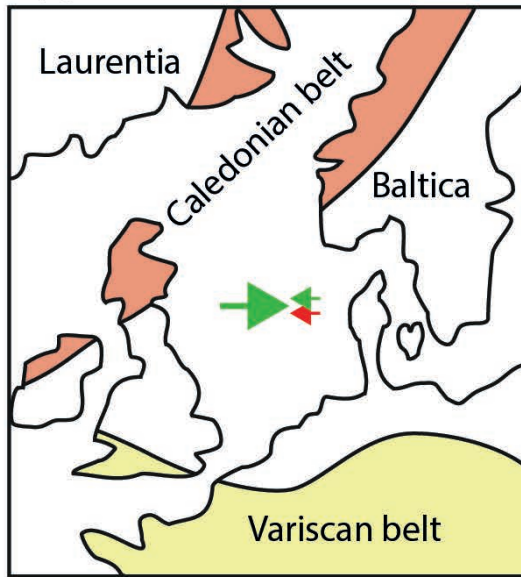
Devonian/Carboniferous



Triassic



Upper Jurassic



Transport of basement material

Transport of reworked sediment

Major sediment supply

Minor sediment supply

Figure 13. Transport history of the zircon grains in the Upper Jurassic sediments in the central North Sea interpreted on basis of their U-Pb ages.

# **Illite distribution and morphology explaining basinal variations in reservoir properties of Upper Jurassic sandstones, Danish North Sea**

Weibel, R., Nielsen, M.T., Therkelsen, J., Jakobsen, F.C, Bjergager, M., Mørk, F., Mathiesen, A., Johannesen, P., Dybkjær, K.

Geological Surveys of Denmark and Greenland (GEUS), Øster Voldgade 10, DK-1350 Copenhagen K, Denmark.

## **Abstract** (max 300 words)

Growth of fibrous illite may destroy an otherwise promising sandstones reservoir, even sandstones characterized by microquartz coatings. Therefore detailed petrographical and diagenetic investigations were performed in order to understand the factors that control illite precipitation and other factors affecting the reservoir properties in the Upper Jurassic Heno Formation. The Heno Formation is encountered in large parts of the Danish Central Graben, where its lower part – Gert Member was deposited in back barrier environment and to a lesser extend shoreface environment and its upper part – Ravn Member was deposited in a shoreface environment influenced by fluvial sourced spit development.

In all 215 cored samples from 15 wells were investigated by optical and scanning electron microscopy. This was supplemented by plug porosity and permeability measurements and X-ray diffraction of bulk and clay fraction. The investigations show among other things that microquartz coatings may help to preserve porosity and permeability, whereas the permeability is reduced when microquartz occurs combined with fibrous illite. Hexagonal illite reduces permeability less than fibrous illite. Illite precipitation is largely governed by K-feldspar abundance during burial. Consequently, the initial abundance of K-feldspar (in the sediment source area) and its alteration during and immediately after deposition, i.e. in the back barrier environment or during aerial exposure (at sequence boundaries), have a major influence on the final reservoir properties of the sandstones. The risk of illite precipitation can largely be predicted from the depositional environment (and the underlying sediments).

## **Graphical abstract** (5x13 cm, 531x1328 pixels)

**Keywords** (max 8)

Weathering of feldspar, kaolinite, illite morphology, hexagonal illite, microquartz, quartz cement, reservoir properties, deep burial

**Highlights** (3 – 5 bullet points, max 85 characters)

## **Introduction**

Alteration of feldspar grains in sandstones may potentially generate secondary porosity and liberate elements promoting clay mineral precipitation. The reservoir properties are influenced by the prevailing process, whether feldspar grain dissolution or clay mineral precipitation. The depositional environment and the climatic conditions affect the composition of the initial pore fluid and define the prevailing precipitation of early diagenetic clays, kaolinite or smectite (e.g. Burley et al. 1985; Jeans et al. 2001; Morad et al. 2010; Weibel et al. 2017). Though feldspar alteration initiates in the hinterland, it continues after deposition with high intensity where meteoric water flushes through the sediments. Feldspar alteration commonly leads to kaolinite precipitation when sediments are flushed with meteoric water (e.g. Hurst and Irwin 1982; Bjørlykke 1984; Stonecipher and May 1990; Glasmann et al. 1989; Bjørlykke et al. 1992). Thus kaolinitization of unstable detrital silicates occur at sequence boundaries and in the lowstand systems tract (e.g. Morad et al. 2010).

However, if K-feldspar survives until deeper burial, its degradation or albitization leads to liberation of potassium (e.g. Bjørlykke et al. 1986, 1992; Bjørkum and Gjelsvik 1988, Chuhan et al. 2001). Potassium may alternatively origin from external sources, such as fluids from adjacent shales (e.g. Gaupp et al. 1993; Furlan et al. 1996; Thyne et al. 2001, Worden and Burley 2003; Clauer et al. 2008) or from migrating fluids (e.g. Robinson et al 1993; Lanson et al. 1996; De Ros 1998; Zwingmann et al. 1999). Any increase of potassium in the formation water promotes illite precipitation, illitization of kaolinite and illite transformation of smectite through mixed-layer illite/smectite phases (e.g. Pollastro 1985; Bjørlykke et al. 1992; Wilkinson et al. 2006; Lander and Bonnell 2010). High supersaturation with potassium promotes precipitation of hexagonal illite, whereas lower saturation result in lath-shaped illite (Bauer et al. 2000; Kuwahara et al. 2001). Especially the fibrous or lath-shaped illite morphology decrease fluid flow in sandstones (e.g. Bauer et al. 2000; Weibel et al. 2017). Therefore, the dominant illite morphology may have major influence on reservoir permeability and the ability to understand illite distribution and morphology is required in order to predict reservoir properties.

Microquartz coatings preserve porosity by inhibiting quartz overgrowth at deeper burial (e.g. Vagle et al. 1984; Aase et al. 1996; Jahren and Ramm 2000; Bloch et al. 2002; Lima and De Ros 2002). However, microquartz occurring in excessive amounts or together with illite or carbonate cement cannot preserve porosity and hence will not have a positive influence on reservoir properties.

The hypothetical question of this work is whether microquartz coatings improve the reservoir properties under all circumstances, or if K-feldspar in addition needs to be removed by weathering in order to avoid enhanced illite precipitation during burial. The Heno Formation is deposited in back barrier (lagoonal) or shoreface environment, and have present day burial depth varying from 3800 – 5400 m. The siliciclastic input was the same with exception of bioclast input in the shoreface sandstones. The degree of weathering on the flood plain and in the shoreface environment varies. Heno Formation represents sandstones with microquartz coatings, microquartz coatings and illite, besides quartz overgrowths with illite of various morphologies. Consequently, the Heno Formation provides the perfect opportunity to investigate the early diagenetic conditions that favours different diagenetic routes during burial.

## **Geological settings**

### **Structural settings**

The Upper Jurassic Heno Formation was deposited on the Gertrud and Heno Plateau in the Danish Central Graben (Fig. 1). The Gertrud and Heno Plateau formed part of a widespread high-lying area in the northernmost part of a Jurassic North Sea rift basin bordered by the Ringkøbing–Fyn High to the east, the Mandal High to the north and the Mid North Sea High to the west (Fig. 1).

Subdivision into three major tectonic phases is possible for the Late Jurassic to Early Cretaceous time; the first phase occurred in Kimmeridgian time, the second in early to Late Volgian and the third in Late Volgian to Ryazanian time (e.g. Gowers and Sæbøe 1985; Møller and Rasmussen 2003; Bruhn and Vagle 2005). Deposition of the Heno Formation occurred during early Kimmeridgian time, when the Gertrud area formed a plateau connecting the Heno Plateau to the south and the Mandal High to the north. The Heno Formation sediments unconformably overlie Palaeozoic rocks and hence follow the topography of these. Mainly N-S trending faults were active along the Feda Graben, though thickness variations of the Heno Formation on the Gertrud Platform show evidence of syn-sedimentary fault activity along WNW-ESE trending faults.

The fault system changed into NW-SE trending faults during Early to Late Volgian time. The fault-induced subsidence developed several fault-controlled half-grabens, which acted as local depocenters for the lower Farsund Formation. The activation of the Mona Fault resulted in development of the Gertrud Plateau into a half graben - the Gertrud Graben. The fault activity ceased during the Volgian times and uniform subsidence of the Gertrud area prevailed during deposition of the upper part of the Farsund Formation.

The third tectonic phase during the Late Volgian – Ryazanian times is characterized by reactivation of the NW-SE trending faults. The tectonic activity was associated with compression and thrusting. Due to this complex tectonic history, areas adjacent to the major faults (e.g. the Mona Fault) were uplifted and exposed to erosion while deposition still occurred within the graben areas.

### **Stratigraphy**

The Heno Formation was redefined and subdivided by Michelsen *et al.* (2003) to include the back-barrier and shoreface sandstones of the Gert Member and the shallow marine sandstones of the Ravn Member. The claystones of the Lola Formation separate the two members in the most wells on the Heno Plateau. The Heno Formation unconformably overlies Carboniferous sediments, Permian lava and volcanoclastic rocks, Triassic Skagerrak Formation and the Middle Jurassic Bryne Formation (Johannessen 2003; Weibel *et al.* 2010b; 2019). The Heno Formation in the Danish sector is roughly time equivalent to the Fulmar Formation in the UK sector and the Ula Formation of the Norwegian sector (Fig. 2; e.g. Partington *et al.* 1993; Johannessen 2003; Gradstein *et al.* 2012).

## **Depositional setting and palaeogeography**

During the Late Jurassic a relative sea-level rise accompanied the normal faulting of the Gertrud Graben/Plateau, resulting in a stepwise transgression towards west (Andsbjerg and Dybkjær 2003; Johannessen 2003).

### **Gert Member**

The Gert Member sandstones in the Gert area contains up c. 60 m of back-barrier sandstones. This is in contrast to the c. 27 m Gert Member sandstones in the Hejre area, where no back-barrier sediments are found. The reason for this could be that the reservoir sandstones in the Hejre area were deposited in a relatively flat or very gently sloping setting, which may form relatively thin but regionally widespread sands in an environment with no tendency of forming barriers, or the former back-barrier sediments may have been removed during transgression. The reason for the large thickness of the Gert Member sandstones in the Gert area compared to the Hejre area may have been a high supply of sand to the area; furthermore, they were deposited in an area of relatively steep palaeotopography and differences in accommodation space. The transgression was retarded due to the high relief and the back-barrier sandstones may therefore have aggraded (Johannessen et al. 2010a, 2010b).

### **Ravn Member**

Interpretation of wireline logs show that offshore mudstones of the Lola Formation are present above the Gert Member and the offshore mudstones are overlain by first regressive and secondly transgressive shallow marine sandstones of the Ravn Member (Johannessen et al. 2010a). The sandstones of the Ravn Member are relatively thin (c. 4-5 m) in the Hejre area compared to areas such as the Gert area and further to the south on the Gertrud Plateau, with thicknesses of 20-40 m in the Jette-1 and Gwen-2 wells (Fig. 3).

The Ravn Member generally consists of shoreface sandstones, with a lower regressive part being prograding, and the upper transgressive part being retrograding (Johannessen 2003; Johannessen et al. 2010a). The lower regressive shoreface sandstones were probably formed due to pause in fault activity and subsidence, whereas the upper transgressive shoreface sandstones were deposited during renewed subsidence (Andsbjerg and Dybkjær 2003). Conglomerates of larger clasts than the typical over-sized clasts in the shoreface sandstones abruptly appear between the coarsening-upwards regressive sandstones and the fining-upwards sandstones. The conglomerates were interpreted as storm event on the beach/shoreface or reworked fluvial deposits formed during maximum regression (Johannessen 2003). Incised valleys (recognized in the Bertel-1 and Ravn-3 wells) and the common presence of coal clasts in the conglomerates support the reworking of fluvial deposits.

## **Burial and thermal history**

The cored Heno Formation has experienced maximum burial temperatures of 125–156°C and pressure of 65–100 MPa. The wells Diamant-1 and W-1 are characterised by temperatures lower than the general trend with depth, which could have been caused by locally lower heat flow (Schovsbo et al. in

prep.). The Ravn-2 well has a relatively high temperature compared with burial depth probably due to hydrothermally influence.

Hydrocarbons are present in several wells. Hydrocarbon migration and introduction into the Heno Formation most likely occurred during the main episode to the maturation of the Kimm-4 sequence of the Farsund Formation.

- Figure 1: Geological map
- Figure 2: Stratigraphic scheme
- Figure 3: Log panel

## **Methods and material**

Polished thin sections were prepared from sedimentary rocks impregnated with blue epoxy, for easy identification of porosity. The polished thin sections were studied by transmitted and reflected light microscope. Descriptive terms for clay minerals are used according to Wilson and Pittman (1977) and for carbonate cement morphologies modified from Harwood (1988). Supplementary studies of crystal morphologies and paragenetic relationships were performed on carbon-coated thin sections and on gold-coated rock chips mounted on stubs using a Phillips XL 40 scanning electron microscope (SEM) equipped with Thermo Nanotracer 30 mm<sup>2</sup> energy dispersive X-ray detector (EDS). The electron beam was generated by a tungsten filament operating at 17 kV and 50–60  $\mu$ A. The total abundance of clay rims were point counted, secondarily the detrital and authigenic clay rim abundances were adjusted according to the SEM observations. The mean grain size for each thin section is obtained by measurement of the long axis of minimum 100 grains intersecting three or more arbitrary straight lines. The grain size nomenclature is applied according to the Wentworth Class (Wentworth 1922). Sorting is estimated petrographically from sorting comparators by Longiaru (1987), which is based on the sorting classes of Folk (1966). The sorting classes are defined for eight relative phi classes that range from very well to poorly sorted. The phi values range from 0 for very well sorted sand to 2.0 for poorly–very poorly sorted sand. Modal compositions of the sandstones were obtained by point counting minimum 400 points, excluding the porosity, in each thin section. Classification of siliciclastic rocks is according to McBride (1968).

Mineral quantification by the Qemscan method is based on carbon coated polished blocks analysed by a scanning electron microscope (SEM) coupled with 2–4 energy dispersive X-ray spectrometers to rapidly image and chemically/mineralogically map samples. Qemscan uses the level of backscatter electron brightness to distinguish the sample from the impregnated epoxy, i.e. ‘background’, in the sample block. Therefore, at each stepping interval, a backscatter electron (BSE) brightness reading is taken and, if above a ‘background’ threshold, an X-ray spectrum is acquired. Conversely, if the BSE value is below the threshold, no X-ray spectrum is acquired. Each analysis point (or pixel in the mineralogical image) is made with a distance of 10  $\mu$ m and a measurement takes between approximately 1 and 4 ms. The resultant X-ray spectrum is compared with a table of known mineral compositions and chemical compositions. If a previously unclassified mineral phase is encountered during analysis, it is marked as ‘other’.

Clay mineralogy is verified on 44 samples by X-ray diffraction (XRD) of bulk rock samples and clay fraction in the sizes 2–0.2 and < 0.2  $\mu$ m. Bulk samples were crushed in a wolfram-carbide mortar, mounted with random orientation and scanned on a Bruker-AXS diffractometer D8 Advance with a primary beam Ge111 monochromated CuK $\alpha_1$  radiation and LynxEye silicon-strip detector. Quantification of major mineral phases was done by Rietveld analysis of X-ray diffractograms of bulk-rock samples. The sandstone samples were crushed manually and dispersed ultrasonically in distilled water. The fraction >30  $\mu$ m was removed by sedimentation and the 2–30  $\mu$ m by centrifugation in a centrifugal particle size analyser using the method described by Slater & Cohen (1962). The suspensions were flocculated in 1 M NaCl and following this excess salt was removed by centrifugation and washing with water and ethanol. Oriented specimens were prepared by pipette of the < 2  $\mu$ m clay fraction, which were either Mg-saturated, K-saturated, Mg-saturated and ethylene glycolated or K-saturated and heated for an hour at 300°C. The

clay specimens were analysed by a Phillips 1050 X-ray diffractometer with  $\beta$ -filtered Co-K $\alpha$  radiation. Criteria for identification of clay minerals are according to Hillier (2003).

Double polished thick sections (~ 100  $\mu$ m) were prepared from five sandstones while ensuring that the temperature was kept below 50°C. The double polished thick sections were studied petrographically in order to characterize the inclusions as primary, or in overgrowths and fracture healings. The fluid inclusions were studied on a Linkam THMSG 600 heating/cooling stage.

Plug porosity and permeability is measured according to the API RP-40 standard (API 1998). Gas permeability was measured at a confining pressure ~ 2.8 MPa (400 psi), and at a mean N<sub>2</sub> gas pressure of ~ 1.5 bar (bar absolute) = 0.15 MPa (permeabilities below 0.05 mD were not measured or measured using a bubble flowmeter). He-porosity was measured at unconfined conditions. The measured effective porosity corresponds to the total porosity, as most reservoir rocks contain only few isolated pores (API 1998). Thin sections were made from the plug trims and cut offs; for which reason the porosity and permeability can be directly correlated to petrographic observations.

Geochemical analyses comprises 'old' data were major elements were determined by XRF (X-ray Fluorescence), trace elements by ICP-MS (inductively coupled plasma - mass spectrometry) and Na<sub>2</sub>O and Cu by atomic absorption spectrometry (AAS) (see Weibel et al. 2010). Additional new analysis of major oxides and several minor elements were analysed by ICP-OES (inductively coupled plasma-optical emission spectrometry); and rare earth and refractory elements were determined by ICP-MS (inductively coupled plasma-mass spectrometry). Both methods applied 0.2 g sample fused by Lithium metaborate/tetraborate and digested in dilute nitric acid. In addition a separate 0.5 g aliquot digested in Aqua Regia (mixture of nitric acid and hydrochloric acid) was analysed by ICP-MS to report the precious and base metals (Au, Ag, As, Bi, Cd, Cu, Hg, Mo, Ni, Pb, Sb, Se, Ti, Zn). Generally, ICP-MS can determine concentrations that are 1 to 2 orders of magnitude lower compared to ICP-OES. Detection limits were 0.01 % for all major elements; with exception of 0.04% for Fe. Detection limits were less than 1 ppm for trace elements including most REE (rare earth elements). The exception were Ba (5 ppm), Co (20 ppm), Nb (5 ppm), Ni (20 ppm), Sr (3 ppm), V (8 ppm), Y (2 ppm), Zn (5 ppm), Zr (5 ppm) and Ce (30 ppm). Total S and C were analysed by LECO with detection limits of 0.01 % and 0.02 %, respectively. Loss on ignition (LOI) was given as weight difference after ignition at 1000°C.

## **Results**

### **Detrital composition of the Heno Formation**

#### **Gert Member**

All sandstones in the studied cores are dominated by quartz and subordinate feldspar, and hence quartzarenites or subarkoses according to the classification of McBride (1968). Monocrystalline quartz dominates most samples, though rare coarse-grained samples may have abundant polycrystalline quartz (e.g. the Rita-1 well). The dominating feldspar type varies between wells, e.g. K-feldspar dominates in the Hejre-2 and Ophelia-1 wells, whereas plagioclase dominates the feldspar assemblage in the Rita-1, Gert-1 and Gert-4 wells (Figs 4 and 5). Alteration of feldspar grains are common and may vary from intensively (e.g. Rita-1, Gert-4) to partially altered (e.g. Gert-1, Hejre-2) (Fig. 6). The K-feldspar abundance may increase from top of the Hejre-2 core and downwards and albite is not present in the uppermost part of the core (Fig. 5).

Muscovite, biotite and chlorite are rare. Rock fragments are typically rare, but common in only the Bertel-1 core. Metamorphic rock fragments are present in most of the sandstones, whereas volcanic rock fragments are less common, except for the Hejre-2 well. Glauconite only occurs occasionally in some wells (e.g. Diamant-1, Rita-1). Chert is typically rare and only occurs in few wells (e.g. Rita-1 and Gert-1). Shell fragments may be common in specific intervals in several wells. Organic matter is of rare or minor abundance. Accessory minerals comprise rutile, Fe-Ti oxides altered to leucoxene, zircon, tourmaline, chromite and rarely apatite.

Detrital smectitic/chloritic clays occur in the back-barrier sandstones of the Gert Member in the Diamant-1 and the estuarine brackish influenced facies of the Rita-1 well. In the lower shoreface deposits of the Hejre-2 well detrital chloritic clays occur as tangential coatings on the detrital grains.

#### **Ravn Member**

Monocrystalline quartz dominates most sandstones of the Ravn Member. Bimodal grain size distribution is common for the Ravn Member and polycrystalline quartz is common as oversize clasts (e.g. Rita-1, Gwen-2, Jeppe-1) and occasionally dominates coarse-grained samples (e.g. Bertel-1). The feldspar content varies between wells (Figs. 4 and 5); some wells are dominated by K-feldspar (e.g. Ravn-2, Ophelia-1), whereas some has equally abundant K-feldspar and plagioclase (e.g. Gwen-2, Jeppe-1) or are even dominated by plagioclase due to later albitization during burial diagenesis (e.g. Ravn-1, Gert-4). In general, albite is more common in the Ravn Member than in the Gert Member. Feldspar content vary within some cores, as the K-feldspar abundance may increase from sequence boundary Kimm-3 and downwards (e.g. Ophelia-1) and the plagioclase content increases from sequence boundary Kimm-3 and downwards (e.g. Gwen-2) (Fig. 5).

Muscovite, biotite and chlorite are rare. Metamorphic rock fragments are present in some samples (e.g. Gwen-2, Jeppe-1), whereas volcanic rock fragments are even more rare (only observed in the Jeppe-1 and Ravn-1 core samples). Glauconite, chert and mud clasts occur sporadically. Glauconite is mainly

present in the very fine to fine-grained sandstones (e.g. Eg-1, Gert-4, Ophelia-1). The degree of illitization of glauconite is most intense immediately below the sequence boundary Kimm-3 and lessens downwards, as the sediments become more fine-grained (e.g. Ophelia-1). Early calcite cemented samples show no illitization of glauconite. Recycled sedimentary quartz grains enclosing kaolinite (Bertel-1) or rounded overgrowths enclosing red dust rims (Diamant-1) occur in some wells. Detrital carbonate clasts (both dolomite crystals and micritic calcite) are common in the westernmost part of the Ravn Member in the Danish Central Graben (e.g. Rita-1, Gert-2, Gert-4, Ravn-1, Ravn-2), but not in the easternmost wells (e.g. Ophelia-1, Jeppe-1, Gwen-2), which on the other hand contain shell fragments. Shell fragments are, in general, less common in the Ravn Member compared to the Gert Member. Biogenic apatite occurs occasionally in the Ravn Member. Organic matter occurs in most wells, but only in small amounts. Heavy minerals are in general rare, and may include zircon, tourmaline, rutile, apatite and altered Fe-Ti oxides. Apatite is generally more common in the Ravn Member than in the Gert Member. Chromite is only very rarely recognised in the Ravn Member (e.g. Jeppe-1).

Detrital clays are possibly originally of smectitic or chloritic composition and have been illitized during burial. Detrital clays vary in abundance from rare in the upper and middle shoreface sandstones and up to abundant in the lower shoreface sandstones (e.g. Gwen-2, Eg-1, Rita-1, Gert-4). Brownish staining, probably due to hydrocarbon, of the detrital clays is typical in some wells (e.g. Ophelia-1).

- Figure 4: Mineralogical distribution on palaeogeographical maps
- Figure 5: K-feldspar and albite distribution through cores from the Heno Formation and characteristic illite morphology
- Figure 6: Petrography – alteration of feldspar grains

## **Diagenesis of the Heno Formation**

### **Gert Member**

Pyrite precipitates very early as framboids followed by octahedral or euhedral pyrite. Although pyrite is ubiquitous, it is typically of low abundance (rare). Occasionally, octahedral pyrite is enclosed in later concretionary cement of minor abundance. Pyrite commonly occurs inside organic matter.

Very early authigenic chlorite pore-filling cement is restricted to sandstones adjacent to the underlying lava or volcanoclastic rocks in the Hejre Field. Zeolite cement is considered a likely early cement in the Hejre Field, which may have stabilized the framework during mechanical compaction until it became unstable at increased burial temperatures (Weibel et al. 2019). The sandstones from the Hejre Field also distinguish themselves from other Gert Member sandstones by having K-feldspar single crystals and K-feldspar overgrowths occur on all detrital K-feldspar grain and most albite grains. K-feldspar overgrowths are not identified in the Gert Member from the Diamant-1, Gert-1, Gert-2, Gert-4 and Rita-1 wells.

Calcite cement occurs as early and late pokilotopic or sparry concretionary cement and as a late patchy cement. The patchy cement is rare to minor in abundance and the concretionary cement is abundant. Albite remnants, possibly after a previous plagioclase grain, are enclosed in some patchy calcite cement. No relationships between sequence boundaries and concretionary calcite could be established. Several episodes of calcite precipitation are documented from variation in oxygen isotope composition in the Hejre area (Weibel et al. 2019).

Dissolved feldspar grains are present in all samples of rare to minor abundance. Dissolution seems to be more intensive of albite grains than of K-feldspar grains. Kaolinite typically occurs as rare scattered booklets in primary pores and oversize (secondary) pores, which could origin from dissolved feldspar grains. Kaolinite has only sporadically formed in association with altered mica. Occasionally kaolinite appears weakly illitized. Kaolinite seems to have its highest abundance below the Kimm-3 sequence boundary in the Diamant-1 and Rita-1 wells. Kaolinite is not observed in the Hejre Field.

Illitization of detrital clay coatings is common and some of these are honeycomb textured. Illitic fibres grow from the clay coatings in several samples (Fig. 7A, C). Condensed illite (i.e. not fibrous) growing around secondary porosity after dissolved K-feldspar or rock fragments characterizes samples of high permeability in the Gert-1 well (Fig. 7B). Hexagonal illite is typical in samples from the Hejre-2 well (Fig. 7E, F).

Anatase is a rare authigenic phase present in many samples, where it occurs as single crystals occasionally enclosing kaolinite booklets.

Albite overgrowths occur as rare overgrowths on detrital albite or remnants of albite in secondary pores (Fig. 6A). The relative timing of albite precipitation varies in different wells and occurs both prior to and post quartz precipitation. Authigenic quartz occurs as overgrowths in amounts varying from minor to common. Especially, samples from the Gert-1 well are characterized by relatively high amounts of authigenic quartz. The lowest abundance of quartz cement appears in early calcite cemented samples, samples of relatively high clay abundance and samples with stylolites.

## **Ravn Member**

Spherulitic calcite occurs in some early calcite cemented samples in the Ophelia-1 well. It is probably formed very early as it is enclosed in early calcite cement, but a detrital origin is another possibility.

Apatite occurs as rare pore lining cement in few samples from the Jeppe-1 well. Pyrite occurs with framboidal and octahedral morphologies and is typically rare in abundance, though present in all samples. Occasionally, pyrite is associated with organic matter.

Microquartz coatings occur in many samples, especially in the coarsest sandstones, i.e. the most proximal settings (e.g. Gwen-2, Diamant-1 wells). Microquartz varies in abundance from minor to common (Fig. 8). Thin microquartz coatings characterize samples of high porosity, whereas samples of excessive microquartz as both pore lining and pore filling cement have lower porosity. Mouldic porosity after sponge spicules is recognized in one sample (Fig. 8A, B). Occasionally rare zeolite occurs in the

mouldic secondary porosity together with microquartz (e.g. Rita-1 well). Zeolite seems to predate the microquartz coatings (Fig. 8B).

Several episodes of carbonate precipitation occur in the Ravn Member. Fe-rich dolomite and ankerite cement occurs as overgrowths on detrital carbonate clasts and is only present in the Ravn Member, not in the Gert Member (Fig. 8E). Ankerite overgrowths are minor to common in abundance and occur on all detrital dolomite clasts (e.g. the Rita-1, Gert-2, Ravn-1, Ravn-2 wells). Ankerite overgrowths are very early in the Rita-1 well, where they enclose microquartz. Ankerite also occurs as micritic or sparry cement and occasionally as replacement of plagioclase.

Early poikilotopic concretionary calcite cement is minor to abundant in few samples (e.g. the Gwen-2 well). This type of samples show “floating” grains indicating that the cementation happened prior to compaction of the sandstone. Oversized calcite-filled pores indicate that the calcite cement has replaced detrital grains (probably feldspar and rock fragments). In the lower shoreface facies the calcite cement is sparry, not poikilotopic.

K-feldspar overgrowths are present in the easternmost wells and vary in abundance from rare (e.g. Gwen-2, Ophelia-1) to common (e.g. Jeppe-1). K-feldspar overgrowths may occur with up to three different zones in samples from the Jeppe-1 well. Alteration of K-feldspar overgrowths, which is either partly dissolution or illitization, is most intensive in the middle zone in case of three zones, in the innermost zone in case of two zones or of the entire overgrowth in case of only one zone.

Feldspar dissolution occurs in all samples but is generally of minor abundance. Secondary porosity, from dissolution of detrital feldspar and feldspar overgrowths, occurs also within calcite cemented areas of the samples, indicating that the secondary porosity formed after the calcite cement. In tightly calcite cemented samples the secondary porosity forms the only porosity within the samples. The degree of feldspar dissolution varies within the cored intervals. Plagioclase dissolution is minor to common in the uppermost part of the Gwen-2 core, whereas the lowermost part of the core has a late phase (after quartz overgrowths and calcite cement) of dissolution of K-feldspar overgrowths. In one sample secondary porosity in particular after feldspar dissolution actually makes up the major part of the porosity.

Kaolinite is of rare (e.g. the Rita-1 well) to minor abundance (e.g. the Diamant-1 well). Kaolinite is filling primary and secondary pores or replacing altered feldspar grains (Fig. 6B). Kaolinite is rare in the Ravn Member compared to the Gert Member.

Anatase is a rare, but ubiquitous authigenic phase which typically occurs as single crystals and only rarely as overgrowths.

Illitization of detrital, probably smectitic, clays results in honeycomb textured coatings. Illitization of glauconite occurs in some wells (e.g. the Ophelia-1 well). Illite appears as protruding fibres from clay rims into open pore spaces. Illitic coatings occur enclosed in quartz overgrowths. Hexagonal illite dominates the lower part of the Ophelia-1 core, whereas fibrous illite is dominant in the uppermost part.

Quartz overgrowths occur in most samples, though with rare occurrences in samples dominated by microquartz cement. Quartz overgrowths are generally of minor abundance. Sutured grain and incipient

stylolites are observed. A peculiar habitus of quartz overgrowths has been observed in some places where it forms elegant quartz overgrowths (with calcite inclusions) into shell fragments replacing the carbonate of the shell fragment (e.g. Gwen-2).

Albite overgrowths occur on detrital albite, though they are only of rare abundance. Rare authigenic albite probably precipitated on remnants of partly dissolved feldspar grains.

Late calcite cement, micritic and sparry, is abundant in some wells (e.g. Jeppe-1, Ravn-1), where it seems to enclose both K-feldspar overgrowths and peculiar quartz overgrowths. Early calcite cement may have stabilized the mesh of framework grains leaving open porosity for quartz cementation. This is then followed by complete calcite cementation and partly calcite replacement of authigenic quartz. Another scenario could be growth of quartz between the calcite crystals or simultaneously growth of calcite and quartz during recrystallization. More detailed isotopic analysis of both authigenic quartz and calcite will hopefully result in a more clear understanding of the peculiar quartz-calcite growth mechanisms. A late episode of calcite dissolution is identified in few wells (e.g. Diamant-1, Ophelia-1).

Mg-rich chlorite occurs as a late pore-filling and fracture-filling phase of minor abundance in the Eg-1 core. Commonly, Mg-rich chlorite fills large pores, which may be secondary porosity after unstable rock fragments or heavy minerals.

Rare barite cement encloses quartz overgrowths. Occasionally, barite cement may be abundant (Weibel et al. 2018). Sulphides, as galena and shpalerite, occasionally accompany barite cement (e.g. Ophelia-1). Anhydrite is rare as fillings in thin fractures. Whether anhydrite is prior to or after barite is not certain.

- Figure 7: Petrography – microquartz
- Figure 8: Petrography – illite morphology
- Figure 9: Petrography – quartz cement

## **Clay mineralogy**

The clay mineral composition has been verified by X-ray diffraction of clay fraction of 2 – 0.2 and < 0.2 µm of samples. Illite is the dominant clay mineral in all investigated sandstones. Illite with hexagonal morphology has a narrow 10 Å peak similar to that of fibrous illite (Fig. 10). The ‘cauliflower’ illite has a broader 10 Å peak (Fig. 10). Kaolinite is documented from the back-barrier sandstones in the Gert area. Chlorite occurs in sandstones in the south-western part of the basin (the Eg-1, Ravn-1??, Ophelia-1?? wells) and in sandstones directly overlying Rotliegendes volcanoclastic deposits (the Hejre-2 and Diamant-1 wells).

- Figure 10: Clay mineralogy

## **Geochemistry**

The geographical mineralogical variations are supported by a larger geochemical dataset. The Heno Formation sandstones have a relatively high Na/Al ratio in the northern and western part of the basin and a relatively high K/Al ratio in the Hejre-2, Ophelia-1, Ravn-2 cores (Fig. 11). A high Na/Al content characterizes the Farsund Formation sandstones close to the Ringkøbing – Fyn High (the NW Adda-1, Deep Adda-1, Iris-1, Tabita-1 wells), whereas an intermediate Na/Al vs. K/Al ratio is typical of the Farsund Formation sandstones close to the Mid North Sea High (the Saxa-1, Wessel-1 wells). A high MgO/CaO ratio, consistent with the dolomite trend, characterizes sandstones from the western part of the basin, whereas a very low MgO/CaO ratio is more common in the eastern part (Fig. 11).

- Figure 11: Geochemistry

## **Porosity and permeability**

Microquartz coatings characterize sandstones having the highest porosity and permeability (Fig. 12). Sandstones with microquartz coatings and illite present show relatively lower permeability at similar porosity. Quartz cement together with kaolinite or limited illitic clays and sandstones inferred to have had an early zeolite cement also have relatively high porosity and permeability. The zeolite cement precursor has been described from the shoreface sandstones in the Hejre-2 core (Weibel et al. 2019). Quartz cemented sandstones with varying amounts of illitic clays represent intermediate porosity and low permeability (Fig. 12). The lowest porosities and permeabilities occur in sandstones dominated by carbonate cement, barite cement and extensive mechanical compaction due to abundant ductile grains (Fig. 12).

Grains size seem to have little influence on the permeability in these samples (Fig. ??). However, depositional environment affects the porosity and permeability by defining the diagenetic path and hence the cementing phases.

- Figure 12: Porosity versus permeability

## Discussion

### Sediment supply

The K-feldspar and albite content show regional variations related to depositional environment, weathering and diagenetic alterations (Fig. 3). This variation is illustrated by the distribution in the Na/Al versus K/Al plot for Upper Jurassic sediments in the Danish Central Graben (Fig. 11). Although the Farsund Formation is stratigraphically younger, it has been included since the same basement source is considered to have been active earlier. The feldspar content could potentially have been altered given rise to kaolinite and hence samples likely to move towards the origin of the plot or status quo by alteration to illite. Sandstones of the Farsund Formation deposited in the westernmost part of the Danish Central Graben consists of a mixture of albite and K-feldspar that were probably sourced from the Mid North Sea High. Plagioclase is the dominant feldspar type in gravity flow sandstones forming local fan systems along the Coffee Soil Fault into the Tail End Graben (Nielsen et al. 2015). The crystalline basement of the Ringkøbing–Fyn High consists mainly of quartz, plagioclase and biotite, though with occasional presence of calcite-replaced K-feldspar (Olivarius et al. 2015). Plagioclase (giving rise to a high Na/Al ratio) is therefore expected to predominate over K-feldspar in sediments derived from the Ringkøbing–Fyn High basement rocks. Locally exposed fault block has been suggested as sources for the volcanic derived K-feldspar in the Gert Member sandstones from the Hejre area (Weibel et al. 2019). These differences in detrital feldspar distribution support previous chemical and heavy mineral investigations, which indicated that Ravn Member was sourced from the Mid North Sea High whereas Gert Member was influenced by more local sources including reworking of the underlying sedimentary successions (Weibel et al. 2010).

The distribution of carbonate clasts in the Ravn Member support that they were sourced from the west, possibly the Mid North Sea High where Zechstein sediments were exposed during the time of deposition. This is supported by a high Mg/Ca ratio in the Ravn Member in the westernmost wells (Ravn-1/-2, Rita-1, Gert-2/-4 in Fig. 1). Whereas fossil fragments occur in both the Gert and Ravn members, carbonate clasts only occur in the Ravn Member. The detrital origin of the carbonate clasts is evident from rounded dolomitic central areas surrounded by rhombohedral ankerite overgrowths, of which the latter may enclose microquartz crystals (Fig.8E). The contents of carbonate clasts is highest in wells in the western part of the Danish Central Graben, indicating that the source of carbonate clasts are located on or close to the Mid North Sea High. The dolomite clasts resemble dolomite described from Upper Jurassic sandstones in the UK Central Graben (Hendry et al. 2000). Dolomite is here considered formed by dolomitization of calcite clasts promoted by Mg from seawater entering the sulphate-reducing intervals of the sediment via bioturbation (Hendry et al. 2000). Dolomite clasts from the Danish Central Graben are typically more rounded and of a smaller average grain size than siliciclastic particles, contrary to the similar grain sizes in the UK Central Graben and the presence of irregular shaped dolomite. It is uncertain whether the dolomite clasts have formed under similar conditions or were recycled from a common sediment source, possibly on the Mid North Sea High, despite a distance of more than 200 km.

Besides fossil fragments Gert Member contains little marine-derived detritus, contrary to Ravn Member which has glauconite, biogenic apatite and occasionally sponge spicules though fewer calcite fossil fragments. The presence of sponge spicules are interpreted from mouldic (monaxon) impressions surrounded by microquartz coatings (Fig. 8A, B). Glauconite is mainly present together with detrital clays in the very fine to fine-grained sandstones (e.g. the Eg-1, Gert-4, Ophelia-1 wells) and hence in the most

fine-grained deposits. Detrital clay abundance highest in the lower and middle shoreface environment and therefore in the positions of Rita-1 well and Ravn-1/-3 wells. Microquartz coatings in Jurassic sandstones has previously been associated with sponge spicules of *Rhaxellid* (e.g. Vagle et al. 1994; Hendry and Trewin 1995; Nielsen et al. 2019) may possibly be used as a proxy for sponge spicules. Some intensively microquartz-cemented sandstones are coalescent with intervals of abundant oversized quartzite clasts occurring at or close to sequence boundaries in the Ravn Member. So the most optimum reservoir sandstones occur were the sediment load from the rivers interacted with sediments from the outer shoreface environment perhaps during transgressions.

Oversized quartzite clasts were probably sourced from the Mid North Sea High and transported by rivers across the flood plain, where local incised valleys formed. Contrary, the sponge spicules must have been sourced from the middle – lower shoreface or offshore environment (Rigby 1987). Sponges grow on sub-sea mounts or platforms, though certain siliceous sponge genera with stalks may grow on muddy or soft substratum (e.g. Rigby 1987; Leinfelder et al. 1996; Abbink et al. 2006). The sponges form reefs similar to corals, though typically at deeper water-depth than corals (e.g. Rigby 1987; Leinfelder et al. 1996; Abbink et al. 2006). The abundance of siliceous sponge reefs vary through geological time with the Late Jurassic representing one of the unique periods of blooming siliceous sponges (e.g. Leinfelder et al. 1996; Kiessling et al. 1999). Other investigations suggest that, besides stratigraphically constrained to Late Jurassic: Oxfordian – Tithonian time, the wave energy level confined the siliceous sponges geographically to specific basins and hence defined the distribution of microquartz cement (Maast et al. 2011). Sponge spicules, pseudomorphed by chalcedony, occur in Volgian - Ryazanian gravity flow deposits in the Tail End Graben (the Iris-1, Tabita-1, NW Adda-1, Deep Adda-1 and Ugle-1 wells), though are not found in the Upper Kimmeridgian gravity flows from the Søgne Basin (the Lulu-2 well) (Nielsen et al. 2015). Consequently, there also seem to be a geographically constrain on the distribution of siliceous sponge spicules in the Danish Central Graben.

## **Intensive weathering**

The back-barrier sandstones of the Gert Member are all characterized by intensive feldspar dissolution and kaolinite precipitation (the Rita-1, Gert-1, -2, -4 and Diamant-1 wells in Fig. 5). Meteoric water, possibly slightly acidic due to common organic matter, flushed through the back-barrier sediments. Feldspar alteration was intensive in this environment (e.g. Bjørlykke 1984; Glasmann et al. 1989; Bjørlykke et al. 1992; Khanna et al. 1997). Most feldspar grains have been dissolved and their mouldic porosity is surrounded by illitic clay coatings and kaolinite has precipitated in adjacent pore spaces or replaced the grain (Fig. 6). A completely different situation existed in the shoreface sandstones in the Hejre area. The marine formation water was less aggressive towards K-feldspar due to influence from underlying ultrapotassic volcanic rocks and volcanic rock fragments in the sandstone in addition to having more abundant initial K-feldspar content (Weibel et al. 2019).

The back-barrier deposits were flooded by marine water and overlain by shoreface and offshore deposits (Johannessen 2003, Johannessen et al. 2010). During the following regression sand deposits of the Ravn Member built out on the Heno Plateau from the Mid North Sea High and eventually a flood plain was formed on the Heno Plateau. Large clasts were transported with rivers, which locally formed incised valleys. Weathering of the shoreface deposits took place on this flood plain, the most intensive weathering occurring at the location of the Diamant-1 well on the centre of the flood plain, where almost all feldspar

grains are dissolved. Weathering profiles from top of cores and downwards can be recognised in the Jeppe-1, Gwen-2, Ophelia-1 and Hejre-2 wells (Fig. 5). Albite alters more intensively than K-feldspar (Jeppe-1 core), however also K-feldspar is affected (Ophelia-1 and Hejre-2 cores). Precipitation of authigenic albite on remnants of dissolved feldspar grains explains the predominance of albite over K-feldspar in intensively altered sandstones (Rita-1, Gert-1/-4; Fig. 6A). Weathering profiles with gradually increasing K-feldspar content in the Ophelia-1 core and increasing albite and K-feldspar contents in the Jeppe-1 core show that the degree of alteration was less intensive the further away from the Mid North Sea High and more into the marine environment (Fig. 5).

## **Microquartz**

Abundant microquartz coatings occur in shoreface sandstones of the Ravn Member. The mouldic porosity after monaxon (ellipsoid) sponge spicules surrounded by excessive microquartz cement in the Rita-1 core document, that microquartz was sourced by siliceous sponge spicules (Fig. 8A, B). Dissolution of biogenic silica, especially siliceous sponge spicules (*Rhaxellid perforate* of the Demospongia group), has previously been suggested as silica sources for microquartz coatings (e.g. Haslett 1992; Vagle et al., 1994; Hendry and Trewin 1995; Aase et al. 1996; Abbink et al. 2006; Maast et al. 2011). Opal-A of sponge spicules is transformed into opal-CT during early diagenesis in the temperature interval of 20–50°C (e.g. Hesse 1990; Huggett et al. 2005). Microquartz typically becomes the dominant silica phase in sediments buried deeper than 2.5 km (e.g. Hendry and Trewin 1995; Stokkendal et al. 2009; Weibel et al. 2010). The effect of temperature may be to speed up reaction rates, since the opal-A via opal-CT to quartz reaction will take place over time in order to reach the thermodynamic least energy demanding stage (Williams et al. 1985).

Microquartz coatings of ordered crystals are controlled by the crystallography of the substratum i.e. the detrital quartz grain. Continued growth of microquartz crystals may increase the likelihood for small crystallographic dislocations, which results in slight crystallographic offset in respect to the underlying quartz (compare Haddad et al. 2006). The cryptocrystalline coatings beneath the microquartz coatings must have formed under an initial very high silica supply followed by a continued high silica supply during microquartz precipitation (compare Williams et al. 1985). Ordered microquartz may eventually (during burial) merge into larger crystals - macroquartz overgrowths, whereas randomly orientated microquartz crystals inhibit focused growth and may preserved porosity and permeability (Weibel et al. 2010). The porosity- and permeability-preserving effect of microquartz coatings is enhanced or supported by emplacement of hydrocarbons and/or generation of overpressure (e.g. Bloch et al. 2002; Nguyen et al. 2013).

Microquartz crystals are recognized on some detrital quartz grains in sandstones from the Gert-1/-2 and Hejre-2 cores. One possible explanation to this scattered occurrence of microquartz crystals could be explained by overgrowth on a polycrystalline quartz grain, since quartz overgrowths tend to grow slower at the prismatic surfaces (Lander et al. 2008). Another explanation could be late exposure of the grain surfaces due to thermodynamic degradation of an earlier cement, for example opal-CT or zeolite (e.g. Hendry and Trewin 1995; Weibel et al. 2010; 2019).

## **K-feldspar**

K-feldspar overgrowths occur in all sandstones having common K-feldspar grains. K-feldspar overgrowths are not present in sandstones exposed to intensive weathering (i.e. Diamant-1, Gert-1,-2, Rita-1). This shows the importance of parent grains in order to reduce the activation energy by nucleation (see Ajdukiewicz and Larese 2012) or it suggests the possibility of an internal source for example by preferential dissolution of K-feldspar having a low Na content followed by precipitation as pure K-feldspar overgrowths on detrital K-feldspar.

Two zones of K-feldspar overgrowths can be recognized in the Jeppe-1 core, whereas they may have been replaced by clay in the Gwen-2 core. In the Hejre Field, authigenic K-feldspar formed overgrowths on detrital albite and numerous tiny discrete crystals, besides two zones of overgrowths on detrital K-feldspar (Weibel et al. 2019). A different diagenetic route is considered for the Hejre Field, since here the Gert Member overlies volcanic rocks and volcanic rock fragments are incorporated in the sandstones. Hence, an early K-rich zeolite cement has inhibited mechanical compaction, and under thermal degradation of K-rich zeolite, the formation water became supersaturated with potassium and K-feldspar precipitated as numerous tiny crystals (Weibel et al. 2019). The double zones of K-feldspar overgrowths in the Jeppe-1 and Hejre-2 cores may be related to higher potassium content in the formation water possibly due to the underlying volcanoclastic sediments.

## **Burial diagenesis**

### **Illite morphology**

Authigenic illite occurs in the Heno Formation with varying morphologies from fibres growing on honeycomb textured coatings, hexagonal crystals and 'cauliflower'-like coatings in addition to replacement of detrital grains (in particular glauconite).

The honeycomb textured illitic coatings are associated with clay-rich sandstones (back-barrier or lower- and middle shoreface) and indicate the presence of former smectitic detrital clays. The clay coatings may have been deposited together with the sand or formed by infiltration of suspended clay-size particles into the recently deposited sand during one of the transgressions. The transformation of a smectitic precursor through mixed-layer illite/smectite clay minerals into illite is documented by the honeycomb textured coatings and the skewness of the 10Å peak (Figs 7, 10; Pollastro 1985). Fibrous illite grows from the honeycomb textured coatings and may severely reduce permeability. Fibrous illite is recognized in the Heno Formation even though the samples have not been critical-point-dried as recommended by Huggett (1982), Kantorowicz 1989). It should be noted that collapsed illite could result in air permeability 2-7 times greater than brine permeability of preserved cores (Grigsby et al. 1992).

Illitization of kaolinite is restricted to sandstones with abundant kaolinite and survival of some K-feldspar grains until deep burial diagenesis (Fig. 7C). When smectitic clays and kaolinite occur together, the smectitic coatings are more prone to be illitized than kaolinite (e.g. the Rita-1 core). No illitization of kaolinite has been recognised in the Diamant-1 core, which completely lack feldspar grains due to intensive weathering. The burial depth of the Heno Formation is here >3800 m corresponding to a temperature of >125°C, hence deeper than the typical onset of illite precipitation (e.g. Fisher & Land 1986;

Bjørkum and Gjelsvik 1988; Ehrenberg and Nadeau 1989; Hamilton et al. 1992; Størvoll et al. 2002). Incipient illitization of kaolinite occurs in sandstones of >4900 m burial depth from the Gert-1 core, where only limited amounts of K-feldspar is present. This corresponds to a temperature of 160°C and hence is way beyond the temperature for maximum illitization. Illitization of kaolinite have previously been suggested to be retarded if K-feldspar is lacking (Wilkinson et al 2006). Likewise, a higher degree of illitization of kaolinite in the Haltenbanken area than in the north Viking Graben is inferred to be caused by a higher abundance of K-feldspar (Chuhan et al. 2000). Kinetic modelling of fibrous illite growth in sandstones where kaolinite is a primary reactant and potassium is derived from K-feldspar dissolution show a strong relation to thermal history and not solely to the maximum burial temperature (Lander and Bonnell 2010). Hence, they concluded that illitization cannot be expected to be a universal function of temperature above 120-140°C as suggested by Ehrenberg and Nadeau (1989) and Bjørlykke et al. (1998).

Hexagonal illite is restricted to the lower parts of the Hejre-2 and Ophelia-1 cores characterized by high K-feldspar contents. Hexagonal illite may grow directly from altered K-feldspar surfaces, though most crystals form on previous tangential clay coatings or as discrete crystals in the pore space (Fig. 7E, F). Hexagonal illite has been described as the end-member morphology as illite/smectite laths changes to more illitic laths and finally hexagonal illite-mica with increased time and temperature (Lanson and Champion 1991). Although, a smectitic precursor may be advocated for the sandstones in the Ophelia-1 core, this is not the case for the sandstones in the Hejre-2 core. Alternatively, the illite morphology has been suggested to be controlled by the potassium saturation in the formation water (Kuwahara *et al.* 2001; Meunier and Velde 2004). Low temperature experiments show that hexagonal crystals form at high growth rates (due to high oversaturation), whereas lower growth rate due to lower saturation of dissolved species results in lath-shaped crystals (Bauer et al. 2000). A high oversaturation may have formed due to instability of K-feldspar at increased burial, which is documented by partial dissolution of K-feldspar overgrowths and discrete crystals.

Illite precipitation is promoted by supply of potassium from dissolution of K-feldspar or from external sources. K-feldspar is stable at shallow burial, hence K-feldspar overgrowths occurs on most detrital K-feldspar grains. K-feldspar becomes unstable at increased temperatures. In sandstones lacking K-feldspar, either due to intensive alteration immediately after deposition in the back-barrier environment or by weathering on the flood plain, the illite precipitation is retarded due to lack of potassium unless it is imported. Illitization as a result of potassium sourced from adjacent shales (Burley et al. 1985) or from migrating fluids is possible, though less likely. The surrounding mudstones, the Lola and Farsund formations, have low  $K_2O/Al_2O_3$  ratio similar to sandstones of low K-feldspar content (Weibel et al. 2010). The exception though is the HA-2 well, which have a high content of K-feldspar and K-rich volcanic rock fragments in the overlying mudstones (Weibel et al. 2019).

Dense illitic 'cauliflower'-like coatings have an occurrence mainly limited to the uppermost part of the Gert-1 core. Contrary to the usual fibrous growth, this atypical restricted growth of illite occurs typically around dissolved feldspar grains. Several possible explanations have been considered: 1) An artefact because the delicate illite morphology was damaged after the core was taken, as these samples were not critical-point-dried, 2) illite replacement of K-feldspar overgrowths on detrital plagioclase as described by Ehrenberg and Boassen (1993), 3) early pedogenetic clay drapings or 4) localised growth in capillary water after hydrocarbon filling of the reservoir. None of the cores taken in the Heno Formation have been treated specifically in order to preserve the illitic clays, hence the fibrous illite could have been damaged. However, this ought to be a problem for all cores. Pedogenetic infiltrated clays would form drapes around

all types of detrital grains (Mora et al 1998), not merely the feldspar grains. Therefore this process seems less likely. The mechanism for the restricted illite growth would be similar to that described for dense chlorite forming in the capillary water rim around detrital grains contrary to fully developed radiating chlorite in the water filled parts (Stokkendal et al. 2009; Friis et al. 2014). Hydrocarbons in a partly oil-wet reservoir may preferentially have remained around oil-wet minerals first of all feldspar and feldspatic rock fragments, which have proven to be more oil-wet than quartz in the Garn Formation from the Haltenbanken area (Storvoll et al. 2002; Ehrenberg et al. 1995). Therefore the 'cauliflower' illite may preferentially have precipitated around former feldspar grains.

### **Quartz cementation**

Quartz overgrowth seems to be retarded by the presence of microquartz coatings and clay coatings. Ubiquitous microquartz coatings in the sandstones of the Diamant-1 and Gwen-2 cores have inhibited or retarded further quartz cementation. Hence, high porosity and permeability characterize the sandstones from the Diamant-1 well, though slightly reduced permeability in the Gwen-2 well due to more common fibrous illite. The burial temperatures in these wells of 125 and 150°C are higher than the typical temperatures (90–100°C) for intensive quartz cementation in the North Sea Basin (e.g. Burley et al. 1989; McBride 1989; Walderhaug 1990; Giles et al. 1992). Illite coatings of detrital and authigenic origin retard quartz overgrowth and promotes smaller quartz outgrowths in the Heno Formation. Contrary to the findings by Chuhan et al (2001), the illite coatings in the Heno Formation do not seem to preserve porosity and permeability, which is probably due to the typically fibrous morphology of illite.

Quartz cementation seems to continue after hydrocarbon introduction in the Hejre-2, Ophelia-1 and Gert-1 wells. This is documented by hydrocarbon-stained kaolinities enclosed in quartz overgrowths in the Gert-1 and Ophelia-1 wells (Fig. 9A). Occasional brownish staining of clays enclosed in quartz overgrowths occurs in the Hejre-2 well, but the major part of the staining is due to bitumen precipitated after quartz overgrowths. The hydrocarbon migration is later in the Rita-1 well, where kaolinite, enclosed in quartz overgrowths, show no brownish staining (Fig. 9B).

## **Conclusion**

The Upper Jurassic Heno Formation in the Danish Central Graben has the optimum settings for investigating the distribution and morphology of illite and its influence on reservoir properties. The initial feldspar type, content besides degree of weathering has strong controls on the succeeding burial diagenesis, including illite precipitation.

Intensive alteration of feldspar results in early kaolinite precipitation immediately after deposition in the back-barrier environment. In a similar way, feldspar grains are altered in shoreface deposits, most intensively in areas subaerially exposed for longer periods. Weathering profiles with downwards decreasing albite and K-feldspar contents are recognised in several wells, where the less stable albite is removed first followed by K-feldspar. This weathering leaves behind clay rims around secondary porosity and kaolinite in the pore spaces. During burial, degradation of detrital K-feldspar supplies potassium for illite precipitation and illitization of kaolinite and smectitic clays. Illite precipitation preferentially occurs in sandstones where K-feldspar survive until deep burial. External potassium sources for example from the adjacent mudstones does not seem to have been active. Early intensive weathering of K-feldspar grains hence improve sandstone reservoir quality by retarding illite precipitation.

Illite precipitates in several morphologies: 1) fibrous, 2) hexagonal and 3) dense 'cauliflower'-like. Fibrous illite commonly grows from honeycomb textured coatings; the latter probably had a detrital smectitic precursor and occur in particular in clayey sandstones. Hexagonal illite is restricted to sandstones having a high K-feldspar content and occasionally grow directly from dissolved K-feldspar surfaces. A high supersaturation with potassium due to K-feldspar instability during increased burial may have promoted this morphology. Dense 'cauliflower'-like illite occurs in particular in the uppermost parts of the Gert-1 cores and is considered to represent clay mineral alteration of K-feldspar in the water rim around K-feldspar grains in a partly hydrocarbon saturated reservoir.

Distribution of other detrital components, like siliceous sponge spicules, also influence in the burial diagenesis. Sponge spicules are in particular deposited in the transgressive systems tract. During burial the opal-A in siliceous sponge spicules becomes unstable and promote microquartz precipitation. Microquartz coatings preserve reservoir porosity and permeability by retarding the otherwise with burial succeeding quartz overgrowths. However, when fibrous illite precipitate the permeability-preserving effect of microquartz is reduced or destroyed depending on abundance.

This study documents a strong palaeogeographical control on the reservoir quality, not merely the distribution of sand deposits, but equally important the intensity of weathering. Hence, the detailed correlation between palaeogeography and reservoir properties (both geometrically and diagenetically) can help predict the optimum location of new potential reservoir sandstones.

## **Acknowledgement**

Thanks to our colleagues at GEUS, who contributed with background information and special thank to Palle Rubæk Andersen, who initiated the diagenesis study in the Danish Central Graben. Thanks to Jette Halskov and Susanne Rømer for preparing the drawings.

## **References**

API. 1998. API RP 40, Recommended practice for core analysis, second edition, American Petroleum Institute, Washington DC.

Bauer, A., Velde, B, Gaupp, R. 2000. Experimental constraints on illite crystal morphology. *Clay Minerals* 35, 587 – 597.

Bjørkum, P.A., Gjelsvik, N. 1988. An Isochemical Model for Formation of Authigenic Kaolinite, K-Feldspar and Illite in Sediments. *Journal of Sedimentary Research* 58, 506–511.

Bjørlykke, K. 1984. Formation of secondary porosity: How important is it? In: McDonald, D. A., Surdam, R. C. (Eds.) *Clastic diagenesis*. American Association of Petroleum Geologists Memoir 37, 277–286.

Bjørlykke, K., 1998. Clay mineral diagenesis in sedimentary basins - a key to the prediction of rock properties. Examples from the North Sea Basin. *Clay Minerals* 33, 15–34.

Bjørlykke, K., Aagaard, P. 1992. Clay minerals in North Sea sandstones. In: Houseknecht, D. W., Pittman, E. D. (Eds.), *Origin, diagenesis and petrophysics of clay minerals in sandstones*, SEPM Special Publication 47, 243 – 268.

Bjørlykke, K., Egeberg, P. K., 1992. Quartz cementation in sedimentary basins, American Association of Petroleum Geologists Bulletin 77, 1538–1548.

Bjørlykke, K., Nedkvitne, T., Ramm, M., Saigal, G.C. 1992. Diagenetic processes in the Brent Group (Middle Jurassic) reservoirs of the North Sea: an overview. In: (Morton, A.C., Hazseline, R.S., Giles, M.R., Brown, S. (Eds.) *Geology of the Brent Group*. Geological Society Special Publication 61, 263 – 287.

Bjørlykke, K., Aagaard, P., Dypvik, H., Hastings, D.S., Harper, A.S., 1986. Diagenesis and reservoir properties of Jurassic sandstones from the Haltenbanken area, offshore mid Norway. In: Spencer, A.M., Holter, E., Campell, C.J., Hanslien, S.H., Nelson, P.H.H., Nysaether, E., Ormaasen, E.G. (Eds.), *Habitat of Hydrocarbons on the Norwegian Continental Shelf*. Graham and Trotman, London, 275– 286.

- Burley, S.D., Kantorowicz, J.D. and Waugh, B. (1985) *Clastic diagenesis*. Geol. Soc. London. Spec. Publ., 18, 189–226.
- Dunham, R.J. (1962). "Classification of carbonate rocks according to depositional texture". In: Ham, W.E. (Ed.) *Classification of carbonate rocks*. American Association of Petroleum Geologists Memoir 1, 108-121.
- Fisher, R.S., Land, L.S. 1986. Diagenetic history of Eocene Wilcox sandstones, South-Central Texas. *Geochimica et Cosmochimica Acta* 50, 551–561.
- Folk, R. L. 1966. A review of grain-size parameters. *Sedimentology* 6, 73-93.
- Friis, H., Molenaar, N., Varming, T. 2014. Chlorite meniscus cement – implications for diagenetic mineral growth after oil emplacement. *Terra Nova* 26, 14 – 21.
- Furlan, S., Clauer, N., Chaudhuri, S., Sommer, F. 1996. K transfer during burial diagenesis in the Mahakam Delta Basin (Kalimantan, Indonesia). *Clays and Clay Minerals* 44, 157 – 169.
- Harwood, P. P. 1988. Microscopical techniques: II. Principles of sedimentary petrography. In: Tucker, M. E. (ed.), *Techniques in sedimentology*. Blackwell Scientific Publications, Oxford, 108-173.
- Hendry, J.P., Wilkinson, M., Fallick, A.E., Trewin, N.H. 2000. Disseminated 'jigsaw piece' dolomite in Upper Jurassic sandstones, Central North Sea: an example of cement growth during bioturbation? *Sedimentology* 47, 631–644.
- Hendry, J.P., Wilkinson, M., Fallick, A.E., Haszeldine, R.S. 2000. Ankerite cementation in deeply buried Jurassic sandstone reservoirs of the Central North Sea. *Journal of Sedimentary Research* 70, 227–239.
- Hillier, S. (2003) Quantitative analysis of clay and other minerals in sandstones by X-ray powder diffraction (XRPD). *Int. Assoc. Sedimentol. Spec. Publ.*, 34, 213–251.
- Jeans, C.V., Mitchell, J.G., Fisher, M.J., Wray, D.S., Hall, I.R. 2001. Age, origin and climatic signal of English Mesozoic clays based on K/Ar signatures. *Clay Miner.*, 36, 515–539.
- Johannessen, P. N. 2003. Sedimentology and sequence stratigraphy of paralic and shallow marine Upper Jurassic sandstones in the northern Danish Central Graben. In: Ineson, J. R. & Surlyk, F. (Eds.) *The Jurassic of Denmark and Greenland*. Geological Survey of Denmark and Greenland Bulletin 1, 367–402.
- Johannessen, P. N., Dybkjær, K., Andersen, C., Kristensen, L., Hovikoski, J. & Vosgerau, H. 2010a: Upper Jurassic reservoir sandstones in the Danish Central Graben: new insights on distribution and depositional environments. In: Vining, B. A. & Pickering, S. C. (Eds.), *Petroleum Geology: From Mature Basins to New Frontiers – Proceedings of the 7th Petroleum Geology Conference*. Geological Society, London, 127–143.
- Kuwahara, Y., Uehara, S., Aoki, Y. 2001. Atomic force microscopy study of hydrothermal illite in Izumiyama pottery stone from Arita, Saga Prefecture, Japan. *Clays and Clay Mineralogy* 49, 300–309.

- Lanson, B., Beaufort, D., Berger, G., Bauer, A. 2002. Authigenic kaolin and illitic minerals during burial diagenesis of sandstones: A review. *Clay Minerals* 37, 1 – 22.
- Lima, R.D., De Ros, L.F. 2002. The role of depositional settings and diagenesis on the reservoir quality of Devonian sandstones from the Solimões Basin, Brazilian Amazonia. *Marine and Petroleum Geology* 19, 1047 – 1071.
- Longiaru, S. 1987. Visual comparators for estimating the degree of sorting from plane and thin sections. *Journal of Sedimentary Research* 57, 791-794.
- McBride, E. F. 1963. A classification of common sandstones. *Journal of Sedimentary Research* 33, 664-669.
- Molenaar, N., Felder, M. 2018. Clay cutans and the origin of illite rim cement: An example from the siliciclastic Rotliegendes sandstone in the Dutch southern Permian Basin. *Journal of Sedimentary Research* 88, 641 – 658.
- Morad, S., Al-Ramadan, K., Ketzer, J.M., De Ros, L.F. 2010. The impact of diagenesis on the heterogeneity of sandstones reservoirs: A review of the role of depositional facies and sequence stratigraphy. *American Association of Petroleum Geologists* 94, 1267 – 1309.
- Meunier, A., Velde, B. 2004. *Illite. Origins, evolution and metamorphism*. Springer, Berlin, 145–187.
- Nielsen, M. T., Weibel, R., Friis, H. 2015. Provenance of gravity-flow sandstones from the Upper Jurassic – Lower Cretaceous Farsund Formation, Danish Central Graben, North Sea. *Marine and Petroleum Geology* 59, 371–389.
- Nielsen, M.T., Weibel, R., Therkelsen, J., Friis, H. 2019. Distribution of porosity-preserving microquartz coatings in sandstones, Upper Jurassic Danish Central Graben. *Submitted*. Review of Survey activities 2018.
- Pollastro, R.M. 1985. Mineralogical and morphological evidence for the formation of illite at the expense of illite/smectite. *Clays and Clay Minerals* 33, 265 – 274.
- Olivarius, M., Friis, H., Kokfelt, T.F., Wilson, R. 2015. Proterozoic basement and Palaeozoic sediments in the Ringkøbing–Fyn High characterized by zircon U-Pb ages and heavy minerals from Danish onshore wells. *Bulletin of the Geological Society of Denmark* 63, 29–44.
- Stokkendal, J., Friis, H., Svendsen, J.B., Poulsen, M.L.K., Hamberg, L. 2009. Predictive permeability variations in a Hermod Sand Reservoir, Stine Segments, Siri Field, Danish North Sea. *Marine and Petroleum Geology* 26, 397 – 415.
- Storvoll, V., Bjørlykke, K., Karlsen, D., Saigal, G., 2002. Porosity preservation in reservoir sandstones due to grain-coating illite: A study of the Jurassic Garn Formation from the Kristin and Lavrans fields, offshore Mid-Norway. *Marine and Petroleum Geology* 19, 767–781.
- Vagle, G.B., Hurst, A., Dypvik, H. 1994. Origin of quartz cements in some sandstones from the Jurassic of the Inner Moray Firth (UK). *Sedimentology* 41, 363–377.

Weibel, R., Whitehouse, M., Olivarius, M., Nielsen, M.T., Jakobsen, F.C., Nielsen, K., Midtgaard, H., Larsen, M. 2018. Non-destructive barite cement in Upper Jurassic sandstones, Danish Central Graben, North Sea. AAPG Annual Conference, Salt Lake City, USA (Abstract).

Weibel, R., Olivarius, M., Jakobsen, F.C., Whitehouse, M., Midtgaard, H., Larsen, M., Nielsen, K. 2019. Thermogenetic degradation of early zeolite cement: An important process for generating anomalously high porosity and permeability in deeply buried sandstone reservoirs? *Marine and Petroleum Geology* 103, 620–645.

Wentworth, C. K. 1922. A scale of grade and class terms for clastic sediments. *Journal of Geology* 5, 377-392.

Wilson, M. D., Pittman, E. D. 1977. Authigenic clays in sandstones: recognition and influence on reservoir properties and paleoenvironmental analysis. *Journal of Sedimentary Petrology* 47, 3 – 31.

## Figures

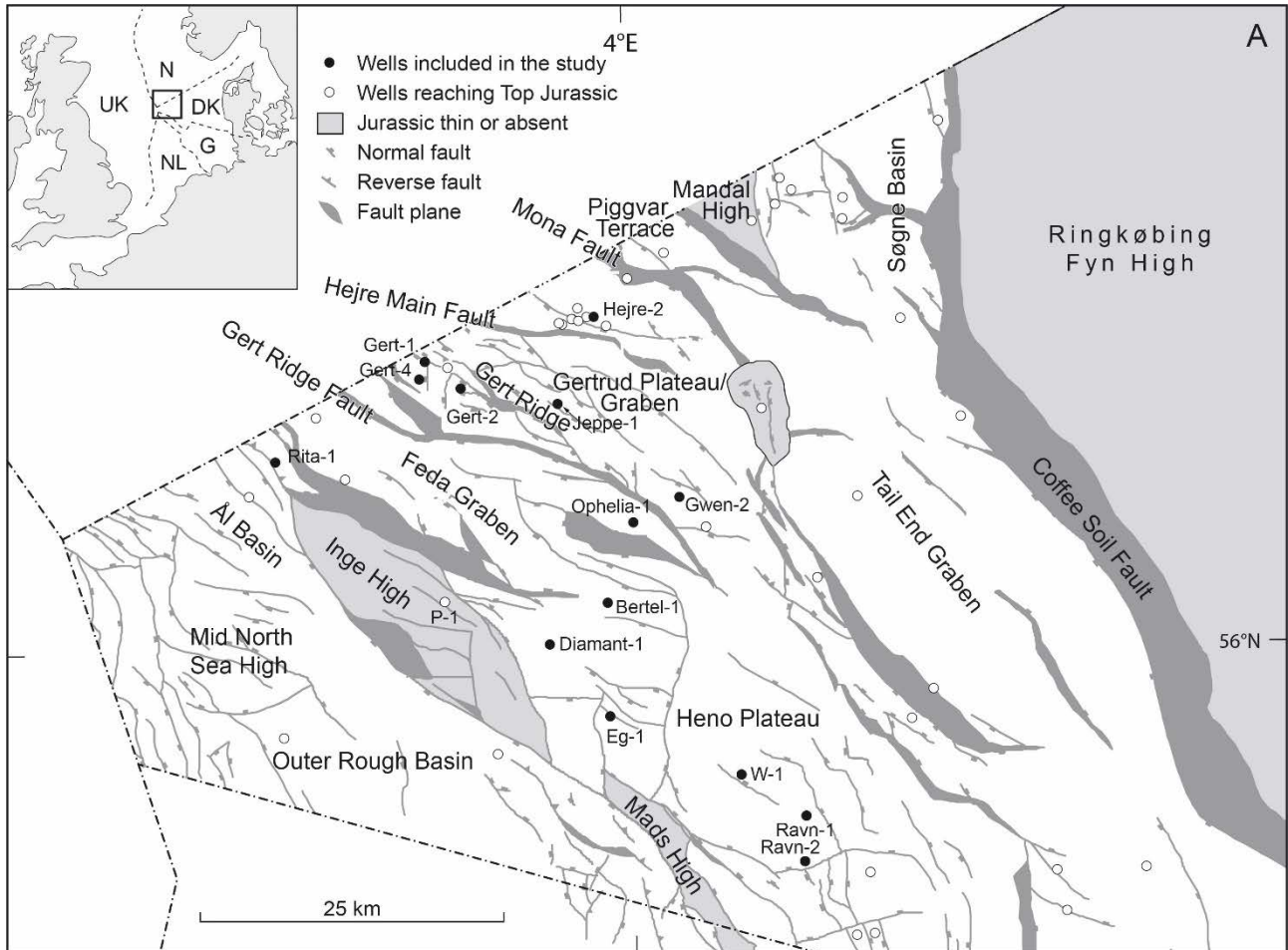


Fig. 1:

Map of the Danish Central Graben showing location of investigated wells and their relationship with structural elements.

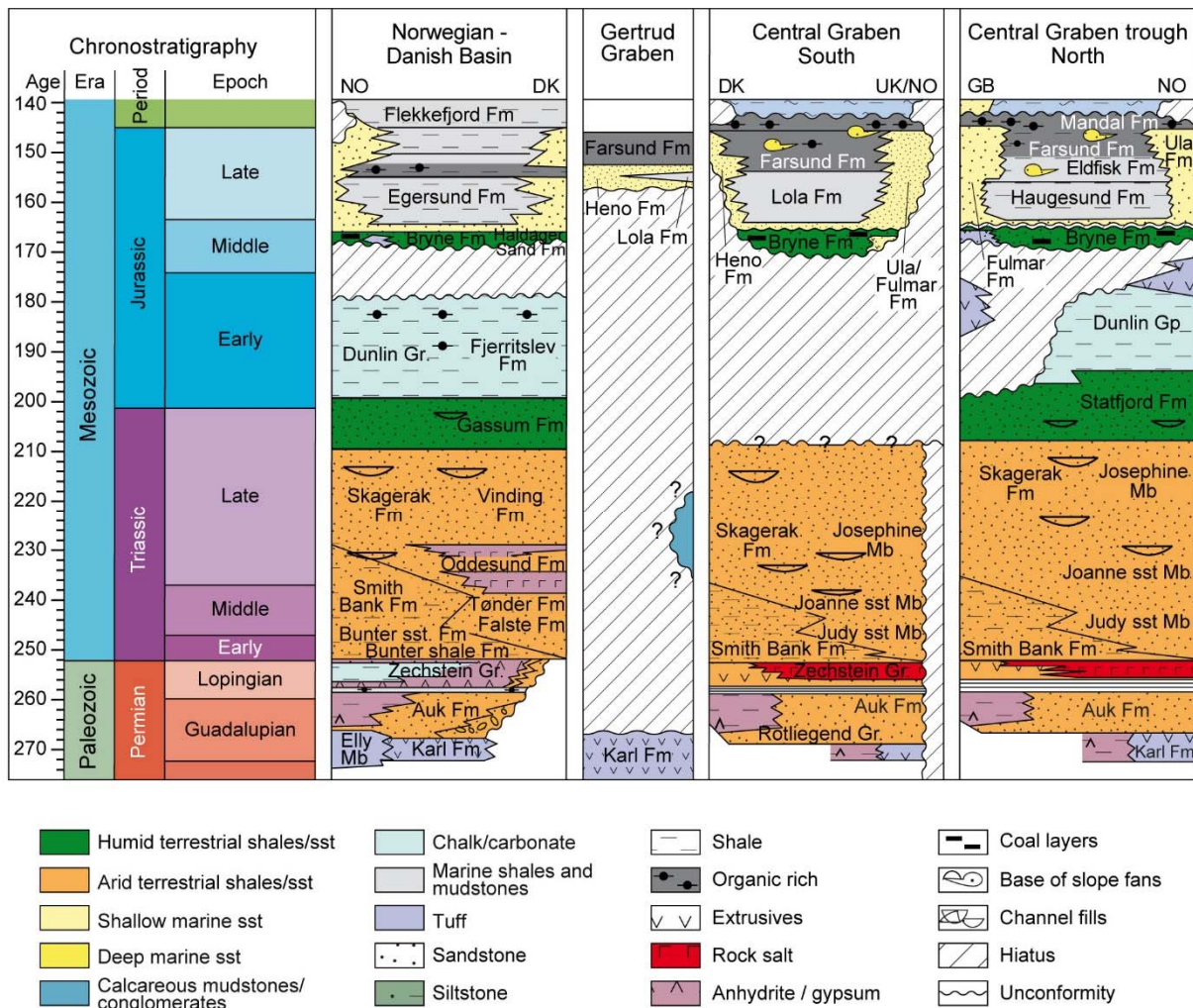


Fig. 2. Lithostratigraphy of Upper Permian to Upper Jurassic of the Gertrud Graben, Danish sector, compared with the lithostratigraphy of the Norwegian–Danish Basin, southern Central Graben and northern Central Graben trough from the Danish (DK), British (GB, UK) and Norwegian (NO) part of the North Sea (modified after Gradstein *et al.* 2012). Focus of this paper is the Upper Jurassic Heno Formation.

*Illite distribution and morphology explaining reservoir properties*

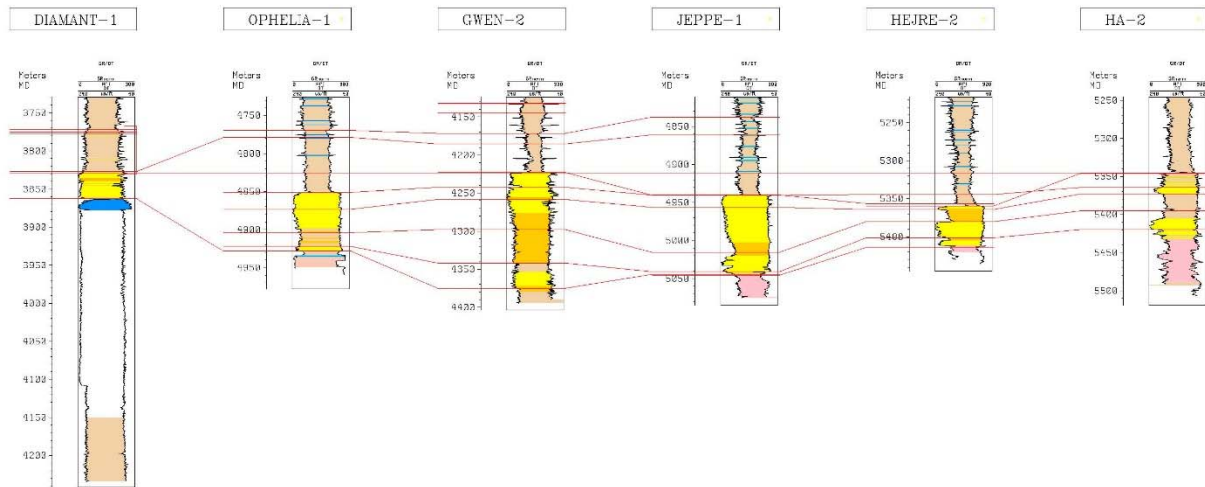


Fig. 3.

Log panel showing the sequence stratigraphic correlation between some of the investigated wells. Note that the sediments in the Diamant-1 and Gwen-2 wells have been exposed longer than the earlier flooded areas and hence may have experienced prolonged weathering compared with other locations in the basin.

*Illite distribution and morphology explaining reservoir properties*

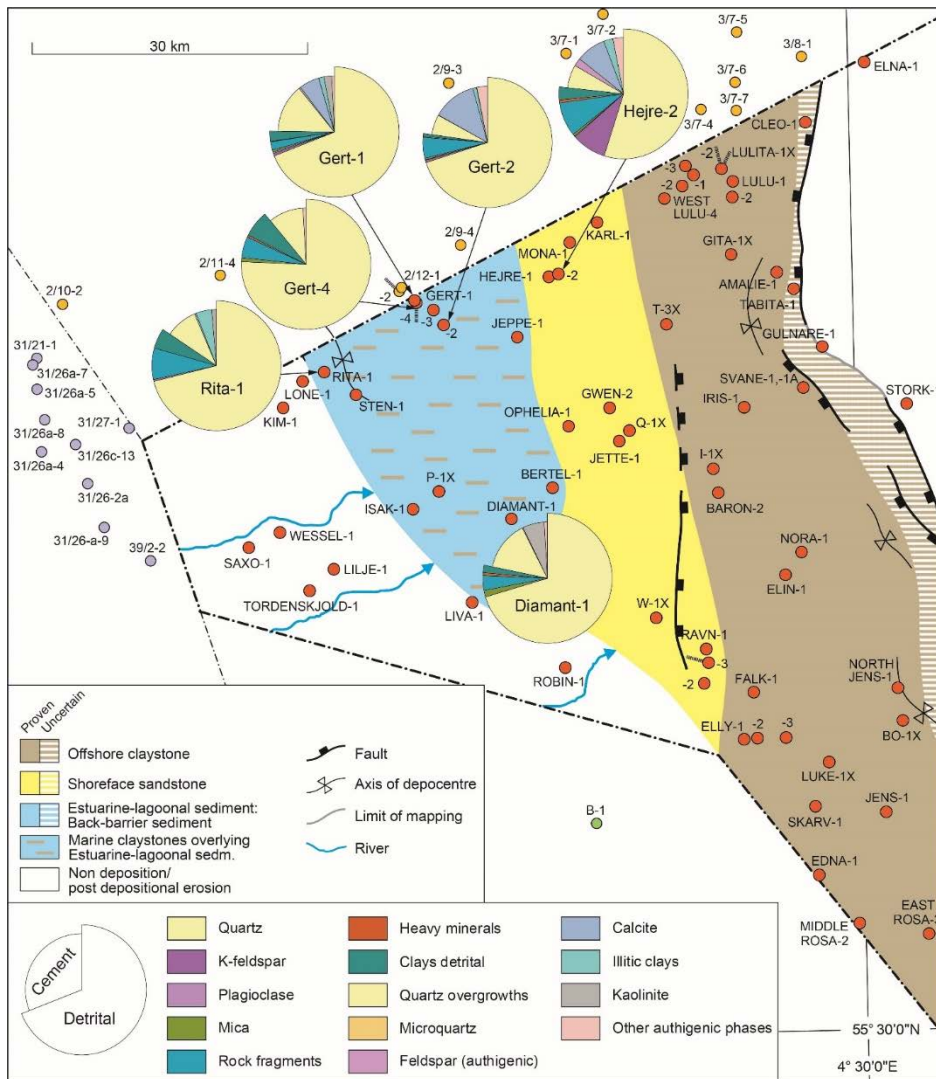


Fig. 4A. Palaeogeographical map of the Kimm-2 to Kimm-3 sequences, i.e. at the time of deposition of the Gert Member (Heno Formation).

*Illite distribution and morphology explaining reservoir properties*

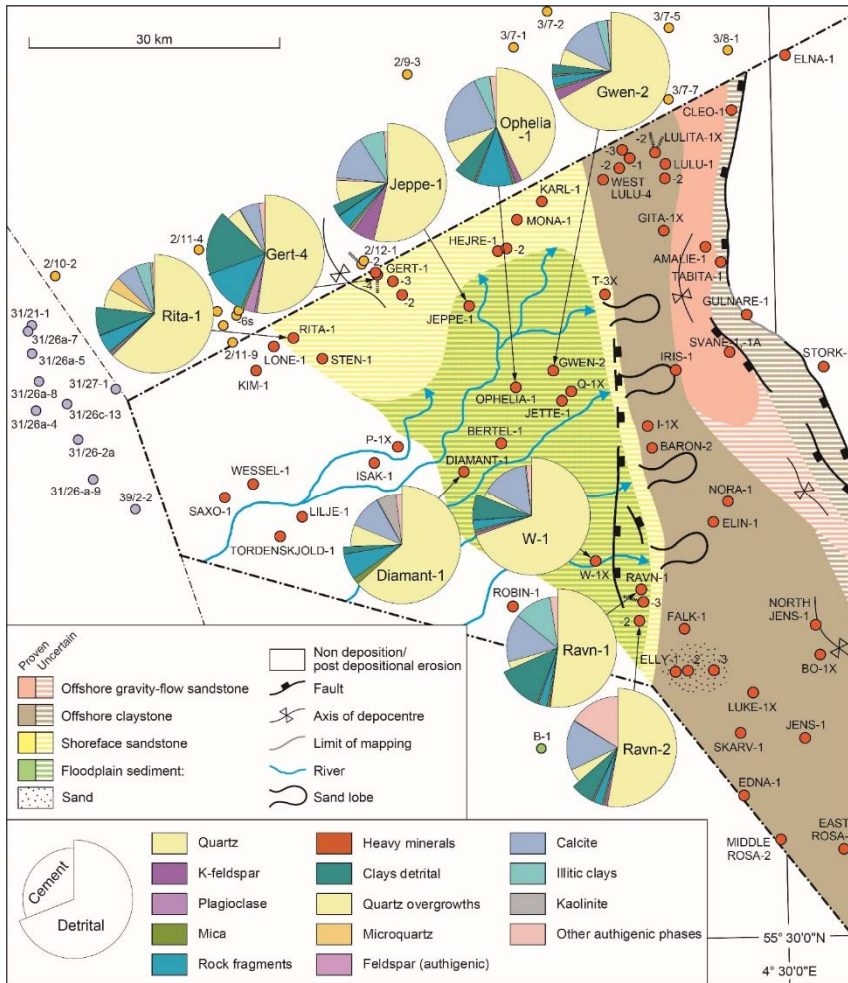
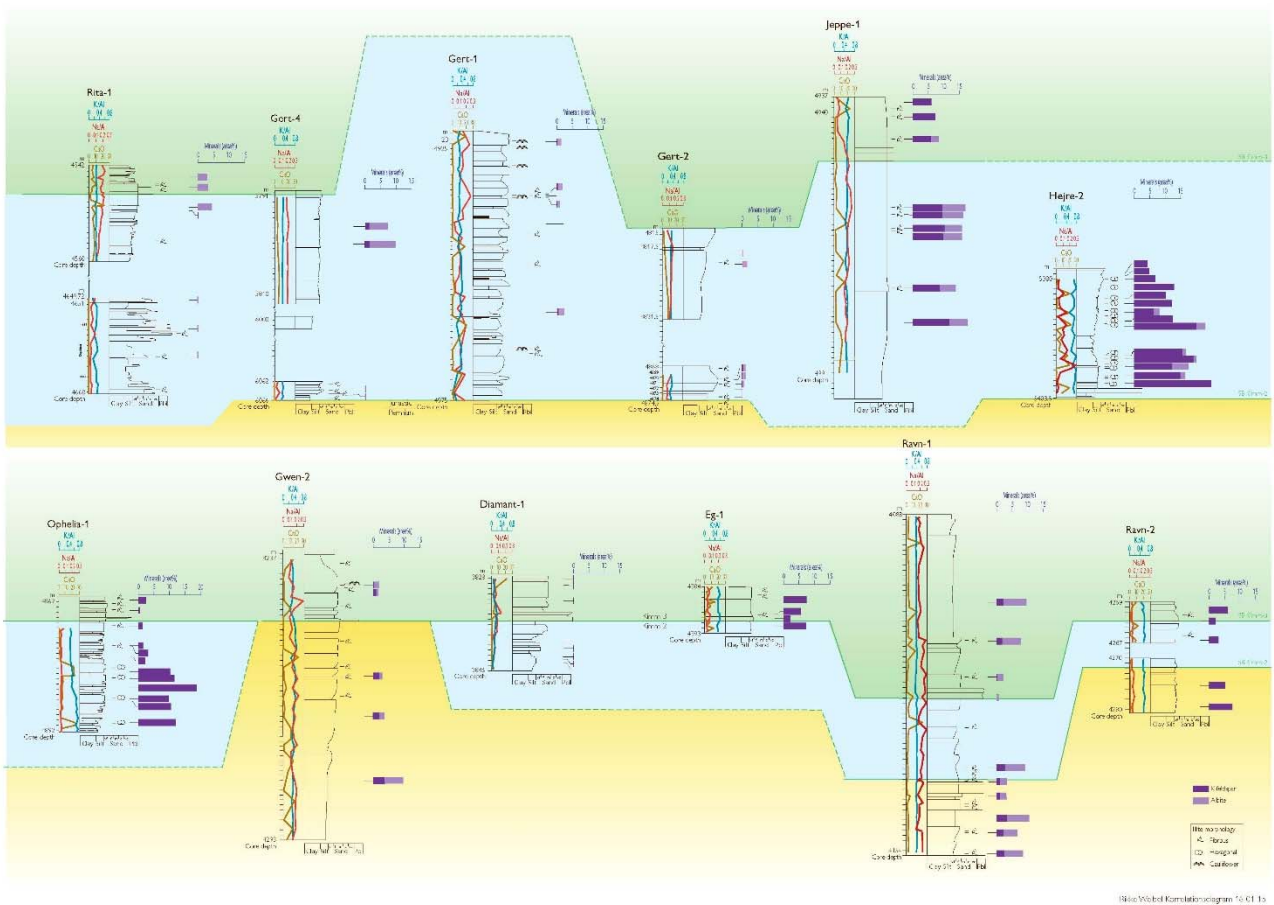


Fig. 4B. Palaeogeographical map of the Kimm-3 sequences, i.e. at the time of deposition of the Ravn Member (Heno Formation). The sandstone in the Ravn-2 well is from the succeeding sequence.

*Illite distribution and morphology explaining reservoir properties*



Illite-Mixed Komatiite program 76.01.15

Fig. 5: Correlation profile of logged core intervals of the Heno Formation. K-feldspar and albite abundances and the dominant illite morphology is shown for each core.

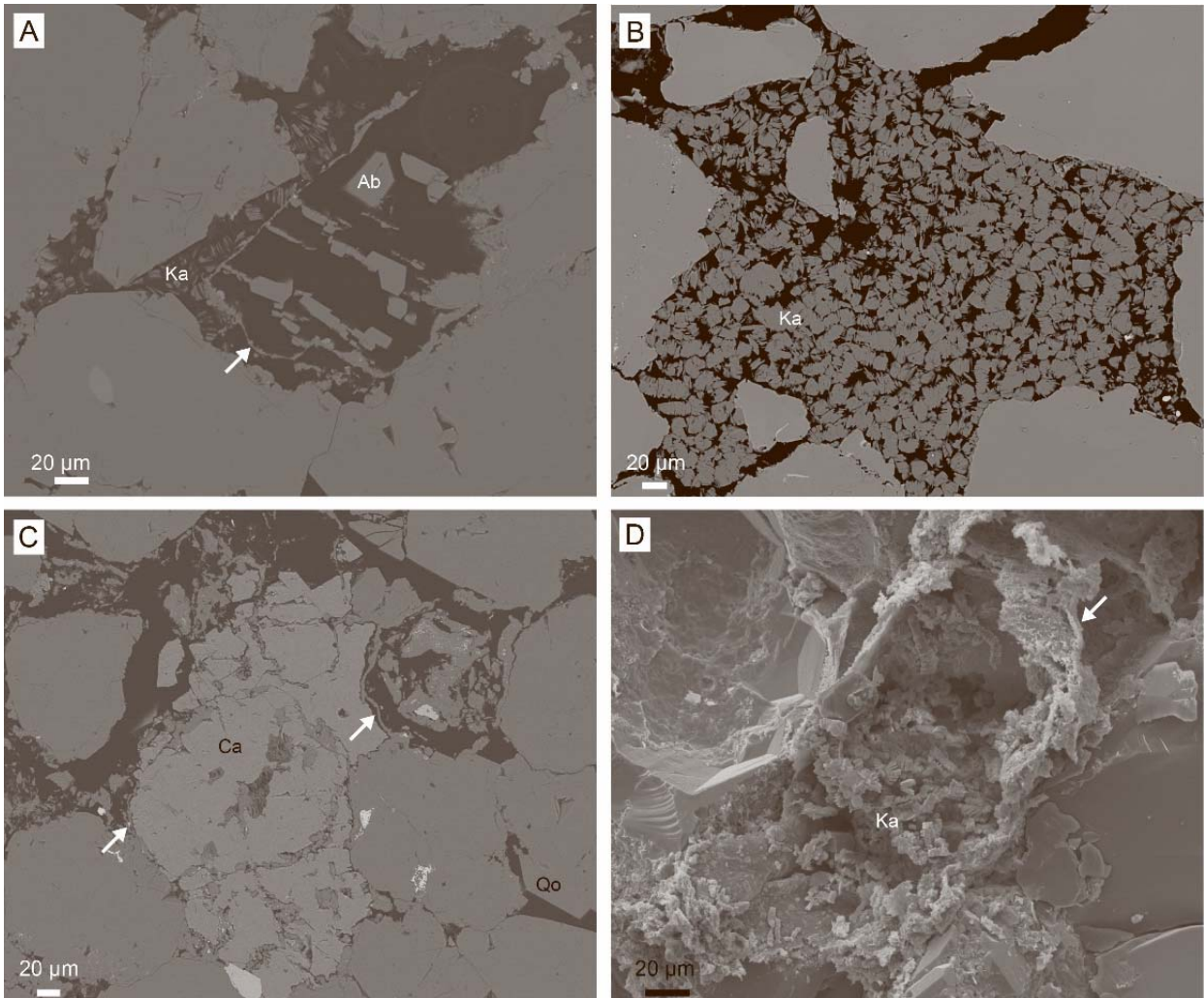


Fig. 6: Feldspar dissolution in the Heno Formation, scanning electron micrographs. **A.** The outline of an altered feldspar grain is marked by illitic coating (arrow) and surrounded by kaolinite (Ka). Authigenic albite crystals (Ab) is growing on remnants of the feldspar grain. Gert-1, 4928.15 m. **B.** Over-sized pored filled with kaolinite (Ka), possibly formed after feldspar dissolution. Diamant-1, 3829.36 m. **C.** Outline of altered feldspar grains and possibly rock fragments are marked by illitic coatings (arrows) and locally enclosed in calcite cement (Ca). Gert-1, 4924.65 m. **D.** Secondary porosity after dissolved feldspar grain marked by illitic clay coating (arrow) and partly filled by kaolinite (Ka). Gert-1, 4935.32 m.

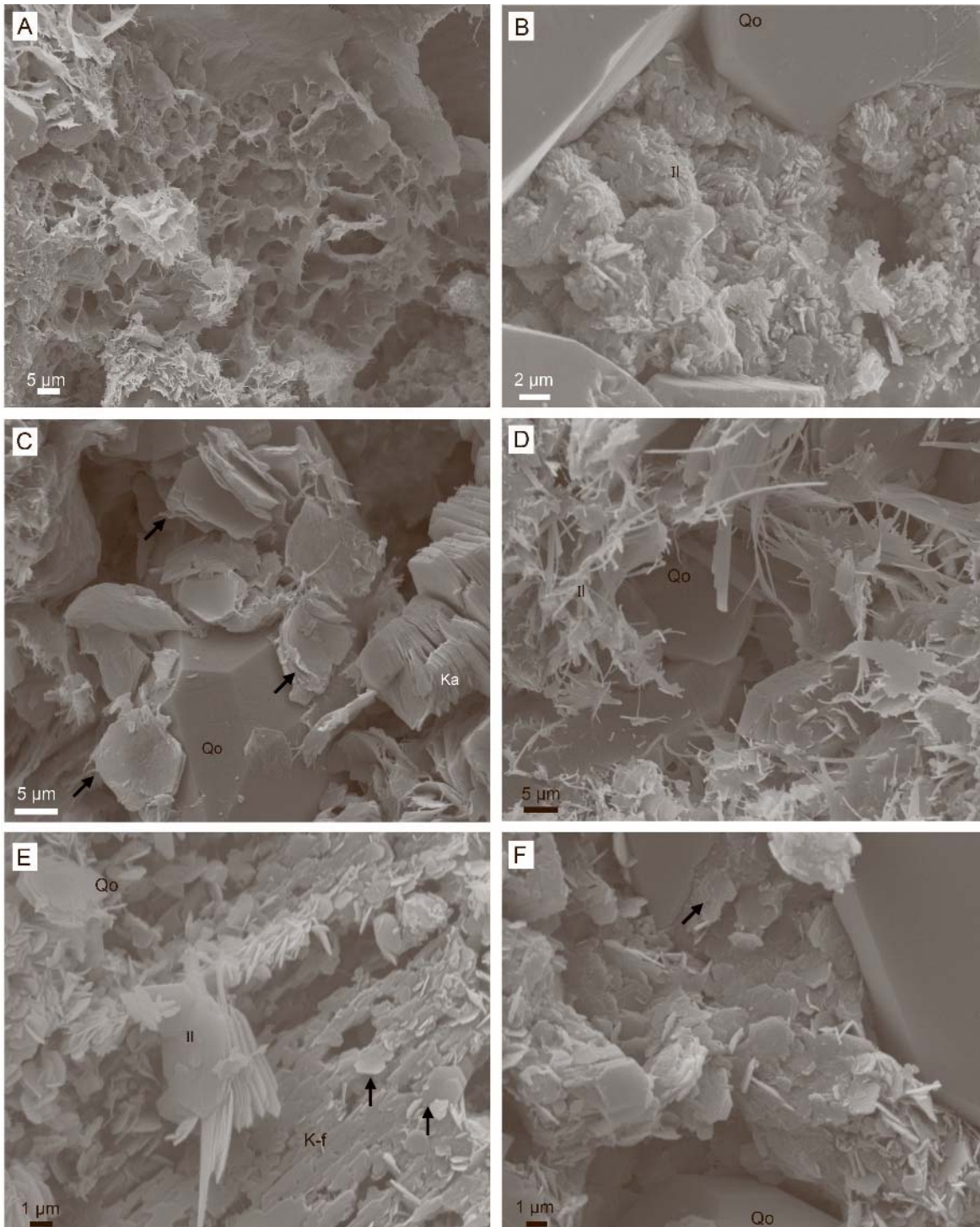


Fig. 7: Illite morphology in the Heno Formation, scanning electron micrographs. **A.** Fibrous illite growing from honeycomb textured coatings. Rita-1, 4667.53 m. **B.** 'Cauliflower'-like illite coatings from the uppermost part of the sandstones in the Gert-1 core, 4624.65 m. **C.** Incipient illitization of kaolinite (arrows) next to unaffected kaolinite (Ka), Gert-1, 4966.94 m. **D.** Fibrous illite (Il) growing after small quartz overgrowths, Jeppe-1, 4985.65 m. **E.** Hexagonal illite (Il) in pore space and locally growing directly from K-feldspar (K-f) grain (arrows). Hejre-2, 5387.35 m. **F.** Hexagonal illite with growth zonation (arrow). Hejre-2, 5399.55 m.

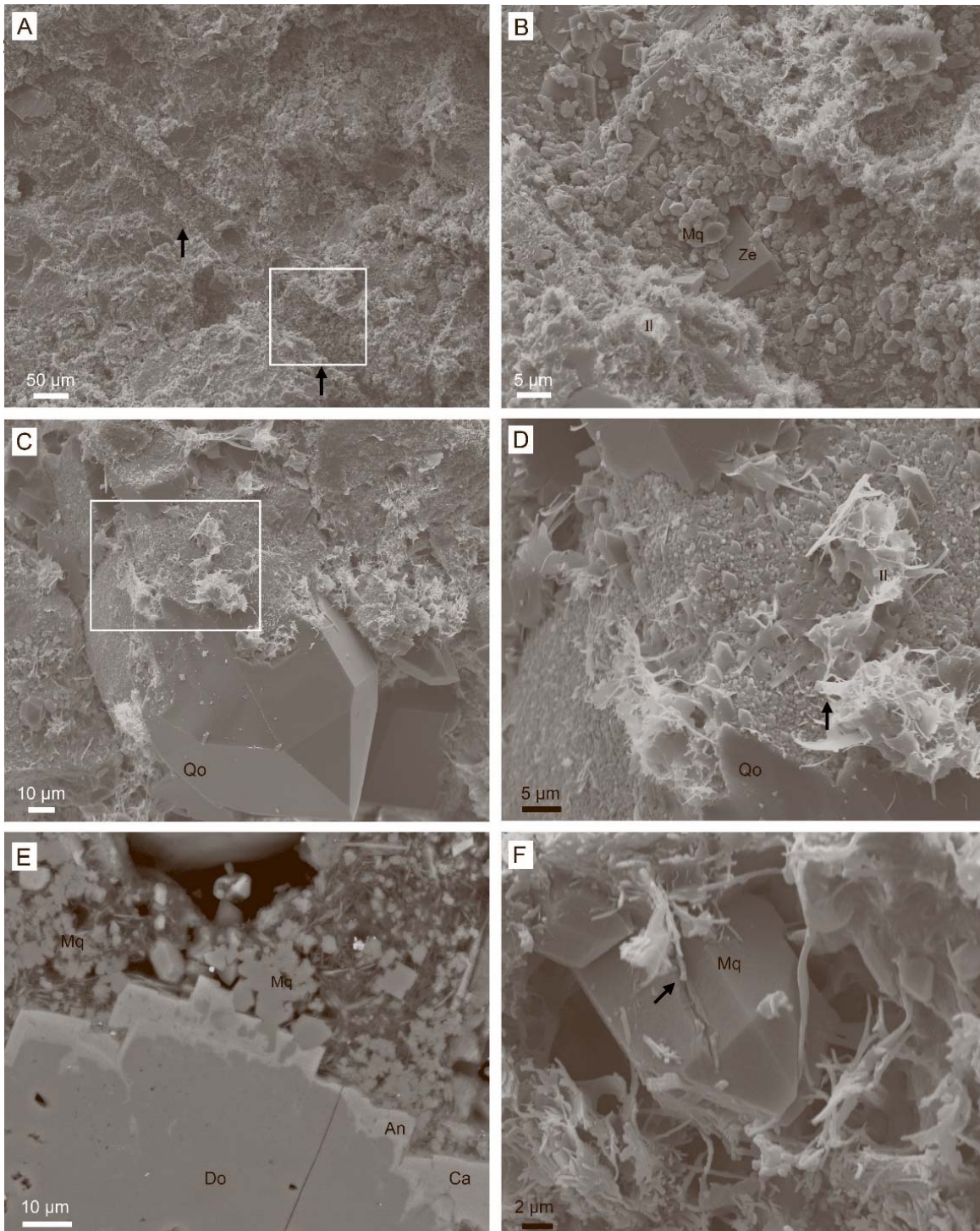


Fig. 8: Microquartz in the Heno Formation. Scanning electron micrographs. **A.** Mouldic impression after dissolved sponge spicule (arrows). Rita-1, 4547.12 m. **B.** Enlarged area of white rectangle in B showing microquartz coatings (Mq) and zeolite (Ze) covering the outline of the former sponge spicule. **C.** Microquartz coating and quartz overgrowth (Qo) on the same quartz grain. Gwen-2, 4246.29 m. **D.** Enlarged area of white rectangle in C showing uniform orientation of the microquartz crystals and that they are covered by later illite (Il). **E.** Rounded dolomite clast (Do) surrounded by ankerite (An) overgrowths, which enclose microquartz (Mq) and are succeeded by calcite cement (Ca). Rita-1, 4547.12 m. **F.**

Microquartz (Mq) crystal, which has continued its growth after fibrous illite precipitation (arrow). Ophelia-1, 4868.64 m.

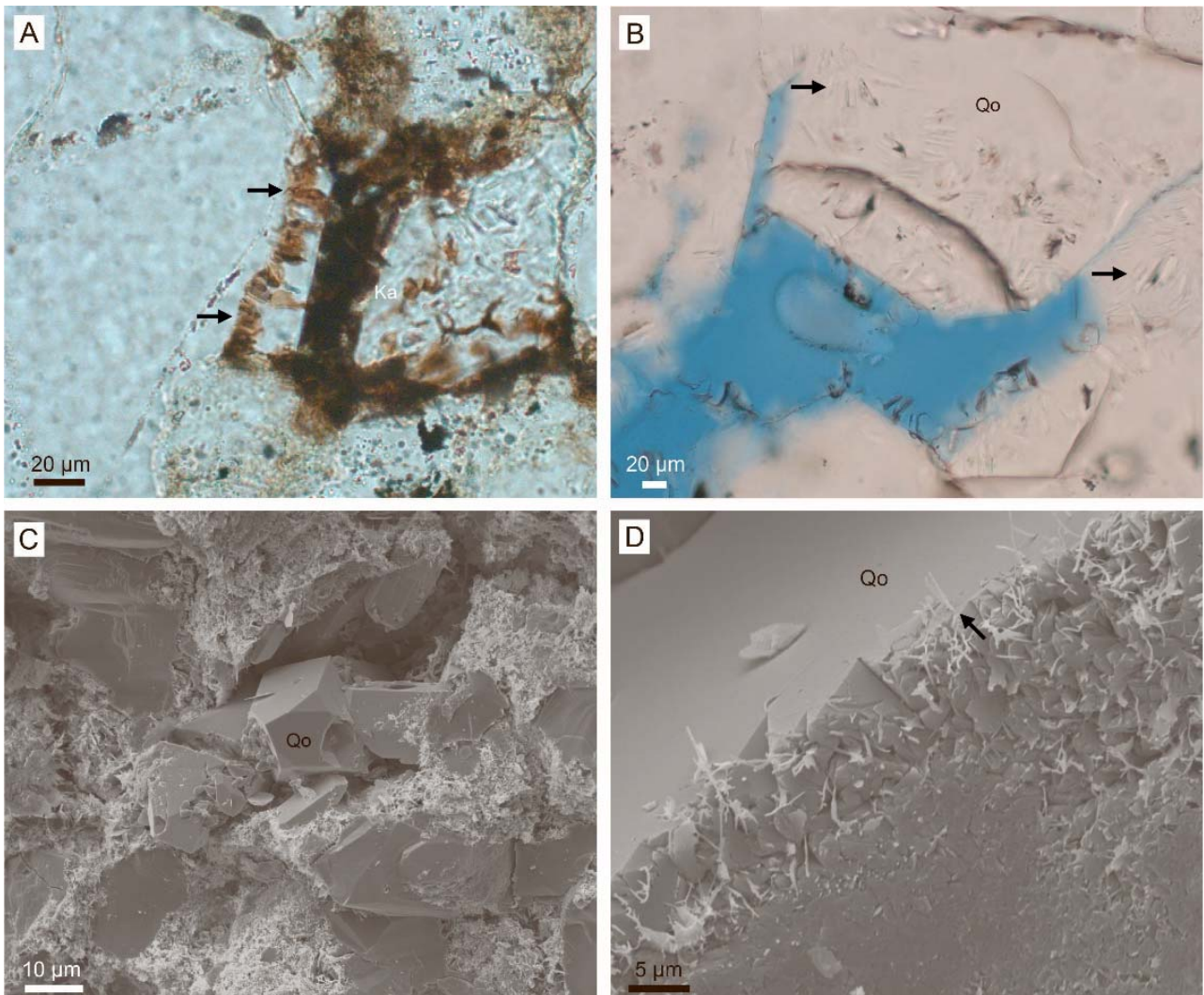


Fig. 9: Quartz cement in the Heno Formation. **A.** Hydrocarbon-stained kaolinite enclosed in quartz overgrowths. Gert-1, 4941-34 m. **B.** Kaolinite enclosed in quartz overgrowths prior to hydrocarbon introduction. Rita-1, 4667.53 m. **C.** Quartz overgrowth inhibited due to illitic coatings. Scanning electron micrograph. Rita-1, 4653.17 m. **D.** Illite fibres (arrow) enclosed in quartz overgrowths (Qo). Scanning electron micrograph. Gwen-2, 4253.14 m.

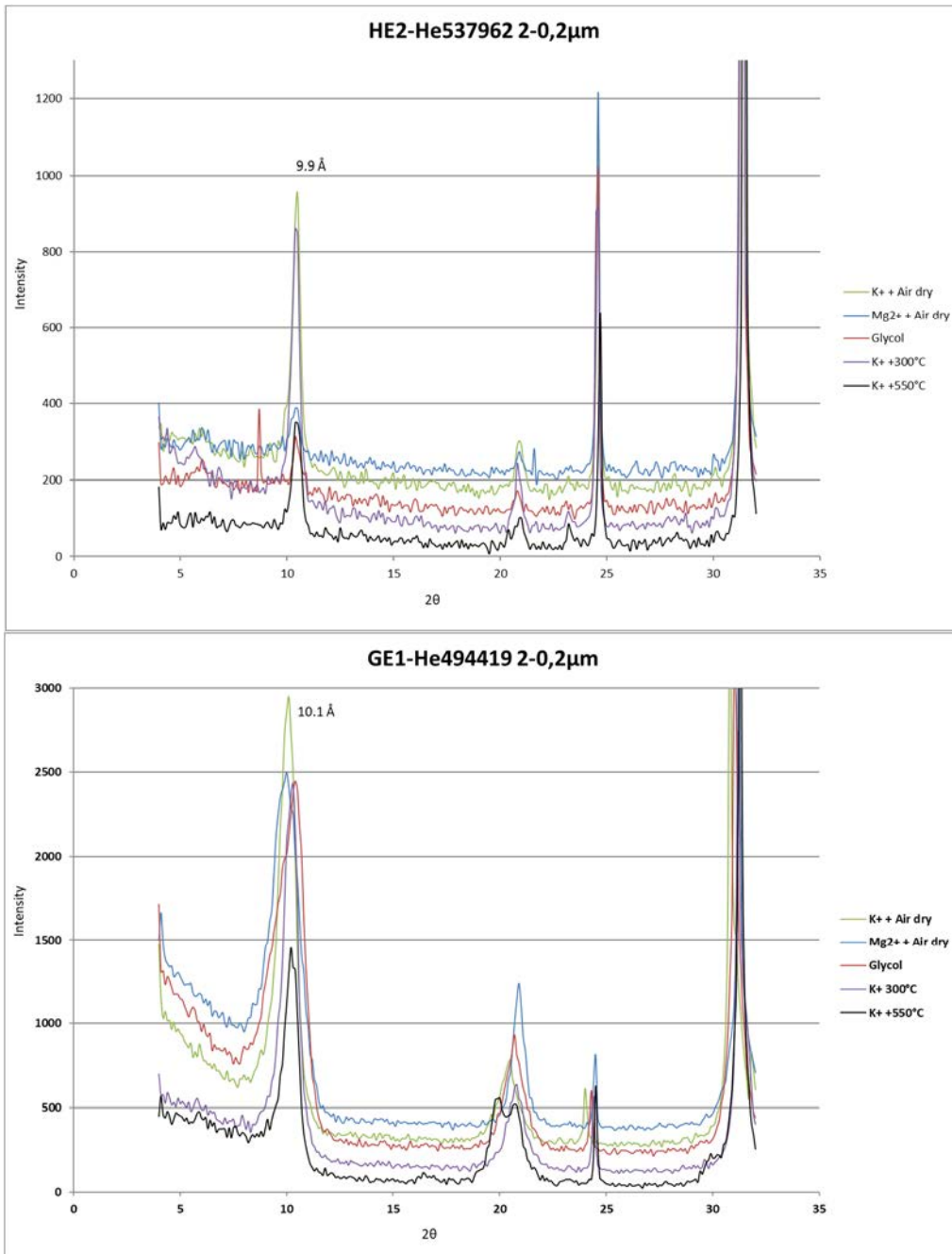


Fig. 10: X-ray diffraction of the clay fraction (2-0.2  $\mu\text{m}$ ) from the Heno Formation. **A.** Narrow 10 Å peak due to dominant hexagonal illite. Hejre-2, 5379.62 m. **B.** Broader 10 Å peak due to more mixed-layer clay minerals besides illite in sandstone with 'cauliflower' type coatings. Gert-1, 4944.19 m.

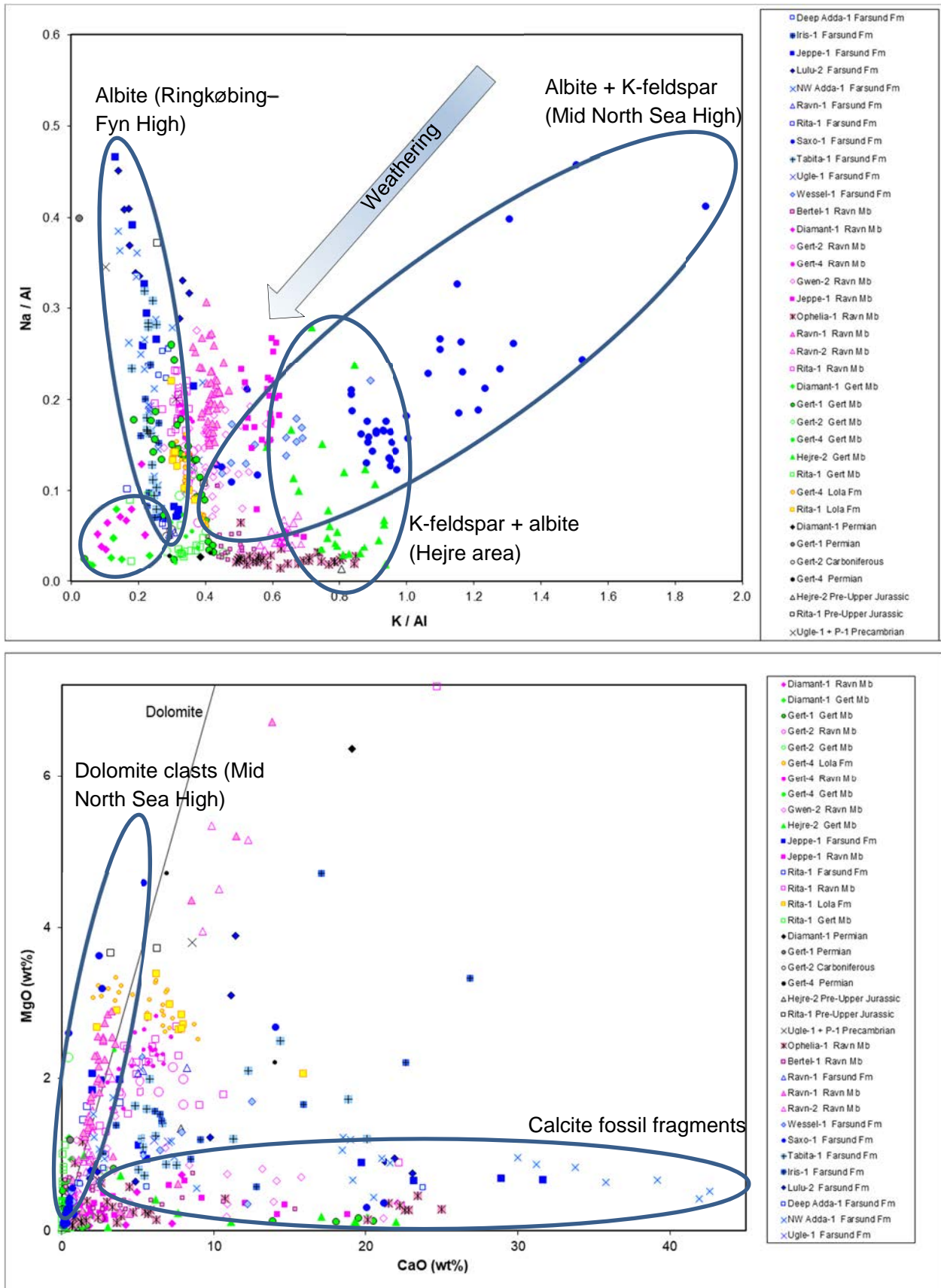


Fig. 11: Chemical composition of Upper Jurassic sediments in the Danish Central Graben.

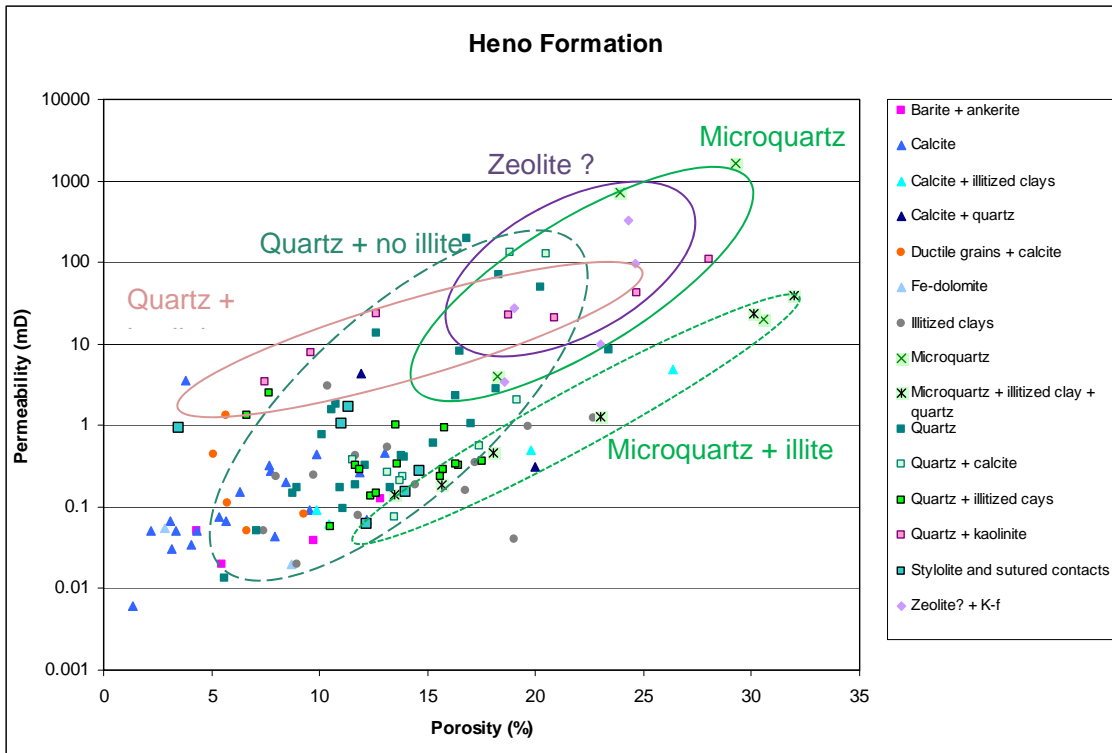


Fig. 12: Porosity and permeability relations for Heno Formation sandstones subdivided according to major diagenetic changes. High porosity and permeability characterize samples with microquartz coatings (light green circle), quartz cement and no clays (dashed green circle), quartz cement together with kaolinite (light pink circle) and samples assumed to have had an early zeolite cement (purple circle). Sandstones having microquartz coatings combined with illite (green dotted circle) have reduced permeability compared with only microquartz cement.

# Combined K-feldspar, zircon, rutile and apatite provenance interpretation, Upper Jurassic sandstones, Danish North Sea

Mette Olivarius <sup>a,\*</sup>, Christian Knudsen <sup>a</sup>, Rikke Weibel <sup>a</sup>, Yann Lahaye <sup>b</sup>, Tonny B. Thomsen <sup>a</sup>, Simon H. Serre <sup>a</sup>, Finn C. Jakobsen <sup>a</sup>, Morten Bjerager <sup>a</sup>, Finn Mørk <sup>a</sup>, Karen Dybkjær <sup>a</sup>

<sup>a</sup> Geological Survey of Denmark and Greenland (GEUS), Øster Voldgade 10, 1350 Copenhagen, Denmark

<sup>b</sup> Geological Survey of Finland (GTK), Betonimiehenkuja 4, 02151 Espoo, Finland

\* Corresponding author: M. Olivarius, mol@geus.dk

## Abstract

Multiple reworking of sediment is a well-known obstruction to provenance studies since although the source area may be evident from geochronological analyses of selected minerals, the transport routes may not or may be misinterpreted. The Upper Jurassic succession in the North Sea offers a unique example of how several stages of reworking can be pinpointed since sediment input from additional source areas were added during each reworking event. The provenance history evident from the detrital zircon and rutile U-Pb ages has some similarities with the provenance history of the K-feldspar grains as shown by their Pb-Pb signature. A large proportion of the K-feldspar grains are sourced by Archean basement, which reveals that the grains have been transported a long distance prior to their final deposition. The proportion of Archean zircon grains is smaller in the sediments, but their presence distinguishes a Laurentian provenance of the majority of those Mesoproterozoic zircons that dominate the age distributions and have ages corresponding to Laurentia/Baltica affinity. The dominant Caledonian age of the rutile grains also points to a northwestern source. Thus, a large proportion of both the light and heavy mineral fractions of the Upper Jurassic sediments is sourced from Laurentia and hence proves a sediment contribution from the northeast of the North Sea. Smaller sediment supplies from Baltica and intra-basinal basement highs are possible. Some of the smaller zircon age populations correspond to the Cadomian and Variscan orogeny, which demonstrates that some of the sediment is sourced from the south of the North Sea, and the Pb isotopic signatures of the K-feldspar grains show that some of these are also derived from the Variscan Orogen. This sediment was probably transported to the central part of the North Sea during the Triassic where it mixed with reworked Devonian/Carboniferous sediment that had been sourced by erosion of Laurentia including the Scottish-Greenlandic Caledonides, Neoproterozoic metasediments and Archean basement complexes. A number of intra-basinal highs were being eroded during the Late Jurassic in the central North Sea, and the erosion of these Triassic, Permian and Carboniferous rocks has presumably sourced the Upper Jurassic sediments in the greater Tail End Graben area.

## 1. Introduction

Provenance interpretation of sediments in the North Sea is hampered by the identical formation ages of Baltica towards the northeast and Laurentia towards the northwest of the basin, and the Sveconorwegian and Grenvillian metamorphic influence on these basement areas happened simultaneous thereby producing a second significant zircon age population in the rocks. Therefore, the provenance of North Sea sediments cannot be inferred from their most prominent age populations, and must instead be interpreted based on the presence of smaller age populations of different affinity.

In this study, a combination of several types of mineralogical provenance indicators is used to decide if this approach can be used to obtain more detailed knowledge of the sediment transport pathways. The interrelationship between heavy minerals that provenance studies are traditionally based on and light minerals that constitute the bulk part of the sediments is of special interest since the light minerals have a much larger impact on the reservoir properties of the sandstones.

The aims of this study are to (1) identify the basement domains that the analyzed minerals are sourced from, (2) interpret the reworking episodes that may have happened from source to sink and (3) deduce the transport pathways that supplied sediment to the Tail End Graben during the Late Jurassic.

## 2. Geological setting

The studied Upper Jurassic succession is present in the Danish Central Graben in the central part of the North Sea between the Ringkøbing-Fyn High to the east and the Mid North Sea High to the west (Fig. 1). These and some smaller intra-basinal highs may have been exposed during the Upper Jurassic deposition. The Tail End Graben is bounded by the Coffee Soil Fault to the east, the Mandal High to the north and the Heno Plateau to the west, which together with the Gertrud Plateau formed a platform area stretching to the Mid North Sea High. This platform was gradually being overstepped during the Late Jurassic. The setting of the Tail End Graben at the time was formed in the extensional North Sea regime during Middle to Late Jurassic rifting when east-dipping stepwise half-grabens were formed in the Danish Central Graben, which constitute the southern part of the North Sea rift complex. Sediment was deposited in paralic and shallow marine depositional environments along the rim of the Tail End Graben (Fig. 2) and deep marine mudstones with petroleum potential formed in the central part, interrupted by episodic gravity flows (Johannessen, 2003; Jakobsen et al., this volume; Schovsbo et al., this volume).

## 3. Material and methods

### 3.1 U-Pb isotope analyses

The U-Pb isotope analyses included both core and cuttings samples. Zircon grains were retrieved from 15 samples including one igneous rock from Ibenholt-1 and the remaining samples are sediments comprising three from Xana-1, three from Gita-1, two from Svane-1, two from Amalie-1, one from Stork-1, two from Gwen-2 and one from 3/7-7. Additionally, rutile grains were collected from the samples from Gwen-2 and from the sample from 3/7-7, and apatite was retrieved from the sample from Ibenholt-1.

U-Pb isotope analyses of zircon, rutile and apatite were performed by laser ablation inductively coupled plasma mass spectrometry (LA-ICPMS) at GEUS, using a NWR 213 laser ablation instrument that is coupled to an Element2 magnetic sector-field ICPMS. The samples were crushed and sieved to extract grains from the 45–750  $\mu\text{m}$  heavy mineral concentrate fraction that was obtained through density separation using a Holman-Wilfley water-shaking table. Zircon, rutile and apatite grains were then handpicked under binoculars, embedded in epoxy mounts, polished and imaged by cathodoluminescence (CL) using a scanning electron microscopy (SEM) prior to LA-ICPMS analysis.

Before loading, all sample mounts and standards were carefully cleaned with ethanol to remove surface contamination. After sample insertion, the ablation cell was flushed with helium carrier gas to minimize gas background level. The mass spectrometer was run for minimum one hour before analysis to lower and stabilize the background signal. The ablated material was swept by the helium carrier gas, which was mixed with argon gas before entering the mass spectrometer. The liberated material was transported through inert Tygon tubing by the helium carrier gas to the mass spectrometer for isotopic determination. Just before analysis, the ICP-MS was optimised for dry plasma conditions through continuous linear ablation of the GJ-1 zircon standard. The sensitivity ratios for the heavy mass range of interest (i.e. from  $^{202}\text{Hg}$  to  $^{238}\text{U}$ ), emphasizing on  $^{238}\text{U}$  and  $^{206}\text{Pb}$ , were maximized, while opting for low element-oxide production levels by minimizing the  $^{254}\text{UO}_2/^{238}\text{U}$  ratio (to be  $<0.05\%$ ).

To minimize instrumental drift, a standard-sample-standard analysis protocol was followed, bracketing all analyses by measurement of the zircon standard GJ-1 (Jackson et al., 2004). For quality control, the secondary standard Plešovice (Slama et al., 2008) was measured during the zircon analyses, yielding an average age accuracy and precision ( $2\sigma$ ) within 3% deviation. For the apatite dating, the McClure and Kovdor apatites (Schoene and Bowring, 2006; Chew et al., 2011; Chew and Donelick, 2012; Chew et al., 2014) were used as

secondary standards, whereas for the rutile analyses, the R10 and R19 rutiles (Luvizotto et al., 2009; Zack et al., 2011) were used as secondary standards, all yielding an averaged age accuracy and precision ( $2\sigma$ ) within 5% deviation.

The geochronology data were acquired from single spots of 25  $\mu\text{m}$  in size, using a laser fluence of  $\sim 10 \text{ J/cm}^2$  and a pulse rate of 10 Hz for the zircons and rutiles, and  $\sim 9 \text{ J/cm}^2$  and 5 Hz for the apatite analyses. To remove additional Pb contamination, the rutiles were pre-ablated using a 40  $\mu\text{m}$  spot size just prior to analyzing. Total acquisition time for single analyses was max. 2 minutes and included 30–40 sec. background measurement followed by laser ablation for 30 or 40 sec. and washout for 40–45 sec. Factory-supplied software from Thermo-Fisher Scientific was used for the data acquisition, obtained through automated running mode of pre-set analytical spot locations. The analyses spots were set at inclusion-free locations free of cracks on the grains.

Data reduction was performed offline through the Iolite software (Hellström et al., 2008; Paton et al., 2011) using the Iolite-integral VizualAge data reduction scheme (Petruš and Kamber, 2012). Probability-density plots (PDP) combined with histograms were produced through the software jAgeDisplay (Thomsen et al., 2016). Any Tera-Wasserburg, Concordia or age-deriving diagram is produced through Isoplot v.4.15 or Iolite v.2.5. For the PDP,  $^{207}\text{Pb}/^{206}\text{Pb}$  ages were used for zircons older than 700 million years (Ma), whereas  $^{206}\text{Pb}/^{238}\text{U}$  ages were used for younger zircons, as the  $^{206}\text{Pb}/^{238}\text{U}$  ages showed more robust ages and lower uncertainties ( $2\sigma$ ) below 700 Ma. To a subset of the analyses from the Ibenholt-1 sample, common-lead correction was applied using measured mass 204 (i.e.  $^{204}\text{Hg} + ^{204}\text{Pb}$ ) corrected for Hg through the  $^{202}\text{Hg}/^{204}\text{Hg}$  natural abundance ratio.

### 3.2 Pb-Pb isotope analyses

K-feldspar Pb-Pb isotope analyses were performed on core samples only since the K-feldspars were not sufficiently well-preserved in the cuttings. A total of nine samples were analyzed including one igneous rock from Ibenholt-1 and the rest are sandstones comprising three from Hejre-2, two from Jeppe-1, one from Ophelia-1 and two from 3/7-7.

Pb-Pb isotope analyses of K-feldspar were performed using a Nu Plasma high-resolution multicollector inductively coupled plasma mass spectrometer (HR MC-ICPMS) at GTK together with a Photon Machine Analyte G2 laser ablation system. The K-feldspars were located and gridded by SEM scanning of the polished sample blocks. Samples were ablated in He gas (gas flows = 0.4 and 0.1 l/min) within a HelEx ablation cell (Müller et al., 2009). The gas mixture was optimized daily for maximum sensitivity. Ablation conditions were: 165–150  $\mu\text{m}$  beam diameter; 20 Hz pulse frequency; 4  $\text{J/cm}^2$  beam energy density. A single Pb–Pb measurement included 1 minute baseline measurement (measure zero) prior to a batch of ratio measurements, each of the latter consisting of data acquisition for 30 seconds with laser on. Breaks in an analytical session, or refilling the Tl solution necessitated a new measure zero.

The MC-ICPMS is equipped with 9 Faraday detectors and amplifiers with  $10^{11} \Omega$  resistors. Baseline and ablation data were measured on peak, collected in static mode (208Pb, 207Pb, 206Pb, 204Pb, 205Tl, 203Tl). The raw data were filtered at 2s and corrected for mass discrimination using an exponential law. The mass discrimination factor for Pb was determined using a  $\sim 20$  ppb Tl solution nebulized at the same time as the sample, using a desolvating nebulizer. The International NIST610 standard with a Pb and Tl concentration of about 500 ppm was used to monitor the precision and accuracy of the measurements for every ten samples over the whole period of analysis. Only data with one standard error of  $< 0.25$  are plotted.

## 4. Results

The sampled sediments were deposited during the Late Jurassic up through the Kimmeridgian, except for the zircon sample from Stork-1 that is of Volgian age (Fig. 2, 3). The seismic markers from Tail End Graben (TEG) have been followed to all the sampled wells and are used to divide the succession into smaller units. The TEG seismic markers coincide in most cases with the sequence stratigraphic boundaries (Fig. 4) that divide the

Kimmeridgian succession into the Kimm-1, -2, -3 and -4 sequences, of which the first three are divided into a lower A and an upper B part (Fig. 2) (Jakobsen et al., this volume).

#### **4.1 Zircon U-Pb geochronology**

The results of the 14 zircon U-Pb age analyses of Upper Jurassic sediments are shown in Fig. 5 as combined histograms and probability-density plots produced through the software jAgeDisplay (Thomsen et al., 2016). Cores were available from the Gwen-2 well and cuttings were sampled from the other wells, often from a large depth interval to obtain a sufficient number of zircons (Fig. 3). Only between 10 and 23 grains were retrieved from each of the samples from the Svane-1 and Amalie-1 wells so their age distributions are not colored grey like the remaining samples in Fig. 5 to signify that the results are not directly comparable since the low number of analyzed grains in Svane-1 and Amalie-1 are not representative. However, although not all age populations are represented in these samples due to the low number of analyzed grains, still the obtained ages are consistent with the age populations found in the remaining samples.

The samples from the Xana-1, Gita-1, Gwen-2, Stork-1 and 3/7-7 wells all have a large span in zircon ages and almost all of them contain the following seven age populations: a small to medium late Archean population, a small middle Paleoproterozoic population, a large late Paleoproterozoic to early Mesoproterozoic population, a large middle to late Mesoproterozoic plus early Neoproterozoic population, a small late Neoproterozoic population, a small early Paleozoic population and a small late Paleozoic population (Fig. 5). Additionally, a few middle Archean, early Paleoproterozoic and middle Neoproterozoic zircons are found in some samples, but they are remarkably few.

The large span in age populations suggest a complicated provenance history with sediment contribution from several source areas. However, the consistency in size and age span of the zircon age populations found in the analyzed samples indicate that the Upper Jurassic sediments in the greater Tail End Graben area have a similar provenance history, although the small variations may also reveal local differences. Thus, all the zircon ages from the analyzed sediments are merged in Fig. 6 to enable interpretation of the overall provenance history of the sediments based on the distribution of these 946 concordant zircon ages.

Basement may have been exposed within the studied basin area during deposition of the Upper Jurassic succession, namely on the Ringkøbing-Fyn High and the Mandal High (Jakobsen et al., this volume). Thus, the presumed age of this local basement is also shown in Fig. 6 based on the results from the analyzed basement in the Ibenholt-1 well and from wells further east on the Ringkøbing-Fyn High (Olivarius et al., 2015). The age of the Ibenholt-1 basement of  $1516 \pm 20$  Ma is calculated as the upper concordia-intercept age of the discordia line by regressing the discordant analyses, which shows that the zircons have suffered lead loss, perhaps during the lower intercept age of  $404 \pm 39$  Ma (Fig. 7). The concordia line of one of the sandstone samples from the Gwen-2 well is shown as an example of how the majority of the detrital zircons in the analyzed Upper Jurassic sediments have concordant ages, although the uncertainties become progressively larger with increasing zircon age. The Wetherill concordia plots are made by the software Isoplot (Wetherill, 1956; Ludwig, 2012).

#### **4.2 Rutile U-Pb geochronology**

The results of the three rutile U-Pb age analyses of Upper Jurassic sediments from the Gwen-2 and 3/7-7 wells show that most of the rutile grains have a similar age centered at 496, 491 and 486 Ma in the samples (Fig. 8). These internally-concordant rutile  $^{206}\text{Pb}/^{238}\text{U}$  ages are calculated by the TuffZirc algorithm in Isoplot (Ludwig and Mundil, 2002; Ludwig, 2012). There is some uncertainty related to the relatively low number of analyzed grains, but the ages found in the three samples are so similar that they seem reliable. All the samples contain some older grains with ages in the intervals of c. 2250-1900 Ma, c. 1300-950 Ma and c. 600-530 Ma, but the uncertainties are large for some of the older rutiles. The only rutile grain that falls outside these age intervals with its age of c. 445 Ma is from the 3/7-7 well.

The U-Pb ages of the zircon grains from the same three samples as the analyzed rutile grains have age distributions that are very different from the rutile ages (Fig. 5, 8). Caledonian-aged grains are dominant among the rutiles, whereas zircons with this age make up a small component. Few Cadomian-aged grains are present among both the rutiles and zircons, whereas Sveconorwegian / Grenvillian-aged grains are more abundant especially among the zircons. The oldest rutile grains correspond approximately to the middle Paleoproterozoic age population found in the zircon grains.

#### **4.3 Apatite U-Pb geochronology**

The apatite U-Pb ages of the basement sample from the Ibenholt-1 well on the Ringkøbing-Fyn High are all discordant so a common Pb correction has been made (Fig. 9). In this way, a good estimate of the lower concordia-intercept age is produced based on the 88 coherent analyses. The resulting apatite age of c. 824 Ma is much younger than the zircon age of  $1516 \pm 20$  Ma from the same sample (Fig. 7).

#### **4.4 K-feldspar Pb-Pb composition**

The Pb isotopic signatures of the analyzed K-feldspar grains from Upper Jurassic sediments (Fig. 10) are compared to the basement domains defined by Tyrrell et al. (2007). Some of the K-feldspar grains from 3/7-7 and Hejre-2 and a few grains from Jeppe-1 have low Pb isotopic ratios comparable to the Archean basement source. Slightly more grains from 3/7-7 and Hejre-2 and many more from Jeppe-1 have compositions that correspond to the Proterozoic II basement domain. A few grains from 3/7-7 are plotting within the Proterozoic I basement category, but most results in this category overlap with the Proterozoic II basement, which is also the case for most grains that plot in the Avalonian basement category. A few grains from 3/7-7, Hejre-2 and Jeppe-1 have Variscan basement affinity. Some K-feldspar grains have different Pb isotopic composition than the defined basement domains, in particular some of the grains from Jeppe-1 that have higher ratios. The K-feldspars from the Ibenholt-1 basement on the Ringkøbing-Fyn High have even higher ratios, with a consistent compositional trend.

### **5. Discussion**

#### **5.1 Provenance of the zircon grains**

A southern provenance of the zircon grains with Cadomian and Variscan ages in the Upper Jurassic sediments is certain since Baltica and Laurentia not contain zircons with similar ages (Fig. 6). However, the zircons were not transported directly from the Variscan Orogen to the central North Sea during the Late Jurassic since they are unlikely to have passed the local highs and depocenters (Johannessen et al., 2010). Furthermore, the extend of the shoreface sandstones points towards sediment supply coming from the west on the western side of the Tail End Graben and perhaps from the east on the eastern side of the graben (Fig. 11). Thus, the zircons from the Variscan Orogen must have been transported northwards to the central North Sea during the late Carboniferous, Permian or Triassic before being reworked into the Upper Jurassic sandstones. This could have happened in a continental setting where long-distance transport was possible by fluvial and aeolian processes, such as during the Triassic when zircons from the Variscan Orogen were transported by wind action across the dry North German Basin and at least as far northwards as to the Ringkøbing-Fyn High (Olivarius et al., 2017).

The majority of the zircon grains in the Upper Jurassic sediments have ages of 1.7-0.9 Ga (Fig. 6), and a 1.8-1.0 Ga gap in zircon ages is characteristic of the southern provenance in the Variscan Orogen, opposed to Baltica and Laurentia that contain plentiful zircons with such ages. Thus, most of the zircon grains have been supplied from these northern areas since the Cadomian and Variscan age populations are small in the studied sediments. Inherited middle Paleoproterozoic basement ages of 2.1-1.8 Ga are present in the Variscan Orogen, while the middle Paleoproterozoic ages in the Scottish and Greenlandic Caledonides are mainly 2.0-1.8 Ga (Linnemann et al., 2000; Thrane, 2002; Gerdes and Zeh, 2006; Cawood et al., 2007). As such, the middle Paleoproterozoic zircons in the studied sediments seem most likely to be derived from the Caledonides since the 2.0-1.8 Ga ages are most abundant.

The presence of Archean zircons reveals a western provenance of the sediments in the Norwegian Sea whereas its absence shows an eastern provenance, together with a less pronounced Caledonian age population (Fonneland et al., 2004). Similarly, the late Archean zircon ages found in the studied sediments must be derived from the northwest of the North Sea since such ages are not present in the Sveconorwegian and Variscan Orogens. Archean basement is exposed locally in northern Scotland and more extensively in eastern Greenland so the zircons have been formed in this basement province, but have probably experienced repeated reworking since the basement erosion. Zircons with Archean and Caledonian ages are rare in sediments in the eastern part of the North Sea, which were primarily sourced by the Sveconorwegian Orogen (Olivarius et al., 2014; Olivarius and Nielsen, 2016; Olivarius et al., submitted). Thus, a dominant sediment contribution to the studied sediments from southwards draining of the Fennoscandian Shield into the North Sea can be excluded since this would have diluted the Archean and Caledonian age populations significantly, which is not the case (Fig. 6).

When ignoring the Variscan and Cadomian age populations, the zircon age distributions of the studied Upper Jurassic sediments in the central North Sea bear a striking resemblance to those found in Devonian, Carboniferous and Upper Jurassic sediments in East Greenland (Slama et al., 2011; Olivarius et al., 2018). However, the 1.5 Ga age population is much more pronounced in the studied sediments than in the Greenlandic sediments, which indicate that Telemarkian basement probably has produced some of the sediment in the North Sea. The Ringkøbing-Fyn High basement is of similar age as the basement in the Telemarkia Terrane in southernmost Norway, as seen from the Ibenholt-1 dating (Fig. 7) and a former study further east (Olivarius et al., 2015). However, the Ringkøbing-Fyn High basement has apparently not been influenced as much by the Sveconorwegian Orogeny since such ages are more abundant in the Telemarkia Terrane (Bingen and Solli, 2009). Thus, distinction between zircons derived from southernmost Norway versus local basement highs in the North Sea can potentially be made by the amount of Sveconorwegian ages. The content of Sveconorwegian/Grenvillian ages is larger in the studied North Sea sediments than in the East Greenland sediments so this indicates that some of the sediment is likely derived from southernmost Norway. This sediment was probably supplied to the central North Sea during the Triassic when fluvial conditions prevailed (McKie and Williams, 2009). So although the zircon ages in the Gothian-Sveconorwegian interval of 1.7-0.9 Ga cannot be used to uniquely distinguish a northeastern versus northwestern source since these ages are abundant both in Baltica and Laurentia, still some interpretable variations within this age interval exist.

A large part of the zircon grains with Mesoproterozoic ages were likely eroded from their basement source already during the Neoproterozoic where the sediment was deposited in large intracratonic basins preceding the breakup of Rodinia (Cawood et al., 2007). Thereby the Krummedal Supracrustal Suite and later the Eleonore Bay Supergroup were formed in proto-East Greenland and correspondingly the Moine Supergroup and later the Dalradian Supergroup were deposited in Scotland. These deposits were afterwards deeply buried and metamorphosed prior to uplift and erosion whereby a thick succession of the metasediments were reworked into the Norwegian Sea and the North Sea.

During the Carboniferous, sediments north of the Mid North Sea High were supplied from the north, and some sediments south of the high also came from the north but some of the upper Carboniferous sediments came from the south as evident by their Cadomian and Variscan zircon ages (Hallsworth et al., 2000; Morton et al., 2001). Devonian sandstones may have sourced some of the Carboniferous sediments in the central North Sea, but were largely covered by younger deposits during the Late Jurassic (Fig. 12). The studied Upper Jurassic sandstones could not have been supplied by reworking of Carboniferous sediments alone since these are dominated either by Cadomian and Variscan zircons or by Caledonian zircons, whereas these age populations are small in the Upper Jurassic sandstones. Carboniferous, Permian and Triassic sediments were exposed on the Mid North Sea High during the Late Jurassic so it is plausible that a mixture of these sediments was supplied to the basin.

The lower of the two analyzed samples from the Gwen-2 well consist of well-sorted, fine-grained sandstone, whereas the upper sample contains sandstone with pebble-sized quartz clasts. Such large clasts are often found

in Upper Jurassic sandstones in the Danish Central Graben so a local source area that supplied coarse clastic material must have been present nearby (Johannessen et al., 2010). However, the zircon age distributions of the two samples from Gwen-2 are comparable regarding which age populations are present so their provenance seem similar (Fig. 5). A Rotliegende source of the clasts is most likely since this volcanic material does not contain zircons so it would not be recognizable in the age distributions of its clastic derivate, which is likely to contain coarse clasts since the volcanic material has only been transported a short distance.

Upper Kimmeridgian to Volgian sandstones along the northeastern flank of the Mid North Sea High were on basis of their heavy mineral assemblage interpreted as eroded off Devonian/Carboniferous and Rotligendes/Triassic sediments on the high (Spathopoulos et al., 2000). A similar provenance of the studied Upper Jurassic sediments seem likely since they cannot have been supplied from Devonian and Carboniferous sediments alone, so they must have been reworked into the Permian and Triassic sediments that were exposed on highs in the central North Sea when the Upper Jurassic succession was being deposited (Fig. 12). These highs comprise the Mid North Sea High, the Heno Plateau, the Mandal High and the Ringkøbing-Fyn High, which were probably covered with sedimentary units that each had a similar provenance signal within the unit on both sides of the Central Graben. Thus, the provenance signal of the studied sediments cannot be used to distinguish whether they were eroded off sediments to the west or the east of the graben during the Late Jurassic. However, basement was exposed on the western flank of the Ringkøbing-Fyn High so a larger content of zircon grains with ages corresponding to timing of the basement formation would indicate that some of the sediment was supplied from this basement.

The sampled basement from the Ibenholt-1 well located centrally on the Ringkøbing-Fyn High cannot have been a sediment source during the Mesozoic as seen by the thick sedimentary succession present on top of the basement (Fig. 3). However, its zircon age of 1.5 Ga (Fig. 7) is consistent with what is found in basement in the Grindsted-1 and Glamsberg-1 wells on the eastern part of the high so this basement has a large extent and its age may be representative for the locally exposed basement in the study area (Olivarius et al., 2015). The analyzed Volgian sandstone from the Stork-1 well was probably deposited in a similar setting as the one represented by the Kimm-3b sequence boundary, where gravity-flow sandstones in the eastern part of the Tail End Graben presumably were sourced from the east (Fig. 11). This would imply erosion of the Ringkøbing-Fyn High basement and its cover, and the Stork-1 sandstone does indeed have a dominant zircon age population that corresponds to the basement age (Fig. 5). However, most of the sand must have been supplied by reworking of older sediments since many other age populations are present. Basement may have been exposed locally on the Mandal High, but only with a small extent.

Zircon grains may not be representative for the bulk part of the sediment they are present in since they have high density so small zircons are deposited in hydraulic equivalence with much larger quartz and feldspar grains (Garzanti et al., 2008). Furthermore, zircon is extremely mechanically and chemically stable and therefore can be reworked multiple times whereas for example feldspar may break down or dissolve. Zircon is present in all the studied sandstones, but in small amounts of <0.1%. Therefore, studying other provenance indicators is important to reveal how representative the zircon transport history is for the bulk sediment.

In this study, the zircon grains have evidently been reworked, and weathering may have changed the mineral assemblage during each reworking episode such that the zircon age distributions may only be representative for the stable mineral assemblage, and perhaps not even for the quartz grains due to hydraulic sorting. Furthermore, mineral fertility in the sediment source rocks is of importance since the other heavy minerals may have formed in other types of rocks than the zircons (Malusá et al., 2016). Zircon is absent in some rocks such as the volcanics in the HA-2 well on the Gertrud Plateau and in the basement in the Per-1 well in the southern part of the Ringkøbing-Fyn High.

In conclusion, the transport history of the zircon grains in the Upper Jurassic sediments in the greater Tail End Graben area can be summarized into at least four events as illustrated in Fig. 13. Firstly, sediments were produced by erosion in Laurentia and deposited in intracratonic basins during the Neoproterozoic. These sediments were later metamorphosed at lower temperatures than the zircon closure temperature and uplift

caused erosion of this succession. This material mixed with eroded material from Archean basement complexes and Caledonian rocks to form Devonian and Carboniferous sediments with multiple age populations in their zircon age distribution. Such sediments were presumably eroded during the Triassic and mixed with sediment transported from the Variscan Orogen and perhaps also from Baltica. The sediment deposited centrally in the North Sea during the Late Jurassic was presumably mainly sourced by erosion of the Triassic sediments on intra-basinal highs and plateaus, besides smaller contributions from older sediments, Permian volcanics and Mesoproterozoic basement, which were also exposed locally in the highs.

### **5.2 Provenance of the rutile grains**

The much lower closure temperature of rutile compared to zircon means that it can record metamorphic events that may not be evident in zircon if the temperature was within the range of c. 400–1000°C. The consistent ages of most rutile grains from sediments in the Gwen-1 and 3/7-7 wells of 496–486 Ma show that the rutiles have been sourced from the same area (Fig. 8). This early Caledonian age is recorded in Scotland where high-grade metamorphism occurred during the Grampian event (Harte, 1988). The rutiles in the Western Gneiss Complex in western south Norway have ages of 385–392 Ma, which are not compatible with those rutile ages found in the studied sediments (Kylander-Clark et al., 2008), so the rutiles have not been sourced from this area. Rutile and zircon grains are transported together due to their high mechanical stability and hydraulic equivalence resulting from comparable densities, so if the rutiles are sourced from Laurentia and not from Baltica then the same is presumably also the case for most of the zircon grains, which is in agreement with the Archean component in the zircon age distributions.

### **5.3 Provenance of the K-feldspar grains**

The K-feldspar analyses are of special importance because the K-feldspar grains represent the bulk part of the sediment, although quartz is the dominant mineral, but quartz and feldspar grains have approximately similar settling equivalence due to their comparable densities so they will normally be transported together (Garzanti et al., 2008). The type and amount of feldspar vary in the studied sandstones, but this may primarily be related to the post-depositional processes (Weibel et al., this volume). The Pb isotopic analyses of the K-feldspar grains in the sandstones show that they originate from several source areas as evident from the large compositional variation (Fig. 10).

The results are of great significance since they reveal that some of the grains have been sourced by distant Archean and Variscan basement, implying that K-feldspar grains are capable of surviving long-distance transport. Furthermore, this shows that zircon age dating is a valuable tool for provenance studies in the North Sea since the provenance interpretation made on this basis does not only apply to the very stable zircon grains but presumably also to the bulk part of the sediment. The relative proportion between Archean and Proterozoic grains is different for zircon and K-feldspar, which shows that the relationship is complex and depends on a number of factors such as mineral fertility in the source rocks and hydraulic sorting during transport (Melusà et al., 2016).

Some of the grains from especially Jeppe-1 plot outside the basement domains. The same is true for some of the grains from Hejre-2, but these have large standard errors so they are not included in Fig. 10. The Hejre-2 and Jeppe-1 wells are both positioned in the Gertrud Graben where local erosion of Permian volcanics has sourced some of the Hejre-2 sediment, and the K-feldspars in these volcanic rocks are formed from albite by potassium metasomatism (Weibel et al., 2019). Thus, the reason for the abnormal Pb isotopic composition of some of the K-feldspar grains in Hejre-2 and Jeppe-1 could perhaps be that they are sourced from metasomatized volcanics. These volcanics would not be identified in the zircon age distributions since they do not contain zircon. Metamorphism can also change the Pb isotopic composition of K-feldspar as seen in the Ibenholt-1 basement, but only a single grain in Jeppe-1 has a comparable composition so this type of Ringkøbing-Fyn High basement is not likely to have sourced a significant part of the studied sediments.

## 6. Conclusions

- The Upper Jurassic sediments in the greater Tail End Graben area were deposited from reworking of older sediments on the intra-basinal highs comprising the Mandal High, Heno Plateau, Mid North Sea High and Ringkøbing-Fyn High.
- The majority of the sediment is sourced from Laurentia, but has been reworked several times before deposition during the Late Jurassic. A smaller sediment supply from the Variscan belt is evident, whereas small sediment contributions from Baltica and local basement highs are possible but not certain.
- Small but consistent stratigraphic variations in the provenance signal suggests that the individual gravity-flow units in the Tail End Graben were supplied by variable sediment contributions from the different intra-basinal highs, probably in response to the repeatedly changing distribution of the depositional environments in the area.
- The combined study of light and heavy minerals has revealed that the provenance history told by the zircon grains is in fact rather comparable to the provenance history of the light mineral fraction represented by the K-feldspar grains.
- The rutile grains with their much lower closure temperature than zircon have consistently recorded an early stage of the Caledonian orogeny, whereas apatite in the Ringkøbing-Fyn High basement were formed during a much earlier metamorphic event that has influenced these Telemarkian-aged rocks.

## Acknowledgements

The authors wish to thank INEOS Oil and Gas Denmark on behalf of the former 4/98 partnership for permission to publish the data. Mojagan Alaei, Høgni Vesturklett, Sebastian N. Malkki and Jette Halskov are thanked for technical assistance.

## References

- Bingen, B., Solli, A., 2009. Geochronology of magmatism in the Caledonian and Sveconorwegian belts of Baltica: synopsis for detrital zircon provenance studies. *Norwegian Journal of Geology* 89, 267–290.
- Cawood, P.A., Nemchin, A.A., Strachan, R., Prave, T., Krabbendam, M., 2007. Sedimentary basin and detrital zircon record along East Laurentia and Baltica during assembly and breakup of Rodinia. *Journal of the Geological Society* 164, 257–275.
- Chew, D.M., Sylvester, P.J., Tubrett, M.N., 2011. U-Pb and Th-Pb dating of apatite by LA-ICP-MS. *Chemical Geology* 280 (1–2), 200–216.
- Chew, D.M., Donelick, R.A., 2012. Combined apatite fission track and U-Pb dating by LA-ICPMS and future trends in apatite provenance analysis. In: Sylvester, P. (Ed.), *Quantitative mineralogy and microanalysis of sediments and sedimentary rocks*. Mineralogical Association of Canada, 219–248.
- Chew, D.M., Petrus, J.A., Kamber, B.S., 2014. U-Pb LA-ICPMS dating using accessory mineral standards with variable common Pb. *Chemical Geology* 363, 185–199.
- Fonneland, H.C., Lien, T., Martinsen, O.J., Pedersen, R.B., Kosler, J., 2004. Detrital zircon ages: a key to understanding the deposition of deep marine sandstones in the Norwegian Sea. *Sedimentary Geology* 164, 147–159.
- Garzanti, E., Andò, S., Vezzoli, G., 2008. Settling equivalence of detrital minerals and grain-size dependence of sediment composition. *Earth and Planetary Science Letters* 273, 138–151.

- Gerdes, A., Zeh, A., 2006. Combined U–Pb and Hf isotope LA-(MC-)ICP-MS analyses of detrital zircons: Comparison with SHRIMP and new constraints for the provenance and age of an Armorican metasediment in Central Germany. *Earth and Planetary Science Letters* 249, 47–61.
- Hallsworth, C.R., Morton, A.C., Claoué-Long, J., Fanning C.M., 2000. Carboniferous sand provenance in the Pennine Basin, UK: constraints from heavy mineral and detrital zircon age data. *Sedimentary Geology* 137, 147–185.
- Harte, B., 1988. Lower Palaeozoic metamorphism in the Moine-Dalradian belt of the British Isles. Geological Society, London, Special Publications 38, 123–134.
- Hellström, J., Paton, C., Woodhead, J., Hergt, J., 2008. Iolite: Software for spatially resolved LA- (quad and MC) ICPMS analysis. In: Sylvester, P. (Ed.) *Laser ablation ICP-MS in the earth sciences: current practices and outstanding issues*. Mineral. Assoc. of Canada, Quebec, 343–348.
- Jackson, S.E., Pearson, N.J., Griffin, W.L., Belousova, E.A., 2004. The application of laser ablation-inductively coupled plasma-mass spectrometry to in situ U–Pb zircon geochronology. *Chemical Geology* 211, 47–69.
- Jakobsen, F., Bjerager, M., Dybkjær, K., Mørk, F., Weibel, R., Olivarius, M., Schovsbo, N.H., Knutz, P., Fyhn, M.B.W., Nielsen, M.T., Lindström, S., Andersen, C., Kristensen, L., Nytoft, H.P., Bojesen-Koefoed, J., Johannessen, P., this volume. Deposition and diagenesis of Upper Kimmeridgian (Upper Jurassic) reservoir sandstones in the Søgne Basin and Tail End Graben, the Danish Central Graben.
- Johannessen, P.N., 2003. Sedimentology and sequence stratigraphy of paralic and shallow marine Upper Jurassic sandstones in the northern Danish Central Graben. *Geological Survey of Denmark and Greenland Bulletin* 1, 367–402.
- Johannessen, P.N., Dybkjær, K., Andersen, C., Kristensen, L., Hovikoski, J., Vosgerau, H., 2010. Upper Jurassic reservoir sandstones in the Danish Central Graben: new insights on distribution and depositional environments. In: Vining, B.A. & Pickering, S.C. (eds): *Petroleum Geology: From mature basins to new frontiers*. Proceedings of the 7th Petroleum Geology Conference. Geological Society London, 127–143.
- Kylander-Clark, A.R.C., Hacker, B.R., Mattinson, J.M., 2008. Slow exhumation of UHP terranes: Titanite and rutile ages of the Western Gneiss Region, Norway. *Earth and Planetary Science Letters* 272, 531–540.
- Linnemann, U., Gehmlich, M., Tichomirowa, M., Buschmann, B., Nasdala, L., Jonas, P., Lützner, H., Bombach, K., 2000. From Cadomian subduction to Early Palaeozoic rifting: the evolution of Saxo-Thuringia at the margin of Gondwana in the light of single zircon geochronology and basin development (Central European Variscides, Germany). *Geol. Soc. Lond. Spec. Publ.* 179, 131–153.
- Ludwig, K.R., 2012. User's manual for Isoplot 3.75. A Geochronological Toolkit for Microsoft Excel. Berkeley Geochronology Center, Special Publication 5, 75 pp.
- Ludwig, K.R., Mundil, R., 2002. Extracting reliable U–Pb ages and errors from complex populations of zircons from Phanerozoic tuffs. *J. Conf. Abstr. 12th Goldschmidt Conference*.
- Luvizotto, G.L., Zack, T., Meyer, H.P., Ludwig, T., Triebold, S., Kronz, A., Münker, C., Stockli, D.F., Prowatke, S., Klemme, S., Jacob, D.E., von Eynatten, H., 2009. Rutile crystals as potential trace element and isotope mineral standards for microanalysis. *Chemical Geology* 261, 346–369.
- Malusà, M.G., Resentini, A., Garzanti, E., 2016. Hydraulic sorting and mineral fertility bias in detrital geochronology. *Gondwana Research* 31, 1–19.

- McKie, T., Williams, B., 2009. Triassic palaeogeography and fluvial dispersal across the northwest European Basins. *Geol. J.* 44, 711–741.
- Morton, A.C., Claoué-Long, J.C., Hallsworth, C.R., 2001. Zircon age and heavy mineral constraints on provenance of North Sea Carboniferous sandstones. *Marine and Petroleum Geology* 18, 319–337.
- Müller, W., Shelley, M., Miller, P., Broude, S., 2009. Initial performance metrics of a new custom-designed ArF excimer LA-ICPMS system coupled to a two-volume laser-ablation cell. *Journal of Analytical Atomic Spectrometry* 24, 209–214.
- Olivarius, M., Rasmussen, E.S., Siersma, V., Knudsen, C., Kokfelt, T.F., Keulen, N., 2014. Provenance signal variations caused by facies and tectonics: Zircon age and heavy mineral evidence from Miocene sand in the north-eastern North Sea Basin. *Marine and Petroleum Geology* 49, 1–14.
- Olivarius, M., Friis, H., Kokfelt, T.F., Wilson, J.R., 2015. Proterozoic basement and Paleozoic sediments in the Ringkøbing-Fyn High characterized by zircon U–Pb ages and heavy minerals from Danish onshore wells. *Bulletin of the Geological Society of Denmark* 63, 29–44.
- Olivarius, M., Nielsen, L.H., 2016. Triassic paleogeography of the greater eastern Norwegian-Danish Basin: constraints from provenance analysis of the Skagerrak Formation. *Marine and Petroleum Geology* 69, 168–182.
- Olivarius, M., Weibel, R., Friis, H., Boldreel, L.O., Keulen, N., Thomsen, T.B., 2017. Provenance of the Lower Triassic Bunter Sandstone Formation: implications for distribution and architecture of aeolian vs. fluvial reservoirs in the North German Basin. *Basin Research* 29 (Suppl. 1), 113–130.
- Olivarius, M., Bjerager, M., Keulen, N., Knudsen, C., Kokfelt, T.F., 2018. Provenance of basinal sandstones in the Upper Jurassic Hareelv Formation, Jameson Land Basin, East Greenland. *Geological Survey of Denmark and Greenland Bulletin* 42, 115–126.
- Olivarius, M., Sundal, A., Weibel, R., Gregersen, U., Baig, I., Thomsen, T.B., Kristensen, L., Hellevang, H., Nielsen, L.H., submitted. Provenance and sediment maturity as controls on CO<sub>2</sub> mineral sequestration potential of the Gassum Formation in Skagerrak. Submitted to *Frontiers in Earth Science*.
- Paton, C., Hellstrom, J.C., Paul, P., Woodhead, J.D., Hergt, J.M., 2011. Iolite: Freeware for the visualisation and processing of mass spectrometric data. *Journal of Analytical Atomic Spectrometry* 26, 2508–2518.
- Petrus, J.A., Kamber, B.S., 2012. VizualAge: A novel approach to laser ablation ICP-MS U-Pb geochronology data reduction. *Geostandards and Geoanalytical Research* 36, 247–270.
- Schoene, B., Bowring, S.A., 2006. U–Pb systematics of the McClure Mountain syenite: thermochronological constraints on the age of the Ar-40/Ar-39 standard. *Contributions to Mineralogy and Petrology* 151, 5, 615–630.
- Schovsbo, N., Ponsaing, L., Mathiesen, A., Bojesen-Koefoed, J.A., Kristensen, L., Dybkjær, K., Johannessen, P.N., Jakobsen, F., this volume. Review of quality and maturity of Lower Jurassic to lowermost Cretaceous petroleum source rocks in the Danish Central Graben.
- Slama, J., Kosler, J., Condon, D.J., Crowley, J.L., Gerdes, A., Hanchar, J.M., et al., 2008. Plesovice zircon - a new natural reference material for U-Pb and Hf isotopic microanalysis. *Chemical Geology* 249, 1–2, 1–35.

Slama, J., Walderhaug, O., Fonneland, H., Kosler, J., Pedersen, R.B., 2011: Provenance of Neoproterozoic to upper Cretaceous sedimentary rocks, eastern Greenland: Implications for recognizing the sources of sediments in the Norwegian Sea. *Sedimentary Geology* 238, 254–267.

Spathopoulos, F., Doubleday, P.A., Hallsworth, C.R., 2000. Structural and depositional controls on the distribution of the Upper Jurassic shallow marine sandstones in the Fife and Angus fields area, Quadrants 31 & 39, UK Central North Sea. *Marine and Petroleum Geology* 17, 1053–1082

Thomsen, T.B., Heijboer, T., Guarnieri, P., 2016. jAgeDisplay: software for evaluation of data distributions in U-Th-Pb geochronology. *Geological Survey of Denmark and Greenland Bulletin* 35, 103–106.

Thrane, K., 2002. Relationships between Archaean and Palaeoproterozoic crystalline basement complexes in the southern part of the East Greenland Caledonides: an ion microprobe study. *Precambrian Research* 113, 19–42.

Tyrrell, S., Haughton, P.D.W., Daly, J.S., 2007. Drainage reorganization during breakup of Pangea revealed by in-situ Pb isotopic analysis of detrital K-feldspar. *Geology* 35, 11, 971–974.

Weibel, R., Nielsen, M.T., Therkelsen, J., Jakobsen, F.C., Bjerager, M., Mørk, F., Mathiesen, A., Johannessen, P.N., Dybkjær, K., this volume. Illite distribution and morphology explaining basinal variations in reservoir properties of Upper Jurassic sandstones, Danish North Sea.

Weibel, R., Johannessen, P.N., Dybkjær, K., Rosenberg, P., Knudsen, C., 2010. Chemostratigraphy of upper Jurassic reservoir sandstones, Danish Central Graben, North Sea. *Marine and Petroleum Geology* 27, 1572–1594.

Weibel, R., Olivarius, M., Jakobsen, F.C., Whitehouse, M., Larsen, M., Midtgaard, H., Nielsen, K., 2019. Thermogenetic degradation of early zeolite cement: An important process for generating anomalously high porosity and permeability in deeply buried sandstone reservoirs? *Marine and Petroleum Geology* 103, 620–645.

Wetherill, G.W., 1956. Discordant uranium-lead ages. *Trans. Amer. Geophys. Union* 37, 320–326.

Zack, T., Stockli, D.F., Luvizotto, G.L., Barth, M.G., Belousova, E., Wolfe, M.R., Hinton, R.W., 2011. In situ U–Pb rutile dating by LA-ICP-MS: 208Pb correction and prospects for geological applications. *Contributions to Mineralogy & Petrology* 162, 515–530.

Figures

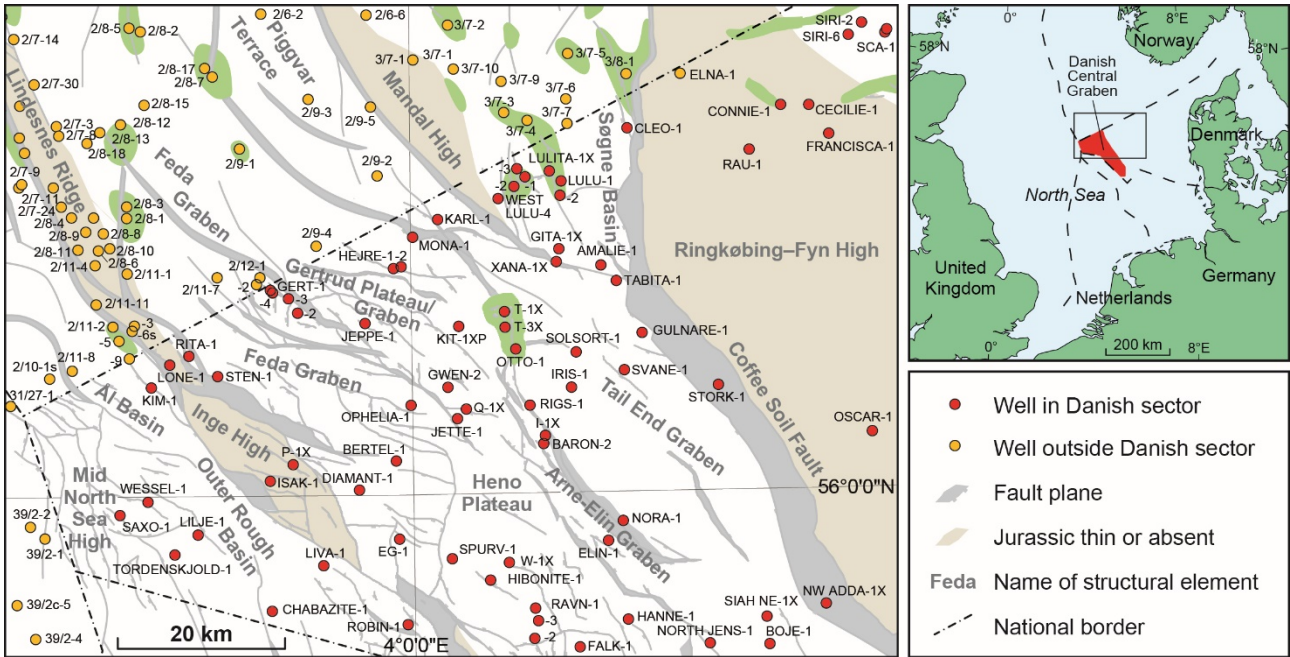


Figure 1. Map of the studied area in the North Sea including wells and structural elements.

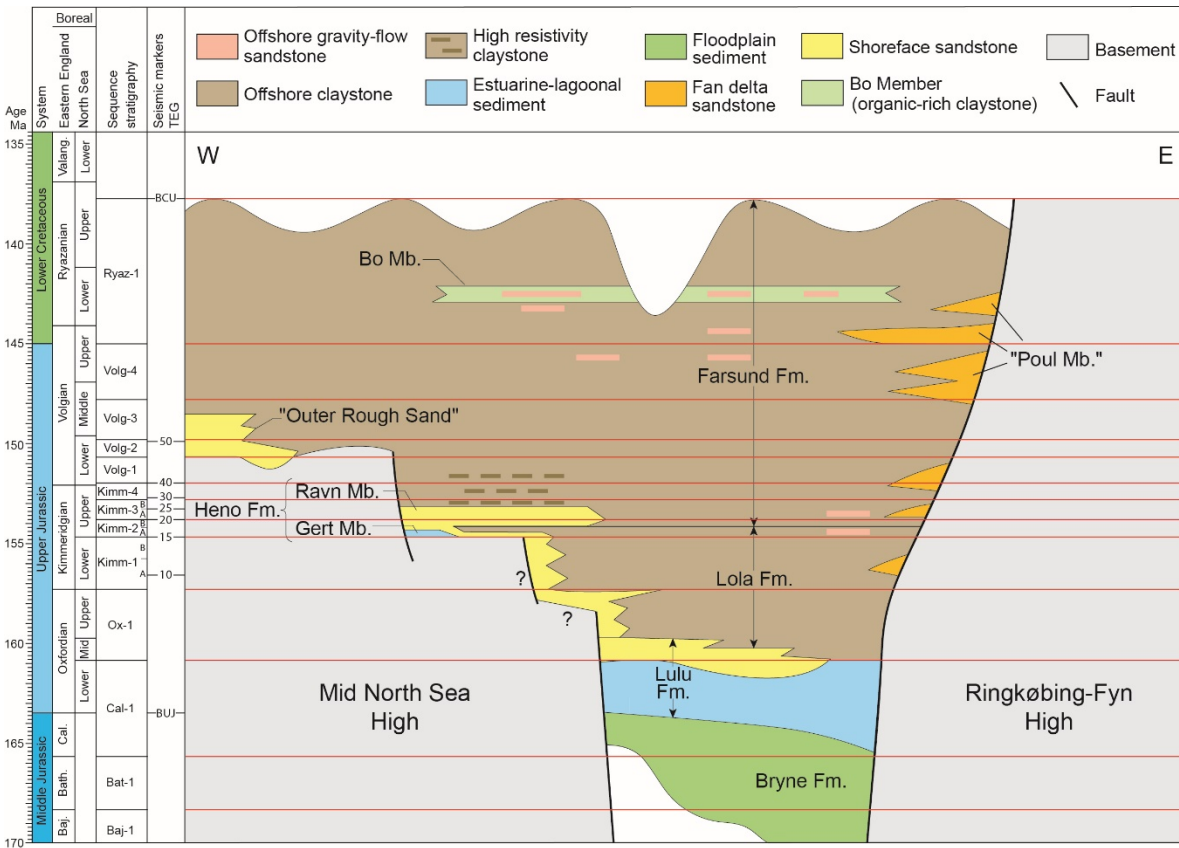


Figure 2. Lithostratigraphic scheme of the Danish Central Graben.

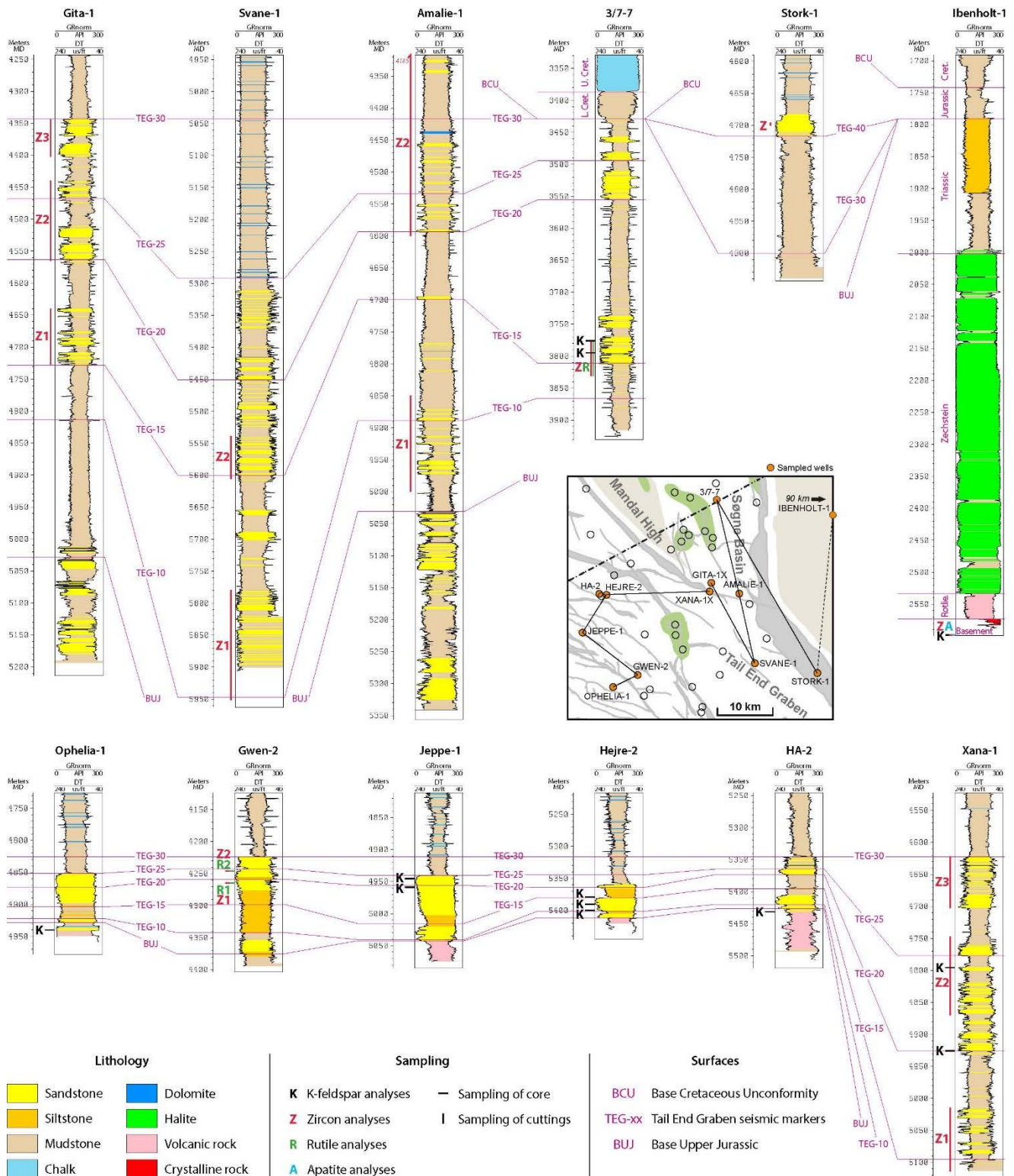


Figure 3. Well-log profile of the wells chosen for provenance analysis. The sample depths are shown for the different isotope analyses.

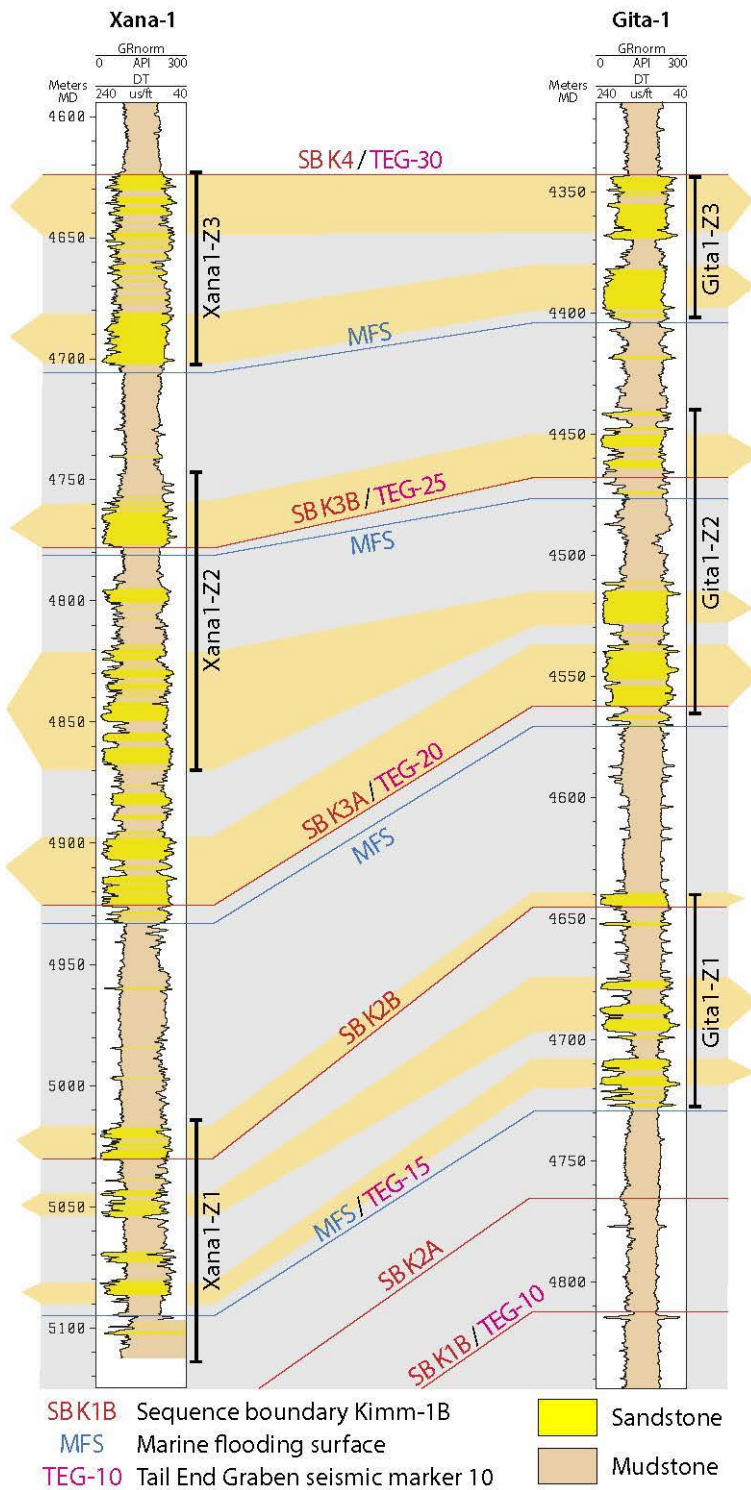


Figure 4. Well-log profile of the stratigraphic correlation of the gravity-flow sandstones in the Xana-1 and Gita-1 wells with indication of sequence stratigraphic surfaces and seismic marker surfaces (see depositional ages in Fig. 2). The depths of cuttings samples used for zircon age analysis are shown.

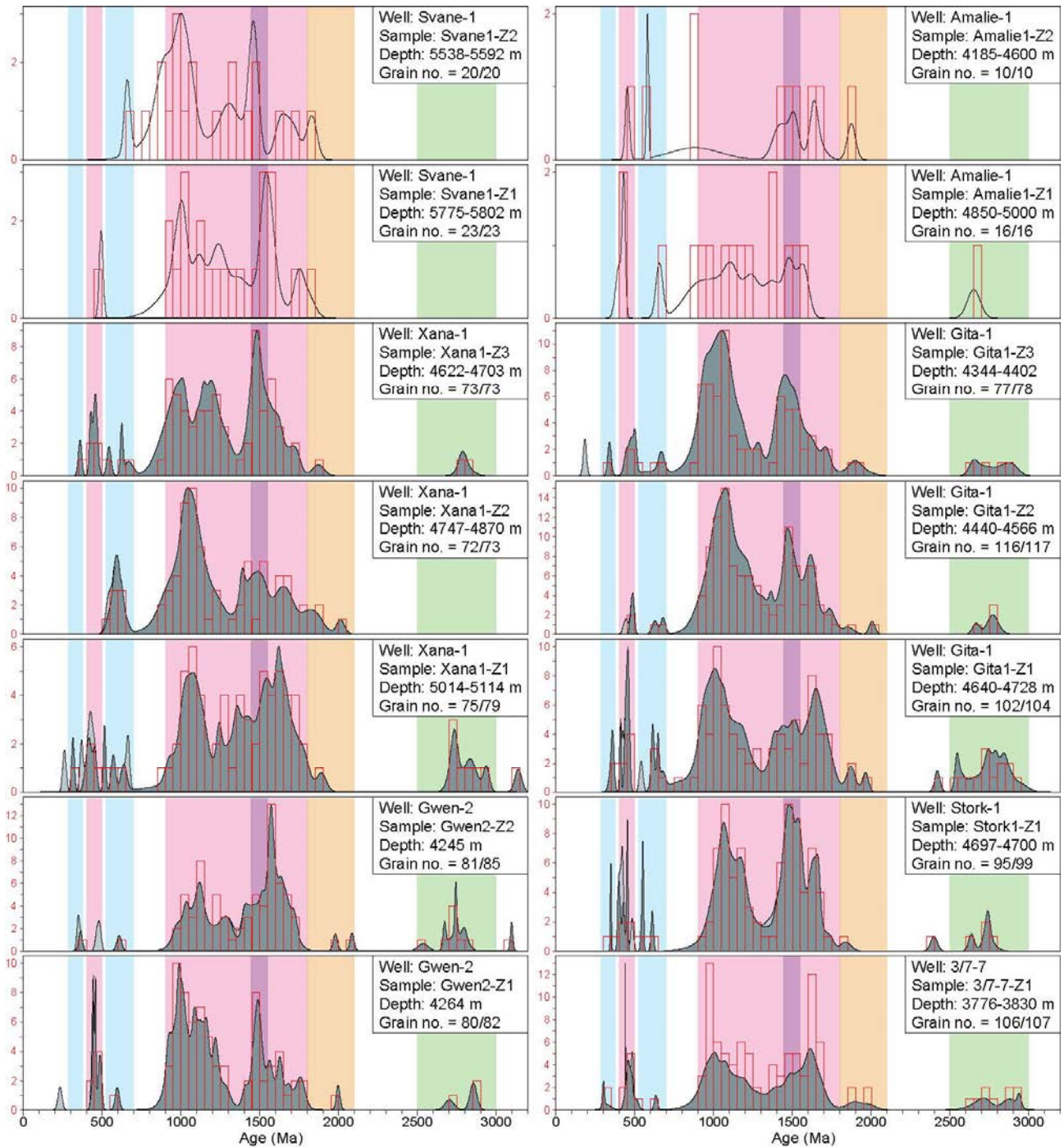


Figure 5. Zircon U-Pb ages from Upper Jurassic sediments in the greater Tail End Graben area. The results are plotted as combined histograms showing the number of concordant grains in red and as probability density distributions where the concordant ages are shown in dark grey and those with discordance >10% in light grey. The age distributions from the Svane-1 and Amalie-1 wells are not grey to signify that the number of analyzed grains is too low to be representative for the entire age spectrum in the sediments. The grain no. displays the number of employed concordant ages out of the total number of measured ages. See Fig. 6 for explanation of the colored age intervals.

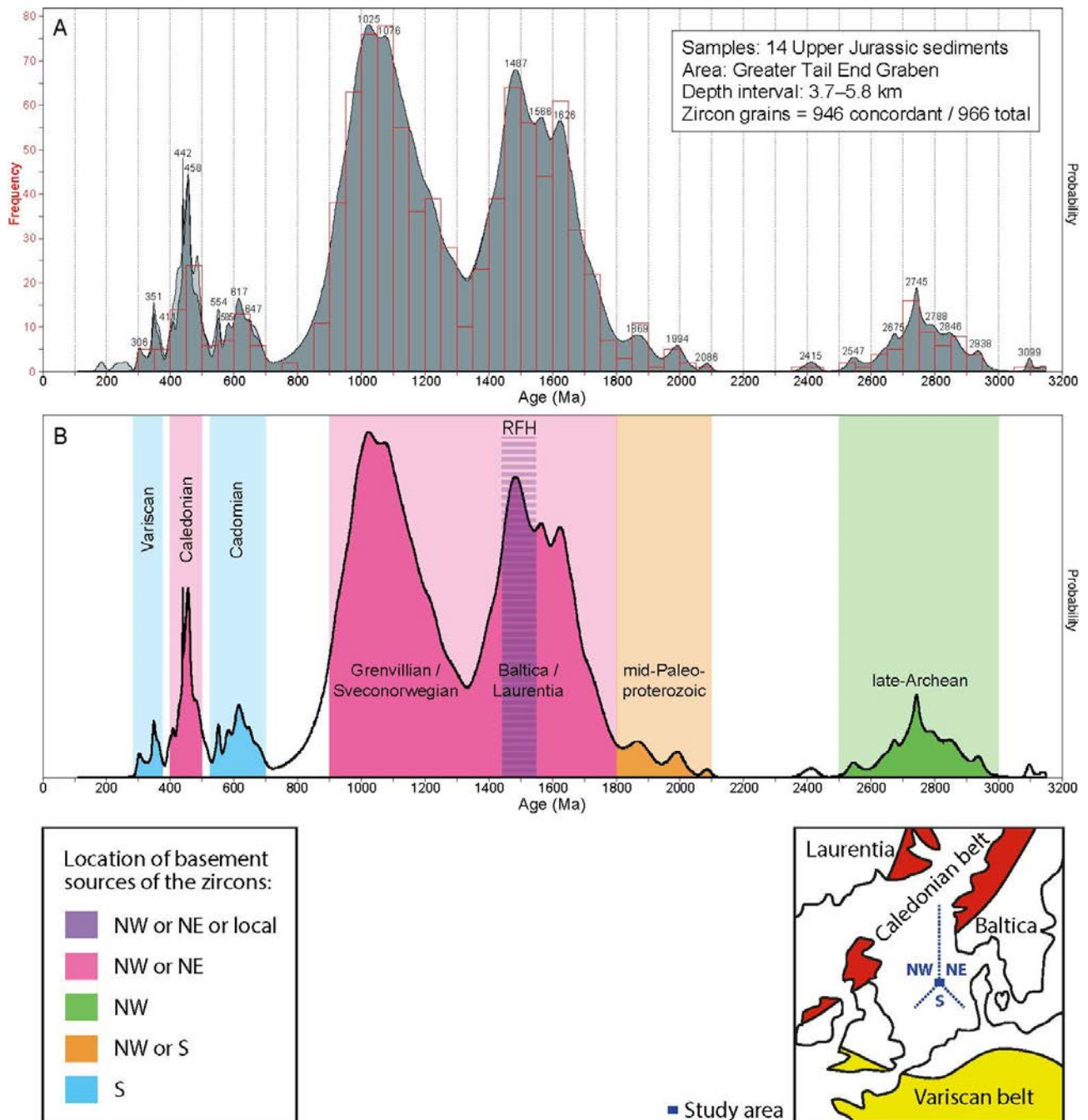


Figure 6. Compilation of all zircon U-Pb age data from Upper Jurassic sediments from this study. A: Peak ages are given in million years (Ma). B: Identification of the possible provenance areas of the age populations. The age of each zircon grain reveals its ultimate basement source, and the grains have most likely been recycled one or several times before their Late Jurassic deposition. The percentages show how large a proportion of the zircon grains have ages within each category. The basement age of the Ringkøbing-Fyn High (RFH) is here presumed to be representative of the intra-basinal basement highs.

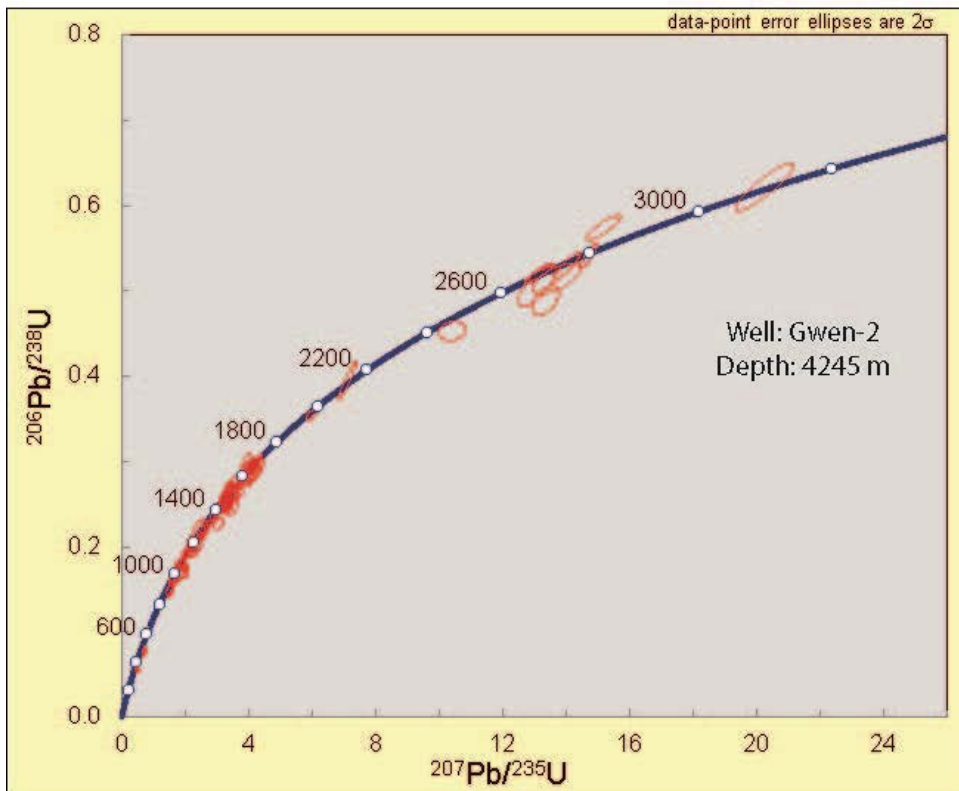
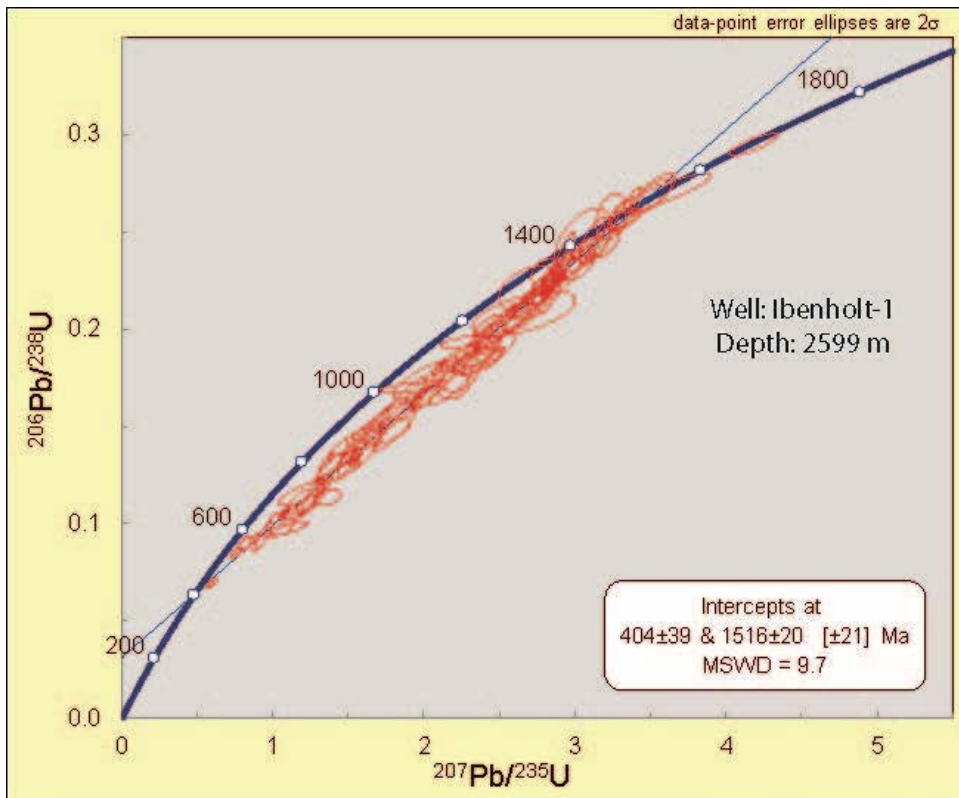


Figure 7. Concordia diagrams of zircon U-Pb data from basement in Ibenholt-1 and sandstone in Gwen-2. The concordia-intercept ages are calculated for the discordant basement ages in Ibenholt-1, whereas the detrital zircons in Gwen-2 are mostly concordant similarly to the rest of the analyzed sediments.

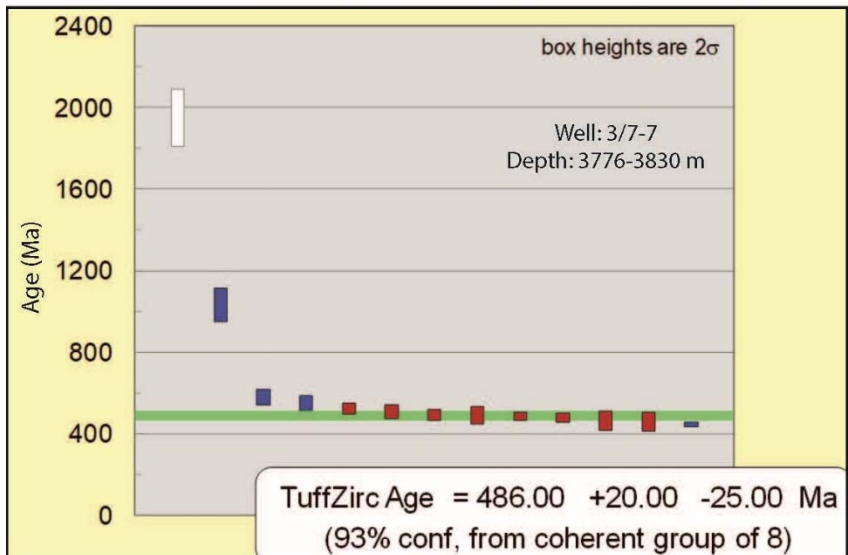
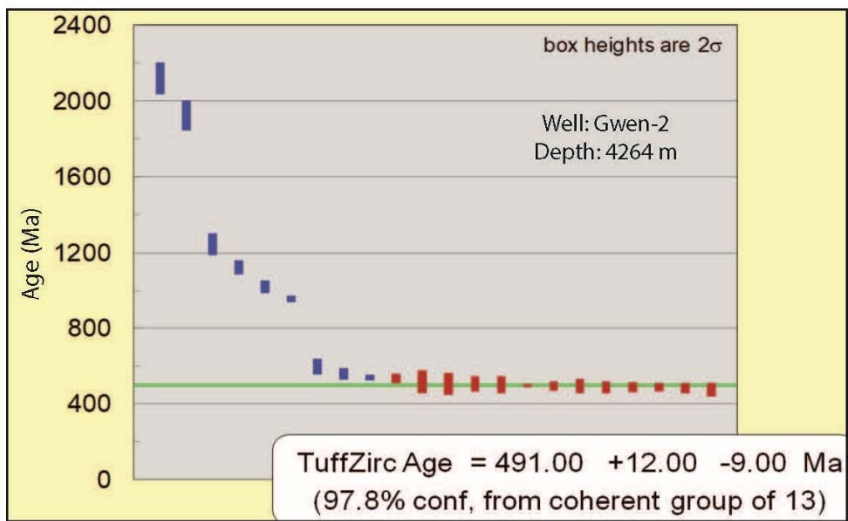
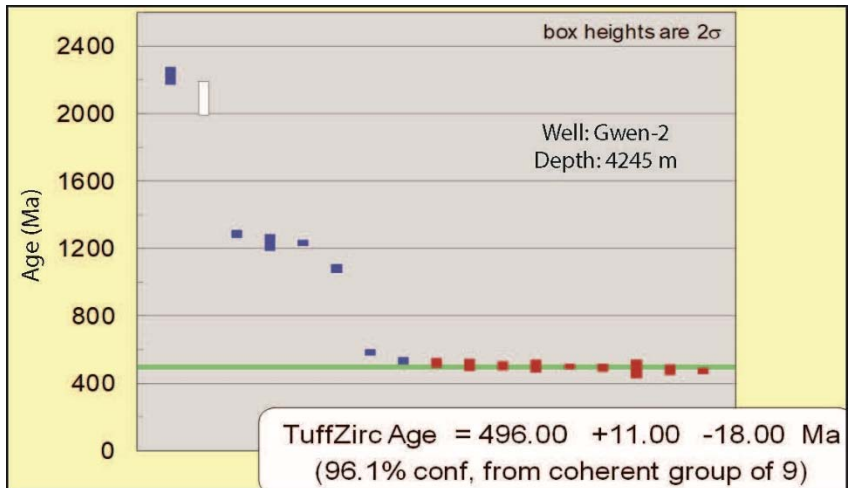


Figure 8. Rutile U-Pb ages from Upper Jurassic sediments in the greater Tail End Graben area. The internally-concordant youngest  $^{206}\text{Pb}/^{238}\text{U}$  ages (in red) are used to calculate an age (in green) of these grains. Some ages were not used in the calculation (in blue) including a few grains with anomalously high errors (in white).

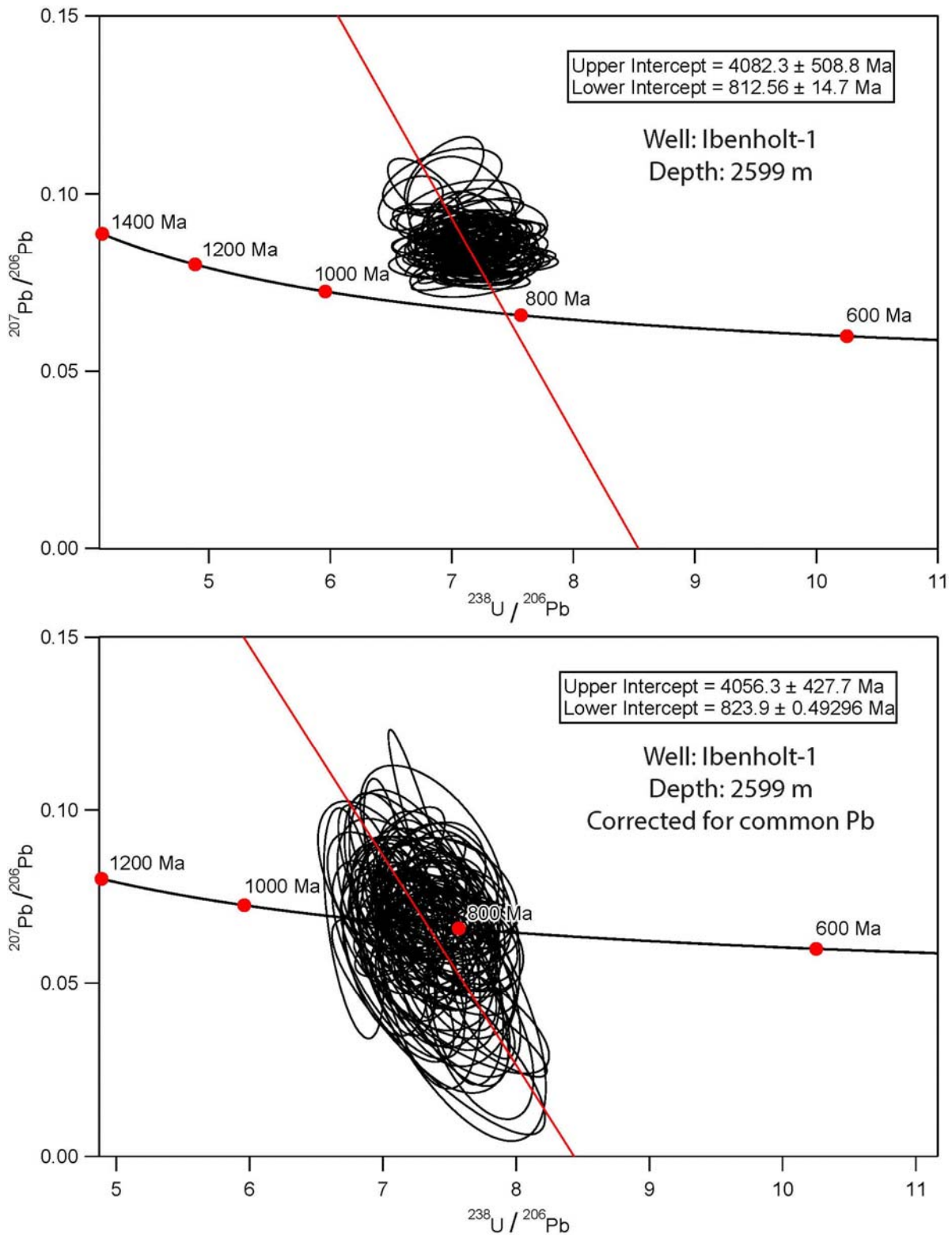


Figure 9. Concordia diagrams of apatite U-Pb data from basement in Ibenholt-1 on the Ringkøbing-Fyn High. The ages are not corrected for common Pb in the upper diagram and they are corrected in the lower diagram whereby a better estimate of the lower concordia-intercept age is made.

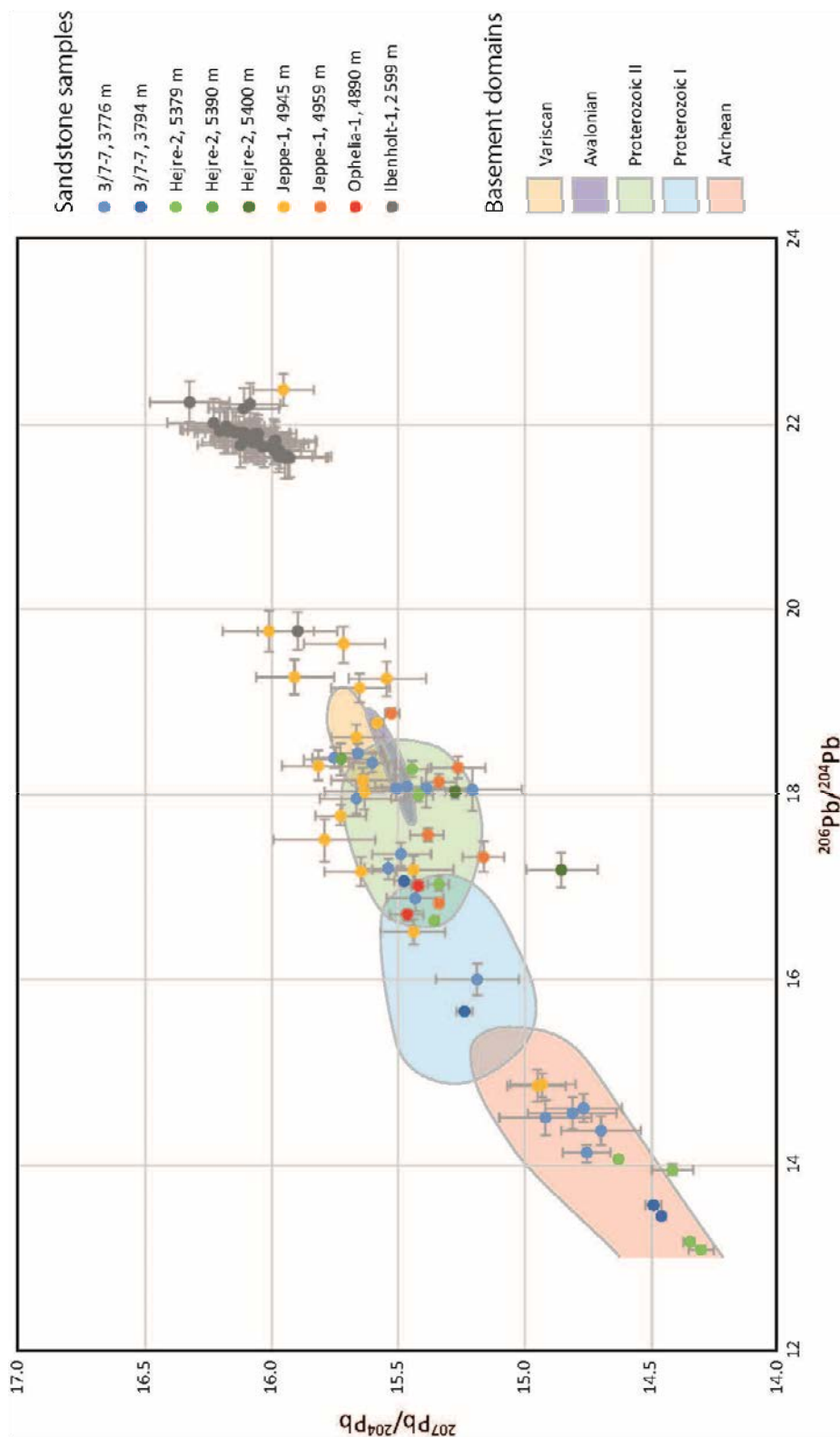


Figure 10. K-feldspar Pb-Pb isotopic signatures from Upper Jurassic sandstones in the greater Tail End Graben area, besides a basement sample from Ibenholt-1 on the Ringkøbing-Fyn High. The basement domains are from Tyrrell et al. (2007).

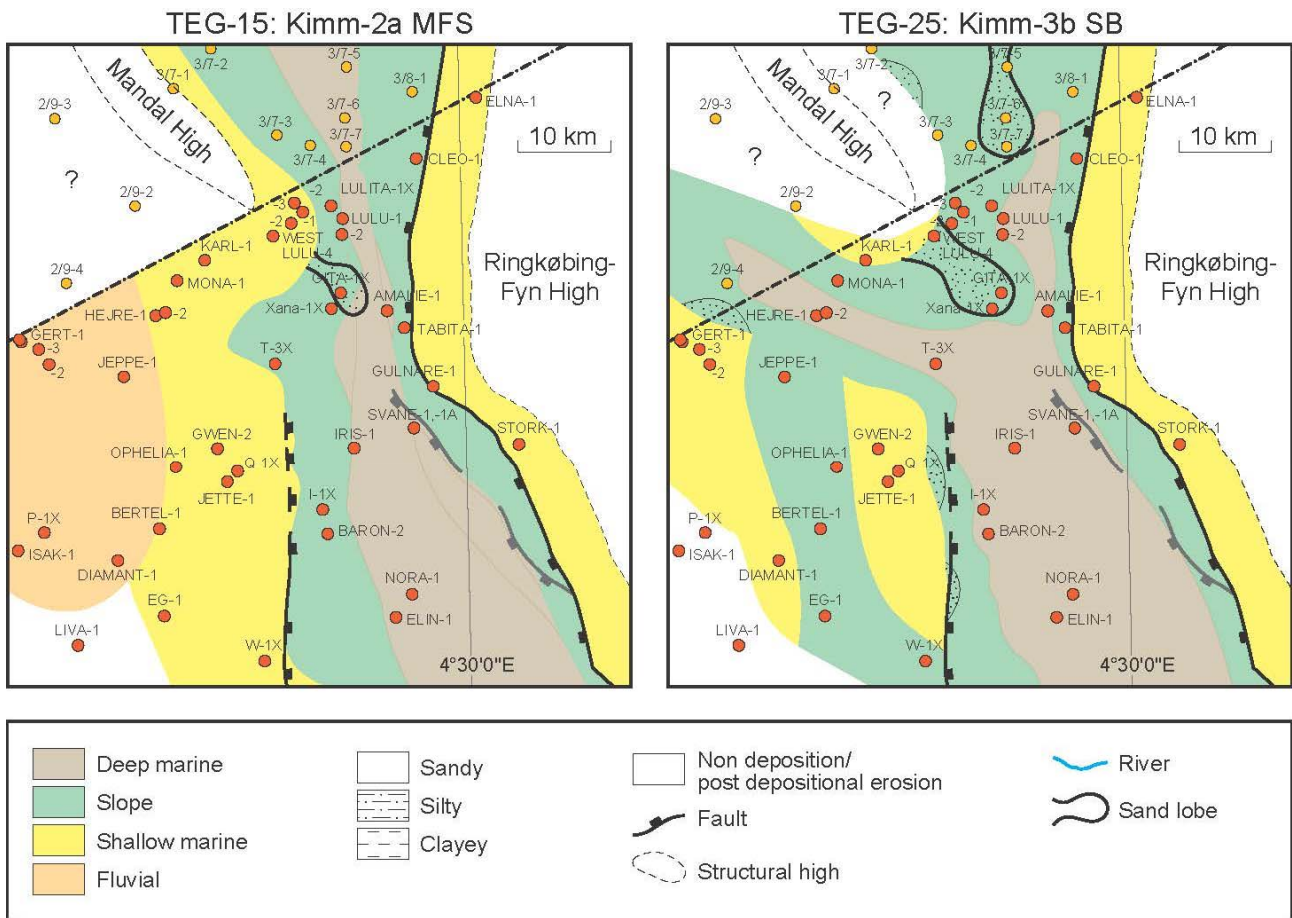


Figure 11. Paleogeographical maps showing the interpreted distribution of depositional environments for two scenarios. MFS: Marine flooding surface. SB: Sequence boundary. From Jakobsen et al. (this volume).

- Upper Jurassic rocks
  - Extent of Upper Jurassic sediments to Upper Kimmeridgian
- Lower to Middle Jurassic rocks
  - Sandstone, claystone and coal
  - M.-U. Callovian volcanic rocks
- Triassic rocks
  - Sandstone and claystone
- Permian rocks
  - Salt, anhydrite and carbonate (Zechstein)
  - Sandstone (Rotliegende)
  - As above, but with underlying volcanoclastic rocks (Rotliegende) which may subcrop locally
- Carboniferous rocks
  - Sandstone, claystone, coal and limestone
- Devonian rocks
  - Sandstone, claystone, and anhydrite
- Basement rocks
  - Metamorphic rocks
- Borders of the North Sea sectors

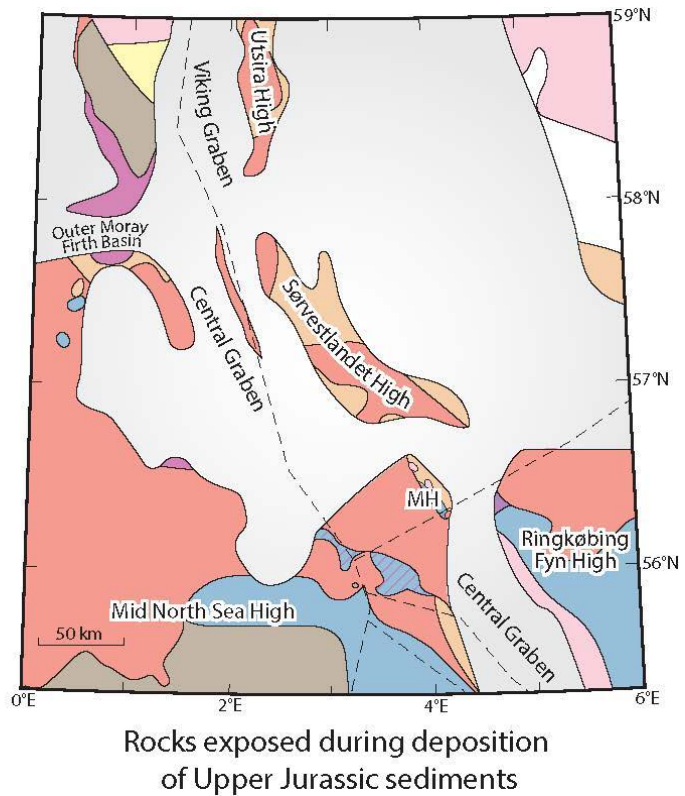
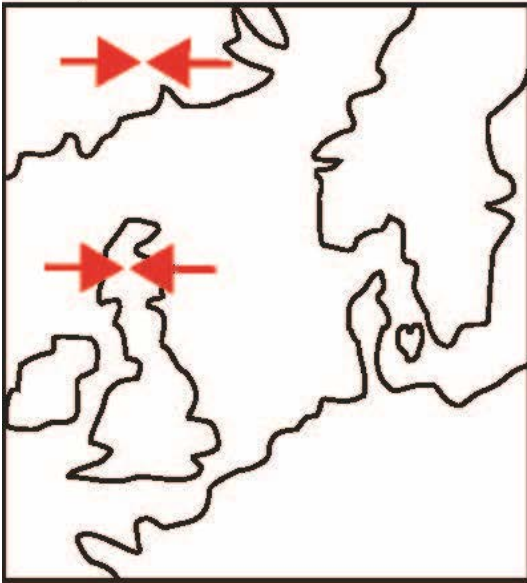
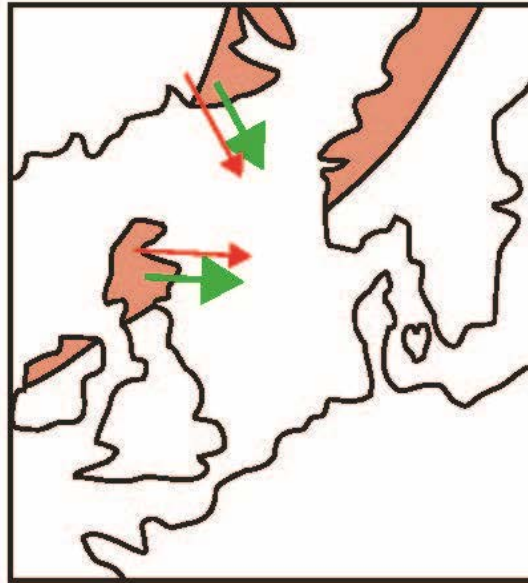


Figure 12. Map of the areas exposed for erosion in the central North Sea during the Late Jurassic. Some areas were gradually overlapped such as the Triassic sediments south of the Mandal High (MH). Modified from Weibel et al. (2010).

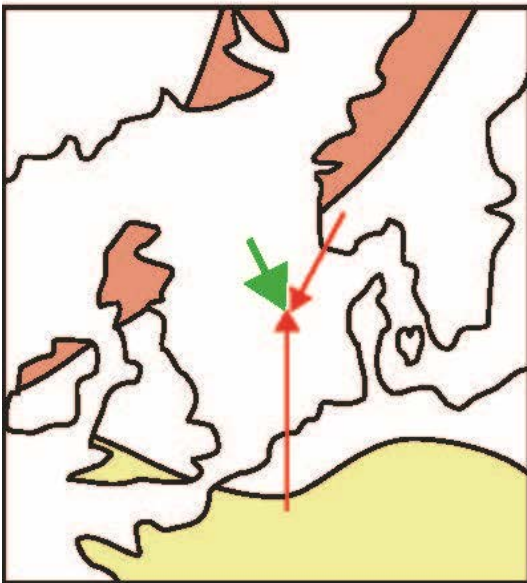
Neoproterozoic



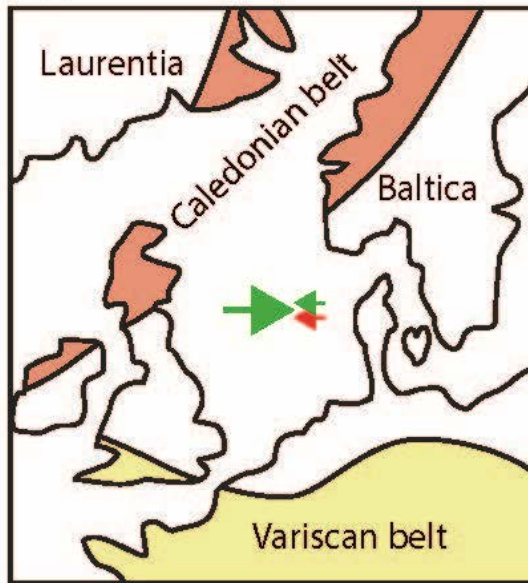
Devonian/Carboniferous



Triassic



Upper Jurassic



Transport of basement material

Transport of reworked sediment

Major sediment supply

Minor sediment supply

Figure 13. Transport history of the zircon grains in the Upper Jurassic sediments in the central North Sea interpreted on basis of their U-Pb ages.

# Review of quality and maturity of Lower Jurassic to lowermost Cretaceous petroleum source rocks in the Danish Central Graben

Niels H. Schovsbo<sup>1\*</sup>, Louise Ponsaing<sup>1</sup>, Anders Mathiesen<sup>1</sup>, Jørgen A. Bojesen-Koefoed<sup>1</sup>, Lars Kristensen<sup>1</sup>, Karen Dybkjær<sup>1</sup>, Peter Johannesen<sup>1</sup>, Finn Jakobsen<sup>1</sup>

<sup>1</sup>Geological Survey of Denmark and Greenland (GEUS), Øster Voldgade 10, DK-1350 Copenhagen K, Denmark. \*nsc@geus.dk

## Abstract

The Danish part of the Central Graben (DCG) is one of the petroliferous basins in the offshore region of Northwestern Europe. In this study a review is made of the source rock quality and maturity, based on an integrated sequence stratigraphic-geochemical investigation to identify and better understand the effective source rocks in the DCG. The review is based on 5556 Rock-Eval pyrolysis data and total organic carbon measurements from 78 wells, and 1175 vitrinite reflectance measurement from 55 wells representing the most data extensive study to date. The thermal maturity is evaluated through 1D-basin modelling. Statistical parameters (average, median, low (P90) and high (P10)) describing the distribution of TOC, HI and  $T_{max}$  are presented for the Lower Jurassic marine Fjerritslev Formation, the Middle Jurassic terrestrial-paralic Bryne, Lulu, and Middle Graben formations and the Upper Jurassic-lowermost Cretaceous marine Lola and Farsund formations in six areas in the DCG. A stratigraphic breakdown of the source rock richness in the Farsund Formation is made for selected Volgian sequences and for the lowermost Cretaceous Ryazanian sequence. The study document that the Farsund Formation is characterized by overall high, but laterally and stratigraphical variable TOC and generative potential. The oil types in the Tail End Graben contain geochemical similarities to a contribution from the topmost Farsund Formation, the Bo Member, that is particularly rich and mature in this area. Oil in the Salt Dome Province is of a subtype characterised by being very immature and lack the geochemical signature from the Bo Member. This oil type mostly originated from deeper levels in the Farsund Formation.

Three maturity maps of the upper and mid part of the Farsund Formation and one representing the Lower to Middle Jurassic formations show that the uppermost Farsund Formation are immature in the southern part of the Salt Dome Province and in the late oil mature in and near the Tail End Graben and the Søgne Basin. The middle part of the Farsund Formation are immature in local areas, but are post mature in the Tail End Graben and in the Rosa Basin within the Salt Dome Province. The Lower Jurassic and the Middle Jurassic Bryne, Lulu and Middle Graben formations is gas prone in most of the DCG.

1-D petroleum modelling show that the uppermost source rock interval (Ryaz-1) in deep wells representing the Gertrud, Søgne and Tail End grabens entered the oil window in the late Paleogene reaching main oil within the last c. 5–10 Ma.

In the DCG the depth of the oil window, as defined by VR of 0.6 %Ro, range between 2200–4500 m. Much of this depth variation can be explained by a simple depth model, the VR-PLS-model, that include the thickness of the Palaeogene to Cretaceous Chalk and Cromer Knoll groups in the VR prediction. According to this model a thick Chalk Group offsets the oil window to deeper levels. The reason for this can be attributed to thermal properties of the highly thermally conductive chalk in contrast to the underlying lesser thermally conductive clays. Higher thermal heat flow in the Salt Dome Province like also contributed to a shallow position of the oil window that occur here.

The DCG is an overpressured basin with several known pressure seals including Palaeocene clays, intra chalk seals, Lower Cretaceous shales and intra Jurassic clays. High pressure > 70 MPa and high temperatures > 150 °C (HPHT conditions) are expected to occur deeper than 3.8 km except for the Fedaa and Gertrud grabens where it is expected to be effective from around 4.7 km due to general lower temperatures here.

## **1. Introduction**

The Danish Central Graben (DCG) is part of the North Sea rift basin offshore NW Europe (Figure 1). In this mature petroleum province the main petroleum source rocks are the Upper Jurassic – lowermost Cretaceous marine shales referred to as the Farsund Formation in the DCG, the Kimmeridge Clay Formation in the UK sector and the Mandal Formation in the Norwegian part of the Central Graben (Damtoft et al., 1987; 1992; Ineson et al., 2003; Petersen et al., 2010, 2012; Verreussel et al., 2018). In the DCG, additional contribution are from Middle Jurassic coaly units of the Bryne and Lulu formations, whereas unknown contribution may come from other source rocks including the Upper Jurassic Lola Formation, the Lower Jurassic Fjerritslev Formation, Permian shales and Carboniferous coals (Damtoft et al., 1987; 1992; Petersen & Nytoft, 2007; Petersen et al., 2016).

The Jurassic-lowermost Cretaceous source rocks mainly charged the Cretaceous – Palaeogene Chalk Group wherefrom the main hydrocarbon production occur in the DCG (Figure 2). Secondary production occur from Middle Jurassic and Paleogene sandstones and more recently also from Upper Jurassic and Miocene sandstone (Goffey et al., 2018; Pedersen et al., 2018). For some time exploration of other Upper Jurassic plays have led to the discoveries of high-pressure and high-temperature (HPHT) such as the Hejre, Amalie-1, Svane-1 and Xana-1X field and discoveries (Figure 2). These discoveries were made in fan delta sandstone and offshore gravity flow deposits (Figure 3). More recently a growing interest, has been seen for also unconventional hydrocarbon resource within the Jurassic shale in the DCG and efforts to map and quantify the resource in Central Graben have recently begun as part of the project: Geological Analysis and Resource Assessment of selected Hydrocarbon systems – GARAH (<https://geoera.eu/projects/garah/>).

The first regional review of the quality and maturity of all Jurassic source rocks in the DCG was presented by Damtoft et al. (1987). Since then, the amount of source rock data and the regional stratigraphic knowledge has advanced considerably with Ineson & Surlyk (2003) being a major

hallmark. A second major advancement in our understanding was gained from the GEUS lead Jurassic Petroleum System Project (Petsys) completed in 2014 that allowed integration of the seismic, bio- and lithostratigraphic framework for the Jurassic. In this project, geochemical databases on source rock quality, maturity and oil chemistry were key deliveries, allowing detailed integrated studies to be made. The main results, however, still awaits publication albeit important contributions on sedimentology (Johannessen et al 2010) and source rock quality and maturation have been published by Petersen et al. (2010, 2011, 2012, 2013) and more recently by Ponsaing et al. (2018, submitted, in preparation).

The remaining challenge is the DCG is to provide a regional overview of the source rock quality and maturity. The present paper aims to 1) refine the geochemical characterization of the Jurassic source rock succession by integrating source rock geochemistry with sequence stratigraphic framework; 2) to map out the maturity of the Jurassic source rocks using 1D maturity models; 3) highlight the interplay of the chalk thickness and pressure on the position of the oil window as outlined by Petersen et al. (2012). An accompanying paper that compare eth source rock quality and maturity with the oil families and oil maturity (c.f. Schovsbo et al. 2018) is under preparation.

## **2. Geological setting**

The DCG is part of the Jurassic North Sea rift complex. It is a major east-dipping half-graben system, consisting of a series of minor NW-SE trending half-grabens bounded by the Coffee Soil Fault to the east and the Mid North Sea High to the west (e.g. Andsbjerg & Dybkjær, 2003; Møller & Rasmussen, 2003; Japsen et al., 2003; Petersen et al., 2011, 2012).

The lithostratigraphy for the Jurassic to Neogene in the DCG is presented in Figure 2. The Jurassic succession has been subdivided into 18 sequences based on integration of the seismic, bio- and lithostratigraphic (Andsbjerg & Dybkjær, 2003; Johannessen et al., 2010). The DCG was in the Early Jurassic characterized by a relatively slow sea-level rise and deposition of the grey, shallow-marine shales of the Fjerritslev Formation occurred (Michelsen et al., 2003; Figures 4). During the latest Early Jurassic – earliest Middle Jurassic, the Triassic and most of the Lower Jurassic succession was removed by erosion, as the area was uplifted (e.g. Andsbjerg & Dybkjær, 2003; Møller & Rasmussen, 2003). As a consequence of this Toarcian erosion, parts of the Fjerritslev Formation is not present in the DCG (Figure 3).

Mid Jurassic rifting caused fault-controlled subsidence in the east, particularly along N-S trending segments of the Coffee Soil Fault (e.g. Japsen et al., 2003; Møller & Rasmussen, 2003; Johannessen et al., 2010; Petersen et al., 2011). As a consequence of the renewed subsidence and subsequent flooding of the DCG the lower part of the Middle Jurassic is dominated by fluvial-channel sandstones assigned to the Bryne Formation whereas the upper part is characterized by a paralic sandstones, shales and coal beds, which are overlain by shore-face and back-barrier deposits. These sediments are, however, restricted to the Søgne Basin, the Tail End Graben and the Salt Dome Province (Figure 1). The paralic and marginally marine upper part is generally referred to the Lulu Formation in north and to the Middle Graben Formation in south. The base of the Middle Jurassic strata overlies the Mid-Cimmerian Unconformity or the Intra-Aalenian Unconformity (Michelsen et al., 2003; Petersen et al., 2011; Petersen & Hertle, 2018).

During Oxfordian – Kimmeridgian, deep-water conditions were established in the DCG and the marine shales of the Lola Formation were deposited. The tectonic trend shifted in the Kimmeridgian from dominantly N-S to NW-SE oriented faulting and at the same time subsidence rates increased. The shallow-marine and back-barrier sandstones of the Heno Formation were deposited on the Heno and Gertrud plateaus during the Late Kimmeridgian. The depositional area gradually extended westwards and thick mudstone-dominated marine succession of the Farsund Formation was deposited over larger areas (Figure 4). During early Volgian, the overall transgression reached the Outer Rough and Ål Basin (e.g. Andsbjerg & Dybkjær, 2003, Johannessen et al., 2010; Petersen et al., 2011, 2012). The subsidence rates were reduced radically in the latest Volgian, and the deposition of the organic rich and highly radioactive ‘hot shales’ of the Bo Member (Volgian – Ryazanian) took place in most areas of the DCG (Figure 4, Michelsen et al., 2003; Ineson et al., 2003).

The transition from the Farsund Formation to the above lying Cromer Knoll Group marks a basinwide facies change, from the black, highly radioactive ‘hot shales’ to carbonate and shelf sediments deposited in open-marine environments. This transition is generally termed the Base Cretaceous Unconformity (BCU). The boundary marks the deposits of the post-rift phase, in the DCG, that are represented by the Cromer Knoll and Chalk groups.

In the Late Cretaceous to early Paleogene, high sea level prevailed and the sedimentation shifted from siliciclastics to chalk, composed of calcareous nanofossils (Anderskov & Surlyk 2011, van Buchem et al., 2017). The tectonic regime shifted to compression tectonics. The thickness of the Chalk Group (Hidra to Ekofisk formations, Figure 2) varies from less than 200 m on inverted ridges to more than 1000 m found in local depocentres in northern Tail End Graben, the Gertrud Graben and on the Heno Plateau (Figure 5). Deep burial of the Jurassic sequence took place in the Paleocene to Neogene (Rasmussen et al., 2005). Depth to the top Jurassic ranges down to 5000 m (Figure 5).

### **3. Database, analytical methods and modelling**

#### **3.1. Source rock, pressure and temperature databases**

The source rock and vitrinite reflectance (VR) data treated here consists mostly of data produced by GEUS during the last almost four decades but also include quality controlled data reported from other sources. The TOC and Rock-Eval data consist of 5556 measurements of Jurassic – lowermost Cretaceous shales from 78 wells in the DCG picked within a cumulated 44.5 km long section. The VR database consist of 1175 samples from 55 wells. For VR the sampling in each well aims to constrain the VR-gradient and measurements are thus included from top to the terminal depth if available.

The quality of the VR measurements is quite variable. The number of VR measurements for each sample varies from 1 to 100 and the associated standard deviation may range between  $\pm 0.02$  and  $0.11$  %R<sub>o</sub> (c.f. Petersen et al., 2012). Albeit histograms of the original measurement population are available for most samples no re-assessment of the measurements has been made for this study.

312 pressure measurements, typical from a repeat formation tester (RFT) tool, are evaluated here. The data are from public available drill reports. Only data that has been quality controlled is here reported. Bore hole temperatures are evaluated from 261 bottom hole temperature measurements from 94 wells. All temperature measurements are reported from public available drill reports and have been “Horner corrected” according to the correction procedures presented by Waples et al. (2004).

Published data in the source rock and VR databases includes data presented by Thomsen et al. (1983); Damtoft et al. (1987, 1992); Østfeldt (1987); Petersen & Rosenberg (1998); Petersen et al. (1998, 2000, 2010, 2011, 2012, 2013); Petersen & Brekke (2001), Ineson et al. (2003); Ponsaing et al. (2018, submitted, in preparation). Included VR measurements outside of DCG are from Norwegian wells 2/11-7, 2/5-9 and 2/12-1; Petersen et al., 2012) that borders the northern part of the DCG (Figure 1).

### **3.2. Analytical methods**

GEUS is by far the largest data contributor to the source rock and VR data and below is a short summary of the analytical methods used at the laboratory. Both oil and water based mud systems have been used in the DCG. Of this oil based mud (OBM) systems are known to have a more severe impact on source rock data quality, if not properly removed prior to analysis (c.f. Petersen et al., 2017). In wells drilled using OBM system, preparative solvent extraction of samples prior to analysis was made. Samples were washed with several batches of dichloromethane (DCM) until the cuttings appeared clean. The 0.25–4.0 mm size-fraction was subsequently recovered by sieving and exhaustively solvent extracted for seven full days using soxhlet instrumentation and dichloromethane/methanol (93+7 vol.%/vol.%) as solvent. In wells drilled using water based mud system cuttings were washed with rinsing tap water. Examination under microscope was made to ensure that the cuttings were complete cleaned.

Since 1992 cuttings for subsequent analysis have been picked from the 1–4 mm size fraction and ground to <0.25mm for Rock-Eval type screening analysis. The selection of this size fraction minimize the impact on cavings that tend to be larger and rather irregular in shape. For older analysis no specific size fraction was used albeit typical from the <2 mm size fraction. Samples for VR measurements were not powdered but imbedded directly in epoxy.

Total Organic Carbon (TOC) content was determined by combustion in a LECO CS-200 induction furnace after elimination of carbonate-bonded carbon by prolonged HCl treatment. In-house and international standards are measured during analysis and the analytical reproducibility is 0.1 wt% TOC. Rock-Eval type pyrolysis was carried out using several types of instrumentation. Most data were produced using a Source Rock Analyzer instrument, manufactured by Humble Instruments and Services (presently Weatherford). Newer analyses were produced by a HAWK instrument (Wildcat Instruments, USA). Some old data were produced by a Rock-Eval 6 instrument or even a Rock-Eval 2 instrument. Irrespective of instrumentation, calibration was done using the IFP-160000 or IFP-55000 standard with sets of one blank and one in-house (Marl Slate) control standard being run for every 10 samples to ensure instrument stability. Based on experience, this procedure serves to assure that different generations of data are comparable.

Based on the Rock-Eval pyrolysis the Hydrogen Index (HI) is calculated from the S<sub>2</sub> yield peak by normalising the S<sub>2</sub> yield by TOC (S<sub>2</sub> / (% TOC/100)). T<sub>max</sub> represent the temperature at which the maximum rate of the hydrocarbon generation (S<sub>2</sub>) occurs. The S<sub>1</sub> peak is not considered here due to the mixed dataset of extracted and non-extracted samples.

VR measurements were carried out following standard procedures (Bustin et al., 1989). Analysts were all accredited and certified by the International Committee for Coal and Organic Petrology (ICCP). The measurements were conducted using a Leitz Orthoplan reflected light microscope equipped with a 50x objective and the Diskus Fossil System (Hilgers Technisches Buero). VR readings were taken at 546 nm (monochromatic light). Before measurement the microscope was calibrated against a YAG 0.903 %R<sub>o</sub> standard with integrated optical zero standard.

### **3.3. Statistical and regression analysis**

The TOC, HI and T<sub>max</sub> frequency distributions are characterized by being skewed and representative statistical properties cannot be calculated by assuming a normal distribution. Instead, to provide the best descriptive statistical properties modelling of the cumulative density frequencies (CDF) were made assuming a log-normal distribution mode. Fitting was made with the SigmaPlot® version 14 from Systat Software that allows iterative modelling to be made in order to obtain the mean and standard deviation of the log-normal distribution. The match of the data and model was evaluated from the goodness of fit (r<sup>2</sup>). All accepted models had r<sup>2</sup> > 0.98. Based on the obtained mean and standard deviation of the log-normal distribution the population mean, standard deviation, and various percentiles (P) of the population were calculated.

The Partial Least Square (PLS) multivariate regression method was used to examine relationships between VR and various depth markers in order to develop predictive models. The PLS regression allows direct correlations to be modelled between y and the multivariate X data, compensating for debilitating co-linearity between x-variables (Esbensen & Swarbrich 2018). A PLS regression model depend on proper validation that is here based on a test set prepared before modelling by randomly splitting the data into two independent data sets, i.e. the training versus the test set, securing a realistic prediction performance validation (Esbensen & Geladi 2010; Esbensen & Swarbrich 2018). All data was auto-scaled [X-X(avr)/std] and the modelling was performed in the software package Unscrambler® 10.5 by CAMO.

### **3.4. Basin modelling**

Basin modelling is made with the PetroMod® software, Integrated Exploration Systems GmbH, Aachen, Germany; v2015.2. The software is used as a tool for integration of geological, geophysical, geochemical and petrophysical data and for testing hypotheses regarding origin and evolution of the petroleum resources. In such models the thermal maturity of the source rock succession is crucial when timing and extent of source rock maturation is assessed (e.g. see Magoon & Dow, 1994 for case studies).

The main object of the basin modelling within this study, was to examine the maturity of the DCG using 1-D basin maturity modelling on 46 wells and 4 pseudo wells. Based on the ‘most likely’ input parameters the regional maturity trend and the position to the oil window was investigated, where the oil window is defined as EASY%Ro= 0.60–1.3%, and gas window as Easy%Ro =1.3–4.0%. The 1-D models uses a tectonic-stratigraphic framework, where each well sequence is divided into layers or events allowing the 1-D PetroMod to quantify all important basin processes as a function of time, including maturity parameters such as temperature and VR. Event-splitting of the Upper Jurassic – lowermost Cretaceous is based on a sequence stratigraphy (Figure 2). The Lower Cretaceous is treated as one event, i.e. the Cromer Knoll Group, while the Chalk Group is divided into two events. The Post Chalk Group is subdivided into 11 Tertiary events based on maps published by Rasmussen et al. (2005) and three Quaternary events, based on an in-house subdivisions. The adapted modelling concept, were adjusted for the Farsund Formation, by applying the Pepper & Corvi (1995) organofacies classification. Absolute ages for the Mesozoic are based on the Chronostratigraphic scheme by Gradstein et al. (2012, 2014); absolute ages for the Tertiary and Quaternary are based on in-house evaluations.

The PetroMod standard LithoFacies library is used and is based on adapted information on depositional facies variation and available information. The boundary conditions are paleo-water-depth, sediment water interface temperature and basal heat flow. The boundary conditions define the basic energetic conditions for the temperature development for all layers, especially the source rock intervals and, consequently, for the maturation of organic matter through time. The paleo-water-depths through time were constructed using information on depositional settings, paleo-environmental information from wells and sediment thickness maps.

## **4. Results**

In order to allow differences in source quality and maturity to be illustrated, the analysed wells (Table 1, Table 4 and Table 5) in the DCG is divided into six areas with as similar basin development as possible (c.f. Japsen et al., 2003; Møller & Rasmussen 2003; Rasmussen et al., 2005). With reference to structural elements presented in Figure 1 the areas includes: 1) the Salt Dome Province including the Rosa and Poul basins, 2) the Tail End Graben including the Arne-Elin Graben, 3) the Feda Graben and Gertrud Plateau/Graben including the Lindesnes and Gert ridges, 4) the Søgne Basin, 5) the Heno Plateau and 6) the Outer Rough including the Ål Basin and the Mid North Sea High. For some wells (see Table 1) the division between the areas are somewhat arbitrary pending on emphasis on the Jurassic or Cretaceous development. This include the Jette-1, Q-1, Gwen-2 and Diamant-1 include here in the Feda Graben (Table 1).

### **4.1. Source rock quality and $T_{max}$ variation within the DCG**

Within each of the six areas outlines above the source rock quality and maturation for following formations are presented (see Figure 2 for stratigraphy):

- 1) The Lower Jurassic (Hettangian – Pliensbachian) marine Fjerritslev Formation

- 2) The Middle Jurassic to lowermost Upper Jurassic (Aalenian – Oxfordian) floodplain to estuarine Bryne, Lulu and Middle Graben formations (hereafter treated together as “Middle Jurassic source rocks”)
- 3) The Upper Jurassic (Oxfordian – Kimmeridgian) marine Lola Formation
- 4) The Upper Jurassic to lowermost Lower Cretaceous (Kimmeridgian – Ryazanian) marine Farsund Formation.

With respect to the Farsund Formation, the source rock data are also tabulated for specific stratigraphical intervals including the Volg-1, the Volg-4 and the Ryaz-1 sequences as these are known to have better than average source rock quality (Ineson et al., 2003; Petersen et al., 2010, 2017; Ponsaing et al., 2018, in review). For each of the six areas the source rock characteristics are presented for each formation as histograms (Figures 7-9) and as population statistical parameters (mean, median (P50), low (P90) and high (P10)) in Table 3. The population statistics are based on modelled log-normal distribution that has been fitted to the cumulative frequency distributions as shown in Figure 10 for the Farsund Formation. The mean and standard deviations of the log-normal distribution together with the goodness of fit ( $r^2$ ) between data and the modelled distribution are presented in Table 2.

The source rock richness is evaluated from a combination of TOC and HI with respect to the present day maturity as indicated by the  $T_{max}$ . The nomenclature follows Peters (1986); TOC below 0.5 wt% is considered poor, between 0.5–1.0 wt% fair, between 1.0–2.0 wt% good and above 2.0 wt% as very good. For evaluation of the generative potential we use the HI (evaluated from immature sample); HI between 0–150 mg HC/g TOC is considered as gas prone; between 150–300 mg HC/g TOC as mixed oil – gas prone and above 300 mg HC/g TOC as oil prone. The top of oil window is assumed to be at a  $T_{max}$  between 435–445 °C (equivalent of 0.6 % $R_o$ ) and the bottom of the oil window is assumed to be at  $T_{max}$  of 470 °C (equivalent of 1.4 % $R_o$ ).

#### 4.11. Fjerritslev Formation

The Fjerritslev Formation was originally defined in the Danish Basin where its maturity and source rock properties are well-described (Thomsen et al., 1987; Petersen et al., 2008). In the DCG the formation is known only as erosional remnants due to extensive mid-Jurassic erosion. Maximum thickness drilled is 257 m found in the Edna-1 well (Michelsen et al., 2003). The formation is dominated by dark grey slightly calcareous claystone with the lower parts being more calcareous and silty (Michelsen et al., 2003). The Fjerritslev Formation has been drilled in both the Salt Dome Province (Figure 7) and on the Heno Plateau (Figure 9). The unit is probably present also in the Tail End Graben, but has not been drilled here (cf. Figure 4a).

The TOC content and source rock properties in the Heno Plateau (wells: Edna-1, Skarv-1) is good with average TOC of 1.3 wt% (median 1.0 wt%). The average HI is 64 mg TOC/g TOC but as the formation is mature (average  $T_{max}$  447 °C) this hampers direct evaluation of the generation potential. In the Salt Dome Province (wells: Jens-1, John Flanke-1, M-8X, N-22X, Olga-1X, O-1X, U-1X), the

formation attains better source rock properties with average TOC values of 2.1 wt% (median of 2.0 wt%). The formation is immature (average  $T_{\max}$  436 °C). The HI distribution is, however, bimodal and no meaningful formation average can be calculated. The formation includes oil prone beds as the HI range up to more than 400 mg HC/g TOC (Figure 7). Since high HI values are yielded by extracted cutting samples, these values are assumed to reflect the kerogen composition of the rock. A mixed oil-gas generative potential is thus assumed for the formation.

#### 4.12. Middle Jurassic source rocks

The Bryne, Lulu and Central Graben formations are treated here as one unit with respect to the source rock evaluation. Of these formations, the source rock quality of the coals and coaly shales of the Bryne and Lulu formations have recently been reviewed by Petersen & Hertle (2018) from the Harald-Lulita-Trym area (Figure 1, wells: West Lulu-1 – 3, Lulu-1, Lulita-1, 3/7-4) and we refer to this publication for specific details on the occurrence in this area.

The Middle Jurassic may attain thickness up to several hundred meters and include both marine to paralic sandstones interbedded with coaly claystone and coals seams up to five meters in thickness (Michelsen et al., 2003; Andsbjerg & Dybkjær, 2003; Petersen & Hertle, 2018). Deposition took place in a variety of environments including fluvial, floodplain, lacustrine and estuarine (Figure 4b). The Middle Jurassic source rocks have been sampled in all areas except for the Feda and Gertrud grabens and the Outer Rough (Table 3). Except for the Søgne Basin the samples generally show < 20 wt% TOC (Figures 7–9) and represent rather thin coaly beds or sediments with disseminated coal. The average TOC range from good to very good (average 1.4–3.3 wt%) with lowest value measured in the Tail End Graben. Here only 24 sample exist from the Nora-1 well. Because of this, no population statistics could be established for the  $T_{\max}$  (Table 3). In the Søgne Basin, a bimodal TOC distribution is seen. For samples with TOC < 20 wt% the average is 2.2 wt% and for samples with TOC > 20 wt% the average is 69.6 wt%. The average HI of the Middle Jurassic source rocks range from 94–171 mg HC/g TOC with the highest values measured in the mature Søgne Basin ( $T_{\max}$  444 °C). Restoring the source rock to its original HI values (pre generative level) suggest that these were around 270 mg HC/g TOC (Petersen & Hertle, 2018) indicating a mixed oil-gas generative potential.

#### 4.13. Lola Formation

The Lola Formation is present in the eastern and southern parts of the DCG where it may attain a thickness of c. 1 km (Michelsen et al., 2003). The formation consists of dark olive-grey to grey claystone deposited in a low energy offshore open marine environment. The average TOC content is fair to good as it varies between 1.2–2.1 wt% (median 0.7–1.7 wt%) with highest concentrations reached in the Heno Plateau and lowest in the Tail End Graben (Table 3). The average HI in the immature Salt Dome Province (average  $T_{\max}$  434°C) is 138 mg HC/g TOC suggesting a gas prone nature of the kerogen, which is in agreement with previous assessments (Michelsen et al., 2003; Ponsaing et al., 2018).

#### 4.14. Farsund Formation

The Farsund Formation is present throughout the DCG and correlates partially with the Kimmeridge Clay Formation and the Mandal Formation in the UK and Norwegian parts of the North Sea (Michelsen et al., 2003, Petersen et al. 2010, 2013; Verreussel et al., 2018). The thickness may exceed 3 km in the Tail End Graben. The Farsund Formation consists of medium to dark grey claystone with numerous thin beds of brownish dolomite. Deposition took place in a relatively deep marine environment and sandstones only occur either as turbidites or as gravity flow deposits especially towards the deeper parts of the basin (Figure 4).

Within the uppermost Jurassic to lowermost Cretaceous sequences (sequence Volg-4 – Ryaz-1, Figure 2) of the Farsund Formation a unit with a conspicuously high gamma ray response occurs, the Bo Member (in older literature the “Hot Unit”, Michelsen et al., 2003). The member is present throughout the DCG albeit it is typically absent (eroded) on structural highs. Thicknesses varies from less than 10 m in the Salt Dome Province to more than 100 m in the Tail End Graben (Ineson et al., 2003). The Bo Member is dominated by black to dark-brown laminated claystone deposited in a low-energy oxygen-deficient environment (Michelsen et al., 2003).

For the entire Farsund Formation the average TOC ranges from good to very good (average 1.8–3.5 wt%, median 1.4–3.0 wt%) with the lowest values in the Søgne Basin and the highest values in the Feda and Gertrud grabens (Table 3). The average HI of the Farsund Formation in the immature Salt Dome Province is 228 mg HC/g TOC, suggesting an overall mix oil–gas generative potential, which is in agreement with previous assessments for this area (Damtoft et al., 1987, 1992; Petersen et al., 2012).

The lowermost Cretaceous (Ryaz-1) part of the formation has very good TOC values (TOC average: 3.6–5.6 wt%, median 3.2–4.4 wt%) with highest values reached on the Heno Plateau and lowest values in the Salt Dome Province (no occurrence in the Søgne Basin and Outer Rough). The HI in the immature Salt Dome Province (average  $T_{\max}$  428°C) is 364 mg HC/g TOC suggesting oil prone kerogen. A high average HI index (339 mg HC/g TOC) also characterises the interval in the early mature Feda and Gertrud grabens (average  $T_{\max}$  439°C) and Heno Plateau (average  $T_{\max}$  438 °C). On the Heno Plateaus the HI range up to 628 mg HC/g TOC (P10) suggesting that the HI was more rich in these areas initially and thus that a considerable regional variability in the oil richness exist. On the Heno Plateau the TOC even range up to 13 wt% (P05, Figure 11).

The Volg-4 sequence shows almost the same overall source rock richness on the Heno Plateau as the Ryaz-1 sequence but for other areas, the Ryaz-1 richness is not matched by the Volg-4 sequence (Figure 11). In general, the Volg-4 interval range between good – very good TOC values (mean 1.9–4.9 wt%, median 1.7–4.6 wt%). The lowest TOC content is measured in the Salt Dome Province where it is very close to the average values of the Farsund Formation. The HI in the immature Salt Dome Province suggest a mixed gas-oil prone generative potential (average 222 mg HC/g TOC). However, the HI in the more mature parts of the DCG is similar to that of the immature Salt Dome Province, suggesting again an initially unequal distribution in oil richness within the DCG.

For the Volg-1 sequence, only the Feda and Gertrud grabens and the Heno Plateau have very good TOC content (average 3.2–3.5 wt%, median 2.9–3.2 wt%). Otherwise, this interval has only good TOC levels as seen in the Tail End Graben (mean 1.8 wt%). In the immature Salt Dome Province the average HI is only 165 mg HC/g TOC, suggesting a rather limited oil generating potential. In the mature and TOC rich basin areas, the average HI range between 168–194 mg HC/g TOC suggesting a higher initial oil generative potential was associated with this unit in these areas compared to the Salt Dome Province (Figure 11, Table 3).

In the Farsund Formation excluding the Volg-1, Volg-4 and Ryaz-1 sequences mentioned above (termed “Farsund other” in Figure 11 and Table 3) the average TOC content vary from 1.6–3.4 wt% with the lowest values measured in the Søgne Basin and the highest in the Feda and Gertrud grabens (Table 3). The second lowest TOC is in the immature Salt Dome Province. Here the average HI is 178 mg HC/g TOC indicative of a mixed oil–gas generative potential.

#### 4.2. Fluid pressure

The DCG is an overpressured basin with several known pressure seals including Palaeocene clays, intra chalk seals, Lower Cretaceous shales and intra Jurassic clays. This leads to rapid fluid pressures build-ups and mean fluid pressures that generally are considerably higher than hydrostatic (Japsen 1998; Dennis et al., 2005; Vejbæk 2008; Petersen et al., 2012). The pressure regimes of the analysed wells (Table 4) all deviate from the general hydrostatic pressure system represented by a gradient of 9.8 KPa/m (Figure 12a). The pressure measurements fall on a common mean fluid pressure versus depth trend that is characterised by a gradient of 24.9 KPa/m (1.1 psi/ft) ( $r^2 = 0.97$ , Figure 12a). This gradient is also slightly higher than the generally assumed lithostatic pressure gradient of 22.6 KPa/m. As a consequence of the faster rise in fluid pressure, the relative difference between fluid pressure and lithostatic pressure decrease; between 2.0–2.5 km the fluid pressure is 40% less than the lithostatic pressure, between 2.5–4.0 km it is 25% less than the lithostatic pressure and at greater depth it is 10% less or almost identical to the lithostatic pressure in the Svane-1 well (3% less than lithostatic pressure). The pressure profile from the wells Jens-1 (Salt Dome Province), Nora-1, (Tail End Graben), Amalie-1, Xana-1X (both Søgne Basin), Gert-1 and Hejre-1 (both Feda/Gertrud Graben) are quite similar as all have a fluid pressure just 10% lower than the lithostatic pressure within the deepest parts (Figure 12).

The occurrence of pressure seals leads to the formation of pressure barriers. To illustrate the effects of these pressure barriers on the pressure–depth relationship, the fluid pressure is also plotted with reference to the top of the Chalk Group (Figure 12b), the base of the Chalk Group (Figure 12c) and the BCU (Figure 12d). No pressure data from post-Chalk Group sediments are included, and the pressure measurements plotted with respect to the top chalk surface (Figure 12b) therefore do not reveal any pressure increase in the topmost part of the hole. When plotted relative to the base of the Chalk Group (Figure 12c), we observe that pressure regime of the Chalk Group reflects the expected hydrostatic trend. Conversely, immediately below the base of the Chalk Group, a distinct increase in fluid pressure is observed in several wells; e.g. the Iris-1 well (Tail End Graben) and the West Lulu-1 well (Søgne Basin). With respect to the BCU, we commonly observe a marked increase in the fluid

pressure somewhat below this structural element; e.g. 100 meters below BCU in the Jens-1 well. Utilizing more data than shown in Figure 13, Carr & Petersen (2004) and Petersen et al. (2012) also showed that the fluid pressure clearly increases below the BCU in the Amalie-1, Hejre-1, Lulita-1, and Svane-1 wells (Figure 12d).

### 4.3. Vitrinite reflectance

A total of 1175 samples from 55 wells have been analysed (Table 1). The VR measurements exhibit a strong statistically significant ( $r^2=0.82$ ,  $n=1175$ ) linear increase with depth when plotted on a semi-logarithmic scale as is customary done for this type of data (Figure 13). Based on the relation in Figure 13 a general and regional model for the DCG can be established according to equation 1:

Regional VR-model

$$VR (\%R_o) = 10^{(0.000122x - 0.617)} \quad (\text{Equation 1})$$

where x is vertical depth below seafloor in m.

The VR slope intercept at surface between 0.1–0.25 %R<sub>o</sub> as expected for non-uplifted basis (see also Petersen et al., 2017). There is, however, a considerable spread around the correlation line amounting to about 1500 m ( $\pm 750$  m) for each R<sub>o</sub> value (Figure 13a). For the VR interval corresponding to earliest oil window and to mid oil window (0.6–0.8 %R<sub>o</sub>) the range in depth is even higher. The depth range for a R<sub>o</sub> measurement of 0.6% is thus considerable as it occurs between 2200–4500 m (Figure 13a). In general terms, the shallowest depths occur in the Salt Dome Province (wells: Bo-1X, M-8X) and the deepest in the Søgne Basin (Gita-1 well) and the Feda and Gertrud grabens (Jeppe-1 well).

The depth range of the 0.5–0.8 %R<sub>o</sub> interval is reduced somewhat if the sample depth is plotted with reference to the top Chalk Group, the base of the Chalk Group or the BCU (Figure 13). This suggests that the part of the depth of the oil window reflect differences in the subsidence history notably the depth of the top and base Chalk Group. It appears that the top of the Chalk Group is immature to slightly mature as the range in VR at the top of the Chalk Group is between 0.3–0.6 %R<sub>o</sub> (Figure 13b). In a similar manner, the base of the Chalk Group is typically within the oil window (0.4–0.8 %R<sub>o</sub>, Figure 13c). For the Jurassic interval the range in VR is 0.4– 1.0 %R<sub>o</sub> with lowest measured in the Salt Dome Province and the highest in the Tail End Graben (Figure 13d). The depth range of the oil window (i.e. 0.6 %R<sub>o</sub>) suggests that it lies up to 1000 m below the BCU in the Salt Dome Province whereas for the remaining areas, the top of the oil window lies either slightly above or within the topmost 200 m of the Jurassic interval (Figure 13d). These observations are in-line with the T<sub>max</sub> variation (Figure 11) where the Farsund Formation in the Salt Dome Province was also shown to be immature and only the deeper stratigraphical levels attained average T<sub>max</sub> above 435 °C (Table 3).

#### 4.4. Conceptual modelling of VR based on the relative distance to depth references

Petersen et al. (2012) has shown that the increase in VR with depth is not just a function of depth itself, but also of the thickness of the Chalk Group and the level of overpressure. This is very similar to what is learned from Figure 13a-d and a series of conceptual models has been made, utilizing the depth below seafloor, the depth below top and base of the Chalk Group and the base of the BCU as reference. For modelling, we applied the PLS regression method as described in section 3.3.

In the final PLS VR-model presented in Figure 14, a one-component model on the depth variables predicts the VR with satisfactory validation results as seen in the prediction versus reference plot in Figure 14c (slope 0.87;  $r^2 = 0.87$ ). This may suggest that the PLS VR-model leads to better VR estimates than normally achieved from any conventional depth plots such as those presented in Figure 13.

By reorganisation of the depth references, the PLS VR-model can be expressed as a modification of the regional VR-model (equation 1) as:

PLS VR-model:

$$VR (\%R_o) = 10^{(0.000126 x - a)} \quad (\text{Equation 2})$$

where  $x$  is depth below sea floor in m. The constant  $a$  is calculated for location of interest as:

$$a = 0.339 + 3.24 \cdot 10^{-5} \cdot \text{Chalk}_{\text{top}} + 3.11 \cdot 10^{-5} \cdot \text{Chalk}_{\text{base}} + 3.15 \cdot 10^{-5} \cdot \text{BCU} \quad (\text{Equation 3})$$

where  $\text{Chalk}_{\text{top}}$  is the depth in m below seafloor of the top of the Chalk Group,  $\text{Chalk}_{\text{base}}$  is the depth in m below seafloor of base Chalk Group and BCU is the depth in m below the BCU.

In Figure 15a-f four well cases are shown to illustrate the model performance of the PLS VR-model versus the regional VR-model. In the four wells the measured VR indicate that the top of the oil window (0.6 % $R_o$ ) range between 2.9–4.2 km with the Jens-1 well (Salt Dome Providence) and the Gert-1 well (Feda Graben) as the shallowest and deepest examples, respectively. For all wells, the regional VR-model predicts the top of the oil window to be at 3.2 km whereas the PLS VR-model have it to range between 2.9–3.8 km (Figure 15a-f). Based on the PLS VR-model a thin Chalk Group as in Jens-1 will lead to a more shallow positioned oil window whereas a thick Chalk Group as encountered in the Amalie-1 and Gert-1 wells will lead to a deeper positioned oil window as compared to the regional VR-model. The thickness of the Lower Cretaceous Cromer Knoll Group also affects the oil window position by shifting it to deeper levels as seen in the Nora-1 well (Figure 15e).

Based on PLS VR-model the depth to the oil window (0.6 % $R_o$ ) has been mapped out in the investigated wells (Figure 16). In the Salt Dome Province the start of the oil window is modelled to occur between 2.2–3.2 km. In contrast deeply positioned oil windows are modelled in the northern part of the DCG especially in the Feda and Gertrud grabens and in the northern Tail End Graben where depths down to c. 3.9 km are seen (Figure 16). The modelling is in agreement with Petersen et al. (2012) who demonstrated a considerable depth to the top of the oil window in this part of the DCG.

#### 4.5. Formation temperature

The bottom hole temperature versus depth was examined in 96 wells in the DCG (Table 5, Figure 17). There is a scatter of about 50 °C for each depth step and some of this scatter undoubtedly reflects poor measurements and/or temperature correction induced by the drilling operation. However, there is a clear geographical distribution, and geothermal gradients range from c. 28 °C/km in the Feda and Gertrud Grabens increasing to 39 °C/km towards the southern Salt Dome Province can be constructed (Figure 17). Temperature data from the DCG has previously been shown by Kubala et al. (2000) and our more complete analysis of the temperature is in-line with their study.

HPHT hydrocarbon exploration in the DCG, is by some authors considered to include areas with fluid pressures above 70 MPa and temperatures above 150 °C (Smithson 2016). Following this definition, the required pressure regime is expected to occur from below 3.8 km based on Figure 12. Temperatures above 150 °C are expected to be reached at same depth in most areas of the DCG, except for the Feda/Gertrud graben where it is expected to be reached around 4.7 km (Figure 17). Using these depth as guideline the HPHT regime includes the Hejre Field and the Amalie-1, Svane and Xana-1X discoveries (Figure 2).

#### 4.6. PetroMod 1-D modelling

The thermal burial history of 46 well locations is optimised against the measured VR data and corrected to present-day temperatures by adjusting the heat flow history to reach an acceptable match (Figure 18). In our comparison we use three kinetic models; the Easy%Ro by Sweeney & Burnham (1990), the Easy%RoDL by Burnham et al. (2017) and the Basin%Ro by Nielsen et al. (2015) to illustrate the possible ranges in VR developments.

The most widely used kinetic model is the Easy%Ro. This kinetic model, however, has been shown to generally calculates higher VR values compared to other models (c.f. Nielsen et al. 2015). As a consequence shallow position of the onset of the oil window (0.6 %Ro) is modelled. This feature can also be seen in our data. Here the depth of start of the oil window (0.6 %Ro) range between 3.1–4.1 km following Easy%Ro whereas the start of oil window range 3.8–4.9 km following the Basin%Ro is four selected wells (Figure 18). For both models the oil window in the Nora-1 well was modelled to lies shallowest and the deepest was found to be in the Gert-1 well. Compared to the VR measurements the model represent an enveloped that encloses the data but does no match them exactly. The PLS VR-model results for Nora-1 and Gert-1 well (Figure 15e,f) provide intermediate estimate of the oil window depth than those obtained by the two kinetic model results.

In all 1-D basin model it was difficult to obtain a reasonable match between modelled VR and measured VR in the Post Chalk Group; possible caused by high contents of reworked organic matter as observed during biostratigraphic studies (Karen Dybkjær personal communication) that generally tend to have too high VR. Main emphasise was therefore to obtain a proper calibration match in the Mesozoic sequence using a constant heat flow model though time as sensitivity studies showed that constant and variable heat flow models provided equally good matches. The heat flow values obtained from the calibration of the 1-D models against VR and bottom hole temperatures data range between

~45 to ~70 mW/m<sup>2</sup> (Figure 19) with a decreasing trend of heat flow values from south to north as also evident in the temperature input data (see section 4.5).

The VR maturity history we show in Figure 20 the Hejre-1 (Gertrud Graben), Amalie-1 (Søgne Basin), Iris-1 and Svane-1 (both Tail End Graben) well examples. For these wells the VR maturation history of the uppermost source rock interval (Ryaz-1) entered the oil window in the late Paleogene reaching main oil within the last c. 5–10 Ma (Figure 20).

#### **4.7. Maturity maps for the Jurassic source rocks**

The VR maturation of the 50 1-D models has been compiled into three maturity maps showing the present day lateral variation of maturity at the upper and mid part of the Farsund Formation and one representing the Lower to Middle Jurassic formations (Figure 21). The maps shows that the present day maturity for the uppermost Farsund Formation (the Volg-3 – Ryaz-1 sequences) ranges from immature in the southern part of the Salt Dome Province to late oil-mature in and near the Tail End Graben and in the Søgne Basin (Figure 21). The underlying part of the Farsund Formation (the Kimm-3 – Volg-3 sequences) are immature in local areas, but are post mature with respect to oil generation in the Tail End Graben and the Rosa Basin within the Salt Dome Province. The Lower Jurassic and the Middle Jurassic Bryne, Lulu and Middle Graben formations is gas prone in most of the DCG area (Figure 21C).

The maturity maps in Figure 21 for the uppermost Jurassic–lowermost Cretaceous source rock interval are in good agreement with previous maps (Damtoft et al., 1987; Thomsen et al., 1990). For the Farsund Formation the upper part of the formation are within the main oil window in most part of the DCG apart from the south–eastern part of the Salt Dome Province and the southern part of the Heno Plateau (Figure 21).

## **5. Discussion**

### **5.1. Representativeness of the source rock database**

The data that form the basis for this study originate from nearly four decades of measurements. For the analytical analysis, the usage of standards adjust for laboratory and machine differences, and since no fundamental shift in analytical concepts have been made, this is not viewed as having any significant impact on the data analysis presented here.

More important and often overlooked are errors induced by the drilling operations and subsequent sampling for analysis i.e. prior to analysis in the laboratory (Minkinen 1987). Our data derive from analysis of both cuttings and core samples. For obtaining average values of parameters that are representative of a formation, using cutting samples with their natural averaging of the sample, is not problematic if the sampling is unbiased, i.e. if all lithologies have equal chance of being sampled. Biases may occur if the lithologies have very different behaviour towards the drill bit. In a mixed shale-sand sequence, less cemented sandy beds may thus be under-represented in the analysed cutting

fraction. Similarly, in shales with cemented limestone beds these latter may be over-represented in the cuttings fraction. In addition, cavings may obscure the lithological information of the cutting sample. These effects is here sought minimized by utilizing a specific size fraction for analysis, namely the 1–4 mm fraction. Hence, both large-size cavings and very tiny recycled fractions from the drilling mud system are prevented from entering the analysed sample.

The second major cause for uncertainty stems from under-sampling of the lithological variation. The minimum sampling frequency aimed at here is 1 sample per 10 meter. For the whole sample database the average is 1 sample per 8 meter as the 5537 samples were picked from a cumulated 44.5 km long interval. However, we know that this estimate does not include the total interval depth and that the real sample frequency is actual less. Moreover, the sample count include core sections where the sampling interval is much higher than in un-cored sections. In some cases the sampling has excluded particular sandy intervals thus biasing the samples towards the shaly part of the formations. Likewise, we note that in a few cases the reported samples were filtered to exclude samples with less than 0.5 wt% TOC.

Currently, the effects of the above-mentioned errors and biases on our calculated formation averages cannot be quantified. Hence, our interpretations come with this uncertainty. However, comparing core data with data obtained from cuttings is one way to probe the errors associated with some of the drill processes. Also, the resulting organic richness interpretation can be compared to similar interpretation obtained from carefully calibrated well logs following models like the delta log R technique of Passey et al. (1990) as a judgment based only on the natural gamma log alone will not be advisable (Petersen et al., 2017).

## **5.2. Source rock quality**

As advised by Cornford et al. (1998) we have used a log-normal distribution model to calculate the population statistics as the distributions are right-end skewed and thus not compatible with a normal distribution. The reason for this is that the arithmetic mean  $\pm$  standard deviation will result in an underestimation of the distributed source rocks because the standard deviation ignores the extreme distributions that else can be captured by a log-normal distribution. Hence, the statistical properties presented in Table 3 allow for a much better representation of the data for further analysis.

Compared to the estimation of source rock richness and quality of the Farsund Formation published by Ponsaing et al. (2018), it should be noted that Ponsaing et al. (2018) only used a limited data set (13 wells) and that the samples were filtered to include only samples with HI > 200 mg HC/g TOC in order to focus the analysis on oil prone samples and to limit the effects of maturation on the averages (Ponsaing et al. 2018). Compared to the tabulation presented in Table 3 this means that their TOC and HI estimates are within the P50–P10 range reported here.

### 5.21 Upper Jurassic–lowermost Cretaceous source rocks

Variation of kerogen type and richness for the DCG was already mapped by Damtoft (1987) based on just a few wells combined with a conceptual approach in which the depositional depth had a strong control on the maceral types. Hence it was assumed and the most oil prone kerogen and rich sources were expected to occur in the deepest parts of the basin where alginites predominantly accumulate. In contrast to this, more lean shales dominated by vitrinite and waxy land plant cuticles were expected to accumulate more shorewards (Damtoft et al., 1987).

Damtoft et al. (1987)'s model predictions are quite similar to the geographical variation in source rock quality and richness documented here (Table 3). Their stratigraphical constraints were, however, poor and we apply a much more precise sequence stratigraphical frame that allow us to analysis the source rock variation with an unpresented high detail level. We can thus unambiguously show that the south to north increase in TOC level exists not only for the topmost Bo Member (i.e. the Volg-4 – Ryaz-1 sequence, Ineson et al., 2003) but also for all other analysed sequences in the Farsund Formation (Figure 11). This suggests that long lasting controls on the accumulation was effective most likely related to the depositional depth of the different basin areas that have a first order control on the seafloor oxygen conditions and depositional energy by preserving the organic matter from decomposition and allow more fine-grained particle to settle. Such regional variation in source rock quality and richness is not surprising as a considerable variation in the Farsund Formation time equivalent Draupne Formation in the South Viking Graben have been mapped out by Justwan et al. (2005).

We have not reconstructed the source rock quality to its original pre-productive state, and the regional changes in generative potential is somewhat overprinted by maturity effects (c.f. Ponsaing et al., submitted). Nevertheless, we can clearly observe that the immature Salt Dome Province have similar or slightly lower HI values for all analysed sequences compared to its mature counterparts (Figure 11). The mixed oil – gas generative potential assessed from the Salt Dome Province was thus likely much more oil prone in the northern part of the DCG as our data in Table 3 suggest.

Studies of the kerogen types in the DCG has mostly focused on the stratigraphic control on the oil richness and little regional comparison has been made (Petersen et al., 2010, 2017; Ponsaing et al., 2018, submitted). According to these studies the stratigraphical variation in oil richness, as expressed by the HI, is mimicked by changes in the organic macerals type such as amorphous organic matter (AOM). Overall the Kimmeridgian i.e. the Lola Formation to lower Farsund Formation witnessed a transition from terrestrial to more marine conditions that followed the transgression of the DCG (Andsbjerg & Dybkjær 2003). The regional variation suggest that tectonic control also played a major role in determining the source rock quality and we thus attribute structural topography and the location of sediment input centres as the ultimate controlling factors as also put forward by Ineson et al. (2003) and Ponsaing et al. (2018).

### 5.22 Middle Jurassic source rocks

One of the major changes in source rock understanding in the DCG since the review by Damtoft et al. (1987) is the recognition of the Middle Jurassic Petroleum system in its own right (see review by Petersen & Hertle 2018). The coaly source rock are primarily gas prone but has an average restored HI of about 280 mg HC/g TOC illustrates the ability to generate liquids hydrocarbons. Paralic parts of the coal beds have a higher generative potential than the landwards parts, however the most significant impact on source rock quality is caused by the presence of sapropelic lacustrine facies (Pedersen & Hertle 2018).

### 5.23 Lower Jurassic source rocks

Data on the Fjerritslev Formation has increased little since the reviews by Damtoft et al. (1987, 1992). The Toarcian part of the Fjerritslev Formation that elsewhere in Europe includes highly oil-prone intervals is generally absent in the DCG (Figure 3) (Damtoft et al., 1987, 1992). The stratigraphically equivalent Posidonia Shale Formation is the most important source rock for oil onshore Germany, and in the German North Sea the Posidonia Shale Formation is the source rock of the Mittelplate field, the only German offshore oil field. In the southern North Sea area, the formation is only preserved in main Mesozoic rift basins and deeper subsided basin parts such as the Central Graben (Lokhorst, 1997). Remnants of the Posidonia Shale Formation are also assumed in the German Central Graben, but are not confirmed by wells (Arfaï & Lutz, 2018). In the DCG the formation have oil – gas generative potential (Table 3) and it may provide an additional source. Main uncertainties to this contribution stems both to the lack of special oil chemistry that may serve to identify a possible contribution (see section 5.4) and to its very patchy distribution in the DCG (Michelsen et al., 2003).

## 5.3. Factors influencing the depth of the oil window

The depth of the oil window, as defined by VR of 0.6 %R<sub>o</sub>, range between 2200-4500 m in the DCG (Figure 13a). Much of this variation in depth can be modelled by using as simple depth model, the VR-PLS-model, that include the thickness of the Palaeogene to Cretaceous Chalk and Cromer Knoll groups in the VR prediction (Figure 15). According to this model a thick Chalk Group offsets the oil window to deeper levels as expected from a regional point of view. An explanation that link a deeply positioned oil window to areas with a thick Chalk Group was put forward by Petersen et al. (2012) based on wells in the northern part of the DCG. According to these authors the effect should be attributed to thermal properties of the highly thermally conductive chalk in contrast to the underlying lesser thermally conductive clays. In addition to this they also invoked a highly pressured system at the base of the Chalk Group to additionally downward displace the oil zone following Carr (1999). Nielsen et al (2015) modelled some of the wells analysed by Petersen et al. (2012) and did not find any pressure effects on the position of the oil window. Instead they attributed the deep position of the oil window to solely thermal conductivity difference of the chalk and shale.

In basin modelling the onset of oil window can be assessed after the model has been calibrated against especially heat flow, thermal conductivities and kinetic models. The most widely used kinetic model is the Easy%Ro kinetic model by Sweeney and Burnham (1990), but due to uncertainties regarding the kinetic model for the calculation of VR based on a given temperature history, alternative kinetic models have been developed over the last years (c.f. Nielsen et al. 2015). These models address various issues, like computational time, effects of pressure and importance of vitrinite suppression due to differences in deposition conditions and maceral interactions. During the last years, it has been argued that Easy%Ro has its weaknesses and that the calculated values are higher compared to the measured values. Thus, it is currently uncertain whether a universal algorithm for VR prediction exists, because maturation of vitrinite and oil-prone kerogen may require local/basin-wide correction for the individual kerogen types, as different calibration of the kinetic model will be required for vitrinite in coals and oil-prone organic matter Schenk et al., (2017).

#### **5.4. Source rocks quality and oil families**

Oil sourced from Middle and Upper Jurassic source rocks can be clearly distinguished from each other and from Permian sources based on oil chemistry (Petersen et al., 2016; Schovsbo et al., 2018). Among the marine Jurassic oil type (type 1 of Schovsbo et al., 2018) four subtypes have been recognised and among these two subtypes have contributed significantly to the accumulated oils namely a “Tail End type” (1A type) that occurs in all fields bordering the Tail End Graben and in the Siri Canyon and a “Salt Dome type” (1D type) that occurs in the southern part of the Salt Dome Province (Figure 20). Compared to our findings on source rock quality and maturity variation in the DCG the two main types can be related to both the stratigraphical and the regional variation in source rock quality and maturation. Type 1A is thus characterised by high bisnorhopane biomarker content indicative of strong marine anoxic conditions typically found in the Bo Member (Ineson et al., 2003; Pedersen et al., 2016; Ponsaing et al., in review, submitted). Type 1D have similar affinity to marine anoxia deposition but among many aspects has less bisnorhopane. The domination of type 1A in the Tail End Graben thus reflect both the thick succession with excellent source rock qualities here and the mature nature of the unit. The presence of the type 1D oil in the Salt Dome province is thus interpreted to reflect other Jurassic sources that the uppermost Farsund Formation since it here is generally immature and has less good source rock qualities developed (Ponsaing et al., submitted).

The oil type potentially generated from the Fjerritslev Formation is poorly known in the DCG as the biomarker composition are only described from five source rock extraction (Schovsbo et al., 2018). Of these the biomarker composition of two source rock extracts (M-8X, Skarv-1) cannot be matched with any reservoir oil whereas three source rock extracts are either pure terrestrial (type 3, U-1X), have a marine anoxic signature “Tail End type” (type 1A, Jens-1) or an oil type known to occur in the Adda and Boje fields (type 1C, N-22X). At current it is not known if this variability reflect the rock itself or migrated oils from other source rock levels. Based on the source rock screening data the compositional variation may, however, be a reflection of the bimodal HI distribution that suggested that the formation both contain terrestrial mixed gas/oil prone and highly oil prone generative potential (Figure 7). GEUS unpublished data suggest that the highly oil prone Toarcian part of the

Posidonia Shale Formation in southwest Germany have a different biomarkers compositions than seen in the DCG (Peter Nytoft personal communication, May 2019). The Toarcian part of the Fjerritslev Formation is also not considered to be present in the DCG (Figure 2) and further studies will aim at characterising the Lower Jurassic source rock biomarker signature.

Terrestrial influenced oils (type 2 and 3 of Schovsbo et al., 2018) are, among many other features, characterised by much higher pristane/phytane ratio than the fully marine Jurassic types (Petersen et al., 2016; Schovsbo et al., 2018). Type 2 occur in the Søgne Basin including northern part of the Tail End Graben and on the eastern Heno plateau (Figure 22). These occurrence are within the Middle Jurassic petroleum System recently reviewed by Petersen & Hertle (2018). Type 3 have been documented from oil stains in the Alma-2, Bertel-1, Gert-1 and Rita-1 wells (Figure 20) and from source rock extracts it is known to occur in the Middle Jurassic Bat-1 to Upper Jurassic Kimm-3 sequences (Schovsbo et al., 2018). These sequences all contain terrestrial dominated kerogen that gas prone (Table 3, Ponsaing et al., 2018).

## 6. Conclusions

- The Danish Central Graben is a mature petroleum province with the principal petroleum source rocks being the Upper Jurassic – lowermost Cretaceous marine Farsund Formation shales and with minor contributions from Middle Jurassic coaly units of the Bryne and Lulu formations.
- Statistical parameters (average, median, low (P90) and high (P10)) describing the distribution of TOC, HI and  $T_{max}$  are presented for the Lower Jurassic marine Fjerritslev Formation, the Middle Jurassic Bryne, Lulu, and Middle Graben terrestrial-paralic formations and the Upper Jurassic-lowermost Cretaceous marine Lola and Farsund formations in six areas in the DCG.
- Within the DCG a clear south to north increase in TOC level exists not only for the topmost Bo Member of the Farsund Formation but also for all other analysed sequences in the Farsund Formation.
- Three maturity maps of the upper and mid part of the Farsund Formation and one representing the Lower to Middle Jurassic formations show that the uppermost Farsund Formation are immature in the southern part of the Salt Dome Province and in the late oil mature in and near the Tail End Graben and the Søgne Basin. The middle part of the Farsund Formation are immature in local areas, but are post mature in the Tail End Graben and in the Rosa Basin within the Salt Dome Province. The Lower Jurassic and the Middle Jurassic Bryne, Lulu and Middle Graben formations is gas prone in most of the DCG.
- 1-D petroleum modelling show that the uppermost source rock interval (Ryaz-1) in deep wells in representing the Gertrud, Søgne and Tail End grabens entered the oil window in the late Paleogene reaching main oil within the last c. 5–10 Ma.
- The depth of the oil window, as defined by VR of 0.6 % $R_o$ , range between 2200-4500 m in the DCG. Much of this variation in depth can be modelled by using as simple depth model, the VR-PLS-model, that include the thickness of the Palaeogene to Cretaceous Chalk and Cromer Knoll groups in the VR prediction. According to this model a thick Chalk Group offsets the oil window to deeper levels. The reason for this can be attributed to thermal

properties of the highly thermally conductive chalk in contrast to the underlying lesser thermally conductive clays. Higher thermal heat flow in the Salt Dome Province like also contributed to a shallow position of the oil window that occur here.

- Our findings on source rock quality and maturity variation in the DCG add further to the effective source rock intervals of the two main Jurassic oil types in the DCG. The domination of type 1A in the Tail End Graben thus reflect both the thick succession with excellent source rock qualities here and the mature nature of the unit. The presence of the type 1D oil in the Salt Dome province is interpreted to reflect other Jurassic sources that the uppermost Farsund Formation since it here is generally immature and has less good source rock qualities developed.
- The source rock screening data the compositional variation of the Fjerritslev Formation indicate both a gas and a highly oil prone generative potential. The source rock extracts from the formation is very limited and variable and it is unknown if this variability reflect the rock itself or migrated oils from other source rock levels.
- The DCG is an overpressured basin. Fluid pressure > 70 MPa and temperatures > 150 °C (HPHT conditions) are expected to occur deeper than 3.8 km except for the Feda and Gertrud grabens where it is expected to be effective from around 4.7 km due to general lower temperatures here.

## 7. Acknowledgement

This paper is published with the permission from the Geological Survey of Denmark and Greenland. We thank Ineos E&P A/S and its partners (Danoil Exploration A/S and Nordsøfonden) in licence 9/95 for financial support to part of this study. Background data originate from existing databases at GEUS and from the work conducted within the multi-client studies PETSYS and CRETSYS, which both were led by GEUS. Erik Thomsen (GEUS) is thanked for his contribution to these projects together with Ditte Kiel-Dühring and Carsten Guvad who made most of the source rock analytical work presented herein. The paper is a contribution to the EU Horizon2020 GeoERA project (The GARAH, H2020 grant #731166 lead by GEUS).

## References

- Anderskov, K., Surlyk, F., 2011. Upper Cretaceous chalk facies and depositional history recorded in the Mona-1 core, Mona Ridge, Danish North Sea. Geological Survey of Denmark and Greenland Bulletin 25, 60 pp.
- Andsbjerg, J., Dybkjær, K., 2003. Sequence stratigraphy of the Jurassic of the Danish Central Graben. Geological Survey of Denmark and Greenland Bulletin 1, 265–300.

- Arfai, J., Lutz, R., 2018. 3D basin and petroleum system modelling of the NW German North Sea (Entenschnabel). Geological Society, London, Petroleum Geology Conference series 8, 67–86.
- Burnham, A.K, Peters, K.E., Schenk, O., 2017. Evolution of vitrinite reflectance models. Search and Discovery Article #41982, 23 p.
- Bustin, R., Cameron, A., Grieve, D., Kalkreuth, W.D., 1989. Coal Petrology – Its principles, methods and applications. Geological Association of Canada, Short Course Notes, v. 3, Victoria, British Columbia, May 8-10, 273 p. Third Edition.
- Carr, A.D., 1999. A vitrinite reflectance kinetic model incorporating overpressure retardation. Marine and petroleum geology 16, 355–377.
- Carr, A.D., Petersen, H.I., 2004. Modelling of the hydrocarbon generation history and volumetric considerations of the coal-sourced Lulita Field, Danish North Sea. Petroleum geoscience 10, 107–119.
- Cornford, C., Gardner, P., Burgess, C., 1998. Geochemical truths in large data sets. I: Geochemical screening data. Organic geochemistry 29, 519–530.
- Damtoft, K., Andersen, C., Thomsen, E., 1987. Prospectivity and hydrocarbon plays of the Danish Central Trough. In: Brooks, J. & Glennie, K.W. (Editors): Petroleum geology of North WestEurope, 403–417. London, Graham & Trotman.
- Damtoft, K., Nielsen, L.H., Johannessen, P.N., Thomsen, E., Andersen, P.R., 1992. Hydrocarbon plays of the Danish Central Trough. In: Spencer, A.M. (Editor). Generation, Accumulation and Production of Europe's Hydrocarbons II. Springer, Berlin. 35–58.
- Dennis, H., Bergmo, P., Holt, T., 2005. Tilted oil–water contacts: modelling the effects of aquifer heterogeneity. In: Dore, A.G. & Vining, B.A. (editors): Petroleum Geology: North-West Europe and Global Perspectives—Proceedings of the 6<sup>th</sup> Petroleum Geology Conference, 145–158. Conferences Ltd. Published by the Geological Society, London.
- Esbensen, K.H., Geladi, P., 2010. Principles of proper validation: use and abuse of re-sampling for validation. Journal of Chemometrics 24, 168–187.
- Esbensen, K.H., Swarbrick, B., 2018. Multivariate data analysis. 6<sup>th</sup> edition Camo software, Oslo, Norway. 462 p.
- Goffey, G., Attree, M., Curtis, P., Goodfellow, F., Lynch, J., Mackertich, D., Orife, T., Tyrrell, W., 2018. New exploration discoveries in a mature basin: offshore Denmark. Geological Society, London, Petroleum Geology Conference series 8, 287–306.
- Gradstein, F., Ogg, J., Ogg, H., Hilgen, F.J., 2012. On the Geologic time scale. Newsletters on Stratigraphy 45, 171–188.
- Gradstein, F.M., Ogg, J.G., Schmitz, M., Ogg, G. (Editors) 2014. The Geologic Time Scale. eBook ISBN: 9780444594488, Paperback ISBN: 9780444594259, Elsevier.

- Ineson, J.R., Surlyk, F., (Editors) 2003. The Jurassic of Denmark and Greenland. Geological Survey of Denmark and Greenland Bulletin 1, 948 p.
- Ineson, J.R., Bojesen-Koefoed, J.A., Dybkjær, K., Nielsen, L.H., 2003. Volgian–Ryazanian ‘hot argillaceous shales’ of the Bo Member (Farsund formation) in the Danish Central Graben, North Sea: Stratigraphy, facies and geochemistry. Geological Survey of Denmark and Greenland Bulletin 1, 403–436.
- Japsen, P., 1998. Regional Velocity-Depth Anomalies, North Sea Chalk: A Record of Overpressure and Neogene Uplift and Erosion. AAPG Bulletin 82, 2031–2074.
- Japsen, P., Britze, P., Andersen, C., 2003. Upper Jurassic–Lower Cretaceous of the Danish Central Graben: structural framework and nomenclature. Geological Survey of Denmark and Greenland Bulletin 1, 1–49.
- Johannessen, P.N., Dybkjær, K., Andersen, C., Kristensen, L., Hovikoski, J., Vosgerau, H., 2010. Upper Jurassic reservoir sandstones in the Danish Central Graben: new insights on distribution and depositional environments. Petroleum Geology Conference 7, 127–143.
- Justwan, H., Dahl, B., Isaksen, G.H., Meisingset, I., 2005. Late to Middle Jurassic source facies and quality variations, South Viking Graben, North Sea. Journal of Petroleum Geology 28, 241–268.
- Kubala, M., Bastow, M., Thomsen, S., Scotchman, I., Oygard, K., 2003. Geothermal regime, petroleum generation and migration. The Millennium Atlas. 289–315.
- Lokhorst, A., (Editor) 1997. NW European Gas Atlas. NITG-TNO (Haarlem). 154 pp.
- Magoon, L.B., Dow, W.G., (Editors) 1994. The petroleum system — from source to trap. AAPG Memoirs 60. DOI: <https://doi.org/10.1306/M60585>,
- Michelsen, O., Nielsen, L.H., Johannessen, P.N., Andsbjerg, J., Surlyk, F., 2003. Jurassic lithostratigraphy and stratigraphic development onshore and offshore Denmark. Geological Survey of Denmark and Greenland Bulletin 1, 147–216.
- Minkinen, P., 1987. Evaluation of the fundamental sampling error in the sampling of particulate solids. Analytica Chimica Acta 196, 237–245.
- Møller, J.J., Rasmussen, E.S., 2003. Middle Jurassic – Early Cretaceous rifting of the Danish Central Graben. Geological Survey of Denmark and Greenland Bulletin 1, 247–264.
- Nielsen, S.B., Clausen, O.R., McGregor, E., 2015. basin%Ro: A vitrinite reflectance model derived from basin and laboratory data. Basin Research 29, 515–536.
- Østfeldt, P., 1987. Oil source rock correlation in the Danish North Sea. In Petroleum Geology of North West Europe, Brooks, J., Glennie, K. (Editors). Graham & Trotman: London, UK, 419–429.

- Passey, Q.R., Creaney, S., Kulla, J.B., Moretti, F.J., Stroud, J.D., 1990. A practical model for organic richness from porosity and resistivity logs. *AAPG Bulletin* 74, 1777–1794.
- Pedersen, S., Weibel, R., Johannessen, P., Schovsbo, N.H., 2018. The diagenetic impact on reservoir sandstones of the Heno Formation in the Ravn-3 well, Danish Central Graben, Denmark. *Geological Survey of Denmark and Greenland Bulletin* 41, 9–12.
- Pepper, A.S., Corvi, P.J., 1995. Simple kinetic models of petroleum formation: Part III. Modelling an open system. *Marine and Petroleum Geology* 12, 417–452.
- Peters, K.E., 1986. Guidelines for evaluating petroleum source rock using programmed pyrolysis. *AAPG Bulletin* 70, 318–329.
- Petersen, H.I., Brekke, T., 2001. Source rock analysis and petroleum geochemistry of the Trym discovery, Norwegian North Sea: a Middle Jurassic coal-sourced petroleum system. *Marine and Petroleum Geology* 18, 889–908.
- Petersen, H.I., Hertle, M., 2018. A review of the coaly source rocks and generated petroleum in the Danish North Sea: An underexplored Middle Jurassic petroleum system? *Journal of Petroleum Geology* 41, 135–154.
- Petersen, H.I., Nytoft, H.P., 2007. Are Carboniferous coals from the Danish North Sea oil-prone? *Geological Survey of Denmark and Greenland Bulletin* 13, 13–16.
- Petersen, H.I., Rosenberg, P., 1998. Reflectance retardation (suppression) and source rock properties related to hydrogen-enriched vitrinite in Middle Jurassic coals, Danish North Sea. *Journal of Petroleum Geology* 21, 247–263.
- Petersen, H.I., Andsbjerg, J., Bojesen-Koefoed, J.A., Nytoft, H.P., Rosenberg, P., 1998. Petroleum potential and depositional environments of Middle Jurassic coals and non-marine deposits, Danish Central Graben, with special reference to the Søgne Basin. *Geological survey of Denmark Bulletin* 36, 81 p.
- Petersen, H.I., Andsbjerg, J., Bojesen-Koefoed, J.A., Nytoft, H.P., 2000. Coal-generated oil: source rock evaluation and petroleum geochemistry of the Lulita oilfield, Danish North Sea. *Journal of Petroleum Geology* 23, 55–90.
- Petersen, H.I., Nielsen, L.H., Bojesen-Koefoed, J.A., Mathiesen, A., Kristensen, L., Dalhoff, F., 2008. Evaluation of the quality, thermal maturity and distribution of potential source rocks in the Danish part of the Norwegian–Danish Basin. *Geological Survey of Denmark and Greenland Bulletin* 16, 66 p.
- Petersen, H.I., Nytoft, H.P., Vosgerau, H., Andersen, C., Bojesen-Koefoed, J.A., Mathiesen, A., 2010. Source rock quality and maturity and oil types in the NW Danish Central Graben: Implications for petroleum prospectivity evaluation in an Upper Jurassic sandstone play area. *Petroleum Geology Conference* 7, 95–111.

- Petersen, H.I., Holme, A.C., Thomsen, E., Whitaker, M.F., Brekke, T., Bojesen-Koefoed, J.A., Hansen, K.H., Larsen, B.T., 2011. Hydrocarbon potential of Middle Jurassic coaly and lacustrine and Upper Jurassic–lowermost Cretaceous marine source rocks in the Søgne Basin, North Sea. *Journal of Petroleum Geology* 34, 277–304.
- Petersen, H.I., Andersen, C., Holme, A.C., Carr, A.D., Thomsen, E., 2012. Vitrinite reflectance gradients of deep wells with thick chalk sections and high pressure: Implications for source rock maturation, Danish-Norwegian Central Graben, North Sea. *International Journal of Coal Geology* 100, 65–81.
- Petersen, H.I., Holme, A.C., Andersen, C., Whitaker, M.F., Nytoft, H.P., Thomsen, E., 2013. The source rock potential of the Upper Jurassic – lowermost Cretaceous in the Danish southern Norwegian sectors of the Central Graben, North Sea. *First Break* 31, 43–53.
- Petersen, H.I., Hertle, M., Juhasz, A., Krabbe, H., 2016. Oil family typing, biodegradation and source rock affinity of liquid petroleum in the Danish North Sea. *Journal of Petroleum Geology* 39, 247–268.
- Petersen, H.I., Hertle, M., Sulsbrück, H., 2017. Upper Jurassic-lowermost Cretaceous marine shale source rocks (Farsund Formation), North Sea: Kerogen composition and quality and the adverse effect of oil-based mud contamination on organic geochemical analyses. *International Journal of Coal Geology* 173, 26–39.
- Ponsaing, L., Bojesen-Koefoed, J.A., Thomsen, E., Stemmerik, L., 2018. Temporal organic facies variations of Upper Jurassic – lowermost Cretaceous source rocks in the Danish Central Graben, North Sea. *International Journal of Coal Geology* 195, 217–237.
- Ponsaing, L., Petersen, H.I., Bojesen-Koefoed, J.A., Nytoft, H.P., Schovsbo, N.H., Stemmerik, L., in review. Source rock quality variations of Upper Jurassic – lowermost Cretaceous marine shales and origin of oils in the Valdemar Chalk Field, Danish North Sea.
- Rasmussen, E.S., Piasecki, S., Andsbjerg, J., Dybkjær, K., Vejbæk, O.V., Jacobsen, C., Britze, P., Bryde-Auken, M., 2005. Cenozoic maps of the Danish North Sea area. *GEUS Report* 2005/33.
- Schovsbo, N.H., Thomsen, E., Nytoft, P., Esbensen, K., 2018. Oil maturity, families and oil-source rock correlations in the Danish North Sea based on biomarker studies. 80<sup>th</sup> EAGE Conference & Exhibition 2018 in Copenhagen, Denmark 5 pp. DOI: 10.3997/2214-4609.201801491.
- Schenk, O., Peters, K.E., Burnham, A.K., 2017. Evaluation of Alternatives to Easy%Ro for Calibration of Basin and Petroleum System Models. 79<sup>th</sup> EAGE Conference and Exhibition 2017. DOI: 10.3997/2214-4609.201700614
- Smithson, T., 2016. HPHT wells. The defining series. *Oilfield Review* 2016, Schlumberger, 2p.
- Sweeney, R.E., Burnham, A.K. 1990. Evaluation of a simple model of vitrinite reflectance based on chemical kinetics. *AAPG Bulletin* 74, 1559–1570.

- Thomsen, R.O., Lerche, I., Korstgård, J.A., 1990. Dynamic hydrocarbon predictions for the northern part of the Danish Central Graben: An integrated basin analysis assessment. *Marine and Petroleum Geology* 7, 123–137.
- Thomsen, E., Damtoft, K., Andersen, C., 1987. Hydrocarbon plays in Denmark outside the Central Trough. In Brooks, J. & Glennie, K.W. (Editors) *Petroleum Geology of North West Europe*. Graham & Trotman, London, 375–388.
- Thomsen, E., Lindgreen, H., Wrang, P., 1983. Investigation on the Source Rock Potential of Denmark. In: Kaasschieter J.P.H., Reijers T.J.A. (Editors) *Petroleum Geology of the southeastern North Sea and the adjacent onshore areas*. Springer, Dordrecht, 221–239.
- van Buchem, F.S., P., Smit, F.W., H., Buijs, G.J.A., Trudgill, B., Larsen, P.-H., 2017. Tectonostratigraphic framework and depositional history of the Cretaceous–Danian succession of the Danish Central Graben (North Sea) – new light on a mature area. *Geological Society, London, Petroleum Geology Conference series*, 8, 9–46.
- Vejbæk, O.V., 2008. Disequilibrium compaction as the cause for Cretaceous–Paleogene overpressures in the Danish North Sea. *AAPG Bulletin* 92, 165–180.
- Vejbæk, O.V., Bidstrup, T., Britze, P., Erlström, M., Rasmussen, E.S., Sivhed, U., 2007. Chalk depth structure maps, Central to Eastern North Sea, Denmark. *Geological Survey of Denmark and Greenland Bulletin* 13, 9–12.
- Verreussel, R.M.C.H., Bouroullec, R., Munsterman, D.K., Dybkjær, K. Geel, C.R., Houben, A.J.P. Johannessen, P.N., Kerstholt-Boegehold, S.J., 2018. Stepwise basin evolution of the Middle Jurassic–Early Cretaceous rift phase in the Central Graben area of Denmark, Germany and The Netherlands. *Geological Society, London, Special Publications* 469, 305–340.
- Waples, D.W., Pedersen, M.R., Kuijpers, P., 2004. Correction of Single Log-Derived Temperatures in the Danish Central Graben, North Sea. – *Natural Resources Research* 3, 229–239.

## Figure captions

**Figure 1.** Structural elements and relevant wells in the southern part of the Central Graben. For well analysed see Tables 1, 4, 5.

**Figure 2.** Stratigraphical overview and petroleum system elements in the Danish Central Graben with indication of discoveries and oil fields. Modified from Ponsaing et al. (in review).

**Figure 3.** Lithostratigraphic scheme through a West to East section through the Danish Central Graben.

**Figure 4.** Selected paleogeography maps representing A) Lower Jurassic Hett-1 – Sin-1 sequences, B) Middle Jurassic Bat-1 sequence, C) Upper Jurassic Kimm-2 – Kimm-3 sequences and D) Lower Cretaceous Ryaz-1 sequence. Modified from Andsbjerg & Dybkjær (2003) and Ponsaing et al. (2018).

**Figure 5.** Depth structure maps of A) top Chalk Group, B) base Chalk Group, C) base Cretaceous Unconformity (BCU) and (D) Chalk Group isochore map. Maps updated from Japsen et al. (2003) and Vejbæk et al. (2007).

**Figure 6.** WSW-ENE section through the central part of the Danish Central Graben. Modified from Møller & Rasmussen (2003).

**Figure 7.** Histograms of TOC,  $T_{max}$  and HI in the Salt Dome Province and Tail End Graben. For list of wells included see Table 1.

**Figure 8.** Histograms of TOC,  $T_{max}$  and HI in the Feda/Gertrud Graben and Søgne Basin. For list of wells included see Table 1.

**Figure 9.** Histograms of TOC,  $T_{max}$  and HI in the Outer Rough and Heno Plateau. For list of wells included see Table 1.

**Figure 10.** Cumulative frequency of the TOC content in the Farsund Formation within the six areas. Each cumulative frequency distribution has been modelled using a log-normal model (black line).

**Figure 11.** Box plot (mean, P95, P75, P50, P25 and P05) for the TOC,  $T_{max}$  and HI populations within the Farsund Formation and selected sequences. The percentile (P) of the distributions are calculated based on Table 2. For list of wells included see Table 1.

**Figure 12.** Pressure measurements versus A) the present sea surface, B) the top Chalk Group, C) the base Chalk Group and D) the base Cretaceous Unconformity (BCU). Depths below reference level in B, C, and D are shown as negative. Grey lines connects pressure measurements within the same well. For comparison the hydrostatic pressure (9.79 KPa/m or 0.433 psi/ft) and lithostatic pressure (22.6 KPa/m or 1 psi/ft) gradient are show assuming a water density of 1.0 g/cm<sup>3</sup> and a average rock density of 2.3 g/cm<sup>3</sup>.

**Figure 13.** Vitrinite reflectance (VR) versus A) the present day sea floor, B) the top Chalk Group, C) the base Chalk Group and D) the base Cretaceous Unconformity (BCU). For reference the  $R_o=0.6\%$  (earliest oil window) is shown. Depths below reference level in B, C, and D are shown as negative.

**Figure 14.** PLS-regression model for the logarithm to VR (LogVR) and the four different depth scales: depth below seafloor (depth), depth with reference to top Chalk Group (Ref Top Chalk), depth with reference to base Chalk group (Ref Base Chalk) and depth with reference to the base Cretaceous unconformity (Ref BCU) [depth references, logVR]. (A) PLS loading-weights plot ( $w_1-w_2$ ), (B) Modelled y-variance, (C) Prediction versus reference plot. Outliers were deleted from the original data set in the final model.

**Figure 15.** A) PLS VR-model versus depth below present sea floor. B) Residual analysis calculates as measured VR – PLS VR-model. Depth profiles for C) Jens-1, D) Amalie-1, E) Nora-1 and F) Gert-1 showing modelled PLS VR-model and regional VR-model and measured VR. Arrows in C-F indicates position of the top oil window ( $VR=0.6\%R_o$ ) estimated either from VR measurements (black), PLS VR-model (green) or linear VR-model (red).

**Figure 16.** Map of estimated depth of the top oil window ( $VR=0.6\%R_o$ ) based on PLS VR-model.

**Figure 17.** Bottom hole temperatures versus present depth below sea floor. Temperatures have been corrected for environmental conditions according to Waples et al. (2004). An average sea floor temperature of 8 °C have been assumed for temperature gradient calculations.

**Figure 18.** 1-D models of A) Hejre-1, B) Gert-1, C) Amalie-1, D) Nora-1 wells showing modelled VR based on the kinetic models: Easy%Ro (black line, Sweeney & Burnham, 1990), Easy%RoDL (blue line, Burnham et al., 2017) and Basin%Ro (red line, Nielsen et al., 2015).

**Figure 19.** Location of the 46 and 4 pseudo wells showing the optimized constant heat flow model values. Notice the general decrease in average values from south to north. The 17 1-D key models are represented by larger symbols.

**Figure 20.** Example of 1-D burial history at the A) Hejre-1, B) Amalie-1, C) Iris-1 and D) Svane-1 well locations showing the VR maturation of the uppermost source rock interval (Ryaz-1) through time. The selected 1-D models show that maturation entered the oil window in the Late Cretaceous reaching main oil within the last c. 5–10 Ma.

**Figure 21.** 1-D modelled maturity based on 46 wells and using Easy%Ro to interpolate the maturity covering A) the Volg-2 to Ryaz-1 sequences (from near the base middle to the top of the Farsund Formation), B) the Kimm-3 to Volg-3 sequences (i.e. from near the base to the middle part of the Farsund Formation) and (C) the Lower and Middle Jurassic (i.e. from Lower Jurassic to near the top Bryne/Lulu/Middle Graben formations).

**Figure 22.** A) Oil types and B) relative oil maturity as depicted by modelled source rock depth. Shallow depths in B indicate less mature oils. From Schovsbo et al. (2018).

## Table captions

**Table 1.** Wells analysed for source rock quality and maturity. Well name in bold have both Rock-Eval and VR data.

**Table 2.** Mean, standard deviation ( $\sigma$ ) and goodness of fit to data ( $r^2$ ) for log-normal distributions.

**Table 3.** Source rock characteristics of Jurassic – lowermost Cretaceous formations and selected sequences in the Danish Central Graben calculated based on Table 2. For list of wells included see Table 1.

**Table 4.** Wells analysed for fluid pressure.

**Table 5.** Wells analysed for bottom hole temperature. Temperatures are corrected according to Waples et al. (1994).

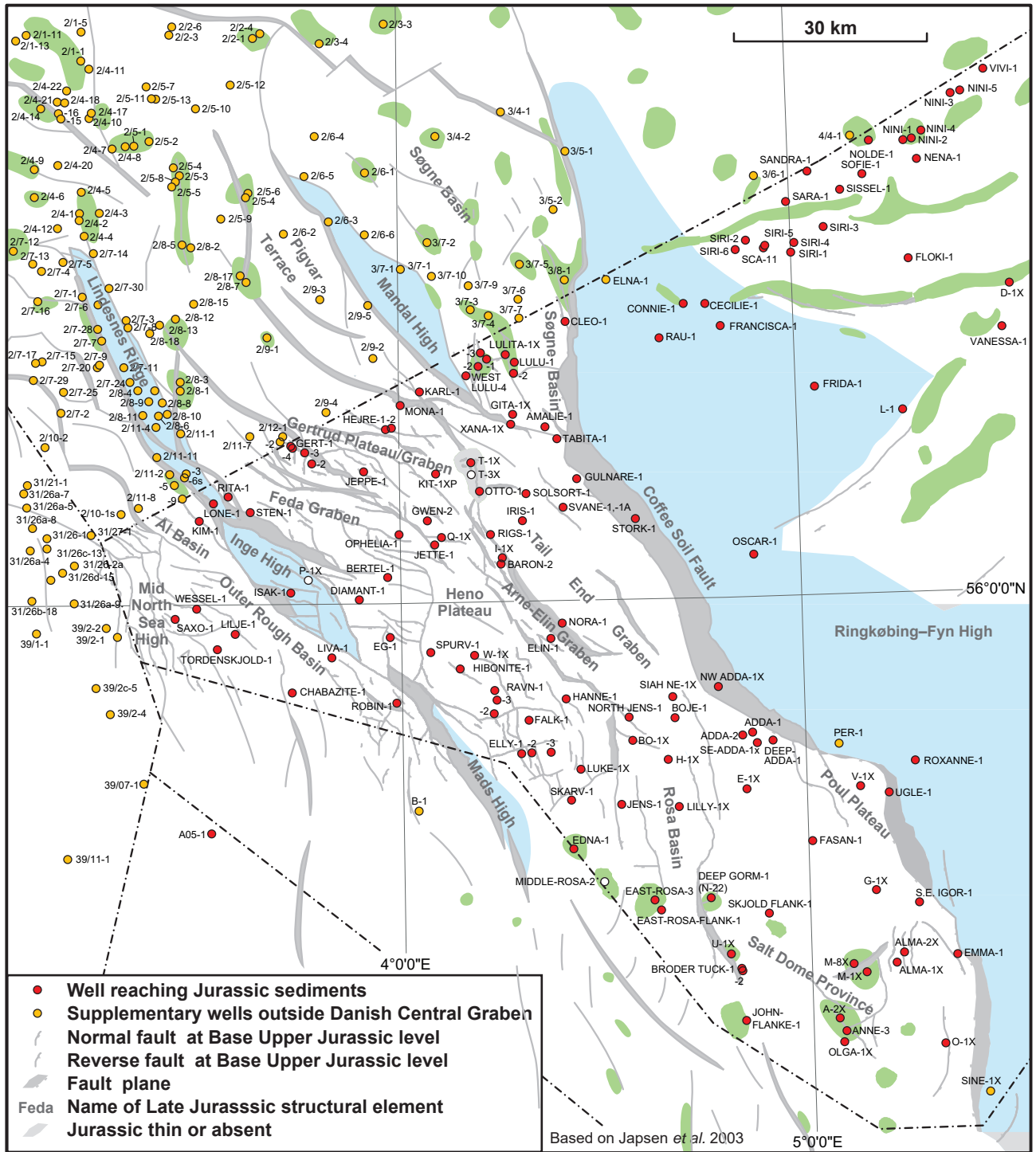
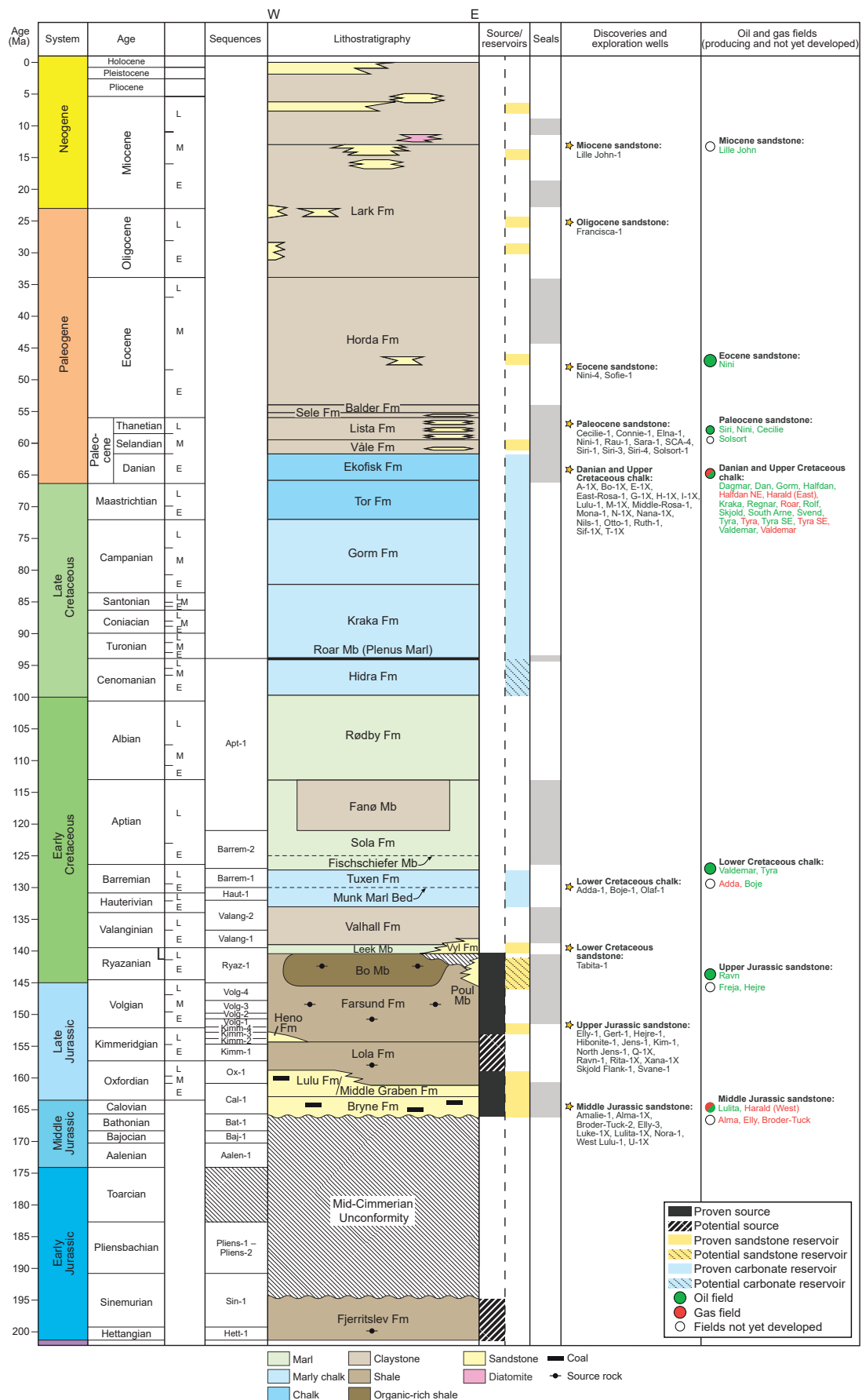


Figure 1. Schovsbo et al.



Figur 2. Schovsbo et al.

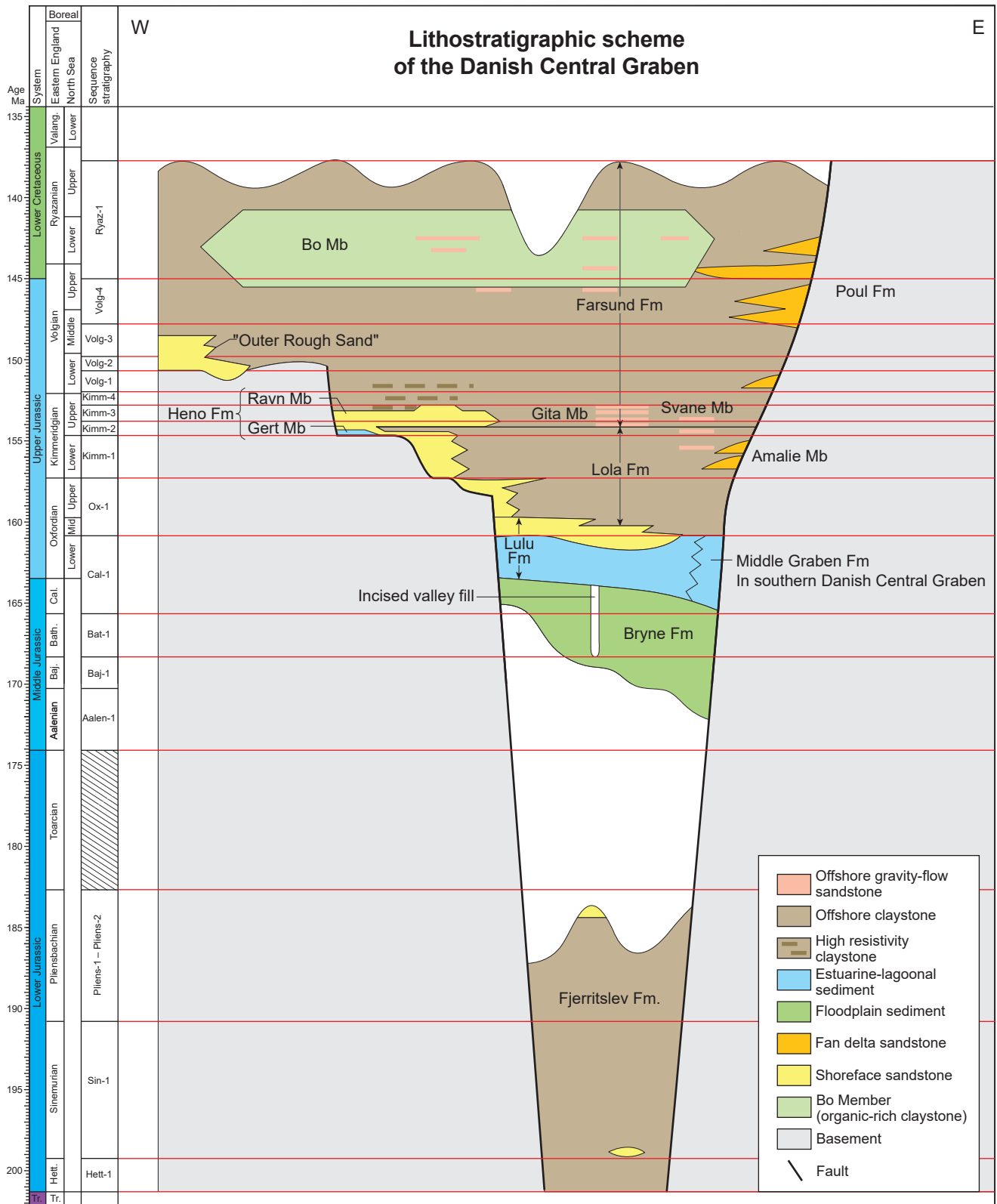


Figure 3. Schovsbo et al.

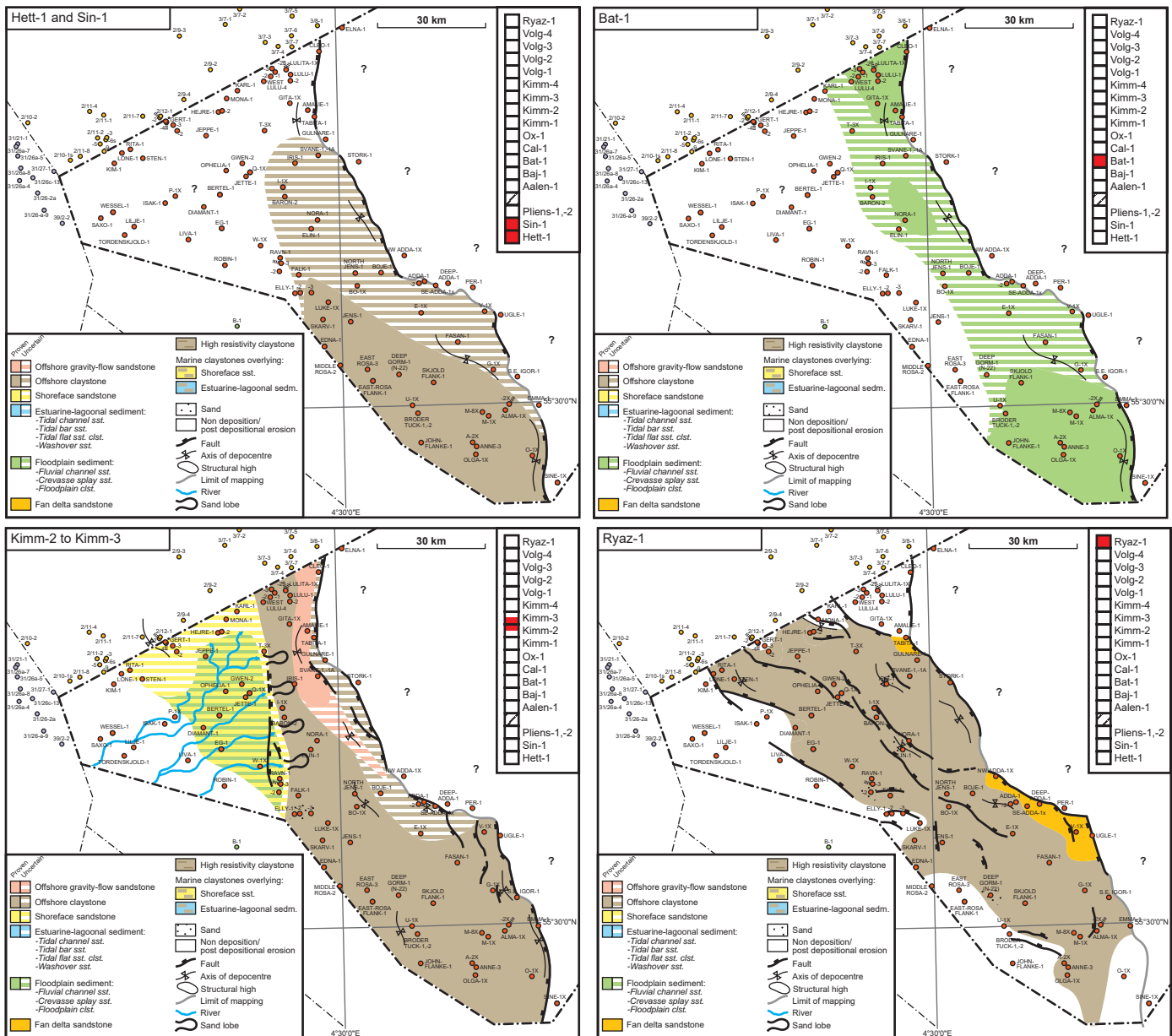


Figure 4. Schovsbo et al.

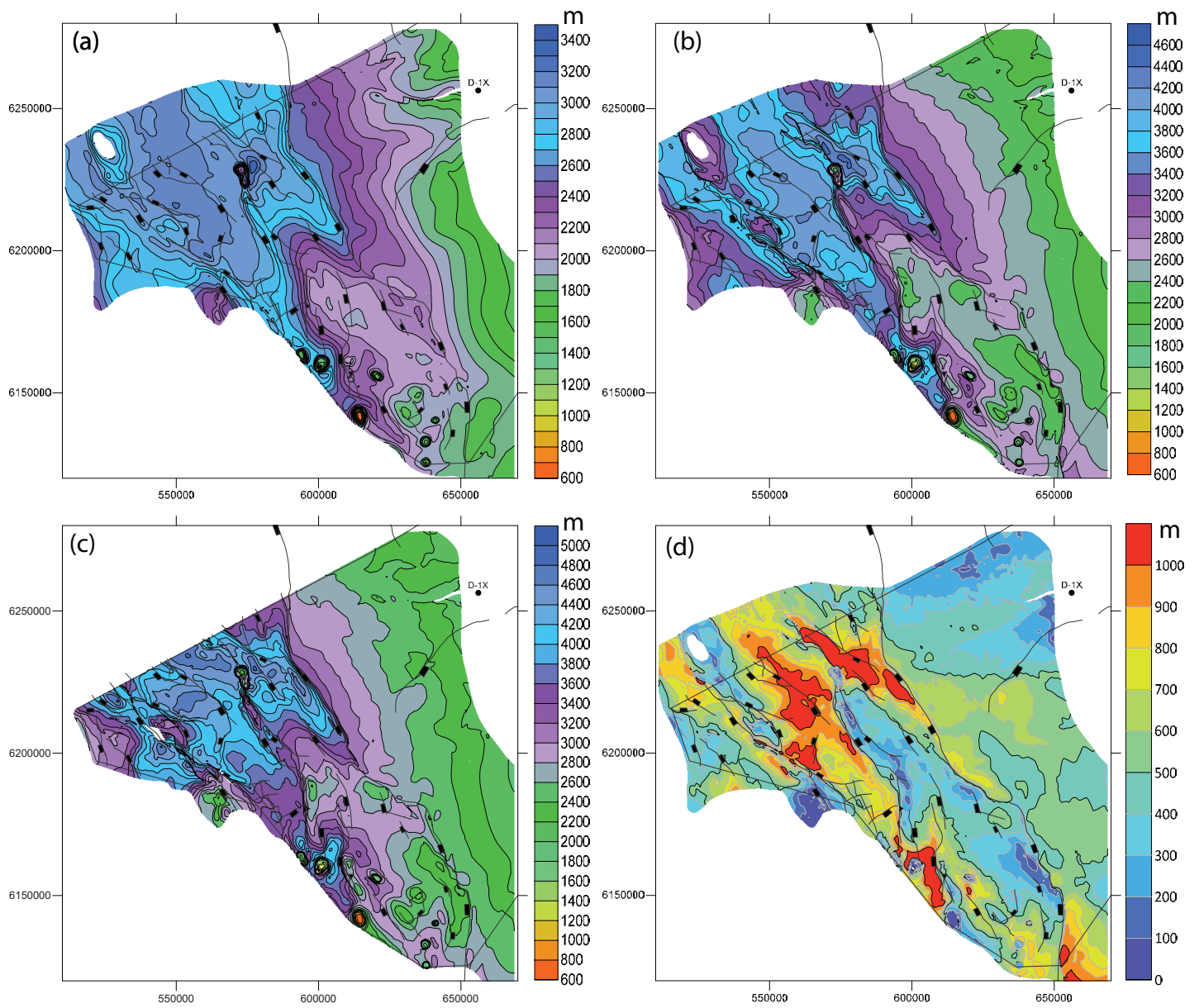


Figure 5. Schovsbo et al.

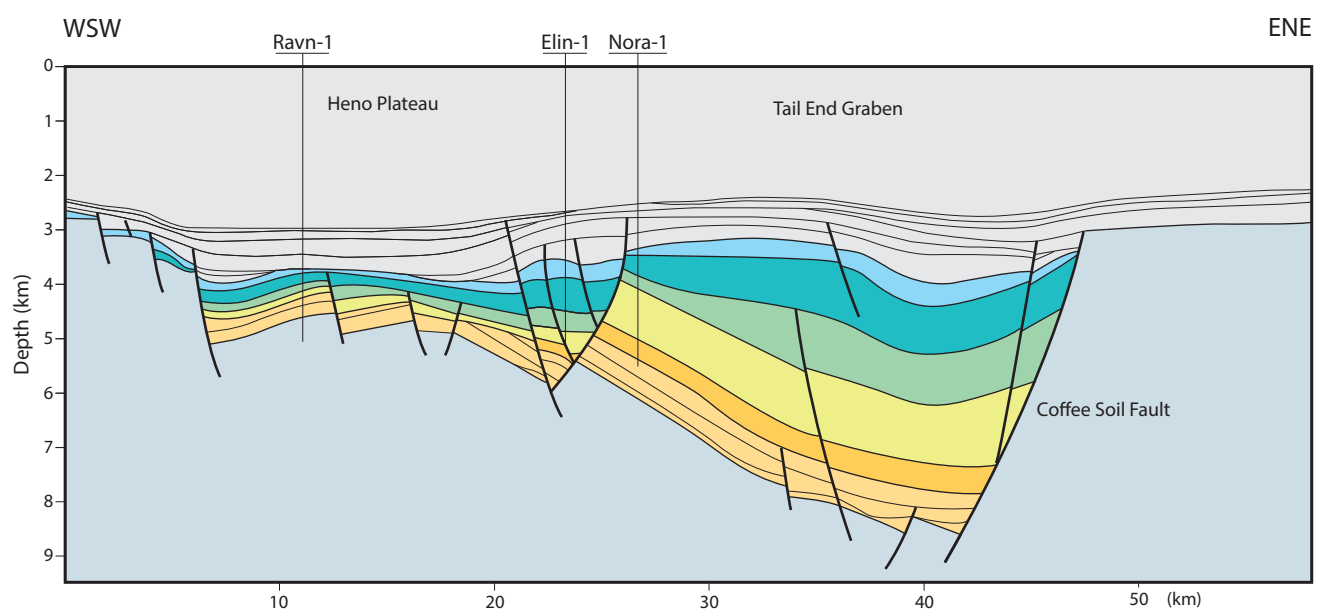


Figure 6. Schovsbo et al.

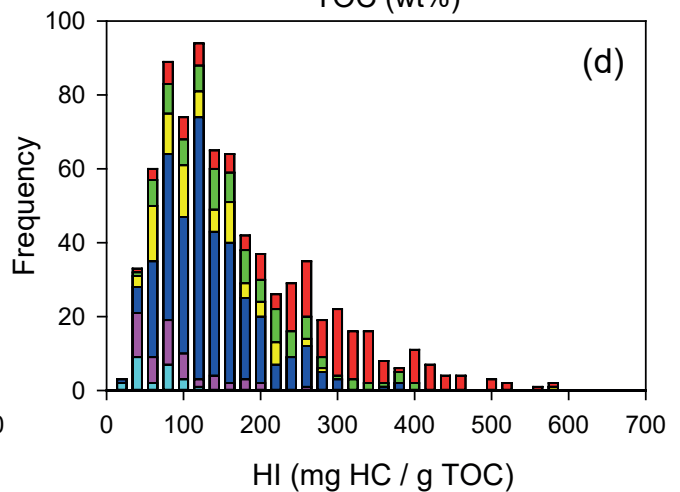
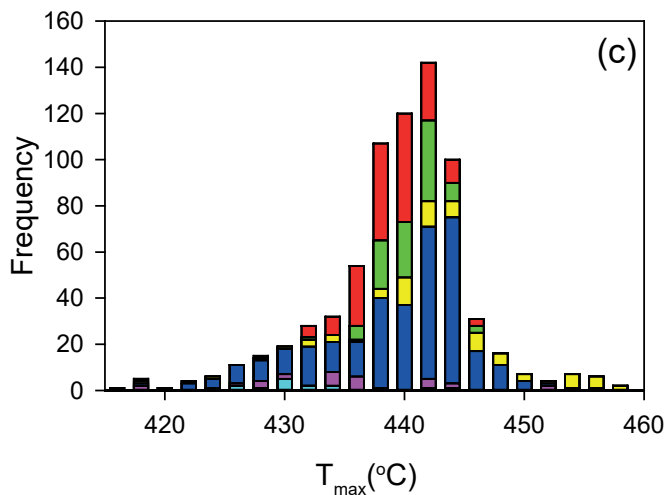
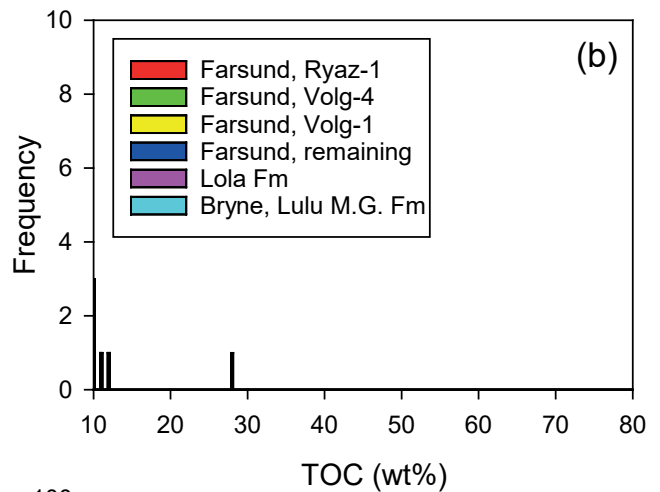
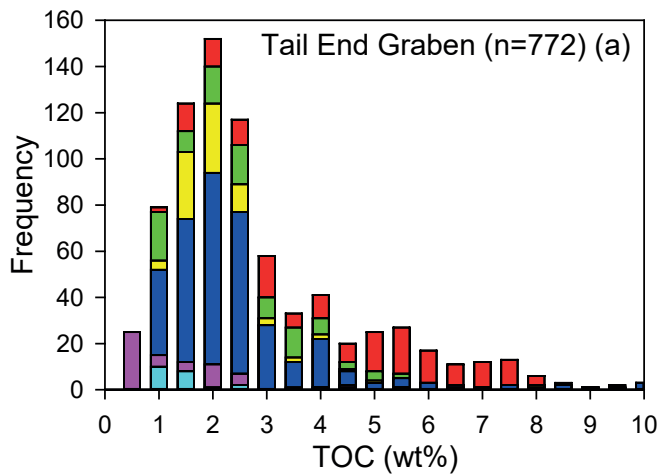
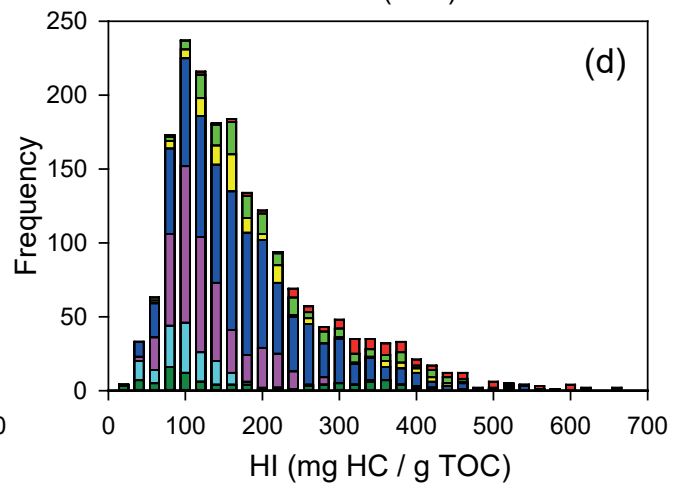
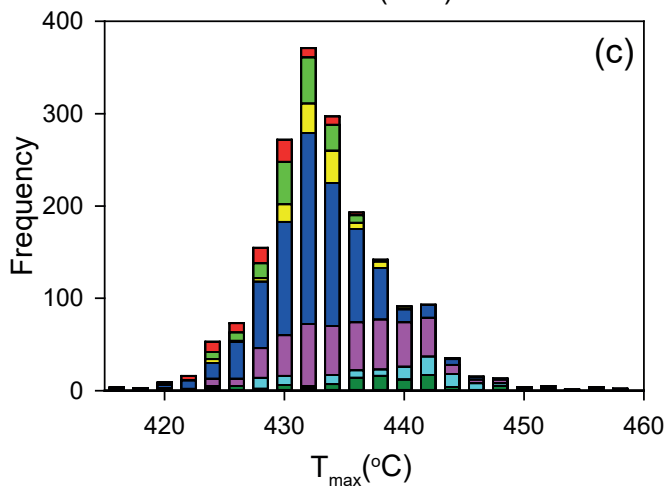
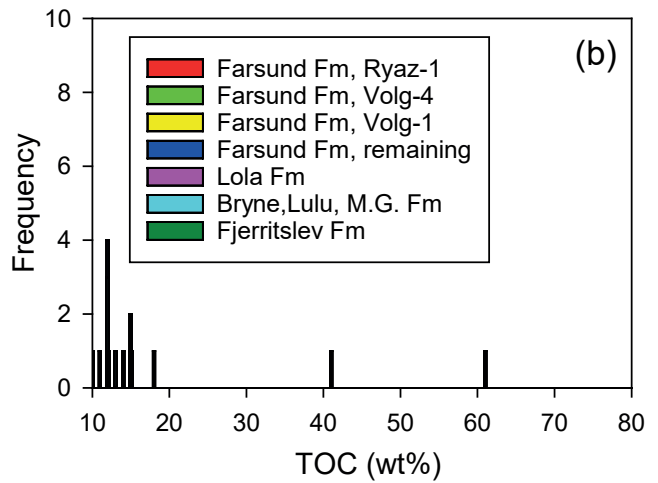
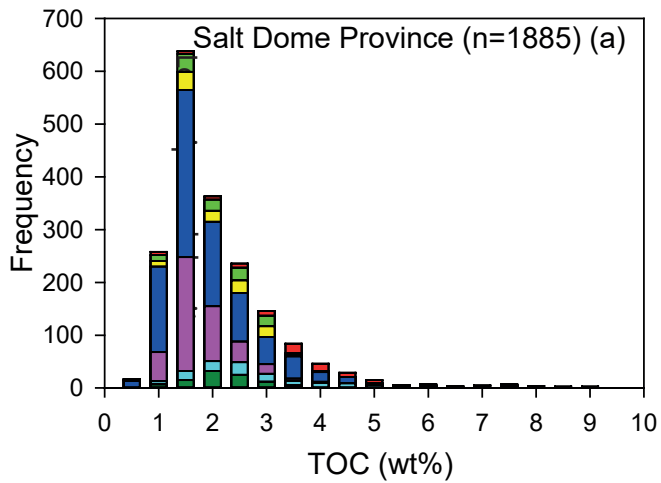


Figure 7. Schovsbo et al.

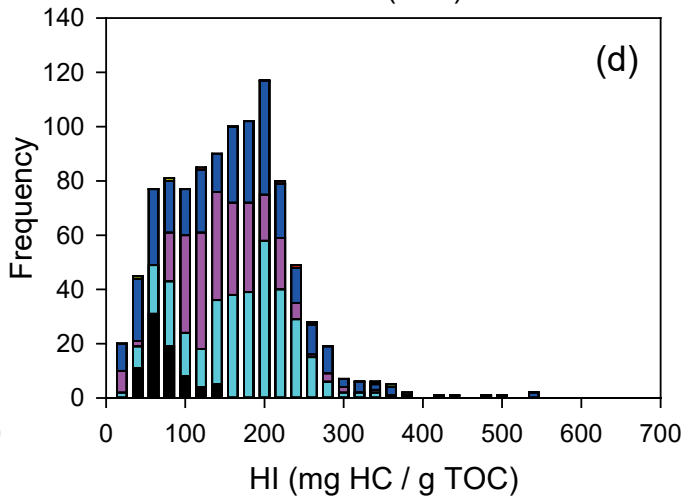
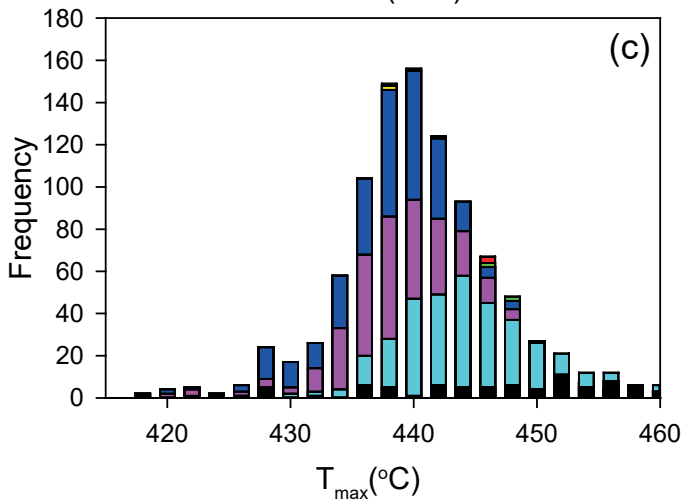
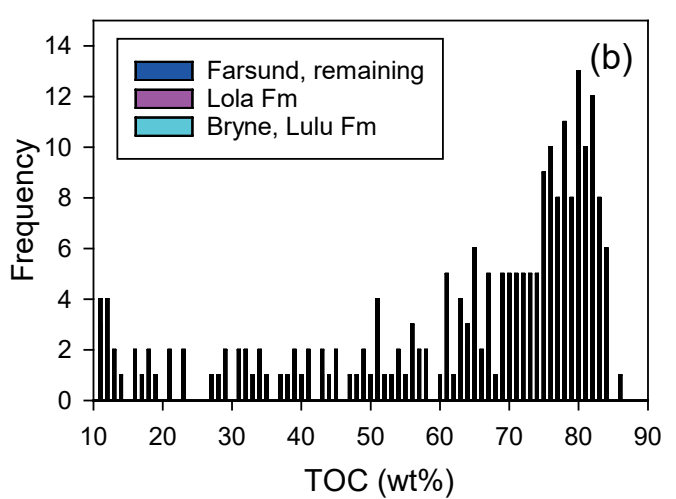
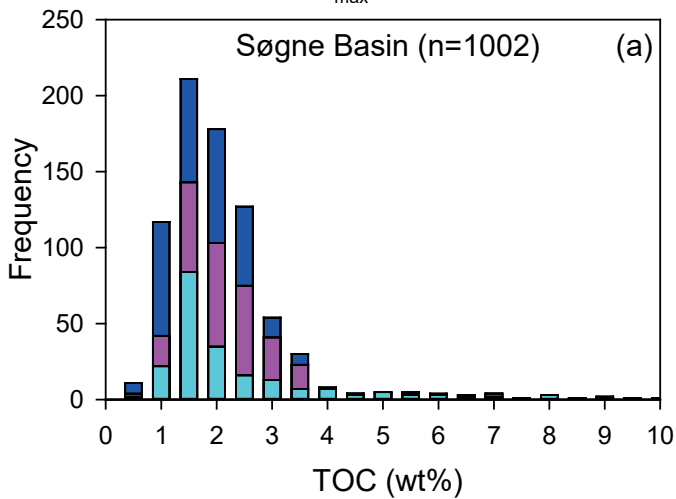
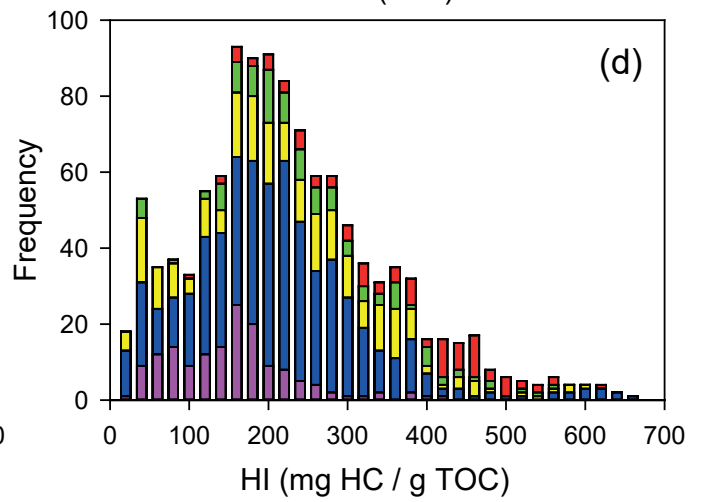
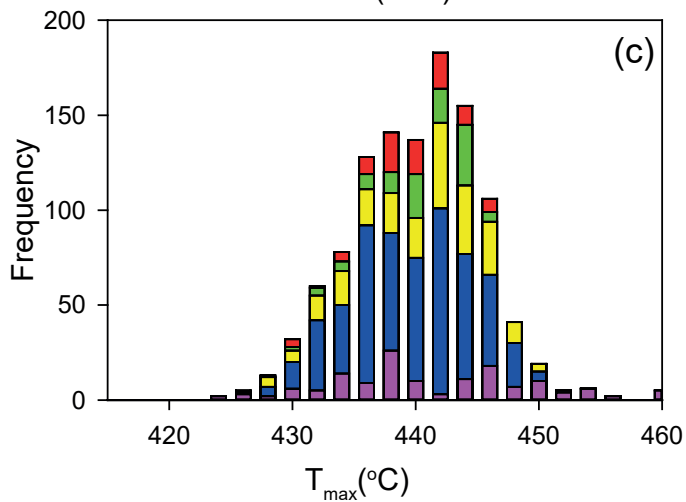
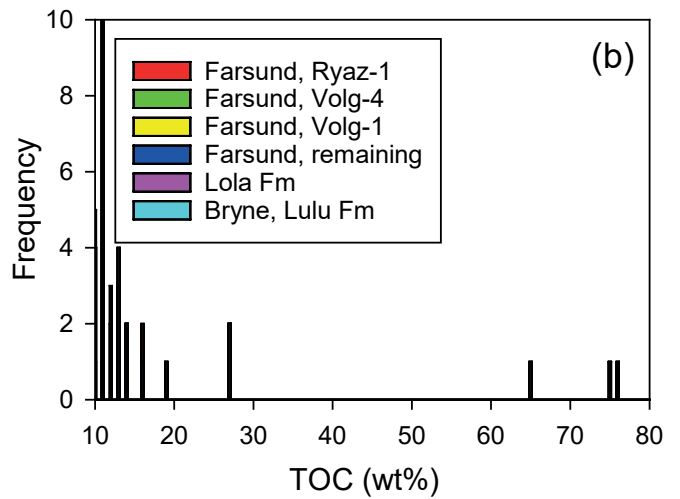
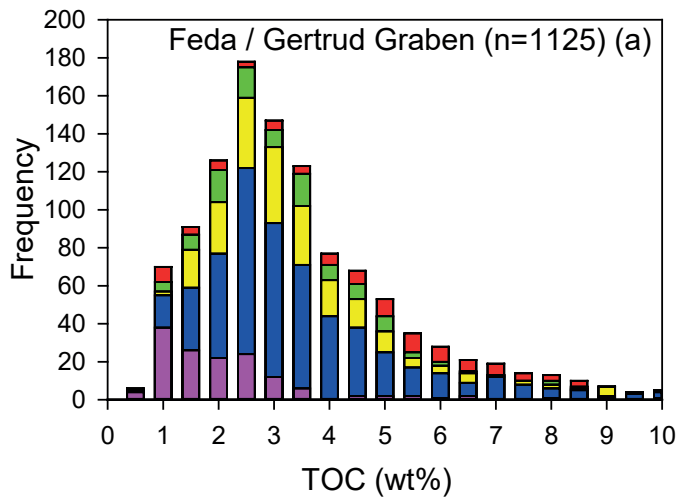


Figure 8. Schovsbo et al.

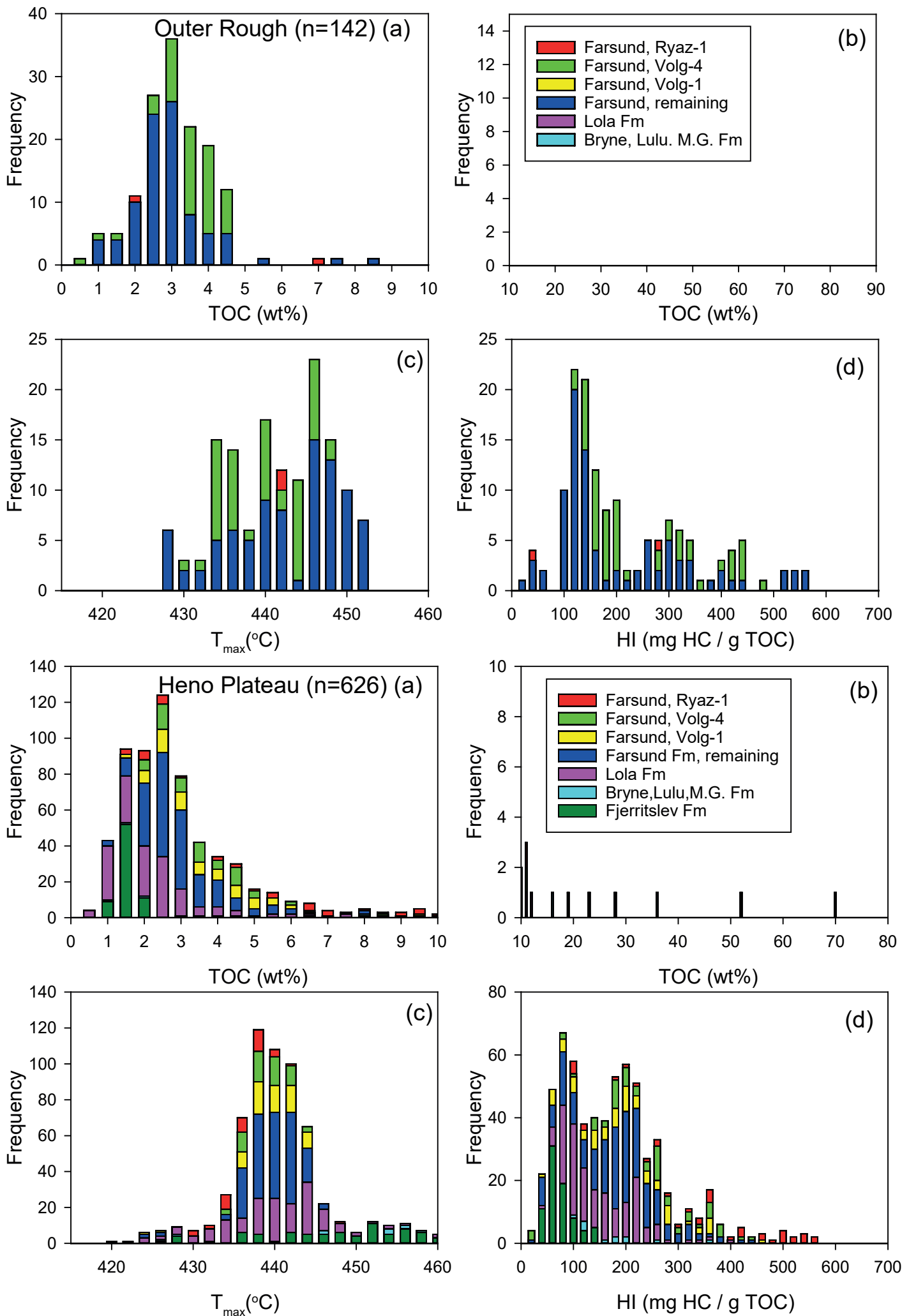


Figure 9. Schovsbo et al.

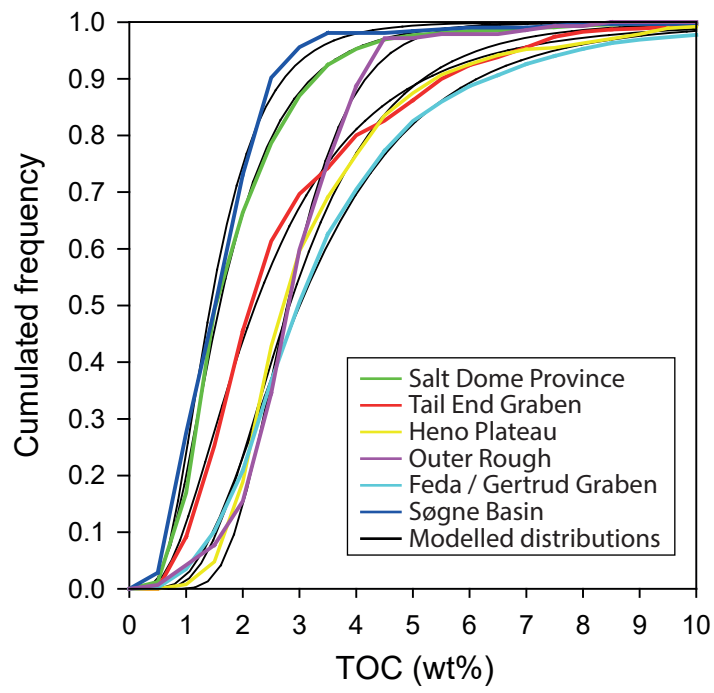


Figure 10. Schovsbo et al.

Figure 10. Schovsbo et al.

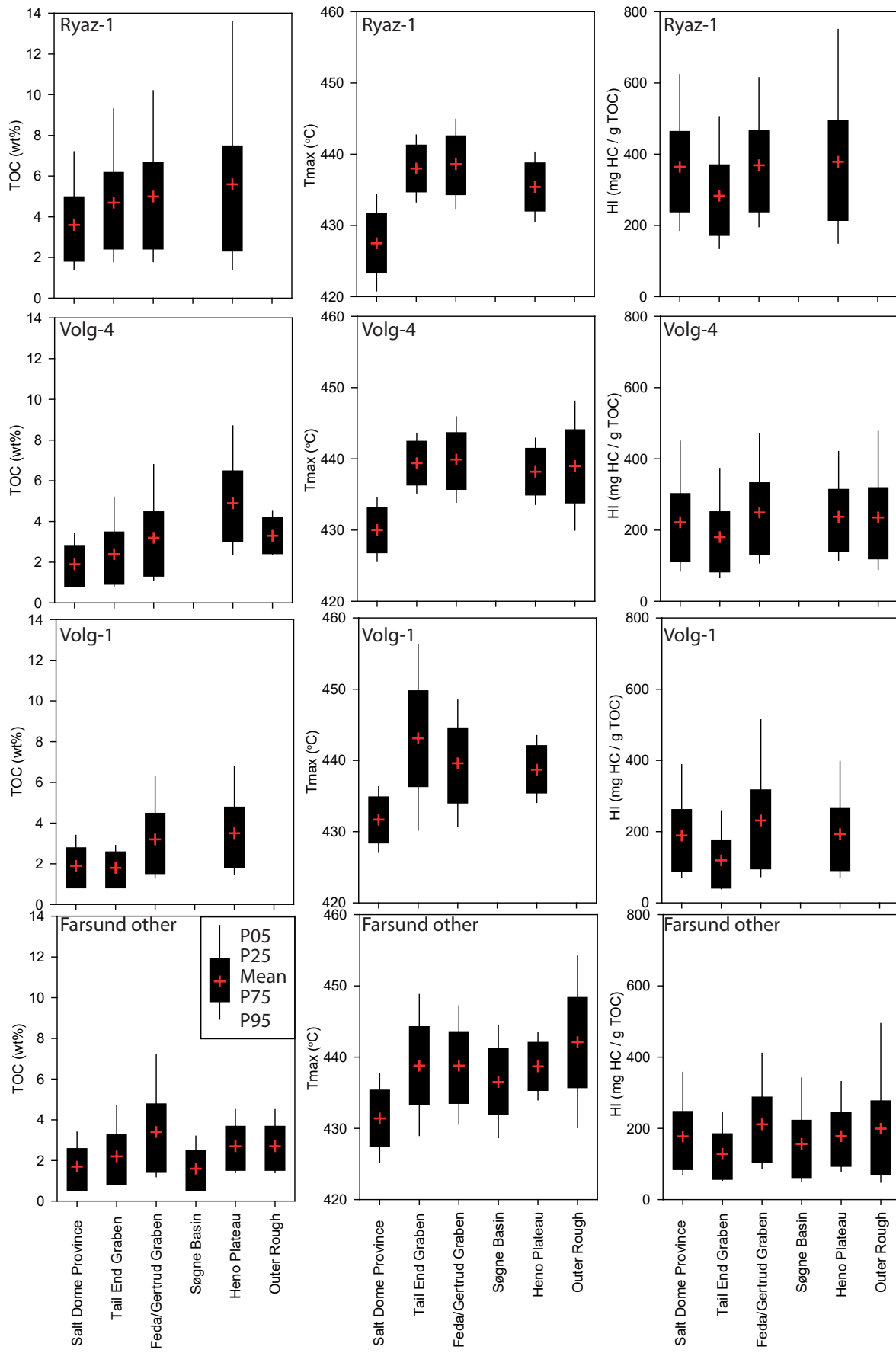


Figure 11. Schovsbo et al.

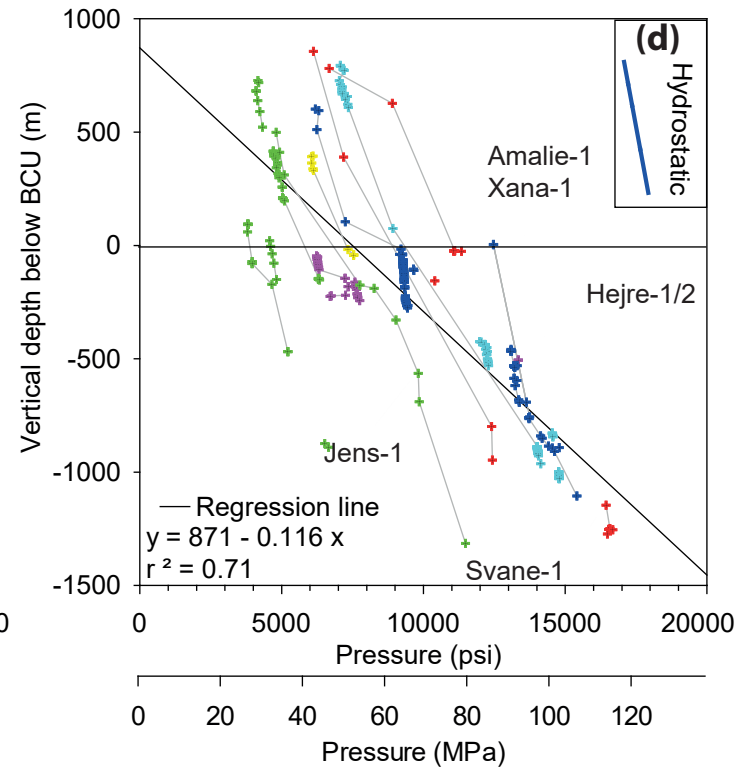
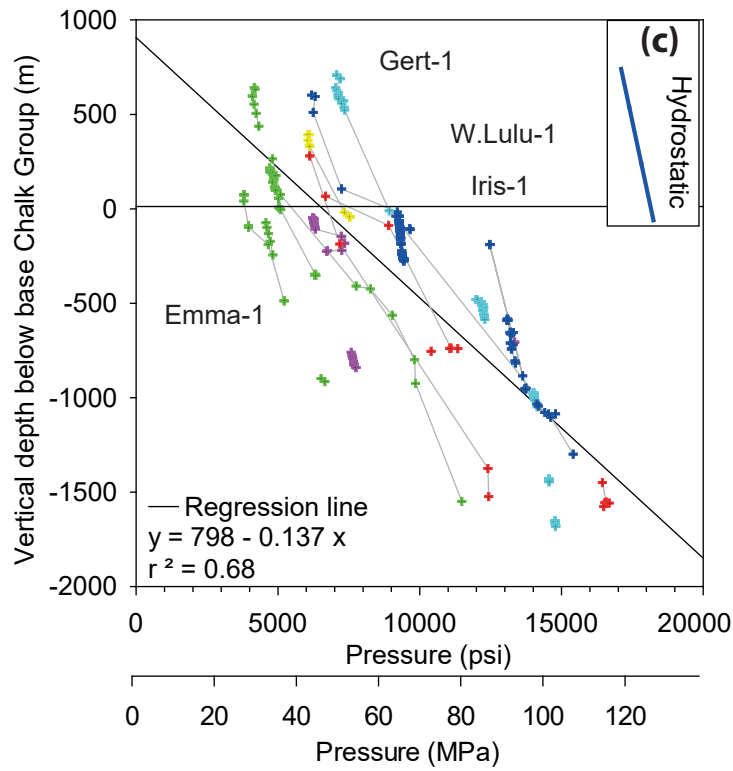
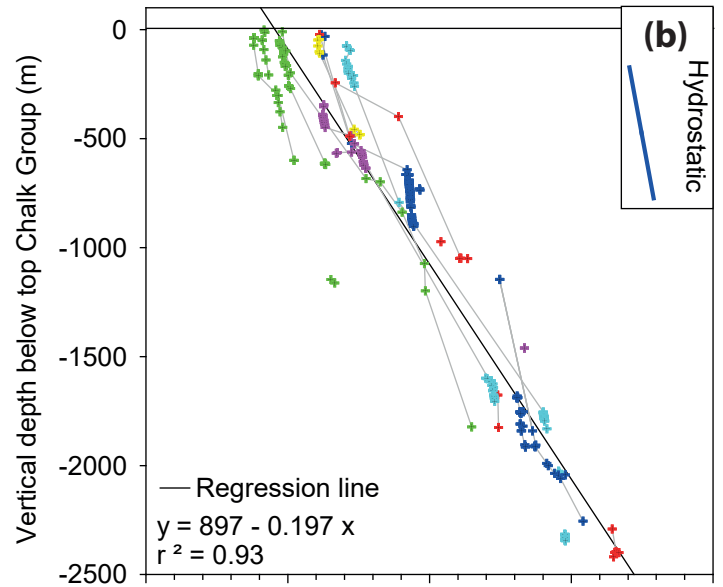
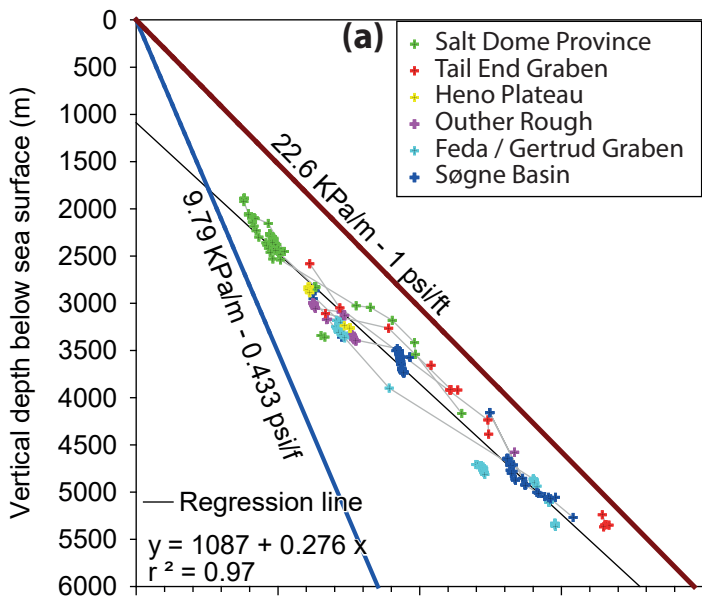


Figure 12. Schovsbo et al.

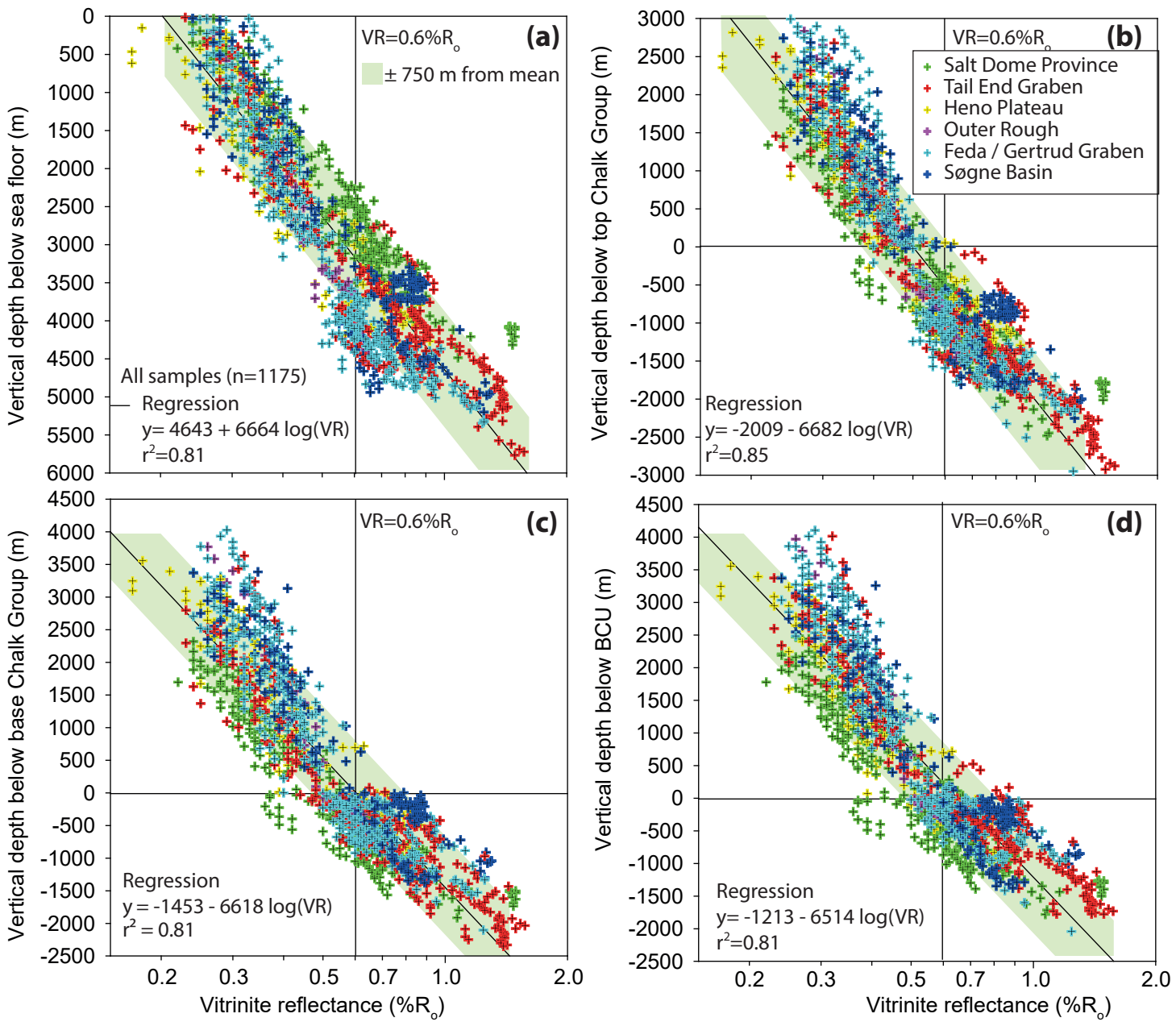


Figure 13. Schovsbo et al.

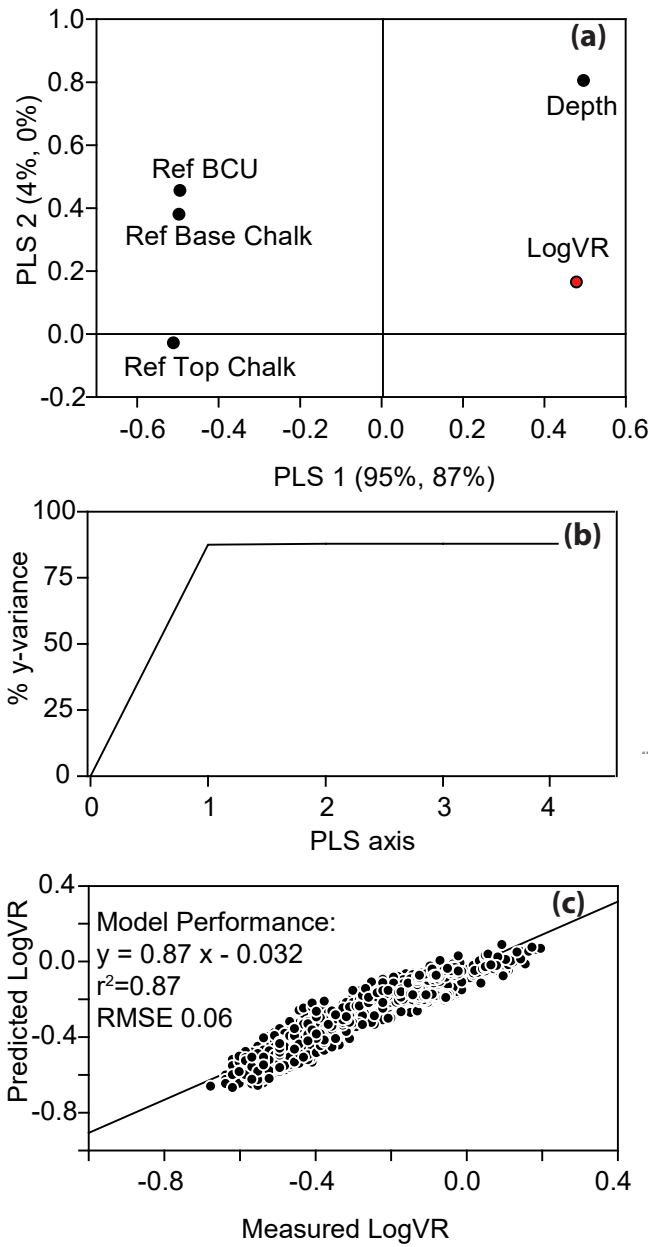


Figure 14. Schovsbo et al.

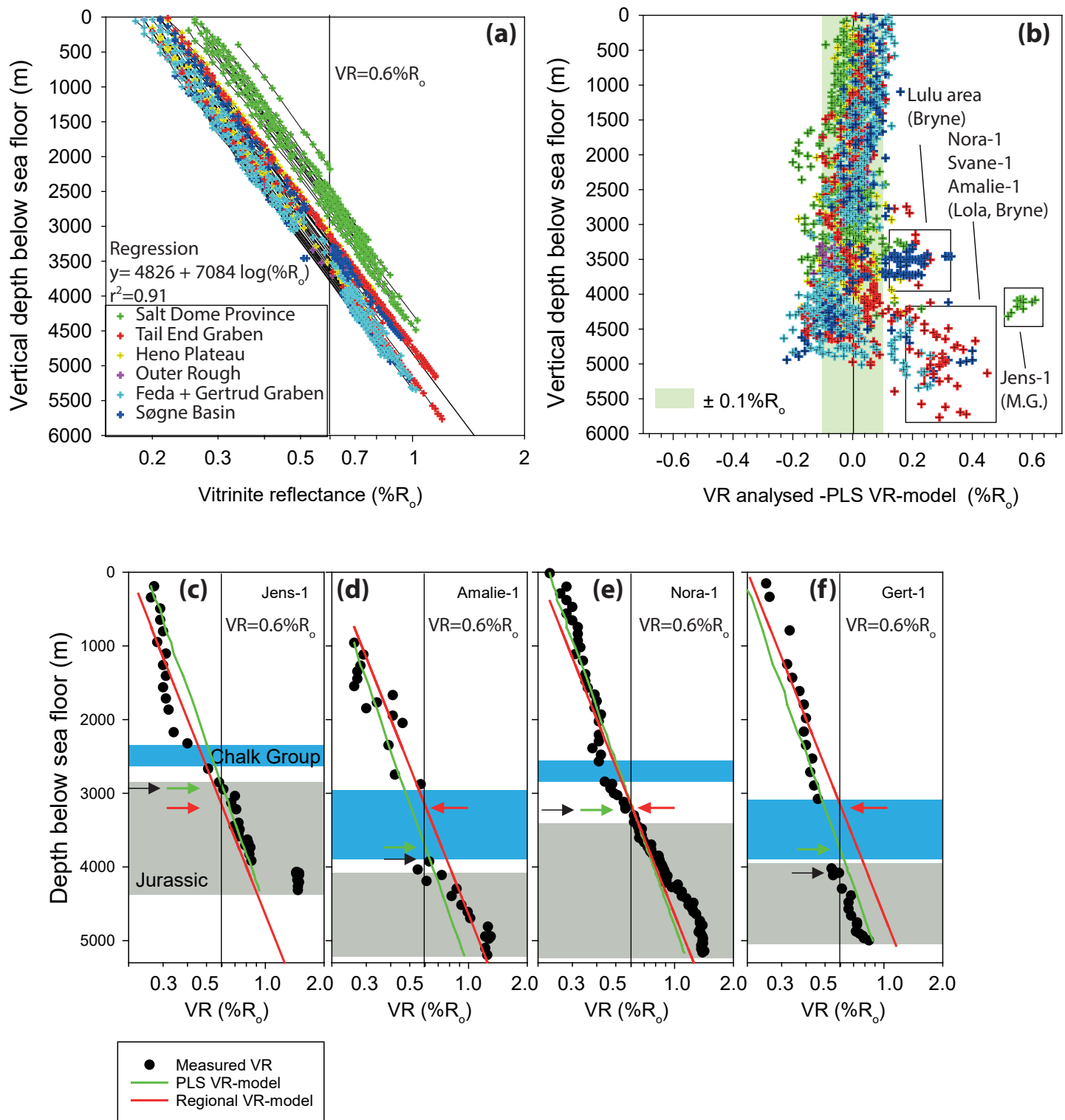


Figure 15. Schovsbo et al.

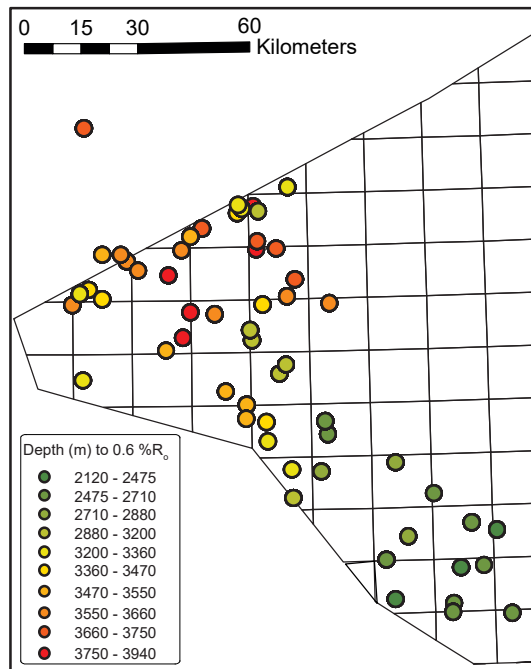


Figure 16. Schovsbo et al.

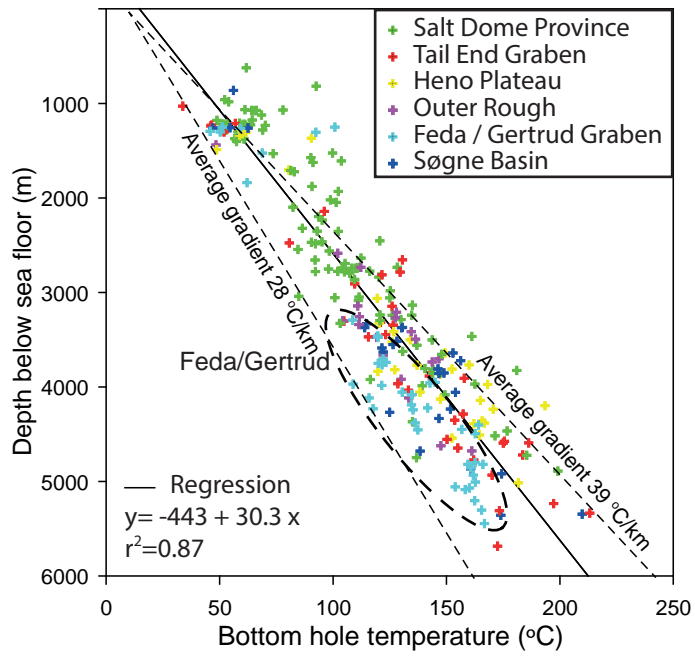
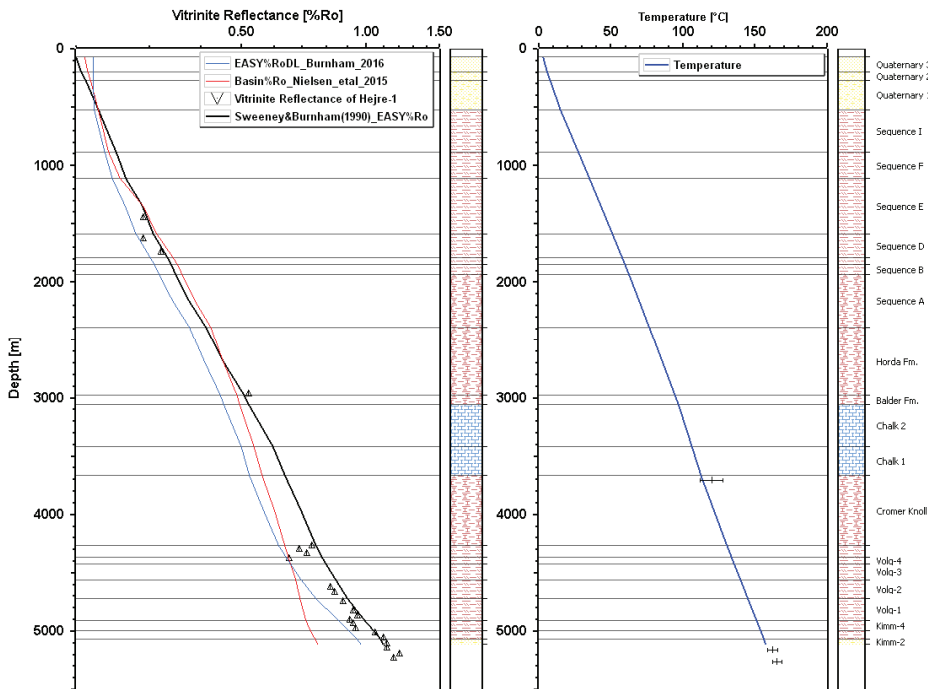


Figure 17. Schovsbo et al.

## Heire-1



## Gert-1

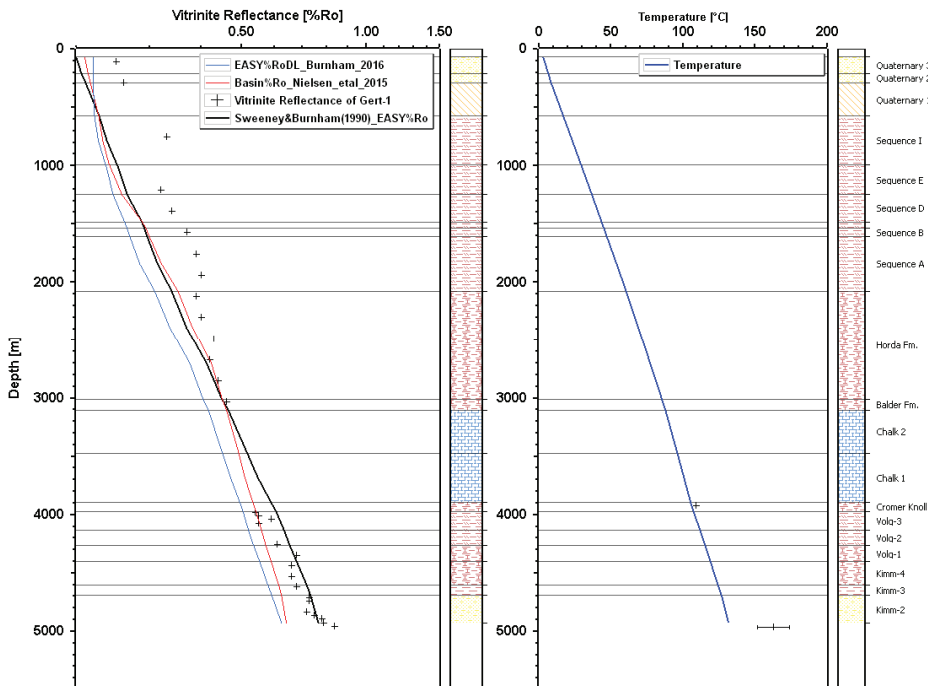
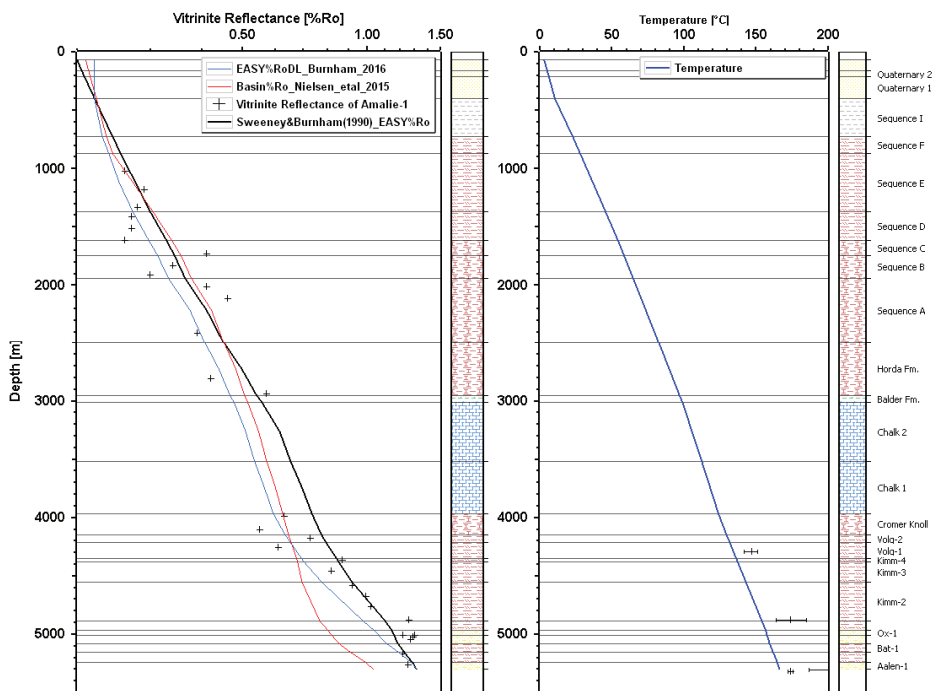


Fig. 18 - Schovsbo et al.,

### Amalie-1



### Nora-1

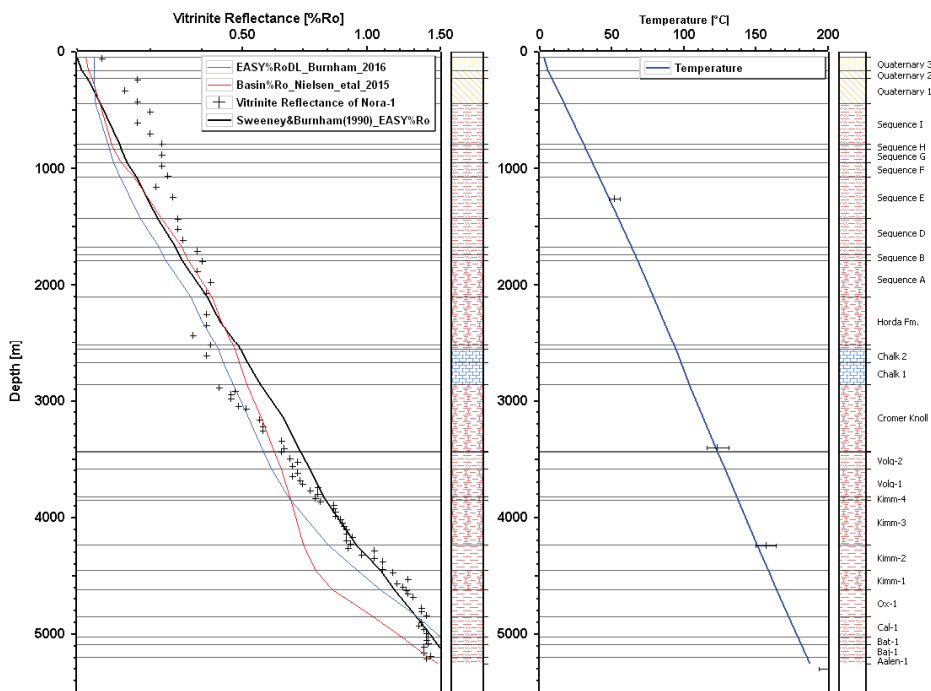


Fig. 18 - Schovsbo et al.,

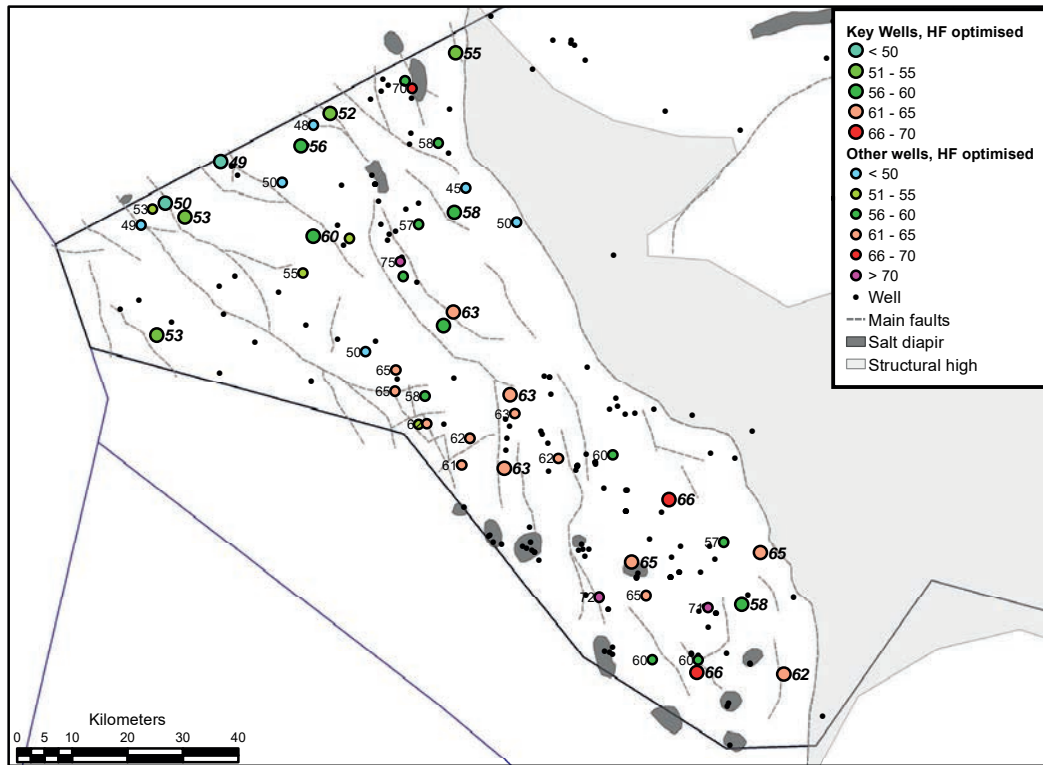


Figure 19. Schovsbo et al.

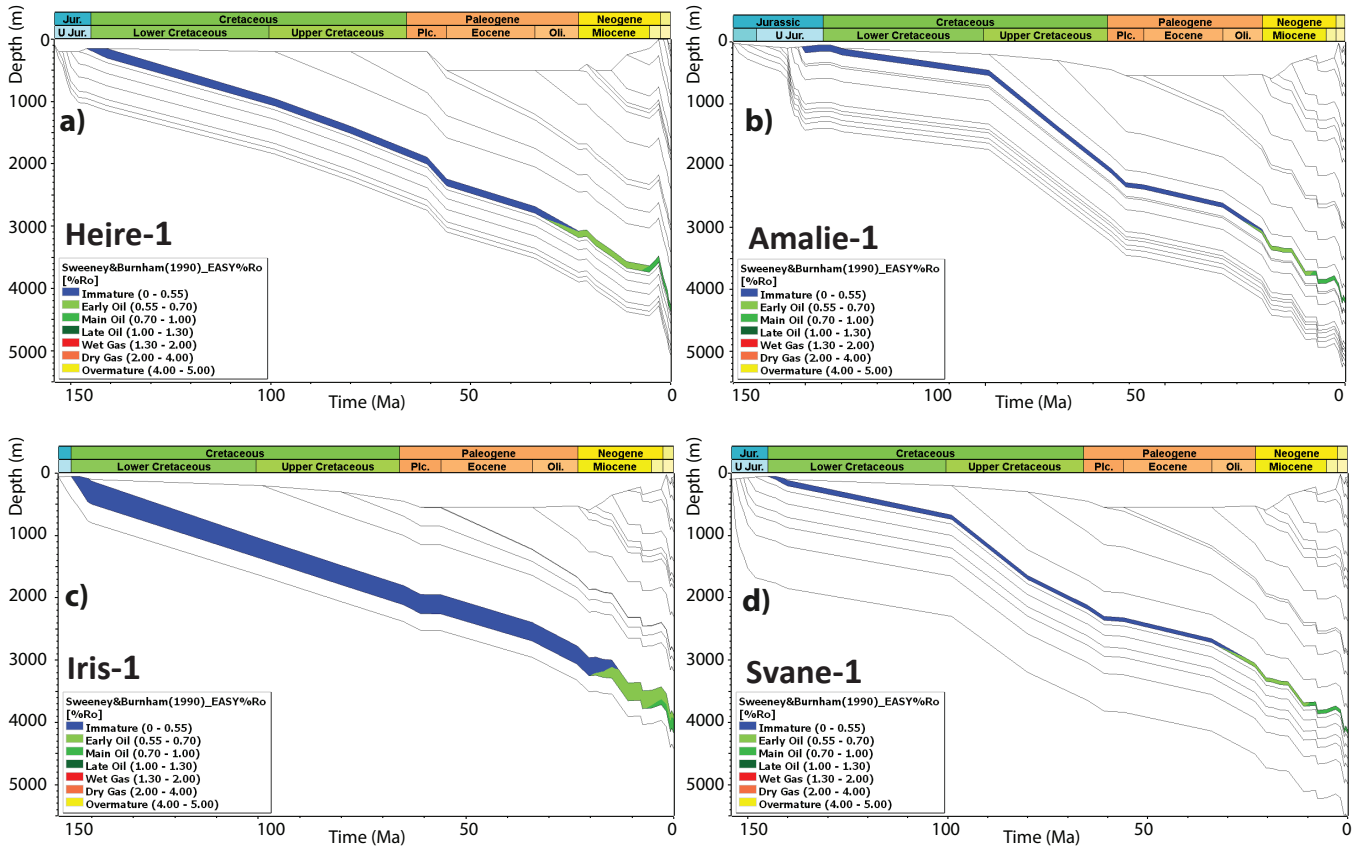


Figure 20. Schovsbo et al.

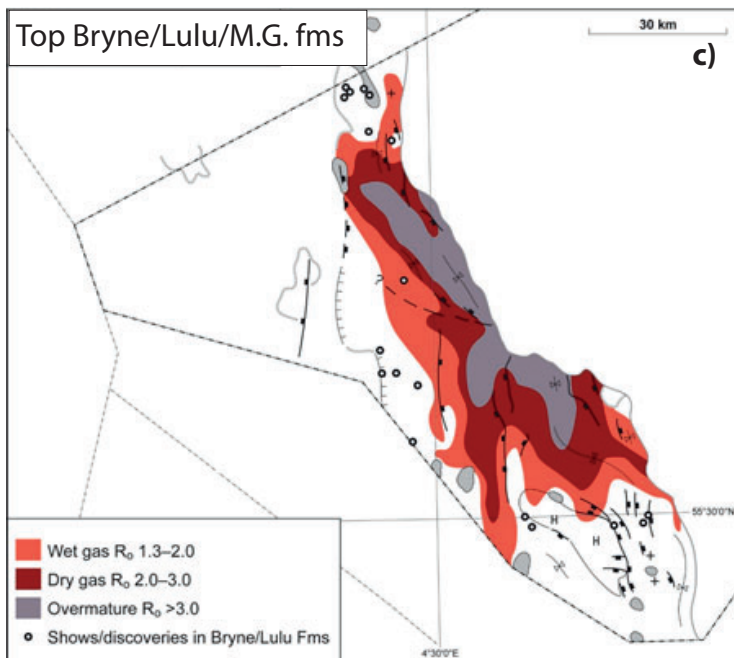
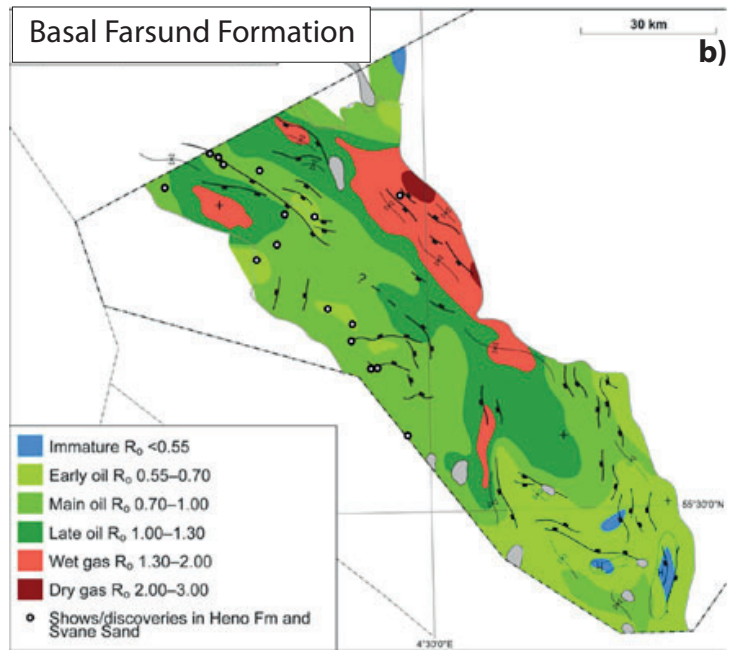
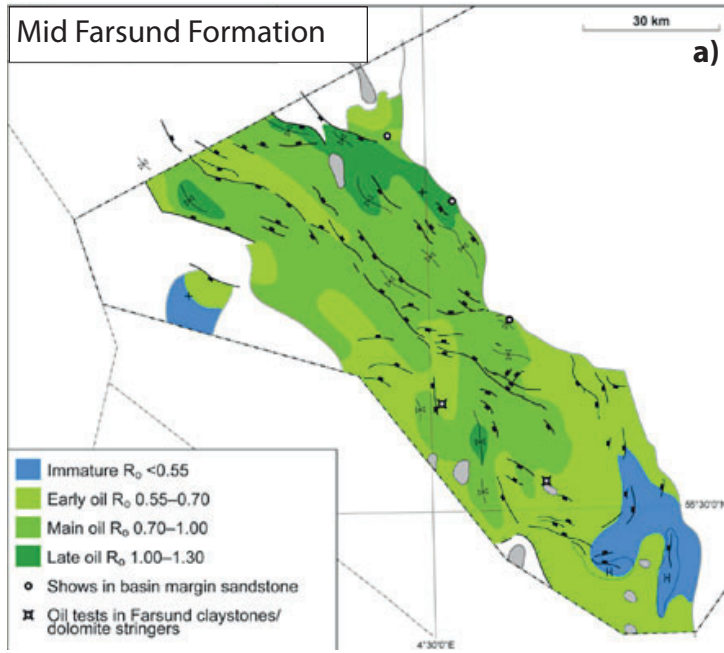


Figure 21. Schovsbo et al.

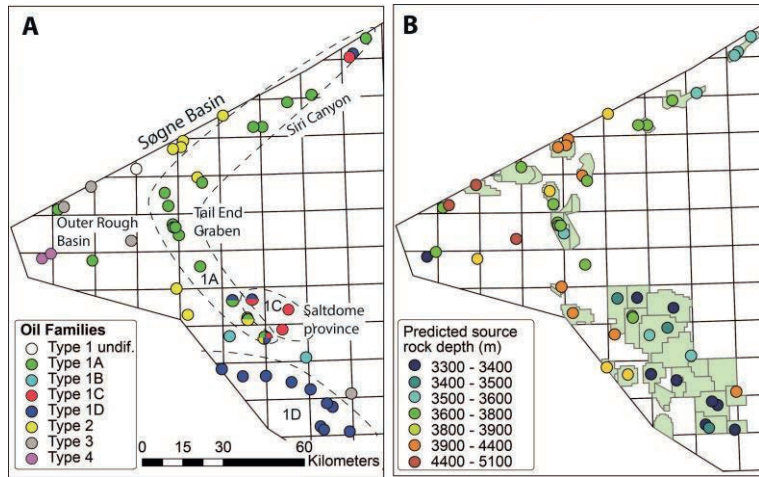


Figure 22. Schovsbo et al.

Table 1.

<b>Salt Dome Province</b>	<b>Outer Rough</b>	<b>Søgne Basin</b>
A-2X	<b>KIM-1</b>	<b>AMALIE-1</b>
ADDA-1	LILJE-1	<b>CLEO-1</b>
<b>ALMA-1X</b>	LIVA-1	<b>GITA-1X</b>
ALMA-2X	ROBIN-1	<b>LULITA-1X</b>
<b>ANNE-3</b>	SAXO-1	<b>LULU-1</b>
<b>BO-1X</b>	<b>TORDENSKJOLD-1</b>	LULU-2
BOJE-1	WESSEL-1	<b>WEST LULU-1</b>
DEEP-ADDA-1		<b>WEST LULU-2</b>
<b>E-1X</b>	<b>Tail End Graben</b>	<b>WEST LULU-3</b>
EMMA-1	<b>BARON-2</b>	<b>XANA-1X</b>
<b>FASAN-1</b>	<b>ELIN-1</b>	
<b>G-1X</b>	<b>GULNARE-1</b>	<b>Feda/Gertrud Graben</b>
<b>JENS-1</b>	I-1X	<b>BERTEL-1</b>
<b>JOHN-FLANKE-1</b>	IRIS-1	<b>DIAMANT-1</b>
<b>M-8X</b>	<b>NORA-1</b>	<b>GERT-1</b>
N-22	<b>STORK-1</b>	<b>GERT-2</b>
<b>NORTH-JENS-1</b>	<b>SVANE-1</b>	<b>GERT-4</b>
NW ADDA-1X	TABITA-1	GWEN-2
<b>O-1X</b>		<b>HEJRE-1</b>
<b>OLGA-1X</b>	<b>Heno Plateau</b>	HEJRE-2
<b>S.E. IGOR-1</b>	<b>EDNA-1</b>	ISAK-1
<b>SKJOLD FLANK-1</b>	EG-1	<b>JEPPE-1</b>
<b>U-1X</b>	ELLY-1	JETTE-1
UGLE-1	<b>ELLY-2</b>	<b>KARL-1</b>
	ELLY-3	<b>LONE-1</b>
	<b>FALK-1</b>	<b>MONA-1</b>
	<b>RAVN-1</b>	<b>OPHELIA-1</b>
	<b>RAVN-2</b>	Q-1X
	<b>SKARV-1</b>	<b>RITA-1X</b>
	<b>W-1X</b>	<b>STEN-1</b>

Table 2

Area	Formation / sequence	TOC (wt.%)			HI (mg HC/g TOC)			T <sub>max</sub> (°C)		
		Mean	$\sigma$	r <sup>2</sup>	Mean	$\sigma$	r <sup>2</sup>	Mean	$\sigma$	r <sup>2</sup>
<b>Salt Dome Province</b>										
	Farsund Formation	0.46	0.55	0.999	5.43	0.16	1.000	6.07	0.0087	1.000
	Ryaz-1	1.17	0.49	0.997	5.83	0.37	0.998	6.06	0.0097	0.996
	Volg-4	0.55	0.41	0.998	5.27	0.51	0.999	6.06	0.0063	1.000
	Volg-1	0.55	0.41	0.998	5.11	0.52	0.995	6.07	0.0065	0.999
	Farsund other*	0.38	0.51	0.999	5.06	0.50	0.998	6.07	0.0088	1.000
	Lola Formation	0.33	0.32	0.996	4.87	0.36	0.999	6.07	0.0126	1.000
	Bryne/Lulu/M.G. fms	0.95	0.68	0.998	4.47	0.38	0.999	6.08	0.0196	0.997
	Fjerritslev Formation	0.67	0.37	0.998	not defined			6.08	0.0146	0.998
<b>Tail End Graben</b>										
	Farsund Formation	0.80	0.67	0.999	4.95	0.62	0.998	6.08	0.0113	0.998
	Ryaz-1	1.41	0.50	0.993	5.57	0.40	0.993	6.08	0.0065	1.000
	Volg-4	0.70	0.57	0.997	5.06	0.53	0.998	6.09	0.0058	0.999
	Volg-1	0.50	0.35	0.999	4.62	0.57	0.999	6.09	0.0179	0.998
	Farsund other*	0.65	0.54	0.999	4.75	0.46	1.000	6.08	0.0137	0.995
	Lola Formation	-0.41	1.11	0.989	4.52	0.50	0.983	6.07	0.0188	0.996
	Bryne/Lulu/M.G. fms	0.15	0.65	0.992	3.84	0.58	0.994	not defined		
<b>Feda and Gertrud Grabens</b>										
	Farsund Formation	1.10	0.56	0.999	5.33	0.52	0.998	6.08	0.0112	1.000
	Ryaz-1	1.47	0.52	0.991	5.85	0.35	0.989	6.08	0.0087	1.000
	Volg-4	1.03	0.54	0.999	5.42	0.45	0.999	6.09	0.0083	0.999
	Volg-1	1.05	0.48	1.000	5.27	0.59	0.990	6.09	0.0122	0.999
	Farsund other*	1.08	0.55	0.999	5.24	0.47	0.996	6.08	0.0115	1.000
	Lola Formation	0.44	0.71	0.998	5.02	0.45	0.997	6.09	0.0176	0.998
<b>Søgne Basin</b>										
	Farsund Fm	0.36	0.50	0.999	4.91	0.60	0.994	6.08	0.0114	0.998
	Farsund other*	0.35	0.49	0.999	4.88	0.58	0.991	6.08	0.0110	0.997
	Lola Fm	0.51	0.42	1.000	4.89	0.41	0.999	6.08	0.0114	0.999
	Bryne/Lulu/M.G. fms (TOC < 20%)	0.81	0.96	0.994	5.07	0.37	0.994	6.10	0.0143	0.998
	Bryne/Lulu/M.G. fms (TOC > 20%)**	69.55	13.89	0.983						
<b>Heno Plateau</b>										
	Farsund Formation	1.04	0.47	0.999	5.20	0.52	0.997	6.08	0.0070	1.000
	Ryaz-1	1.48	0.69	0.987	5.82	0.49	0.975	6.08	0.0069	1.000
	Volg-4	1.52	0.39	0.999	5.39	0.39	0.996	6.08	0.0065	0.998
	Volg-1	1.16	0.46	0.999	5.13	0.52	0.996	6.08	0.0065	1.000
	Farsund other*	0.92	0.35	0.999	5.09	0.43	0.994	6.08	0.0066	1.000
	Lola Formation	0.55	0.61	0.998	4.99	0.44	0.998	6.08	0.0138	0.998
	Fjerritslev Formation	0.25	0.22	0.996	4.08	0.40	1.000	6.10	0.0207	0.999
<b>Outer Rough</b>										
	Farsund Formation	1.02	0.32	0.999	5.16	0.63	0.996	6.09	0.0155	0.999
	Volg-4	1.19	0.19	0.998	5.33	0.51	0.991	6.08	0.0126	0.997
	Farsund other*	0.92	0.35	0.999	5.05	0.70	0.992	6.09	0.0166	0.997

\*Excluding Volg-1; -4; Ryaz-1; \*\* Normal distribution. M.G.: Middle Graben Formation

Table 3

Area	Formation / sequence	TOC (wt.%)				HI (mg HC/g TOC)				T <sub>max</sub> (°C)			
		Mean	P90	P50	P10	Mean	P90	P50	P10	Mean	P90	P50	P10
<b>Salt Dome Province</b>													
	Farsund Formation	1.8	0.8	1.6	3.2	231	186	228	280	431	426	431	436
	Ryaz-1	3.6	1.7	3.2	6.0	364	213	341	546	428	422	428	433
	Volg-4	1.9	1.0	1.7	2.9	222	102	195	374	430	427	430	433
	Volg-1	1.9	1.0	1.7	2.9	189	85	165	322	432	428	432	435
	Farsund other*	1.7	0.8	1.5	2.8	178	83	157	298	431	427	431	436
	Lola Formation	1.5	0.9	1.4	2.1	138	82	130	205	434	427	434	441
	Bryne/Lulu/M.G. fms	3.3	1.1	2.6	6.2	94	54	88	142	439	428	439	450
	Fjerritslev Formation	2.1	1.2	2.0	3.2	Bimodal distribution				436	428	436	444
<b>Tail End Graben</b>													
	Farsund Formation	2.8	0.9	2.2	5.2	171	63	141	313	439	433	439	445
	Ryaz-1	4.7	2.2	4.1	7.8	283	156	261	437	438	434	438	442
	Volg-4	2.4	1.0	2.0	4.2	180	80	157	308	439	436	439	443
	Volg-1	1.8	1.1	1.7	2.6	119	49	102	211	443	433	443	453
	Farsund other*	2.2	1.0	1.9	3.8	128	64	115	208	439	431	439	447
	Lola Formation	1.2	0.2	0.7	2.7	104	48	92	175	434	424	434	445
	Bryne/Lulu/M.G. fms	1.4	0.5	1.2	2.7	55	22	47	98	not defined			
<b>Feda and Gertrud Grabens</b>													
	Farsund Formation	3.5	1.5	3.0	6.1	238	106	207	405	439	433	439	445
	Ryaz-1	5.0	2.2	4.3	8.5	369	223	347	542	439	434	439	444
	Volg-4	3.2	1.4	2.8	5.6	249	127	226	401	440	435	440	445
	Volg-1	3.2	1.5	2.9	5.3	232	91	194	415	440	433	440	446
	Farsund other*	3.4	1.5	3.0	5.9	212	104	189	346	439	432	439	445
	Lola Formation	2.0	0.6	1.5	3.8	168	85	152	270	440	430	440	450
<b>Søgne Basin</b>													
	Farsund Fm	1.6	0.8	1.4	2.7	161	63	135	290	437	430	437	443
	Farsund other*	1.6	0.8	1.4	2.7	156	63	132	277	437	430	437	443
	Lola Fm	1.8	1.0	1.7	2.9	144	78	133	225	438	431	438	444
	Bryne/Lulu/M.G. fms (TOC < 20%)	3.5	0.7	2.2	7.6	171	99	160	256	444	436	444	452
	Bryne/Lulu/M.G. fms (TOC > 20%)	69.6	51.7	69.6	87.4								
<b>Heno Plateau</b>													
	Farsund Formation	3.2	1.5	2.8	5.2	207	94	181	351	438	434	438	442
	Ryaz-1	5.6	1.8	4.4	10.6	379	180	336	628	435	432	435	439
	Volg-4	4.9	2.8	4.6	7.6	238	133	220	364	438	435	438	442
	Volg-1	3.5	1.8	3.2	5.8	193	86	168	329	439	435	439	442
	Farsund other*	2.7	1.6	2.5	3.9	178	93	162	283	439	435	439	442
	Lola Formation	2.1	0.8	1.7	3.8	161	84	146	256	439	431	439	447
	Fjerritslev Formation	1.3	1.0	1.3	1.7	64	35	59	98	447	435	447	459
<b>Outer Rough</b>													
	Farsund Formation	2.9	1.9	2.8	4.2	213	77	174	393	441	432	441	450
	Volg-4	3.3	2.6	3.3	4.2	235	108	207	397	439	432	439	446
	Farsund other*	2.7	1.6	2.5	3.9	199	63	155	383	442	433	442	451

\*Excluding Volg-1; -4; Ryaz-1. M.G.: Middle Graben Formation. P10 indicate the value that 10% of the population will exceed; P50 indicate the median of the population; P90 indicate the value that 90% of the population will exceed.

Table 4

<b>Salt Dome Province</b>	<b>Feda/Gertrud Graben</b>
EMMA-1	BERTLE-1
JENS-1	GERT-1
NW ADDA-1X	HEJRE-1
SKJOLD FLANKE-1	HEJRE-2
U-1X	
UGLE-1	<b>Tail End Graben</b>
	ELIN-1
<b>Heno Plateau</b>	IRIS-1
ELLY-1	NORA-1
	SVANE-1
<b>Søge Basin</b>	
AMALIE-1	<b>Outer Rough</b>
WEST LULU-1	KIM-1
XANA-1X	ROBIN-1
	SAXO-1
	WESSEL-1

Table 5

<b>Salt Dome Province</b>	<b>Salt Dome Province</b>	<b>Søgne Basin</b>
A-2X	SKJOLD FLANK-1	AMALIE-1
ADDA-1	TOVE-1	CLEO-1
ADDA-2	U-1X	LULITA-1X
ALMA-1X	UGLE-1	LULU-1
ALMA-2X	V-1X	LULU-2
ANNE-3	VAGN-2	WEST LULU-1
BO-1		WEST LULU-2
BOJE-1	<b>Feda/Gertrud Graben</b>	WEST LULU-3
DEEP-ADDA-1	BERTEL-1A	WEST LULU-4
E-1X	DIAMANT-1	
EAST-ROSA-1	GERT-1	<b>Tail End Graben</b>
EAST-ROSA-2	GERT-2	BARON-2
EAST-ROSA-3	GERT-3	ELIN-1
EAST-ROSA-FLANK-1	GWEN-2	GULNARE-1
ELNA-1	HEJRE-1	I-1X
EMMA-1	HEJRE-2	IRIS-1
FASAN-1	JEPPE-1	NORA-1
G-1X	JETTE-1	OTTO-1
JENS-1	KARL-1	STORK-1
JOHN-1	LONE-1	SVANE-1A
JOHN-FLANKE-1	MONA-1	T-1X
M-1X	OPHELIA-1	T-3X
M-8X	STEN-1	TABITA-1
MIDDLE-ROSA-1	RITA-1X	
MIDDLE-ROSA-2		<b>Outer Rough</b>
N-22	<b>Heno Pleateau</b>	ISAK-1
NORTH-JENS-1	EDNA-1	KIM-1
NW ADDA-1X	EG-1	LILJE-1
OLGA-1X	ELLY-1	LIVA-1
PER-1	ELLY-2	P-1X
Q-1X	ELLY-3	ROBIN-1
RUTH-1	FALK-1	SAXO-1
S.E. ADDA-1X	RAVN-1	TORDENSKJOLD-1
S.E. IGOR-1	RAVN-2	WESSEL-1
SINE-1XP	SKARV-1	
	W-1X	